THE EFFECT OF EXTRUSION PROCESSING

UPON THE PROPERTIES OF 8090

ALUMINIUM ALLOYS

by

James N. Waring

A thesis submitted for the degree of
Doctor of Philosophy in the University of London
and Diploma of Imperial College

April 1996



John Percy Group, Department of Materials,
Imperial College of Science, Technology and Medicine,
London, SW7 2BP.

BIBL.
LONDIN.
UNIV.

ABSTRACT

Wrought aluminium-lithium alloys possess high specific property values, making them highly desirable for aerospace applications. The production of components from these alloys by extrusion methods does, however, produce several problems.

The inherent nature of the extrusion process is to produce highly elongated deformed grains. This factor combined with the stress concentration characteristics of the aluminium lithium alloys - coplanar slip, P.F.Z's and grain boundary precipitates- causes these alloys to exhibit relatively poor transverse tensile properties and low longitudinal toughness values, particularly in thin sections.

This project set out to initiate work on a series of investigations concerned with the effect of processing modifications upon property values. The ultimate aim of the investigation sequence was to analyse the effects of conically shaped dies upon the production of thin section bar extrudates. The two main areas of investigation carried out in this project towards this end were as follows:-

(i) Characterisation of the microstructure and properties associated with rectangular cross section 'slab' extrusions produced from shear face dies. From examination of these extrudates correlations between microstructure, property values and processing conditions for relatively thin section extrusions were established.

Process conditions of extrusion/aspect ratio, extrusion temperature and ageing treatment were varied with tensile properties of yield stress, U.T.S, and % elongation to failure, together with fracture toughness being measured. The main microstructural changes considered were changes in % recrystallisation, grain/subgrain size and texture, and in order that the microstructural/processing correlation occurring independent of compositional fluctuations could be established, two different 8090 alloy batches were extruded.

Analysis of a method that could successfully be used for the toughness measurement of thin extrudate sections was also carried out.

(ii) Utilisation of axi-symmetric extrusions in order to investigate the effects of conically shaped dies upon the deformation field, hence property values of extruded products. Process conditions of extrusion temperature, die cone angle and ageing treatment were varied, and as with the 'slab' extrudates, yield stress, U.T.S. and fracture toughness measurements were made. Microstructural evaluations of % recrystallisation, grain/subgrain sizes and texture were also made, hence correlations between processing conditions, property values and microstructure were obtained.

An investigation into the use of visioplasticity and finite element techniques, in order to analyse the deformation process were also carried out.

LIST OF CONTENTS

	Page
Abstract.	2
List of Figures.	7
Chapter One INTRODUCTION	25
Chapter Two LITERATURE SURVEY	
2.1 Physical Metallurgy of Lithium Containing Aluminium Alloys.	28
2.1.1 Binary Systems.	28
- Al-Li Binary System.	28
- Al-Zr Binary System.	29
2.1.2 Ternary Systems.	30
- Al-Li-Cu Ternary System.	30
2.1.3 Al-Li-Cu-Mg Quaternary System.	31
2.1.4 Impurities, As Cast Material and homogenisation.	32
2.2 Mechanical Properties of Lithium Bearing Alloys.	34
2.2.1 Tensile properties.	34
-Factors affecting strength.	35
2.2.2 Fracture Toughness.	38
Coplanar slip, due to δ'.	39
Preferential deformation in P.F.Z's.	40
Precipitation of grain boundary phases.	40
Grain structure and texture.	41
Constituent phases.	42
Dispersoids and tramp elements.	42
2.3 Textural Systems of Wrought Aluminium Lithium Alloys.	44
2.3.1 Texture representation.	44
2.3.2 Wrought aluminium texture systems.	45
Extrusion Textures.	45
Rolling Textures.	46
2.4 Hot Working Process.	48
2.4.1 Analysis of Metal Forming Process.	48
Finite Element Analysis.	48
Upper Bound Analysis.	49
Visioplasticity Analysis.	51
2.4.2 Hot Working.	52
2.4.3 Microstructural Restoration Processes.	54
Chapter Three EXPERIMENTAL PROCEDURE.	
3.1 Extrusion Press and Tooling.	58

3.2 Billet Preparation. 59

3.3 Material Specification. 60

3.4 Heat treatments. 60
3.4.1 Homogenisation
3.4.2 Billet heating
3.4.3 Ageing

3.5 Sample preparation. 62

3.6 Microstructural Investigation. 64
Transmission Electron Microscopy.
Optical Analysis.
Texture Determination.
Microhardness Analysis.

3.7 Fracture Characterisation. 65

3.8 Deformation Analysis. 65

Chapter Four RECTANGULAR CROSS-SECTION, 'SLAB', EXTRUSIONS RESULTS, DISCUSSIONS AND CONCLUSIONS

4.1 Optical Microscopy 68
4.1.1 General Extrudate Structures 68
4.1.2 Variation in Microstructure with solution heat treatment & Ageing 68
4.1.3 Variation in Microstructure with Extrusion Temperature 70
4.1.4 Variation in Microstructure with Extrusion and Aspect Ratios 72
4.1.5 Discussion. 73

4.2 Transmission Electron Microscopy. 85
4.2.1 Microstructural Variation with Processing. 85

4.3 Texture Analysis. 90
4.3.1 Texture Variation with Processing. 90
4.3.2 Texture-Microstructure Correlations. 91
4.3.3 Discussion and Conclusions. 93

4.4 Toughness Analysis. 105
4.4.1 Correlation of Toughness Measurements. 105
4.4.2 Fracture & Toughness Variation with Ageing Condition. 106
4.4.3 Fracture & Toughness Variation with Extrusion Temperature. 110
4.4.4 Fracture & Toughness Variation with Extrusion/Aspect Ratios. 113
4.4.5 General Discussion and Conclusions. 115
Fracture characterisation. 115
Correlation Between Properties and Microstructure. 116
Effect of Extrusion Temperature upon Toughness. 118
Effect of Aspect Ratio and Extrusion Ratio Upon Toughness. 118

Effect of Ageing Condition upon Toughness. 119
4.5 Tensile Properties. 134
4.5.1 Variation in Tensile Properties with Extrusion Temperature. 134
4.5.2 Variation in Tensile Properties with Extrusion/Aspect Ratios. 137
4.5.3 Variation in Tensile Properties with Ageing Condition. 138
4.5.4 Conclusions. 139

Chapter Five AXI-SYMMETRIC, CONICAL DIE EXTRUSIONS RESULTS, DISCUSSIONS AND CONCLUSIONS

5.1 Optical Microscopy. 145
5.1.1 General Extrudate Structures. 145
5.1.2 Variation in Microstructure with Changes in Extrusion Temperature and Die Cone Angle. 145
5.1.3 Discussion and Conclusions. 147

5.2 Transmission Electron Microscopy. 156
5.2.1 Variation in Microstructure with Processing. 156

5.3 Texture Analysis. 160
5.3.1 Texture Variation with Processing. 160
5.3.2 Texture-Microstructure Correlations. 160
5.3.3 Conclusions. 161

5.4 Deformation Flow Analysis. 166
5.4.1 Split Gridded Billet Analysis. 166
5.4.2 Visioplasticity. 168
5.4.4 Finite Element Analysis. 169
Flow Patterns. 170
Extrusion Loads. 170
Temperature Fields. 171
Strain Rate Fields. 172
Temperature Compensated Strain Rate. 174
5.4.5 Discussion and Conclusions. 175

5.5 Toughness Analysis. 196
5.5.1 Fracture Characterisation. 196
5.5.2 Effect of die Cone Angle upon Toughness, Anisotropy. and Centre to Surface Property Variations. 197
5.5.3 Effect of Extrusion Temperature upon Toughness and Anisotropy. 200
5.5.4 Conclusions. 200
Fracture Characterisation. 200
Correlation between Properties, Processing Conditions and Microstructure. 201

5.6 Tensile Properties. 212
5.6.1 Variation in Tensile Properties with Die Cone Angle. 212
5.6.2 Variation in Tensile Properties with Extrusion Temperature. 213
5.6.3 Variation in Tensile Properties with Ageing Condition. 214

5.6.4 Conclusions. 215

Chapter Six CONCLUSIONS AND FURTHER WORK. 219

6.1 Conclusions. 219

6.2 Further Work. 224

Appendix I 226
Toughness measurements. 226
Toughness Parameter. 226
Testing Procedure. 227
Chevron Notch Samples. 228
Toughness Calculation using chevron notch bars. 230

Appendix II 234
Visioplasticity Deformation Analysis. 234
Experimental Determination of Distortion Field. 235

Appendix III 237
Finite Element Analysis. 237
Material Properties During Deformation. 237
Friction Conditions. 238
Thermal Properties of Material. 238
Forge 2 Package. 238

Appendix IV 240
Calculation of Z value. 240

References 242

List of Figures

2.1 Physical Metallurgy of Lithium Containing Aluminium Alloys.

Fig 2.1.1 Equilibrium Al-Li Binary phase diagram suggested by McAlister[46].

Fig 2.1.2 Al-Li-Cu ternary system.

(a) Isothermal section of the phases present at 350°C in the Al-Li-Cu system (Hardy and Silcock[44]).

(b) Representation of the phases identified by Silcock[45] after ageing for 16 hours at 165°C.

2.3 Textural Systems of Wrought Aluminium Lithium Alloys

Fig 2.3 Diagram illustrating the angles associated with texture representation according to Bunges' notation.

2.4 Hot working Process

Fig 2.4.1 Kinematically admissible velocity field.

Fig 2.4.1 Schematic representation of the variation in extrusion stress with variations in die cone angle.

3.0 Experimental

Fig 3.1.1 Plan Views of shear face, 'slab', dies. Indicating the range in orifice geometry and the associated extrusion and aspect ratios.

Fig 3.1.2 Typical conically shaped die, shown in elevation with the associated geometry.

Fig 3.2.1 Diagram illustrating the split billet specification and associated machined grid pattern.

Fig 3.3.1 Chemical composition of alloys A, B & C.

Fig 3.4.1 Table illustrating the extrusion ageing treatment schedules carried out for both the 'slab' and axi-symmetric extrusions.

Fig 3.5.2 Diagram illustrating the extrudate sectioning for the various alloy extrusions.

4.1 Optical Microscopy

Fig 4.1.1 Optical Micrographs
Alloy B material.
As-Extruded material.

(a) 15:1 extrusion ratio.
400° C extrusion temperature.
Edge of extrudate.
(b) 15:1 extrusion ratio.
500° C extrusion temperature.
Core of extrudate.
(c) 30:1 extrusion ratio.
500° C extrusion temperature.
Edge of extrudate.
(d) 30:1 extrusion ratio.
500° C extrusion temperature.
Core of extrudate.

Fig 4.1.2 Optical Micrographs.
Alloy A material.
As-Extruded material.
(a) 30:1 extrusion ratio.
500° C extrusion temperature.
Edge of extrudate.
'Rear' of extrudate.
(b) 30:1 extrusion ratio.
500° C extrusion temperature.
Core of extrudate.
'Rear' of extrudate.
(c) 15:1 extrusion ratio.
400° C extrusion temperature.
Edge of extrudate.
'Front' of extrudate.

Fig 4.1.3 Optical Micrographs.
Overaged Condition.
'Core' of extrudate.
(a) 6:1 extrusion ratio.
400° C extrusion temperature.
Alloy A material.
'Front' of extrudate.
(b) 15:1 extrusion ratio.
400° C extrusion temperature.
Alloy B material.
(c) & (d) 15:1 extrusion ratio.
400° C extrusion temperature.
Alloy A material.
'Front' of extrudate.

Fig 4.1.4 Optical Micrographs
Alloy A material.
Underaged Condition.
'Core' of extrudate.
(a) 30:1 extrusion ratio

450° C extrusion temperature.
'Back' of extrudate.
(b) & (c) 30:1 extrusion ratio.
400° C extrusion temperature.
'Front' of extrudate.

Fig 4.1.5 Optical Micrographs.
15:1 Extrusion Ratio.
Alloy A material.
Overaged Condition.
'Surface' of extrudate.
(a) 400° C extrusion temperature.
'Front' of extrudate.
(b) 450° C extrusion temperature.
'Front' of extrudate.
(c) 500° C extrusion temperature.
'Back' of extrudate

Fig 4.1.6 Optical Micrographs
30:1 Extrusion Ratio
500° C extrusion temperature.
Underaged Condition.
'Core' of extrudate.
(a) & (b) Alloy A Material
'Front' of extrudate.
(c) Alloy B Material

Fig 4.1.7 Optical Micrographs
30:1 Extrusion Ratio
500° C extrusion temperature.
Alloy A material
Overaged Condition.
'Back' of extrudate.
(a) 'Surface' of extrudate.
(b) & (c) 'Core' of extrudate.

Fig 4.1.8 Variation in recrystallised grain size, subgrain size and % recrystallisation with changes in processing conditions. Alloy A material, 'front' of extrudate.

Fig 4.1.9 Calculated Z values for various extrusion condition combinations.

4.2 Transmission Electron Microscopy.

Fig 4.2.1 **T.E.M. Micrographs**
(a) 30:1 Extrusion Ratio.
500° C extrusion temperature.
Alloy A material
As-Extruded condition.
Longitudinal section

'Core' region of extrudate.
This micrograph illustrates a very clean microstructure. No grain boundary precipitation is evident, but the 'mottled effect associated with the micrograph is due to δ' precipitation.

(b) 15:1 Extrusion Ratio.
400° C extrusion temperature.
Alloy B material
As-Extruded condition.
Longitudinal section
'Core' region of extrudate.
This micrograph illustrates the constituent grain boundary phases observed in all the extrudates, irrespective of processing histories.

(c) 30:1 Extrusion Ratio.
500° C extrusion temperature.
Alloy B material
Peak-aged condition.
Longitudinal section
'Core' region of extrudate.
This micrograph is a bright field image along the (100) Al-orientation illustrating the δ' precipitation.

Fig 4.2.2 **T.E.M. Micrographs**

(a) & (b) 15:1 Extrusion Ratio.
500° C extrusion temperature.
Alloy A material
Overaged condition.
Longitudinal section
'Core' region of extrudate.
These micrographs illustrating the S and T_1 matrix precipitation. δ' and β' precipitation is also present, evident by the 'mottled' effect associated with each micrograph.

(c) & (d) 30:1 Extrusion Ratio.
400° C extrusion temperature.
Alloy B material
Overaged condition.
Longitudinal section
'Core' region of extrudate.
These T.E.M. micrographs highlight the grain boundary I phase (Al-Cu-Li) precipitation. δ', β' and S phase precipitation is also clearly evident.

(e) & (f) 30:1 Extrusion Ratio.
500° C extrusion temperature.
Alloy A material
Overaged condition.
Longitudinal section
Core region of extrudate.
Micrograph (e) illustrates the δ' and β' precipitation observed in all the aged extrudates. Micrograph (f) illustrates the S phase grain boundary precipitation.

Fig 4.2.3 **T.E.M. Micrographs**

(a) & (b) 15:1 Extrusion Ratio.
500° C extrusion temperature.
Alloy A material
Underaged condition.
Longitudinal section
'Core' region of extrudate.
The elongated nature of the original grains, together with the internal subgrain structures, are illustrated by these micrographs. No substantial S or T_1 matrix precipitation is evident, but the 'mottled' effect associated with the micrographs is due to substantial δ' precipitation. At grain boundaries I phase precipitation, based upon the Al-Li-Cu system, were observed, and subgrain sizes of approximately 1->5μm were indicated.

(c) 30:1 Extrusion Ratio.
400° C extrusion temperature.
Alloy B material
Overaged condition.
Transverse section
2/3 radius position.
This micrograph illustrates grains/subgrains with generally equiaxed appearances, due to its transverse sectioning from the extrudate. Subgrain sizes of approximately 2->4μm were evident. It also illustrates the substantial proportions of grain boundary I phase, that were observed in all the extrudates processed to the overaged condition.

(d) 30:1 Extrusion Ratio.
500° C extrusion temperature.
Alloy A material
Overaged condition.
Longitudinal section
2/3 radius position.
This micrograph illustrates very clearly the elongated nature of the original grains, together with the internal subgrain structures.
Subgrain/recrystallised grain sizes of 2->10μm were observed.

(e) & (f) 15:1 Extrusion Ratio.
400° C extrusion temperature.
Alloy A material
Overaged condition.
Longitudinal section
'Core' region of extrudate.
These micrographs illustrate the S and T_1 matrix precipitation present in the overaged material.

4.3 Texture Analysis

Fig 4.3.1 Textural system variations with processing condition changes.
Aged condition. Alloy A material.

Fig 4.3.2 Tabulation of the textural system variations observed with changes in processing conditions. Aged conditions, alloy A material.

Fig 4.3.2 {111} Pole Figure Plots.
8090 alloy A.
'Core' of Extrudate.
'Rear' of Extrudate.
Overaged condition
(a) & (b) 15:1 extrusion ratio
400° C extrusion temperature.

Fig 4.3.3 {111} Pole Figure Plots.
8090 alloy A.
'Core' of Extrudate.
'Rear' of Extrudate.
Overaged condition
(a) 15:1 extrusion ratio
500° C extrusion temperature.
(b) 9:1 extrusion ratio
500° C extrusion temperature.

Fig 4.3.4 {111} Pole Figure Plots.
8090 alloy A.
'Core' of Extrudate.
Overaged condition
(a) 30:1 extrusion ratio
400° C extrusion temperature.
'Rear' of Extrudate.
(b) 30:1 extrusion ratio
400° C extrusion temperature.
'Front' of Extrudate.

Fig 4.3.5 {111} Pole Figure Plots.
8090 alloy A.
'Surface' of Extrudate.
Overaged condition
(a) 15:1 extrusion ratio
500° C extrusion temperature.
'Rear' of Extrudate.
(b) 30:1 extrusion ratio
500° C extrusion temperature.
'Front' of Extrudate.

Fig 4.3.6 {111} Pole Figure Plots.
8090 alloy A.
'Core' of Extrudate.
Overaged condition
(a) & (b) 30:1 extrusion ratio
500° C extrusion temperature.

'Rear' of Extrudate.

Fig 4.3.7 {111} Pole Figure Plots.
8090 alloy A.
'Surface' of Extrudate.
Overaged condition
(a) & (b) 30:1 extrusion ratio
400° C extrusion temperature.
'Front' of Extrudate.

Fig 4.3.8 {111} Pole Figure Plots.
8090 alloy A.
'Surface' of Extrudate.
Overaged condition
(a) & (b) 15:1 extrusion ratio
400° C extrusion temperature.
'Front' of Extrudate.

Fig 4.3.9 Variation in % volume fraction of texture components with variations in processing conditions.
(a) Variation in Brass, S, Copper and Cube texture components with increases in extrusion temperature, for 30:1 extrudates.
(b) Variation in Brass, S, Copper and Cube texture components with increases in extrusion ratio, for extrudates produced at 400°C.

4.4 Toughness Analysis

Fig 4.4.1 Comparison between (T-L) toughness measurements made using short rod and chevron notch bar specimens.

Fig 4.4.2 Variation in (T-L) and (L-T) toughness values with changes in ageing condition. Alloy A material.

Fig 4.4.3 Graphical representation of the observed variations in (T-L) and (L-T) toughness values with changes in ageing condition. Alloy A material.
(a) 15:1 extrusion ratio, 400°C extrusion temperature.
(b) 15:1 extrusion ratio, 450°C extrusion temperature.
(c) 30:1 extrusion ratio, 400°C extrusion temperature.
(d) 30:1 extrusion ratio, 450°C extrusion temperature.

Fig 4.4.4 Variation in (T-L) and (L-T) toughness values with changes in ageing condition. Alloy B material.

Fig 4.4.5 Graphical representation of the observed variations in (T-L) and (L-T) toughness values with changes in ageing condition. Alloy B material.
(a) 15:1 extrusion ratio, 400°C extrusion temperature.
(b) 15:1 extrusion ratio, 450°C extrusion temperature.
(c) 30:1 extrusion ratio, 400°C extrusion temperature.
(d) 30:1 extrusion ratio, 450°C extrusion temperature.

Fig 4.4.6 (T-L) S.E.M. Fractographs
As-Extruded Condition.
'Front' Regions of Extrudates.
(a) Alloy A material
6:1 Extrusion Ratio.
500° C Extrusion Temperature.
(b) Alloy A material
15:1 Extrusion Ratio.
500° C Extrusion Temperature.
(c) Alloy A material
30:1 Extrusion ratio.
500° C Extrusion Temperature.

Fig 4.4.7 (L-T) S.E.M. Fractographs
Alloy B material
As-Extruded Condition.
(a) 15:1 Extrusion Ratio.
400° C Extrusion Temperature.
(b) 15:1 Extrusion Ratio.
450° C Extrusion Temperature.
(c) 15:1 Extrusion ratio.
500° C Extrusion Temperature.

Fig 4.4.8 S.E.M. Fractographs
Alloy A Material
Underaged Condition.
9:1 Extrusion Ratio
400° C Extrusion Temperature.
'Front' of Extrudate.
(a) & (b) (T-L) Fracture
(c) & (d) (L-T) Fracture.

Fig 4.4.9 S.E.M. Fractographs
Alloy A material
15:1 Extrusion Ratio
Underaged Condition.
'Front' Regions of Extrudates.
(a) (T-L) Fracture
400° C Extrusion Temperature.
(b) (L-T) Fracture.
400° C Extrusion Temperature.
(c) (T-L) Fracture
500° C Extrusion Temperature.
(d) (L-T) Fracture.
500° C Extrusion Temperature.

Fig 4.4.10 (T-L) S.E.M. Fractographs
Alloy A Material

Overaged Condition.
'Rear' of Extrudate.
(a) 6:1 Extrusion Ratio
400° C Extrusion Temperature.
(b) 9:1 Extrusion Ratio
400° C Extrusion Temperature.
(c) 30:1 Extrusion Ratio
400° C Extrusion Temperature.

Fig 4.4.11 S.E.M. Fractographs
Alloy A material
15:1 Extrusion Ratio
Overaged Condition.
'Front' Regions of Extrudates.
(a) (T-L) Fracture
400° C Extrusion Temperature.
(b) (L-T) Fracture.
400° C Extrusion Temperature.
(c) (T-L) Fracture
500° C Extrusion Temperature.
(d) (L-T) Fracture.
500° C Extrusion Temperature.

Fig 4.4.12 S.E.M. Fractographs
Alloy B material
30:1 Extrusion Ratio
Overaged Condition.
(a) (T-L) Fracture
400° C Extrusion Temperature.
(b) (T-L) Fracture.
500° C Extrusion Temperature.
(c) (L-T) Fracture
500° C Extrusion Temperature.

Fig 4.4.13 S.E.M. Fractographs
Alloy A Material
Overaged Condition.
30:1 Extrusion Ratio
500° C Extrusion Temperature.
'Rear' of Extrudate.
(a) (T-L) Fracture
(b) & (c) (L-T) Fracture.

Fig 4.4.14 Variation in (T-L) and (L-T) toughness values with increasing extrusion temperature. Alloy A extrudates.

Fig 4.4.15 Variation in (T-L) and (L-T) toughness values with increasing extrusion temperature. Alloy B extrudates.

Fig 4.4.16 Calculated variations in (T-L) and (L-T) fracture toughness values, with increases in extrusion temperature. Alloy A extrudates.
(a) 15:1, 'Front' of Extrudate, Overaged Condition
(b) 15:1, 'Rear' of Extrudate, Overaged Condition
(c) 30:1, 'Front' of Extrudate, Overaged Condition
(d) 30:1, 'Rear' of Extrudate, Overaged Condition
(e) 15:1, 'Front' of Extrudate, Underaged Condition
(f) 30:1, 'Front' of Extrudate, Underaged Condition

Fig 4.4.17 Calculated variations in (T-L) and (L-T) fracture toughness values, with increases in extrusion temperature. Alloy B extrudates.
(a) 15:1, Underaged Condition
(b) 30:1, Underaged Condition
(c) 15:1, Peak aged Condition
(d) 30:1, Peak aged Condition
(e) 15:1, Overaged Condition
(f) 30:1, Overaged Condition

Fig 4.4.18 Variation in (T-L) and (L-T) toughness values with increasing extrusion and aspect ratio. Alloy A extrudates.

Fig 4.4.19 Variation in (T-L) and (L-T) toughness values with increasing extrusion and aspect ratio. Alloy A extrudates.
(a) 400°C, 'front' of extrudate, underaged condition.
(b) 450°C, 'front' of extrudate, overaged condition.

4.5 Tensile Properties

Fig 4.5.1 Variation in tensile property values with increasing extrusion temperature, for alloy A extrudates.

Fig 4.5.2 Graphical representation of the variation in tensile property values with increases in extrusion temperature.
(a) Longitudinal samples, 15:1 extrusion ratio,
400° C extrusion temperature, Overaged condition,
'Front' of extrudate.
(b) Longitudinal samples, 15:1 extrusion ratio,
400° C extrusion temperature, Overaged condition,
'Back' of extrudate.
(c) Longitudinal samples, 30:1 extrusion ratio,
400° C extrusion temperature, Overaged condition,
'Front' of extrudate.
(d) Longitudinal samples, 15:1 extrusion ratio,
400° C extrusion temperature, Overaged condition,
'Back' of extrudate.

(e) Transverse samples, 15:1 extrusion ratio,
400° C extrusion temperature, Overaged condition,
'Front' of extrudate.
(f) Transverse samples, 15:1 extrusion ratio,
400° C extrusion temperature, Overaged condition,
'Back' of extrudate.
(g) Longitudinal samples, 15:1 extrusion ratio,
400° C extrusion temperature, Underaged condition
'Front' of extrudate.
(h) Longitudinal samples, 30:1 extrusion ratio,
400° C extrusion temperature, Underaged condition
'Front' of extrudate.

Fig 4.5.3 Variation in tensile property values with increases in extrusion/aspect ratios.
alloy A extrudates, 'front' of extrudate.

Fig 4.5.4 Graphical representation of the variation in tensile property values with increases in extrusion/aspect ratio.
(a) Longitudinal samples.
400° C extrusion temperature, underaged condition,.
(b) Longitudinal samples.
450° C extrusion temperature, overaged condition.

5.1 Optical Analysis

Fig 5.1.1 Optical Micrographs
(a) 30° die cone angle.
460° C extrusion temperature.
Underaged condition.
Surface region of extrudate.
(b) & (c) 30° die cone angle.
460° C extrusion temperature.
Underaged condition.
Core region of extrudate.

Fig 5.1.2 Optical Micrographs
(a) 45° die cone angle.
400° C extrusion temperature.
Overaged condition.
Core region of extrudate.
(b) & (c) 45° die cone angle.
460° C extrusion temperature.
Overaged condition, core region of extrudate.

Fig 5.1.3 Optical Micrographs
(a) 60° die cone angle.
400° C extrusion temperature.
Underaged condition.

Surface region of extrudate.
(b) 60° die cone angle.
400° C extrusion temperature.
Underaged condition.
Core region of extrudate.
(c) & (d) 60° die cone angle.
460° C extrusion temperature.
Overaged condition.
Core region of extrudate.

Fig 5.1.4 Optical Micrographs
(a) 90° die cone angle.
460° C extrusion temperature.
Underaged condition.
Surface region of extrudate.
(b) 90° die cone angle.
460° C extrusion temperature.
Overaged condition.
Core region of extrudate.
(c) 90° die cone angle.
430° C extrusion temperature.
Overaged condition.
Core region of extrudate.

Fig 5.1.5 Variation in % recrystallisation, grain size and subgrain size, with increasing extrusion temperature and die cone angle.

Fig 5.1.6 Variation in surface region microhardness values.
(a) 460°C extrusion temperature.
(b) 430°C extrusion temperature.

5.2 Transmission Electron Microscopy.

Fig 5.2.1 **T.E.M. Micrographs**
(a) 60° die cone angle.
460° C extrusion temperature.
Overaged condition.
Longitudinal section
Core region of extrudate.
This micrograph illustrates the elongated nature of the original grains, together with internal substructure. Matrix precipitation, together with grain boundary I phase precipitation (Al-Cu-Li) are also illustrated.
(b) Higher magnification of (a)
(c) Higher magnification of (b), highlighting the matrix S phase precipitation.
(d) 30° die cone angle.
400° C extrusion temperature.
Underaged condition.
Transverse section

Core region of extrudate.
(e) Higher magnification of (d) illustrating the absence of matrix S and T_1 precipitation in the underaged condition.

Fig 5.2.2 **T.E.M. Micrographs**

(a) 90° die cone angle.
400° C extrusion temperature.
Underaged condition.
Transverse section
Core region of extrudate.
(b) Higher magnification of (a) illustrating the absence of significant matrix precipitation other than δ', which gave rise to the mottled effect associated with the subgrains.

(c) 90° die cone angle.
460° C extrusion temperature.
Underaged condition.
Transverse section
Core region of extrudate.
These micrographs illustrate the absence of S and T_1 matrix precipitation associated with the underaged material. δ' matrix precipitation along with dislocation loops, however, are clearly seen in the subgrains. Grain boundary precipitation of I phase and based upon the Al-Cu-Li are also clearly shown.

(d) 90° die cone angle.
400° C extrusion temperature.
Overaged condition.
Transverse section
Core region of extrudate.
This micrograph illustrates the grain boundary precipitation of I phase (Al-Cu-Li), with associated precipitate free zones.

(e) & (f) 90° die cone angle.
460° C extrusion temperature.
Overaged condition.
Transverse section
Core region of extrudate.
These Micrographs illustrate the matrix precipitation of S phase, together with the δ' precipitation, which has given rise to the 'mottled' effect associated with the micrographs.

5.3 Texture Analysis

Fig 5.3.1 {111} pole figure plots.
(a) 30° die cone angle.
430°C Extrusion Temperature.
(b) 45° die cone angle.
430°C Extrusion Temperature.

Fig 5.3.2 {111} pole figure plots.
(a) 60° die cone angle.
430°C Extrusion Temperature.
(b) 90° die cone angle.
430°C Extrusion Temperature.

Fig 5.3.3 {111} pole figure plots.
(a) 45° die cone angle.
400°C Extrusion Temperature.
(b) 45° die cone angle.
460°C Extrusion Temperature.

Fig 5.3.4 Variation in % volume fraction of texture components with increasing die cone angle.

5.4 Deformation Flow Analysis

Fig 5.4.1 Distortion patterns obtained from extrusion of machine gridded split billets at 430°C extrusion temperature.
(a) 90° die cone angle.
(b) 60° die cone angle.
(c) 45° die cone angle.
(d) 30° die cone angle.

Fig 5.4.2 Schematic illustration of the distortion field obtained from extrusion of a 5mm square grid pattern.

Fig 5.4.3 (a), (b) and (c), schematic illustrations of the variations in dead metal zone formation as the die cone angle altered.
(d) Schematic, relating the relative material position in the deformation zone with the transverse and longitudinal sections within the extrudate

Fig 5.4.4 Variation in experimental and predicted extrusion loads as processing conditions varied.
(a) Variation in the experimentally obtained and theoretically predicted extrusion loads as die cone angle and extrusion temperature were varied. 8090 alloy extrusions.
(b) Variation in the experimentally obtained and theoretically predicted extrusion loads as die cone angle and extrusion temperature were varied. 7075 alloy extrusions.
(c) Graphical representation of the extrusion loads as die cone angle increased. 8090 alloy extrusions.

Fig 5.4.5 X-ray contact print of distorted gold mesh.
8090 alloy, 45° die cone angle, 430°C extrusion temperature.

Fig 5.4.6 Strain rate distributions produced from visioplasticity analysis.
(a) 7075 alloy, 45° die cone angle, 430°C extrusion temperature.
(b) 8090 alloy, 45° die cone angle, 430°C extrusion temperature.
(c) 8090 alloy, 60° die cone angle, 430°C extrusion temperature.

Fig 5.4.7 Flow line pattern results produced from finite element analysis
(a) 7075 alloy, 90° die cone angle, 430°C extrusion temperature.
(b) 8090 alloy, 60° die cone angle, 430°C extrusion temperature.
(c) 7075 alloy, 60° die cone angle, 430°C extrusion temperature.
(d) 8090 alloy, 45° die cone angle, 430°C extrusion temperature.
(e) 7075 alloy, 45° die cone angle, 430°C extrusion temperature.
(f) 8090 alloy, 30° die cone angle, 430°C extrusion temperature.
(g) 7075 alloy, 30° die cone angle, 430°C extrusion temperature.

Fig 5.4.8 Temperature distributions, produced from finite element analysis
(a) 7075 alloy, 30° die cone angle, 430°C extrusion temperature.
(b) 8090 alloy, 30° die cone angle, 430°C extrusion temperature.
(c) 8090 alloy, 60° die cone angle, 430°C extrusion temperature.
(d) 8090 alloy, 90° die cone angle, 430°C extrusion temperature.

Fig 5.4.9 Strain rate distributions, produced from finite element analysis
(a) 8090 alloy, 45° die cone angle, 430°C extrusion temperature.
(b) 8090 alloy, 90° die cone angle, 430°C extrusion temperature.
(c) 8090 alloy, 30° die cone angle, 430°C extrusion temperature.
(d) 7075 alloy, 60° die cone angle, 430°C extrusion temperature.

Fig 5.4.10 Temperature compensated strain rate distributions, produced from finite element analysis
(a) 8090 alloy, 45° die cone angle, 430°C extrusion temperature.
(b) 8090 alloy, 30° die cone angle, 430°C extrusion temperature.
(c) 8090 alloy, 90° die cone angle, 430°C extrusion temperature.

5.5 Toughness Analysis

Fig 5.5.1 (R-L) S.E.M. Fractographs
Underaged Condition.
Core Regions of Extrudates.
(a) 45° Die Cone Angle.
400° C Extrusion Temperature.
(a) 90° Die Cone Angle.
430° C Extrusion Temperature.
(c) & (d) 45° Die Cone Angle.
430° C Extrusion Temperature.

Fig 5.5.2 (R-L) S.E.M. Fractographs
Underaged Condition.
Core Regions of Extrudates.
460° C Extrusion Temperature.
(a) 30° Die Cone Angle.

(b) 45° Die Cone Angle.
(c) 60° Die Cone Angle.
(d) 90° Die Cone Angle.

Fig 5.5.3 (R-L) S.E.M. Fractographs
Overaged Condition.
Core Regions of Extrudates.
430° C Extrusion Temperature.
(a) 60° Die Cone Angle.
(b) & (c) 30° Die Cone Angle.

Fig 5.5.4 (L-R) S.E.M. Fractographs
Underaged Condition.
(a) 45° Die Cone Angle.
430° C Extrusion Temperature.
Core of Extrudates
(a) 45° Die Cone Angle.
460° C Extrusion Temperature.
Core of Extrudates
(c) 45° Die Cone Angle.
430° C Extrusion Temperature.
Surface of Extrudates

Fig 5.5.5 (L-R) S.E.M. Fractographs
Underaged Condition.
Core Regions of Extrudates.
400° C Extrusion Temperature.
(a) 30° Die Cone Angle.
(b) 90° Die Cone Angle.
(c) & (d) 45° Die Cone Angle.

Fig 5.5.6 (L-R) S.E.M. Fractographs
Overaged Condition.
Core Regions of Extrudates.
460° C Extrusion Temperature.
(a) 30° Die Cone Angle.
(b) 60° Die Cone Angle.
(c) & (d) 45° Die Cone Angle.

Fig 5.5.7 Variation in (R-L) and (L-R) toughness values with changes in die cone angle and extrusion temperature.

Fig 5.5.8 Graphical representation of the variation in (R-L) and (L-R) toughness values with changes in die cone angle, for extrudates produced at different extrusion temperatures and aged to either the underaged or overaged conditions.
(a) Underaged material, 8090 alloy.

Variation in (R-L) toughness values with increases in die cone angle.
(b) Underaged material, 8090 alloy.
Variation in (L-R) toughness values with increases in die cone angle.
(c) Underaged material, 8090 alloy.
Variation in toughness anisotropy with increases in die cone angle.
(d) Overaged material, 8090 alloy.
Variation in (R-L) toughness values with increases in die cone angle.
(e) Overaged material, 8090 alloy.
Variation in (L-R) toughness values with increases in die cone angle.
(f) Overaged material, 8090 alloy.
Variation in toughness anisotropy with increases in die cone angle.

Fig 5.5.9 Variation in (L-R) fracture toughness values from the centre of the extrudates to the surface. All extrudates were produced at 430°C and aged to the underaged condition.

Fig 5.5.10 Variation in (R-L) and (L-R) toughness values with changes in extrusion temperature, for extrudates produced using dies of varying die cone angle and aged to either the underaged or overaged conditions.

(a) Underaged material, 8090 alloy.
Variation in (R-L) toughness values with increases in extrusion temperature.
(b) Underaged material, 8090 alloy.
Variation in (L-R) toughness values with increases in extrusion temperature.
(c) Underaged material, 8090 alloy.
Variation in toughness anisotropy with increases in extrusion temperature.
(d) Overaged material, 8090 alloy.
Variation in (R-L) toughness values with increases in extrusion temperature.
(e) Overaged material, 8090 alloy.
Variation in (L-R) toughness values with increases in extrusion temperature.
(f) Overaged material, 8090 alloy.
Variation in toughness anisotropy with increases in extrusion temperature.

5.6 Tensile Properties

Fig 5.6.1 Variation in longitudinal tensile property values with changes in die cone angle, extrusion temperature and ageing condition. Alloy A extrudates.

Fig 5.6.2 Graphical representation of the variation in longitudinal tensile property values with increasing die cone angle.
(a) 8090 alloy A, underaged condition. Variation in the yield stress values with increases in die cone angle.
(b) 8090 alloy A, underaged condition. Variation in the ultimate tensile stress values with increases in die cone angle.

(c) 8090 alloy A, overaged condition. Variation in the yield stress values with increases in die cone angle.
(d) 8090 alloy A, overaged condition. Variation in the ultimate tensile stress values with increases in die cone angle.

Fig 5.6.3 Graphical representation of the variation in longitudinal tensile property values with increases in extrusion temperature
(a) 8090 alloy A, underaged condition. Variation in the yield stress values with increases in die cone angle.
(b) 8090 alloy A, underaged condition. Variation in the ultimate tensile stress values with increases in die cone angle.
(c) 8090 alloy A, overaged condition. Variation in the yield stress values with increases in die cone angle.
(d) 8090 alloy A, overaged condition. Variation in the ultimate tensile stress values with increases in die cone angle.

Appendices

Fig 7.1 The configuration of the chevron notch bar specimens used to measure (L-R) and (L-T) fracture toughness values.

CHAPTER ONE

Introduction

Aluminium lithium alloys are particularly attractive for aerospace applications, due to their high elastic modulii combined with their ability to attain intermediate strength levels. These strength values are attributable to the precipitation of coherent $\delta'^{(1)->(6)}$. The addition of major solute elements such as magnesium and copper has also been shown to further increase the strength values and fracture toughness through the co-precipitation of other metastable phases. It is obvious therefore that microstructure, hence property values, can be controlled by manipulation of composition and heat-treatment schedule.

The hot working procedures are also very influential in the development of microstructure. The local conditions of deformation, temperature and strain rate together with the local microstructural features determine the rates of dislocation annihilation and generation, the shape of grains and sub-grains, along with the degree of recrystallisation.

This project has set out to investigate the influence of processing upon the property values and anisotropy of rectangular cross-section, 'slab', extrusions.

Thin bar extrusions are being used in a number of aerospace applications. Westland helicopters utilise AA8090, where properties matching those of 7075 have been achieved[7]. Thin bar 8090 extrusions down to 1.6mm may also be used in the leading and trailing edges of the wing structure within the Airbus A330/A340 aircraft[6][8].

Problems encountered with thin bar extrusions however, have been:-

(1) Lower tensile properties than thicker sections.

This may be due to increased levels of recrystallisation removing the substructure, and/or textural effects.

Alcan have shown that by using an ageing temperature of 210° C and increasing the magnesium and copper contents to the top of the AA8090 specification tensile requirements of 400MPa proof, 450MPa U.T.S and 4% elongation can be obtained in thin bar sections.

(2) Anisotropy in property values.

If recrystallisation is not substantial, the inherent nature of the extrusion process is to produce highly elongated grains in the direction of extrusion. The subsequent application of stresses perpendicular to these boundaries leads to delamination along the grain boundaries resulting in poor mechanical properties. This factor together with the stress concentration characteristics of aluminium lithium alloys - coplanar slip, precipitate free zone formation and grain boundary precipitation - have caused these alloys to exhibit relatively poor transverse tensile properties and low longitudinal toughness values.

Many researchers have investigated precipitation as a means of affecting the stress concentration characteristics of aluminium lithium alloys, but it may also be possible to affect the stress concentration phenomena by altering the deformation process. Alcoa have shown how disruption of the flow pattern within axisymmetric extrusions can modify the texture present and achieve desired changes in mechanical properties and improvements in the isotropy of the microstructure across the thickness directions may also be possible with alterations in the deformation process.

Initially this project set out to investigate the variation in the property values of 'slab' extrusions as the process conditions were varied. Standard process conditions of extrusion ratio, aspect ratio, extrusion temperature and ageing treatment were varied, but the effect of varying die cone angle upon the property values was also of interest. Due to the difficulty in producing conical slab dies, and the problems associated with the implementation of visioplasticity and finite element techniques in order to quantify flow changes, die cone angle variations were carried out upon axi-symmetric extrusions. Once possible property improvements due to changes in die cone angle were identified and the problems associated with the analytical techniques resolved, however, the modification of die cone angle was to be extended to the thin section extrusion situation.

The project, therefore, consisted of two main sections;- One involving 'slab' extrusions and the second axi-symmetric extrusions.

For the 'slab' extrusions, extrusion/aspect ratio, extrusion temperature and ageing condition were varied. The tensile and toughness property values were then measured as processing conditions, testing orientation and distance along the extrudate, were varied. In order to identify the particular microstructural changes affected by the changing process conditions and subsequent effects, if any, upon property values and anisotropy, microstructural analyses of texture, % recrystallisation and grain size were carried out.

For the axi-symmetric extrusions die cone angle, extrusion temperature and ageing condition, were varied and once again the variations in property values with changes in processing conditions established. Microstructural analysis of texture, recrystallisation and grain size, were then carried out in order to correlate with processing variations and explain any property variations that may have occurred. In addition, due to the manipulation of the die cone angle, analyses involving gridded billets, visioplasticity and finite element techniques were carried out in order to define the changes in the deformation field.

Overall, therefore, each section established property-microstructure correlations and the process conditions necessary to produce desired microstructures, hence property values.

CHAPTER TWO

LITERATURE SURVEY

2.1 Physical Metallurgy of Lithium Containing Aluminium Alloys

The most important precipitate phase in Al-Li alloys is the metastable coherent δ' (Al_3 Li) phase. This precipitate not only strengthens the material[46][47][48], but also gives rise to severe coplanar slip[49][50][51] and subsequent increases in localised strain concentration. This strain localisation, in connection with weak internal boundaries, results in decreased ductility and fracture toughness. In order to improve properties, additions of copper and magnesium can be made to the binary Al-Li alloys. These additional elements cause solid solution strengthening and the precipitation of semi-coherent and incoherent phases. These phases disperse slip and thereby improve toughness and ductility values [6].

The phases considered most important in the quaternary Al-Li-Cu-Mg-(Zr) alloy used in this project are listed below:-

δ' - (Al_3Li)	S - (Al_2CuMg)	I - (Al-Li-Cu)
β' - (Al_3Zr)	T_1 - (Al_2CuLi)	Al-Fe-Cu intermetallics

Several alloy systems will now be discussed in connection with the above phases:-

2.1.1. Binary Systems

Al-Li Binary System

Since δ' precipitates play such an important role in the strengthening of aluminium lithium alloys, knowledge of the binary phase diagram and the precipitation characteristics of metastable δ' and the equilibrium δ is very important. Fig 2.1.1 illustrates the equilibrium Al-Li phase diagram suggested by McAlister[43].

Several different α/δ solvus lines have been suggested. A solvus line coinciding with the α/δ' solvus line below approximately 7 at% lithium, and approaching 5 at% lithium solubility at room temperature, has been developed[1][2][3]. This is not expectable thermodynamically, however, because of the large free energy difference between δ and δ'. Other researchers[4][5] have produced more acceptable α/δ solvus lines, which approach 1 at% at room temperature.

As far as heat treatment is concerned, however, the α/δ' solvus line is of more practical importance, since the δ'(Al_3 Li) is the main strengthening phase in Al-Li alloys. Good agreement up to 13 at% has been found for the shape of the δ' solvus[6][7][3], but it is not possible to extend experimental measurements beyond this point, due to eutectic formation. This does not apply to theoretical models, however, and two models predicting the continuation of the metastable phase diagram to higher lithium

concentrations have been put forward by Sigli & Sanchez[8] and Khachaturyan[9]. The development of such models beyond experimental observations is purely of academic interest.

The δ'(Al_3 Li) forms as small coherent spherical precipitates and has an $L1_2$ type structure with a lattice parameter of a=4.038 angstroms[7]. The similarity in crystal structure between the δ' and the aluminium matrix results in low coherency strains, hence a low nucleation barrier for δ' precipitation. This low nucleation energy barrier means that the δ' precipitates homogeneously throughout the material, forming a fine uniform distribution. It also means that δ' precipitation is not affected by the presence of structural defects such as dislocations or grain boundaries.

The actual mechanism of δ' precipitation has been the subject of much debate. At commercial ageing temperatures δ' precipitates form by homogeneous nucleation and growth[11], they then grow by diffusion controlled kinetics[6][11][12][13][14]. Ordering before phase separation has been shown to occur through the use of different experimental techniques such as high resolution electron microscopy (H.R.E.M) and electron diffraction[20], small angle X-ray scattering (S.A.X.S) and T.E.M.[21], and S.A.X.S. and superlattice X.R.D. [22]. This process of ordering also agrees with the theoretical model proposed by Kachaturyan[9]. In this model Kachaturyan predicted that under certain conditions of rapid quenching a disordered solid solution, α, would become ordered on the $L1_2$ lattice, decompose into two ordered phases of differing lithium content, and finally the low % lithium phase would become disordered. The microstructure would then consist of ordered δ' particles and disordered matrix. This spinodal decomposition has been concluded by Radmilocov[20] and Miyasato[23] also.

As the temperature drops, however, thermal analysis[15][16], S.A.X.S.[18][19] and resistivity measurements[17] have indicated pre-cursors to δ' formation. This is not supported by the analyses stated above or the theoretical model.

Ageing within the δ' phase field will eventually lead to the formation of the equilibrium δ phase - particularly at grain boundaries. The δ phase has a B_{32} (NaTl) type of structure with lattice parameter a=6.37 Angstroms[12]. The δ' precipitate may be a precursor to the δ precipitation or just a separate metastable phase.

Nozato and Nakai[10] have suggested that δ forms from the metastable δ', but Williams[32] and Sanders and Balmuth[52] suggest that the δ nucleates independently of the δ' and growth of the δ particles is accompanied by dissolution of the metastable δ' phase.

Al-Zr Binary System

Dispersoid forming elements are added to commercial lithium alloys in order to (a) retard recrystallisation and grain growth, and (b) reduce the propensity towards coplanar slip.

Zirconium forms a fine dispersion of β' (Al_3 Zr) particles, which have a tetragonal structure and incorporate no lithium[24] . Due to its low diffusivity, the zirconium remains in solid solution during casting. This is in contrast to the lithium which segregates out during casting producing a cored structure. Upon homogenisation the lithium re-dissolves, whereas the zirconium precipitates out, due to its low solid solubility. The distribution of zirconium in solid solution is not uniform, however, owing to the solidification coring which occurred during casting. As a result the β' particles precipitate out in a non-uniform distribution [25] . This non-uniformity of β' means that some regions deficient in β' may recrystallise.

The β' particles may not incorporate lithium, but they do affect the precipitation of δ'. The δ' particles not only nucleate homogeneously throughout the matrix, but also heterogeneously upon the β' precipitates. This creates composite particles, which behave as large δ' precipitates[26][27] .

2.1.2 Ternary Systems

Up to the peak aged condition the volume fraction of δ' increases, and by definition so do the strength levels. The maximum strength level obtainable through δ' precipitation is limited, however, due to the fact that it is a coherent precipitate showing little misfit. Few interface dislocations are consequently present in order to interact with other dislocations. The addition of a third element to the binary Al-Li system may, however, be used to enhance properties. This additional element may cause the precipitation of less coherent phases, as well as increasing the solid solution strengthening of the material.

In commercial aluminium lithium alloys, copper and magnesium are added as solute additions in order to improve properties.

Al-Li-Cu System

The presence of copper in solid solution decreases the maximum solubility of lithium in aluminium[28] , but does not affect the precipitation mechanism of δ'[29] . The presence of copper does, however, cause the precipitation of additional lithium bearing phases, which may affect the volume fraction of δ'. The phases produced as a consequence of the copper additions have been shown to be dependent upon the Cu:Li ratio, and ageing temperature[28] . Fig 2.1.2 (a) illustrates an isothermal section of the phases present at 350° C in the ternary system[44], whereas fig 2.1.2(b) indicates the phases identified by Silcock[45] after 16hrs at 165° C.

In commercial aluminium lithium alloys T_1 (Al_2CuLi) phase is the predominant copper bearing strengthening phase present after ageing, and it nucleates heterogeneously on dislocations, low angle grain boundaries and other defects. T_1 has

an hexagonal crystal structure with a = 0.497nm and c = 0.934nm and develops as thin platelets parallel to the {111} planes of the aluminium matrix.

Since both δ' and T_1 phases contain lithium, the precipitation of T_1 subsequent to the formation of δ' may cause a reduction in the volume fraction and distribution of δ'. Some researchers [30][31] consider T_1 precipitation to be sustained by lithium in solid solution, whereas Sanders showed T_1 passing through δ' and possibly consuming them.

The precipitation of T_1 is considered beneficial, however, since it is a powerful strengthening phase and appears to reduce the tendency for strain localisation. Evidence has been provided that T_1 precipitates are initially sheared and then looped by dislocations, as are the δ'. Since both precipitates are sheared the beneficial nature of T_1 in reducing coplanar slip is unexpected. T_1 platelets do have greater lattice mismatch and different internal structures compared with δ'[33], however, consequently their strengthening contribution is greater than that of δ', which is mainly due to order hardening. These additional mechanisms of strengthening, due to T_1 are not as greatly reduced by coplanar slip as is the mechanism of strengthening provided by the δ'. Consequently coplanar slip is reduced and strength increased if T_1 is present.

Since the presence of T_1 phase is beneficial and it precipitates by heterogeneous nucleation upon defects, researchers have considered pre-ageing stretches in order to promote precipitation[42].

As well as T_1 precipitates, T_2 (Al_3CuLi_3) precipitation also occurs at high angle boundaries. The formation of T_2 phase particles along grain boundaries leads to the development of δ' precipitate free zones (PFZ's). The presence of T_2 and PFZ's causes loss in ductility and fracture toughness, hence their presence is undesirable.

2.1.3 Al-Li-Cu-Mg System

When magnesium is added to Al-Li-Cu alloys the additional precipitation of S (Al_2 CuMg) occurs.

In high lithium, low copper alloys, such as 8090, S phase is the main copper bearing phase [31][34]. The S phase is semi-coherent and has an orthorhombic crystal structure. It forms as rods aligned along <100> Al directions. These rods then widen on {210} planes. When these laths meet, corrugated precipitate sheets are formed[35].

The precipitation of S within the matrix has been shown to increase ductility and fracture toughness values [36][37]. This is because S phase precipitates do not have densely packed slip planes parallel to the matrix slip planes and as a result they resist shearing by dislocations, hence reducing the tendency for coplanar slip [31].

The S phase does precipitate homogeneously within the matrix, but mainly forms heterogeneously upon structural defects. The heterogeneous precipitation of S at high and low angle grain boundaries also occurs, and since it contains no lithium it is not

associated with PFZ formation. Researchers[38][39] have identified a number of grain boundary phases that form in commercial alloys and are associated with PFZ formation . The actual boundary phases formed have been found to depend upon the Li:Cu and Cu:Mg ratios [38]->[41] . C phase (Al-Li-Cu-Mg) has been observed in material of low Cu:Mg ratio, but as this ratio increases I phase (Al-Li-Cu) and T_2 phase (Al-Li-Cu) develop.

The phases considered above are of interest as a consequence of ageing, but precipitates may persist from processes carried out before ageing. We must, therefore, briefly consider the phases remaining after solution treatment, and prior to ageing.

2.1.4 Impurities, As-Cast Material and Homogenisation

The main impurity elements present in aluminium lithium alloys are iron, silicon, sodium, potassium and calcium. Iron and silicon often combine with the alloying elements during casting to form insoluble constituent phases at high angle grain boundaries. These phases then form stringers in the extruded product.

This combination with the available solute atoms and the alignment of these constituent phases along the extrusion direction, makes iron and silicon within the alloys generally undesirable. They may be useful in small amounts, however, due to their combination with sodium and potassium, which prevents the formation of sodium and potassium grain boundary films [28].

Many phases have been reported in the as-cast Al-Li-Mg-Cu-Zr alloy system [38][39] and the homogenisation treatment chosen must remove these non-equilibrium phases, together with features such as coring. The homogenisation must, however, remain a practical operation. The homogenisation temperature employed, therefore, will be determined by the solidus temperature of the material. The homogenisation time will depend upon the degree of non-uniformity in composition, the size of the non-equilibrium phases, and the diffusivities of the phase forming elements.

Homogenisation schedules have been developed whereby all but Al-Fe-Cu phases are dissolved. These phases then form stringers in the final wrought product. Such practices have been employed in this project, therefore the only intermetallic phase anticipated is one from the Al-Fe-Cu system.

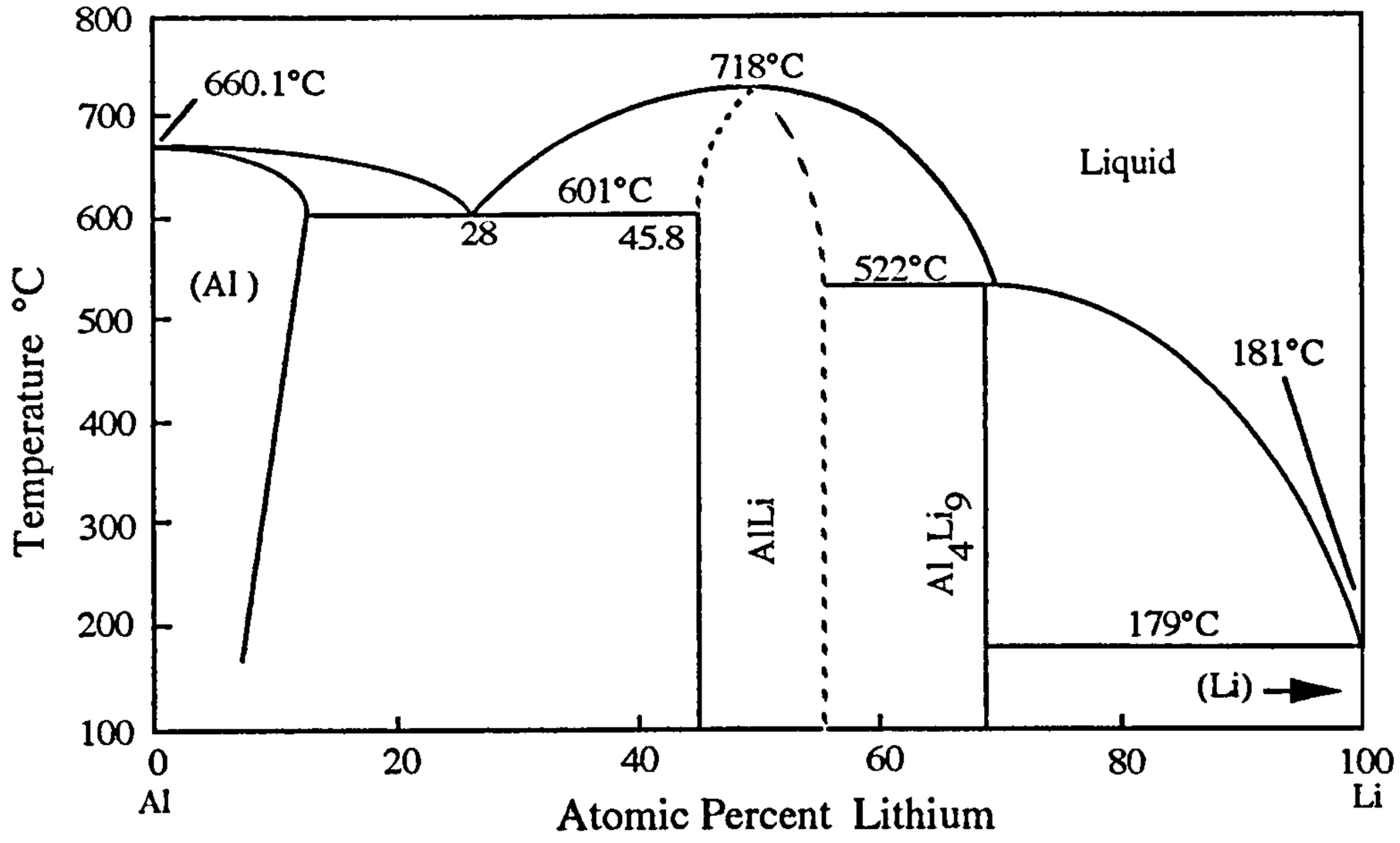
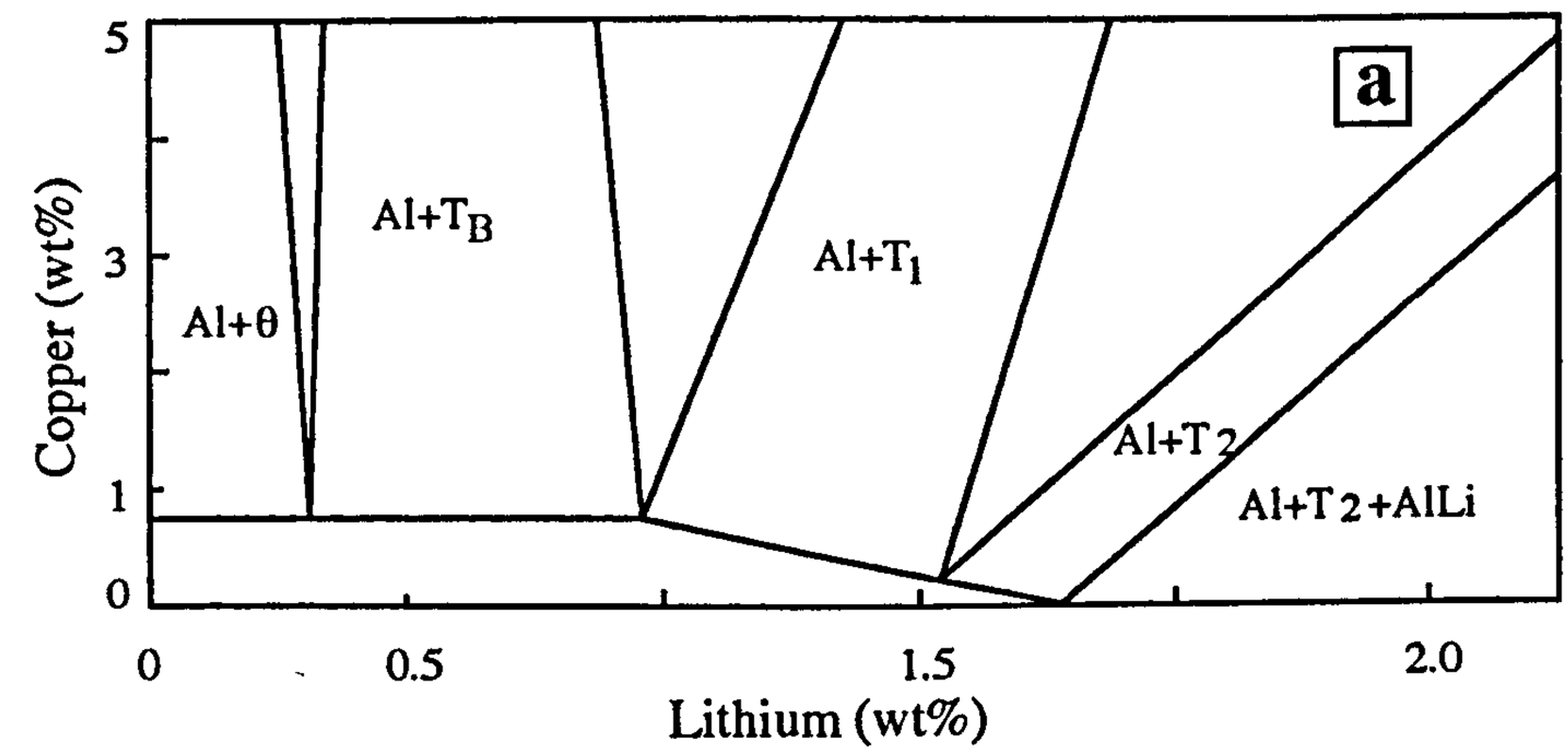


Fig 2.1.1 Equilibrium Al-Li binary diagram suggested by McAlister.



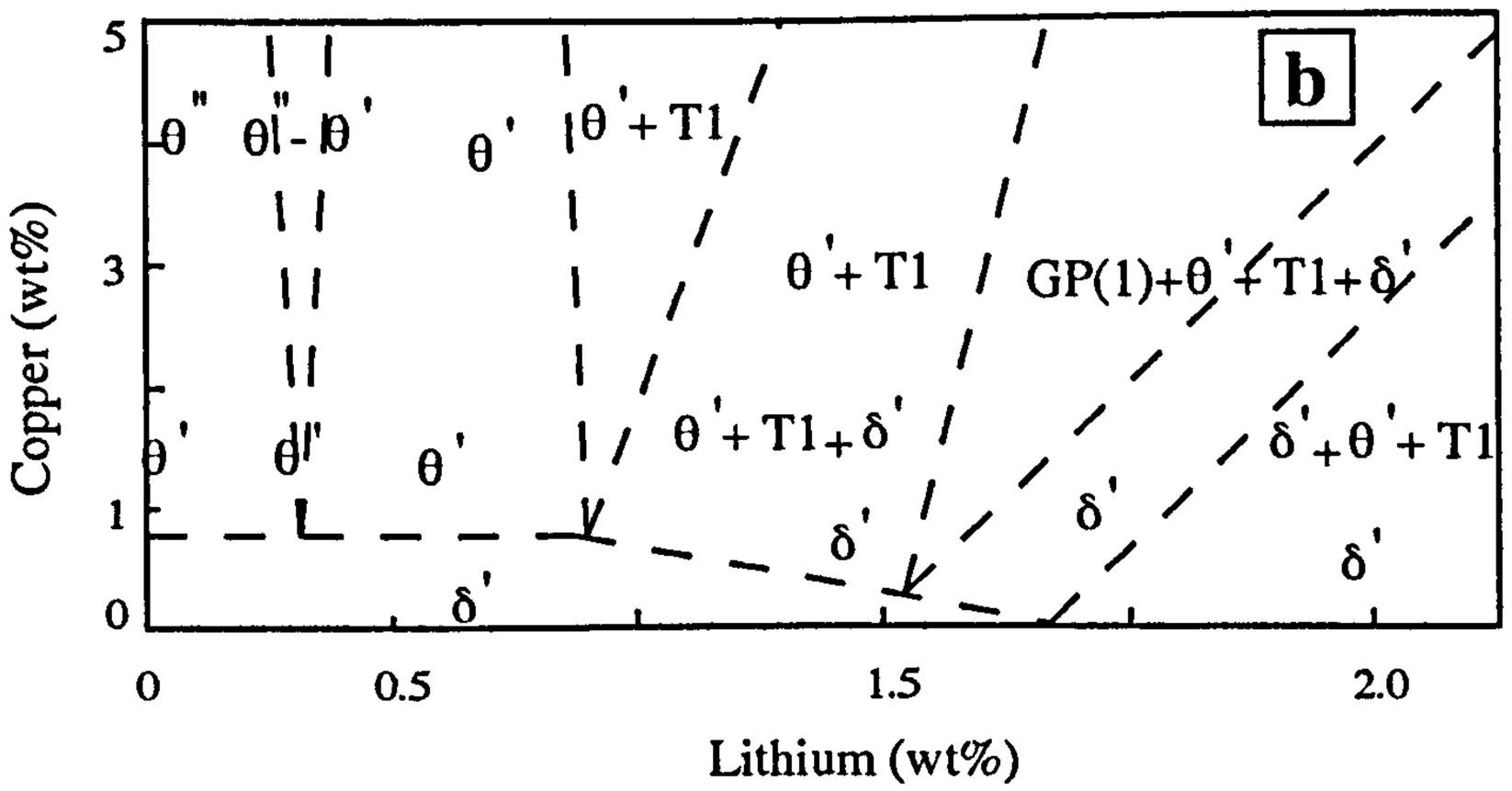


Fig 2.1.2 (a) Isothermal section of the phases present at 350°C in the Al-Li-Cu system.
(b) Representation of the phases identified by Silcock after ageing for 16 hours at 165°C.

2.2 Mechanical Properties of Lithium Bearing Aluminium Alloys

The mechanical properties of any material will depend upon the microstructural features and the intrinsic nature of the matrix. Aluminium lithium alloys have the potential for high yield strengths, combined with low densities and high moduli[1][2]. Their fracture toughness values, however, are low, and their anisotropy in properties developed after working, can be high.

The main microstructural features that will affect the mechanical properties of an 8090 aluminium alloy are as follows:-

(1) Fine precipitates.

These precipitates form as a result of age hardening. The most important of these phases, with regard to the effect upon mechanical properties, is δ' (Al_3Li), which is a major contributor to strength within the 8090 alloy.

Other phases which precipitate out upon heat treatment and affect mechanical properties include S (Al_2CuMg), T_1 (Al_2CuLi) and I (Al-Cu-Li) phases.

(2) Dispersoids.

Al_3Zr dispersoids form in 8090 alloys[3]. They are stable at the alloy solutionising temperature and are present in order to retard recrystallisation and grain growth.

(3) Coarse intermetallics

These phases contain impurity elements such as iron and silicon and form during ingot solidification. These phases may survive homogenisation treatments to a certain degree, due to the low diffusivities of their constituent elements, resulting in their appearance as stringers in the final wrought product[5][6].

(4) Texture.

Texture has been shown to be more pronounced in aluminium lithium alloys compared with other common aluminium alloys. As a result the effect of texture upon properties is considered to be of considerable importance in Al-Li alloys, especially when combined with their propensity for coplanar slip[7][8].

(5) Grain and subgrain size and shape.

The grain and sub-grain structures present within a material affect the yield characteristics and the work hardening capacity of the material. Consequently the yield strength, ultimate tensile strength and fracture toughness values will be affected.

2.2.1 Tensile Properties

The tensile properties of any material are dependent upon the way in which the material deforms in the absence of macroscopic cracks. The microstructural features of

interest when considering tensile properties are those which interact with dislocations to a significant degree, thereby modifying the slip and the stresses required for slip.

For the aluminium 8090 alloys considered in this project, there are several mechanisms of strengthening, which may operate[4][9][10].

(1) Solid solution strengthening - due to Li, Cu and Mg in solid solution.

(2) Precipitation strengthening caused by δ' (Al_3 Li), S (Al_2 CuMg) and T_1 phases.

(3) Dispersion strengthening as a result of Al_3 Zr dispersoids.

(4) Grain or subgrain boundary strengthening.

Miller et al [9] considered the various contributory factors defining the overall strength of aluminium lithium alloys. δ' was accepted as the main strengthening phase, but the importance of substructure was also clearly shown. He concluded that substructure did not only provide intrinsic strength, but also provided a high density of nuclei for the precipitation of S and T_1. This dependence of strength upon substructure meant that recrystallised structures were considered unable to achieve the same strength levels as unrecrystallised material, unless the material had a very fine recrystallised grain size.

In commercial 8090 alloys, the strength contributions made by various mechanisms has also been summarised as follows [10] :- In underaged tempers, δ' precipitation and solid solution hardening govern the matrix strength, whereas in the peak temper, strengthening by δ' and S is dominant. The contribution to strength from the presence of Al_3 Zr is considered small, owing to its small volume fraction. It has been reported, however, that the Al_3Zr precipitates affect mechanical properties by reducing particle shear, and strengthening precipitate free zones within the alloy [4]. The contribution to strength of other ageing phases, such as grain boundary I phase or the coarse intermetallics, are also not of great importance with regard to dislocation hindrance. These phases do cause stress concentration and lower the resistance of the inter-granular region to crack propagation, however, and hence affect the ultimate tensile strength and strain to fracture.

Since precipitation hardening due to δ', S and T_1 is of such importance, this mechanism of strengthening will be now discussed in more detail.

Precipitate Strengthening

When dislocations interact with precipitates there are a number of mechanisms, which may contribute to strength:- (a) Coherency strengthening.

(b) Surface strengthening.

(c) Modulus hardening

(d) Order hardening.

(e) Stacking fault strengthening.

(f) Orowan strengthening.

(a)->(e) apply for shearing of precipitates, whereas (f) applies when the precipitates are by-passed.

The most prevalent precipitate in aluminium lithium alloys is the δ' phase[11][12] . These precipitates have a high lattice coherency with the matrix, and as such are sheared by dislocations. Not all of the above mentioned strengthening mechanisms associated with shearing of particles have, however, been found to be important with regard to the shearing of δ'.

Huang[13] and Froaomeni[14] showed coherency and surface strengthening components to be negligible. Order and modulus strengthening mechanisms, however, were found by Noble et al[1] and Jensrud[15] to be the dominant mechanisms in a binary alloy near peak temper. Sainfort and Guyot[16] , Huang and Ardell[17][18] and Fragomeni[14] also concluded order strengthening to be the most dominant strengthening mechanism.

Coherency Strengthening:- This strengthening mechanism arises due to misfit strains between precipitate and matrix. Many researchers[1][13][15][16][19][20] have reported that the contribution of coherency strengthening to the critical resolved shear stress (CRSS) is relatively small. This is a consequence of the small misfit strain between the δ' and the matrix, which has been reported[21] as being ε=0.08 (0.02%).

Ardell modelled strengthening based upon coherency strengthening. This model worked well when the precipitates were small, and only interacted weakly with edge dislocations, but was inaccurate when the particles were larger and caused substantial bending of the dislocations, as is the case in Al-Li alloys.

Surface Strengthening:- When the precipitates are sheared there is an increase in surface area of the particles, hence an associated surface energy which must be overcome by the dislocations. Brown and Ham[22] analysed this strengthening mechanism, and by using an interfacial energy of γ_S =0.014 J/m^2 [23] , found only a 1MPa increase in strength.

Modulus strengthening:- This strengthening mechanism arises from the fact that the matrix and precipitate have different shear moduli, hence the dislocations will have different strain energies depending upon their situation within the matrix or precipitate. Kelly and Nicholson [24] have attempted to model this strengthening mechanism, but the accuracy was doubtful.

Order Strengthening:- This mechanism of strengthening arises in ordered lattice structures, due to the movement of a dislocation causing the formation of an anti-phase boundary. In reality unit dislocations move as superlattice dislocations in ordered

materials . In this arrangement of paired dislocations, one dislocation creates the anti-phase boundary and the subsequent dislocation restores the ordered lattice.

Brown and Ham[22] and Raynor and Silcock[25] developed models which predict the contribution to strength, due to order hardening.

$$\tau \alpha \gamma_{APDB}^{3/2} r^{1/2} f^{1/2}$$

τ = Shear flow stress γ_{APDB} = The antiphase boundary energy,
r= The precipitate size, and f = The volume fraction of precipitate

Orowan Strengthening:- As ageing proceeds the precipitates grow, resulting in a decrease in the stress required to cause dislocations to loop around the particles. Eventually the Orowan looping mechanism becomes the dominant strengthening mechanism. Many researchers have developed models for Orowan looping[26][27].

The above are the various strengthening mechanisms which occur in aluminium binary alloys, and in quaternary alloys due to the precipitation of δ'. Other precipitate phases of prime importance are S (Al_2 CuMg) and T_1 (Al_2CuLi) . The balance between S and T_1 precipitation is dependent upon the relative concentrations of lithium, magnesium and copper. High copper and lithium contents relative to magnesium result in a dominance of T_1 , whereas high copper and magnesium relative to lithium produce a dominance of S.

The contribution to strength attributable to the presence of T_1 precipitation within different Al-Li-Cu-(Zr) alloys has been reported[35][36][37] to be considerably greater that that of δ'. The T_1 phase has an hexagonal structure and forms as thin platelets parallel to the{111} planes within the aluminium matrix. Direct evidence has shown that the T_1 precipitates are sheared by dislocations, but the tendency for strain localisation, due to work softening on the dislocation glide plane is reduced when T_1 is present. This is due to the increase in lattice misfit and differing internal structure of the T_1 compared with δ' [40].

The S contribution to the hardness of Al-Cu-Mg alloys has been analysed by Silcock[38], who demonstrated an increase in yield strength as the S phase formed.

S precipitates do not have any densely packed slip planes parallel to the matrix slip planes and as a result they resist shear by dislocations[41], thereby promoting cross-slip. Crooks et al [42] and Crooks and Starke[43] have clearly shown that when S is present in Al-Li-Cu-Mg alloys strain localisation is suppressed.

2.2.2 Fracture Toughness

The fracture toughness of a material is its ability to resist the unstable growth of flaws, with this ability depending upon the crack growth energy requirements.

The energy requirements for crack propagation will depend upon:-

(1) The character of the crack (fast/slow, sharpness, size and shape).

(2) The energy requirements associated with the straining necessary to operate the micromechanism of failure.

Appendix I illustrates how a toughness parameter can be developed from the stress distribution ahead of the crack, with the stress state at failure depending upon:-

(1) Applied stress.

(2) Crack configuration-sharpness, shape and size.

(3) Stress State.

(4) Deformation characteristics of the material.

The resulting equation from this development[55] is shown below:-

$$K=C\sigma\sqrt{\pi a} \qquad \text{.....} \quad 2.2.1$$

K = Stress Intensity factor

σ = applied stress

$C=f\left(\frac{a}{w}\right)$ = This is a dimensionless parameter that depends upon the geometry of the specimen, w, and crack size, a.

Even though the equation above does not show any obvious relation to microstructure, deformation characteristics which are controlled by microstructure, have been included in the list of factors controlling the stress distribution ahead of a crack at failure. The deformation characteristics of the alloy will determine the micromechanism which is activated first during crack propagation, and also the path that the crack follows. Essentially, therefore, this factor is responsible for the applied stress necessary for a given crack to grow under a given stress state, and as such influences equation 2.2.1.

In aluminium alloys the failure mechanism is usually microvoid coalescence. In this mechanism voids nucleate at various internal discontinuities and as the local stresses increase the microvoids grow, coalesce and eventually form a continuous fracture surface[29] . The important factor for crack growth is, therefore, the attainment of a critical amount of strain on a local scale.

The local strains necessary for crack propagation will depend upon microstructural inhomogeneities. The local stresses required in order to produce these local strains will depend upon the yield character of the material, and the stress concentration factors will

determine the applied stress necessary to produce these local stresses. The microstructural factors of interest when considering fracture toughness in 8090 alloys are, therefore, as follows:-

(1) The factors affecting strain requirements for microvoid coalescence:-

(i) The distribution of particles at which void formation occurs.

(ii) The ability of the particles and their interfaces with the matrix, to resist cleavage and/or decohesion.

(2) The factors affecting strain concentration phenomena:-

(i) Coplanar Slip- δ' precipitates.

(ii) Grain size.

(iii) Precipitates that may disperse slip (S and T_1 phases).

(iv) Precipitate free zones (P.F.Z.'s).

(v) Texture.

(3) The factors affecting the yield stress of the material:-

(i) Precipitates- δ', S, T_1 .

(ii) Subgrain/grain size.

(iii) Texture.

The various factors affecting toughness will now be considered in more detail.

Factors Affecting Fracture Toughness

Coplanar slip due to δ':- Upon quenching, after extrusion or solution treatment, a uniform distribution of spherical δ' precipitates out[30] . The volume fraction of these precipitates then increases during subsequent ageing up to the peak aged condition.

The δ' has an ordered lattice structure, which has very similar lattice parameters to that of the matrix[11] . As a consequence, small δ' precipitates (50->200nm) are easily sheared by dislocations. After being sheared by a dislocation subsequent dislocation movement through the precipitate is facilitated and intense coplanar slip develops.

The process of coplanar slip gives rise to regions of intense shear, which in turn produce high strain and stress concentration levels at grain boundaries. The stress concentration at grain boundaries encourages the breakdown of the inter-granular region, resulting in an inter-granular failure[31][32][33] .

If the grain boundary strength is high or the textural systems present within the material are such that grain boundary stress concentration is reduced, breakdown of the shear region itself may occur before grain boundary failure. This results in a transgranular rather than intergranular fracture path. Coplanar slip may, therefore, encourage intergranular or transgranular failure, depending upon the texture present, the grain boundary strength and the ageing condition of the material.

Severe coplanar slip is a phenomenon which highlights weak points within the material and thereby decreases toughness. Consequently the prevention of coplanar slip would be desirable. Increase in the matrix/δ' misfit energy (discourages particle shear) or the use of additional precipitates to disperse the slip, may reduce coplanar slip.

The method of using a second precipitating phase, such as S (Al_2 CuMg) has been shown to improve the fracture toughness by increasing the total deformation associated with failure[57]. Unlike δ' and T_1, S phase has an open packed structure, hence there are no uniform densely packed potential slip planes which lie parallel to the matrix slip planes. The laths of S phase are, therefore, unlikely to be penetrated by dislocations. This encourages dislocation bowing and thereby increases the local work-hardening rate, preventing the development of bands of coplanar slip. In Al-Cu-Mg alloys considerable S phase precipitation could be achieved by precipitation upon dislocation loops and helices. In lithium containing alloys, however, the concentrations of loops and helices is low, due to the relatively high vacancy-lithium atom binding energy-(0.25-0.03ev)[16]. This inhibits the formation of helices and loops, thereby reducing the opportunity for S phase precipitation. Gregson and Flower[65] carried out experiments upon 8090 rolled strip in order to investigate the effect of S phase precipitation upon fracture toughness. They observed a change in the failure mechanism from one of transgranular planar slip to intergranular failure, which was associated with the inhibition of coplanar slip by the non-coherent S phase precipitation.

Preferential deformation in Precipitate Free Zones:- In aluminium alloys, where the grain boundary precipitates are formed from the same solute additions as the matrix precipitates, the existence of precipitate free zones (PFZ's) is inevitable. P.F.Z.'s have been reported in 8090 alloys, with the PFZ formation being explained by vacancy and solute depletion.

The PFZ is considerably softer than the surrounding material owing to the lack of strengthening precipitates. As a result the plastic flow is concentrated in this region causing grain boundary stress concentration.

Roven and Starke[53] produced a PFZ free microstructure in a pre-stretched 8090 alloy by lowering the ageing temperature to 121° C. This PFZ free microstructure contained only δ' precipitation, due to the low ageing temperature and was found to exhibit a higher strength, ductility and work hardening capacity.

Precipitation of Grain Boundary Phases:- Many researchers have found that grain boundary precipitation affects the toughness of aluminium alloys[45][51]. Vasudevan and Doherty[44] carried out reversion experiments with Al-Li alloys, and distinguished two different reasons for the reduction in toughness from the underaged to overaged condition.

(i) The increase in planar slip associated with the increase in the amount of δ' phase.

(ii) The increase in the size of the grain boundary precipitates.

The surface slip markings observed within this analysis, suggested that slip was initiated at the large grain boundary δ precipitates, and Vasudevan and Doherty showed that if the area fraction of large stable precipitates was increased, whilst maintaining the same matrix structures and yield strengths, the toughness decreased. Intergranular failure was identified from the fracture surfaces, which showed dimples with spacings approximating to that of the grain boundary precipitate separation. This type of failure was termed grain boundary ductile failure (G.B.D.F), with the incidence of this type of failure increasing from the under to overaged condition.

Vasudevan and Suresh[45] have observed an intergranular failure in high purity Al-Li-Cu-Zr alloys, that was controlled by T type (Al_x Cu_y Li_z) grain boundary phases. Suresh et al[46] also showed that in combination with coplanar slip, void formation around δ and T_2 particles caused reductions in toughness. Colvin and Starke[50] also concluded T_2 precipitation to be directly correlated with a decrease in toughness.

In Al-Li-Cu-Mg-Zr alloys Mukapadyay[5] has reported precipitation of C type phase (Al-Cu-Mg) at grain and subgrain boundaries with no δ present. Owen [6] has also reported no δ phase in such alloys, but instead an icosohedral phase was observed to be the major grain boundary precipitate, and responsible for both the δ' PFZs and embrittlement of the grain and subgrain boundaries. Cassada et al[66] have also shown that in Al-Li-Cu alloys aged at 190°C or higher, rather than the δ phase, a T_2 (Al_6CuLi_3) [icosohedral(I phase)] was present at the grain boundaries.

It is obvious from these analyses that grain boundary precipitation is a major problem with regard to toughness, especially when combined with the stress concentration phenomenon occurring within lithium bearing aluminium alloys.

A number of techniques have been employed to reduce grain boundary precipitation. A low ageing temperature, below 150° C has been found by Lewis et al[47] to produce the required precipitation in heavy section forgings of AA8090 without extensive T_2 precipitation at grain boundaries. A pre-ageing stretch has also been found to accelerate the matrix ageing kinetics, by providing heterogeneous nucleation sites for T_1 and S, without affecting grain boundary precipitation[48][49].

Grain Structure and Texture:- The combination of grain structure and texture can alter the slip length within any material. Larger grain sizes will increase the slip length and the presence of intense texture systems can cause the subgrains to exhibit low misorientations. These changes in slip length will affect stress concentration levels, hence the applied stress levels associated with the failure mechanism, and consequently toughness values. In 8090 aluminium lithium alloys, however, zirconium, is present in order to act as a grain refiner and recrystallisation inhibitor[3][64] . The hot worked microstructures, therefore, usually consist of highly elongated grains aligned in the

extrusion direction. This fibering of the microstructures then causes high levels of anisotropy, with S-L and S-T orientations displaying much lower toughness values than L-T orientations[51]. Recrystallisation will occur in selected localised areas, however, due to the absence of Al_3 Zr dispersoids or favourable localised conditions of strain, strain rate and temperature. This recrystallisation will then modify the average grain size and in itself affect toughness.

Peel et al [52] suggested that the optimum grain structure for improved properties depends upon the stress state to which the material will be subjected. Under plane stress conditions (thin sections) fracture is controlled by the plastic deformation occurring within the large plastic zone. A fine recrystallised grain structure would, therefore, generate maximum strains to failure. Under plane strain conditions, however, failure initiates at the weakest feature ahead of the crack tip, therefore a large grain size would be preferable in order to improve toughness.

In practice, sheet products are most often supplied with a fine, recrystallised grain structure, while plate material exhibits a large unrecrystallised grain structure.

With regard to texture present within these alloys, researchers such as Tempus et al [54], have shown that in axi-symmetric bar extrusions a pronounced <111> + <100> double fibre texture existed, consisting of 75% <111> and 22% <100>, whereas in slab bar extrusions a texture system similar to that found in rolling (Brass, S and copper components) was observed. By comparison of property values, the strength levels were found to increase and elongations to decrease, as the texture changed from double fibre to rolling type. The textures present within the material will, therefore, affect not only the material response to applied stress, but also ductility, and hence toughness.

Constituent Phases:- These coarse intermetallic compounds, consisting of impurity elements, form during ingot solidification and appear as stringers in the final wrought product. Owen [6] showed that in Al-Li-Cu-Mg-Zr alloys these intermetallic particles are fractured by coplanar slip impingement, causing void formation and premature intergranular failure, hence low material toughness. The stringers, along with the elongated grains, cause anisotropy in tensile and toughness properties. Tensile properties, notably ductility, are greatest in the longitudinal direction and least in the short transverse direction. The amount of intermetallic phases containing iron and silicon can be reduced by decreasing the iron and silicon content of the material. The limit to which such elements can be realistically reduced is 0.1wt%, but major improvements in fracture toughness have arisen, due to control of these impurity elements [63].

Dispersoids and Tramp Elements:- Al_3Zr (β') precipitates are present within commercial 8090 aluminium alloys in order to impede recrystallisation and grain growth[56]->[61]. They range in size from 0.05->1μm, but since they encourage δ'

precipitation[62] , may occur as composite precipitates, where they are coated in δ'. Owing to their limited size, coherency and distribution, Al_3 Zr particles do not participate directly in the fracture process.

Many researchers have shown that poor fracture toughness can be as a result of tramp elements, such as sodium, potassium and Sulphur, segregating to grain boundaries[53] . As a result of these studies standard commercial practice is to minimise such impurities.

2.3 Textural Systems of Wrought Aluminium Lithium Alloys

2.3.1 Texture Representation

The basis for texture analysis is a desire to determine the preferred orientation of grains within the material with respect to some pre-determined set of axes. One way to perform texture determination would be to analyse each grain individually and determine crystal orientations from diffraction patterns. This would give a microscopic texture determination. Pole figure analysis[1], however, is a method in which texture determination is carried out on a much more macroscopic level. A pole figure is a stereographic projection of the poles of specific planes and illustrates graphically the orientation of grains with respect to reference axes. These reference axes are related to the worked material section and are usually the longitudinal, transverse and short transverse directions. Actual pole figure production involves the alignment of an x-ray generator and detector at the precise Bragg angle for a given set of planes eg{111}. The sample is then rotated in 3 dimensions and the orientation of the specific planes calculated. The poles of the planes, together with the diffraction intensities, are then plotted giving a complete picture of the orientation of one set of planes within the sample. A draw-back to pole figure determinations is that the poles of one plane orientation may overlap with that of a another plane orientation - a problem which is most acute when complex, rather than ideal, texture systems are present. In order to determine the texture of a material precisely, therefore, a number of pole figures need to be produced and analysed in relation to each other. A technique in which the data from a number of pole figures is combined into a single set of output data involves the orientation distribution function (O.D.F.)[2][3]. In this technique several pole figures are produced and mathematical models are then used in order to combine the data and show graphically the grain orientations.

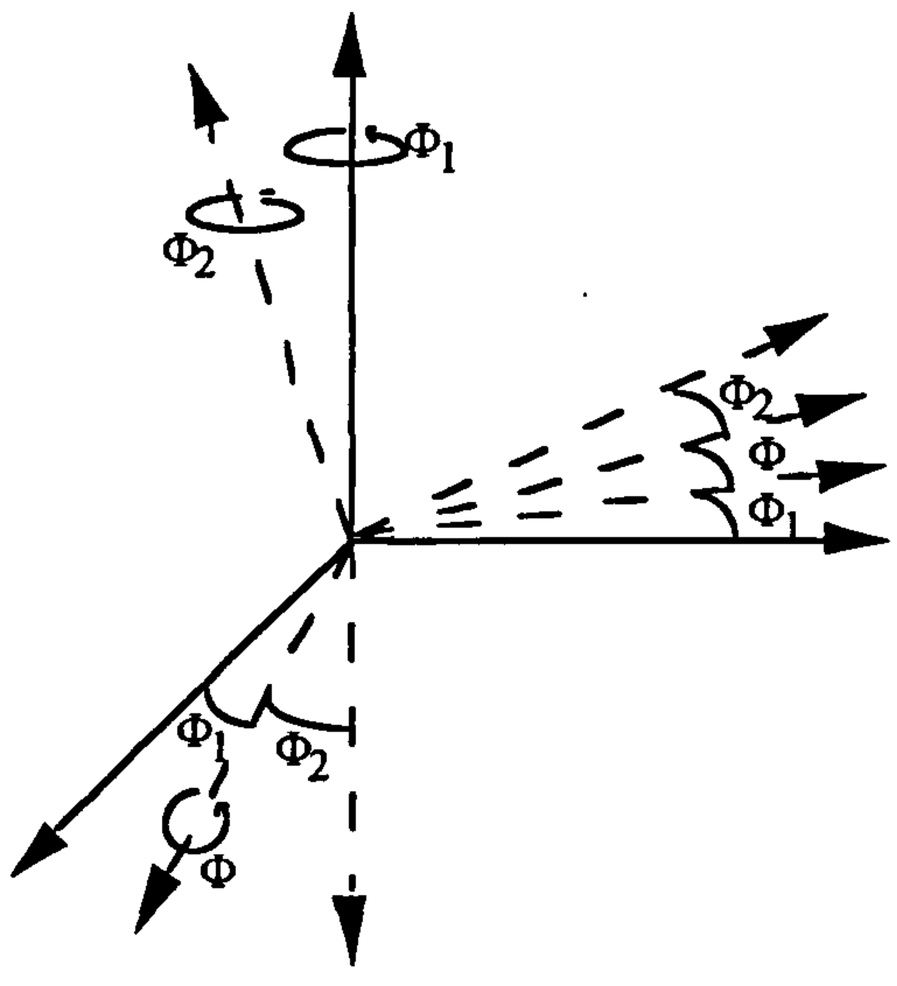


Fig 2.3 - Angles associated with texture representation according to Bunge notation

In O.D.F. analysis the orientation relationships between two sets of orthogonal axes are determined. One set of orthogonal axes is related to the crystal lattice and one set to the sample section. The angles of rotation necessary to cause coincidence of these axes are then determined, with each unique set of three rotation angles -Euler angles- corresponding to a specific lattice orientation. The two main O.D.F. analysis systems are due to Bunge and Roe[3][10] . The basic idea is identical in each case, with differences occurring only in Euler angle definition. In this project Bunge's notation is used and is shown in the figure 2.3. Bunge uses rotation angles of Φ, Φ_1 and Φ_2, crystal orientations represented by the three cube axes <100>, <010> & <001>, and specimen orientations of longitudinal, transverse and short transverse directions.

There are problems associated with O.D.F. analysis, which arise from experimental limitations and subsequent analysis, but these have been generally resolved and O.D.F. can be used as a very precise technique for measuring texture.

2.3.2 Wrought Aluminium Textures Systems

The development of deformation textures depends upon the shape changes imposed by the tooling and the modes of shear deformation operating in the individual crystals. As such, therefore, different texture systems are associated with axi-symmetric extrusions and rolled material.

Extrusion Textures

Fibre textures are formed during deformation processes which produce uniaxial strain. Axi-symmetric extrusion textures in F.C.C. metals are reported as having double fibre textures with some grains having <111> directions and others <100>, directions parallel to the deformation axes[5][8][11][12] . It has been reported[5] that (i) Hibbard considered the <111> to be the true end texture and that <100> results from recrystallisation during deformation, (ii) Roberts and Butt considered the <100> texture component to arise from the <115> component by deformation after recrystallisation and (ii) McHague considered that the elastic stresses during deformation favoured the formation of <100> recrystallisation nuclei. Both Roberts and Mc Hague, however, demonstrated that the <100> components had lower dislocation densities than the <111>, hence may be associated with recrystallised grains rather than deformed grains.

In super pure aluminium extrudates exhibiting <111> and <100> textures, it has been reported[5] that Gow and Cahn found recrystallisation to produce a minor <111> component and a major component with a range between <103> and <113>. They were able to show (through etch pit methods) that the minor <111> recrystallisation component arose from the <111> deformation component and was related by a 46° rotation about the common <111> pole. Components in the <103> -> <113> range

were derived from both the <111> and <100> components by rotation about the non-axial <111> poles. In the case of <111> deformation component 46° rotations took place, whereas 22° rotations occurred in the <100> component.

Rolling Textures

For deformation at low strains, the main feature of F.C.C. rolling textures are α and β fibres [4][6]. The α fibre is a range of orientations from Goss {011} <100> -> Brass {011} <211> -> {011} <011>. The β fibre is the range of orientation components from copper {112} <11-1> -> S {124} <21-1> -> brass {011} <211>. As the strain increases the α fibre breaks down into a major component of brass, together with a scatter towards Goss. The β fibre, however, develops maxima at some or all of the ideal components of copper, S and brass.

Two theories by Taylor and Sachs have attempted to model deformation behaviour, hence have been used to model texture formation. Taylor assumed that each grain strains equally and undergoes multiple slip i.e a specific shape change is assumed, and that in order for this shape change to occur five independent slip systems are considered to operate (the five slip systems with the lowest Schmidt factor), with the Taylor factor being defined as the combined ratio of the resolved shear stress to the applied shear stress for all of the operating slip systems. Sachs, however, assumed each grain to be stressed equally and to undergo single slip i.e. the Sachs theory predicts that slip will occur upon the close packed planes with the highest Schmidt factor (ratio of the resolved shear stress/axial stress).

Full constraint, and relaxed constraint Taylor models[13]->[17], successfully predict the development of the β fibres, and its three main components, during deformation. Whereas the Sachs model predicts the development of strong brass components.

Not only have these models been shown to predict the change in grain orientations towards given stable texture systems as deformation occurs, but they also predict the rapid movement towards these orientations as deformation commences together with the progressive slowing down of this movement as deformation continues.

When considering texture development, however, not only must the deformation texture be considered, but also recrystallisation textures. Recrystallisation may occur concurrently with deformation, or subsequent to deformation in a separate annealing process. In either case, however, if a given texture component is enhanced by recrystallisation it can only be explained by the preferred formation of recrystallisation nuclei with this enhanced texture, or the preferred growth of recrystallisation nuclei with this enhanced texture.

With regard to the growth of the recrystallised grains, it is possible to define the kinetics of the process by an Avrami equation [7]:-

$$x=1-\exp(-Kt^{\beta})$$

x= Volume fraction of recrystallised material, t= time.
K and β = constants characteristic of the process.

This type of equation - modified to include an incubation time- can then be used in order to describe the development of texture components [9].

$$I(t) = I\infty - (1 - I_o) \exp [-K (t - t_o)^{\beta}]$$

Io and I∞ are measured intensities at time zero and infinity, t_o= Incubation time.

For pure aluminium, cold rolled (90%) and subsequently annealed, researchers[7][9] have predicted texture development during the annealing stage by utilising the above equations. They observed an incubation time of 11 ±2 mins for the cube grains, whereas for the grains with random texture, no incubation time was found necessary. It was also observed, however, that the cube grains grew faster than the grains with random orientations. There was, therefore, a significant volume fraction of cube-orientated grains in the fully recrystallised sample, even though there were approximately fifty times as many grains of random orientation. These results consequently indicated that the preferred growth scenario was most likely responsible for the observed correlation between cube texture and recrystallisation.

With regard to 8090 material, rolling processes and asymmetric extrusions have been observed to produce combinations of rolling ({112} <111> copper texture, {110} <112> brass texture and {124} <211> S texture), and cube textures, with the cube orientations being related to recrystallisation. In axi-symmetric extrusions the double fibre texture system has been observed, with the occurrence of cube texture again being associated with recrystallisation. In both cases, however, no conclusions concerning whether preferred nucleation or preferred growth was responsible for the cube texture-recrystallisation relationship have been developed.

The type of texture systems present within any worked material will depend upon the pre-existing, deformation and recrystallisation textures. If grain refining additions are used, the as-cast ingots of aluminium usually possess random texture. (If not, columnar grains will form orientated with the <100> direction parallel to the casting direction). The factors producing the type and proportions of the texture systems observed within the 8090 extruded and rolled material, as stated above, will, therefore, depend upon:-

(i) The strain fields associated with the specific deformation process, and the modes of shear deformation occurring in order to accommodate this strain.

(ii) The mechanism of recrystallisation (subgrain rotation or grain boundary bulging), and the factors affecting the % of recrystallisation (dispersion forming elements, precipitation, second phase particles), which are discussed further in section 2.4.

2.4 Hot Working Process

When considering heat treatable alloys, the variables which may be altered in order to modify the microstructure, hence properties, are:-

(i) Composition.

(ii) Heat treatment schedules.

(iii) Processing conditions (strain, strain rate and temperature).

In this project the effects of changes in extrusion processing conditions upon microstructure and properties were investigated.

Microstructural variations were not only observed between extrudates subjected to different processing conditions, but due to variations in strain, strain rate and temperature within the extrusion deformation zones, transverse and longitudinal variations in microstructure were also observed within each extrudate. Complete deformation analysis of each extrusion would, therefore, be necessary in order to provide complete explanations for the observed variations in microstructure and properties within and between extrudates.

2.4.1 Analysis of Metal Forming Process

The complete analysis of a deformation process would involve determination of strain, strain rate, flow stress and temperature distributions throughout the deformation zone. In order to accomplish this task, therefore, the physical limits imposed by the tooling boundaries, together with plastic theory related to the deformation of the material, must be considered simultaneously.

Complete explanations of deformation analysis can be found in may text books, but a brief outline of the basic concept is set out below.

From the solution of static stress equilibrium equations[1]-[7] , yield criteria[1]-[7] and stress boundary conditions imposed by the tooling, stress distributions associated with the deformation process can be developed. In order to then relate these stresses to resulting strains it is necessary to utilise constitutive equations. In 1871 Levy and later Von Mises proposed that the increments of plastic strain were related to the stress deviators[1][11] . In addition Von Mises also proposed a constitutive equation which described the behaviour of metal in the plastic range[1] , and related stresses with strain rates. Both of these constitutive equations can, however, be used to relate the stresses associated with deformation to the resulting distortions of the material. Velocity fields can then be developed from the strain rate distributions, but the law of incompressibility must be obeyed, as well as the conditions imposed by the tooling.

For solution of plastic forming processes, therefore, the following equations must be solved simultaneously:-

(1) Stress equilibrium equations

(2) Stress boundary conditions (tooling boundary conditions for stress)
(3) Yield criterion (the stress condition necessary for yield)
(4) Stress/strain or stress/strain rate constitutive equations (relationship between the stresses and resultant distortions)
(5) Velocity field equations (i) Linear velocity field.
(ii) Continuity equations obeyed (incompressibility).
(iii) Tooling boundary conditions upon velocity.

One additional problem at this point is that the flow stress of the material is a function of microstructure, strain rate, and temperature. The specific flow stress used in the yield criteria must, therefore, be representative of the prevailing local conditions.

Even though the complete analysis of the deformation process is very complex, finite element analysis is a technique which can be used to supply a complete solution for the deformation process. Appendix III highlights the basics of a finite element analysis as carried out in this project. There are also a number of theories and techniques available in which the analysis process is simplified, making solutions more easily attained. Two such examples are:-
(1) Upper bound techniques
(2) Visioplasticity

The simplification associated with these techniques makes the analysis of the deformation process easier, but does create limitations in the accuracy and extent of the information obtainable.

Upper Bound Technique

In the upper bound technique an assumed kinematically admissible velocity field is constructed. No attempt, however, is made to satisfy the stress equilibrium equations at any point in the field. From this situation, numerous expressions for processing requirements can be formulated[1][7]. Even strain, strain rate and stress distributions can be produced[1]. The more representative the assumed velocity field is of the practical situation, the more accurate are the results obtained from subsequent analysis.

Since die cone angle variations during processing are of interest in this project a brief outline of some results obtainable from an upper bound analysis of the kinematically admissible velocity field shown in fig 2.4.1, are outlined below:-

BIBL. LONDIN. UNIV.

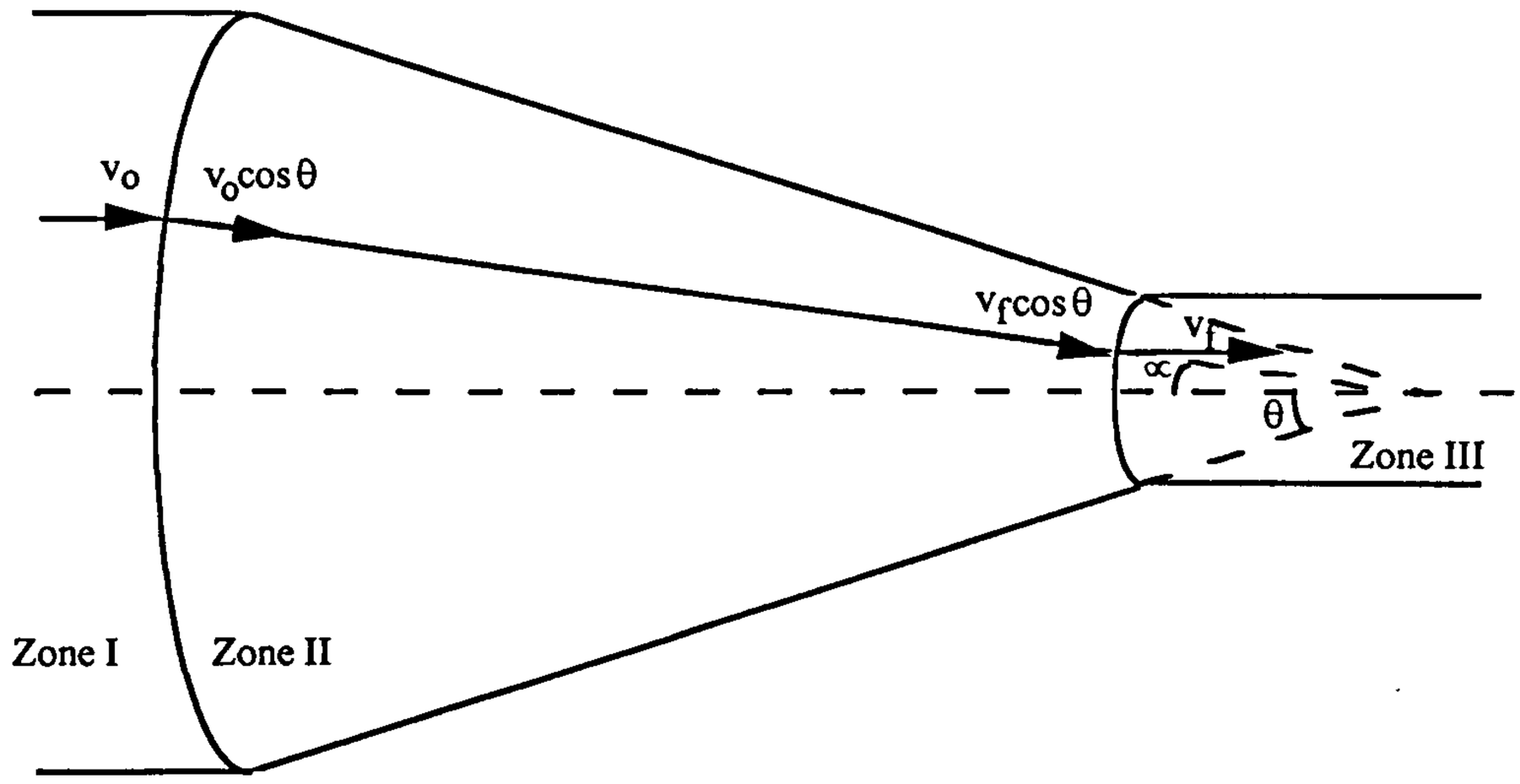


Fig 2.4.1. Kinematically admissible velocity field.

The velocity field above, has three regions in which the velocity is continuous. In zones I and III the velocity is uniform and only has axial components of v_o and v_f respectively. In zone II the velocity is directed towards the apex of the cone.

Using the assumed velocity field and considering ideal deformation energies, together with energy absorption at velocity discontinuities, it is possible to derive an expression for the extrusion load[1] . Fig 2.4.2 represents schematically the variation in extrusion stress with cone angle predicted by this expression.

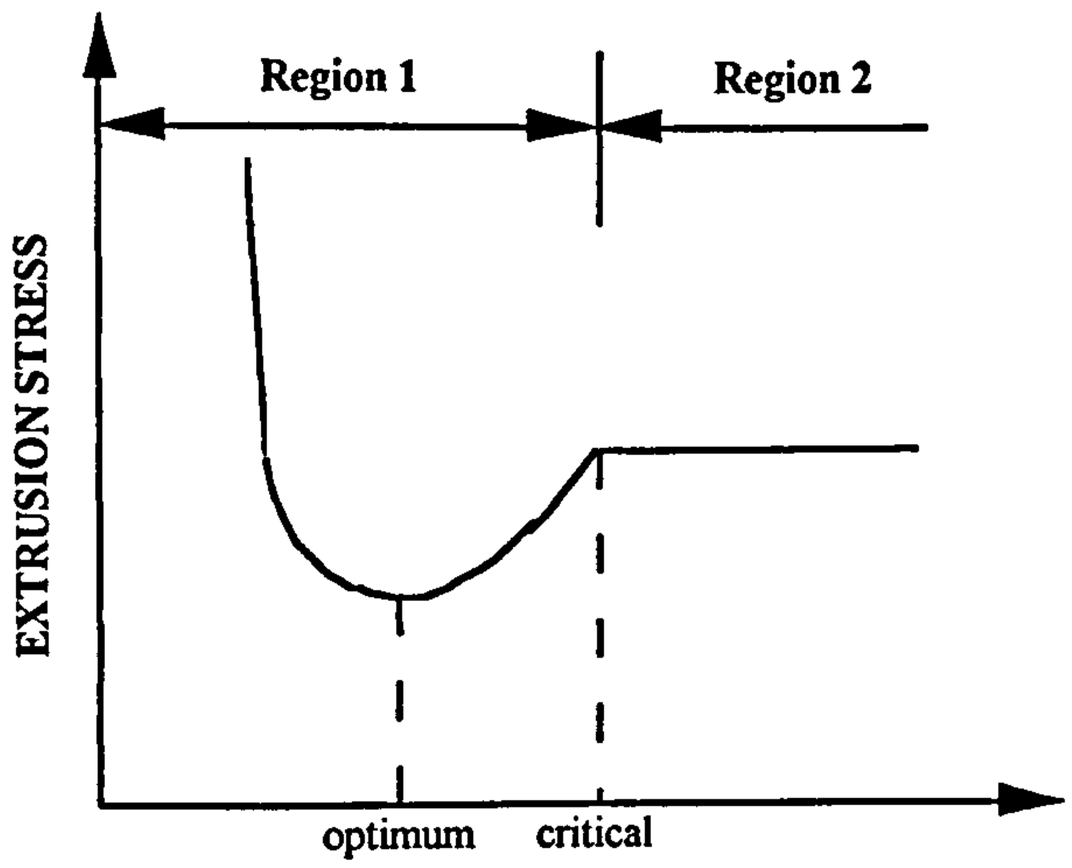


Fig 2.4.2 :- Variation in extrusion stress with increases in die cone angle.

In region I the cone angle is small, and as a result the contact surface between the material and the die is large, giving rise to high frictional forces and high extrusion loads. As the cone angle increases the frictional forces decrease, but the distortion of

the material increases, thereby increasing the work of deformation. There is, therefore, an optimum cone angle, where a minimum combination of frictional work and deformation is achieved, resulting in a minimum extrusion load.

As the cone angle increases, flow around the periphery of the deformation zone becomes more and more difficult until eventually the shear stresses developed within the material exceed the shear yield stress of the material and a dead-metal zone is formed. This upper bound approach predicts that the dead metal zone formation will occur at a constant cone angle. Once this critical cone angle has been reached, therefore, the extrusion pressure will no longer increase with increasing cone angle - as is shown in region II. The critical die cone angle is defined as the angle which just prevents dead zone formation and varies with the conditions of extrusion as follows [1] :-

(1) As the reduction increases the critical cone angle increases.

(2) As the friction between the material and die decreases the critical cone angle increases.

(3) The critical cone angle is always less than 90°. Only if the reduction approaches infinity will the critical cone angle approach 90°, thus for square faced dies (α=90°), and for a finite reduction, a dead metal zone will form at an angle less than 90°.

The above discussion has shown how useful this type of analysis can be for determining processing requirements and has highlighted economic reasons, which have to be considered when the suitability of varying cone angle in order to improve properties is investigated. Economic reasons may be outweighed by improved properties, however, therefore a more in depth analysis of the deformation process is necessary in order to understand the deformation changes occurring.

Visioplasticity

The visioplasticity approach does not develop an assumed velocity or stress field, but an experimentally found flow field is utilised. The physical laws of deformation are, therefore, automatically obeyed. In order to obtain this experimental flow field a regular grid is usually marked onto a central plane within the extrusion billet and the subsequent grid distortions analysed after deformation. The visioplasticity approach is, therefore, an empirical approach in which distortion data is found and then analysed according to assumptions of:-(i) Volume constancy.

(ii) Equilibrium equations.

(iii) Constitutive equations.

(iv) Plastic theories.

Even though a real flow field is developed, due to the numerous criteria which need to be simultaneously solved, a complete analysis of the deformation process is still very complex.

Visioplasticity analyses[1][3]->[6] have shown that there is substantial variation in strain and strain rate from the centre of the extrudate to the edge and along any given flow line within the deformation zone. These differences in strain and strain rate lead to differences in microstructure and produce anisotropic properties within the extrudate.

An outline of the visioplasticity process as carried out in this project is shown in appendix II.

Some basic methods for analysing the deformation process have been discussed above, with only brief reference to the concepts used within these analytical methods - such as ideas concerning the deformation behaviour of the material. The deformation behaviour of material during extrusion is more commonly referred to as hot working behaviour and will now be discussed in a little more detail.

2.4.2 Hot Working

During hot working, softening mechanisms counteract the strain hardening effect associated with the deformation. This allows large strains to be achieved without the need for any separate annealing stage. The temperature of such deformation is usually greater than 0.6Tm, where Tm is the material melting point in Kelvin[13] . Other benefits of hot working are the relatively low energy input required for deformation, due to the decrease in material flow stress associated with the high temperatures, and the greater compositional homogeneity within material as a result of increased diffusion. Draw backs connected with hot working, however, are the increased reaction of the material with the atmosphere, and the difference in structure, hence properties, between the centre of the work piece and the edge caused by temperature variations.

As has already been stated, a knowledge of the flow stress during deformation, is required for complete analysis of the deformation process.

The value of the mean equivalent flow stress $\bar{\sigma}_f$ will depend upon[9][12][13][14] :-

(1) The intrinsic property of the matrix, which essentially defines the Peierls Nabarro stress.

(2) The microstructure of the material. This structure factor term, S, will include all features that affect the deformation mechanism, such as dislocations, solute atoms, vacancies, grain boundaries and precipitates. Its value will depend upon the arrangement, number and distribution of these defects, and as such is dependent upon strain rate, strain and temperature $f(\bar{\dot{\varepsilon}}, \varepsilon, T)$.

(3) Strain Rate. The flow stress increases as strain rate increases.

(4) Temperature. The deformation mechanisms will be aided by thermal activation, hence the flow stress will be temperature dependent.

In its simplest form, therefore, a hot working constitutive equation, for a given material, would be as follows:-

$$\bar{\sigma}_f = f\{ S(\dot{\bar{\varepsilon}}, T, \varepsilon), \dot{\bar{\varepsilon}}, T\}$$

S = Structure Factor.
$\dot{\bar{\varepsilon}}$ = Mean equivalent strain rate.
$\bar{\sigma}_f$ = Mean equivalent Flow stress.
T= Temperature.
ε = Strain.

During hot working the strain increases, but once a critical strain has been exceeded, a dynamic equilibrium is established between work hardening and softening processes i.e. no net work hardening. The structure factor, therefore, becomes independent of further strain i.e. it is only a function of strain rate and temperature.

$$\bar{\sigma}_f = f\{(\dot{\bar{\varepsilon}}, T\} \qquad (\bar{\sigma}_f = \text{steady state flow stress})$$

Assuming that the dislocation movement processes are the same for creep and hot working, Sellers and Tegart[16] adopted the general empirical equation relating steady state creep to stress and temperature to hot working studies and produced:-

$$\dot{\bar{\varepsilon}} = A(\sinh \alpha \bar{\sigma}_f)^{n'} \exp\left(\frac{-\Delta H}{RT}\right) \qquad \text{.....2.4.1}$$

$\bar{\sigma}_f$ = Mean equivalent flow stress.
$\dot{\bar{\varepsilon}}$ = Mean equivalent strain rate.
T = Absolute temperature.
$-\Delta H$ = Activation energy.
R = Universal gas constant.
A, α and n' are experimentally determined temperature independent constants.

($-\Delta H$) is the activation energy of the rate controlling deformation mechanism occurring, and $\Delta H = f(\sigma_{app}, T, S)$. At high temperatures ($-\Delta H$) has been found to be equivalent to the energy for self diffusion.
The equation above has been shown to fit high temperature deformation over a wide range of strain rates and temperatures, and has been reviewed extensively[9][10][13][16].

At low stresses ($\alpha\sigma > 0.8$) the above equation reduces to a power relation:-

$$\dot{\bar{\varepsilon}} = A' \bar{\sigma}_f^{n}$$

n = Temperature independent constant
A' = Temperature dependent constant

At high stresses ($\alpha\sigma > 1.2$) equation 2.4.1 has an exponential relationship:-

$$\dot{\bar{\varepsilon}} = A'' \exp(B \bar{\sigma}_f)$$

B is a temperature independent constant

$\dot{\bar{\varepsilon}} = A'' \exp(B\ \bar{\sigma}_f)$ B is a temperature independent constant

Re-arrangement of equation 2.4.1 gives:-

$$\dot{\bar{\varepsilon}}\ \exp\left(\frac{\Delta H}{RT}\right) = A[\ \sinh(\alpha\ \bar{\sigma}_f)]^n$$

The L.H.S of the above expression incorporates both the strain rate and temperature of deformation and is known as the temperature compensated strain rate or Zener-Hollomon parameter (Z), where $Z = \dot{\bar{\varepsilon}}\ \exp\left(\frac{\Delta H}{RT}\right)$

Equation 2.4.1 can, therefore, written as:- $Z = A[\ \sinh(\alpha\ \bar{\sigma}_f)]^n$

If this expression is expanded using the sinh function, the following is obtained:-

$$\bar{\sigma}_f = \frac{1}{\alpha}\ \mathrm{Ln}\left(\left(\frac{Z}{A}\right)^{\frac{1}{n}} + \sqrt{\left(\frac{Z}{A}\right)^{\frac{2}{n}} + 1}\right)$$

This is a steady state constitutive equation relating stress, strain rate and temperature. α, n and A are hot working temperature independent constants.

2.4.3 Microstructural Restoration Processes

In an annealed material the dislocation density can range from between 10^5->10^8 cm^{-2}. During hot working, however, dislocations are created, and the dislocation density can rise to 10^{10}->$10^{11}cm^{-2}$. Owing to the fact that strain energies are associated with dislocations, a driving force for re-arrangement and annihilation of the dislocations is consequently produced as a result of the deformation. These microstructural re-arrangements and annihilations may occur concurrently with deformation, in which case they are referred to as dynamic restoration processes, or after deformation in which case they are referred to as static processes. The two principle restoration processes are known as recovery and recrystallisation.

Recovery is the re-arrangement of dislocations into cells and their subsequent movement within these cells to form low angle boundaries. During hot working the dislocation generation rate, hence the dislocation density, increases. The annihilation rate then increases as recovery processes take place, producing a microstructure consisting of subgrains with low misorientations. Eventually the annihilation rate equals that of the generation rate and a steady state microstructure is formed, where the dislocation density, subgrain size, and misorientation, do not alter with further straining. This constancy of the subgrains persists during dynamic recovery even though the grains elongate in conformity with the deformation process. This is a consequence of the repeated unravelling and reformation of the subgrains.

The higher the temperature of deformation or lower the strain rate, the larger the subgrains become[8][18][19] , with their centres containing fewer dislocations and their boundaries fewer and more orderly arranged dislocations. The reasons for the decrease in the dislocation density as the temperature increases or the strain rate decreases is due to the changes in the balance between the dislocation generation an annihilation rates.

The dependence of the mean subgrain size upon temperature and strain rate has been found to obey the following relationship[20][21] :-

$$d^{-p} = a + b\ln\left(\frac{Z}{A}\right) \qquad \text{.....2.4.2}$$

p=1->3 (normally 1), Z = Zener Hollomon parameter.

Since the room temperature properties of a material are related to the subgrain size by a Hall Petch type relationship[17][24] :-

$$\sigma_y = \sigma_0 + Nd^{-q} \qquad \text{.....2.4.3}$$

σ_0 = Inherent friction stress of the lattice.

d= Grain size and N= Alloy specific coefficient.

Combination of equations 2.4.2 and 2.4.3, can be used to relate the room temperature yield stress with the processing parameters:-

$$\sigma_y = e + f\mathrm{Ln}\left(\frac{Z}{A}\right)$$

The yield stress of the material increases with decreasing subgrain size, therefore the yield stress can be controlled by the deformation conditions, i.e. strain rate and temperature.

The above paragraphs have highlighted the mechanism of recovery, and since the dislocation movements associated with the recovery process occur by climb and cross-slip, recovery will take place more readily in metals such as aluminium, which have high stacking fault energies . Not only have deformed grains with internal substructures been observed within aluminium lithium alloys, however, but recrystallisation has also been identified. Since the potential for dynamic recrystallisation is highly reduced in material that dynamically recovers (cannot reach critical strain for recrystallisation) the presence of recrystallised grains in aluminium alloys may be attributed to static processes. Static recrystallisation requires an incubation time after extrusion and its extent and the resulting grain size depend upon a number of variables:- (i) amount of prior deformation, (ii) temperature, (iii) time, (iv) initial grain size, (v) composition, and (vi) amount of recovery or polygonisation prior to the start of recrystallisation.

The process of recrystallisation involves the nucleation of strain free regions, the boundaries of which transform the strained matrix into strain free material as they move. This requires a high angle grain boundary i.e. a large degree of misfit to accommodate the dislocations. The driving force for recrystallisation is provided by high elastic strain energy associated with the deformed structure. In general the critical strain for recrystallisation, ε_c, increases with increasing strain rate and decreasing

temperature (ε_c decreases as Z increases). This signifies that at higher Z values the sub-boundary dislocation density is higher before recrystallisation is nucleated.

The alloying of aluminium, however, has been observed to cause lower levels of recovery, thereby increasing the strain energy associated with the steady state, hence increasing the possibility of dynamic recrystallisation[8][22][23].

Commercially available 8090 aluminium lithium alloys are highly alloyed. They also contain zirconium, which forms Al_3Zr dispersoid particles and inhibits static recrystallisation. The process of dynamic recrystallisation cannot, therefore, be ruled out for these alloys. Indeed Mukapadyay[24] has concluded the presence of dynamic recrystallisation, with different nucleation mechanisms being associated with changing rates of deformation. At low strain rates, recrystallisation nucleation was considered to occur by grain boundary bulging and by subgrain rotation at higher deformation rates.

The as-quenched structure of the extruded 8090 material may, therefore, contain both static and dynamically recrystallised grains. The dynamic recrystallisation may be present by virtue of the nature of the alloy composition, and also to a certain extent due to the localised deformation conditions of strain, strain rate and temperature. The statically recrystallised grains, however, may be present due to the inability to quench the extrudate fast enough immediately after emergence from the die orifice, or as a consequence of solution heat treatment. The only way to definitely distinguish between dynamically and statically recrystallised grains is through the use of transmission electron microscopy technique. Theoretically, the statically recrystallised grains should be free of internal dislocations. The dynamically recrystallised grains, however, will exhibit high internal dislocation densities.

CHAPTER THREE

EXPERIMENTAL PROCEDURE

3.1 Extrusion Press and Tooling

All extrusions were carried out on an Enefco vertically acting 5MN press, with a container liner of 75mm internal bore. The container was maintained 25° C below the extrusion temperature in order to prevent overheating during extrusion. A ram speed of 3mm/s was initially set, which gave rise to approximately 2.5mm/s during extrusion.

In this project both shear face dies with rectangular die orifice geometry - 'slab' extrusions -, and conically shaped dies with round axi-symmetric die orifices were utilised. Fig 3.1.1 illustrates the range of shear face die orifice geometry and the associated extrusion and aspect ratios. For the axi-symmetric extrusions the extrusion ratio did not alter from 15:1, and fig 3.1.2 illustrates a typical conically shaped die in elevation, with the associated geometry. As can be seen, four conically shaped dies of 30°, 45°, 60° and 90° die cone angles were produced.

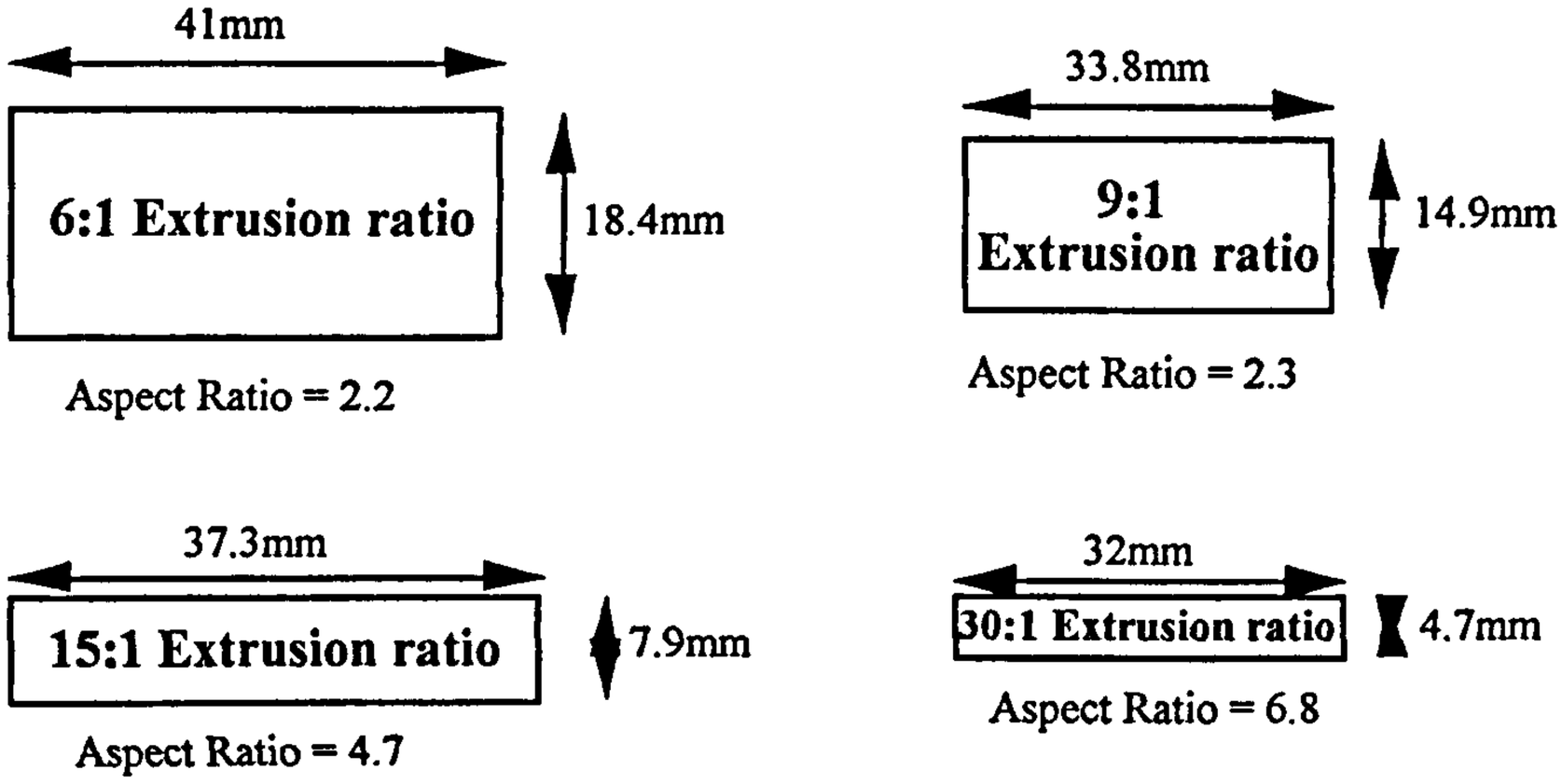


Fig 3.1.1

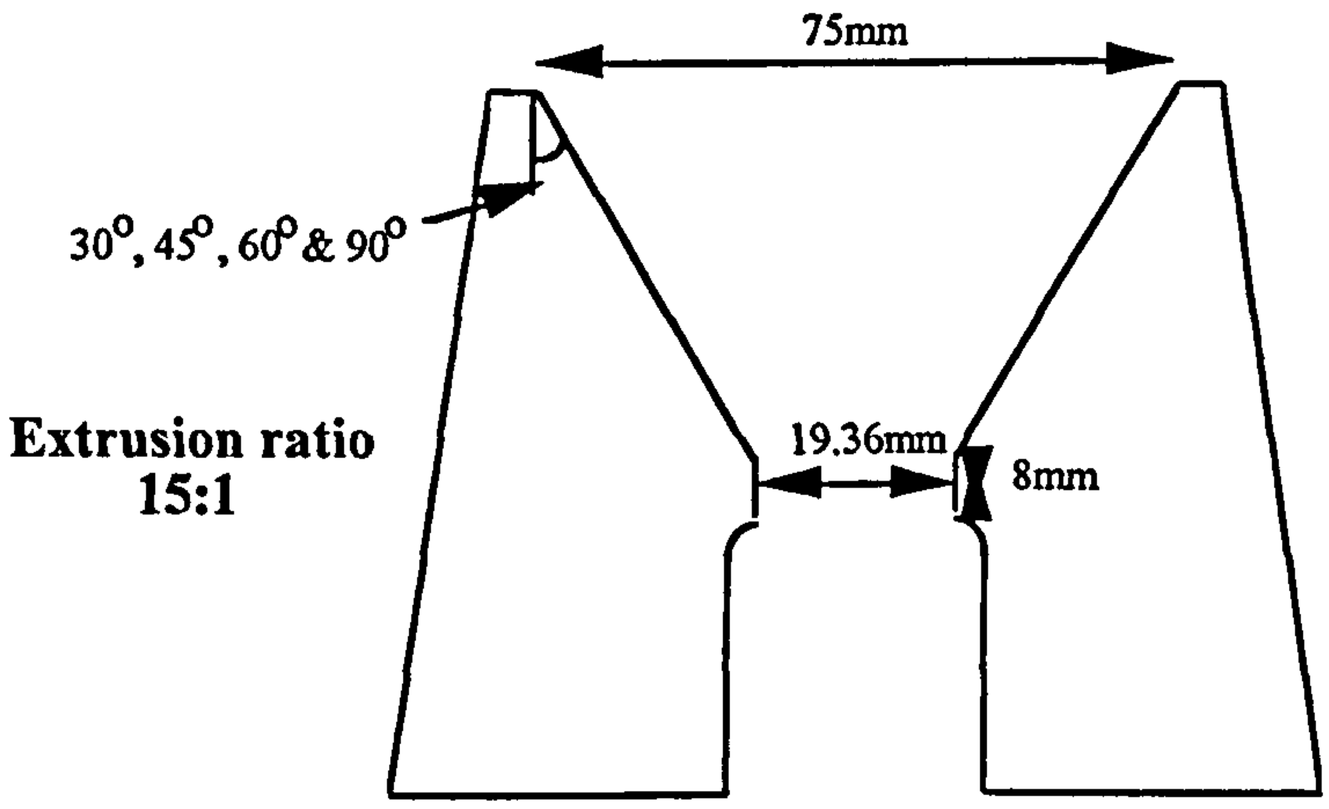


Fig 3.1.2

The slab dies were heated in-situ on the extrusion press, but due to a lack of die heating from the container heaters, the conical dies were initially heated in an air-circulating furnace prior to being fitted into the extrusion press.

3.2 Billet Preparation

For all the extrusions performed using the shear face dies with rectangular orifice geometry, solid extrusion billets of 72.5mm in diameter and 100mm in length were used. For the axi-symmetric extrusions, however, flow field analysis involving gridded billet analysis was carried out. This required the use of split gridded billets, both with and without gold wire meshing. For the axi-symmetric extrusions, therefore, the following solid and 'split' extrusion billets were used:-

(i) Solid billets. 72.5mm diameter x 100 mm in length

(ii) Split billets. Split billets were used in order to observe the flow during conical die extrusion. The billets consisted of two halves with a 5mm square grid machined onto the internal face of one half. Each billet was tapered to fit a specific die and the parallel section of each billet was 100 mm. For simple flow analysis a certain number of split billets had a graphite lubricant coated onto their internal meridian planes, before extrusion was carried out. The presence of this lubricant allowed separation of the two billet halves after extrusion and observation of the resulting grid distortion field to be made. For visioplasticity analysis of the extrusion process, however, gold wire was placed into the grooves of the machined grid, before the two halves were joined and the split billet extruded. Investigations into the methods of rejoining the split billets by welding and clamping before extrusion, were carried out, but the most effective and least disruptive way of rejoining the billets was found to be by the use of a steel 'U' tack. Fig 3.2.1 illustrates a schematic of a typical split billet arrangement.

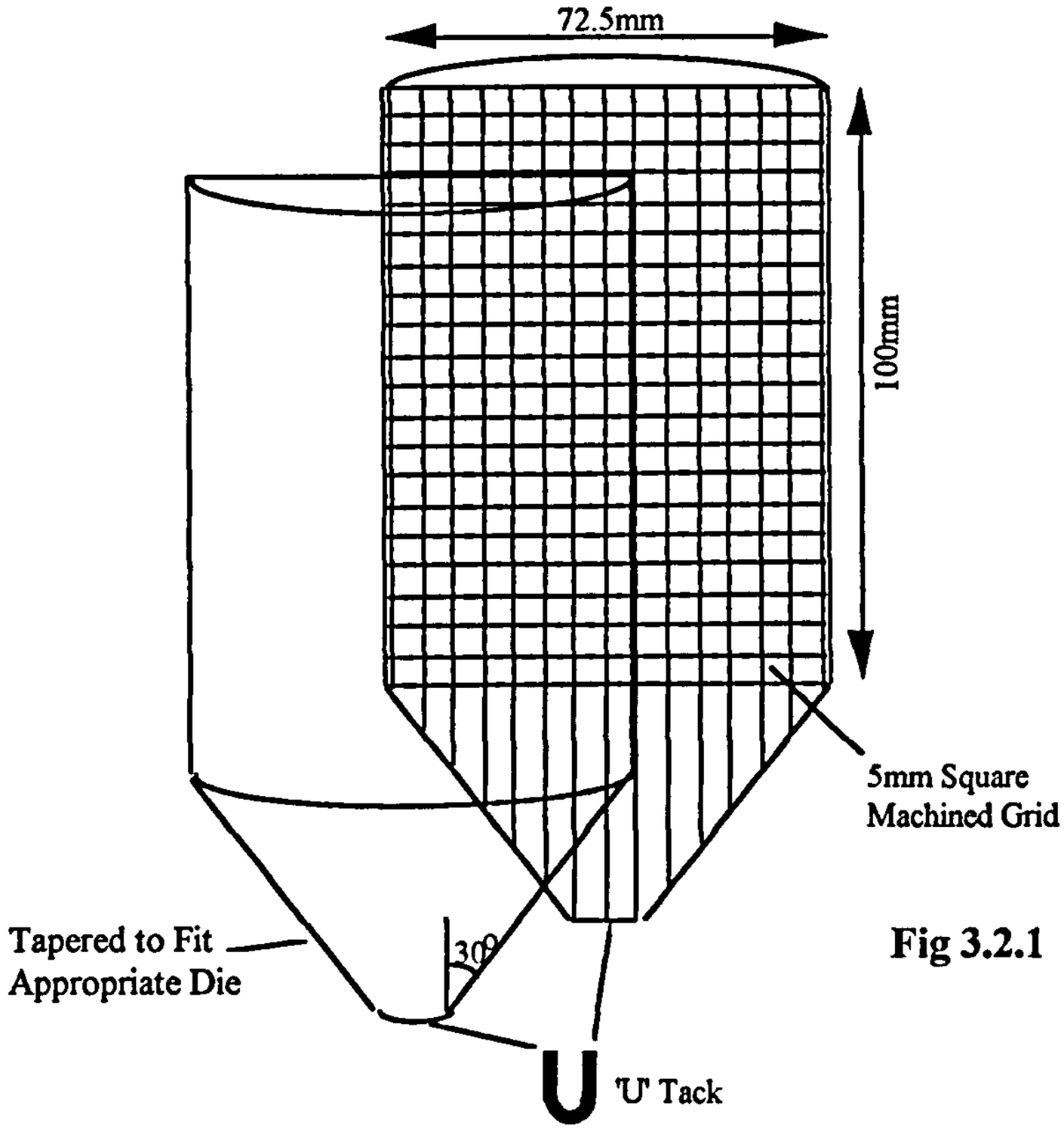


Fig 3.2.1

3.3 Material Specification

Both 8090 and 7075 alloys were utilised in this project.

	Li	Cu	Mg	Zn	Si	Fe	Ti	Zr	Cr	Balance
Alloy A 8090	2.33	1.24	0.72	0.016	0.05	0.04	0.02	0.12	/	Al
Alloy B 8090	2.25	1.03	1.00	0.016	0.05	0.04	0.01	0.15	/	Al
Alloy C 7075	/	1.57	2.5	5.5	0.01	0.00	/	/	0.01	Al

Fig 3.3.1

Both 'slab' and axi-symmetric extrusions were carried out using alloy A material. This alloy was also used in the preparation of split billets for distortion pattern and visioplasticity analyses.

Alloy B was used in the production of 15:1 and 30:1 'slab' extrusions alone, and the 7075 material was only used in the production of split billets for visioplasticity analysis.

3.4 Heat Treatments

3.4.1 Homogenisation

The 8090 billets were homogenised at 535° C for 24 hours, in an air circulating furnace. They were then quenched in water maintained at room temperature, and the surface oxidation removed in order produce the desired billet size.

3.4.2 Billet heating

All the solid extrusion billets were induction heated prior to extrusion, the split billets, however, were heated in an air circulating furnace maintained at 5° C above the extrusion temperature.

3.4.3 Ageing

All the extrudates were quenched after extrusion, using a cold water jet that surrounded the extrudate, and was situated approximately 50cms from the die base. The extrudates were then either retained in the as-extruded condition or subsequently solution heat treated and aged, according to the schedule shown below:-

Alloy A, 'slab', Extrusions

Extrusion Ratio	6:1			9:1			15:1			30:1		
Extrusion Temp	400	450	500	400	450	500	400	450	500	400	450	500
As-Extruded	●	/	●	/	/	/	●	●	●	/	/	●
Under-aged	●	/	/	●	●	/	●	●	●	●	●	●
Over-aged	●	●	●	●	●	●	●	●	●	●	●	●

Alloy B, 'slab', Extrusions

Extrusion Ratio	15:1			30:1		
Extrusion Temp	400	430	460	400	430	460
As-Extruded	●	●	●	●	●	●
Under-aged	●	●	●	●	●	●
Peak-aged	●	●	●	●	●	●
Over-aged	●	●	●	●	●	●

Alloy A, Axi-symmetric Extrusions

Die Cone Angle	30°			45°			60°			90°		
Extrusion Temp	400	430	460	400	430	460	400	430	460	400	430	460
Under-aged	●	●	●	●	●	●	●	●	●	●	●	●
Over-aged	●	●	●	●	●	●	●	●	●	●	●	●

Fig 3.4.1

Solutionising consisted of a 30 minute soak at 530° C for the 15:1 and 30:1 material, and a 35 minute soak for the 6:1 and 9:1 material, with an additional 10 minutes required in each case for temperature stabilisation of the furnace. The solution treatments were carried out in muffle and air-circulating furnaces, with the extrudates being water quenched to room temperature after treatment.

The under-aged condition was obtained by heating the solutionised extrudates in an air-circulating oven, maintained at 190° C, for 1 hour 40 minutes. 10 minutes was also required for temperature stabilisation of the oven. The extrudates were subsequently quenched in a water bath maintained at room temperature.

The over-aged condition was obtained by heating the solutionised extrudates in an air-circulating oven, maintained at 190° C, for 26 hours. 10 minutes was again required for temperature stabilisation of the oven, and the extrudates were also quenched in a water bath at room temperature.

3.5 Sample Preparation

The relative positioning of the sample preparation within the various extrudates is illustrated in fig 3.5.1.

In order to concentrate on the property values obtained from the relatively stable flow region of extrusion, the initial sections of all the extrudates were discarded. For the 15:1 and 30:1 extrudates produced from alloy A material, investigations into microstructural and property changes occurring from the 'front' of the extrudate to the 'rear' were investigated, hence were sectioned as shown. For all other extrusions sample preparation occurred from the mid position of the extrudate.

From the various sections of the extrudates the following specimens were prepared:-

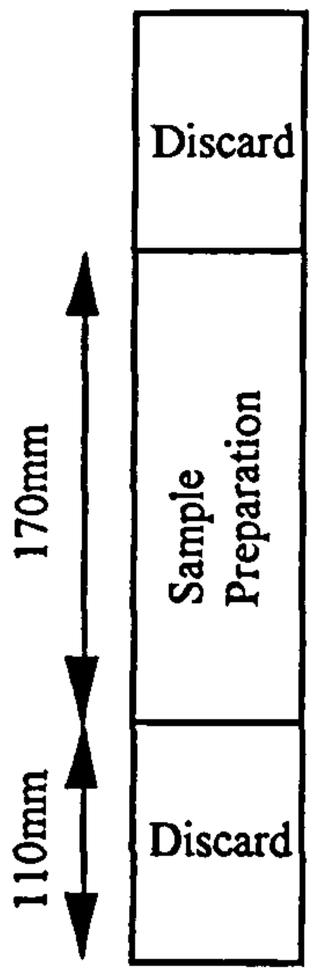
(1) Houndsfield '11' round tensile specimens. These were prepared from the 6:1, 9:1 and 15:1 rectangular bar extrusions as well as the axi-symmetric extrusions. For the rectangular slab material transverse and longitudinal sample orientations were prepared, whereas only longitudinal samples could be prepared for the round bar extrusions. All samples were prepared from the centre of the extrudates.

(2) Flat tensile specimens. Due to thickness limitations, Houndsfield '11' tensile specimens could not be made from the 30:1 material. Instead, longitudinal flat tensile specimens were prepared from the centre of the 30:1 extrudates.

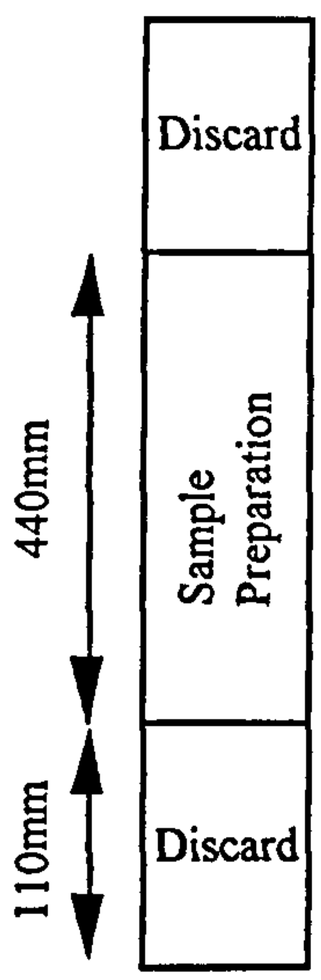
(3) Chevron notch bar fracture toughness specimens. For the rectangular slab material both T-L and L-T chevron notch fracture toughness samples were prepared. For the axi-symmetric rod extrusions, however, only L-R specimens could be produced. The majority of the toughness specimens were machined from the centre of the extrudates, but some L-R samples were prepared from the edge regions of the round bar extrudates.

(4) Short rod fracture toughness specimens. R-L short rod specimens were produced from the axi-symmetric extrusions, and T-L short rod specimens produced from the 6:1 and 9:1 rectangular slab material.

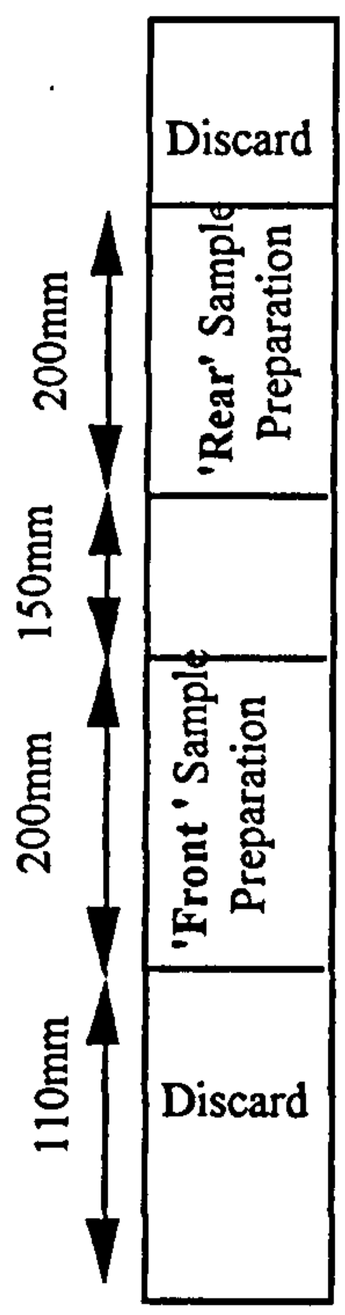
8090, Alloy A, 'Slab' Extrudates



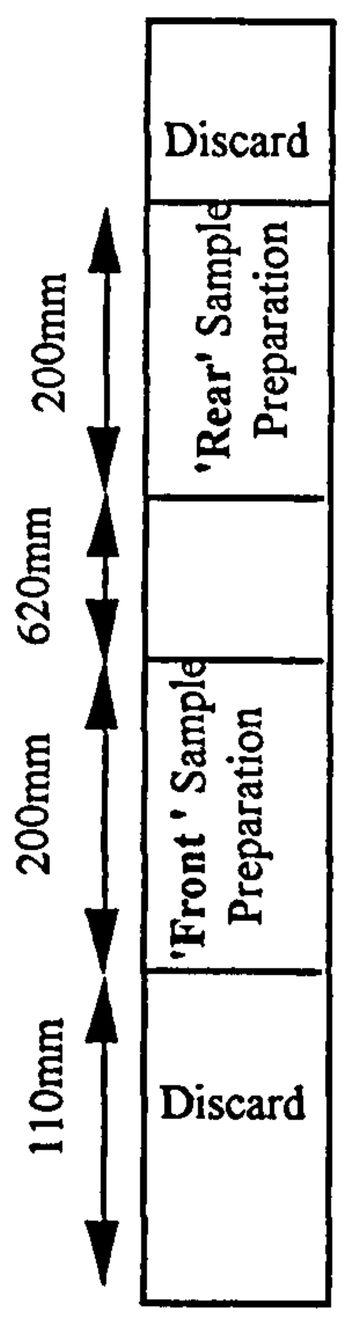
6:1 Extrusion Ratio



9:1 Extrusion Ratio

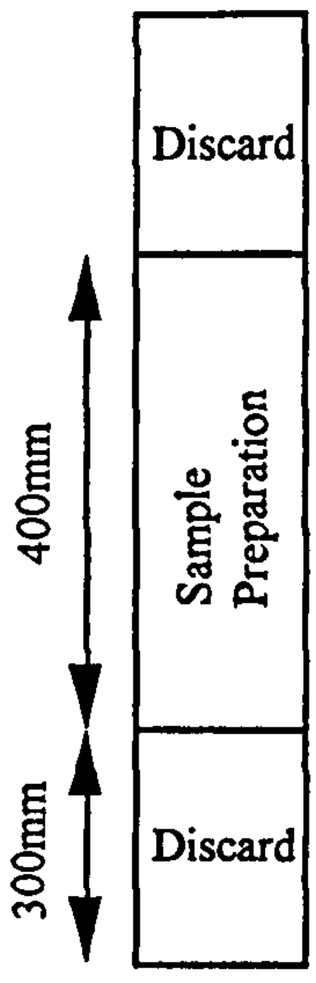


15:1 Extrusion Ratio

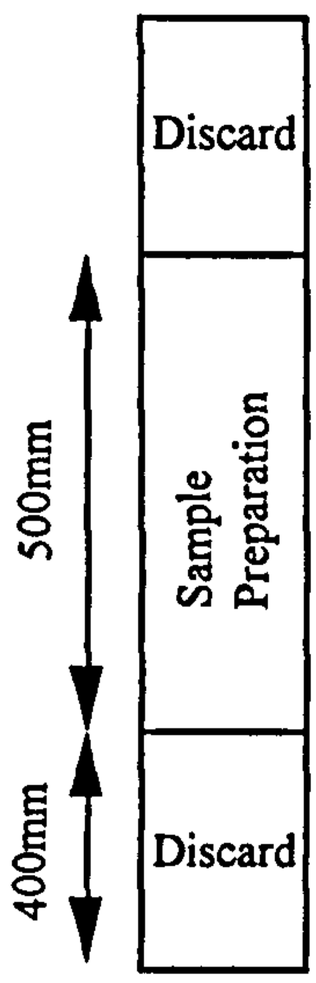


30:1 Extrusion Ratio

8090, Alloy B, 'Slab' Extrudates



15:1 Extrusion Ratio



30:1 Extrusion Ratio

8090, Alloy A, Axi-symmetric extrudates produced from conically shaped dies

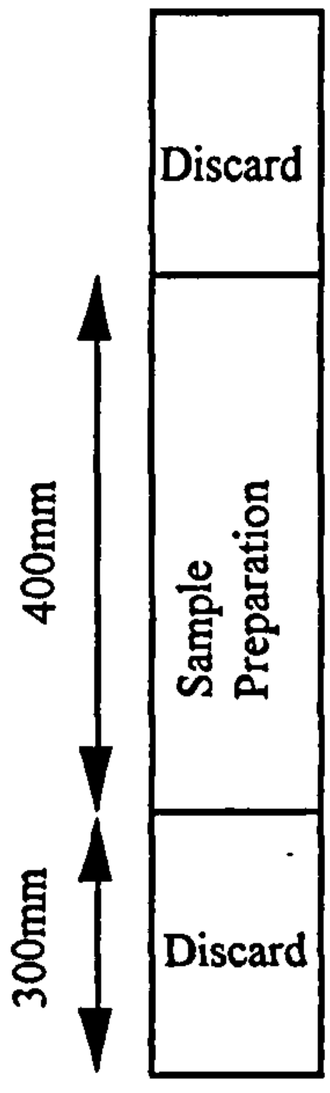


Fig 3.5.1

3.6 Microstructural Investigation

Various techniques were employed in order to characterised the microstructures of the various extrudates.

(1) Transmission Electron Microscopy (T.E.M.)

Longitudinal and transverse wafers were cut from the extrudates using a slow cutter. The wafers were then ground down to a thickness of 0.3mm using SiC paper. Discs, 3mm in diameter, were subsequently punched from these wafers and electro-thinned using a Struers tenupol jet polishing machine. The jet polisher was operated at 20V and an etching solution of 70% methanol and 30 % nitric acid (by volume) maintained at a temperature of -30°C, was used.

Once sample preparation had been carried out by electrothinning, transmission electron microscopy analysis was carried out on a Philips EM 301 and JEOL 120 Cx TEMSCAN operating at 100kV.

(2) Optical analysis

Longitudinal and transverse sectioning of the extrudates was carried out using a slow cutter. The internal surfaces of the sectioned extrudates were then ground using SiC paper and polished down to 1μm using diamond paste. The specimens were subsequently electro-etched using Barkers reagent [3.5gms H_3BO_3 (Boric acid), 23ml HBF_3 (tetraflouric acid) and 500 ml of water], at a potential of 20 V

The optical analysis provided a very good overview of the extrudate microstructure and clearly illustrated:-

(i) Recrystallisation - size/shape and percentage.

(ii) The directionality of the microstructure.

(iii) Grain/subgrain size and shape variations throughout the extrudate.

In order to quantify percentage recrystallisation values, an image analyser consisting of a Bosch camera linked to an Ibas system was utilised. In this analysis optical micrographs were scanned and assessed.

(3) Texture determination

Texture analysis of the 'slab' extrudates was carried out using a Philips PW1078 texture goiniometer interfaced to a microcomputer to provide pole figure plots. The samples prepared for textural analysis were approximately 2.5 cm^2 and were cut longitudinally from the extrudates and polished down to 1μm using diamond paste. Texture analysis of the rod extrudates, however, was carried out at Alcan Laboratories, Banbury, which provided pole figure plots and O.D.F analysis. The samples were cut longitudinally from the centre of the extrudates, with the sample size encompassing the entire extrudate width.

(4) Microhardness Analysis

Optical analysis had continually shown the surface regions of the extrudates to be distinct from the core areas. As a result, microhardness testing was carried out in order to provide further information upon the centre to surface microstructural differences.

Micro-hardness measurements were carried out upon several axi-symmetric rod extrusions using a Leitz micro-hardness tester. Longitudinal samples were sectioned from the extrudates, mounted and polished down to 1μm using diamond paste.

3.7 Fracture Characterisation

S.E.M. analysis of the fracture samples was necessary in order to provide knowledge of the fracture characteristics of the extrudates. The contribution of various microstructural features to the mechanical properties of the material could then be suggested and correlations between processing and property values facilitated.

All the fracture characterisations were carried out upon Joel T220 and T200 scanning microscopes, and no special preparation of the fracture samples was necessary before analysis.

3.8 Deformation Analysis

A simple deformation characterisation, involving Z calculation, was carried out for the 'slab' material. Appendix IV outlines the theory and equations used. This analysis produced bulk Z values for each extrudate. No information concerning the strain rate and temperature distributions within each extrusion was provided.

For the axi-symmetric extrusions, however, several methods of deformation characterisation were carried out, with information upon temperature, strain rate and Z value distributions, for each extrusion being provided.

The simplest analysis involved observations of the distortion patterns produced from extrusion of split gridded billets. The distortion patterns produced from the gridded billets illustrated the instantaneous deformations of various elemental blocks and any changes that occurred in these deformations as die cone angles were altered.

Visioplasticity analyses were also carried out upon the axi-symmetric extrusions. In this technique split gridded billets were again utilised, but they were combined with gold wire meshes in order to facilitate the determination of deformation field, hence strain rate distributions. A full outline of the visioplasticity technique as performed in this project is shown in appendix II.

The final analysis performed upon the axi-symmetric extrusions, was a finite element technique. This was the most complex analysis performed and as such required

computer assistance. This analysis provided information upon temperature, strain rate, and Z value distributions throughout the extrusion deformation zones and extrudates. An outline of the finite element analysis, as carried out in this project is shown in appendix III.

CHAPTER FOUR

Rectangular Bar Extrusions Results and Discussion

This project set out to establish correlations between mechanical properties, processing conditions and microstructure, within 8090 rectangular section, 'slab', extrusions. The results were, therefore, split into the following areas:-

(1) Optical Microscopy
(2) Transmission Electron Microscopy
(3) Textural Analysis
(4) Toughness Analysis
(5) Tensile Properties

In each area of analysis the effects of processing conditions were examined, which lead to correlations between processing, properties and microstructure.

The analysis of an Alcan 8090 alloy -alloy A- was of main concern, but in order to confirm the general variation in grain structure and property values with processing, irrespective of the specific material compòsition (particularly zirconium), a commercially available alloy from Alcoa - alloy B-, with a greater zirconium level was also extruded.

Alloy A:-Li-2.33, Cu-1.24, Mg-0.72, Zn-0.016, Si-0.05, Fe-0.04, Ti-0.020, Zr-12%,+Al
Alloy B:-Li-2.50, Cu-1.03, Mg-1.00, Zn-0.016, Si-0.05, Fe-0.04, Ti-0.010, Zr-15%,+Al

Errors

The tensile strength and toughness values were obtained from averaging a minimum of four samples. Error bars were not included on the graphs showing property variations with processing, since it caused a certain amount of confusion. Standard deviations, at the 80% confidence level, are shown in the property tables, however, which indicates the measurement variations.

The toughness results and standard deviations were rounded to the nearest decimal with the percentage error varying from approximately 2->8%. The tensile strengths and associated standard deviations were rounded to the nearest whole number and again a percentage error varying from 2->8% was present. It must be remembered that the anisotropy results were produced by subtraction of property measurements, hence measurement errors were cumulative, causing constant trends to be diluted.

4.1 Optical Microscopy

4.1.1 General Extrudate Structures

Optical analysis of the extrudates produced a very good overview of the extrudate microstructures, providing information on the directionality of the microstructure and recrystallisation variations throughout the extrudate sections. Due to etching of the subgrain boundaries, the subgrain structures within the extruded material were also evident optically. The accuracy of the subgrain size observed under the optical microscope was checked, however, by comparison with the results obtained from T.E.M analysis.

From a general observation of the optical micrographs, fig 4.1.1->7, the basic extrudate microstructures were shown to consist of highly elongated original grains containing internal subgrain structures. In combination with this basic microstructure colonies of grain boundary recrystallisation were also observed. The proportion of recrystallisation varied with processing conditions, and increased continually from the centre of the extrudates to the surface, as well as from the 'front' of the extrudates to the 'rear'.

The deformation process was unlubricated forward extrusion, producing a dead metal zone adjacent to the tooling surfaces, a cone of heavy shear adjacent to the dead metal zone, and a central region in which reduced amounts of more ideal deformation occurred. The high degree and type of straining associated with the flow consequently produced the elongated appearance of the extrudate. A complete analysis of the deformation process was not carried out, but fig 4.1.9 does show the calculated Zener-Hollomon values for each extrusion. Appendix IV outlines the theory and equations used in the calculations of the Z values.

The variation in recrystallisation with processing conditions, together with the longitudinal and transverse variations within each extrudate were associated with changes in the temperature and deformation histories experienced by the extruded material, and will be outlined in more detail in the subsequent sections.

4.1.2 Variation in Microstructure with Solution Heat-Treatment & Ageing

As already mentioned the as-extruded core microstructures of both alloy A & B extrudates were characterised by elongated original grains containing internal substructure. Recrystallised grains were also observed at the original grain boundaries, with the size and percentage volume fraction of the recrystallised grains increasing as the extrusion temperature and extrusion/aspect ratios increased, fig 4.1.1.

Towards the surfaces of these extrudates the incidence of recrystallisation increased until at the extreme outer surfaces of the extrudates annuli of 100% recrystallisation existed, fig 4.1.2. As with the core regions, however, the proportion of the recrystallised grains, present in the surface regions, increased as the extrusion temperature and extrusion/aspect ratios increased, fig 4.1.2 (a) & (c).

For the solution heat treated and aged extrudates no significant differences were observed between the grain structures obtained from the underaged and overaged material. As with the as-extruded material, however, considerable microstructural variations between the core and surface regions of the aged extrudates were present. The effects of ageing upon the core and surface regions will, therefore, be considered separately.

Core Regions. The effect of solution heat treatment and ageing upon the extrudate core microstructures depended upon the processing conditions.

For the 6:1, 9;1, 15:1 extrudates produced at all temperatures and the 30:1 extrudates produced at 400° C, solution heat treatment and ageing increased the relative proportion of the small (10-20μm) recrystallised grains present at the grain boundaries, fig 4.1.3->4. For the 30:1 extrudates produced at 450° C and 500° C, however, solution heat treatment and ageing caused not only the proportion of recrystallisation to rise, but also the size of the recrystallised grains to increase. These extrudate cores consequently consisted of elongated original grains, combined with small (10->20μm) recrystallised grains present at the original grain boundaries, together with much larger recrystallised grains varying in size between 20->100μm, fig 4.1.6->7.

The basic microstructural features and changes occurring with the heat treatment processes were similar in extrudates produced from both alloys A and B. Only the relative proportions of recrystallisation were observed to be slightly lower in alloy B extrudates, fig 4.1.6 (c) & 4.1.7 (b).

Surface Regions As with the core regions, the effect of solution heat treatment and ageing upon the as-extruded surface microstructures depended upon processing conditions. For 6:1, 9:1, 15:1 extrudates produced at 400° C & 450° C, and 30:1 extrudates produced at 400° C, solution heat treatment and ageing caused considerable grain growth in the extreme outer surfaces of the extrudates. This produced grains in excess of 100μm, as indicated in fig 4.1.5. Below these narrow surface layers of exaggerated grain growth, however, there was an abrupt change to microstructures consisting of elongated original grains. In addition to elongated original grains these sublayers exhibited grain boundary recrystallisation, as with the as-extruded material. Solution heat treatment and ageing had, however, increased the volume fraction of recrystallisation relative to the as-extruded condition.

For the 15:1 extrudates produced at 500° C, and the 30:1 extrudates produced at 450° C & 500° C, solution heat treatment and ageing did not cause the formation of outer annuli of extremely large grains. Instead, surface regions characterised by large (50μm) equiaxed recrystallised grains, fig 4.1.5 (c) & 4.1.7 (a), were observed. 100% recrystallisation was again present at the extreme outer regions of the extrudates, with the volume fraction of recrystallisation then decreasing towards the core regions of the extrudates.

4.1.3. Variation in Microstructure with Extrusion Temperature

Core regions. Irrespective of extrusion ratio, increasing the extrusion temperature was found to increase the volume fraction of recrystallisation, within the as-extruded material, fig 4.1.1. The recrystallised grain or subgrain sizes present within the as-extruded material were not, however, significantly altered by extrusion temperature increases.

In the core regions of 15:1 extrudates that had been solution heat treated and aged, increases in extrusion temperature were also observed to increase the proportion of the small (10->20μm) recrystallised grains, without affecting their size, or the size of the subgrains (1->10μm) significantly, fig 4.1.3. For 30:1 extrudates that had been solution heat treated and aged, however, increases in extrusion temperature caused not only the proportion of recrystallisation to rise, but also the recrystallised grain size to increase. At 400° C the 30:1 microstructures were characterised by small (10->32μm) recrystallised grains present at the original grain boundaries, together with the occasional large (40μm) recrystallised grain, fig 4.1.4 (b). At the higher temperature of 450° C, however, a significant proportions of larger (20->100μm) recrystallised grains were present, fig 4.1.4 (a). Finally at 500° C the proportion of the larger grains had increased still further, fig 4.1.6 & fig 4.1.7.

For all the core extrudates, the microstructural variations with extrusion temperature were consistent for both alloy compositions. It was evident, however, that the extrudates produced from alloy B extrudates had slightly lower volume fractions of recrystallisation, irrespective of the recrystallised grain size, fig 4.1.6 (c), & 4.1.7 (b).

With regard to the variation in microstructure from the 'front' of the extrudate to the 'rear', it was observed that for both the 15:1 and 30:1 extrudates higher extrusion temperatures enhanced the longitudinal increase in recrystallisation.

Surface regions The surface regions of the as-extruded 15:1 extrudates produced at 400° C and 450° C possessed outer annuli of 100% recrystallisation, fig 4.1.2 (c). Below these outer annuli, however, there were abrupt changes to microstructures exhibiting elongated original grains with internal substructure, together with small

(10μm) grain boundary recrystallisation. As the extrusion temperature increased to 500° C the volume fraction of surface recrystallisation increased.

These changes in surface microstructures with increases in extrusion temperature were also evident for the 30:1 as-extruded material. At 400° C the surface microstructures of the 30:1 extrudates were found to consist of a narrow outer band of large (20->60μm) recrystallised grains, which changed abruptly to microstructures characterised by elongated original grains, internal substructure and small (10μm) grain boundary recrystallisation. In extrudates produced at 450° C and 500° C, however, the proportion of recrystallisation in the outer regions increased, fig 4.1.2 (a).

For the 15:1 extrudates produced at 400° C and 450° C, and processed to the T6 condition, the extreme outer surfaces of the extrudates were characterised by exaggerated growth, producing grains in excess of 100μm, fig 4.1.5 (a) & (b). Below these outer annuli, abrupt changes to microstructures consisting of elongated original grains, internal subgrain structures (1->10μm), together with small (10->20μm) recrystallised grains present at the original grain boundaries, again occurred. No obvious changes in the depth to which the outer annuli of exaggerated grain growth extended, or degree of recrystallisation in the outer regions, could be identified as the extrusion temperature was increased from 400° C to 450° C. Increasing the extrusion temperature to 500° C, however, caused the surface regions to be characterised by large equiaxed recrystallised grains varying in size from between 20->80μm. 100% recrystallisation was still present at the extreme outer surfaces, but this decreased towards the centre of the extrudate, revealing a microstructure of elongated original grains, substructure and small (10->20μm) grain boundary recrystallised grains.

For the 30:1 extrudates processed to the T6 condition, similar variations in the surface microstructures with increases in extrusion temperature were found to those observed for the 15:1 extrudates. In 30:1 extrudates produced at 400° C the extreme outer surfaces were populated by grains in excess of 100μm. The microstructure immediately below these outer annuli, however, were shown to consist of elongated original grains, internal subgrains (1->10μm), and small (10->40μm) grain boundary recrystallised grains. In extrudates produced at 450° C and 500° C the surface microstructures exhibited large (20->80μm) equiaxed recrystallised grains, fig 4.1.7 (a). In the extreme outer regions of the extrudates 100% recrystallisation was present, but this decreased towards to centre of the extrudates. The depth to which the 100% recrystallised surface regions extended, was found to increase from the front of the extrudate to the rear, but did not alter significantly as the extrusion temperature was increased from 450° C to 500° C.

All the above changes in core and surface microstructures as the extrusion temperature varied were observed for both the Alcan and Alcoa material. The extrudates produced

from the alloy B material were, however, consistently shown to exhibit slightly lower proportions of recrystallisation compared with the extrudates produced from alloy A.

4.1.4 Variation in Microstructure with Extrusion/Aspect Ratios

The two factors of extrusion ratio and extrusion aspect ratio have been grouped together, since a change in one factor was in general linked with a change in the other.

Core Regions For the slab extrudates produced at 400° C and processed to the T6 condition, increases in the extrusion/aspect ratio caused the volume fraction of the small (10->30μm) recrystallised grains to increase, fig 4.1.3(a) & (c) and fig 4.1.4(b). The subgrain size, however, was found to remain approximately constant at 1->10μm, fig 4.1.3(d) & 4.1.4(c).

For slab extrudates produced at the higher extrusion temperatures of 450° C and 500° C, increases in the extrusion/aspect ratio also caused the proportion of the small recrystallised grains present at the original grain boundaries to increase. For increases in extrusion ratio from 15:1 to 30:1, however, marked increases in the presence of large (20->100μm) recrystallised grains were also observed.

Since variations in extrusion ratio and aspect ratio usually occurred concurrently, it was difficult to assess which was responsible for the microstructural variations. Only the 6:1 & 9:1 extrusions had comparable aspect ratios, but due to their similar extrusion ratios, no significant microstructural changes were observed between the extrudates.

By comparison of the 15:1 'slab' extrudate microstructures with the microstructures obtained from the 15:1 axi-symmetric extrudates, however, it was found that the increase in aspect ratio from 1:1->4.7:1 caused a very slight increase in the proportion of recrystallisation.

Surface Regions The surface regions of the slab extrudates produced at 400° C and subsequently solution heat treated and aged, were characterised by outer annuli of exaggerated grain growth. Below these regions of recrystallisation, however, the extrudate microstructures were characterised by elongated original grains, substructure, and small recrystallised grains. It was observed that increasing the extrusion/aspect ratio caused the depth of the outer annuli of exaggerated growth to increase, and the proportions of recrystallisation in the lower surface regions to increase.

For the extrudates produced at 450° C and 500° C, there was a substantial change in the microstructures of the outer regions, as extrusion/aspect ratio increased. For 6:1, 9:1 and 15:1 extrudates produced at 450° C the extreme outer regions of the extrudates were characterised by outer annuli of exaggerated grain growth. As the extrusion ratio was increased from 6:1->15:1 the depth to which the exaggerated growth extended

increased, as did the proportion of recrystallisation in the lower surface regions. Increasing the extrusion ratio still further from 15:1 to 30:1, however, caused the characteristics of the surface regions to completely change. Instead of the exaggerated grain growth, the outer regions were characterised by large (20->80μm) equiaxed recrystallised grains, with the proportion of recrystallisation decreasing gradually towards the centre of the extrudates. The extrudates produced at 500° C, also exhibited changes in their surface microstructures. Again exaggerated grain growth altered to that of large equiaxed grains, as extrusion ratio increased. In contrast with the material produced at 450° C, however, this change in microstructural characteristics occurred as the extrusion ratio was increased above 9:1 and not 15:1.

4.1.5 Discussion

In the previous paragraphs, the microstructural variations with heat treatment condition, extrusion temperature and extrusion/aspect ratio were highlighted. Not only were microstructural changes observed as processing conditions were varied, but longitudinal and transverse increases in the percentage recrystallisation were observed within each extrudate. All these observed variations in microstructure occurring due to changes in processing conditions and relative position within the extrudates, naturally suggested microstructural dependencies upon strain rate, strain and temperature. In an attempt to relate the microstructural characteristics to the extrusion/aspect ratio and extrusion temperatures experienced during processing, Z values were calculated using the formula suggested by Sheppard[8], fig 4.1.9.

The percentage recrystallisation and grain sizes observed in the core regions of the aged extrudates, calculated using an image analyser, are tabulated in fig 4.1.8. As can be seen no constant relationship between the proportions or sizes of the recrystallised grains and the Z values were evident. Due to the fact that subgrain size fluctuations within the core of the extrudates were insignificant, no common correlation between subgrain size and Z values could be made either.

This inability to relate the microstructures with Z values indicated that the actual influence of strain rate and temperature values upon the microstructure was probably different from that suggested by the Z function.

Any relationship between strain rate and temperature with microstructure depends upon the effect of these conditions upon the restoration mechanism. With regard to the actual mechanisms of restoration, numerous investigators[2] have previously shown that during hot deformation, pure and dilute aluminium alloys have a high propensity towards dynamic recovery. Consequently the occurrence of recrystallisation during the hot working process itself is reduced, and a finite time at elevated temperature after working is necessary for recrystallisation to occur. In this project, although the

extrudates were water quenched after extrusion there was a short distance between die orifice and water jacket. Inevitably, therefore, there was a finite time interval before the temperature of the extrudate dropped to room temperature. The observed equiaxed grains in both alloy compositions may, therefore, have formed after deformation, by static recrystallisation.

The driving force for recrystallisation is the stored energy present within the material. Recrystallisation will, therefore, increase as the rate of hot working increases and the extrusion temperature decreases. On this basis the observed increases in recrystallisation with extrusion/aspect ratio can be explained, but the enhancement of recrystallisation as the extrusion temperature increased, cannot. It must be remembered, however, that increasing the extrusion temperature will increase the temperature of the emerging extrudate. The thermal activation of the recrystallisation mechanism, as well as the grain growth rates will, therefore, increase. Consequently, the variation in static recrystallisation occurring with increases in extrusion temperature will depend upon the relative effects of decreases in driving force and increases in thermal activation of the recrystallisation process.

Even though static processes may explain the observed microstructural changes, dynamic recrystallisation will be affected in a similar way by the changes in processing, hence cannot be ruled out.

No conclusive identification of the specific static and dynamic processes taking place during extrusion could be made without extensive T.E.M. analysis. This was outside the parameters of this project, with T.E.M. analysis only being used to establish precipitate size, shape, and distribution, together with the confirmation of subgrain sizes. From previous researchers, who did set out to analyse these factors, however, it has been shown that dynamic processes other than recovery were considered present, and Mukapadyay[3] determined that at higher deformation rates and temperatures localised regions of dynamic recrystallisation occurring by subgrain rotation were present.

Even though definite conclusions concerning whether recrystallisation occurred after or concurrently with deformation could not be drawn, it was observed that recrystallisation increased with extrusion temperature and extrusion/aspect ratio. The differences in the as-extruded microstructure were, therefore, attributed to:-

(1) Severity of deformation - At the higher extrusion/aspect ratios, greater amounts of recrystallisation occurred throughout the extrudate, due to higher levels of straining and strain rate. The proportion of recrystallisation also increased from the centre of the extrudates to the edge, due to higher levels of straining and greater strain rates in the surface regions.

(2) Temperature - Higher extrusion temperatures caused enhancement of the recrystallisation mechanisms and recrystallised grain growth rates, hence greater amounts of recrystallisation were observed.

Temperature differentials between the core and surface regions of the extrudates also caused the proportion of recrystallisation to increase towards the extrudate surfaces.
(3) Zirconium Level - Zirconium inhibits grain boundary movement[4][6] , therefore discouraged growth after extrusion and before quench. Alloy A extrudates consequently exhibited slightly higher proportions of recrystallisation than alloy B extrudates.

Upon solution heat treatment these as-extruded microstructures were then modified still further by the process of growth, which again depended upon the stored energy and zirconium levels of the extruded material. Solution heat treatment caused the % volume fraction of recrystallisation to increase most dramatically in alloy A extrudates produced at the high extrusion ratios and temperatures.

All the observations regarding microstructural changes occurring with processing conditions and relative positions within the extrudates were, therefore, associated with either (i) increased deformation levels and increased temperature causing increased recrystallisation and/or (ii) increased temperature and time enhancing grain growth.

As well as transverse differences in temperature and strain rate, textural differences and/or solute depletion may also have been responsible for the microstructural changes occurring between the centre and edge of the extrudates.

Differences in the straining, strain rate and temperature between the core and surface regions of the extrudates may have caused differences in the deformation and recrystallised textures. Recrystallisation and grain growth rates may, therefore, have varied across the extrudates. High numbers of large equiaxed grains in the surface regions may have been produced by the nucleation of a high number of grains with moderate growth rates, whilst the presence of excessively large grains may have been produced by the nucleation of a low number of grains with very high growth rates. Textural analysis of both core and near surface regions was, therefore, carried out, with the results shown in section 4.3. From this analysis, it appeared that the textures did indeed alter from the centre of the extrudates to the surface regions, but no identification of the texture systems associated with the exaggerated growth regions was possible.

With regard to the influence of solute depletion upon surface microstructures Friedrich[5] found that the surface provided a diffusion path for Mg and Li when heated in a non-protective atmosphere, causing loss of important hardening elements at the surface. In his investigations of rolled sheet, he used S.I.M.S and microhardness techniques to produce a good correlation between the loss of alloying elements and the reduction in age-hardening potential of the material. Friedrich also observed increased grain size towards the surface of the material, and associated this increased grain size with solute depletion, and not increased temperature and strain at the surface.

If magnesium and lithium are depleted, the precipitation of δ', T_1 and S will be reduced. This would explain the hardness profile observed by Friedrich, but how, if at all, this influenced recrystallisation or grain growth is less obvious. The T_1 and S phases co-precipitate with the δ', and nucleate on matrix dislocations and subgrain boundaries[7] . The presence of T_1 and S or δ', therefore, may cause pinning of grain boundaries to a certain extent, along with localised increases in dislocation densities. The absence of such precipitation, due to solute depletion, may consequently increase the recrystallisation nucleation and/or grain growth.

The explanation of increased recrystallisation in the surface regions of the extrudates may, therefore, be considered as having a number of contributory factors:-

(i) Increased straining, strain rate and temperature towards the surface of the extrudates enhancing the recrystallisation mechanism and facilitating grain growth.

(ii) Textural differences between the core and surface regions causing variations in the degree of recrystallisation and/or grain growth.

(iii) Solute depletion within the surface regions enhancing recrystallisation and/or grain growth.

Fig 4.1.1 Optical Micrographs
Alloy B material.
As-Extruded material.
(a) 15:1 extrusion ratio.
400° C extrusion temperature.
Edge of extrudate.
(b) 15:1 extrusion ratio.
500° C extrusion temperature.
Core of extrudate.
(c) 30:1 extrusion ratio.
500° C extrusion temperature.
Edge of extrudate.
(d) 30:1 extrusion ratio.
500° C extrusion temperature.
Core of extrudate.

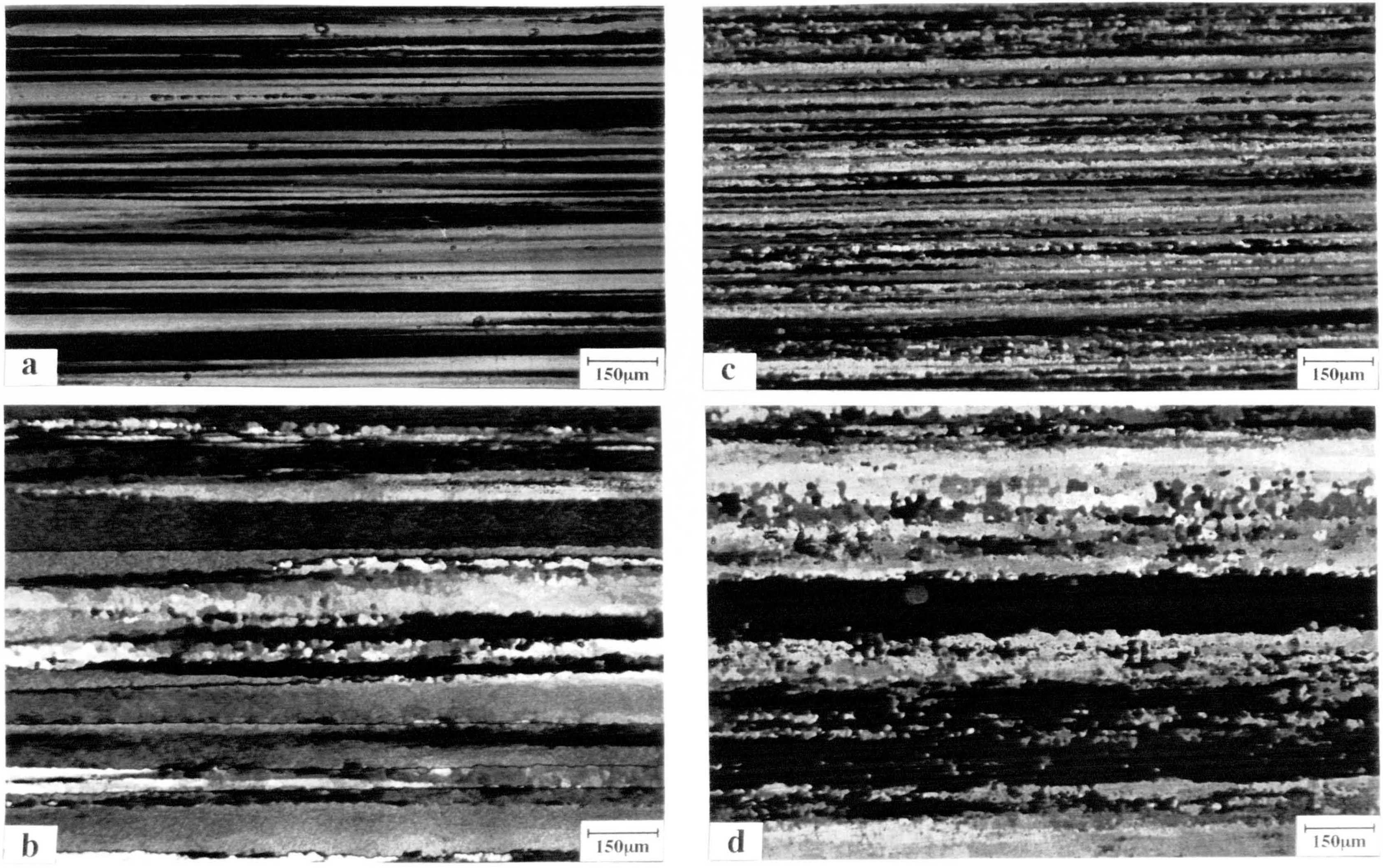


Fig 4.1.1

Fig 4.1.2 Optical Micrographs.
Alloy A material.
As-Extruded material.
(a) 30:1 extrusion ratio.
500° C extrusion temperature.
Edge of extrudate.
'Rear' of extrudate.
(b) 30:1 extrusion ratio.
500° C extrusion temperature.
Core of extrudate.
'Rear' of extrudate.
(c) 15:1 extrusion ratio.
400° C extrusion temperature.
Edge of extrudate.
'Front' of extrudate.

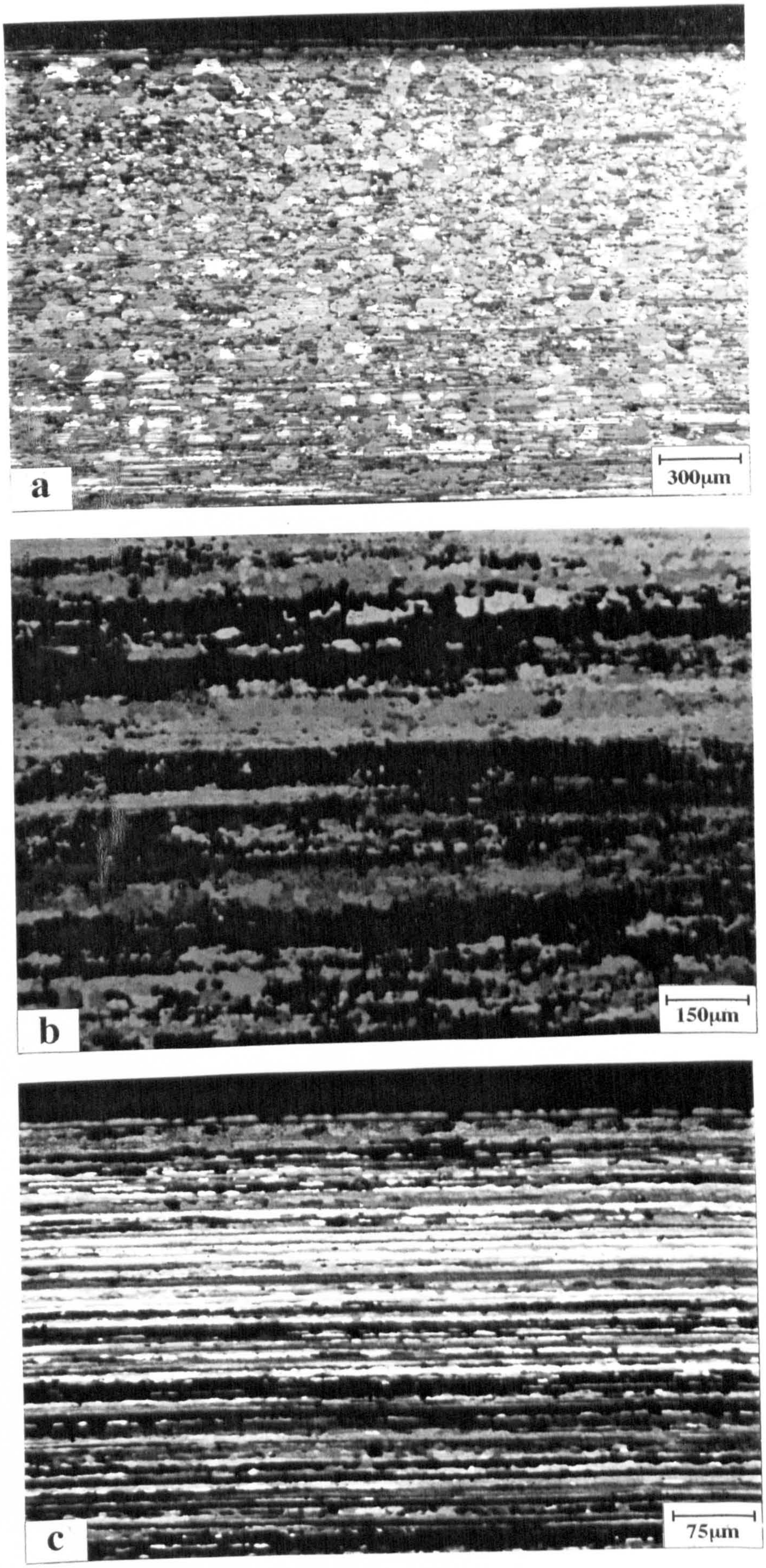
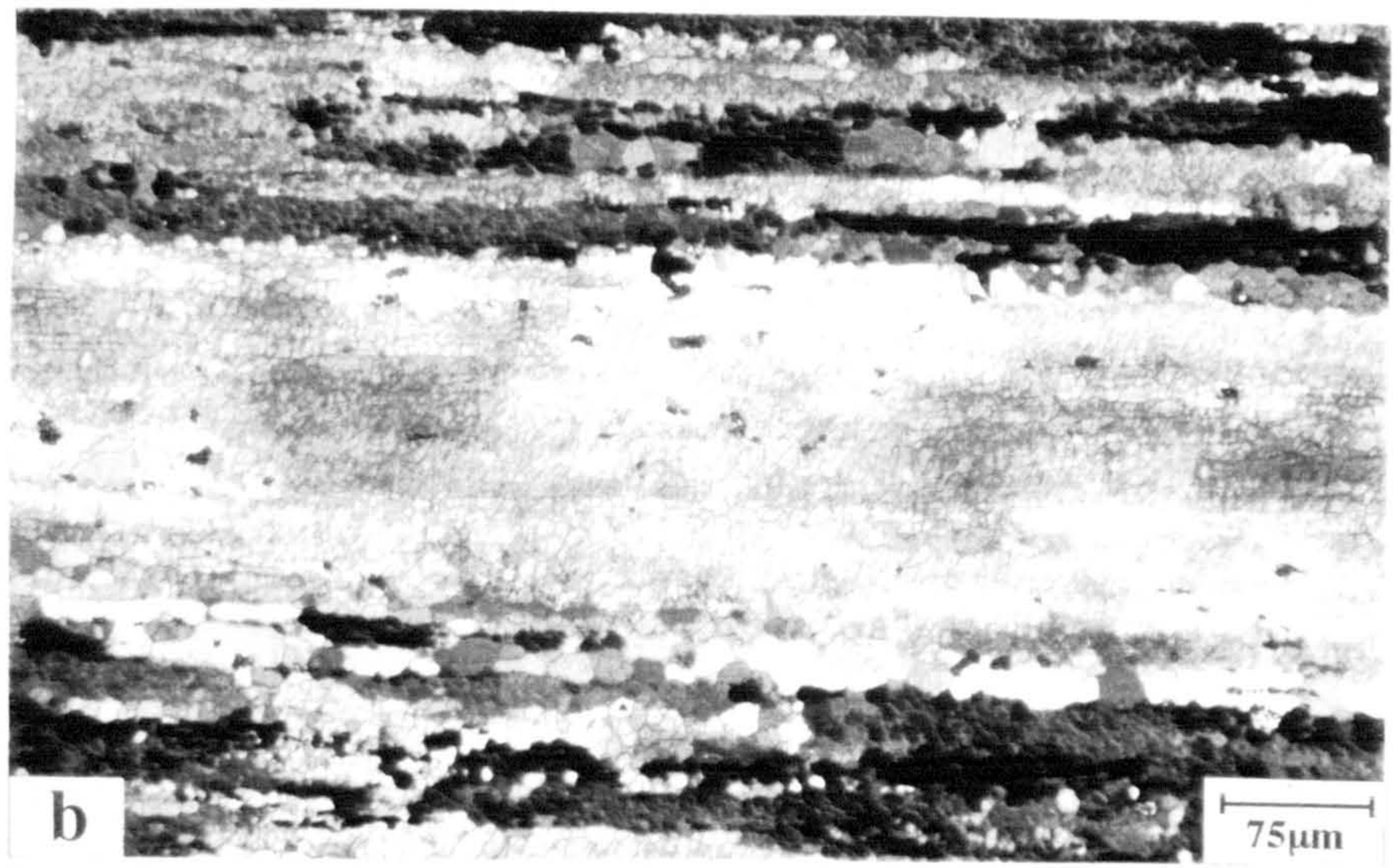
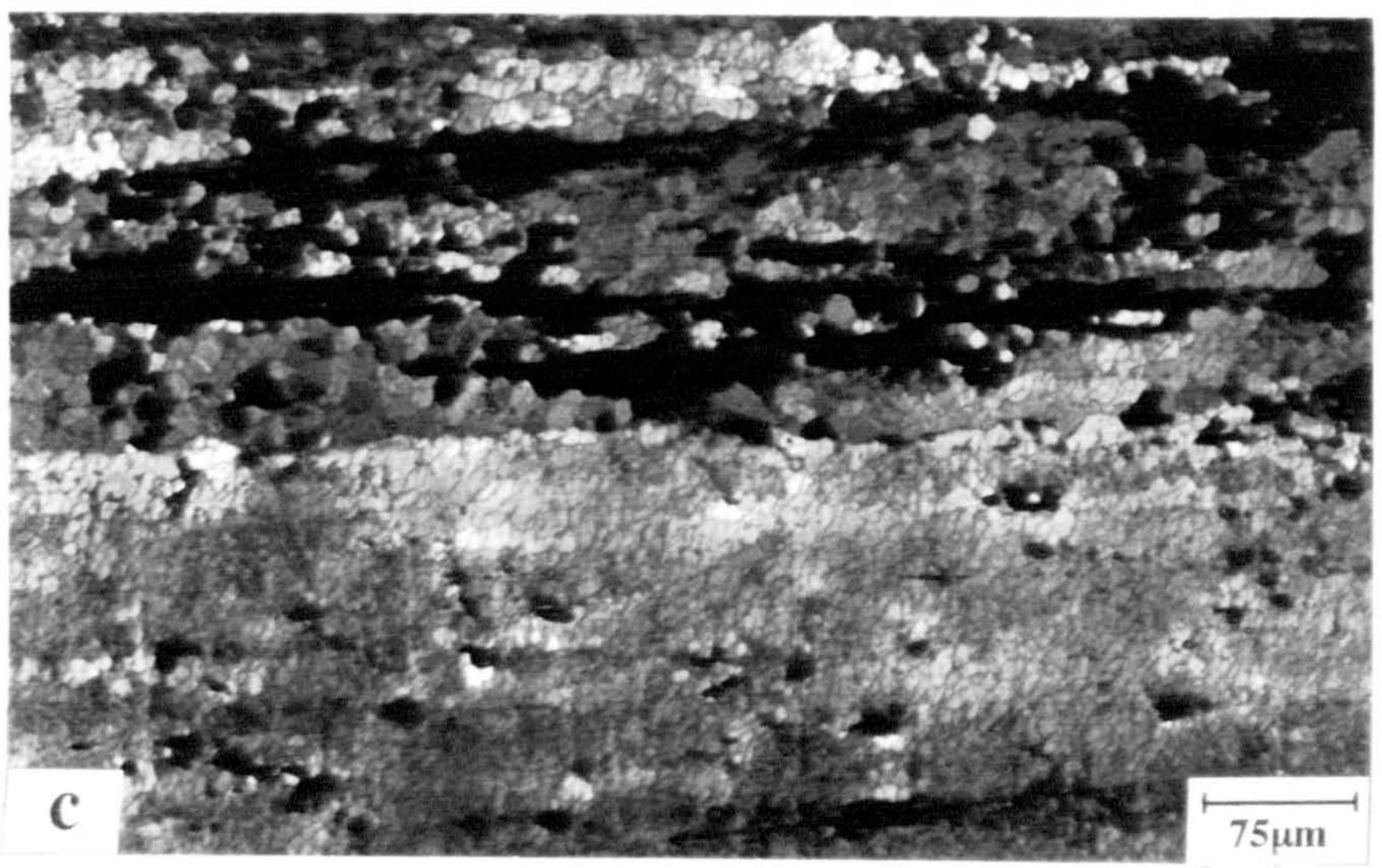


Fig 4.1.2

Fig 4.1.3 Optical Micrographs.
Overaged Condition.
'Core' of extrudate.
(a) 6:1 extrusion ratio.
400° C extrusion temperature.
Alloy A material.
'Front' of extrudate.
(b) 15:1 extrusion ratio.
400° C extrusion temperature.
Alloy B material.
(c) & (d) 15:1 extrusion ratio.
400° C extrusion temperature.
Alloy A material.
'Front' of extrudate.







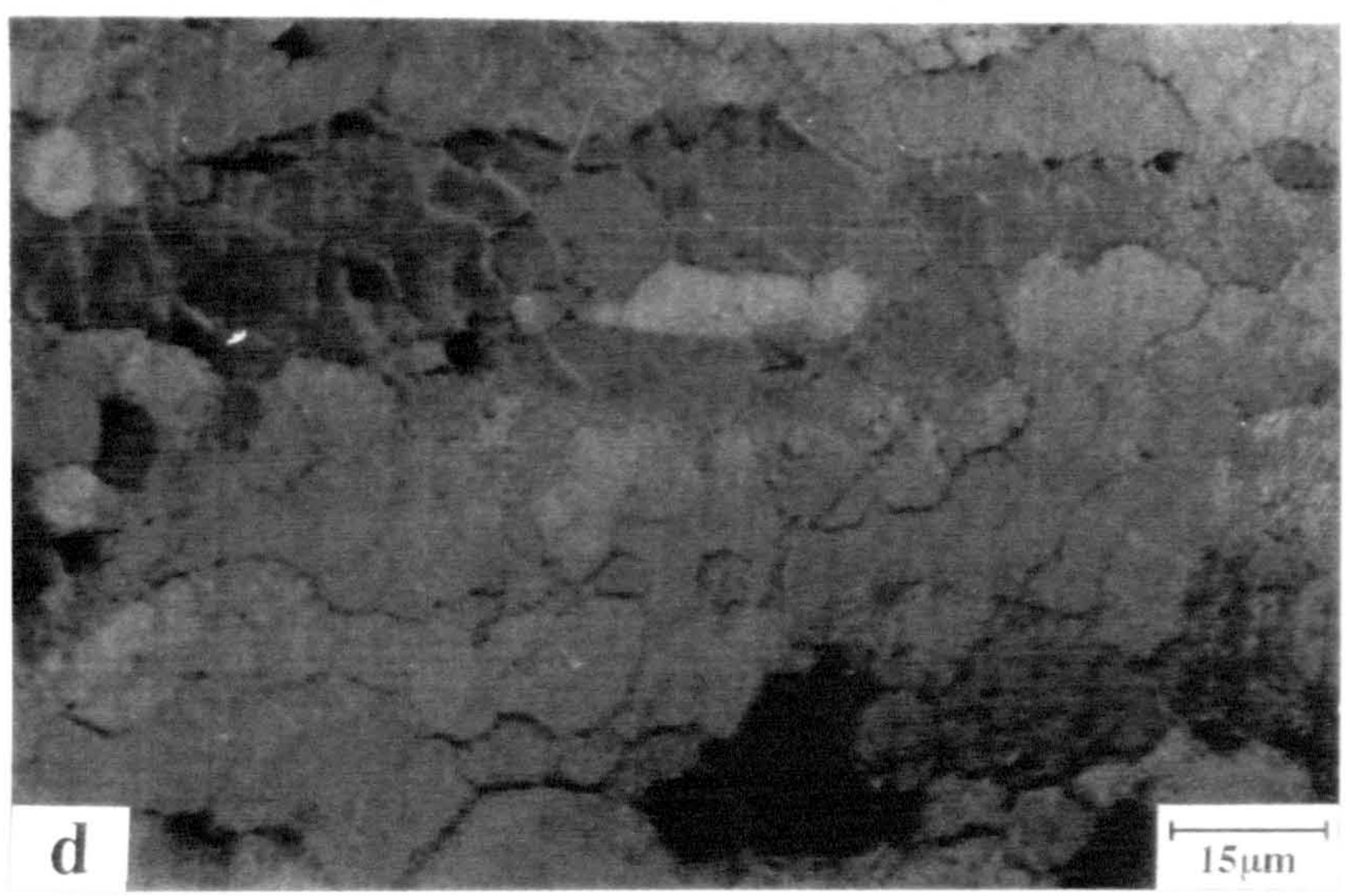
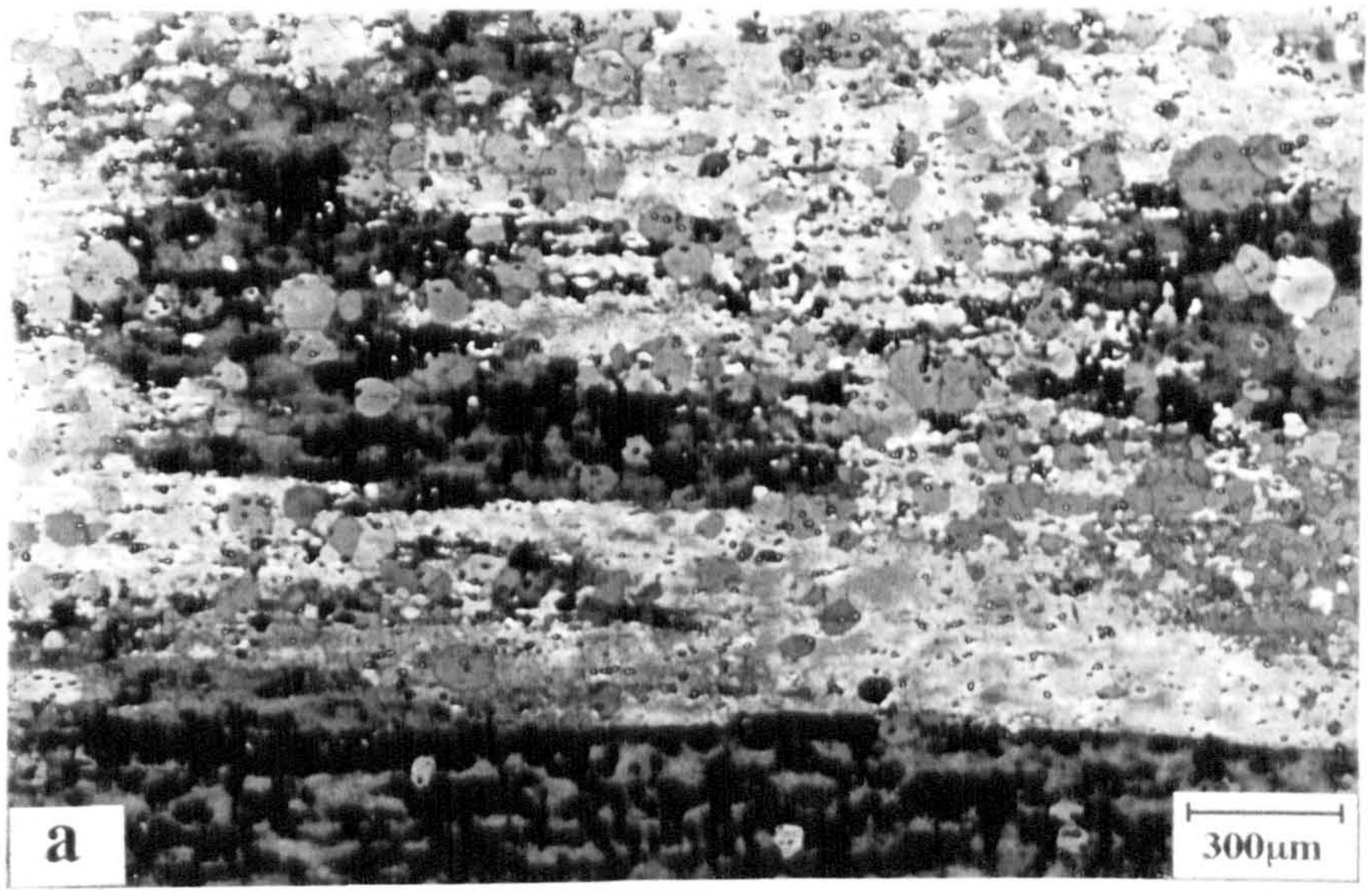
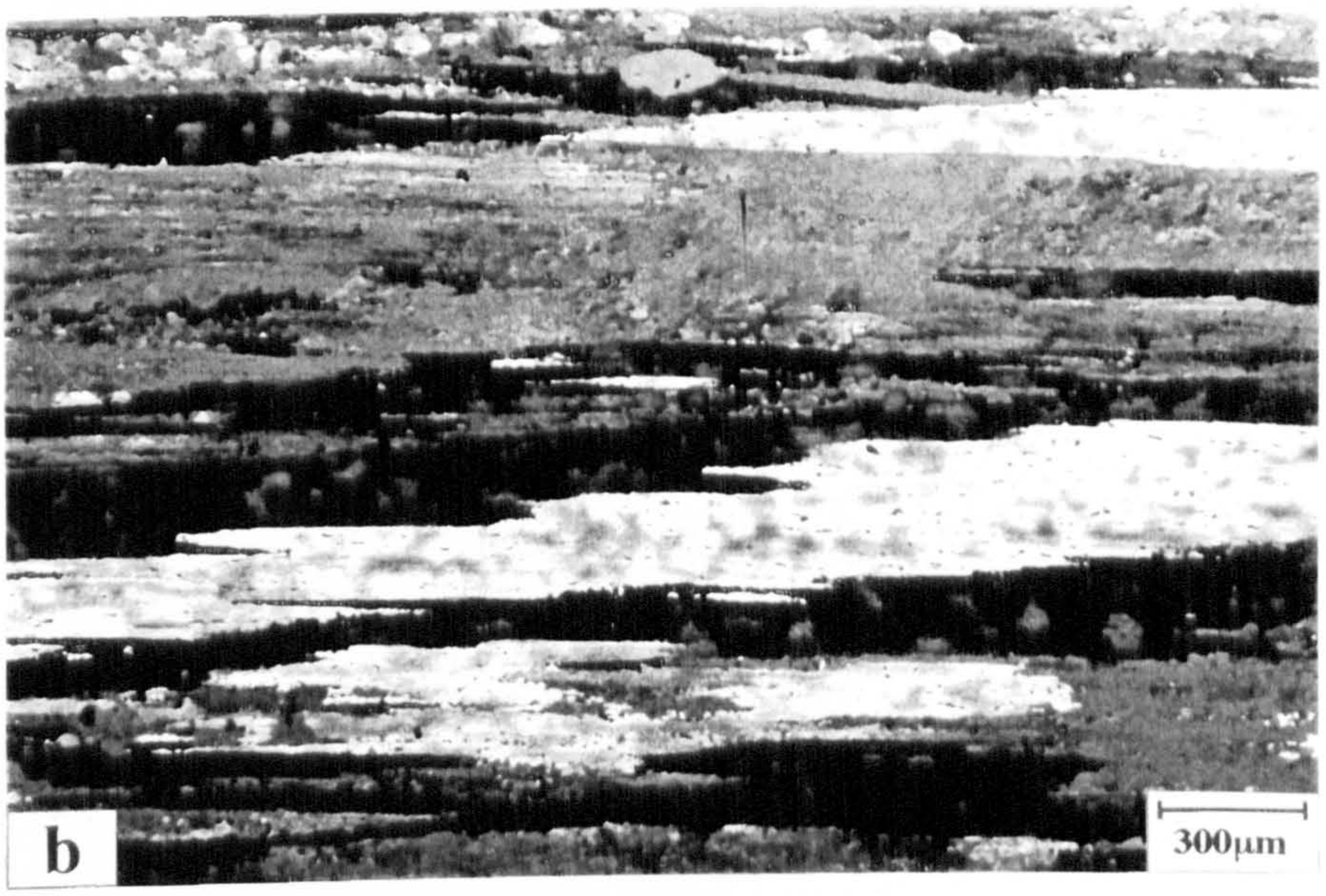


Fig 4.1.3

Fig 4.1.4 Optical Micrographs
Alloy A material.
Underaged Condition.
'Core' of extrudate.
(a) 30:1 extrusion ratio
450° C extrusion temperature.
'Back' of extrudate.
(b) & (c) 30:1 extrusion ratio.
400° C extrusion temperature.
'Front' of extrudate.





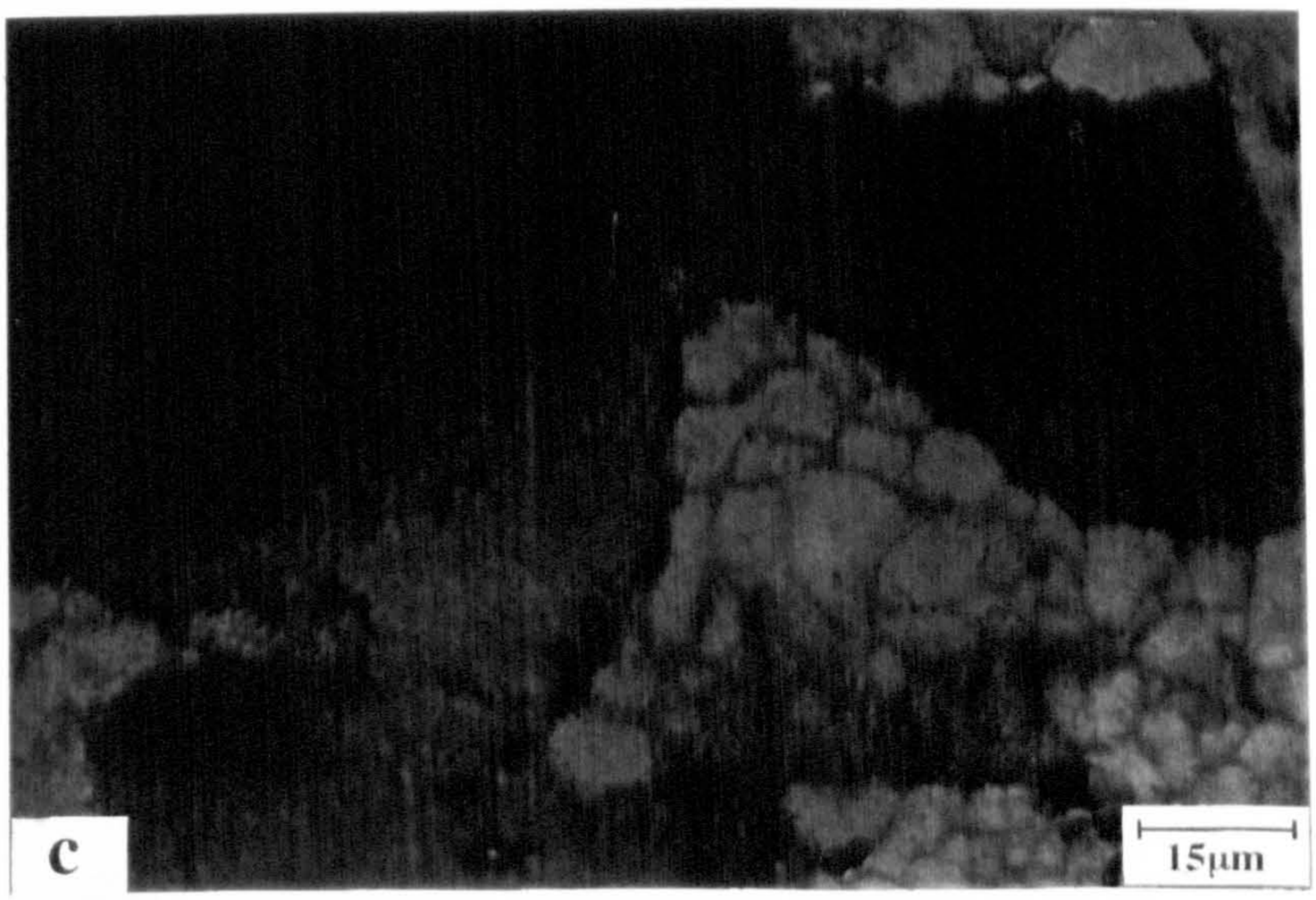


Fig 4.1.4

Fig 4.1.5 Optical Micrographs.
15:1 Extrusion Ratio.
Alloy A material.
Overaged Condition.
'Surface' of extrudate.

(a) 400° C extrusion temperature.
'Front' of extrudate.

(b) 450° C extrusion temperature.
'Front' of extrudate.

(c) 500° C extrusion temperature.
'Back' of extrudate

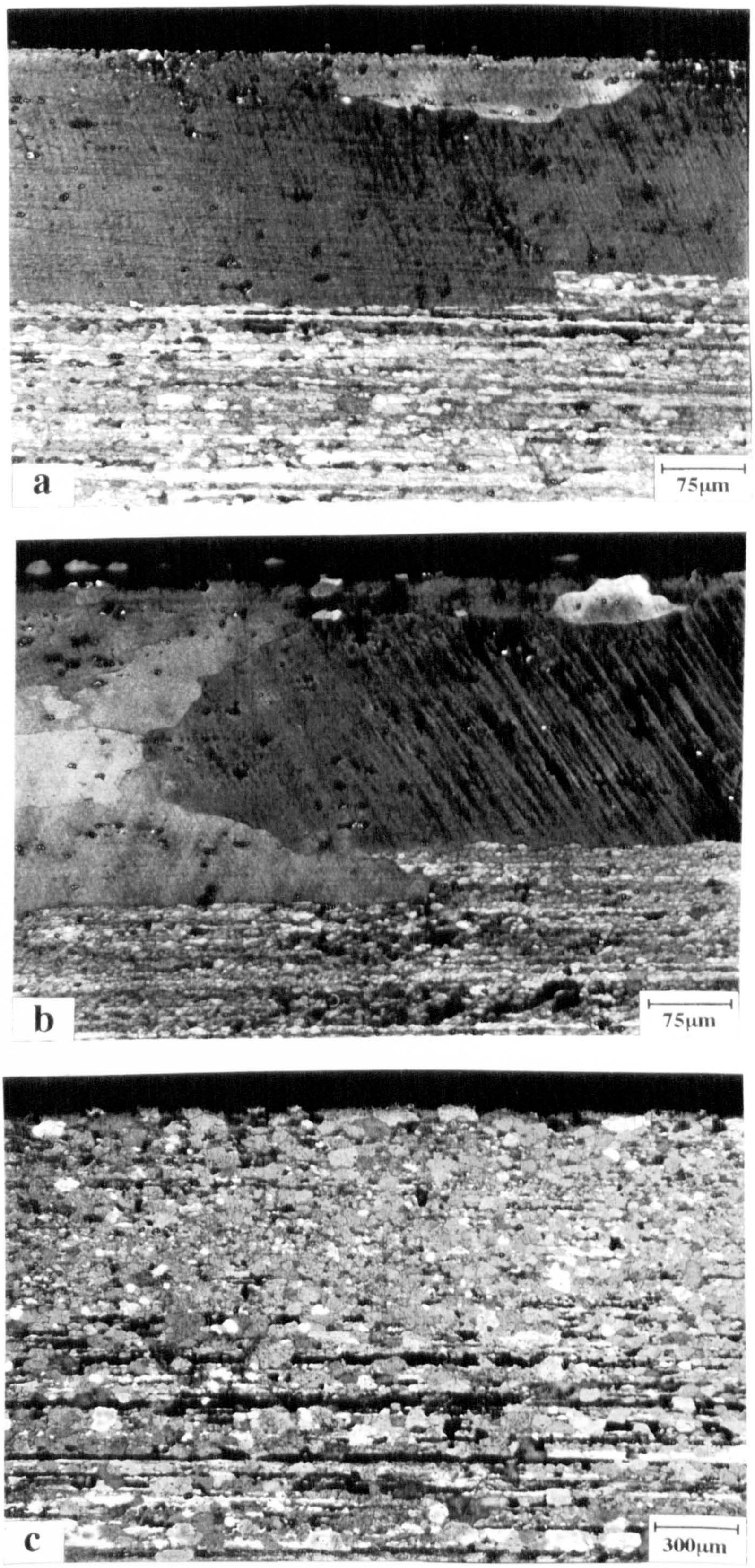
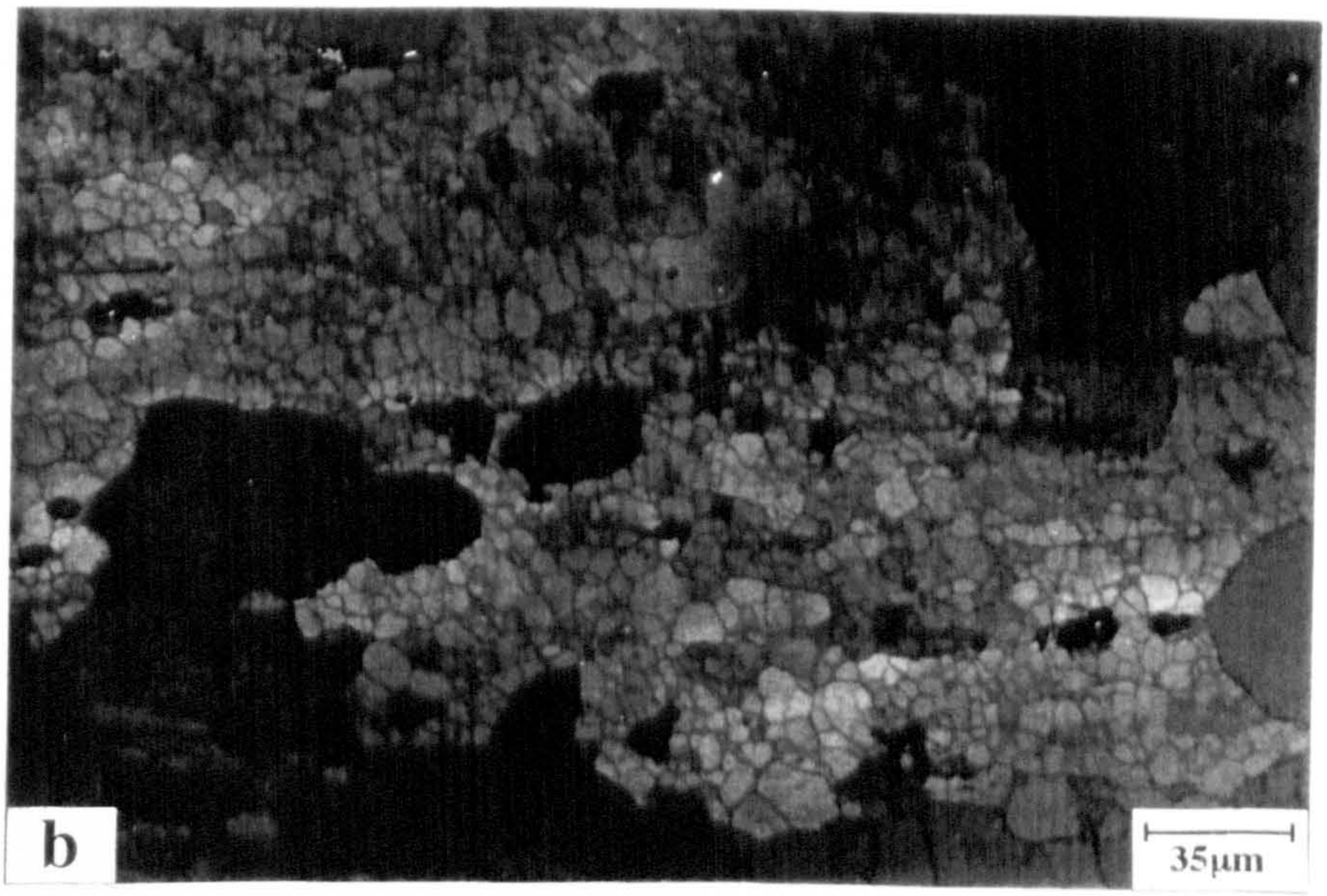


Fig 4.1.5

Fig 4.1.6 Optical Micrographs
30:1 Extrusion Ratio
500° C extrusion temperature.
Underaged Condition.
'Core' of extrudate.
(a) & (b) Alloy A Material
'Front' of extrudate.
(c) Alloy B Material





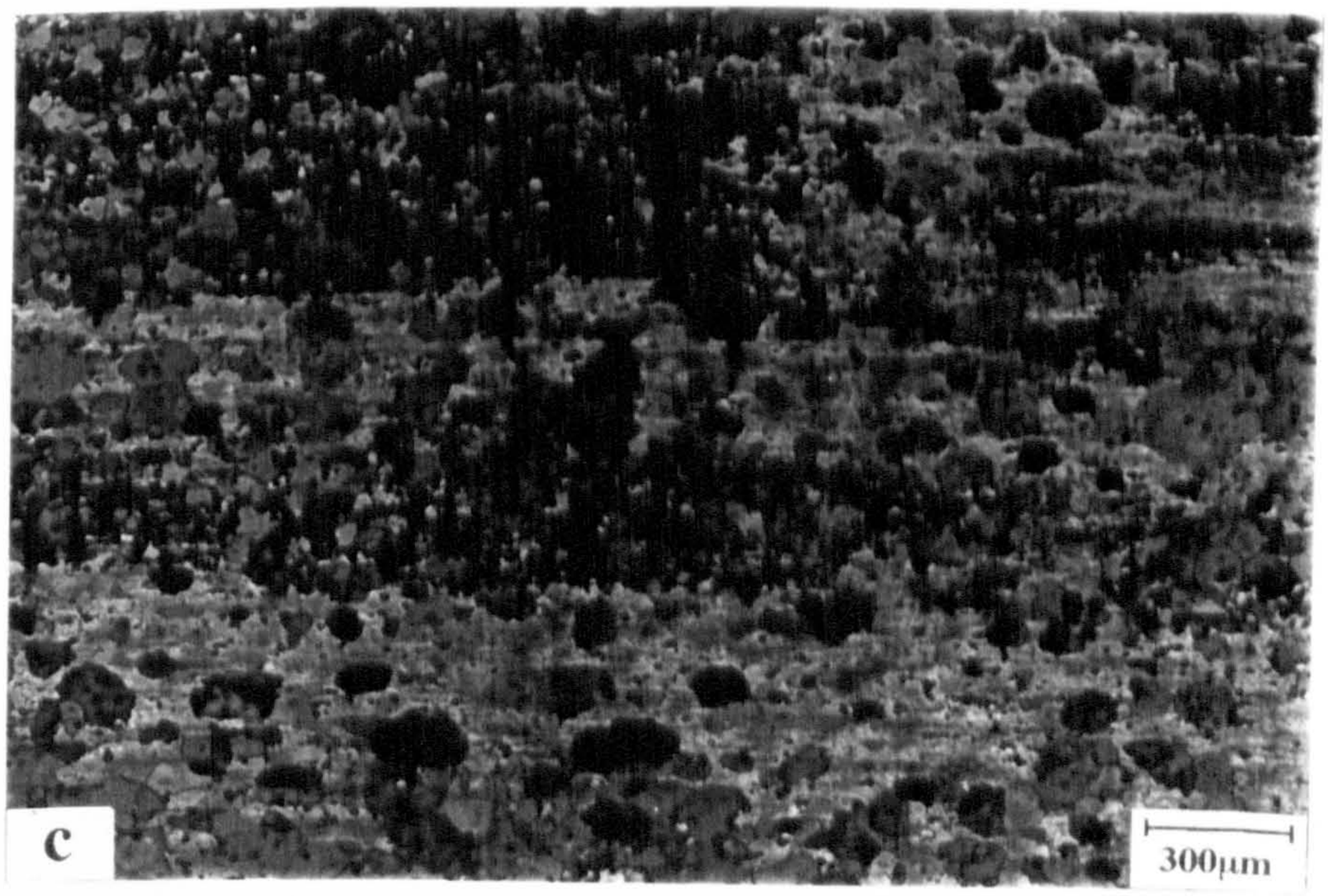


Fig 4.1.6

Fig 4.1.7 Optical Micrographs
30:1 Extrusion Ratio
500° C extrusion temperature.
Alloy A material
Overaged Condition.
'Back' of extrudate.
(a) 'Surface' of extrudate.
(b) & (c) 'Core' of extrudate.

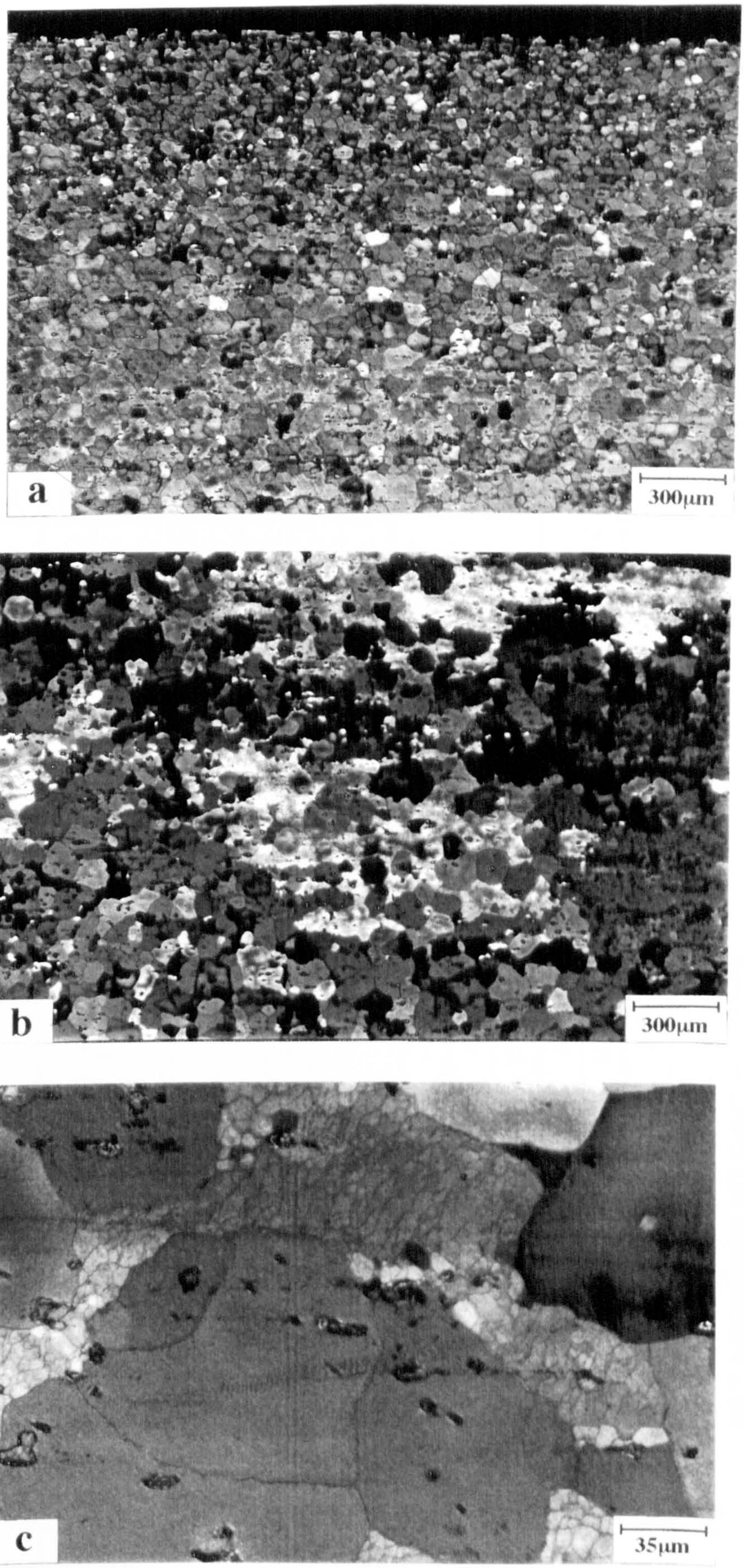


Fig 4.1.7

Extrusion Ratio	Extrusion Temp (°C)	Ln Z	Percentage of core recrystallisation	Grain size of core recrystallisation (μm)	Grain size of edge recrystallisation (μm)	Core subgrain size (μm)
6:1	400	28.867	0			1->10
9:1	400	29.141	0 -> 5% Grain boundary equiaxed grains	10		1->10
15:1	400	29.701	12% Grain boundary equiaxed grains	10 -> 20	> 100 Exaggerated growth	1->10
	450	27.72	20% Grain boundary equiaxed grains	10 -> 20	> 100 Exaggerated growth	1->10
	500	25.871	24% Grain boundary equiaxed grains	10 -> 20	20 -> 80 Large equiaxed grains	1->10
15:1 Axi-symmetric	400	29.377	10 %	10 -> 20	10 -> 50	1->10
30:1	400	30.146	15% Grain boundary equiaxed grains	10 -> 40	> 100 Exaggerated growth	1->10
	450	28.2	20% Large equiaxed grains	20 -> 100	20 -> 80 Large equiaxed grains	1->10
	500	26.39	35% Large equiaxed grains	20 -> 100	20 -> 80 Large equiaxed grains	1->10

Fig 4.1.8 Variation in recrystallised grain size, subgrain size, and % recrystallisation with changes in processing conditions. Alloy A, aged material, 'front' of extrudate.

Extrusion ratio & cross-section gemetry (mm)	Aspect Ratio	Billet cross-section (mm)	Semi-cone angle	Pe	Pr	Pe/Pr	R'	Total Strain LnR'	Ram Speed mm/s	Strain rate (/s)	Extrusion Temp (°C)	Ln Z
6:1 18.4 x 41	2.2:1	75	60	118.8	96.2	1.1	6.7	1.9	2.44	0.642	400	28.867
9:1 14.9 x 33.8	2.2:1	75	62	96.6	78.5	1.1	10.1	2.3	2.44	0.844	400	29.141
15:1 7.9 x 37.3	4.7:1	75	65	90.4	60.8	1.22	18.3	2.91	2.96	1.478	400	29.701
									3.1	1.548	450	27.72
									2.85	1.423	500	25.871
15:1 Axi-symmetric 19.36 diameter	1:1	75	65	60.8			15	2.71	2.3	1.069	400	29.377
									2.6	1.209	450	28.250
									3.0	1.395	500	27.244
30:1 4.7 x 32	26.81	75	70	73.3	43.0	1.31	39.2	3.67	2.86	2.307	400	30.146
									3.1	2.501	450	28.2
									2.96	2.388	500	26.389

Fig 4.1.9 Calculated Z values for various extrusion condition combinations. (See Appendix IV for calculation method).

4.2 Transmission Electron Microscopy

Transmission electron microscopy (T.E.M.) was carried out in order to provide general information on the distribution and proportion of phases present within the extrudates, together with knowledge of the subgrain sizes, and variation in these sizes with process conditions.

An in depth analysis of the phases present was considered unnecessary, since it was possible to identify the matrix and grain boundary precipitates to the required degree from the published literature[1][2][3][4][8].

4.2.1 Microstructural Variation with Processing

For both alloy compositions T.E.M. analysis of the as-extruded material revealed the matrix precipitation to be characterised by δ' and Al_3 Zr. Fig 4.2.1(a) illustrates a typical micrograph obtained from the as-extruded material. It exhibits a mottled appearance, due to the presence of the δ', but no grain boundary precipitation is evident. Constituent phases that survived homogenisation were clearly observed at many grain boundaries within the as-extruded material, however, as fig 4.2.1 (b) indicates. These precipitates were in general elongated, having an axial length up to 2μm and an aspect ratio ranging from 1:1 -> 5:1. A complete analysis of these phases was not carried out, since many researchers[1][2] have previously established them to be based upon the Al-Fe-Cu system.

The variation in both matrix and grain boundary precipitation within the as-extruded material, was found to be negligible as the extrusion temperature and extrusion/aspect ratio increased. The subgrain sizes within the as-extruded material, which ranged from 2->6μm, were also found to be constant as process conditions were varied.

After solution heat treatment and ageing the amount of both grain boundary and matrix precipitation was observed to increase. In the underaged, peak-aged and overaged material considerable amounts of homogeneously precipitated δ' were evident, together with β' precipitates formed from the heterogeneous nucleation of δ' on Al_3 Zr particles, fig 4.2.1(c) & fig 4.2.2(e). The homogeneously nucleated δ' precipitates were observed to grow from 20->40nm, and the duplex Al_3 Zr / δ' precipitates from 35->60nm as ageing proceeded from the underaged to the overaged condition. Very little S(Al_2 CuMg) or T_1 (Al_2CuLi) was detected in the matrix after short ageing times (i.e. underaged), fig 4.2.3(a) & (b) , but as ageing proceeded, T_1 and S phase precipitation clearly increased, fig 4.2.2. Heterogeneous nucleation of S was indicated by its sporadic occurrence throughout the matrix, and has been reported[2][5] to grow as rods, which then widen to form laths resulting in a corrugated sheet appearance in the T.E.M micrographs, fig 4.2.2(b). Colonies of heterogeneous nucleated T_1 phase were also present, appearing as regular stripes in the T.E.M. micrographs. This is due to the fringe contrast caused by the associated stacking faults. Fig 4.2.2(f) indicates the heterogeneous nucleation of

ageing precipitates upon grain boundaries. No δ' P.F.Z's were associated with this precipitation, since S phase contains no lithium, hence did not compete with the δ' for the available lithium. Also, when the copper content is relatively low in comparison with the lithium present, it has been reported that no competition between the δ' and T_1 phases for the available lithium occurs either.

With greater ageing times increasing proportions of small precipitates, with associated P.F.Z's, were observed to populate high angle grain boundaries, fig 4.2.2(c) & (d). These precipitates were observed to grow from an average of 0.05 μm in the under-aged condition to 0.1μm in the over-aged condition. The presence of the P.F.Z.'s suggested that they contained lithium. Researchers such as Mukapadyay[1] have also observed grain boundary precipitates, and by using x-ray E.D.S. analysis, he found these particles to be rich in copper (13-17 wt %), determining them to be based upon the Al-Li-Cu-Mg system. Other researchers[2][6] have found that in AA 8090, I phase forms at the grain boundaries. The I phase having a composition based upon the Al-Cu-Li system (70% Al and 30% Cu) and being responsible for the P.F.Z formation. There are, therefore, conflicting results as to the specific composition of these grain boundary phases. The majority of the evidence, however, does suggest these phases to be I phase, hence they will be referred to as such subsequently in this project.

The largest I phase precipitates were observed at high angle boundaries, indicating an ease of formation, associated with lower lattice strains and greater diffusion rates. The dependence of the I phase precipitation upon boundary misorientation has also been observed by other researchers[1][7] . The I phase precipitates shown in fig 4.2.2(d) were approximately 0.1μm in size, but they were found to range in size up to 0.2μm.

With regard to the variations in the microstructures of the aged material, with changes in processing, no significant variations in precipitation with increases in extrusion temperature or aspect/extrusion ratio, for both the underaged and overaged material, were observed. Tempus[9] also observed no variations in precipitation in lital 8090 extrudates as the aspect ratio was increased.

Not only were the microstructural variations between extrudates produced under different conditions of interest, but microstructural variations across the transverse sections of each extrudate were also investigated. Fig 4.2.3 (c)->(d) show T.E.M. micrographs obtained near the surface regions of the extrudates at the 2/3 radius position. Fig 4.2.3 (d) illustrates the outline of the original deformed grains, together with the internal substructure ranging in size between 2->6μm. The extrudates were processed to the overaged condition, hence homogeneously and heterogeneously nucleated δ', together with S and T_1 phases, were observed. For both alloy compositions, however, no definite variations in δ', T_1 or S precipitation were observed to occur towards the outer regions of the extrudate, irrespective of ageing condition. The subgrain sizes were also found to be constant from the core regions to the 2/3 radius positions of the extrudates.

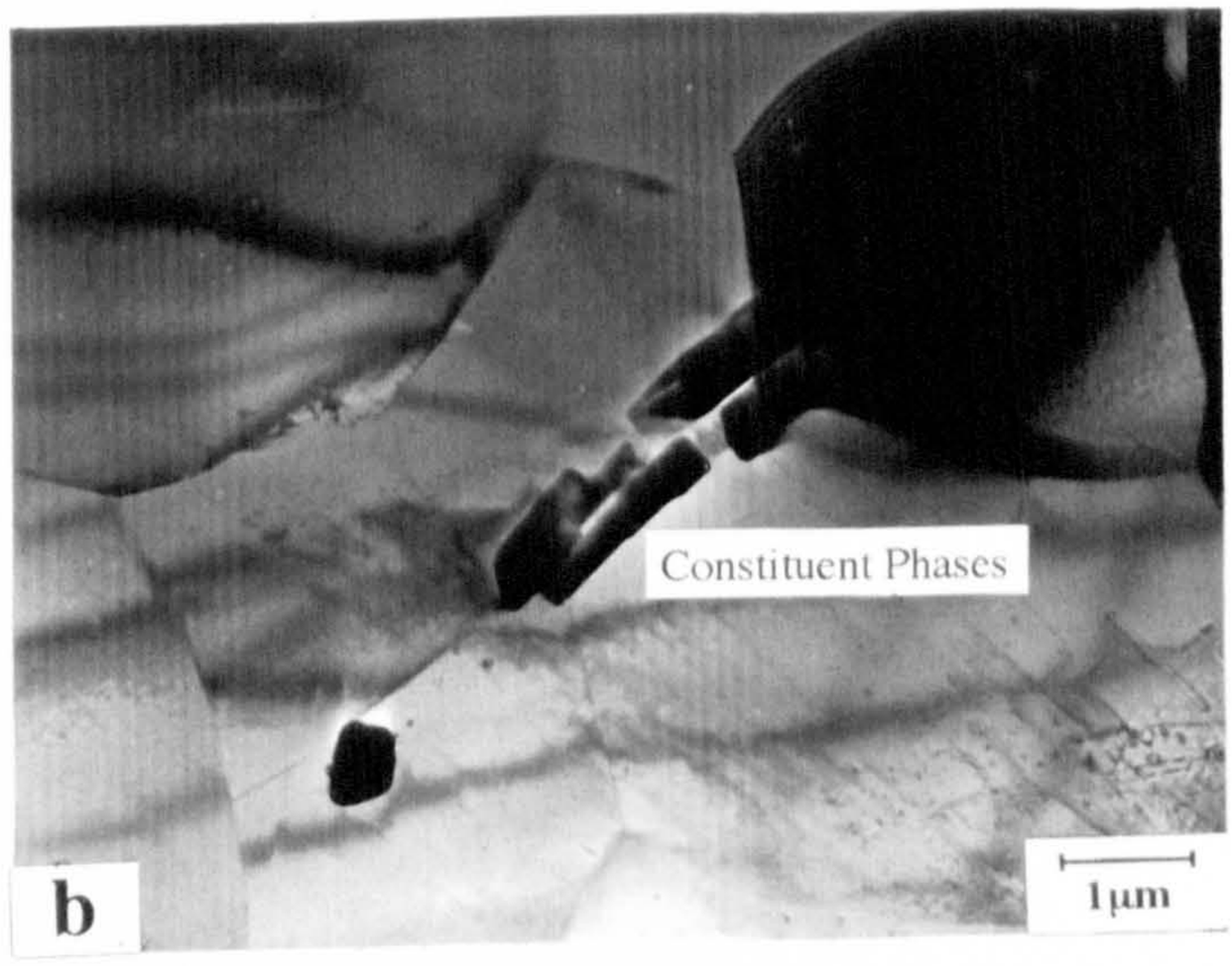
Fig 4.2.1 T.E.M. Micrographs.

(a) 30:1 extrusion ratio.
500° C extrusion temperature.
Alloy A material.
As-extruded condition.
Longitudinal section.
'Core' region of extrudate.
This micrograph illustrates a very clean microstructure.
No grain boundary precipitation is evident, but the
'mottled' effect associated with the micrograph is due to δ'
precipitation.

(b) 15:1 extrusion ratio.
400° C extrusion temperature.
Alloy B material.
As-extruded condition.
Longitudinal section.
'Core' region of extrudate.
This micrograph illustrates the constituent grain boundary
phases observed in all the extrudates irrespective of
processing histories.

(c) 30:1 extrusion ratio.
500° C extrusion temperature.
Alloy B material
Peak-aged condition.
Longitudinal section.
'Core' region of extrudate.
This micrograph is a bright field image along the (100) Al-
orientation illustrating the δ' precipitation.





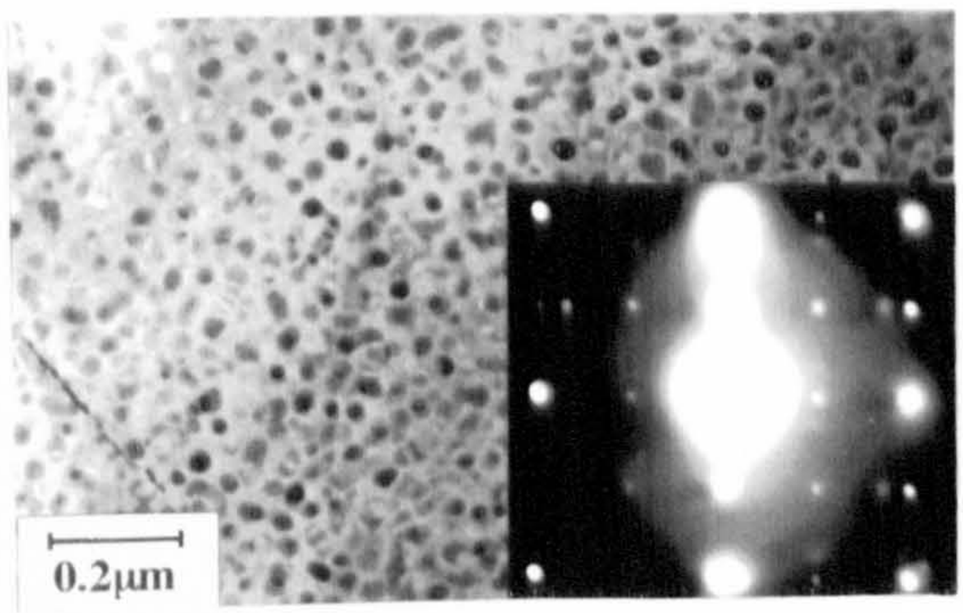


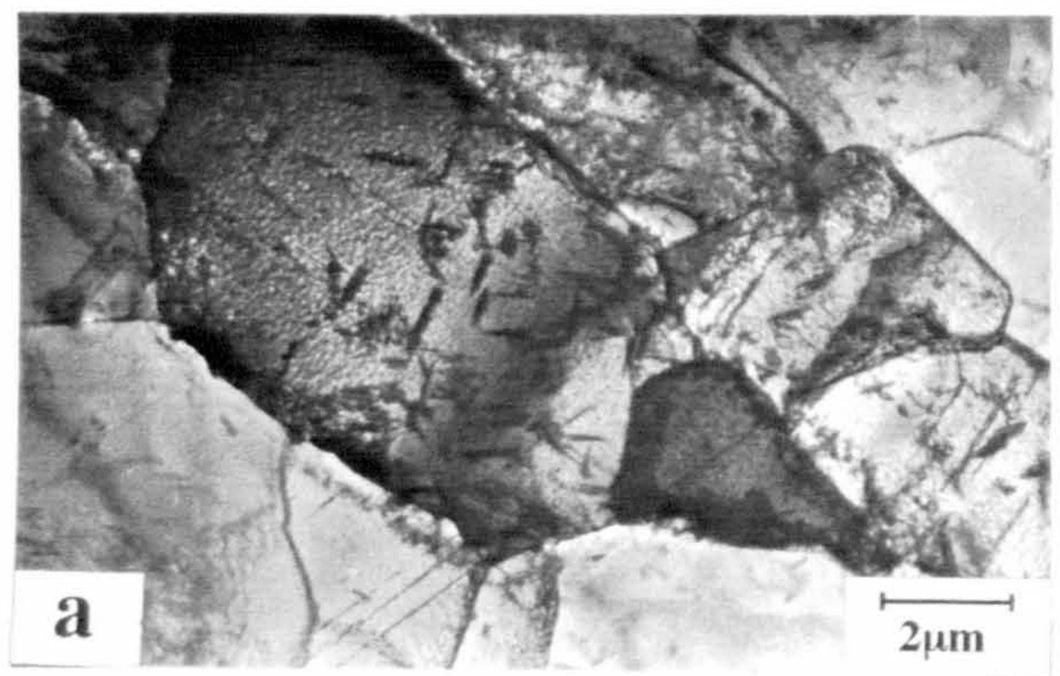
Fig 4.2.1

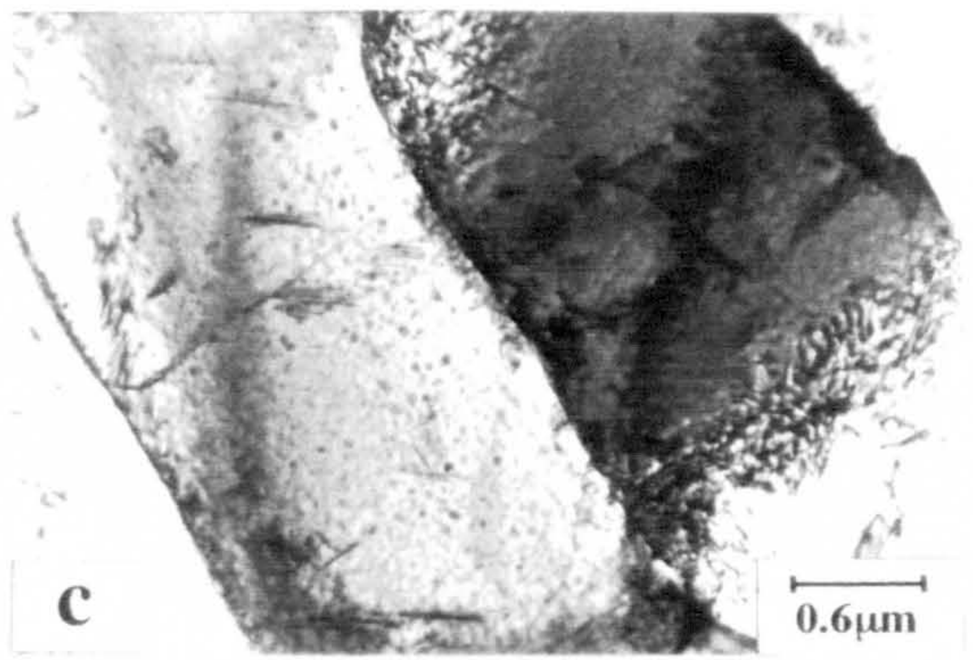
Fig 4.2.2 T.E.M. Micrographs.

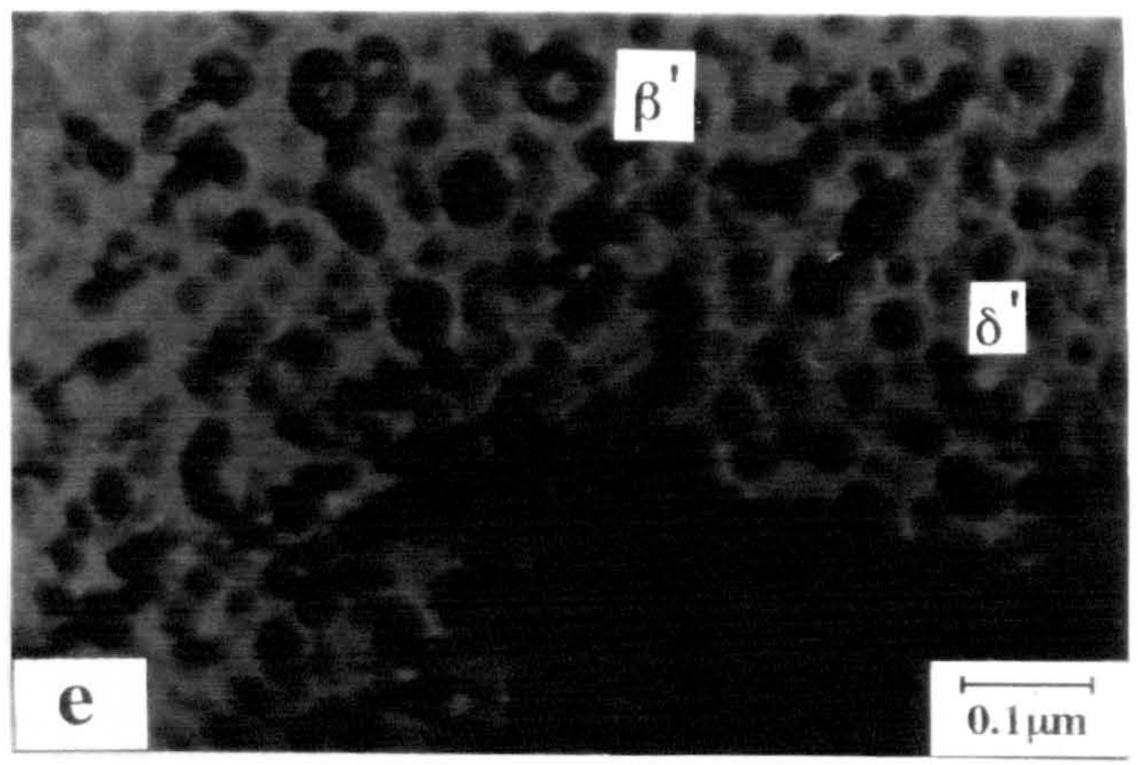
(a) & (b) 15:1 extrusion ratio.
500° C extrusion temperature.
Alloy A material.
Overaged condition.
Longitudinal section.
'Core' region of extrudate.
These micrographs illustrate the S and T_1 matrix precipitation. δ' and β' precipitation is also present, evident by the 'mottled' effect associated with each micrograph.

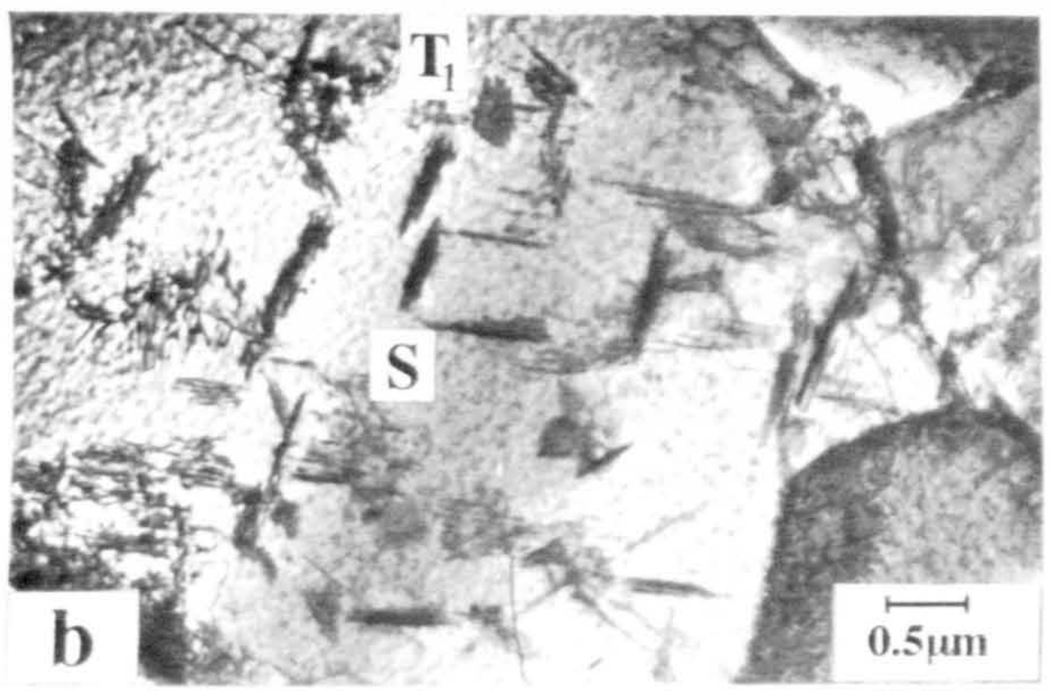
(c) & (d) 30:1 extrusion ratio.
400° C extrusion temperature.
Alloy B material.
Overaged condition.
Longitudinal section.
'Core' region of extrudate.
These T.E.M. micrographs highlight the grain boundary I phase (Al-Cu-Li) precipitation.
δ', β' and S phase precipitation is also clearly evident.

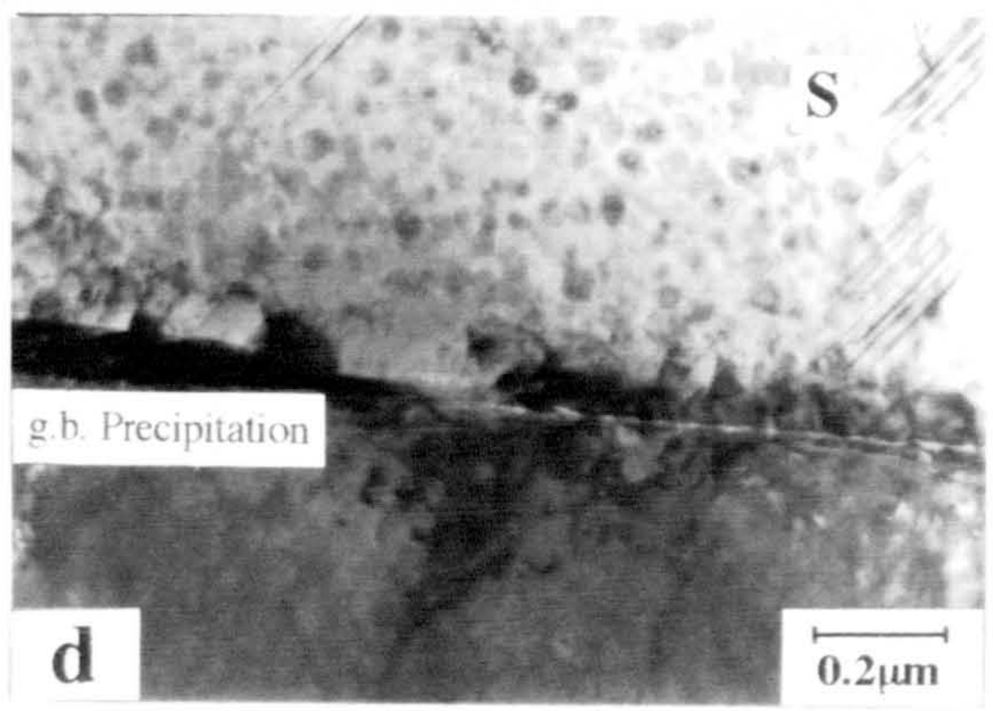
(e) & (f) 30:1 extrusion ratio.
500° C extrusion temperature.
Alloy A material.
Overaged condition.
Longitudinal section.
Core region of extrudate.
Micrograph (e) illustrates the δ' and β' precipitation observed in all the aged extrudates.
Micrograph (f) illustrates the S phase grain boundary precipitation.


a
2μm


c
0.6μm


β'
δ'
e
0.1μm


T1
S
b
0.5μm


S
g.b. Precipitation
d
0.2μm

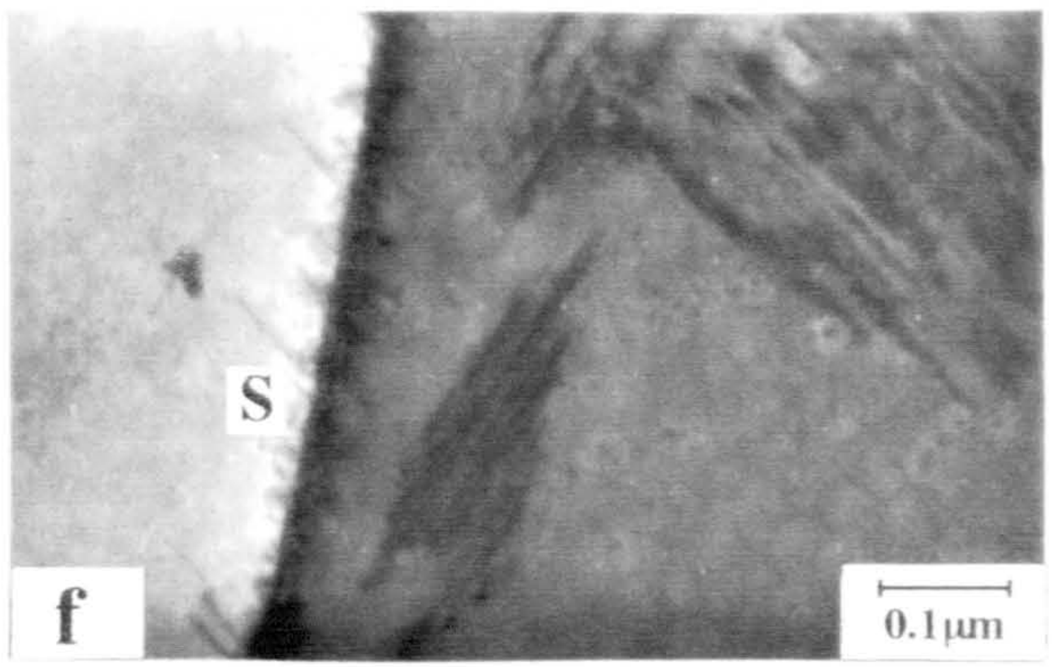

S
f
0.1μm

Fig 4.2.2

Fig 4.2.3 T.E.M. Micrographs.

(a) & (b) 15:1 extrusion ratio.
500° C extrusion temperature.
Alloy A material
Underaged condition.
Longitudinal section.
'Core' region of extrudate.
The elongated nature of the original grains, together with the internal subgrain structures, are illustrated by these micrographs.
No substantial S or T_1 matrix precipitation is evident, but the 'mottled' effect associated with the micrographs is due to substantial δ' precipitation.
Grain boundary I phase precipitation based upon the Al-Li-Cu system is evident, and subgrain sizes of approximately 1->5μm were indicated.

(c) 30:1 extrusion ratio.
400° C extrusion temperature.
Alloy B material.
Overaged condition.
Transverse section.
2/3 radius position.
This micrograph illustrates subgrain sizes of approximately 2->4μm. The grains/subgrains were generally equiaxed in appearance, due to the transverse sectioning of the sample from the extrudate.
It also illustrates the substantial proportions of grain boundary I phase precipitation evident in all extrudates that were processed to the overaged condition.

(d) 30:1 extrusion ratio.
500° C extrusion temperature.
Alloy A material.
Overaged condition.
Longitudinal section.
2/3 radius position.
This micrograph illustrates very clearly the elongated nature of the original grains, together with the internal subgrain structures. Subgrain/recrystallised grain sizes of 2->10μm were observed.

(e) & (f) 15:1 extrusion ratio.
400° C extrusion temperature.
Alloy A material.
Overaged condition.
Longitudinal section.
'Core' region of extrudate.
These micrographs illustrate the S and T_1 matrix precipitation present in the overaged material.

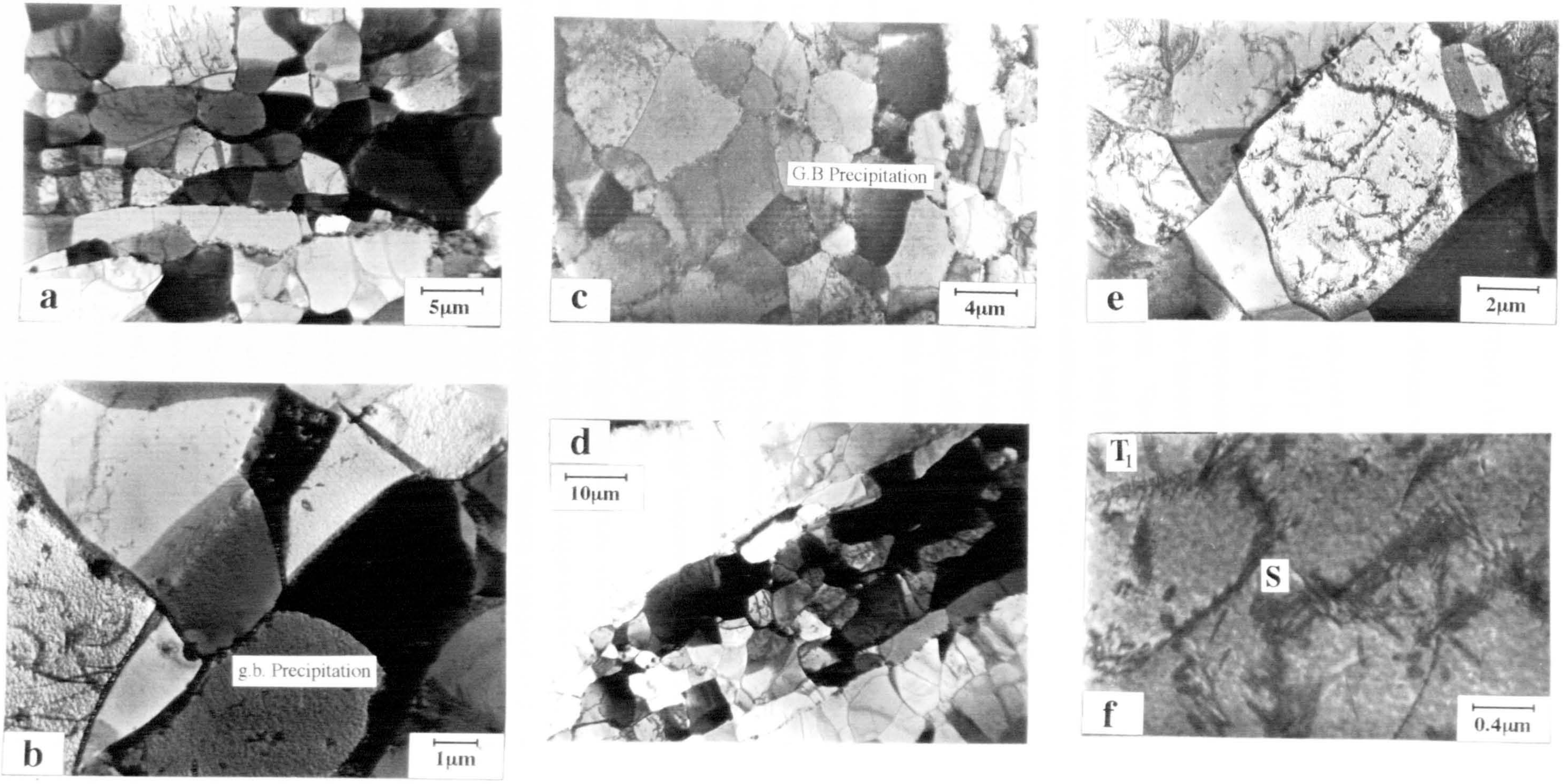

a
5μm
c
G.B Precipitation
4μm
e
2μm
b
g.b. Precipitation
1μm
d
10μm
T_1
S
f
0.4μm

Fig 4.2.3

4.3 Texture Analysis

4.3.1 Texture Variation with Processing

In order to investigate the variation in texture with processing conditions, O.D.F. and pole figure analyses were carried out. O.D.F. analysis enabled percentage volume fractions of specific textural components to be calculated, whilst pole figure plots illustrated general trends in texture with variations in processing condition.

Many previous researchers[1][2][3] have investigated the various textures associated with both rolling and extrusion processes. Four (ideal) orientations situated on two principal rolling texture fibres called the α and β fibres[4][8] have been associated with rolled F.C.C. metals and alloys, whilst extrusions have been found to develop double fibre, <111> <100>, texture with the <111> component being dominant[7][9].

Fig 4.3.1 tabulates the observed variations in texture as the processing conditions were altered, for solution heat treated and aged alloy A material. The variation in as-extruded texture with increasing extrusion temperature were also examined, but no changes were observed.

At the centres of the aged extrudates produced at the lower extrusion temperatures and ratios, strong rolling type textures, consisting of copper {112} <111>, brass {110} <112>, Goss {110} <001>, and S {124} <211> components, were evident, fig 4.3.2->3. At the higher extrusion temperatures and extrusion ratios, however, these rolling textures began to break down and a cubic component became more evident, compare fig 4.3.3 with fig 4.3.5, and fig 4.3.4 with fig 4.3.6.

The material extruded at 15:1 exhibited no significant texture variations with increases in extrusion temperature other than a slight increase in the cube texture component, fig 4.3.1. For the 30:1 material, however, more significant texture variations with increases in extrusion temperature were observed. Fig 4.3.9 illustrates how the Brass, S, Copper and cube components were observed to vary with extrusion temperature. No significant changes in the Goss texture component were found. From these graphs it is evident that a correlation between Brass, S and Copper textures was present, with these components decreasing as extrusion temperature increased. The cube texture on the other hand was observed to increase as extrusion temperature increased. Previous researchers[4] have also reported correlations between texture components, associating copper & S components with cube textures, and Goss textures with brass components, but neither of these associations were evident in this project.

With regard to the variation in texture with extrusion/aspect ratio, extrudates produced at 400° C exhibited an increase in both the rolling type textures and cube components as the extrusion ratio increased from 9:1->30:1, fig 4.3.1. At 500° C, however, the increase in extrusion ratio from 15:1->30:1 appeared to cause a decrease in rolling type textures and increases in cube components. It was considered, therefore, that increases

in extrusion ratio caused the basic deformed matrix orientations to exhibit greater degrees of rolling type textures, but when higher levels of recrystallisation was present, this rolling texture increase was masked by the increase in cube component associated with the recrystallised grains.

In addition to the core textures, near surface textures were also analysed, fig 4.3.5. & figs 4.3.7->8 The exact surface of the material could not be analysed, due to the necessity for grinding and polishing of the extruded product before texture analysis. This meant that approximately 0.5mm was removed from the surface before analysis. In material extruded at the higher extrusion temperatures and ratios, near surface textures consisting of Cube {001} <100>, Goss, Brass and S orientations were evident, fig 4.3.5. These textures were similar to those found in the central core regions, but rolling texture components were greatly reduced. At the surface of the material extruded at lower temperatures, deformation rolling texture components were very difficult to observe, even the cube orientations seemed to be absent, fig 4.3.7->8. From studying pole figure plots, however, these near surface regions appeared to have texture systems close to {311}<0-11>, and {322} <0-11> components.

Other researchers have also observed transverse variations in texture components within wrought material. Bowen[10] investigated the texture variations in sheet material and found considerable texture component changes, but none were consistent with the results observed in this project. Bowen did, however, require recrystallised material in order to obtain the damage tolerant properties for the 8090 alloy. The lack of correlation could, therefore, be attributed to the microstructural differences between Bowens sheet material and the slab extrudates produced in this project.

4.3.2 Texture-Microstructure Correlations

Extrudate Core Regions

Optical analysis revealed the basic extrudate core microstructures to consist of elongated original grains with internal substructure. The amount of equiaxed recrystallised grains, of various sizes, were then observed to increase throughout this basic framework, as the extrusion temperature and extrusion/aspect ratio increased.

Increases in the amount of small (10->20μm) equiaxed recrystallised grains at the original grain boundaries occurred in the 15:1 extrudates as the extrusion temperature increased from 400° C->500° C. No obvious variations in the rolling type texture components were observed as a result of increases in extrusion temperature, but the cube texture components did increase. Within the 30:1 extrudates the amount of large (20->100μm) equiaxed recrystallised grains increased as the extrusion temperature increased from 400° C->500° C. Once again the cube texture was observed to increase with rising extrusion temperature, but in addition, the rolling type texture components were observed to decrease, fig 4.3.1.

Just as the variation in microstructure with extrusion temperature depended upon extrusion/aspect ratio, so the microstructural changes occurring with increasing extrusion/aspect ratio depended upon extrusion temperature. In extrudates produced at 400° C increases in the amount of small (10->20μm) equiaxed recrystallised grains at grain boundaries occurred as the extrusion ratio was increased from 9:1-> 30:1. Slight cube texture component increases were associated with this increase in extrusion/aspect ratio, but the major texture increases occurred in the rolling texture components. These increases in rolling type textures were associated with the increase in aspect ratio and not recrystallisation. In extrudates produced at 500° C increases in extrusion ratio from 15:1->30:1 caused the amount of large (20->100μm) equiaxed grains to increase, and was associated with an increase in cube components. Decreases in the rolling type textures were also observed as the recrystallisation increased. From the data obtained from extrudates produced at 400° C, however, it was concluded that increases in extrusion/aspect ratio caused increases in rolling type textures. It was considered, therefore, that for the extrudates produced at 500° C, any increases in the intensity of the rolling texture orientations that occurred due to changes in aspect ratio, were masked by the increase in cube texture, associated with the substantial increase in recrystallisation.

Not only were the core texture changes occurring as a result of variations in processing conditions investigated, but the variation in texture along the extrudates were also analysed. Within extrudates produced at the higher extrusion ratios and/or temperatures, increases in cube texture from the 'front' of the extrudates to the 'rear' were significant, fig 4.3.1. This was associated with the increases in recrystallisation from the front of the extrudate to the rear. Under the action of the more moderate processing conditions, however, lower general recrystallisation levels were present, and consequently the texture variation from front to back did not appear to be significant.

From the above texture results it appeared that increased recrystallisation was at least linked with increased cube texture components. This is a conclusion previously arrived at by many authors[5][10] , and two possible explanations for increased cubic texture component with increased recrystallisation have been suggested[6] :-

(i) Cubic grains are preferentially nucleated during recrystallisation, hence have higher concentration than other orientations.

(ii) Faster growth rates of the cubic grains, compared with other common orientations, produce a cubic texture in the solution treated structure.

From the observations stated above, it was considered that the recrystallisation caused the formation of a basically random texture system, ruling out a preferred nucleation theory. The theory of enhanced cube grain growth was accepted, however, with preferred growth of the recrystallisation nuclei of cube orientations causing the % volume of cube texture to increase.

Extrudate Near Surface Regions

Microstructural analysis identified two basic types of surface microstructure:-

(1) In extrudates produced at the higher extrusion temperatures and/or extrusion/aspect ratios, surface regions consisting entirely of equiaxed recrystallised grains, with the grains ranging in size from 20->80μm, were observed.

(2) In extrudates produced at the lower extrusion temperatures and/or extrusion/aspect ratios, narrow outer regions of exaggerated grain growth, which abruptly changed to microstructures consisting of elongated original grains with internal substructure, were observed.

In extrudates exhibiting surface regions consisting of equiaxed grains, texture systems dominated by the cube component were evident, fig 4.3.5. Rolling type components that were present in the core regions of these extrudates were revealed at the surface, however, due to the increased degree of recrystallisation.

For extrudates exhibiting the narrow annulus of exaggerated grain growth, texture analyses could only be carried out on the sub-surface regions below the exaggerated grains. It was found that this region had a texture close to {322} <0-11> and {311}<0-11> components, and not the typical rolling deformation textures of the core structures, fig 4.3.7->8. The microstructure of these near surface regions consisted of elongated grains with internal substructure and only differed from the core regions in the elongation of the original grains and the degree of recrystallisation. Since it was considered that recrystallisation was associated with cube texture components, the texture differences between the centre and edge of these extrudates were believed to be as a result of strain, strain rate and temperature variations altering the orientation of the grains, and not connected with increases in recrystallisation.

As with the core regions, the variation in surface textures from the front of the extrudates to the rear were most evident in extrudates produced at the higher extrusion temperature and extrusion/aspect ratios. For these extrudates an increase in the cube texture was observed, and again was associated with increased recrystallisation.

4.3.3 Discussion and Conclusions

The observed texture variations occurring as a result of variations in processing conditions were due to increases in recrystallisation, and changes in the deformation texture. From the texture analysis the following observations were highlighted:-

(1) The centre of the aged 'slab' extrudates were characterised by a texture system consisting of rolling (copper, brass, S and Goss) and cube textures.

(2) The degree of cube texture at the centre of the extrudate increased with increasing extrusion temperature -an effect more apparent for higher extrusion ratios. Cube

textures were correlated with recrystallisation, with preferred growth of cube grains, rather than preferred nucleation, giving rise to the correlation.

(3) The degree of brass, S, and copper textures appeared to decrease with increasing extrusion temperature.

(4) Both the rolling and cube texture components increased as the extrusion/aspect ratio increased.

(5) The cube texture component at the centre of the extrudate increased from the front of the extrudate to the back, and this was associated with increased recrystallisation.

(6) In extrudates produced at the higher extrusion temperatures and ratios the surface texture, associated with equiaxed recrystallised grains, consisted of dominant cube textures and reduced rolling type textures.

(7) In extrudates produced at the lower extrusion temperatures and ratios the surface regions below the exaggerated growth region consisted of a subgrain structure exhibiting texture components close to the {322}<0-11> and {311}<0-11> orientations, rather than the rolling or cube texture components.

From these results, therefore, the following scenarios concerning the microstructural development were produced.

In extrudates produced at the high extrusion temperatures and ratios (15:1 at 500° C and 30:1 at 400° C & 500° C) the formation of randomly orientated recrystallised grains occurred during extrusion. Within the time interval between extrusion and quench further recrystallisation may also have occurred. In addition, due the high exit temperatures, grain growth occurred, with the Cube grains possessing enhanced growth rates. Upon solution heat treatment growth of the recrystallised grains continued, thereby increasing the cube texture component still further. A centre to edge variation in texture was set up, due to the temperature and strain variations causing increased recrystallisation at the surface. Textural variations from the front of the extrudate to the back also occurred within these extrudates, due to the increase in recrystallisation along the extrudate.

For extrudates produced at the lower extrusion temperatures and ratios, recrystallisation was present, but not encouraged. Consequently after extrusion the reduced amounts of recrystallised nuclei, combined with the low temperature, meant that few equiaxed grains were observed in the as-extruded material. Upon solution heat treatment a few grains at the extreme outer surfaces of the extrudates were encouraged to grow considerably, creating the outer annuli of large grains. Within the majority of the material, however, the presence of Al_3Zr meant that grain boundary movement was in general discouraged, causing the elongated grains with internal substructure to be retained. Since recrystallisation varied only slightly from the centre of the extrudates to the edge, and was usually associated with cube texture, the observed centre to edge texture changes were attributed to deformation differences rather than increased

recrystallisation. The texture observations made, showed that the increases in strain and temperature associated with the near surface subgrain regions, caused the development of textures close to {322} <1-11>, {311} <1-11> components, rather than the rolling type texture systems.

With regard to the variation in texture from the front of the extrudates to the back, it was observed that texture changes were reduced, owing to the general lower levels of overall recrystallisation.

Extrusion Ratio	Extrusion Temperature (°C)	Sample Position	Textural Systems
6:1	400	Core region of extrudate	Rolling Textures Dominant
	500	Core region of extrudate	Rolling Textures Dominant Cube component (2*Random)
9:1	400	Core region of extrudate	Brass = 6.62 Goss =1.04 Cube= 1.90 S = 4.26 Copper = 1.14
	500	Core region of extrudate	Rolling Textures Dominant
15:1	400	Near surface region Front of extrudate	{322}<0-11> & {311}<0-11>
		Near surface region Rear of extrudate	{322}<0-11> & {311}<0-11>
		Core region Front of extrudate	Brass = 10.4 Goss =1.67 Cube= 2.20 S = 8.42 Copper = 2.74
		Core region Rear of extrudate	Brass = 11.4 Goss =2.12 Cube= 3.81 S = 9.13 Copper = 2.74
	500	Near surface region Rear of extrudate	Rolling Textures Cube component (3-4 Random)
		Core region Front of extrudate	Brass = 10.0 Goss =1.82 Cube= 4.02 S = 7.98 Copper = 2.51
		Core region Rear of extrudate	Rolling Textures Cube component (2-3 Random)
30:1	400	Near surface region Front of extrudate	{322}<0-11> & {311}<0-11>
		Near surface region Rear of extrudate	{322}<0-11> & {311}<0-11>
		Core region Front of extrudate	Brass = 14.9 Goss =1.95 Cube= 2.94 S = 10.4 Copper = 4.02
		Core region Rear of extrudate	Rolling Textures
	500	Near surface region Front of extrudate	Rolling Textures Cube component (4*Random)
		Core region Front of extrudate	Brass = 6.05 Goss =1.18 Cube= 8.43 S = 7.38 Copper = 1.21
		Core region Rear of extrudate	Brass = 4.03 Goss = 2.09 Cube= 17.2 S = 5.12 Copper = 1.04
15:1 Axi-symmetric	400 & 500	Throughout extrudate	<111> &<100> Double Fibre Texture

Fig 4.3.1 Textural system variations with processing conditions.
Aged condition. Alloy A material.

Fig 4.3.2 {111} Pole Figure Plots.
8090 alloy A.
'Core' of extrudate.
'Rear' of extrudate.
Overaged condition.
(a) & (b) 15:1 extrusion ratio.
400° C extrusion temperature.

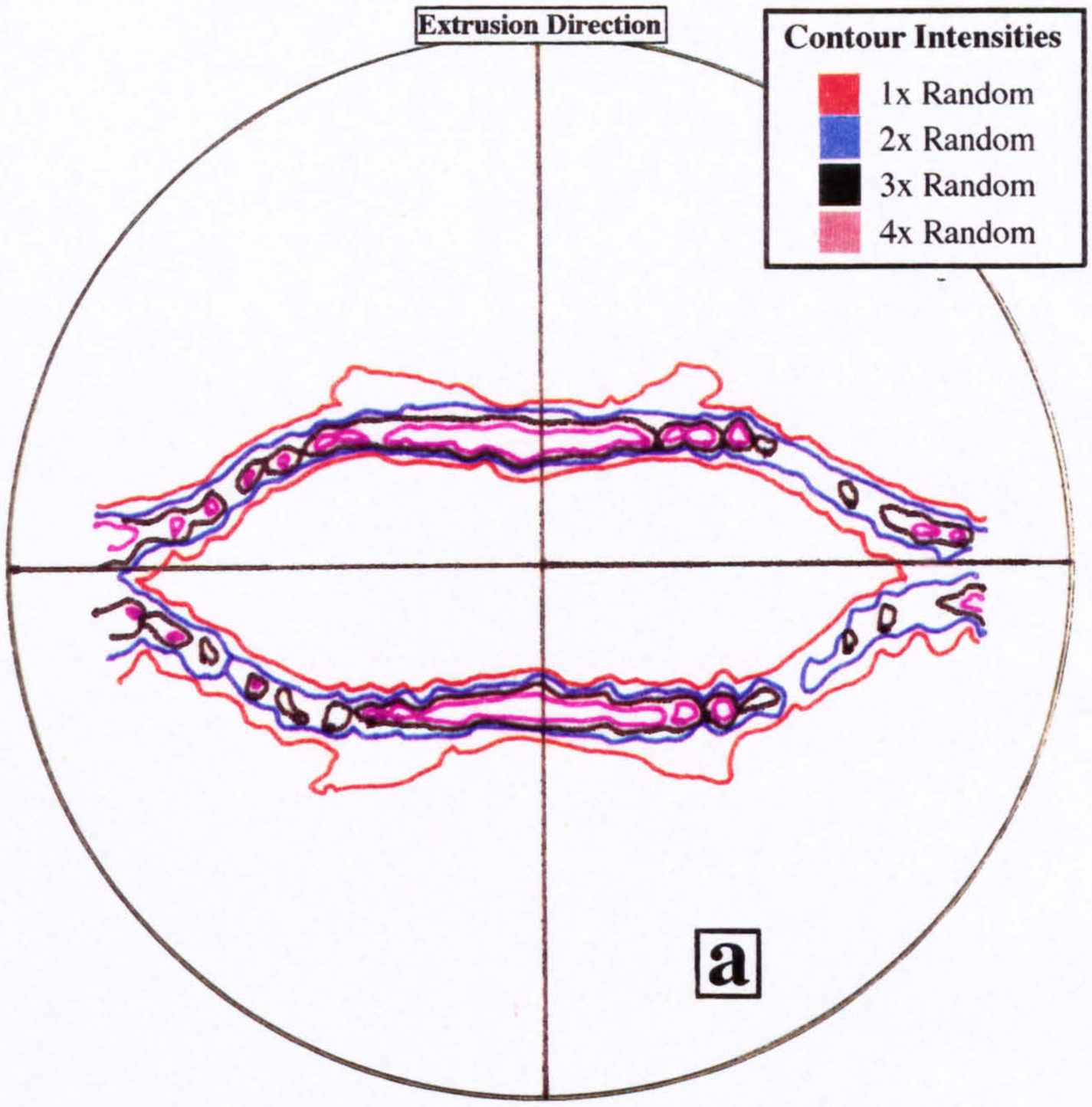
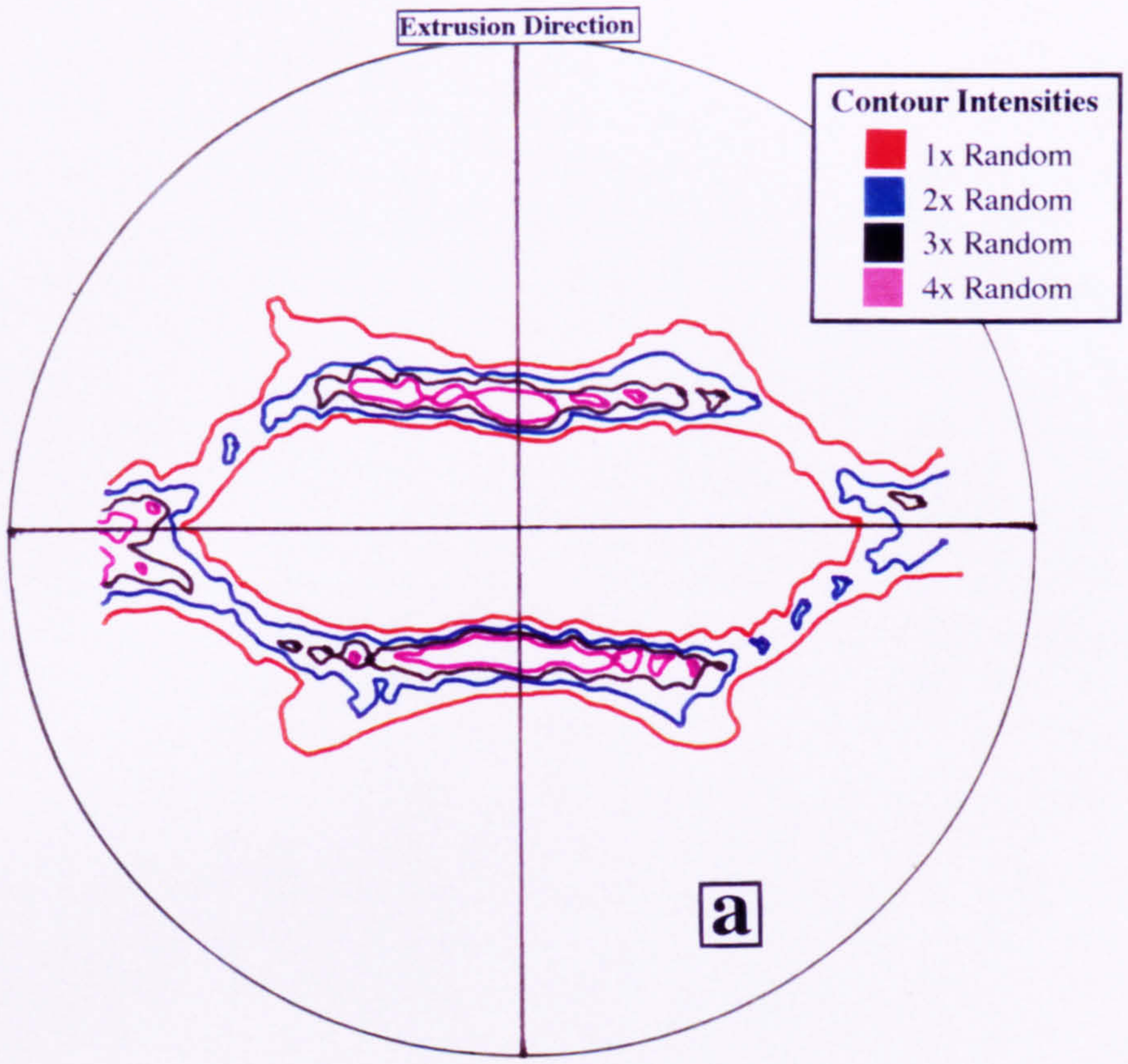

Extrusion Direction
Contour Intensities
1x Random
2x Random
3x Random
4x Random
a
Extrusion Direction
Contour Intensities
3x Random
4x Random
5x Random
6x Random
b

Fig 4.3.2

Fig 4.3.3 {111} Pole Figure Plots.
8090 alloy A.
'Core' of extrudate.
'Rear' of extrudate.
Overaged condition.
(a) 15:1 extrusion ratio.
500° C extrusion temperature.
(b) 9:1 extrusion ratio.
500° C extrusion temperature.


Extrusion Direction
Contour Intensities
1x Random
2x Random
3x Random
4x Random
a

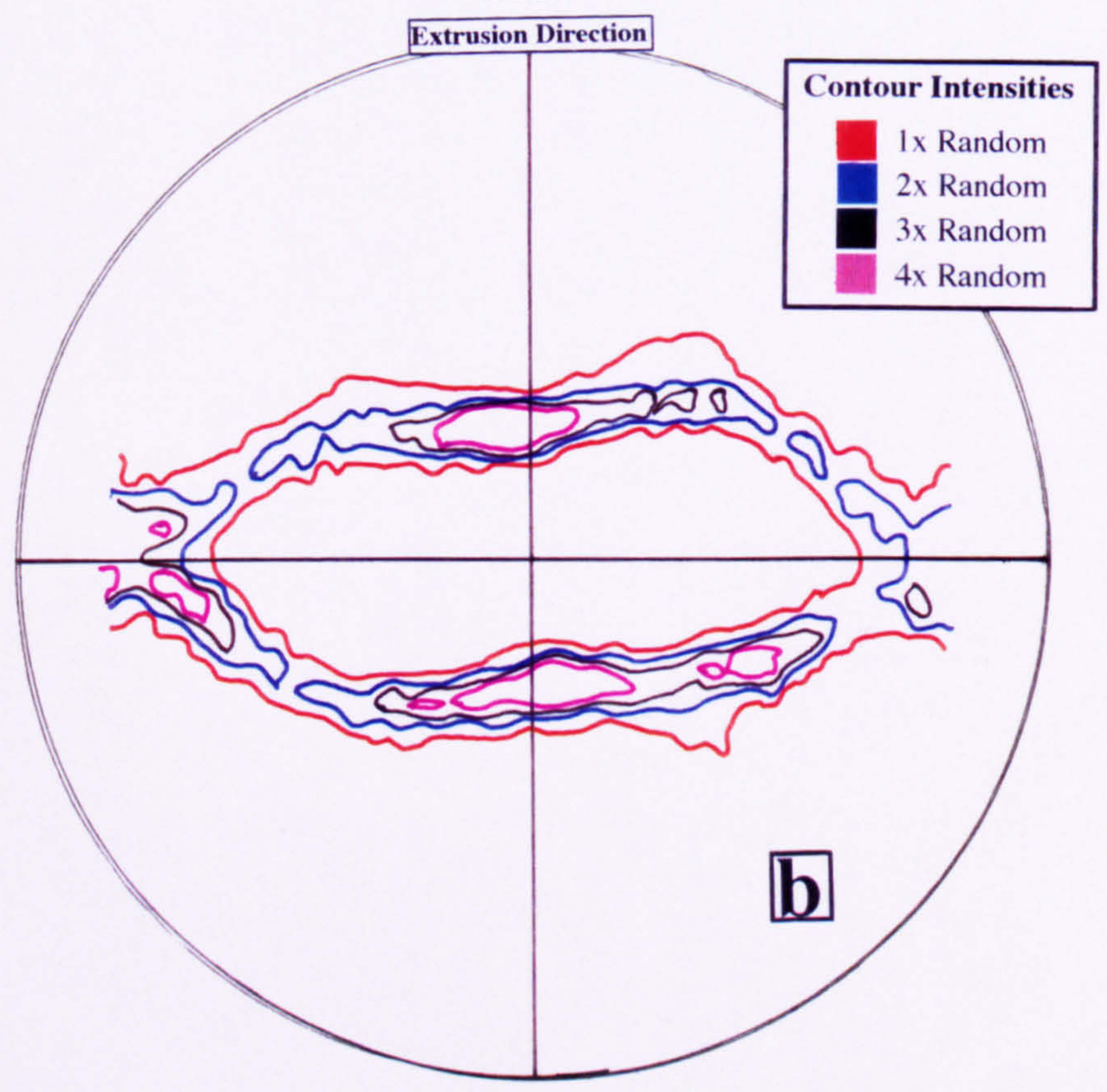

Extrusion Direction
Contour Intensities
1x Random
2x Random
3x Random
4x Random
b

Fig 4.3.3

Fig 4.3.4 {111} Pole Figure Plots.
8090 alloy.
'Core' of extrudate.
Overaged condition.
(a) 30:1 extrusion ratio.
400° C extrusion temperature.
'Rear' of extrudate.
(b) 30:1 extrusion ratio.
400° C extrusion temperature.
'Front' of extrudate.

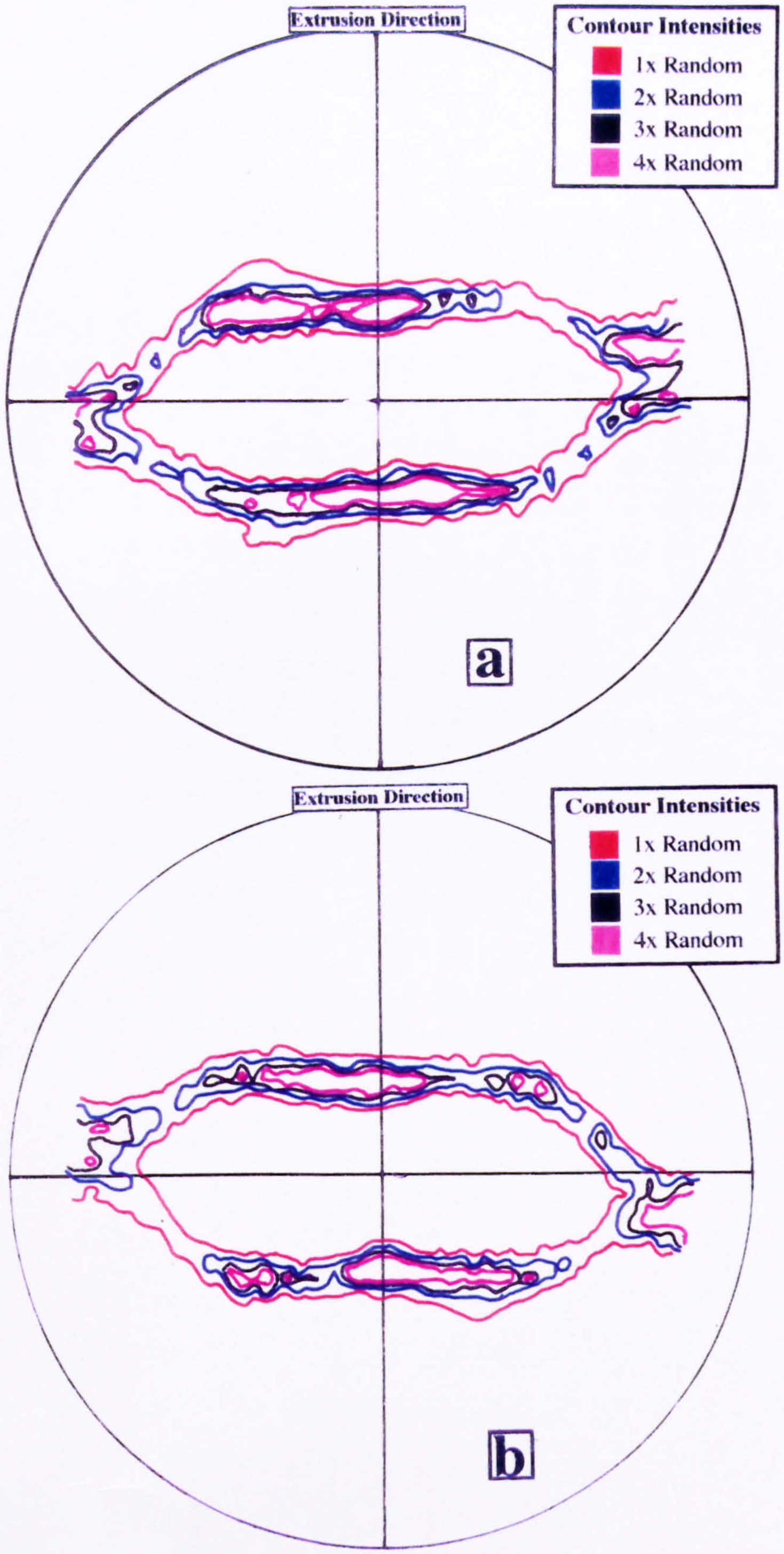

Extrusion Direction
Contour Intensities
1x Random
2x Random
3x Random
4x Random
a
Extrusion Direction
Contour Intensities
1x Random
2x Random
3x Random
4x Random
b

Fig 4.3.4

Fig 4.3.5 {111} Pole Figure Plots.
8090 alloy A.
'Surface' of extrudate.
Overaged condition.
(a) 15:1 extrusion ratio.
500° C extrusion temperature.
'Rear' of extrudate.
(b) 30:1 extrusion ratio.
500° C extrusion temperature.
'Front' of extrudate.

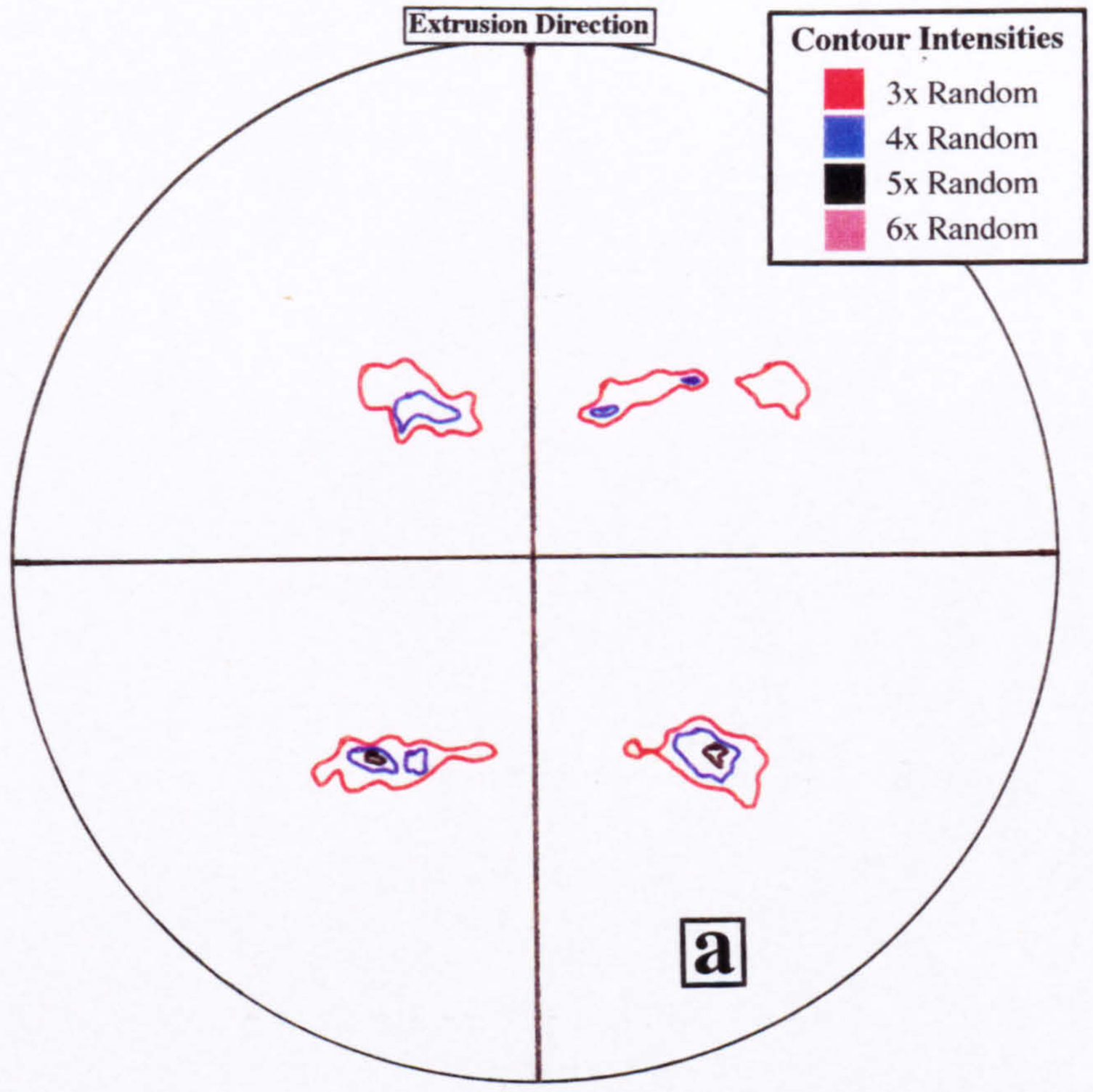

Extrusion Direction
Contour Intensities
3x Random
4x Random
5x Random
6x Random
a
Extrusion Direction
Contour Intensities
3x Random
4x Random
5x Random
6x Random
b

Fig 4.3.5

Fig 4.3.6 {111} Pole Figure Plots.
8090 alloy A.
'Core' of extrudate.
Overaged condition.
(a) & (b) 30:1 extrusion ratio.
500°C extrusion temperature.
'Rear' of Extrudate.

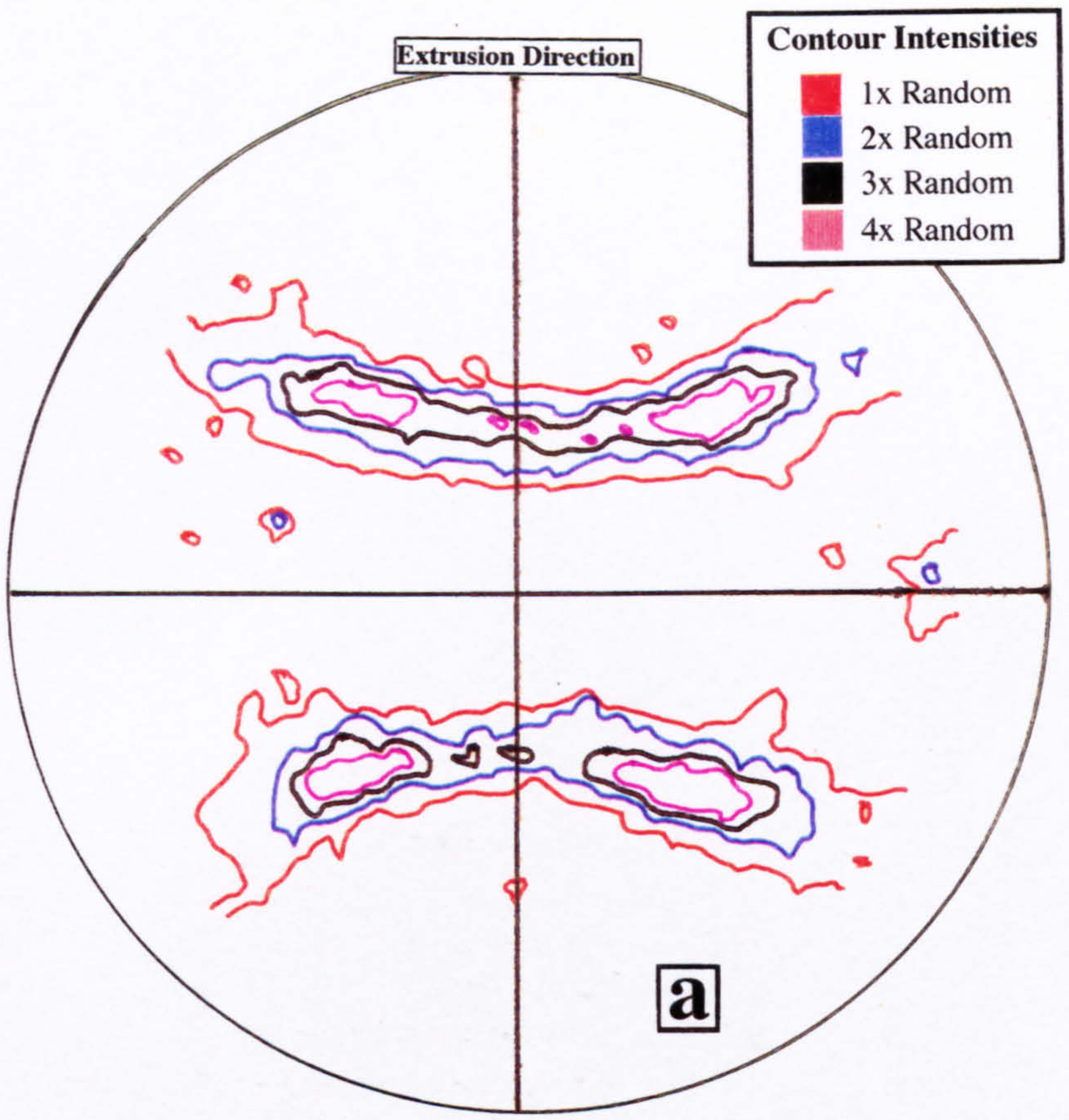
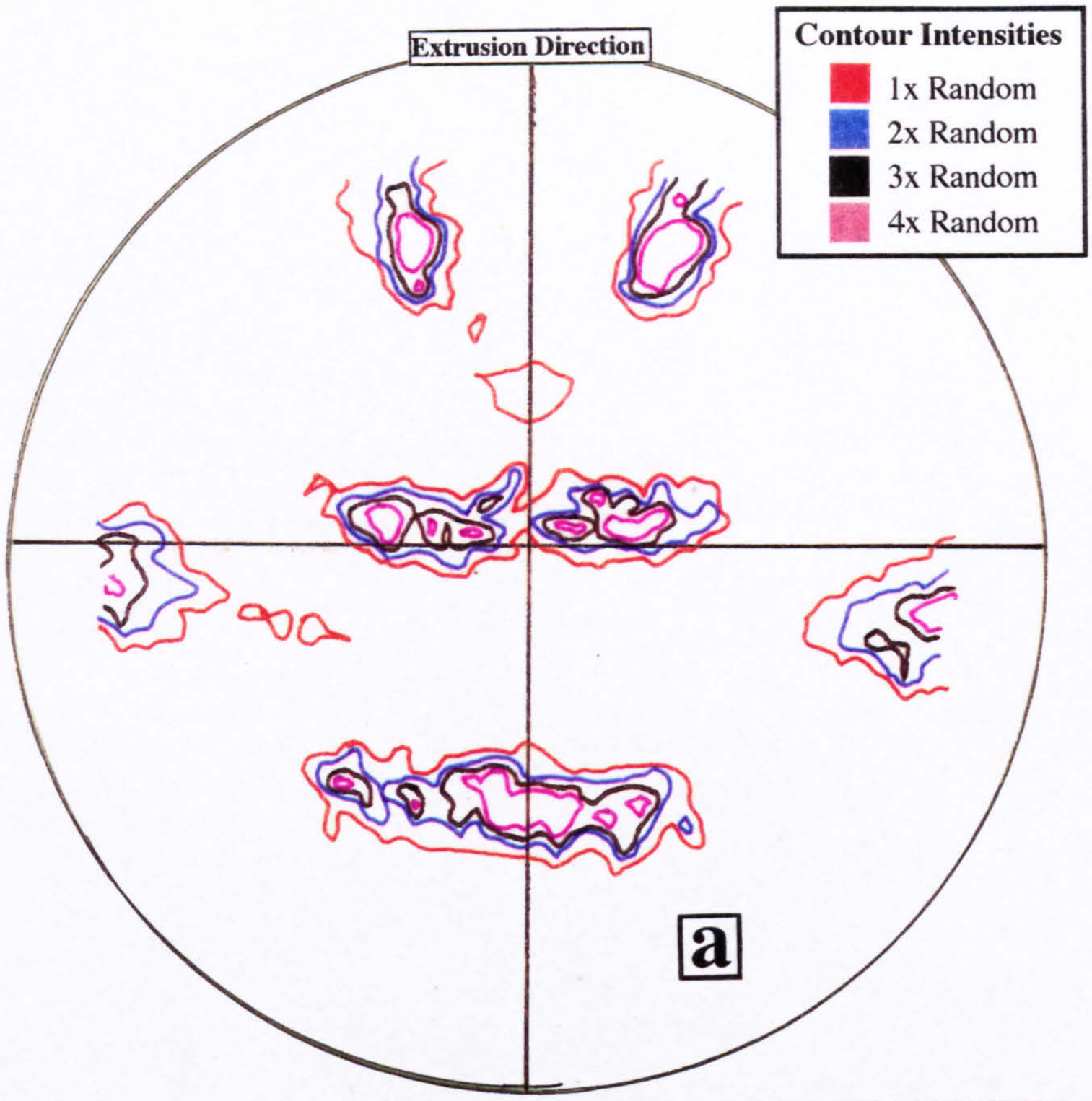

Extrusion Direction
Contour Intensities
1x Random
2x Random
3x Random
4x Random
a
Extrusion Direction
Contour Intensities
3x Random
4x Random
5x Random
6x Random
b

Fig 4.3.6

Fig 4.3.7 {111} Pole Figure Plots.
8090 alloy A.
'Surface' of extrudate.
Overaged condition.
(a) & (b) 30:1 extrusion ratio.
400° C extrusion temperature.
'Front' of Extrudate.


Extrusion Direction
Contour Intensities
1x Random
2x Random
3x Random
4x Random
a

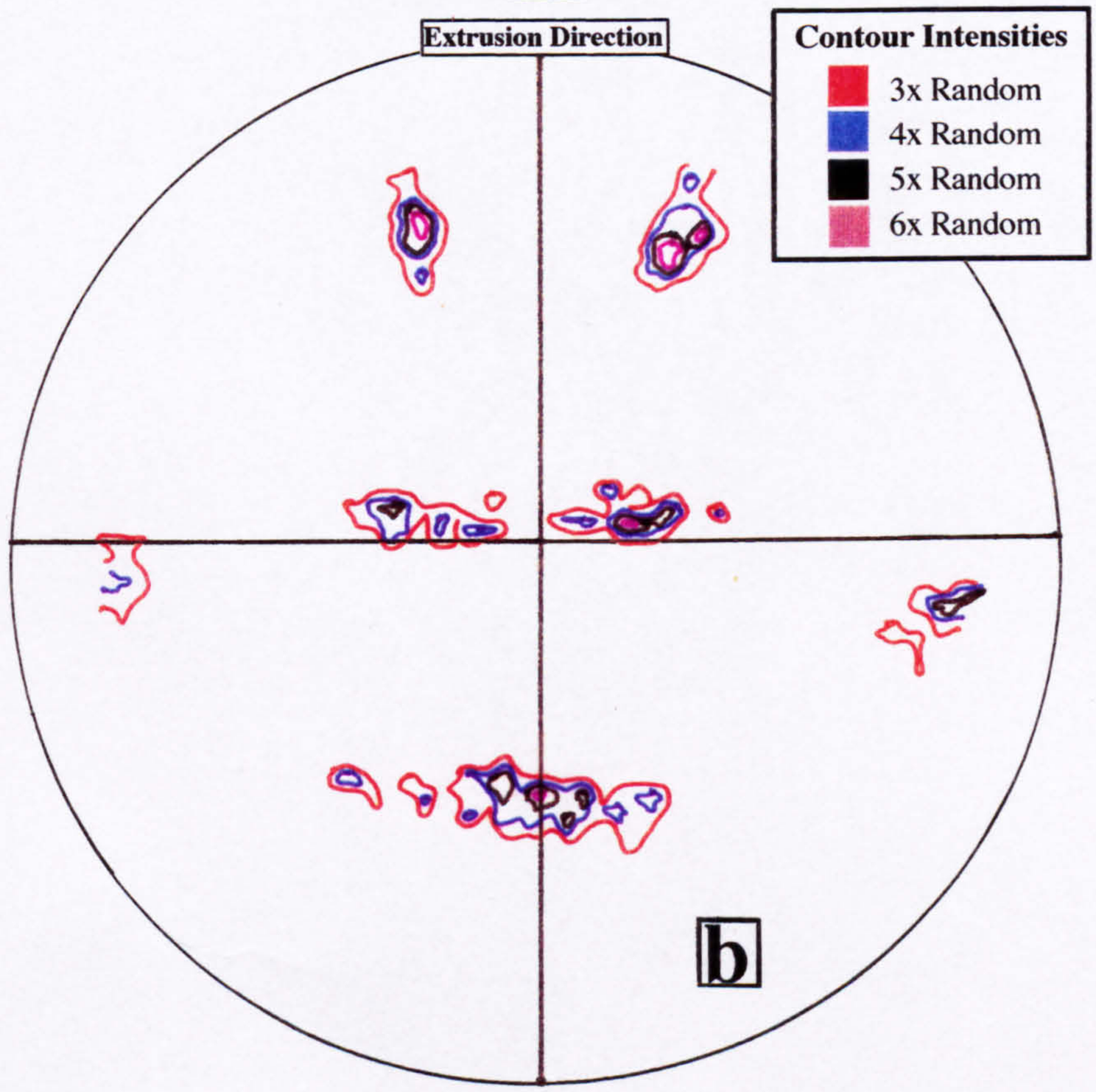

Extrusion Direction
Contour Intensities
3x Random
4x Random
5x Random
6x Random
b

Fig 4.3.7

Fig 4.3.8 {111} Pole Figure Plots.
8090 alloy A.
'Surface' of extrudate.
Overaged condition.
(a) & (b) 15:1 extrusion ratio.
400° C extrusion temperature.
'Front' of extrudate.

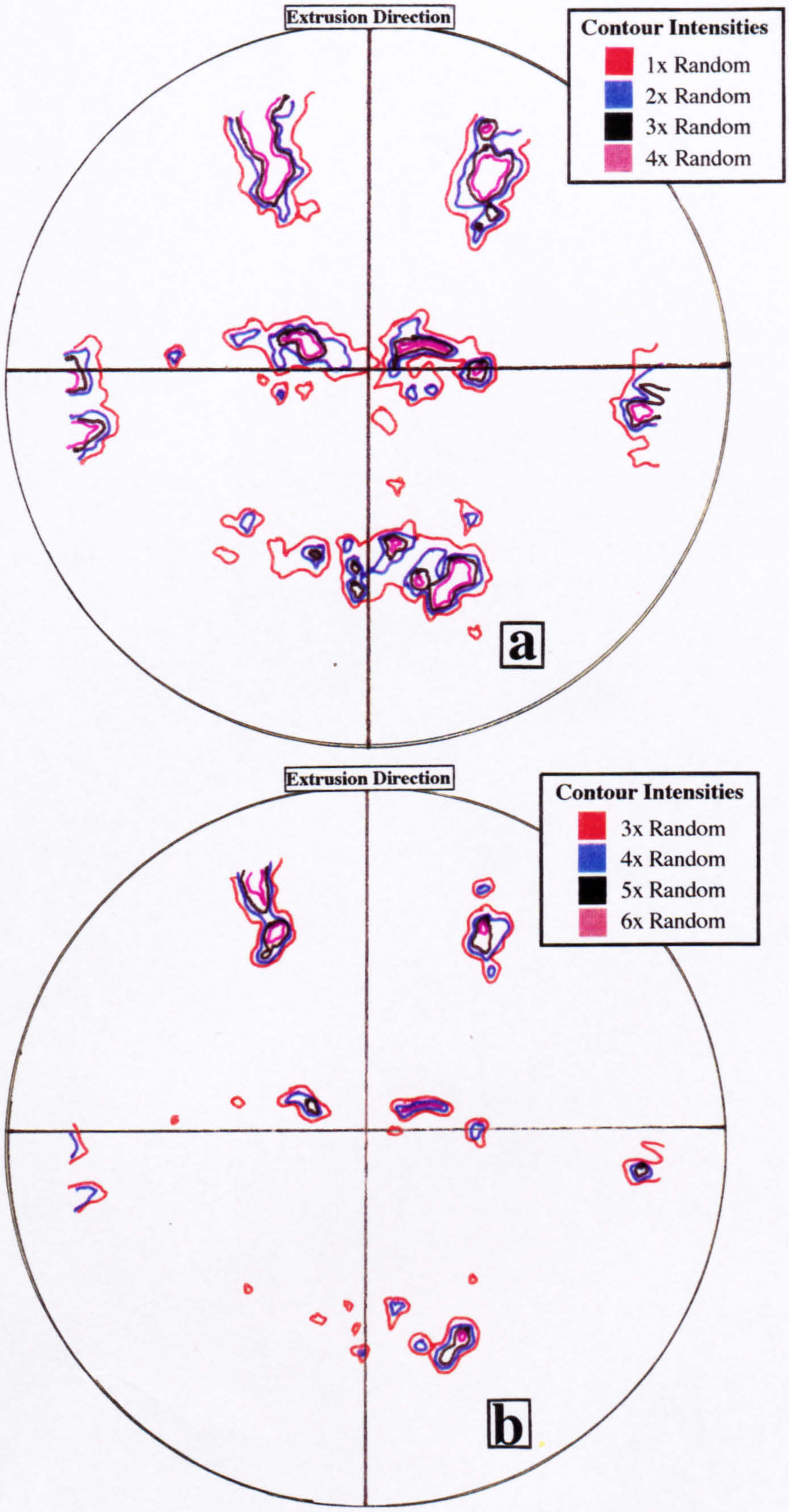
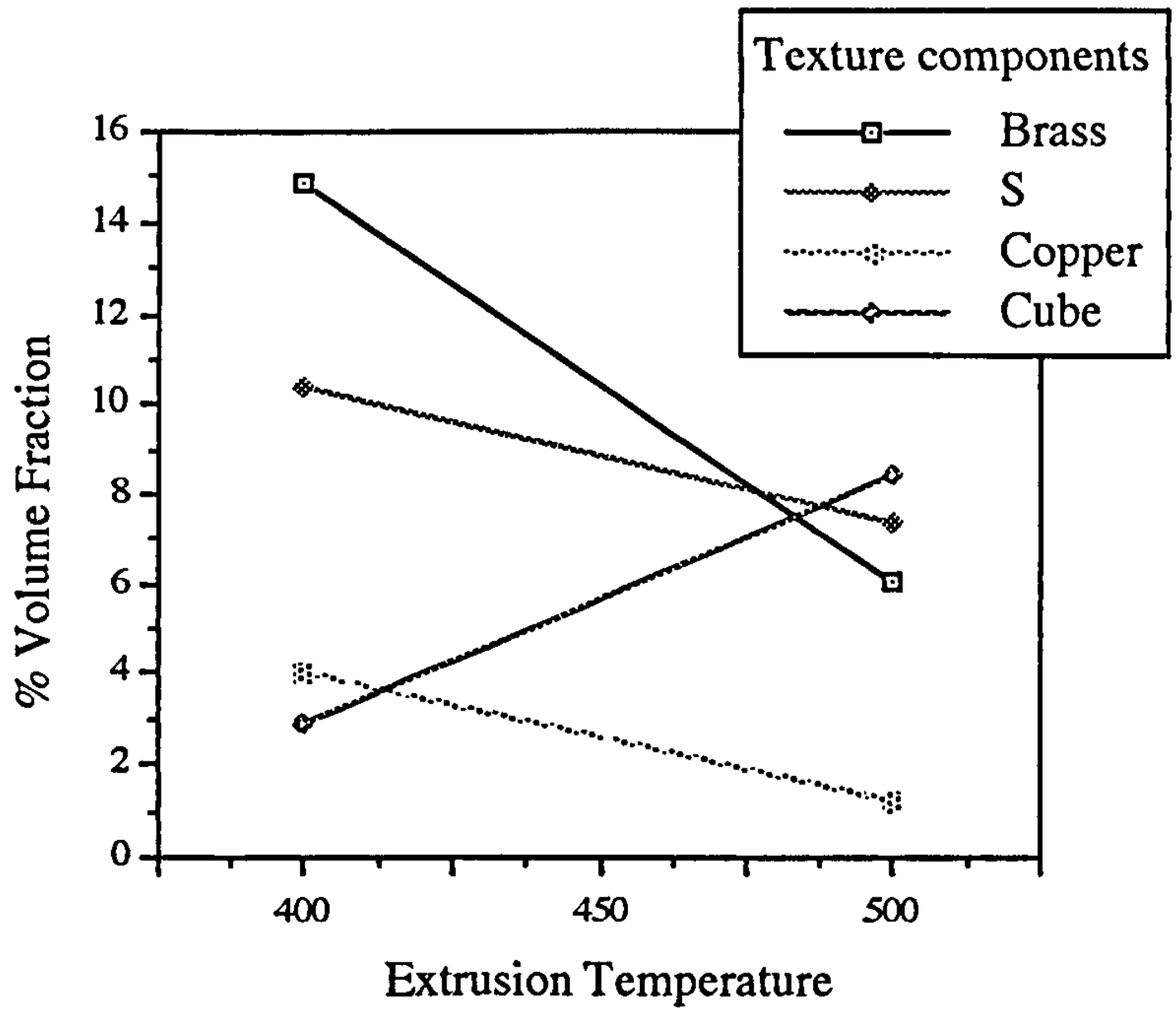

Extrusion Direction
Contour Intensities
1x Random
2x Random
3x Random
4x Random
a
Extrusion Direction
Contour Intensities
3x Random
4x Random
5x Random
6x Random
b

Fig 4.3.8



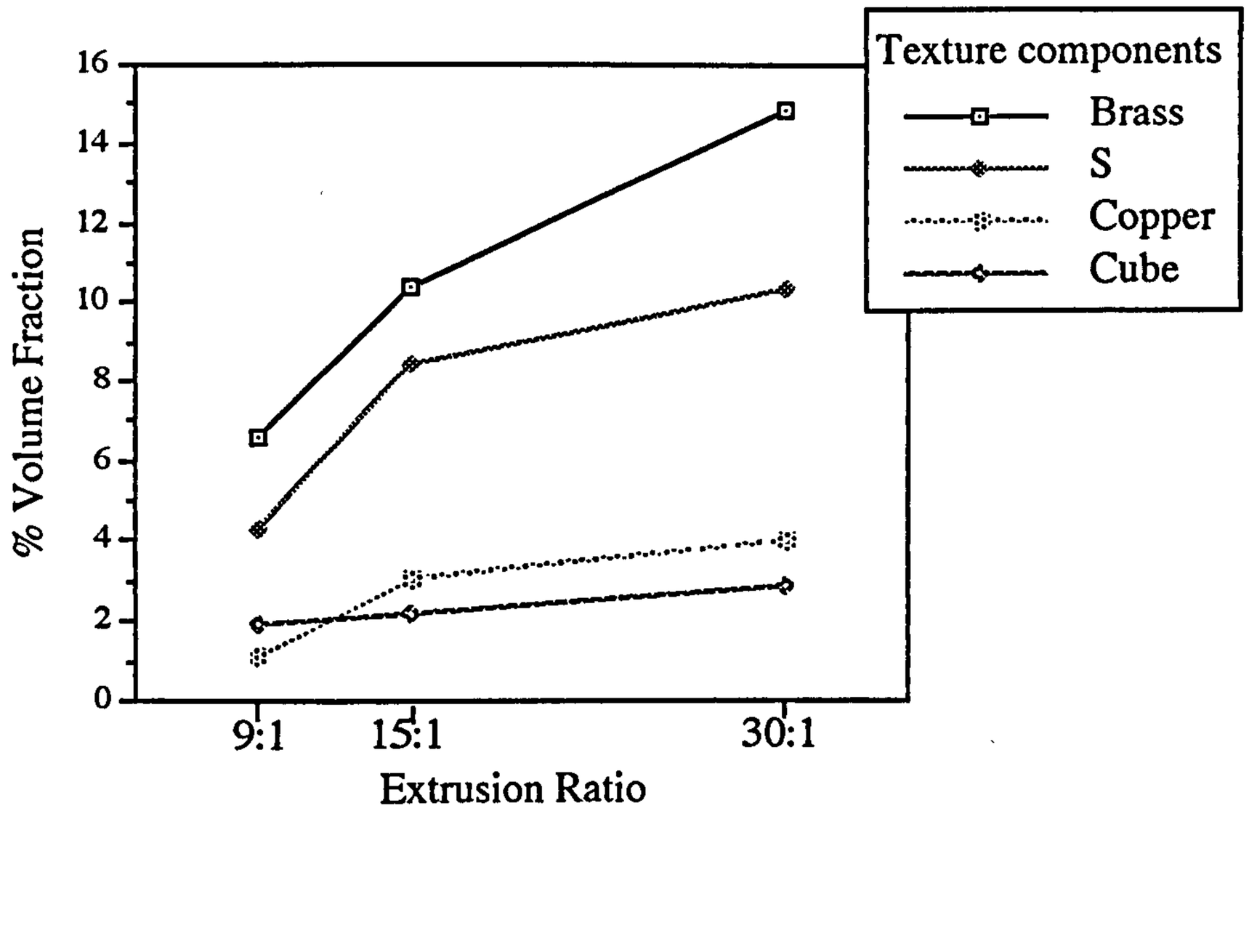


Fig 4.3.9 Variation in % volume fraction of texture components with variations in processing conditions.
(a) Variation in Brass, S, Copper and Cube textures components with increases in extrusion temperature, for 30:1 extrudates.
(b) Variation in Brass, S, Copper and Cube textures components with increases in extrusion ratio, for extrudates produced at 400 °C.

4.4 Toughness Analysis

4.4.1 Correlation of Toughness Measurements

Due to the generally small extrudate sectional dimensions, toughness measurements were primarily made using chevron notch bar specimens[15] . These bar specimens were, however, capable of measuring both longitudinal, (T-L), and transverse, (L-T), toughness values. In order to assess the accuracy of the measurements made by these relatively small bar specimens, T-L toughness values were also measured by the more widely used short rod[13][14] toughness samples, and the results compared.

Fig 4.4.1 tabulates the toughness values obtained from 'slab' extrusions produced at 400° C. In each case a minimum of six samples were tested, and the standard deviations of the results at the 80% confidence level calculated. It was evident that for material in the as-extruded condition the chevron bar specimens produced lower toughness values compared with the short rod samples. In the aged condition, however, the toughness measurements from the different samples were comparable.

Due to the varying extrudate section geometry the chevron bar specimen size also varied. Changes in the dimensions of the chevron bar samples did not appear to affect toughness measurements to any significant degree, however, as indicated in fig 4.4.1.

Extrusion Ratio	Ageing Condition	Chevron notch bar specimens (A)		Short rod Specimens (B)	Ratio A/B
		Large specimens Cross-section 5mm * 7mm	Small Specimens Cross-section 4mm * 6mm		
6:1	As-Extruded	17.3 (±0.6)	16.9 (±0.6)	21.8 (±0.5)	1.26
	Under-aged	24.5 (±0.4)	24.3 (±0.4)	24.8(±0.5)	1.01
9:1	As-Extruded	15.8 (±0.4)	15.7 (±0.4)	20.7 (±0.5)	1.31
	Under-aged	25.6 (±0.7)	26.1 (±0.2)	25.0 (±0.2)	0.98

Fig 4.4.1 Comparison between T-L toughness measurements made using short rod and chevron notch bar specimens

A brief analysis to determine the effect of notch depth i.e. α_o (see Appendix I) upon toughness measurement was also carried out. The size of α_o was found to affect toughness measurement to a limited degree, with higher toughness values being obtained when larger α_o values were used. For consistency in results, therefore, it was decided that an α_o of approximately zero would be used in each case, i.e. the chevron

notch was cut such that the apex of the notch was incident with the surface of the specimen.

4.4.2 Fracture & Toughness Variations with Ageing Condition

The variation in fracture toughness values with ageing condition are tabulated in fig 4.4.2 and fig 4.4.4, for alloy A and B extrudates respectively. Fig 4.4.3 and fig 4.4.5 also illustrate graphically the observed variations in the toughness values.

Irrespective of extrusion processing conditions, the longitudinal and transverse toughness values of both alloy extrudates consistently increased from the as-extruded to the underaged condition. As already mentioned in section 4.4.1, however, due to the occurrence of substantial ductility, the chevron notch bar specimens may have under-estimated the toughness values of the as-extruded material by a factor of approximately 1.3. If the toughness values obtained from the as-extruded material are corrected by a factor of 1.3, it can be seen that the actual toughness values of the as-extruded and underaged material are much more comparable. The response of the extrudates to further ageing, however, was observed to be dependent upon the alloy composition.

For alloy B extrudates further ageing to the peak aged and then to the overaged conditions caused an initial decrease and subsequent increase in toughness values, with the overaged condition exhibiting improved toughness compared with the underaged state. For alloy A material, however, the relative toughness values between the underaged and overaged material depended upon extrusion ratio. In general, the 15:1 alloy A extrudates exhibited improved toughness values in the overaged state compared with the underaged condition. for the 30:1 extrudates, however, the underaged material exhibited superior toughness properties.

Previous researchers[1][12] have stated a consistent decrease in both T-L and L-T fracture toughness values as ageing occurred. In order to explain the toughness variations observed in this project, therefore, fractographs of the as extruded and aged material were examined and related to the microstructural characteristics of the extrudates.

As-Extruded Material

T-L and L-T fractographs obtained from alloy A and B as-extruded material are illustrated in fig 4.4.6->7.

From observation of these fractographs it can be seen that longitudinal crack propagation through the T4 extrudates of both alloys resulted in a highly dimpled fracture surface, with occasional stepping of the surface topography. The majority of the observed dimpling varied in size from 5->25μm, and due to their slight

axisymmetric proportions, a certain directionality along the extrusion axis was observed.

Optical and T.E.M. analyses of alloy A & B extrudates in the T4 condition revealed a core grain structure consisting of elongated grains, with internal subgrains of 1->10μm. Grain boundary recrystallisation (10->20μm) was also observed, the proportion of which varied with extrusion temperature and ratio. With regard to precipitation, no substantial matrix precipitation, other than δ', was observed, and grain boundary precipitation was found to be limited to constituent phases. From this knowledge and the appearance of the fractographs, it was determined that T-L crack propagation occurred along the general path of the original grains by a microvoid coalescence mechanism involving void initiation at grain boundary constituent phases. The void growth associated with the microvoid crack propagation produced the dimpling, and the stepping of the fracture surface was associated with crack front movement across the elongated deformed grains in the transverse direction.

Transverse crack propagation through the T4 extrudates of both alloys also resulted in highly dimpled fracture surface, fig 4.4.7. As with the longitudinal fracture, the majority of the dimples varied in size from approximately 5->25μm, but were more equiaxed, thereby causing the overall transverse fracture surface to exhibit no directionality, fig 4.4.7. The mechanism of transverse crack propagation was again considered to occur by microvoid coalescence with void initiation at 2nd phase particles. The decrease in the directionality of the transverse fracture surface compared to that of the longitudinal fracture, was attributed to a difference in the distributions of the void nucleating precipitates in the L-T and T-L planes. The spacing between the particles in the long transverse and short transverse directions (i.e. L-T plane) were comparable, producing equiaxed dimpling as a result of transverse crack propagation. Due to the high degrees of elongation, however, the spacing between the particles in the longitudinal direction were greater than in the short transverse direction. This consequently produced the asymmetric dimpling as a result of longitudinal crack propagation.

Aged Material

Fig 4.4.8->9 are fractographs obtained as a result of longitudinal and transverse crack propagation through extrudates produced under different processing conditions, but all aged to the underaged condition.

Longitudinal crack propagation through these extrudates produced nodular fracture relief varying in size from between 1->10μm. Regions varying in size from 10->50μm and exhibiting a slightly rippled appearance were also observed. Both these fracture surface features exhibited axi-symmetric proportions thereby causing the fractographs

to exhibit distinct directionalities in the extrusion direction, fig 4.4.8 (a)&(b), and fig 4.4.9 (a)&(c).

Optical analysis of the underaged extrudates revealed a core structure of elongated grains, together with the presence of grain boundary recrystallisation. The proportion and grain size of the grain boundary recrystallisation was then observed to increase as the extrusion temperature and extrusion/aspect ratio increased. T.E.M. analysis of the underaged material revealed substantial δ' matrix precipitation, together with I phase and constituent precipitates present at grain boundaries. From consideration of the S.E.M. and optical analysis, therefore, the following failure process was suggested in connection with the underaged material. Upon straining, deformation would commence upon primary slip systems resulting in intense shear regions. The subsequent impedance of dislocation motion by grain boundaries then produced intense dislocation pileups and strain concentrations. At this point, the operation of a secondary slip system became feasible. As the strain concentration at the grain boundaries increased, cracks nucleated at grain boundary precipitates. These voids then grew with further straining and subsequently coalesced. These basic processes produced the fracture surfaces with characteristic protuberances and indentations comparable in size to the dimensions of the subgrain and recrystallised grains. The flat faceted regions were considered to occur as a consequence of transgranular failure, caused by a breakdown of the intense coplanar regions within the grains. Again a microvoid coalescence mechanism operated, causing voiding, but the operation of secondary slip systems produced steps upon the fracture surface, creating the slightly corrugated appearance.

The transgranular failure was much more in evidence when the fractures produced from L-T samples were examined, fig 4.4.8 (c) & (d), fig 4.4.9 (b) & (d). For L-T crack propagation it was necessary for the crack to cross the line of the original grains. Consequently transgranular failure by the breakdown of shear regions was more common, producing an increased proportion of flat faceted areas (10->50μm) with 'rippled' or 'stepped' topography. Intergranular failure was also evident within the L-T fractographs and again occurred by a microvoid coalescence crack propagation mechanism involving void formation at grain boundary precipitation.

From analysis of the fractographs obtained from underaged material, therefore, two failure paths were identified -intergranular and transgranular- with the specific path followed being dependent upon (i) The relative strength of the grain boundaries & coplanar shear regions, and (ii) The testing orientation.

Figs 4.4.10->13 illustrate fractographs obtained from transverse and longitudinal crack propagation through extrudates produced under varying conditions, but all aged to the overaged condition.

The fracture surfaces produced as a result of longitudinal crack propagation through the overaged material was found to be dependent upon processing conditions. In

extrudates produced at the lower extrusion ratios and temperatures the fracture surfaces exhibited nodular relief varying in size from between 1->20μm, fig 4.4.10, fig 4.4.11(a) and 4.4.12(a). In extrudates produced at the higher extrusion ratios and temperatures, however, larger relief regions varying from 20->80μm were also in evidence fig 4.4.12(b), fig 4.4.13 (a).

The fractograph appearance produced by transverse crack propagation through the overaged extrudates also depended upon processing conditions. In extrudates produced at the lower extrusion temperatures and ratios, a combination of nodular relief varying in size between 1->20μm, together with regions exhibiting a stepped appearance and varying in size between 10->50μm were present, fig 4.4.11 (b). For extrudates produced at higher extrusion ratios and temperatures, however, the fracture surface exhibited a combination of nodular relief varying in size between 5->20μm, together with an underlying larger relief varying in size between 20->100μm, fig 4.4.12 (c), fig 4.4.13 (b) & (c).

For both the longitudinal and transverse failures precise correlations between the fracture surface relief and the grain sizes within the extrudates were evident. The basic failure process occurring within the overaged material was, therefore, considered identical to that occurring within the underaged material. Compared with the underaged material, however, T.E.M. analysis revealed the overaged material to exhibit increased proportions of δ', T_1 and S matrix precipitation, together with increased proportions of grain boundary I phase precipitation. This increased precipitation was considered to affect the specific deformation characteristics within the overaged material, thereby increasing the incidence of intergranular failure within both the longitudinal and transverse failures.

From the above results it was evident that for both the as-extruded and aged material, fracture occurred by a microvoid coalescence crack growth mechanism. Due to different precipitate and grain structure characteristics, however, the microvoid coalescence mechanism produced very different fracture topographies, hence toughness values, as ageing occurred.

A distinct change in the fracture appearance was evident between the as-extruded and underaged extrudates produced from both alloy compositions. This was initially correlated with an increase in toughness, but an inability of the chevron notch bar specimens to measure the toughness values of the as-extruded material accurately, made these specific toughness value changes unreliable. Toughness measurement of the aged material was considered accurate, however, with the response of the extrudate to progressive ageing being shown to be dependent upon alloy composition.

For alloy B extrudates ageing to the peak aged and then to the overaged conditions caused an initial decrease and subsequent increase in toughness values, with the overaged condition exhibiting improved toughness compared with the underaged state. For alloy A material, however, the relative toughness values between the underaged and overaged material depended upon extrusion ratio. In general, the 15:1 alloy A extrudates exhibited improved toughness values in the overaged state compared with the underaged condition. for the 30:1 extrudates, however, the underaged material exhibited superior toughness properties.

From the subsequent correlation of these observed toughness variations with microstructural features the effect of ageing upon properties appeared to be directly related to the grain structures present. When processing was such as to produce relatively low degrees of small grain boundary recrystallisation, the disruption of the coplanar slip process by matrix precipitation of S and T_1 , outweighed the concurrent phenomenon of boundary weakening by precipitation. The overaged material was consequently tougher than the underaged material. As the recrystallisation grain size increased, however, the factor of grain boundary weakening increased in importance, hence the underaged material became tougher.

The peak aged material consistently exhibited the lowest toughness values, because it possessed maximum volume fractions of δ', without the benefit of additional S and T phase precipitation.

Since the aged material offered the best property values in all respects, further analysis was concentrated upon the aged conditions.

4.4.3 Fracture & Toughness Variation with Extrusion Temperature

The variations in the T-L and L-T fracture toughness values observed with increasing extrusion temperature are tabulated in fig 4.4.14 and fig 4.4.15, for alloys A and B respectively. Fig 4.4.16 and fig 4.4.17 also illustrate graphically the variation in the aged extrudate toughness values, as extrusion temperature increased.

T.E.M. analysis of the as-extruded material revealed no significant changes in precipitation as extrusion temperature increased. The texture systems were also found to remain approximately constant. Optical analysis of both alloy extrudates did, however, reveal increases in the proportion of small grain boundary recrystallisation as the extrusion temperature increased. These increases in recrystallisation may, therefore, have been associated with decreases in the transverse toughness and increases in the longitudinal toughness values. As the results show, however, the changes in the toughness values were relatively small, hence no definite relationships between toughness values and microstructural features could be established.

For extrudates processed to the under-aged condition, the L-T toughness values for both alloy extrudates consistently decreased as the extrusion temperature increased, irrespective of extrusion/aspect ratio. The T-L toughness values, however, exhibited variations with extrusion temperature that were dependent upon extrusion/aspect ratios. For the 15:1 extrudates, the longitudinal fracture toughness values were observed to increase with increasing extrusion temperature, whereas for the 30:1 extrudates a decrease in the longitudinal fracture toughness values were observed as the extrusion temperature increased.

Microstructural analysis of the 15:1 extrudate cores revealed that increases in the extrusion temperature caused the amount and size of the relatively small recrystallised grains present at the original deformed grain boundaries to increase. The cube texture components present within the extrudates were also found to increase slightly as the extrusion temperature increased. With regard to the precipitation, however, no significant changes occurred as the extrusion temperature increased.

In the previous section the processes occurring during T-L and L-T fracture were identified as microvoid coalescence mechanisms, producing both intergranular and transgranular failure. Due to the fibering effect of the extrudate microstructures, however, the longitudinal failure process was dominated by intergranular failure along the line of the original grain boundaries, whilst during transverse crack propagation movement across the grains was prominent.

The increase in the T-L toughness with extrusion temperature for the 15:1 extrudates was, therefore, attributed to the increase in the small recrystallised grains enhancing disruption of the failure along the line of the original grain boundaries. This consequently caused an increase in the incidence of fracture relief corresponding to the recrystallised grain sizes (1->10μm), fig 4.4.9 (a) & (c). In relation to the L-T failure, however, the small recrystallised grains were considered as points of stress concentration, and hence caused the observed decrease in the transverse toughness as the extrusion temperature increased. A consequence of the differing response of the transverse and longitudinal toughness values to increasing recrystallisation, was a decrease in anisotropy as the extrusion temperature increased.

In contrast with the failure of 15:1 extrudates, the longitudinal and transverse fracture surfaces produced from failure of the 30:1 material were very similar in appearance. For the 30:1 extrudates, microstructural analysis revealed an increase in the amount of large recrystallised grains as extrusion temperature increased, and it was a simple matter to associate the fracture topography with the large recrystallised grain and subgrain sizes. The decreases in both the T-L and L-T toughness values as the extrusion temperature increased were, therefore, attributed to the increases in stress concentration at grain boundaries associated with the increase in grain size. The simultaneous decrease in both the longitudinal and transverse toughness values as the proportion of

the large recrystallised grains increased, consequently decreased the anisotropy of the material.

For extrudates aged to the overaged condition similar variations in toughness values with increasing extrusion temperature were observed as those evident for the underaged material. For extrudates produced from both alloy compositions the L-T toughness values decreased as extrusion temperature rose, irrespective of extrusion/aspect ratio. The T-L toughness values, however, exhibited variations with extrusion temperature that were dependent upon extrusion/aspect ratios. For the 15:1 extrudates the T-L fracture toughness was observed to increase as the extrusion temperature rose, whereas for the 30:1 extrudates a decrease in the longitudinal toughness was observed as the extrusion temperature increased.

Fig 4.4.11 illustrates the variation in the appearance of both the T-L and L-T fracture surfaces as extrusion temperature increased, for the overaged 15:1 extrudates. The T-L fracture was characterised by intergranular failure along the line of the original deformed grain boundaries, giving rise to a highly directional fracture. The topography on the fracture surface did not vary significantly with extrusion temperature and the majority of relief varied in size from between 5->20μm. The transverse fracture, however, was characterised by a combination of relief varying in size between 5->20μm, together with regions exhibiting a stepped appearance and varying in size from between 10->50μm. The incidence of the flatter regions appeared to decrease as the extrusion temperature increased, and was attributed to the increased presence of the small grain boundary recrystallised grains. As with the underaged material, therefore, the differing effect of the increased presence of small recrystallised grains upon the transverse and longitudinal toughness values, resulted in a decrease in anisotropy as extrusion temperature rose. It must be remembered that the anisotropy was produced from subtraction of two property values, hence measurement errors were cumulative.

The homogeneity of toughness properties from the 'front' of the extrudates to the 'rear' was observed to increase as the extrusion temperature increased, for both the longitudinal and transverse toughness values.

Fig 4.4.12->13 illustrate T-L and L-T fracture surfaces, obtained from 30:1 extrudates produced from both alloy compositions, and aged to the overaged condition.

For the 30:1 extrusions carried out at the lower extrusion temperature of 400° C, the T-L fracture surfaces were characterised by directional fractures exhibiting nodular relief varying in size from between 1->20μm, fig 4.4.12(a). The L-T failure within these extrudates, however, exhibited no directionality, but again relief varying in size from approximately 1->20μm were evident. As the extrusion temperature increased, the appearance of the fracture surfaces altered considerably. For both T-L and L-T fracture propagation within extrudates produced at 500° C, the fracture surface exhibited nodular relief varying in size from 5->20μm, together with underlying relief regions

varying in size from between 20->100μm, fig 4.4.12(c) & fig 4.4.13. Both of the dimensions associated with these fracture surface features could be related to the recrystallised grains present within the microstructure, which indicated an intersubgranular/granular failure.

The anisotropy in property values for the 30:1 extrudates remained approximately constant with increased extrusion temperature, for both alloy extrudates, even though the orthogonal fractures became much more similar in appearance. The homogeneity in toughness values from the 'front' of the extrudates to the 'rear' also remained relatively constant at comparatively low values.

From the above results, therefore, it was obvious that the effect of extrusion temperature upon microstructure and properties was dependent upon the specific values of other processing parameters. This made it impossible to categorically state whether or not a certain variation in extrusion temperature would improve or decrease toughness values. Two conclusions that could be drawn from these results, however, were:-

(i) If the variation in extrusion temperature increased the proportion of small recrystallised grains at the original grain boundaries, an improvement in the T-L toughness values would result, the intensity of which would decrease as ageing occurred. The L-T toughness values, however, would decrease as a result of this recrystallisation.

(ii) If the variation in extrusion temperature increased the proportion of large recrystallised grains, both the T-L and L-T toughness values would decrease, irrespective of ageing condition.

4.4.4 Fracture and Toughness Variation with Extrusion/Aspect Ratio

The measured variations in longitudinal and transverse toughness values produced by increases in extrusion/aspect ratios, for alloy A extrudates, are tabulated in fig 4.4.18. These toughness variations are also illustrated graphically in fig 4.4.19.

Fig 4.4.19(a) illustrates the measured variations in toughness values, obtained from extrudates produced at 400° C and aged to the underaged condition. As the extrusion/aspect ratios increased, the L-T toughness values of the 'slab' extrudates were found to decrease, whilst the axi-symmetric 15:1 extrudates exhibited the greatest L-T toughness values. The T-L toughness values of the 'slab' extrusions, however, were generally found to increase as the extrusion/aspect ratios increased, with the axisymmetric 15:1 extrusions exhibiting the lowest specific toughness values. The anisotropy of the slab extrudates was also observed to decrease as the extrusion/aspect ratio increased, with the axi-symmetric material exhibiting the greatest anisotropy.

From microstructural analysis of these extrudates it was revealed that as the extrusion/aspect ratios increased so did the percentage of small recrystallised grains present at the deformed grain boundaries. These increased proportions of recrystallised grains may have decreased the L-T toughness values by increasing the stress concentration points for void formation. They may have also increased the T-L toughness values by significantly disrupting crack propagation along the line of the original grains.

Not only may the recrystallisation changes have affected toughness values, but the concurrent changes in texture may also have influenced property values. It was concluded from the texture section that recrystallisation was associated with increased cube texture component. The enhanced T-L toughness and decreased L-T toughness values may, therefore, also be associated with increases in cube texture. Changes in the deformation texture systems must not be forgotten either. Changes in the deformation texture occurred most evidently between the 'slab' and axi-symmetric extrusions. microstructural analysis revealed a slightly higher proportion of grain boundary recrystallisation within the 'slab' material, and a major difference in texture, with the slab material exhibiting a rolled type texture and the axisymmetric extrusion exhibiting double fibre texture. This change in deformation texture from one of rolling to double fibre may, therefore, also be responsible for decreases in T-L and increases in L-T toughness values.

Fig 4.4.19 (b) illustrates the variation in toughness values brought about by increases in extrusion/aspect ratio, for extrudates produced at 450° C and aged to the overaged condition. For the 'slab' material, no consistent variation in T-L toughness values were observed as the extrusion/aspect ratio increased. As with the underaged extrudates the L-T toughness values were observed to decrease with increasing extrusion/aspect ratio. In contrast with the underaged materials, however, the 15:1 axi-symmetric material did not exhibit the maximum specific L-T toughness values. With regard to anisotropy, the difference between the L-T and T-L toughness values for the slab extrudates was observed to decrease as the extrusion/aspect ratio increased, whilst the axi-symmetric material exhibited the greatest anisotropy.

As the extrusion ratio rose from 9:1->15:1 microstructural analysis revealed an increase in the proportion of small recrystallised grains present at the original deformed grain boundaries. The increase in the T-L toughness values as the extrusion ratio increased from 9:1->15:1 may, therefore, be attributed to the disruption of crack propagation by these grains. The concurrent decrease in the L-T toughness may also be due to these recrystallised grains acting as stress concentration points for void formation. As the extrusion ratio rose from 15:1->30:1, however, microstructural analysis revealed an increase in the amount of large equiaxed recrystallised grains . The decreases in both T-L and L-T toughness values as the extrusion ratio increased from

15:1->30:1 may, therefore, be due to this recrystallisation increasing stress concentration values at the grain boundaries.

As with the material produced at 400° C, the effects of changes in texture upon properties must not be forgotten. No constant correlation between cube texture and T-L toughness values was evident, but a possible correlation between increases in cube texture and decreases in L-T toughness values was observed. Changes from rolling type textures to double fibre, also appeared to decrease T-L toughness values.

From the above results the toughness values were shown to be dependent upon the combined effects of grain structure, texture systems and precipitation condition. Single microstructure property value correlations may be made, however, but the observed property variations will be as a result of all microstructural changes. Care must, therefore, be exercised in determining any conclusions from these simple associations.

4.4.5 General Discussion and Conclusions

(1) Fracture characterisation

T-L toughness specimens:- Due to the 'weakness' of the internal grain boundaries, T-L fracture occurred predominantly by an intergranular microvoid coalescence failure mechanism. The boundary 'weakness' was caused by grain boundary precipitation, and accentuated by the strain concentration phenomena occurring within the material - coplanar slip & P.F.Z formation. Transgranular failure was also evident, but was usually associated with transverse crack propagation. This failure occurred when the grain boundary strength and textural systems present within the material, were such that the shear stress developed within the coplanar slip regions caused transgranular failure initiation, before the shear stress necessary for boundary failure was achieved. The transgranular failure again occurred by a microvoid coalescence, with void initiation occurring at second phase matrix precipitates, β' particles, and at the junction of three or four slip bands.

L-T toughness samples:- Failure in the transverse direction involved crack propagation across the elongated deformed grains, and consequently transgranular rather than intergranular failure was necessary. The problem of crack growth along elongated grain boundaries at low applied stresses was, therefore, not present. As a result the L-T toughness values were always higher than the T-L values.

The mechanism of trans-granular crack propagation was microvoid coalescence, and the slightly corrugated appearance of the flat faceted transgranular regions was due to the manifestation of secondary slip systems upon the fracture surface.

(2) Correlation Between Properties and Microstructure

Property values and processing conditions were connected through the influence of processing upon microstructure. The main mechanism of crack advancement within these alloys was identified as microvoid coalescence[2][3][4][7] , with the following microstructural features found to influence the property values:-

(i) The localised deformation phenomena - Coplanar slip and textural effects.

Coplanar slip, due to δ' precipitation, caused intense shear upon slip planes, and has previously been shown[8][9] to enhance intergranular failure at lower than expected applied stresses. The proportion of δ' increased as ageing occurred, but it was found that it was the combined effect of δ', S, T_1 and grain size that determined whether or not ageing improved or decreased toughness values. It was considered, however, that the increase in δ' precipitation, due to ageing was detrimental with respect to both the longitudinal and transverse toughness values.

The presence of a definite texture denotes preferred crystallographic orientations within the material. Under the action of a given stress state this may cause an increase in the strain concentration at grain boundaries, hence increase grain boundary failure. It may also, however, serve to reduce the effect of the grain boundaries to inhibit dislocation movement, by reducing the crystallographic misorientation across grains. This will decrease the stress concentration at boundaries, consequently increasing the possibility of transgranular failure. It was concluded in this section that the presence of double fibre texture, compared with that of rolling type components (Copper, Brass, S, and Goss), decreased the T-L toughness values and increased L-T toughness values. It was also indicated that increases in rolling textures caused the T-L toughness to increase, and the L-T toughness to decrease. Since cube texture variations were correlated with recrystallisation, it was difficult to determine whether it was changes in grain structure that effected properties, or the change in texture. The conclusion as to whether or not cube texture was good or bad with regard to property values was, therefore, impossible to make.

(ii) Grain size. Larger grain sizes allow greater strain concentration build-ups at grain boundaries, thereby enhancing failure at low stresses. Smaller grains may not only help to prevent this, but they may also disperse the strain during deformation.

The effect of grain size upon toughness has actually been found to be dependent upon the stress-state[10][11] . In plane strain (thick sections) microvoid coalescence initiates from the nearest weak point ahead of the crack, suggesting that a large grain size would be beneficial for plate and extrusion products. For thin extrudates, however, 6mm or less, plane stress prevails, causing the formation of a larger plastic zone. Under these

conditions maximum amounts of straining, rather than the prevention of void initiation is of prime importance, hence a small grain size is desirable.

In this project the size of the recrystallised grains varied with processing conditions. Large equiaxed recrystallisation tended to be present in the central regions of aged material extruded at higher temperatures and ratios,-30:1 450° C & 500° C, with grain boundary recrystallisation of relatively small equiaxed grains present in material extruded at lower temperatures and ratios. It was found that increases in the amount of large recrystallised grains decreased both longitudinal and transverse toughness values, but increased isotropy. The increase in the presence of the small recrystallised grains at the original grain boundaries, however, tended to increase the T-L toughness, decrease the L-T toughness values, and increase the isotropy. The large equiaxed recrystallisation decreased both longitudinal and transverse properties, due to the increased stress concentration at boundaries associated with the larger grains. The small equiaxed recrystallised grains disrupted the microvoid coalescence crack propagation along the continuous line of the original grain boundaries. Their relatively small size, however, did not increase the strain concentration within the grains greatly, hence the longitudinal toughness values increased. With regard to transverse crack growth the presence of the recrystallised grains at the original grain boundaries represented points of discontinuity, hence decreased toughness.

(iii) Grain boundary Phases. Grain boundary phases may be regarded as weak points within the matrix, encouraging the formation and expansion of voids at grain boundaries. Many researchers have previously highlighted the effect of such precipitates upon fracture[2][3]. In this project ageing caused increased grain boundary precipitation and was considered to decrease T-L and L-T toughness values. It must be remembered, however, that the exact effect of ageing upon property values not only depended upon grain boundary recrystallisation, but also upon the matrix precipitation and the existing grain structure.

(iv) Fibering. The alignment of grains and particles within the material provides a pre-determined crack path. This has been found to be highly influential in determining many of the fracture surfaces observed, hence the toughness values measured, particularly for the T-L specimens[4][6][7][12].

During extrusion the grains became highly elongated in the extrusion direction. This 'fibering' of the extrudate microstructure essentially provided pre-determined crack paths along the extrudate, which were weakened by the presence of grain boundary precipitation. For the T-L fracture specimens, the combined effect of weak longitudinal boundaries, the strain localisation phenomena occurring within the material, and the application of the applied stress perpendicular to the extrusion direction, caused relatively low energy failure along the elongated grain boundaries. This fibering effect

was determined to be the major factor responsible for the difference between T-L and L-T toughness values.

The above paragraphs have described how property values were correlated with microstructural characteristics. It must be remembered, however, that in this project specimens were produced in order to simulate plane strain conditions, so that a material property could be defined. The microstructural features which improve the plane strain fracture toughness, therefore, may not necessarily improve the plane stress fracture toughness[11].

(3) Effect of Extrusion Temperature Upon Toughness

Extrusion temperature affected toughness by its direct effect upon the recrystallisation present within the material. As already mentioned, in the as-extruded conditions both alloy compositions exhibited an increase in recrystallisation as the extrusion temperature increased. Increases in extrusion temperature consequently increased T-L toughness and decreased the L-T toughness values.

In the solution heat treated and aged condition increases in the extrusion temperature tended to increase the amount of small equiaxed recrystallised grains in extrudates produced at lower ratios, and the amount of large equiaxed grains in extrudates produced at higher ratios. The effect of extrusion temperature upon toughness consequently depended upon which type of recrystallisation was present. Since higher extrusion temperatures were generally associated with the formation of the large equiaxed grains, it was suggested that the optimum extrusion temperature with regard to longitudinal toughness should be low enough to prevent excessive grain growth, but high enough to produce substantial recrystallisation. This would result in a high degree of small equiaxed grain boundary recrystallisation, and hence improve longitudinal toughness. The optimum extrusion temperature for improved transverse toughness values would be low enough to prevent all recrystallisation.

When considering the manipulation of processing conditions such as temperature, however, extrusion limit diagrams must be consulted in order that surface quality and tooling limitations are satisfied[17][18]

(4) Effect of Aspect Ratio and Extrusion Ratio Upon Toughness

Extrusion ratio and aspect ratio affected toughness values through their effect upon recrystallisation and texture.

Through changes in the deformation fields, increases in aspect ratio enhanced the formation of rolling type textures, and encouraged recrystallisation. Increases in

extrusion ratio also caused increased recrystallisation, and consequently affected the texture systems present within the extrudates. Extrusion ratio changes did not, however, cause texture changes through modification of the deformation field characteristics.

Variations in aspect ratio and extrusion ratio could, therefore, be utilised to modify microstructure, hence properties. The alteration of extrusion ratio in order to control microstructure is possible, but economic reasons may make this impractical. With regard to the aspect ratio, it must be remembered, that even though aspect ratio has a considerable effect upon microstructure, varying the aspect ratio in order to control the structure would be impractical, since the finished product usually has a given aspect ratio for a design reason. The control of texture may be achieved, however, by using working techniques to provide pre-textures to extrusion billets, which when extruded produce a more desirable extrusion texture. The modification of the deformation process may also be possible, in order to control the extrusion textures produced.

(5) Effect of Ageing Condition Upon Toughness

The effect of ageing upon properties appeared to be directly related to the grain structures present. When processing was such as to produce small grain boundary recrystallised grains, the disruption of the coplanar slip process by matrix precipitation of S and T_1 , outweighed the concurrent phenomenon of boundary weakening by precipitation. The overaged material was consequently tougher than the underaged material. As the recrystallisation grain size increased, however, the factor of grain boundary weakening increased in importance, hence the underaged material became tougher.

The peak aged material consistently exhibited the lowest toughness values, because it possessed maximum volume fractions of δ', without the benefit of additional S and T phase precipitation.

Extrusion Ratio	Extrusion Temp. (°C)	Sample Posit.	Ageing Condition	(L-T) Toughness ($MPam^{1/2}$)	(T-L) Toughness ($MPam^{1/2}$)
15:1	400	Front of Extru.	As-Extruded	20.3 (±0.6)	20.0 (±0.5)
			Under-aged	29.6 (±0.4)	25.2 (±0.4)
			Overaged	31.9 (±0.4)	26.6 (±0.4)
		Rear of Extru.	As-Extruded	21.0 (±0.3)	20.4 (±0.9)
			Overaged	32.3 (±0.3)	27.1 (±0.3)
	450	Front of Extru.	As-Extruded	20.5 (±0.4)	19.9 (±0.4)
			Under-aged	28.9 (±0.4)	26.4 (±0.5)
			Over-aged	29.3 (±0.4)	27.0 (±0.5)
		Rear of Extru.	As-Extruded	20.2 (±0.7)	19.9 (±0.3)
			Overaged	30.2 (±0.7)	27.4 (±0.5)
	500	Front of Extru.	Under-aged	28.4 (±0.2)	27.4 (±0.6)
			Over-aged	28.2 (±0.5)	27.8 (±0.3)
30:1	400	Front of Extru.	Under-aged	28.7 (±0.3)	27.6 (±0.5)
			Over-aged	27.1 (±0.4)	25.1 (±0.5)
	450	Front of Extru.	Under-aged	27.2 (±0.7)	26.1 (±0.5)
			Over-aged	26.2 (±0.3)	24.1 (±0.5)
	500	Front of Extru.	Under-aged	27.1 (±0.5)	26.2 (±0.6)
			Overaged	25.1 (±0.3)	23.2 (±0.2)

Fig 4.4.2 Variation in (T-L) & (L-T) toughness values with changes in ageing condition. Alloy A material.

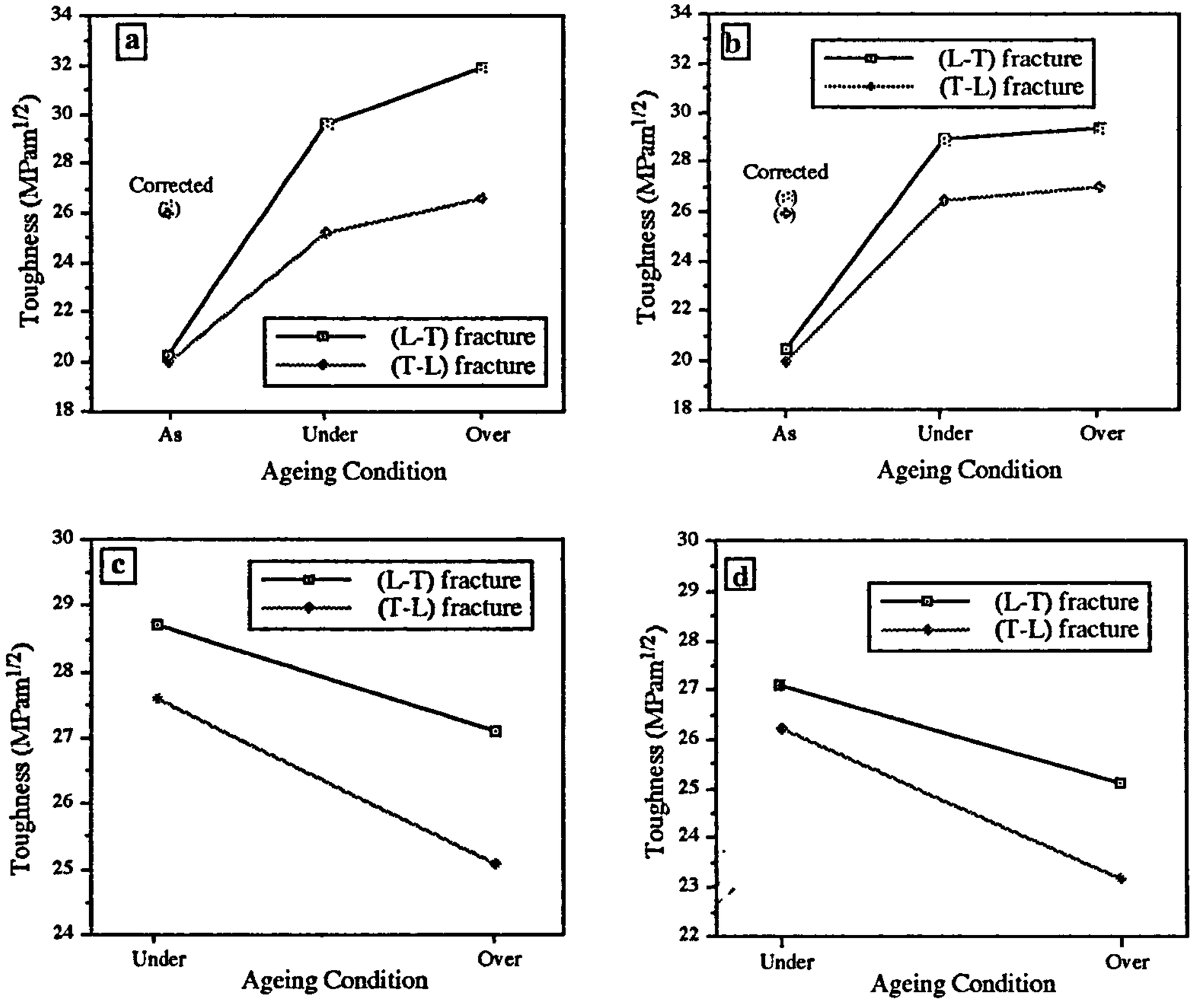


Fig 4.4.3

Alcan 8090. Alloy A.
Variation in (T-L) and (L-T) toughness values with changes in ageing times
(a) 15:1 extrusion ratio, 400 °C extrusion temperature.
(b) 15:1 extrusion ratio, 450°C extrusion temperature.
(c) 30:1 extrusion ratio, 400 °C extrusion temperature.
(d) 30:1 extrusion ratio, 500°C extrusion temperature.

Extrusion Ratio	Extrusion .Temp. (°C)	Ageing Condition	(T-L) Toughness ($MPam^{1/2}$)	(L-T) Toughness ($MPam^{1/2}$)
15:1	400	As-Extruded	20.8 (±0.4)	21.4 (±0.4)
		Under-aged	27.5 (±0.4)	31.6 (±0.4)
		Peak-aged	25.3 (±0.5)	29.9 (±0.4)
		Overaged	28.2 (±0.5)	33.5 (±0.4)
	450	As-Extruded	20.5 (±0.5)	21.2 (±0.4)
		Under-aged	28.5 (±0.5)	31.1 (±0.4)
		Peak-aged	26.4 (±0.5)	28.2 (±0.3
		Over-aged	30.5 (±0.5)	32.2 (±0.3)
	500	As-Extruded	20.5 (±0.6)	20.3 (±0.5)
		Under-aged	29.0 (±0.6)	29.8 (±0.5)
		Peak-aged	26.9 (±0.2)	27.2 (±0.3)
		Over-aged	30.5 (±0.2)	31.9 (±0.3)
30:1	400	As-Extruded	21.6 (±0.5)	22.8 (±0.5)
		Under-aged	27.2 (±0.5)	28.8 (±0.4)
		Peak-aged	26.2 (±0.3)	28.2 (±0.2)
		Overaged	28.8 (±0.5)	31.6 (±0.7)
	450	As-Extruded	20.4 (±0.5)	22.6 (±0.7)
		Under-aged	25.7 (±0.5)	29.1 (±0.5)
		Peak-aged	25.3 (±0.8)	27.4 (±0.2)
		Over-aged	27.5 (±0.5)	31.5 (±0.5)
	500	As-Extruded	20.3 (±0.6)	21.4 (±0.5)
		Under-aged	25.5 (±0.6)	28.2 (±0.2)
		Peak-aged	24.9 (±0.5)	26.2 (±0.4)
		Over-aged	26.9 (±0.4)	29.8 (±0.4)

Fig 4.4.4 Variation in (T-L) & (L-T) toughness values with changes in ageing condition. Alloy B material.

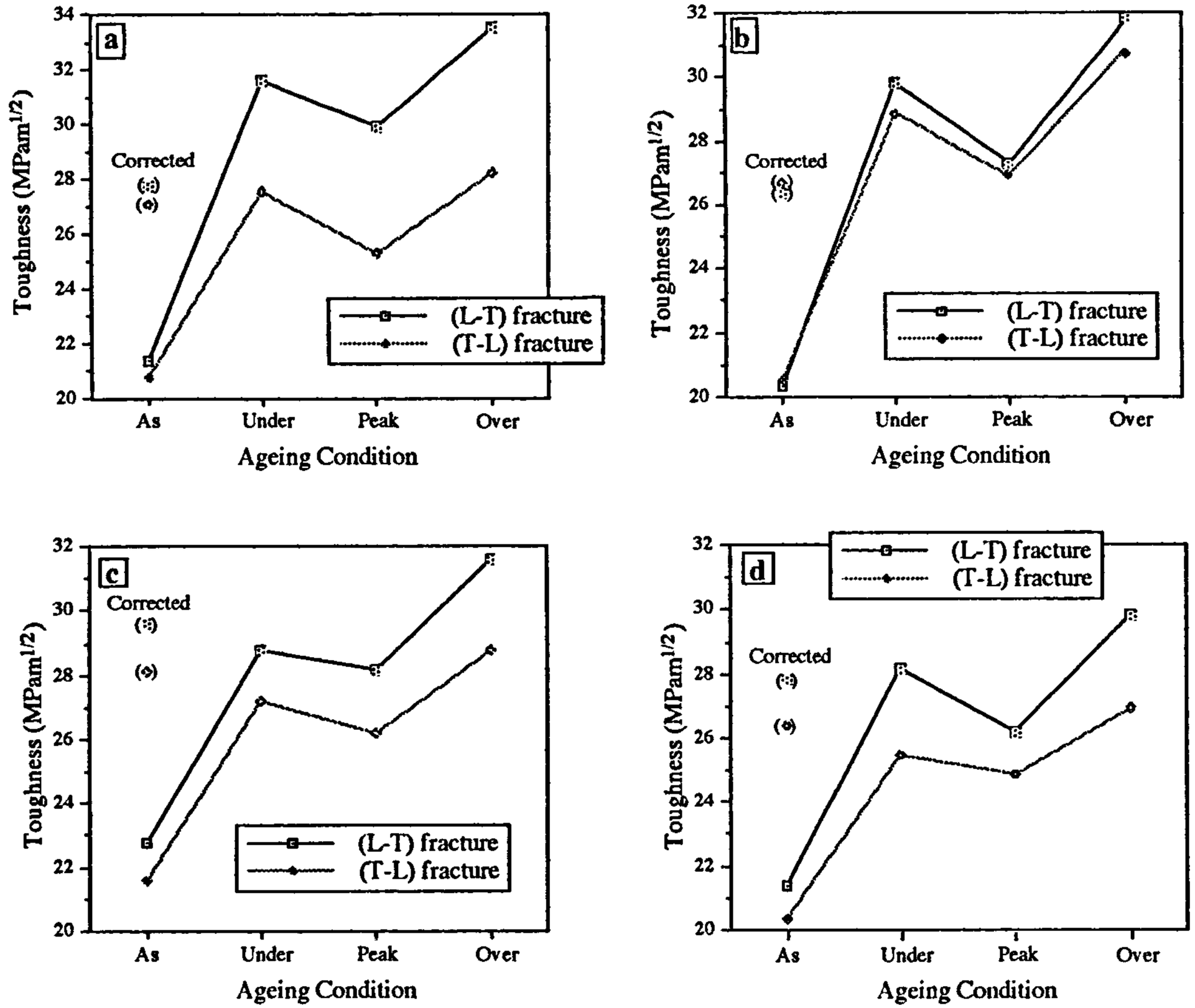
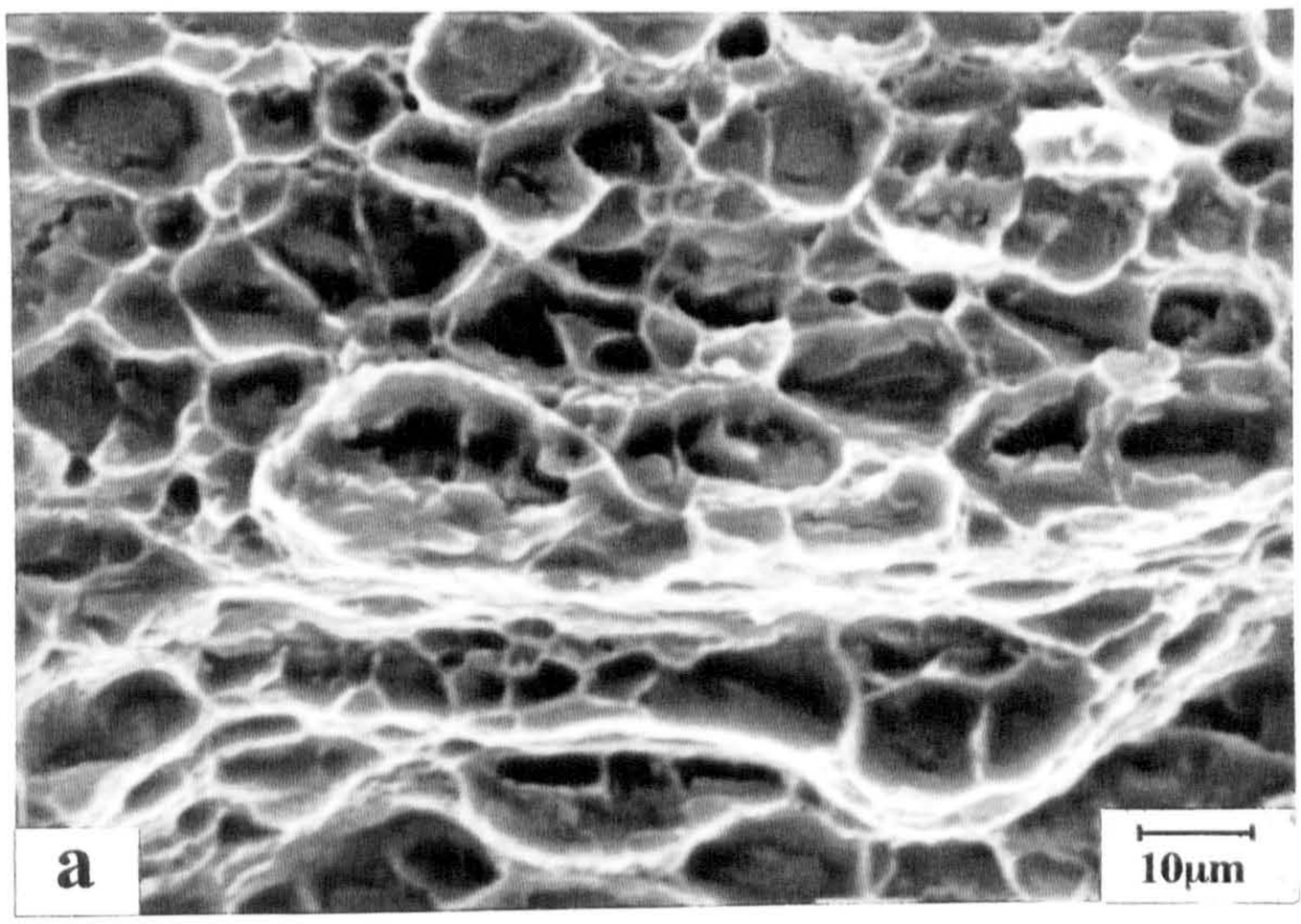
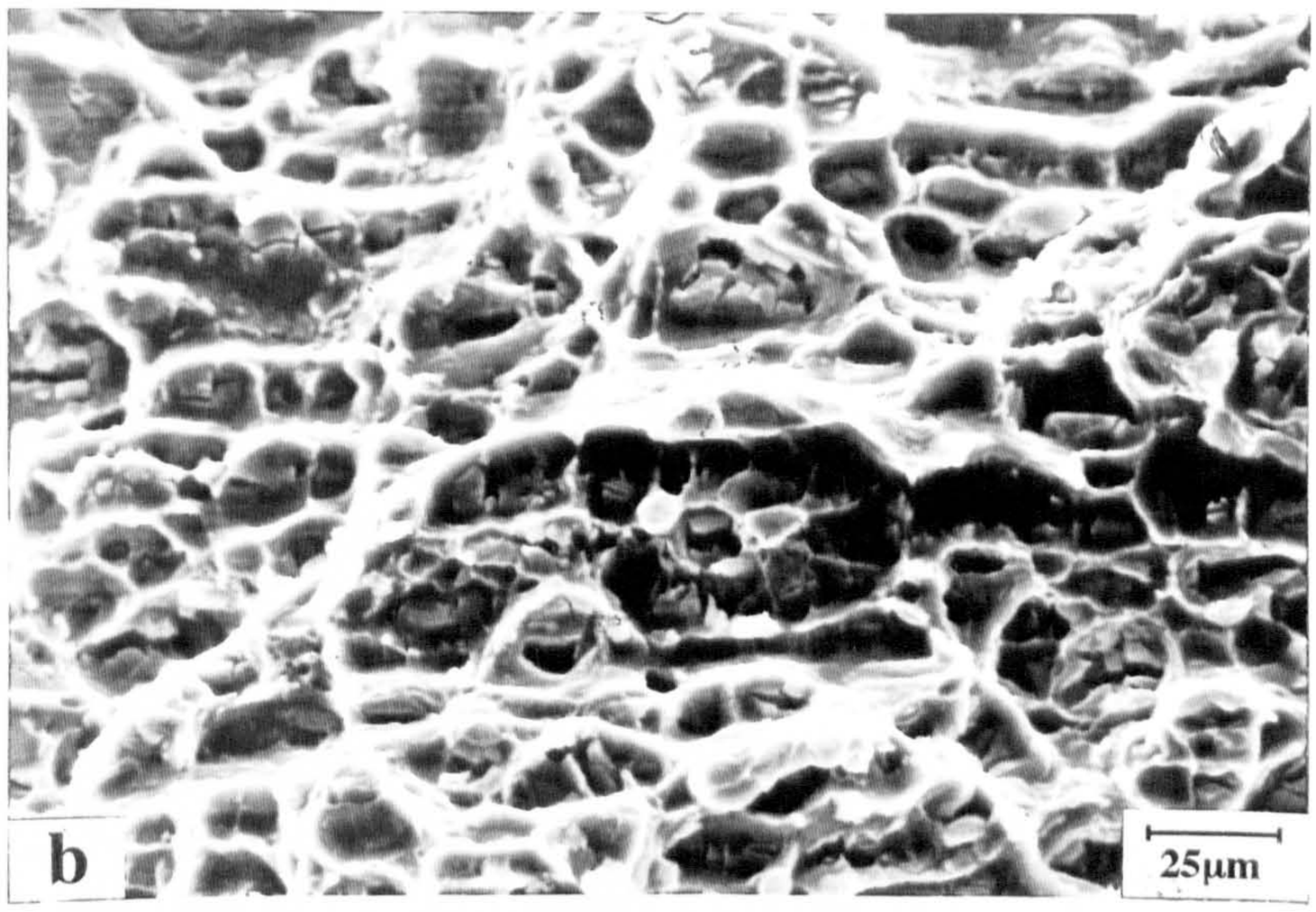


Fig 4.4.5

Alcoa 8090, Alloy B.
Variation in (T-L) and (L-T) toughness values with changes in ageing times.
(a) 15:1 extrusion ratio, 400°C extrusion temperature.
(b) 15:1 extrusion ratio, 500°C extrusion temperature.
(c) 30:1 extrusion ratio, 400°C extrusion temperature.
(d) 30:1 extrusion ratio, 500°C extrusion temperature.

Fig 4.4.6 (T-L) S.E.M. Fractographs.
As-extruded condition.
'Front' regions of extrudates.
(a) Alloy A material.
6:1 extrusion ratio.
500° C extrusion temperature.
(b) Alloy A material.
15:1 extrusion ratio.
500° C extrusion temperature.
(c) Alloy B material.
30:1 extrusion ratio.
500° C extrusion temperature.





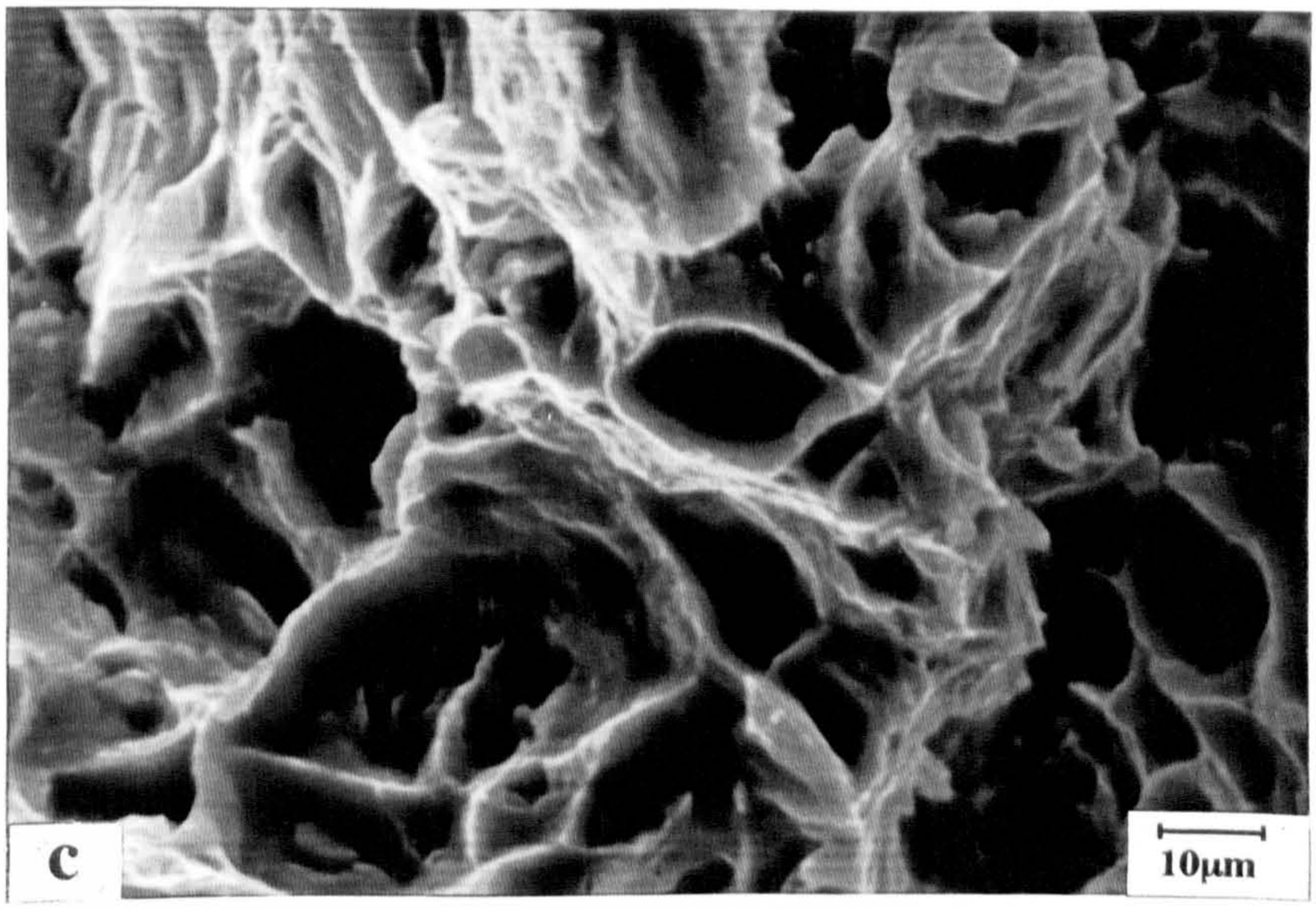


Fig 4.4.6

Fig 4.4.7 (L-T) S.E.M. Fractographs.
Alloy B material.
As-extruded condition.
(a) 15:1 extrusion ratio.
400° C extrusion temperature.
(b) 15:1 extrusion ratio.
450° C extrusion temperature.
(c) 15:1 extrusion ratio.
500° C extrusion temperature.

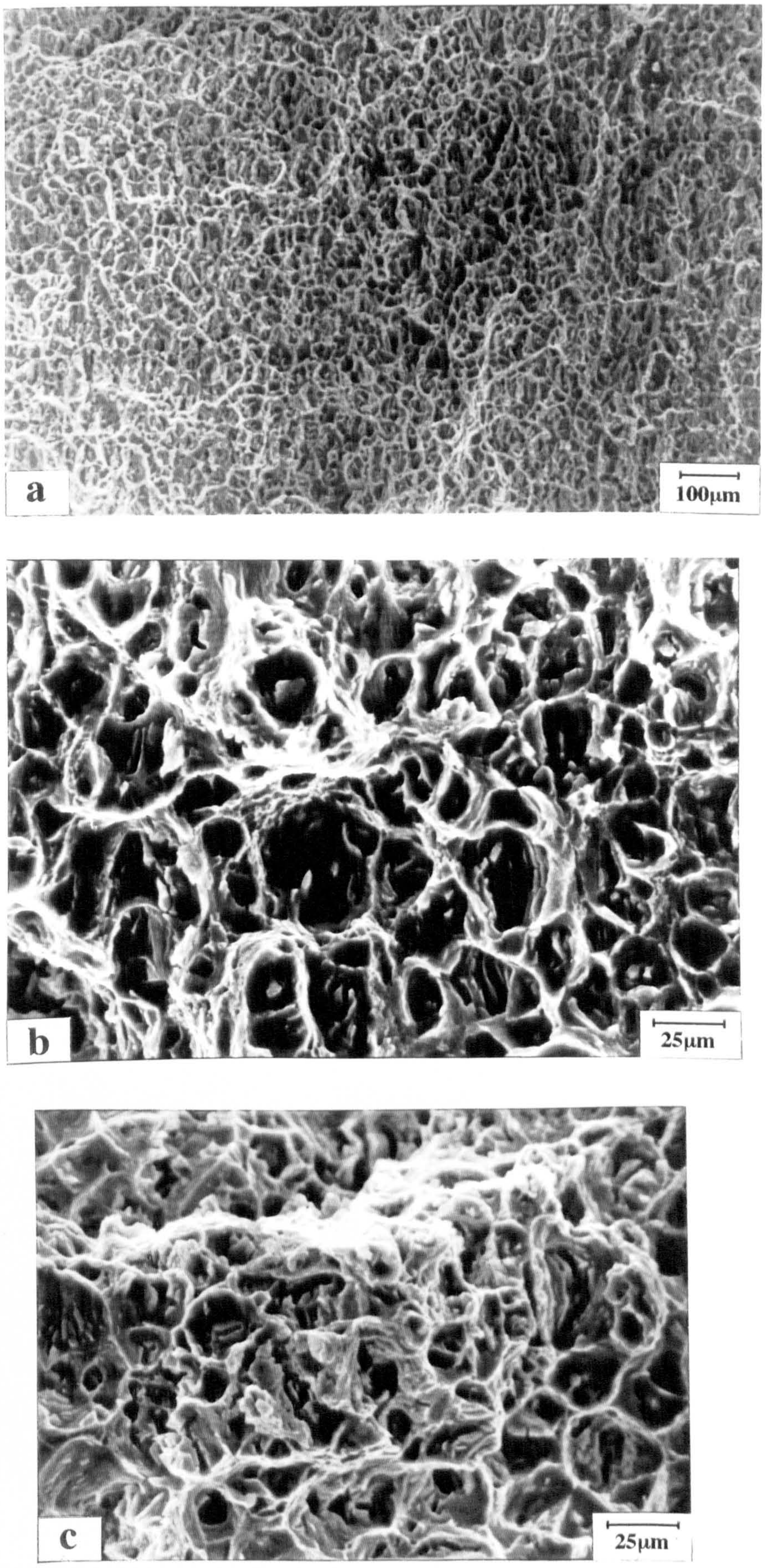
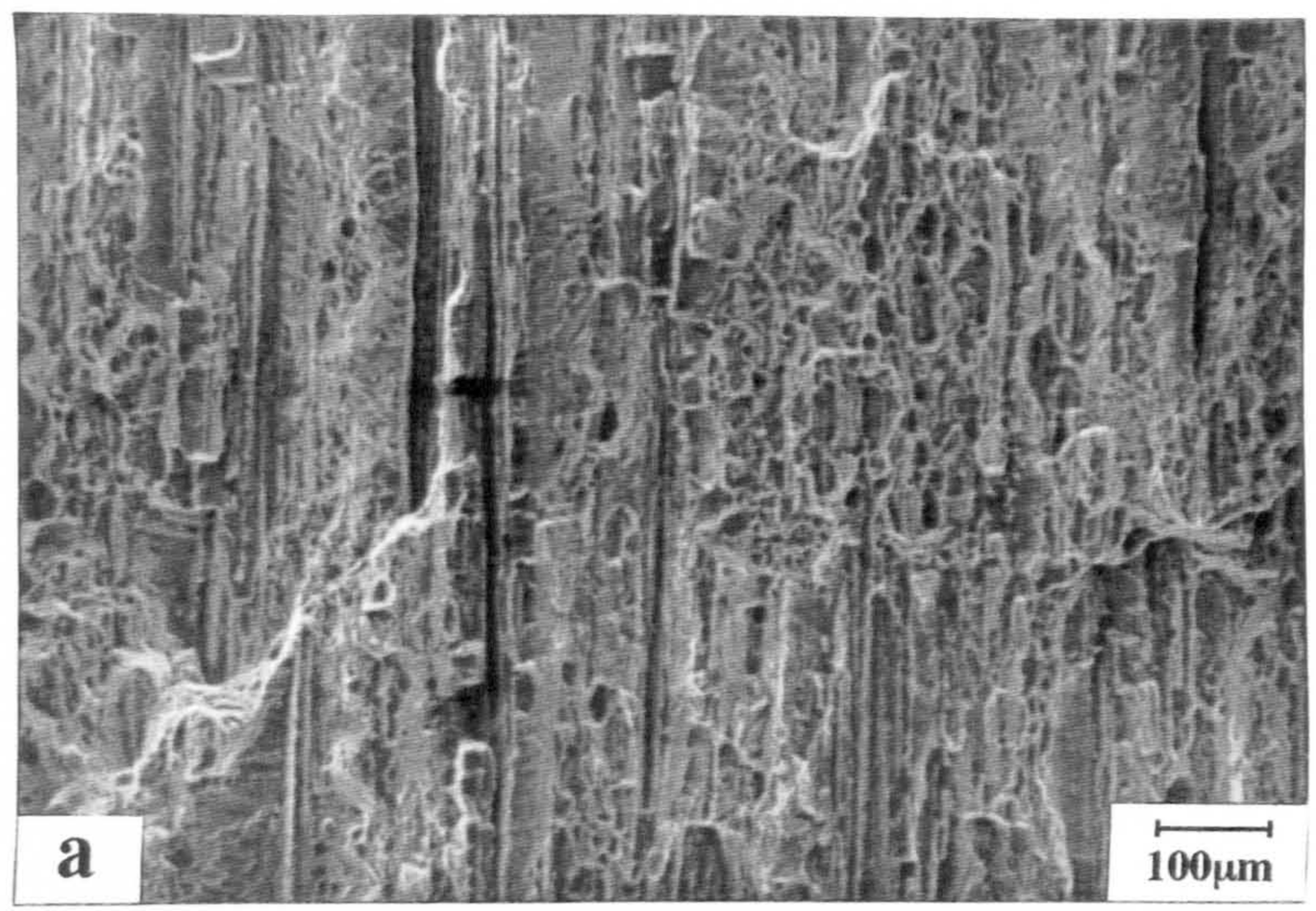
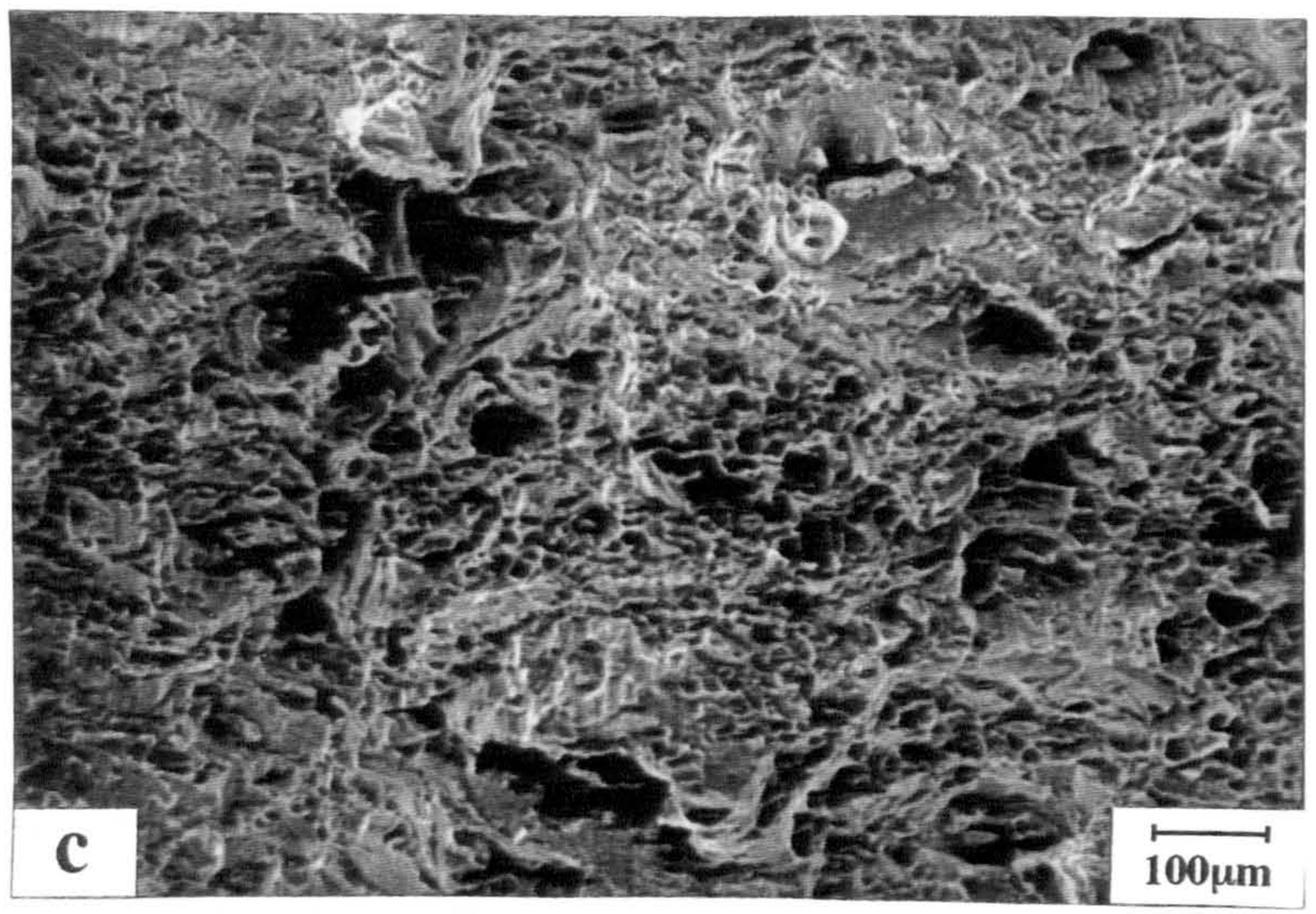
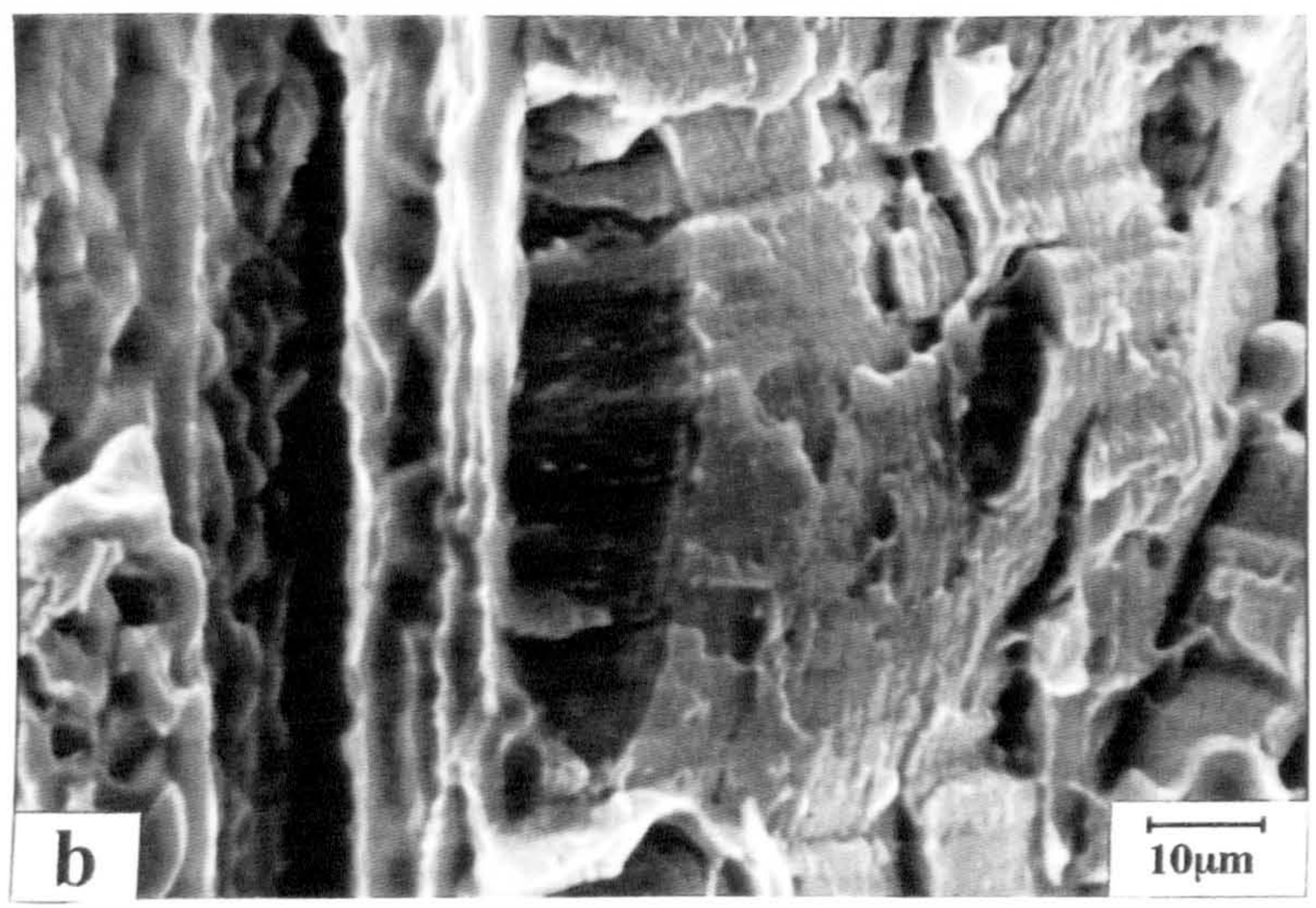


Fig 4.4.7

Fig 4.4.8 S.E.M. Fractographs.
Alloy A material.
Underaged condition.
9:1 extrusion ratio.
400° C extrusion temperature.
'Front' of extrudate.
(a) & (b) (T-L) Fracture.
(c) & (d) (L-T) Fracture.







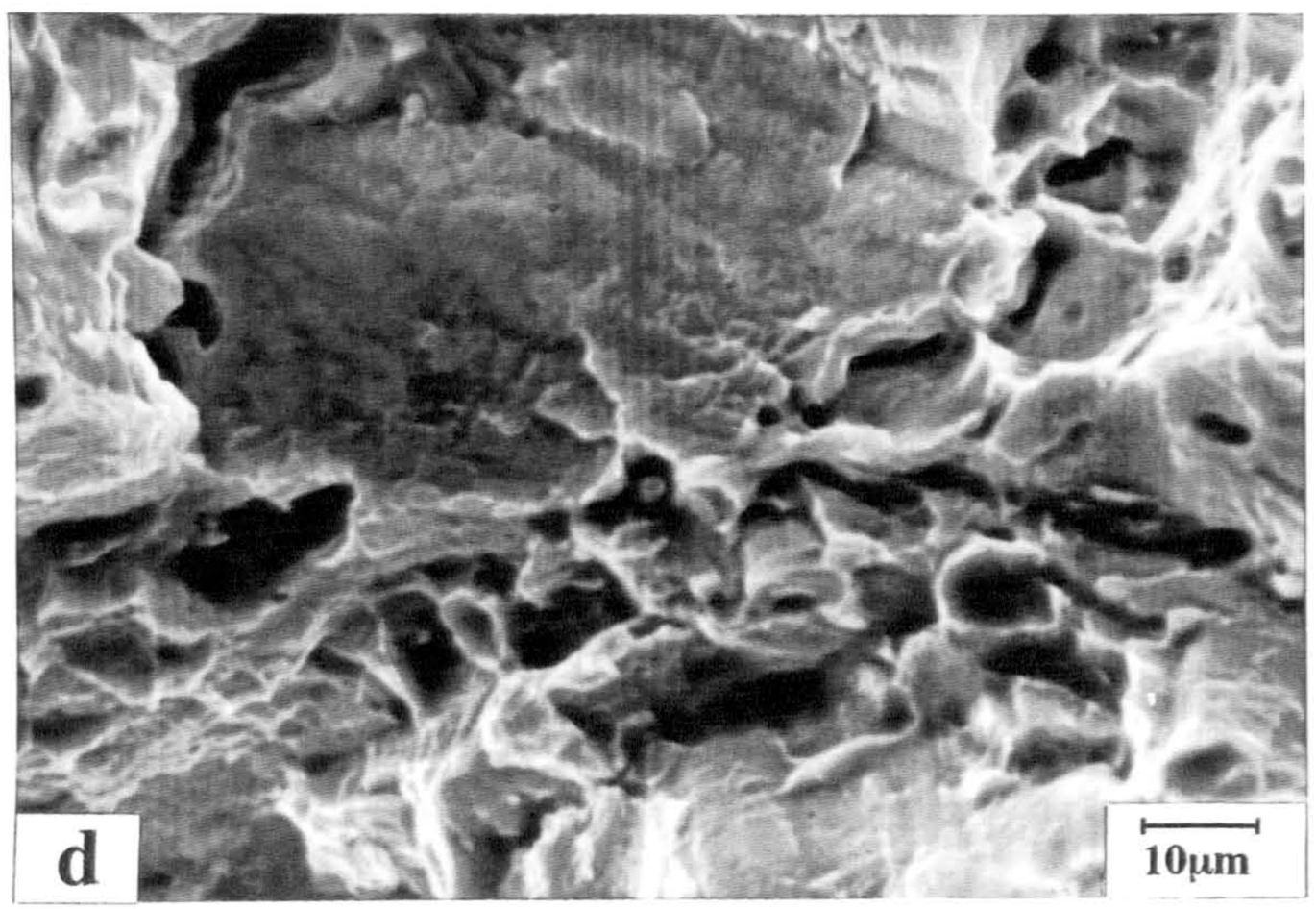


Fig 4.4.8

Fig 4.4.9 S.E.M. Fractographs.
Alloy A material.
15:1 extrusion ratio.
Underaged condition.
'Front' regions of extrudates.
(a) (T-L) Fracture.
400° C extrusion temperature.
(b) (L-T) Fracture.
400° C extrusion temperature.
(c) (T-L) Fracture.
500° C extrusion temperature.
(d) (L-T) Fracture.
500°C extrusion temperature.

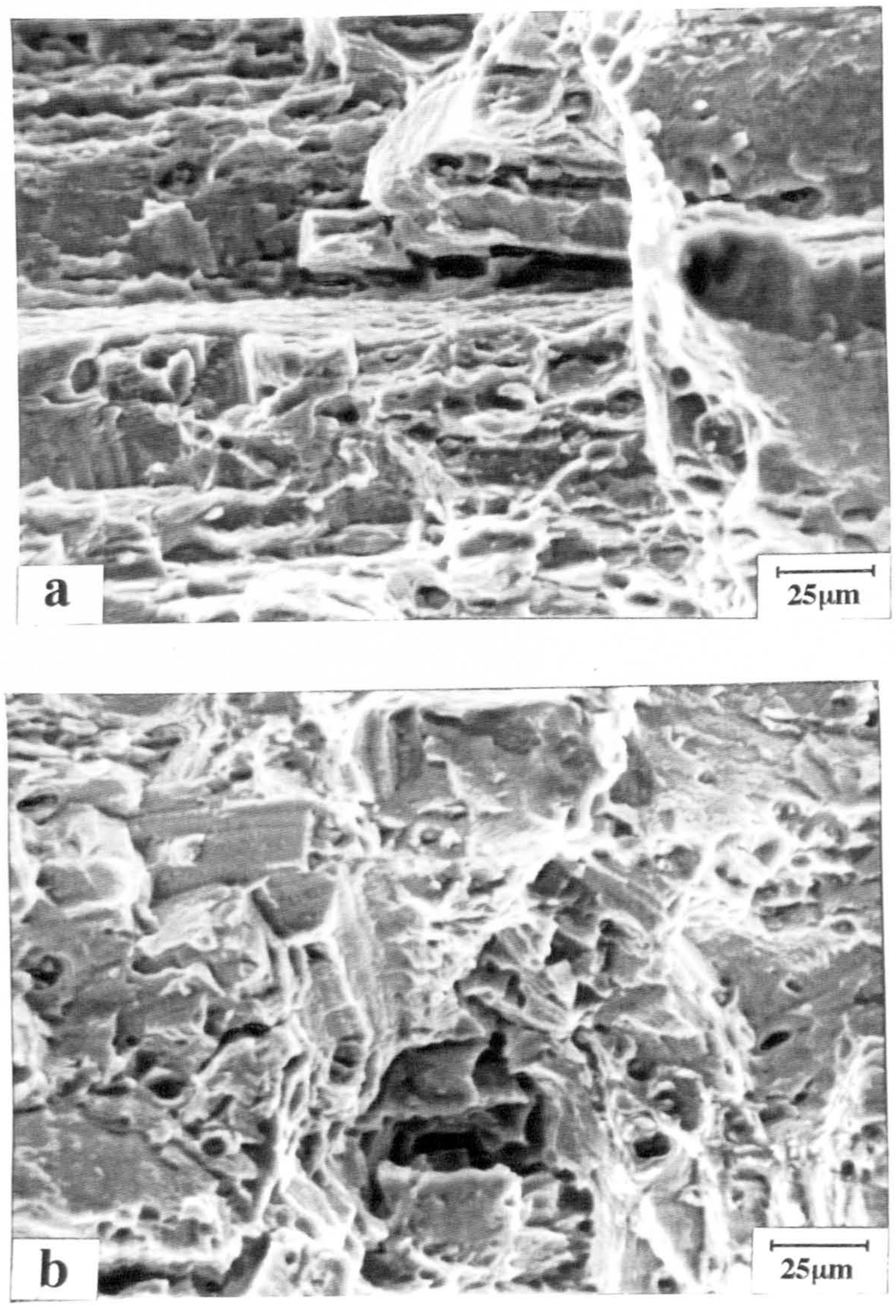


Fig 4.4.9

Fig 4.4.10 (T-L) S.E.M. Fractographs.
Alloy A material.
Overaged eondition.
'rear' of Extrudate.
(a) 6:1 extrusion ratio.
400° C extrusion temperature.
(b) 9:1 extrusion ratio.
400° C extrusion temperature.
(c) 30:1 extrusion ratio.
400° C extrusion temperature.

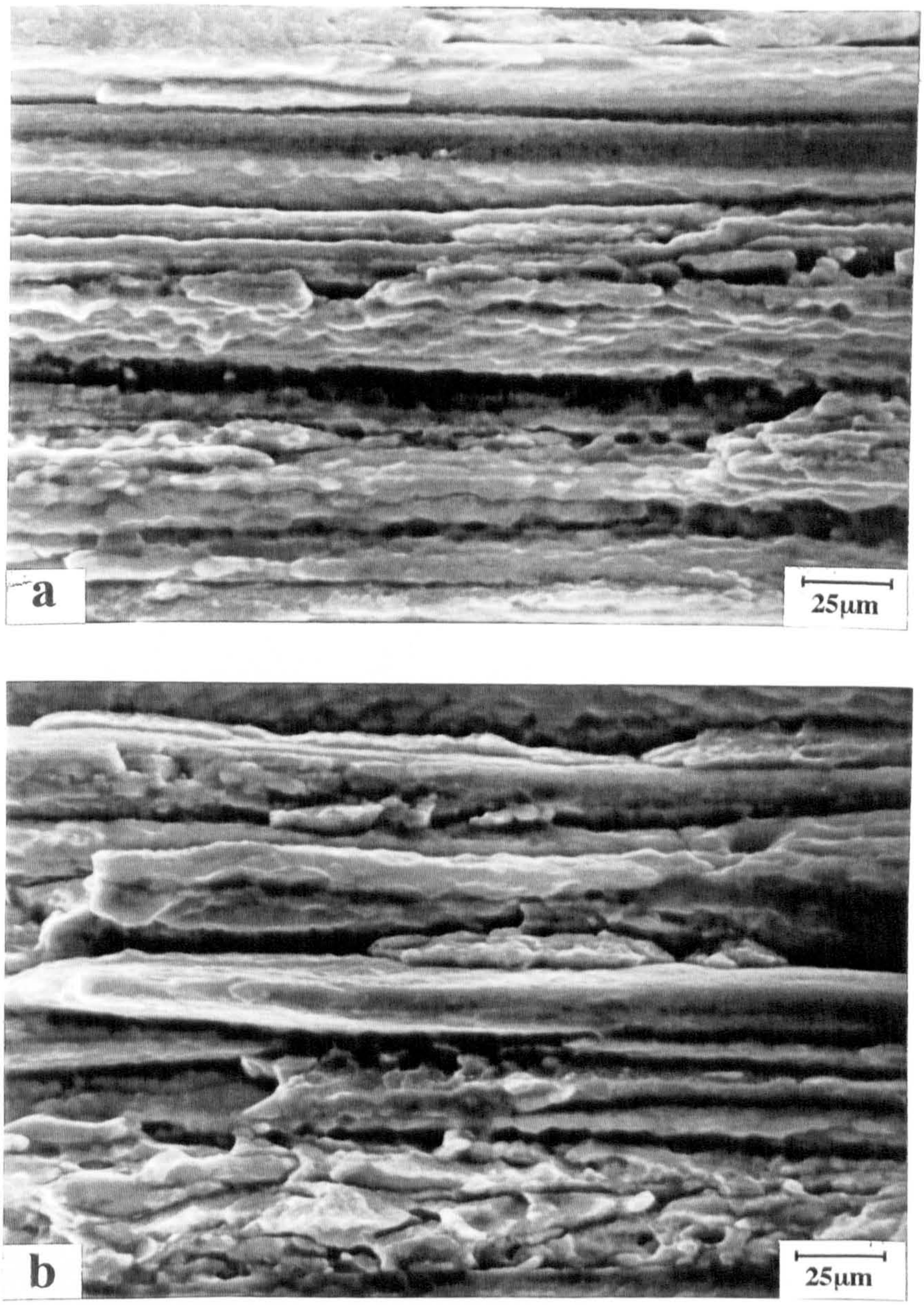
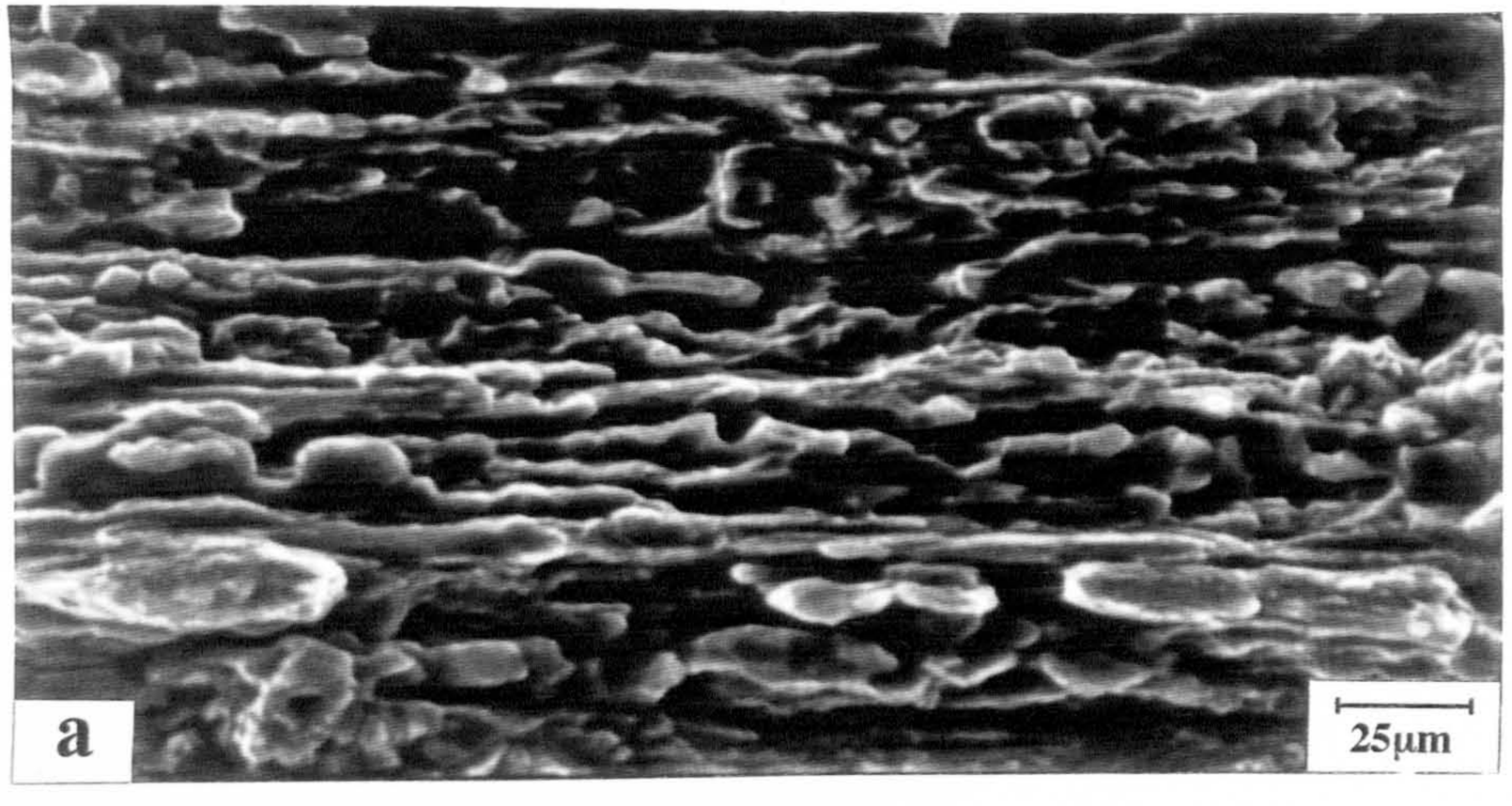
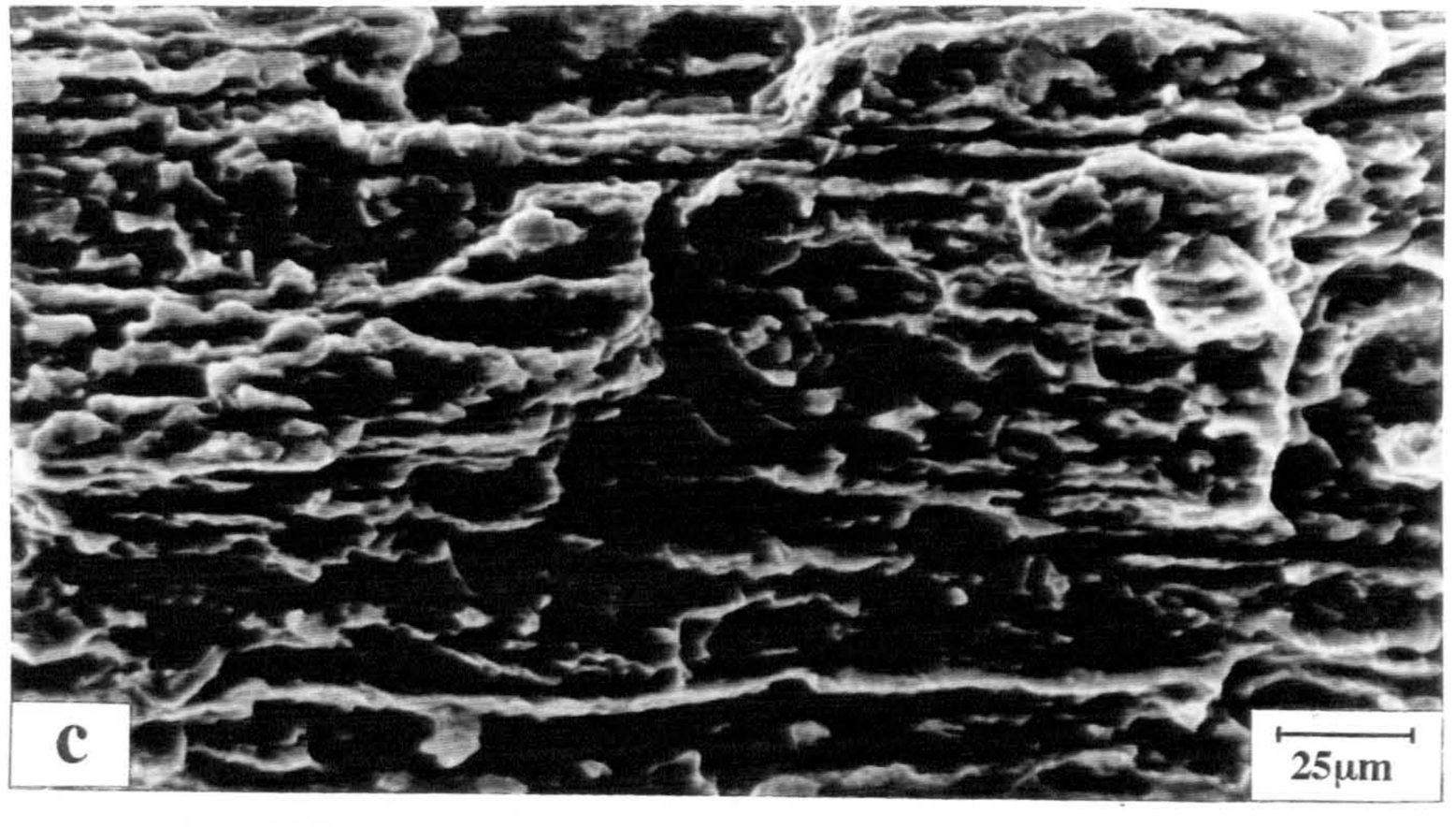
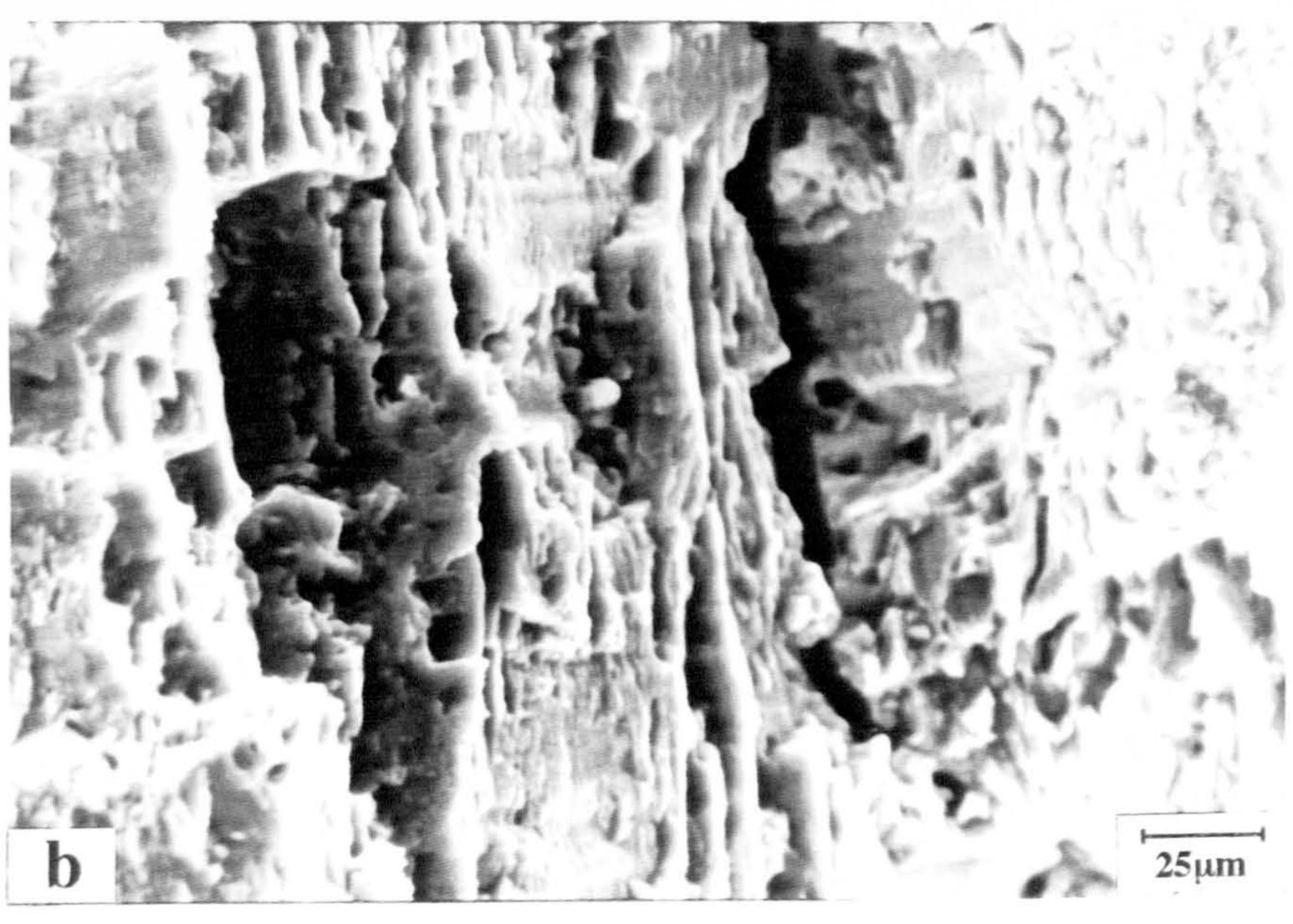


Fig 4.4.10

Fig 4.4.11 S.E.M. Fractographs.
Alloy A material.
15:1 extrusion ratio.
Overaged condition.
'Front' regions of extrudates.
(a) (T-L) Fracture
400° C extrusion temperature.
(b) (L-T) Fracture.
400° C extrusion temperature.
(c) (T-L) Fracture
500° C extrusion temperature.
(d) (L-T) Fracture.
500° C extrusion temperature.







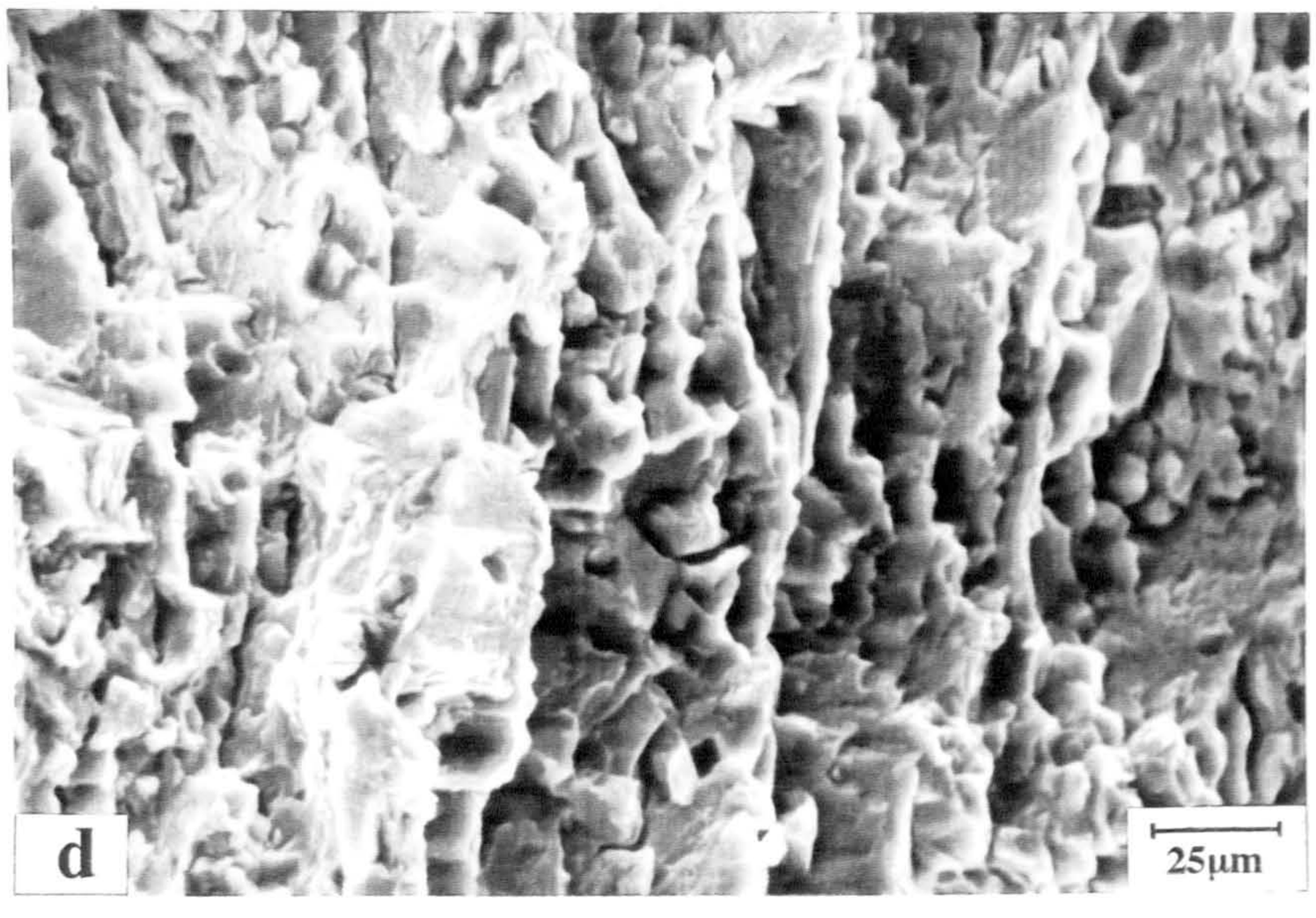
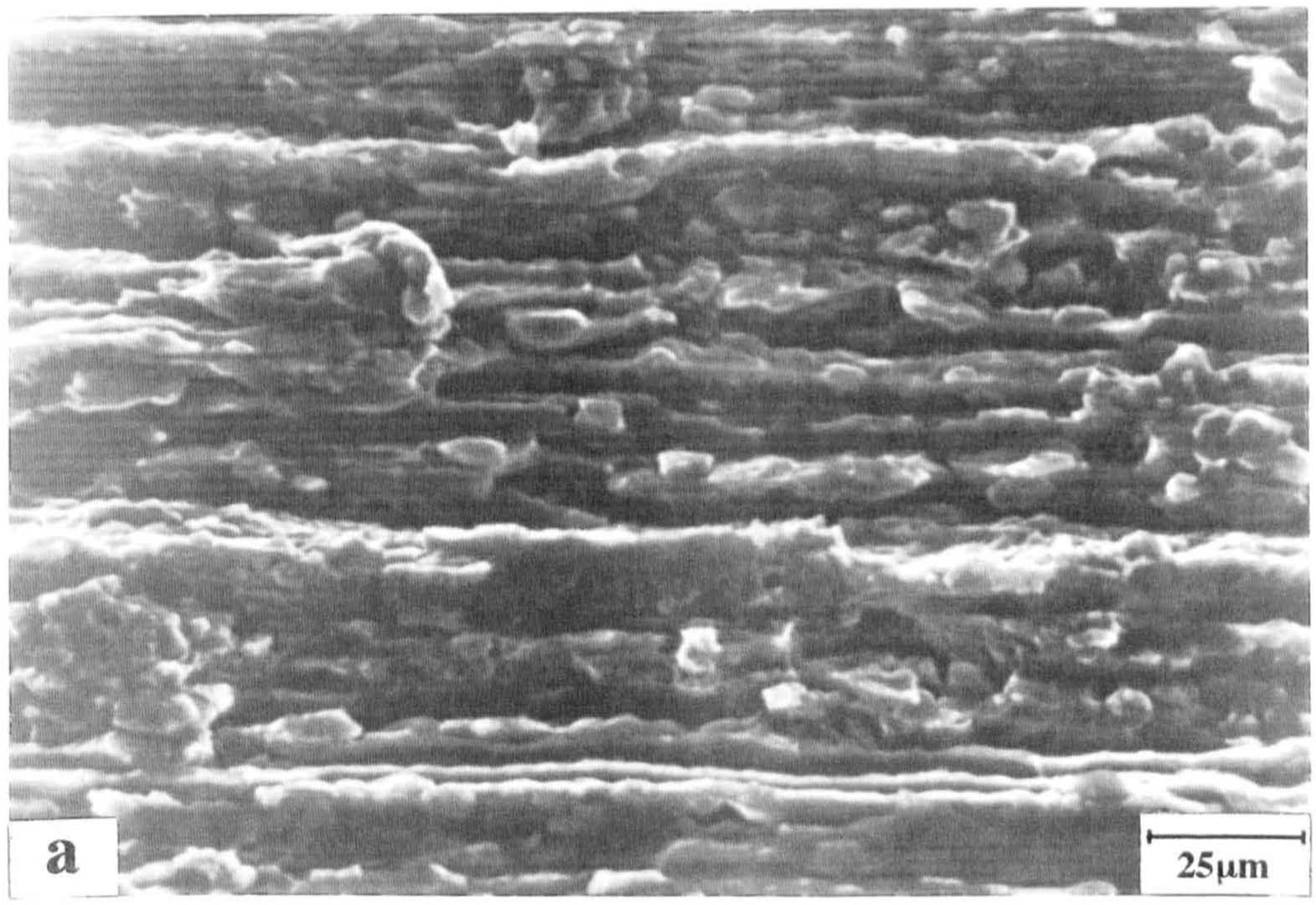
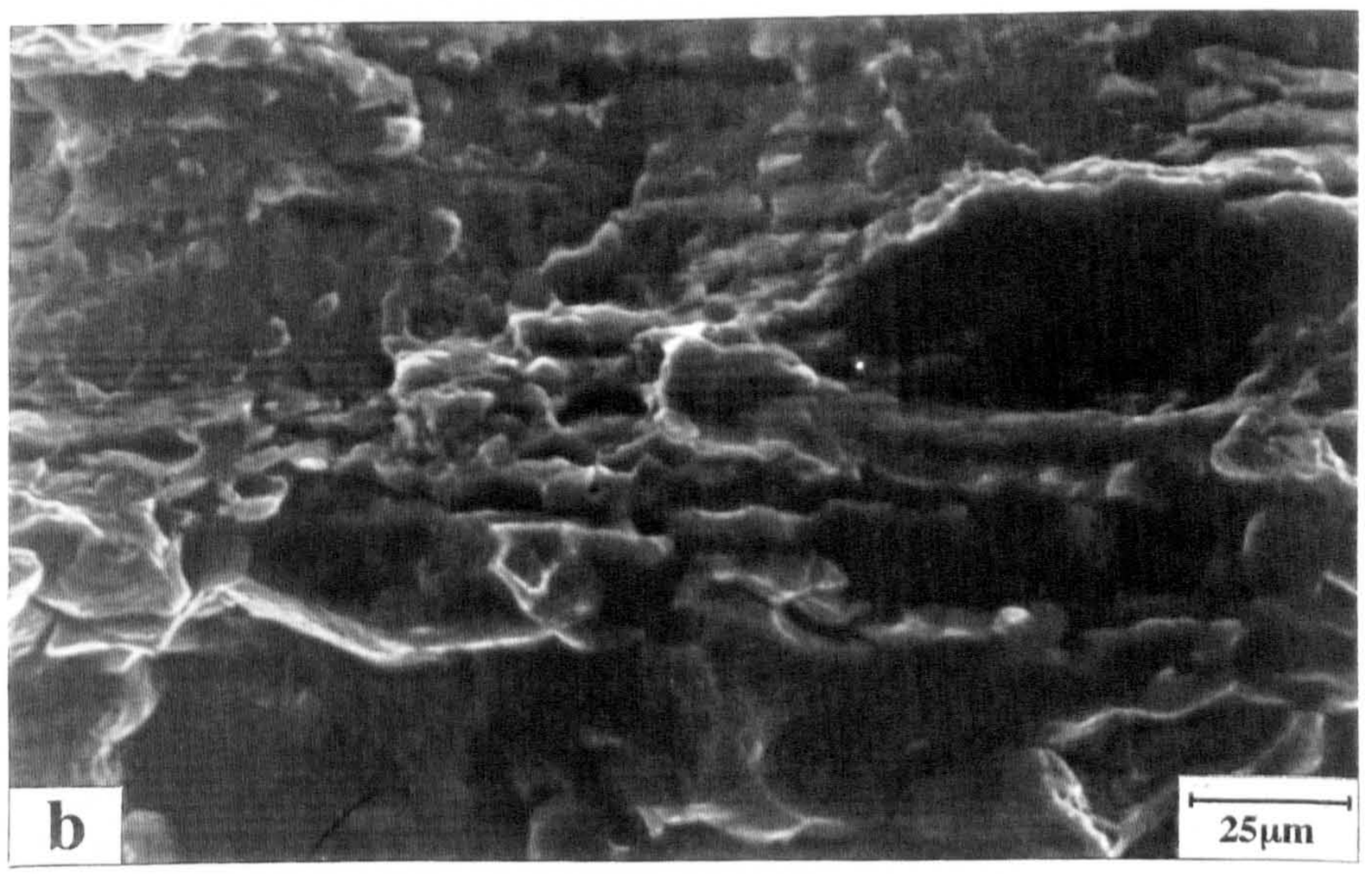


Fig 4.4.11

Fig 4.4.12 S.E.M. Fractographs.
Alloy B material.
30:1 extrusion ratio.
Overaged condition.
(a) (T-L) Fracture
400° C extrusion temperature.
(b) (T-L) Fracture.
500° C extrusion temperature.
(c) (L-T) Fracture
500° C extrusion temperature.





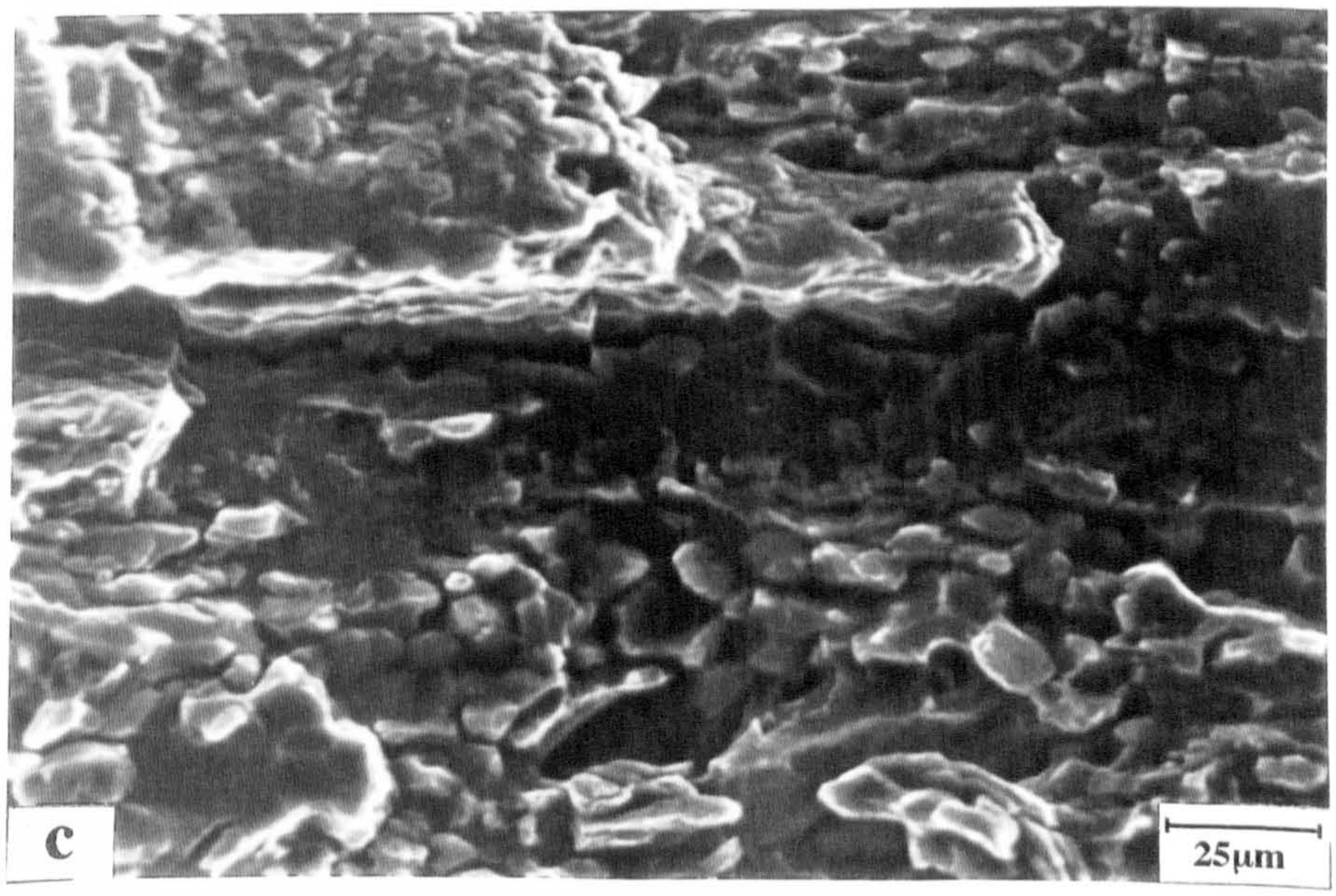


Fig 4.4.12

Fig 4.4.13 S.E.M. Fractographs.
Alloy A material.
Overaged condition.
30:1 extrusion ratio.
500° C extrusion temperature.
'rear' of extrudate.
(a) (T-L) Fracture.
(b) & (c) (L-T) Fracture.

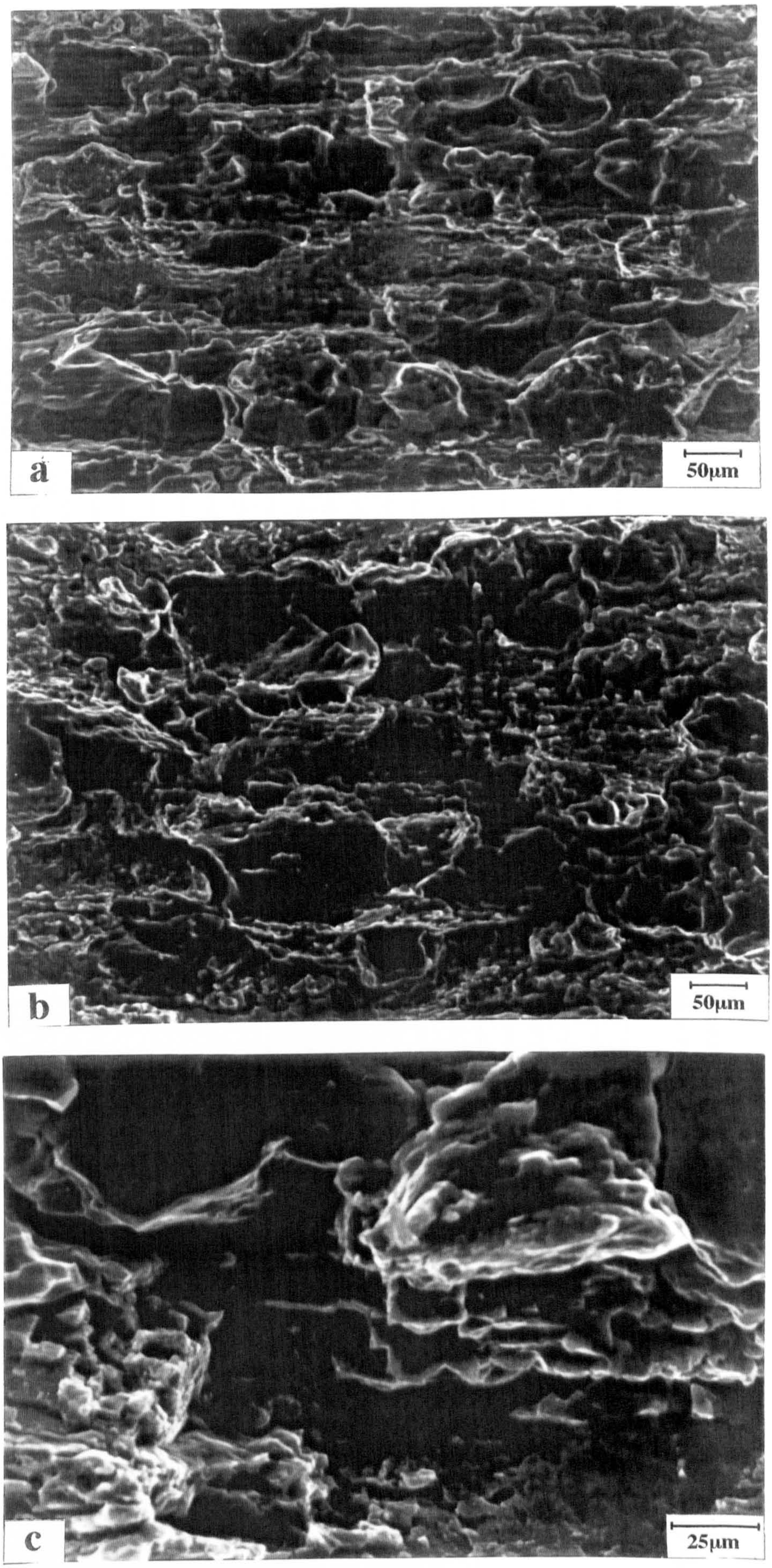


Fig 4.4.13

Ageing Condition	Extrusion Ratio	Sample Position	Extrusion Temp (°C)	(L-T) Toughness ($MPam^{1/2}$)	(T-L) Toughness ($MPam^{1/2}$)
AS	15:1	Front of Extrudate	400	20.3 (±0.6)	20.0 (±0.5)
			450	20.5 (±0.4)	19.9 (±0.4)
		Rear of Extrudate	400	21.0 (±0.3)	20.4 (±0.9)
			450	20.2 (±0.7)	19.9 (±0.3)
Under-aged	15:1	Front of Extrudate	400	29.6 (±0.4)	25.2 (±0.4)
			450	28.9 (±0.4)	26.4 (±0.5)
			500	28.4 (±0.5)	27.4 (±0.6)
	30:1	Front of Extrudate	400	28.7 (±0.3)	27.6 (±0.5)
			450	27.2 (±0.7)	26.1 (±0.5)
			500	27.1 (±0.5)	26.2 (±0.6)
Over-aged	15:1	Front of Extrudate	400	31.9 (±0.4)	26.6 (±0.4)
			450	29.3 (±0.4)	27.0 (±0.5)
			500	28.2 (±0.5)	27.8 (±0.3)
		Rear of Extrudate	400	32.3 (±0.3)	27.1 (±0.5)
			450	30.2 (±0.7)	27.4 (±0.5)
			500	29.5 (±0.5)	29.2 (±0.6)
	30:1	Front of Extrudate	400	27.1 (±0.4)	25.1 (±0.5)
			450	26.2 (±0.3)	24.1 (±0.5)
			500	25.1 (±0.3)	23.2 (±0.2)
		Rear of Extrudate	400	27.4 (±0.2)	25.3 (±0.3)
			450	26.0 (±0.2)	24.9 (±0.8)
			500	25.0 (±0.4)	23.3 (±0.5)

Fig 4.4.14 Variation in (T-L) & (L-T) toughness values with increasing extrusion temperature. Alcan -alloy A- extrudates.

Ageing Condition	Extrusion Ratio	Extrusion Temp (°C)	(L-T) Toughness ($MPam^{1/2}$)	(T-L) Toughness ($MPam^{1/2}$)
AS	15:1	400	21.4 (±0.7)	20.8 (±0.6)
		450	21.2 (±0.4)	20.5 (±0.7)
		500	20.3 (±0.2)	20.5 (±0.6)
	30:1	400	22.8 (±0.5)	21.6 (±0.6)
		450	22.6 (±0.6)	20.4 (±0.2)
		500	21.4 (±0.5)	20.3 (±0.5)
Under-aged	15:1	400	31.6 (±0.5)	27.5 (±0.4)
		450	31.1 (±0.4)	28.5 (±0.5)
		500	29.8 (±0.2)	29.0 (±0.2)
	30:1	400	28.8 (±0.5)	27.2 (±0.4)
		450	29.1 (±0.5)	25.7 (±0.2)
		500	28.2 (±0.2)	25.5 (±0.7)
Peak-aged	15:1	400	29.9 (±0.4)	25.3 (±0.5)
		450	28.2 (±0.4)	26.4 (±0.5)
		500	27.2 (±0.4)	26.9 (±0.5)
	30:1	400	28.2 (±0.6)	26.2 (±0.8)
		450	27.4 (±0.5)	25.3 (±0.5)
		500	26.2 (±0.4)	24.9 (±0.5)
Over-aged	15:1	400	33.5 (±0.2)	28.2 (±0.5)
		450	32.2 (±0.2)	30.5 (±0.5)
		500	31.9 (±0.2)	.. ±
	30:1	400	31.6 (±0.7)	28.8 (±0.5)
		450	31.5 (±0.5)	27.5 (±0.5)
		500	29.8 (±0.4)	26.9 (±0.4)

Fig 4.4.15 Variation in (T-L) & (L-T) toughness values with increases in extrusion temperature. Alcoa -alloy B- extrudates.

Fig 4.4.16 Calculated variations in (T-L) & (L-T) fracture toughness values with increases in extrusion temperature. Alloy A extrudates.
(a) 15:1, 'front' of extrudate, overaged condition.
(b) 15:1, 'rear' of extrudate, overaged condition.
(c) 30:1, 'front' of extrudate, overaged condition.
(d) 30:1, 'rear' of extrudate, overaged condition.
(e) 15:1, 'front' of extrudate, underaged condition.
(f) 30:1, 'front' of extrudate, underaged condition

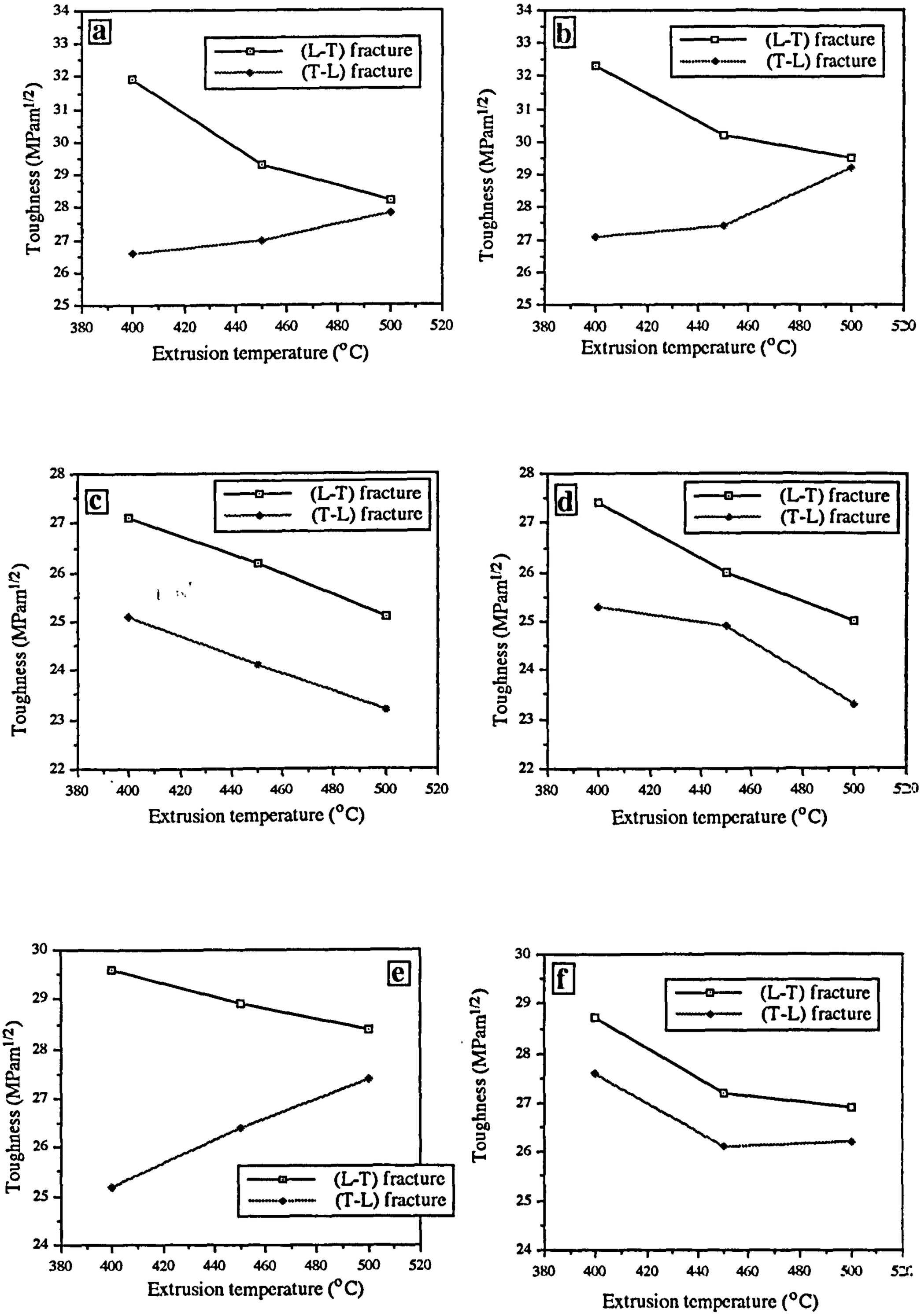

a
b
c
d
e
f
(L-T) fracture
(T-L) fracture
Toughness (MPam1/2)
Extrusion temperature (°C)

Fig 4.4.16

Fig 4.4.17 Calculated variations in (T-L) and (L-T) fracture toughness values, with increases in extrusion temperature. Alloy B extrudates.
(a) 15:1, underaged condition.
(b) 30:1, underaged condition.
(c) 15:1, peak aged condition.
(d) 30:1, peak aged condition.
(e) 15:1, overaged condition.
(f) 30:1, overaged condition.

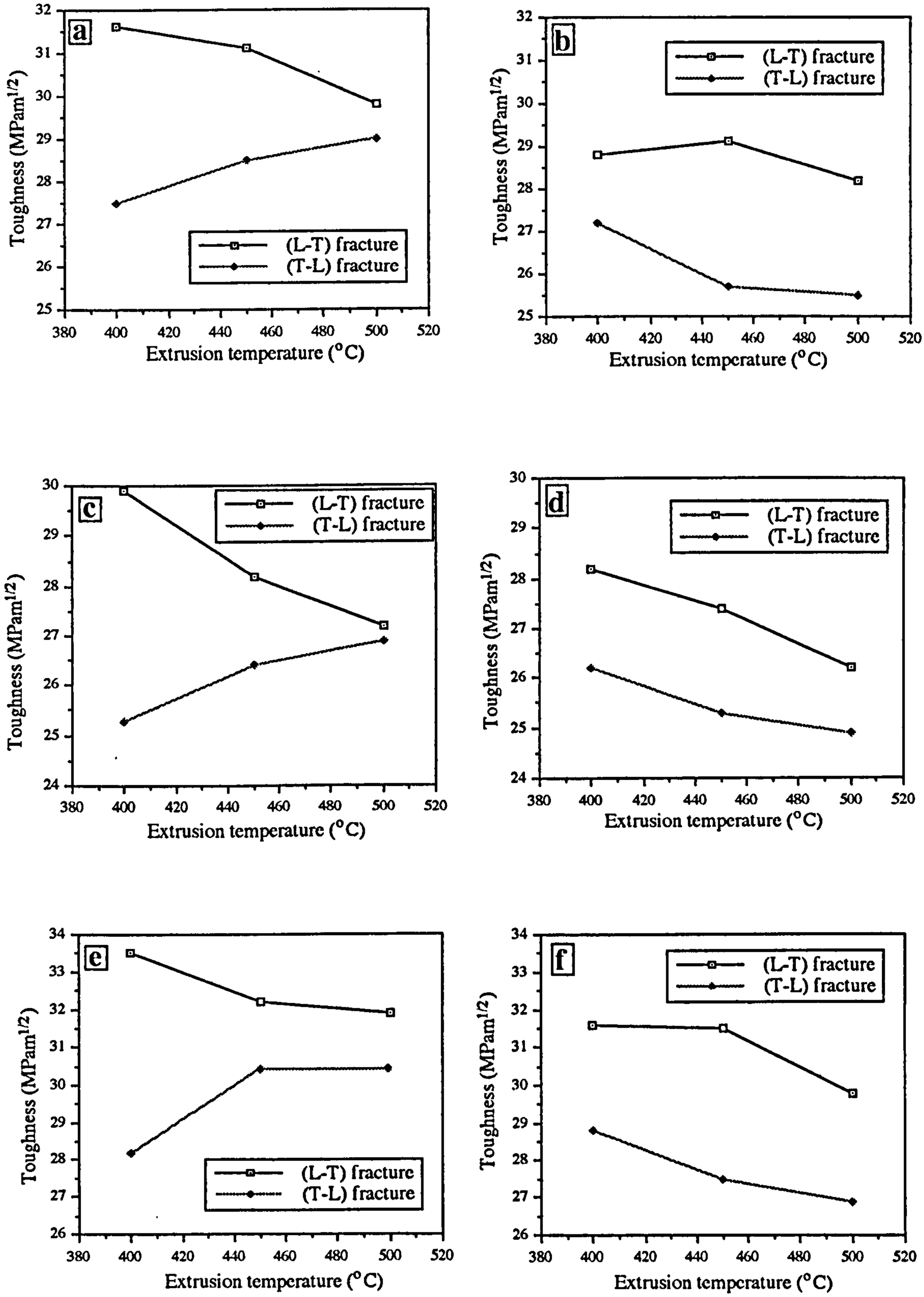
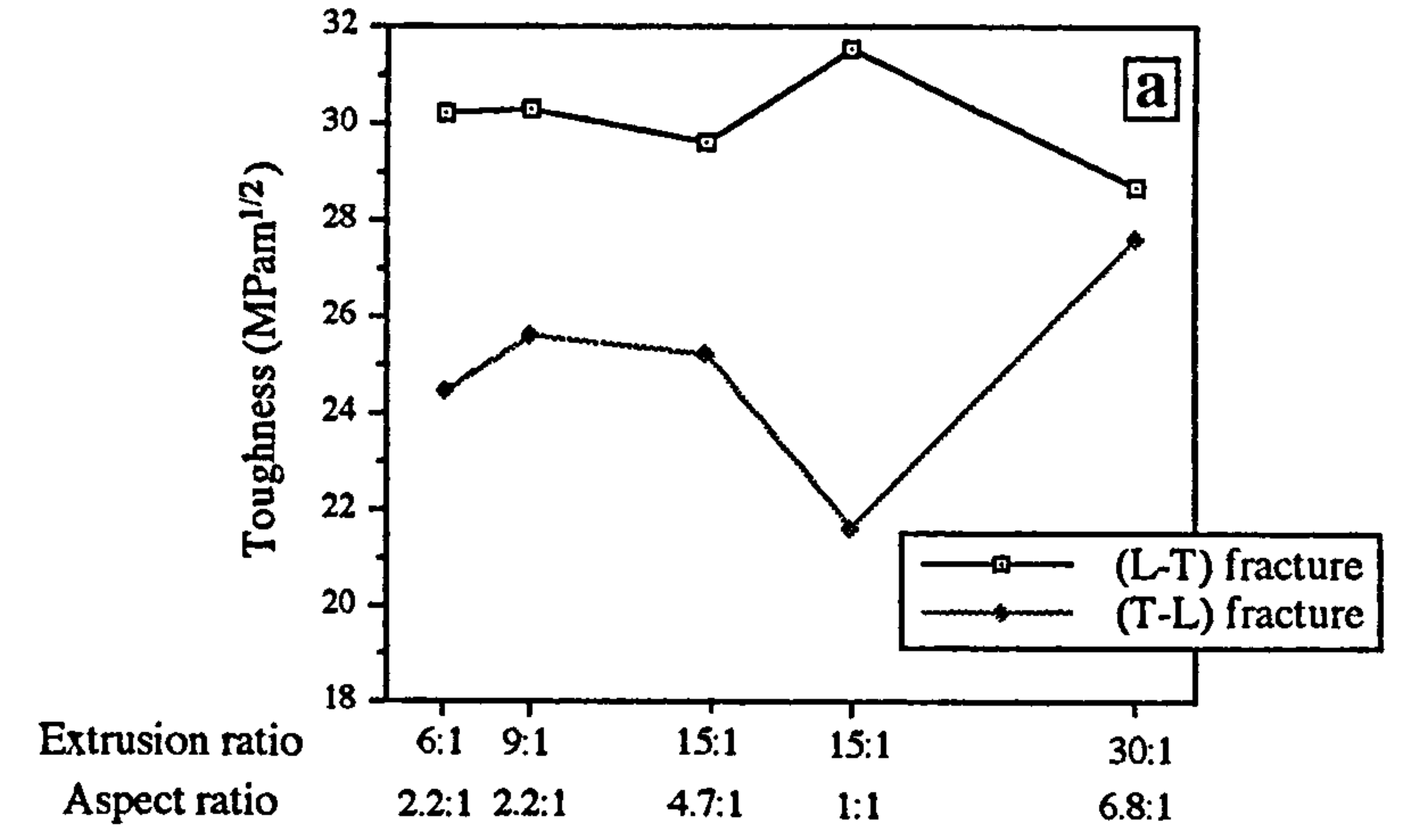

a
b
c
d
e
f
(L-T) fracture
(T-L) fracture
Toughness (MPam1/2)
Extrusion temperature (°C)

Fig 4.4.17

Extrusion Temperature (°C)	Ageing Condition	Extrusion Ratio	Aspect Ratio	(L-T) Toughness (MPam$^{1/2}$)	(T-L) Toughness (MPam$^{1/2}$)
450	Over-aged	9:1	2.2:1	29.9 (±0.8)	24.6 (±1.1)
		15:1	4.7:1	29.3 (±0.4)	27.0 (±0.5)
		15:1	Axi-symmetric	29.0 (±0.3)	21.5 (±0.3)
		30:1	6.8:1	26.2 (±0.3)	24.1 (±0.5)
400	Under-aged	6:1	2.2:1	30.2 (±0.4)	24.5 (±0.4)
		9:1	2.2:1	30.3 (±0.2)	25.6 (±0.7)
		15:1	4.7:1	29.6 (±0.4)	25.2 (±0.4)
		15:1	Axi-symmetric	31.5 (±0.8)	21.6 (±0.9)
		30:1	6.8:1	28.7 (±0.3)	27.6 (±0.5)

Fig 4.4.18 Variation in (T-L) & (L-T) toughness values with extrusion/aspect ratio. Alloy A.



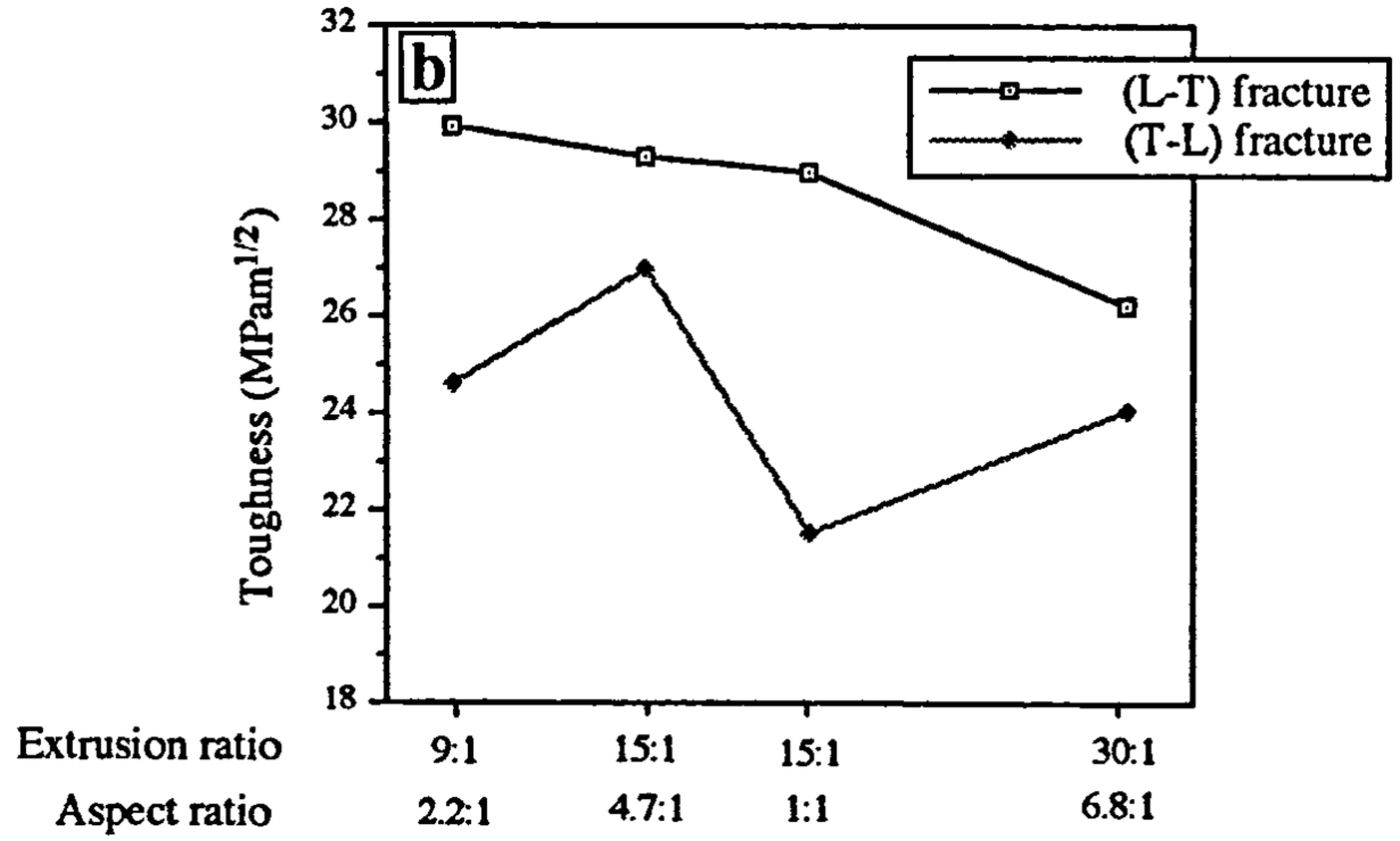


Fig 4.4.19

Variation in (T-L) and (L-T) toughness with increasing extrusion/aspect ratio. Alloy A extrudates.
(a) 400°C, 'front' of extrudate, underaged condition.
(b) 450°C, 'front' of extrudate, overaged condition.

4.5 Tensile Properties

This project set out to suggest processing improvements for slab extrusions, hence required correlations between property values and processing conditions to be made. In order for explanations of these observed property variations to be formulated, correlations between property values and microstructure were also carried out.

The tensile property values evaluated were yield stress, ultimate tensile stress (U.T.S.), and percentage elongation to failure. The yield stress was calculated at 0.2% strain, and the U.T.S. represented the stress at instability. The % elongation to failure as measured, however, consisted of a number of components:-

(1) Stretching of the equipment (systematic error).

(2) Elongation to the point of instability.

(3) Elongation between the instability point and failure.

In subsequent discussions of tensile property variations, therefore, the variation in strength values were of main concern. The % elongations to failure were quoted, but not discussed in detail.

4.5.1 Variation in Tensile Properties with Extrusion Temperature

Fig 4.5.1 tabulates the observed variations in longitudinal and transverse tensile property values, as extrusion temperature was altered. For material processed to the as-extruded condition no substantial variations in tensile property values with increasing extrusion temperature, were observed. For the aged material, however, greater variations in the tensile property values were evident. Both the yield stress and U.T.S. of the aged extrudates were generally observed to decrease with extrusion temperature, as is illustrated graphically in fig 4.5.2. The actual variations in property values were still relatively small, however, with only % property changes of between 3->12% being observed for increases in temperature from 400° C to 500° C.

Optical analysis of the aged extrudates revealed that increases in extrusion temperature caused the degree of recrystallisation to increase, with the size of the recrystallised grains depending upon the associated extrusion/aspect ratio. For the 15:1 extrudates, increases in extrusion temperature were found to increase the volume fraction of small (10->20μm) equiaxed grains present at the grain boundaries, whilst for the 30:1 extrudates the proportion of large (20->100μm) equiaxed grains increased considerably as extrusion temperature increased.

There are many factors that affect the yield stress and U.T.S. of a material, such as grain size, texture, substructure and precipitation[1][2][3][4][8]. For both extrusion ratios, therefore, the yield stress would be expected to decrease with increasing extrusion temperature, due to the observed changes in recrystallisation causing increased grain

size and decreased substructure. The U.T.S. would also be expected to decrease with increased grain size and decreased substructure, since it represented the instability point, and thereby depended upon the work hardening mechanisms present within the material, and the propensity towards localised deformation.

As well as grain structure changes, textural variations were also observed with increases in extrusion temperature. Textural analysis of the extrudates revealed increases in cube texture component and decreases in rolling type texture as the extrusion temperature increased. These changes in texture were as a result of increased recrystallisation, however, and hence the specific identification of the effect of texture changes upon properties was difficult, due to the concurrent changes in recrystallisation.

With regard to variations in precipitation as the extrusion temperature increased, T.E.M analysis of the overaged extrudates revealed no significant changes in the volume fraction of either the matrix or grain boundary phases.

Overall, therefore, it was concluded that the decrease in strength levels associated with increases in extrusion temperature were due to increased recrystallisation producing (i) An increase in grain size and decrease in substructure and/or (ii) An increase in cube texture and/or decrease in rolling texture.

In addition to the correlations between specific property values and processing conditions, fig 4.5.1 also indicates the variation in properties between orthogonal axes, and the homogeneity in property values between the 'front' and 'rear' of certain extrudates. It was observed that the longitudinal tensile properties were consistently greater than the transverse property values. The yield stress of any metal is dependent upon the factors hindering dislocation motion such as the number of grain boundaries (grain size), the extent and size of precipitation (δ',S, T_1) and the degree of substructure present. On a more basic level the yield stress is also dependent upon the texture present, since this affects the energy requirements necessary for slip activation when a given force is applied in a given direction. Since the grain size, substructure and precipitation were consistent, the difference in yield stresses between the orthogonal axes must have been due to textural differences. The grain shape was axi-symmetric in nature, however, which may also have been responsible for axi-symmetric tensile properties. The elongated nature of the grains would only cause anisotropy in yield stress if the average grain slip lengths associated with each orthogonal testing directions were different. This would only occur if the orientation of the operating slip systems changed as testing direction altered, which in turn would be dependant upon the crystallographic plane orientations i.e. texture. The axi-symmetric nature of the grains cannot, therefore, be stated as causing anisotropy on its own, but that it may increase the potential for anisotropy.

With regard to U.T.S. values, not only do the yield properties of the material affect specific values, but the work hardening capacity and localised deformation characteristics of the extrudates are also important. This suggested, therefore, that the differences in the U.T.S. values between orthogonal axes was again as a result of texture, but the highly directional character of the extrudate grain structures may also have had an effect.

Even though a distinct difference in the orthogonal tensile properties was observed, no consistent variations in anisotropy with extrusion temperature were evident.

With regard to the homogeneity in tensile properties from the 'front' of the extrudate to the 'rear', it was observed that for the aged material both the longitudinal and transverse yield and U.T.S. values were, in general, slightly greater at the 'front' of the extrudate than at the 'rear'. As the extrusion temperature was increased, however, no consistent variations in these property differences were observed.

Microstructural analysis revealed an increase in recrystallisation and cube texture component from the 'front' of the extrudate to the 'rear', with these increases being enhanced as the extrusion temperature rose. No significant variations in precipitation were evident, however, hence the observed decrease in yield stress and U.T.S. from the 'front' of the extrudate to the rear was attributed to the grain structure and/or texture changes. At this point it must be pointed out that the percentage property changes from the 'front' of the extrudate to the rear were on average no greater than 4%. Caution must, therefore, be taken in correlating the slight microstructural changes with the small changes in tensile properties.

Other researchers have also investigated tensile property variations with increases in extrusion temperature for aluminium lithium alloys[1][5][6][7]. From these investigations processing-property correlations both consistent with those stated above and different from those found in this project, have been concluded. The reason for these inconsistencies in processing-property correlations, however, was due to differences in microstructural variations. For example, Reynolds and Creed[1] investigated the variation in tensile property values with increases in extrusion temperature for commercially extruded 8090, 100mm x 25mm and 20mm x2mm, flat bar sections. They observed an increase in the tensile property values as both the extrusion temperature decreased and from the 'front' of the extrudates to the 'back'. For the 100mm x 25mm extrudates, no core recrystallisation was observed, hence the property variations were attributed to changes in the substructure strengthening. For the 20mm x 2mm section extrudates, however recrystallisation was shown to occur, but no variations with extrusion temperature were stated, again, therefore, they attributed the property changes to variations in substructure strengthening alone.

In this project recrystallisation and texture changes were observed with increases in extrusion temperature. As a result the tensile properties increased with increases in

LnZ, as found by Reynolds and Creed, but decreased from the 'front' of the extrudates to the 'rear', which was the converse to the observations made by Reynolds.

Processing-property correlations can be stated, therefore, but they will not be consistent for all combinations of processing conditions. The microstructure-property correlations, however, will be consistent, irrespective of processing

4.5.2 Variation in Tensile Properties with Extrusion/Aspect Ratios

The observed variation in tensile properties with increases in the extrusion/aspect ratios, for alloy A material solution heat treated and aged either to the underaged or overaged condition, are tabulated in fig 4.5.3.

For the rectangular cross section, 'slab', extrudates produced at 400° C and tempered to the underaged condition, no substantial variations in the longitudinal or transverse tensile properties were observed as the extrusion/aspect ratios increased, fig 4.5.4 (a)&(b).

Microstructural analysis of these extrudate cores revealed that increases in the extrusion/aspect ratio from 15:1->30:1 caused no significant variations in precipitation. The proportion of small (10->30μm) equiaxed recrystallised grains present at the original grain boundaries did, however, increase as the extrusion ratio increased, along with an associated increase in cube and rolling texture components.

Even though the 'slab' extrudate property variations with increasing extrusion/aspect ratio were not substantial, a significant decrease in the transverse, and in particular the longitudinal, property values was evident between the 15:1 axi-symmetric and 15:1 'slab' extrudates, as found by other researchers[1][3]. Microstructural analysis of the two extrudates revealed a slight increase in the % recrystallisation as the aspect ratio increased, but no significant changes in precipitation. Textural analysis also revealed a change from rolling type texture to one of double fibre, as the aspect ratio increased. The major differences in tensile property values between the axi-symmetric and 'slab' extrusions were, therefore, attributed to the texture changes. Tempus also concluded this detrimental effect of changes in texture from double fibre to rolling, upon the tensile property values.

For rectangular cross-section 'slab' extrudates, produced at 450° C and tempered to the overaged condition, fig 4.5.4(b), more significant decreases in both the yield and ultimate tensile stress values were observed as the extrusion/aspect ratio increased, than was observed for the underaged material.

Optical analysis of these extrudates revealed a general increase in original grain boundary elongation, together with an increase in the proportion of small (10->20μm) recrystallised grains as the extrusion ratio increased from 9:1->15:1. Increases in the proportions of the large (20->100μm) recrystallised grains were then observed as the

extrusion ratio increased from 15:1->30:1. Textural analysis of the extrudates also revealed that increases in aspect ratio enhanced the degree of rolling type textures, whilst cube texture increases were associated with the higher levels of recrystallisation. With regard to precipitation, however, negligible changes were identified as the extrusion/aspect ratio increased.

The decrease in the property values associated with the increase in extrusion ratio from 9:1->15:1 was consequently attributed to the greater proportions of small (10->20μm) equiaxed recrystallised grains present at the original grain boundaries. The decreases in the property values with the increase in ratio from 15:1->30:1, however, were associated with the increase in the number of large (20->100μm) equiaxed recrystallised grains, together with texture change to include more cube component. It must not be forgotten, however, that due to extrudate thickness values flat tensile specimens were prepared from the material extruded at 30:1, and round Houndsfields from material extruded at a ratio of 15:1 and below. Geometric effects introduced by the different specimens may, therefore, have affected the property differences between the 15:1 and 30:1 material.

With regard to anisotropy, no consistent variations in the anisotropy with increases in extrusion/aspect ratio were observed.

As with the underaged material a significant increase in the transverse, and in particular the longitudinal, property values was evident between the 15:1 'slab' and 15:1 axi-symmetric extrudates, as found by other researchers[1][3]. Microstructural analysis of the two extrudates revealed a slight decrease in the % recrystallisation, but no significant changes in precipitation. Textural analysis also revealed a change from rolling type texture to one of double fibre as the aspect ratio increased. The major differences in tensile property values between the 'slab' and axi-symmetric extrusion were, therefore, again attributed to the texture change.

4.5.3 Variation in Tensile Properties with Ageing Condition

Fig 4.5.1 indicates the variation in tensile properties with ageing. The underageing and overageing times were chosen to correspond to the 80% strength level, hence the yield stress did not alter with different ageing treatment. Ageing from the underaged to overaged conditions did, however, increase U.T.S. values. Ageing from the as-extruded to underaged or overaged condition increased both yield and U.T.S values, whilst the % elongation to failure decreased.

These variations in property values with ageing, have been found by many researchers, and can be explained in terms of the changes in precipitation[8][9].

Microstructural analysis revealed ageing to produce increased matrix precipitation of δ', T_1 & S phases, together with increased grain boundary precipitation of I and S

phases. The δ', T_1 and S phases increased the strength of the material by impeding dislocation motion[9]->[15]. The grain boundary precipitation, however, was not a factor in determining deformation characteristics, hence had no bearing upon yield strength levels[16]. The increase in matrix precipitation was, therefore, responsible for the increase in strength values between the as-extruded to aged material.

The increase in coplanar slip associated with the δ' precipitation has been reported to affect the deformation characteristics of the material to such an extent, that two different models have been suggested for aged and non-aged material[3] i.e. the Sachs and Taylor models. Aluminium has an F.C.C. lattice structure, hence 12 slip systems- four close packed {111} slip planes and three {100} close packed directions- within each grain. The Sachs model assumes slip occurs on only one of the possible slip systems. It determines the slip system with the highest Schmidt factor and assumes this to be the primary one. The Taylor model, however, assumes multiple slip with at least five independent slip systems operating, which is the minimum number of slip systems required for an arbitrary shape change, when there is no volume change. Each model predicts the likelihood of slip occurring on a given slip system when the load is applied in a specified direction. The Sachs model is more applicable to aged material, than the Taylor model, due to coplanar slip producing unhomogeneous slip. For the Sachs model a minimum M_S value (max Schmidt factor) and for the Taylor model a minimum M_t value predicts the primary slip system.

With regard to the U.T.S. values, the observed variations with ageing, not only depended upon the yield characteristics, but also upon the work hardening capacity and strain localisation phenomena present within the material. The U.T.S. value increases observed between the under and overaged material were, therefore, attributed to reduced localised deformation associated with the additional precipitation of S and T_1 matrix phases.

4.5.4 Conclusions

In all the alloy A extrudates the transverse tensile property values were consistently found to be lower than the longitudinal values. This anisotropy in property values was attributed to textural effects and the highly elongated nature of the matrix, but no consistent variations in the material anisotropy values were evident as the extrusion temperature or extrusion/aspect ratio varied.

Increases in extrusion temperature did, however, cause decreases in the tensile strength levels. This was attributed to enhanced recrystallisation, which influenced:-

(i) Grain size. Recrystallisation and growth caused grains of various sizes to be produced. Greater grain boundary stress concentrations were associated with the larger grains, which decreased both the yield stress and U.T.S. values.

(ii) Substructure. Increased recrystallisation decreased the substructure present, thereby decreasing the U.T.S. and yield stress values.
(iii) Texture. Recrystallisation was associated with increased cube texture. The conclusive effect of cube texture upon tensile properties could not be determined, however, due to concurrent changes in grain structure.

Changes in the extrusion/aspect ratio also affected the tensile property values of the slab extrusions, due to the changes brought about in:-.
(a) Recrystallisation. Changes in the recrystallisation affected grain size, substructure and texture as mentioned above.
(b) Texture. Increases in aspect ratio increased the rolling texture components, which was considered to decrease tensile properties.

Ageing Condition	Extrusion Ratio	Sample Posit.	Sample Orient.	Extrusion Temp (°C)	Yield Stress ($MPa^{1/2}$)	Ultimate Tensile stress ($MPa^{1/2}$)	% Elong.
As -Extruded	15:1	Front of Extrudate	Long-itudinal	400	131 (±6)	313 (± 5)	14.7
				500	125 (±10)	300 (±6)	19.0
			Trans.	400	125 (±6)	275 (±7)	15.2
				500	120 (±6)	279 (±5)	17.9
		Rear of Extrudate	Long-itudinal	400	131 (±5)	283 (±6)	14.3
				500	126 (±7)	294 (±6)	18.4
			Trans.	400	131 (±5)	266 (±7)	15.8
				500	116 (±6)	276 (±5)	18.1
Under-aged	15:1	Front of Extrudate	Long-itudinal	400	348 (±5)	450 (±6)	7.3
				450	333 (±7)	449 (±9)	7.7
				500	325 (±8)	439 (±6)	7.4
	30:1	Front of Extrudate	Long-itudinal	400	336 (±5)	457 (±10)	6.5
				450	304 (±5)	444 (±5)	6.0
				500	299 (±7)	369 (±6)	7.5
Over-aged	15:1	Rear of Extrudate	Long-itudinal	400	339 (±7)	473 (±7)	6.0
				450	314 (±5)	458 (±6)	6.8
				500	320 (±5)	467 (±6)	7.4
			Trans.	400	317 (±5)	436 (±7)	6.5
				450	313 (±6)	438 (±8)	7.7
				500	296 (±5)	426 (±6)	7.5
		Front of Extrudate	Long-itudinal	400	351 (±6)	471 (±5)	7.0
				450	338 (±6)	483 (±5)	7.7
				500	329 (±7)	464 (±7)	6.5
			Trans.	400	321 (±6)	434 (±7)	7.7
				450	317 (±6)	453 (±7)	7.8
				500	305 (±5)	432 (±5)	8.0
	30:1	Rear of Extrudate	Long-itudinal	400	322 (±6)	468 (±6)	8.0
				450	298 (±7)	441 (±6)	8.0
				500	292 (±9	406 (±5)	5.7
		Front of Extrudate	Long-itudinal	400	338 (±7)	470 (±7)	8.2
				450	310 (±6)	461 (±5)	8.0
				500	303 (±8)	455 (±6)	6.7

Fig 4.5.1 Variation in tensile property values with increasing extrusion temperature, for alloy A extrudates

Fig 4.5.2 Variation in tensile property values with increases in extrusion temperature.
(a) 15:1 extrusion ratio,
400° C extrusion temperature, overaged condition, longitudinal samples, 'Front' of extrudate.
(b) 15:1 extrusion ratio,
400° C extrusion temperature, overaged condition, longitudinal samples, 'Back' of extrudate.
(c) 30:1 extrusion ratio,
400° C extrusion temperature, overaged condition, longitudinal samples, 'Front' of extrudate.
(d) 15:1 extrusion ratio,
400° C extrusion temperature, overaged condition, longitudinal samples, 'Back' of extrudate.
(e) 15:1 extrusion ratio,
400° C extrusion temperature, overaged condition, transverse samples,' Front' of extrudate.
(f) 15:1 extrusion ratio,
400° C extrusion temperature, overaged condition, transverse samples, 'Back' of extrudate.
(g) 15:1 extrusion ratio,
400° C extrusion temperature, underaged condition, longitudinal samples, 'Front' of extrudate.
(h) 30:1 extrusion ratio,
400° C extrusion temperature, underaged condition, longitudinal samples, 'Front' of extrudate.

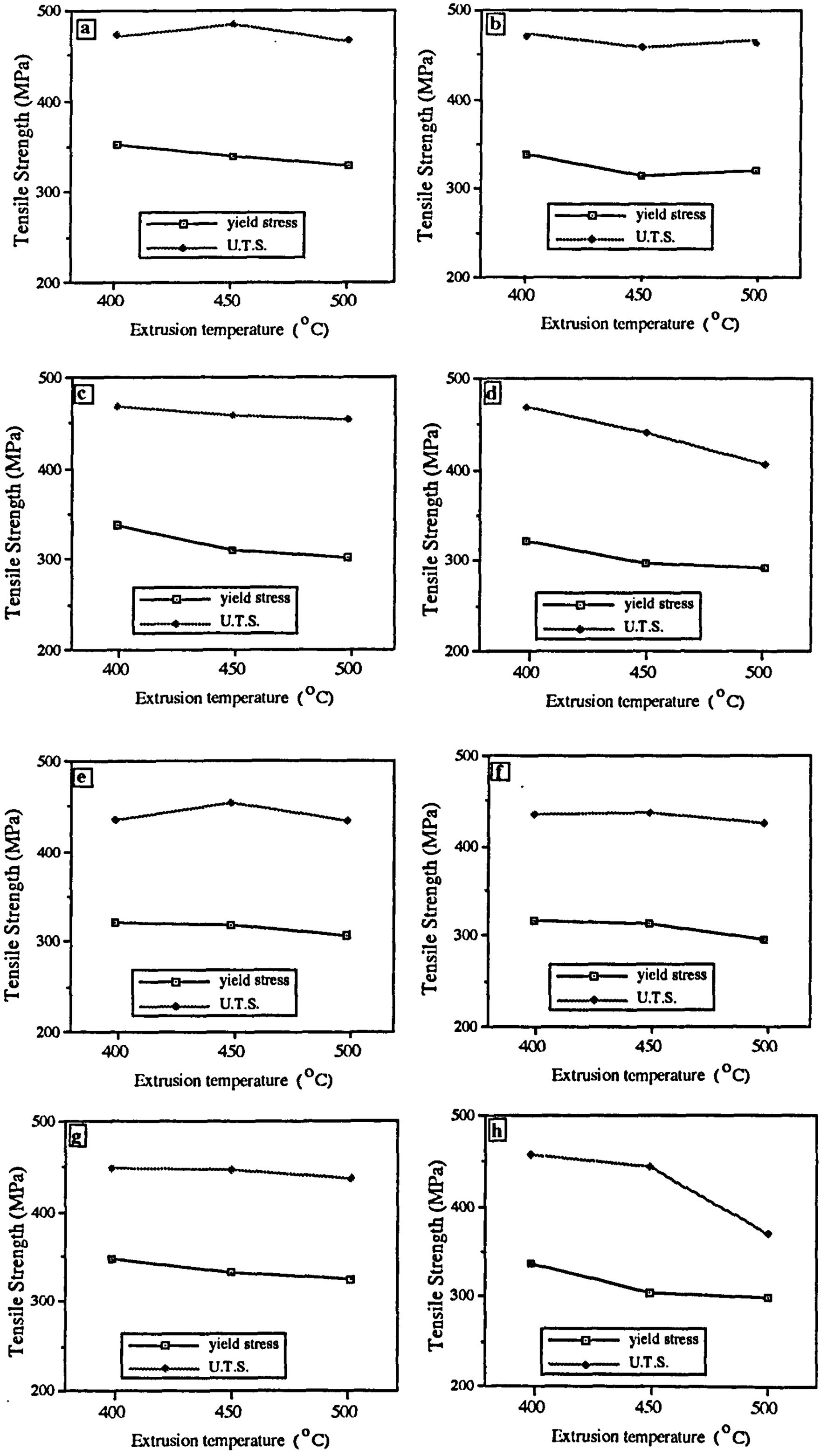

a
b
c
d
e
f
g
h
Tensile Strength (MPa)
Extrusion temperature (°C)
yield stress
U.T.S.
500
400
300
200
400
450
500

Fig 4.5.2

Extrusion Temp (°C)	Ageing Cond.	Sample Orient.	Extrusion Ratio	Aspect Ratio	Yield Stress ($MPa^{1/2}$)	Ultimate Tensile stress ($MPam^{1/2}$)	% Elong.
450	Over-aged	Longitudinal	9:1	2.2:1	374 (±7)	490 (±4)	7.2
			15:1	4.7:1	338 (±6)	483 (±5)	7.7
			15:1	Axi-symmetric	430 (±6)	540 (±7)	4.7
			30:1	6.8:1	310 (±6)	461 (±5)	8.0
400	Under-aged	Longitudinal	6:1	2.2:1	346 (±4)	449 (±6)	7.8
			9:1	2.2:1	352 (±7)	462 (±5)	8.4
			15:1	4.7:1	348 (± 5)	450 (±6)	7.3
			15:1	Axi-symmetric	445 (± 5)	493 (±5)	5.7
			30:1	6.8:1	336 (±5)	457 (±10)	6.5
		Transverse	6:1	2.2:1	272 (± 5)	362 (±6)	3.0
			9:1	2.2:1	284 (±5)	376 (±5)	2.9
			15:1	4.7:1	289 (± 9)	380 (±7)	7.3

Fig 4.5.3 Variation in tensile property values with increases in extrusion/aspect ratio 'Front' of extrudate.

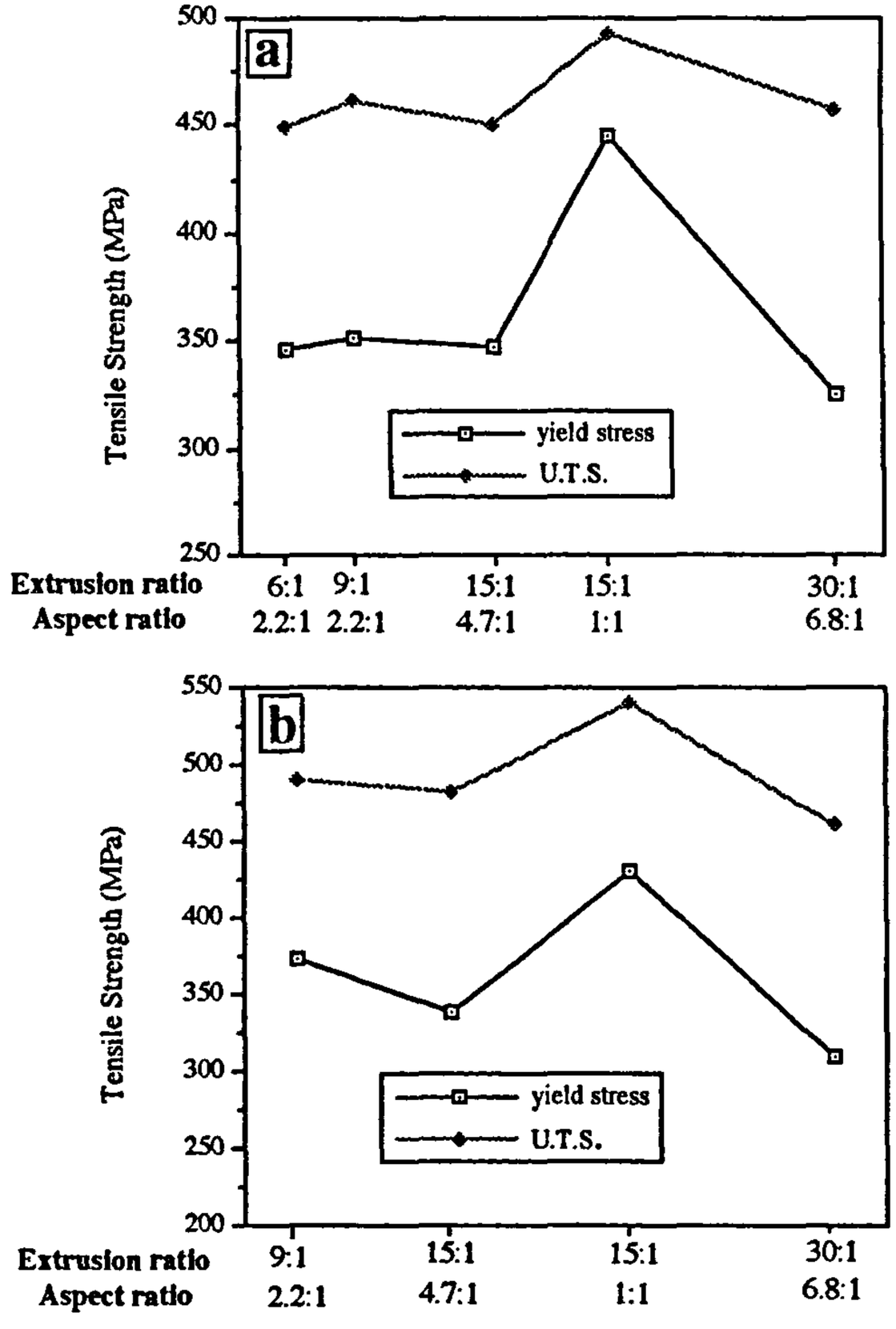


Fig 4.5.4

Variation in tensile strengths with increasing extrusion/aspect ratio
(a) 400°C extrusion temperature, underaged conditon, longitudinal sample.
(b) 450°C extrusion temperature, overaged condition, longitudinal sample.

CHAPTER FIVE

Axi-symmetric Conical Die Extrusions Results and Discussion

In this section of the project an investigation into the effects of die cone angle and extrusion temperature upon the property values of aged axi-symmetric extrudates was carried out. In order to fully explain the effects of these process conditions upon property values, it was necessary to investigate the changes occurring in the deformation flow pattern, together with the variations in microstructure. The results were, therefore split into the following areas:-

(1) Optical Microscopy.
(2) Transmission Electron Microscopy.
(3) Textural Analysis.
(4) Deformation Characterisation.
(5) Toughness Properties.
(6) Tensile Properties.

In each area of analysis the effects of processing conditions were examined, which lead to correlations between processing, properties and microstructure. The composition of the material remained constant, and is shown below, in weight % :-

Li-2.33, Cu-1.24, Mg-0.72, Zn-0.016, Zr-0.12, Si-0.05, Fe-0.04, Ti-0.020, Bal. Al

Errors

The tensile strength and toughness values were obtained from averaging a minimum of four samples. Error bars were not included on the graphs showing property variations with processing, since it caused a certain amount of confusion. Standard deviations, at the 80% confidence level, are shown in the property tables, however, which indicates the measurement variations. The toughness results and standard deviations were rounded to the nearest decimal with the percentage error varying from approximately 2->8%.

The tensile strengths and associated standard deviations were rounded to the nearest whole number and again a percentage error varying from 2->8% was present. It must be remembered that the anisotropy results were produced by subtraction of property measurements, hence measurement errors were cumulative, causing constant trends to be diluted.

5.1 Optical Analysis

5.1.1 General Extrudate Structures

From the analyses carried out on the 'slab' extrudates, it was clear that the aged material offered the most desirable properties, with the slightly overaged material offering marginally better property combinations. For this reason only the aged axisymmetric extrudates were analysed, with particular attention being paid to the slightly overaged condition.

Optical analysis of the aged extrudates provided a very good overall view of the extrudate microstructures, producing information on the directionality of the microstructure, and recrystallisation variations throughout the extrudate section. Due to the etching of the subgrain boundaries, the subgrain structures within the extruded material were also evident optically. The accuracy of the subgrain size observed under the optical microscope was checked, however, by comparison with the results obtained from T.E.M. analysis.

From a general observation of the optical micrographs, figs 5.1.1->4, the basic extrudate microstructure was shown to consist of highly elongated original grains containing internal subgrain structures. In combination with the elongated fibrous grains, colonies of grain boundary recrystallisation were also observed. The proportion of recrystallisation and recrystallised grain size varied with processing and increased continually from the centre of the extrudates to the surface, with annuli of 100% recrystallisation present at the extreme outer surface regions.

5.1.2 Variation in Microstructure with Changes in Extrusion Temperature and Die Cone Angle

For any given set of process conditions, no significant differences in microstructure were observed between the underaged and overaged material. Microstructural variations were observed, however, between extrudates produced under different processing conditions, and also across the transverse section within each extrudate. The variation in microstructure with changes in extrusion temperature and die cone angle will, therefore, be considered separately for the surface and core regions of the extrudates.

Optical analysis allowed changes in the sizes and proportions of the recrystallised grains, the distortion of the original matrix and the subgrain sizes to be analysed. It must be remembered, however, that the % recrystallisation within the extrudates was calculated using an optical analyser, hence a certain amount of variation in the calculated % recrystallisation was found depending upon the micrograph used for

analysis. Fig 5.1.5, tabulates the general variations in the % recrystallisation and grain size at the core of the aged material, as the process conditions varied.

Core Regions

As already mentioned the core regions of all the axi-symmetric extrusions were characterised by elongated original grains, internal subgrain structures and small (10-40μm) recrystallised grains present at the original grain boundaries, fig 5.1.1->4.

Increases in the extrusion temperature were observed to increase the percentage of recrystallisation, along with the recrystallised grain sizes, fig 5.1.2. The specific changes in recrystallisation with extrusion temperature were, however, dependent upon die cone angle, as the table in fig 5.1.5 illustrates. The subgrain sizes were observed to remain approximately constant (2->10μm) as the extrusion temperature varied.

With regard to the effect of changes in die cone angle upon the recrystallisation within the core regions of the extrudates, no constant correlations could be found. As the die cone angle was increased from 30° ->45° , the percentage of core recrystallisation and recrystallised grain sizes were observed to decrease, fig 5.1.1(b) & 5.1.2(a). Subsequent increases in die cone angle to 60° and then to 90° , however, caused the percentage of recrystallisation to increase. The nature of these changes in recrystallisation was consistent for all extrusion temperatures, but the magnitude of the changes and specific proportions of recrystallisation were found to be greater for higher extrusion temperatures, fig 5.1.5.

Surface Regions

The surface regions of the extrudates were characterised by outer annuli of 100% recrystallisation consisting of large (20->100μm) grains. The proportion of this recrystallisation was then observed to decrease towards the centre of the extrudates, with the microstructures becoming increasingly characterised by elongated original grains, internal subgrains, and small (10->40μm) equiaxed recrystallised grains.

For any given extrudate, increasing the extrusion temperature was observed to produce a slight increase in the depth to which the outer annulus of 100% recrystallisation extended into the extrudate. The proportion of small (10->40μm) recrystallised grains present in the regions below this outer annulus was also observed to increase. The recrystallised grain sizes throughout the surface regions, however, did not appear to alter significantly with variations in extrusion temperature.

No substantial changes in the surface microstructures were observed as the die cone angle was altered, but the proportion of the large equiaxed grains present within the surface regions did decrease slightly as the die cone angle increased.

5.1.3 Discussion and Conclusions

As already stated, the central regions of the extrudates were characterised by elongated original grains with internal subgrains (2->10μm), together with colonies of small (10->40μm) recrystallised grains present at the original grain boundaries. The proportion and size of recrystallisation was observed to increase from the centre of the extrudates to the surface, with annuli of 100% recrystallisation consisting of significantly larger (20->100μm) grains at the extreme outer surface areas of the extrudates.

Increasing the extrusion temperatures was observed to increase the % recrystallisation and grain size within the core regions of the extrudates, and the % recrystallisation in the surface regions. With regard to the effect of die cone angle upon microstructures, no constant variations in recrystallisation or grain size were observed as the die cone angle was increased. Maximum proportions of recrystallisation were observed within the core regions of extrudates produced using dies with 30° and 90° cone angles, whilst minimum levels of recrystallisation were associated with the 45° cone angle.

As with the 'slab' extrudates, the obvious reason for the general fibrous appearance of the microstructures was due to the basic extrusion flow pattern. A complete analysis of the deformation is shown in section 5.4, but basically the unlubricated forward extrusion produced a dead metal zone adjacent to the tooling surfaces, a cone of heavy shear adjacent to the dead metal zone, and a central region in which reduced amounts, but more ideal deformation occurred. The high degree and type of straining associated with this flow pattern consequently produced the elongated appearance of the extrudate.

The variations in recrystallisation observed as the extrusion temperature was increased depended upon the effects of temperature upon the recrystallisation mechanism. As stated in section 4.1, investigators have previously shown pure and dilute aluminium alloys to have high propensities for dynamic recovery. Consequently the occurrence of recrystallisation during the hot working process itself is reduced, and a finite time at elevated temperature after working is necessary for recrystallisation to occur.

The axi-symmetric extrusions were quenched after working, but there was a finite time interval between the completion of working and the quenching process. Static recrystallisation may, therefore, have occurred within the extrudates. The driving force for recrystallisation is the elastic strain energy present within the material. Increases in temperature facilitate recovery processes, hence decrease the stored energy within the material. This on its own would decrease the tendency for recrystallisation. It must not be forgotten, however, that the higher temperature would also increase the thermal activation of the recrystallisation mechanisms and the recrystallised grain growth rates. The relationship between the recrystallisation and increasing extrusion temperature would, therefore, depend upon the relative effects of the decreases in stored energy, the increases in thermal activation and the increases in growth rates.

Even though static processes could explain the observed microstructural changes, dynamic recrystallisation could equally explain the observed increases in recrystallisation with extrusion temperature. The exact mechanism of recrystallisation, be it static or dynamic, could not be determined, however, without T.E.M. analysis. As with the 'slab' extrusions this was beyond the scope of this project.

With regard to the variations in recrystallisation observed as the die cone angle increased, analysis of the deformation process, shown in section 5.4, revealed that decreases in the extrusion die cone angle had the following effects:-

(i) Increased the general temperature levels throughout the deformation zone.
(ii) Increased the average temperatures experienced by the material forming the extruded product.
(iii) Increased the average temperature differences between the centre and surface regions of the extrudates.
(iv) Caused higher levels of strain rate to be experienced at greater distances from the die orifice, particularly in the surface regions of the deformation zone.
(v) Increased the average strain rates experienced by the material forming the extruded product.
(vi) Increased the average strain rate differences between the centre and surface regions of the extrudate.
(vii) Decreased the specific cumulative Z values associated with each elemental section within the extrudates..
(viii) Decreased the difference in the cumulative Z values between elemental sections within the extrudates.

It was obvious from these results, therefore, that changes in the temperatures and strain rate combinations experienced by the extruded material caused the observed changes in recrystallisation as the die cone angle altered. The Zener Hollomon parameter represents a term which incorporates both temperature or strain rate, but even though changes in the deformation histories were identified with changes in die cone angle, no definite relationships between the microstructure and Z values could be established. This inability to relate the microstructures with Z values suggested that either cumulative Z values were not the most appropriate Z values to associate processing histories with final microstructures, or that the relationship between strain rate, temperature, and microstructure assumed by the Z function was not applicable to these extrudates. No conclusions concerning the exact relationships between strain rate, strain and temperature with microstructures could, however, be made. Even though an exact function relating strain rate and temperature with microstructure could not be determined, it was evident that increases in the temperatures and strain rates increased recrystallisation.

Not only were microstructural variations observed between extrudates, but also transversely within each extrudate. Temperature field analysis of the extrusion distortion zones indicated more severe temperature histories and final exit temperatures to be associated with the outer regions of the extrudates. Strain rate analysis also showed more severe strain rate histories to be experienced by the extrudate surface material. Once again, therefore, correlations between temperature and strain rate with the volume fraction of recrystallisation could be made.

At the extreme outer surfaces of the extrudates, not only did the % volume fraction of recrystallisation increase, but a dramatic increase in grain size was also observed. Exaggerated or abnormal grain growth in metals is usually associated with a decrease in surface energy and not stored energy. The highest levels of strain, strain rate and temperature occurred within the extreme outer regions of the extrudates, the resulting enhancement of growth may, therefore be associated with these extremes in processing.

Friedrich[1] also observed increased grain size at the surface of rolled sheet, however, and associated this increased grain size with solute depletion, and not increased temperature and strain rate at the surface. He investigated the solute losses, due to heat treatment, and found that the surface provided a diffusion path for Mg and Li when heated in a non-protective atmosphere, causing loss of important hardening elements at the surface. In his investigations of rolled sheet he used S.I.M.S and microhardness techniques to produce a good correlation between the loss of alloying elements and the reduction in age-hardening potential of the material.

Microhardness profiles obtained from the axi-symmetric extrudates produced in this project are illustrated graphically in fig 5.1.6. It was observed that a distinct drop in hardness occurred at the surface. As the extrusion temperature increased, the general hardness level also appeared to decrease. Changes in cone angle, however, did not appear to have a substantial effect upon the microhardness profile.

The distinct drop in microhardness values associated with the surface regions of the extrudates may have been solely due to increases in grain sizes. If magnesium and lithium concentrations were depleted in the surface regions as found by Friedrich, however, the precipitation of δ', T_1 and S would have been reduced, which could also be correlated with the hardness profiles observed in this project and by Friedrich. How, if at all, this solute depletion would influence recrystallisation or grain growth, however, was less obvious. The T_1 and S phases, co-precipitate with the δ', and nucleate on matrix dislocations and subgrain boundaries[2]. The presence of T_1 and S or δ', therefore, may cause pinning of grain boundaries to a certain extent, along with localised increases in dislocation densities. The absence of such precipitation, due to solute depletion, may consequently increase the recrystallisation nucleation and/or grain growth.

In addition to variations in process histories and solute depletion, textural differences between the core and surface regions of the extrudates may also have influenced the microstructures produced. The more severe processing experienced by the surface regions may have encouraged the nucleation of grains possessing textures associated with high growth rates. This would consequently produce larger grain sizes.

The explanation of increased growth as well as increased recrystallisation towards the surface, therefore, may be considered to have a number of contributory factors:-

(1) Increased severity in processing conditions towards the extrudate surface encouraging recrystallisation and facilitating growth.

(2) Solute depletion causing enhanced recrystallisation and/or growth.

(3) Textural differences may have caused differences in recrystallised grain growth rates.

The dependence of recrystallisation and grain growth upon strain rate and temperature was, therefore, responsible for the changes in microstructure observed between extrudates as well as within each extrudate. Likewise, the effect of processing conditions upon the strain rate and temperature distributions determined the correlations between processing and microstructure.

Fig 5.1.1 Optical Micrographs.
(a) 30° die cone angle.
460° C extrusion temperature.
Underaged condition.
Surface region of extrudate.
(b) & (c) 30° die cone angle.
460° C extrusion temperature.
Underaged condition.
Core region of extrudate.

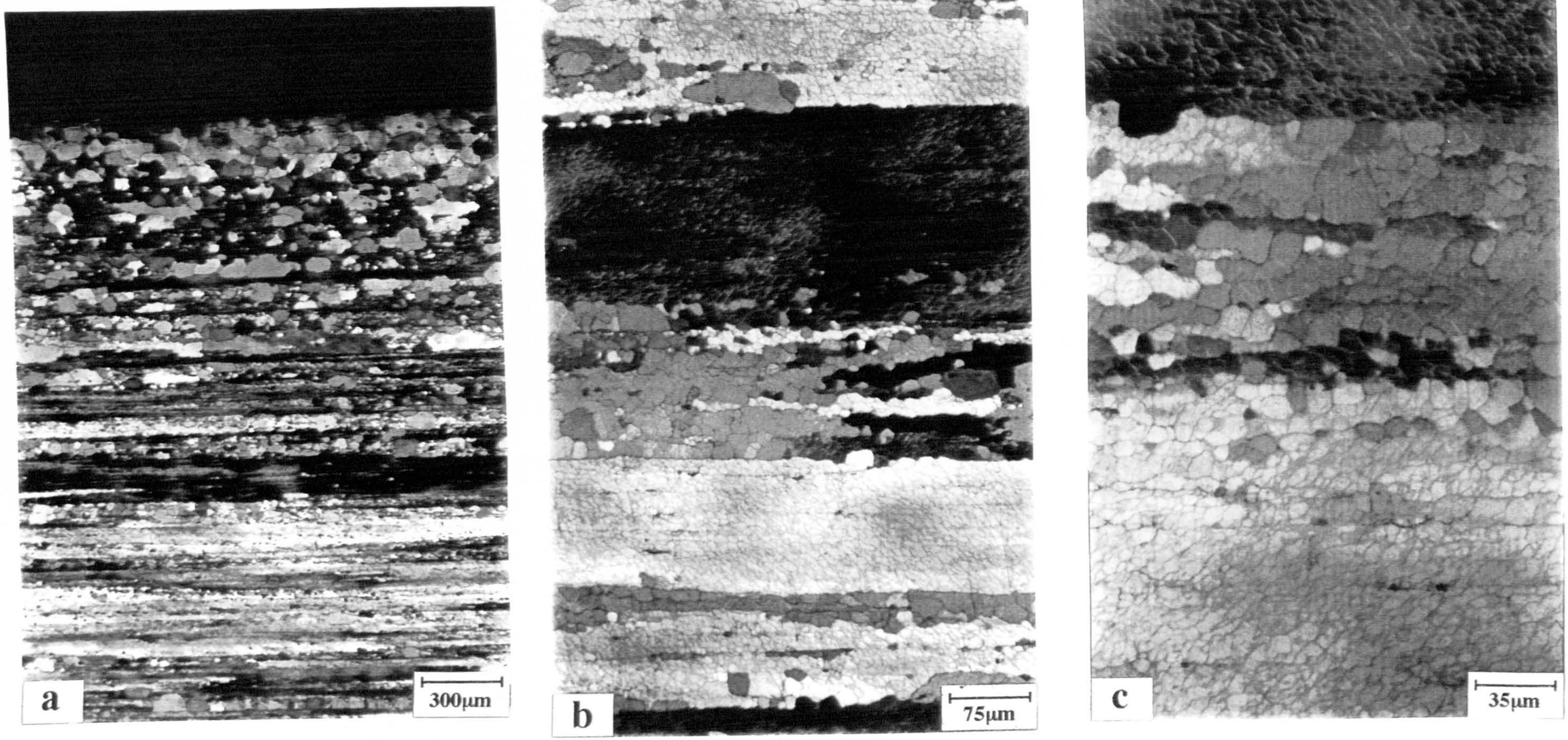


Fig 5.1.1

Fig 5.1.2 Optical Micrographs.
(a) 45° die cone angle.
400° C extrusion temperature.
Overaged condition.
Core region of extrudate.
(b) & (c) 45° die cone angle.
460° C extrusion temperature.
Overaged condition, core region of extrudate.

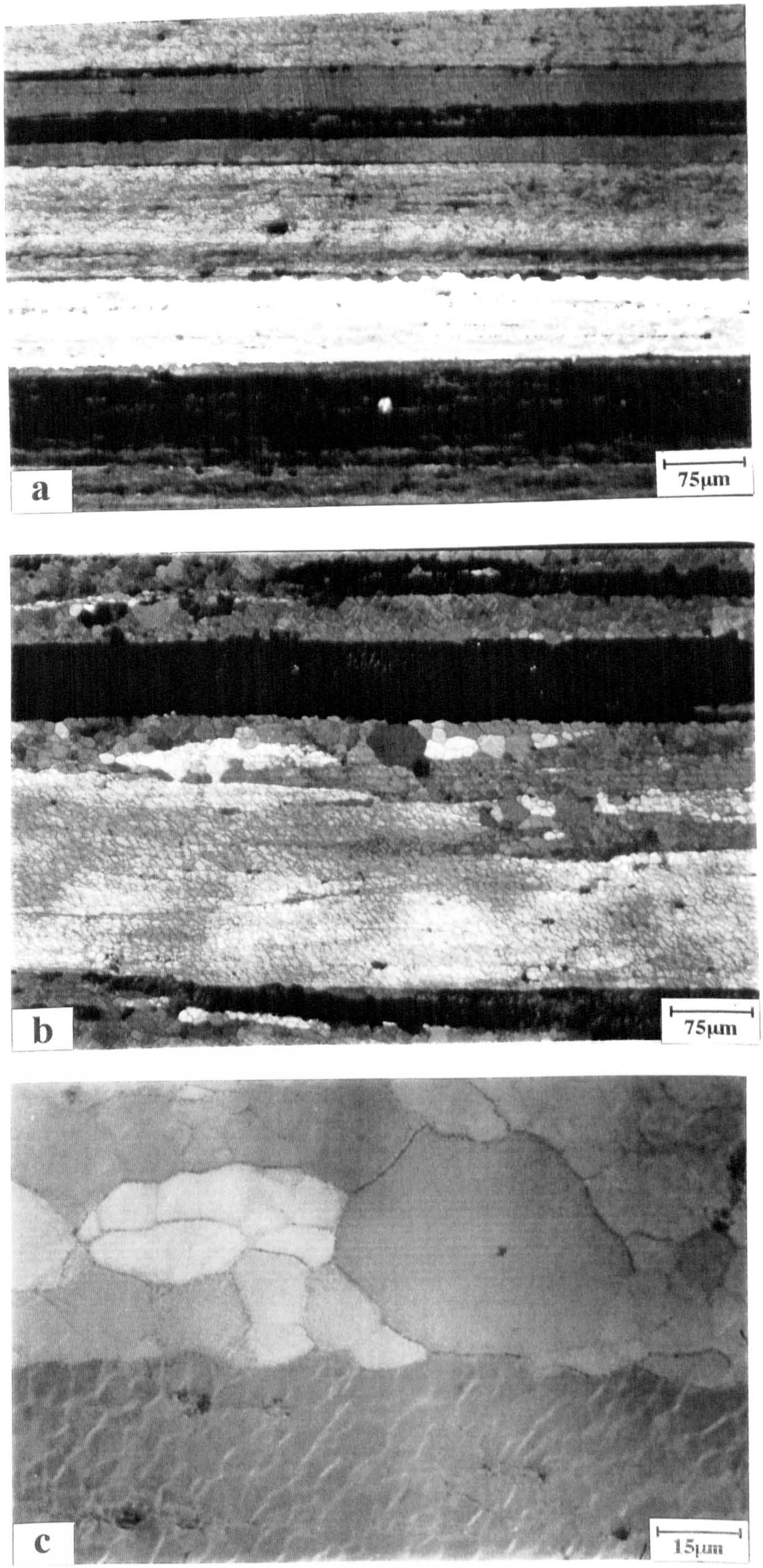


Fig 5.1.2

Fig 5.1.3 Optical Micrographs.
(a) 60° die cone angle.
400° C extrusion temperature.
Underaged condition.
Surface region of extrudate.
(b) 60° die cone angle.
400° C extrusion temperature.
Underaged condition.
Core region of extrudate.
(c) & (d) 60° die cone angle.
460° C extrusion temperature.
Overaged condition.
Core region of extrudate.

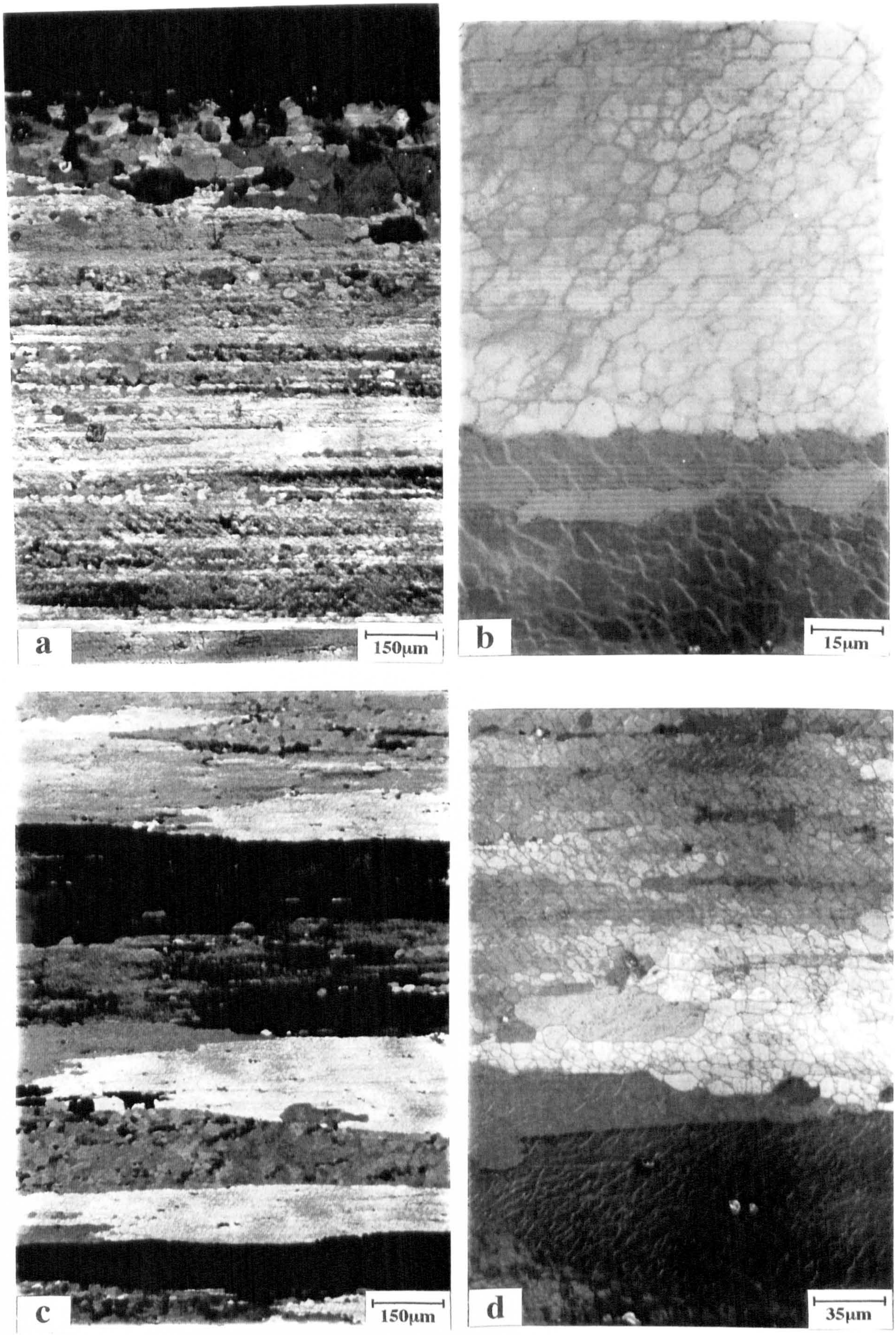
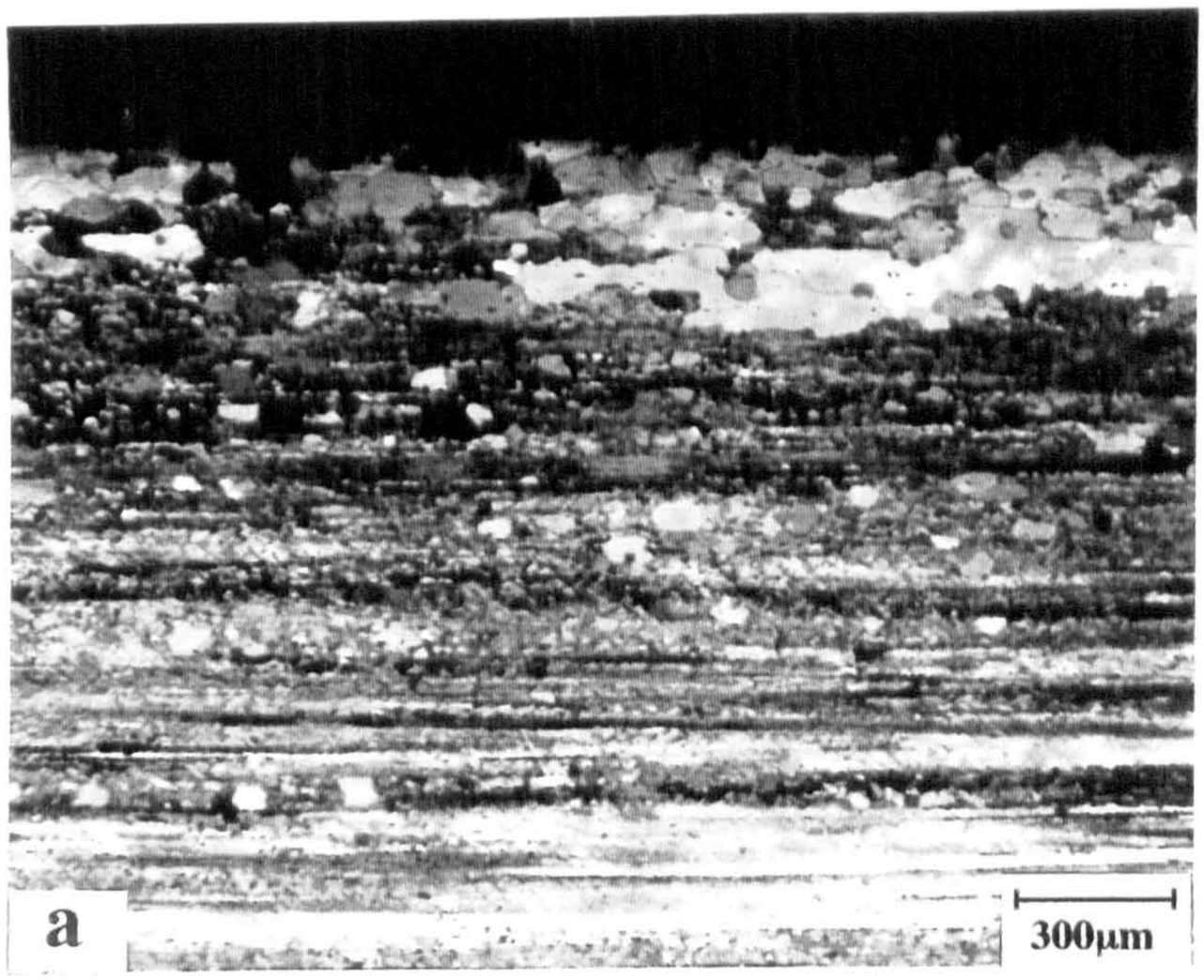


Fig 5.1.3

Fig 5.1.4 Optical Micrographs.
(a) 90° die cone angle.
460° C extrusion temperature.
Underaged condition.
Surface region of extrudate.
(b) 90° die cone angle.
460° C extrusion temperature.
Overaged condition.
Core region of extrudate.
(c) 90° die cone angle.
430° C extrusion temperature.
Overaged condition.
Core region of extrudate.





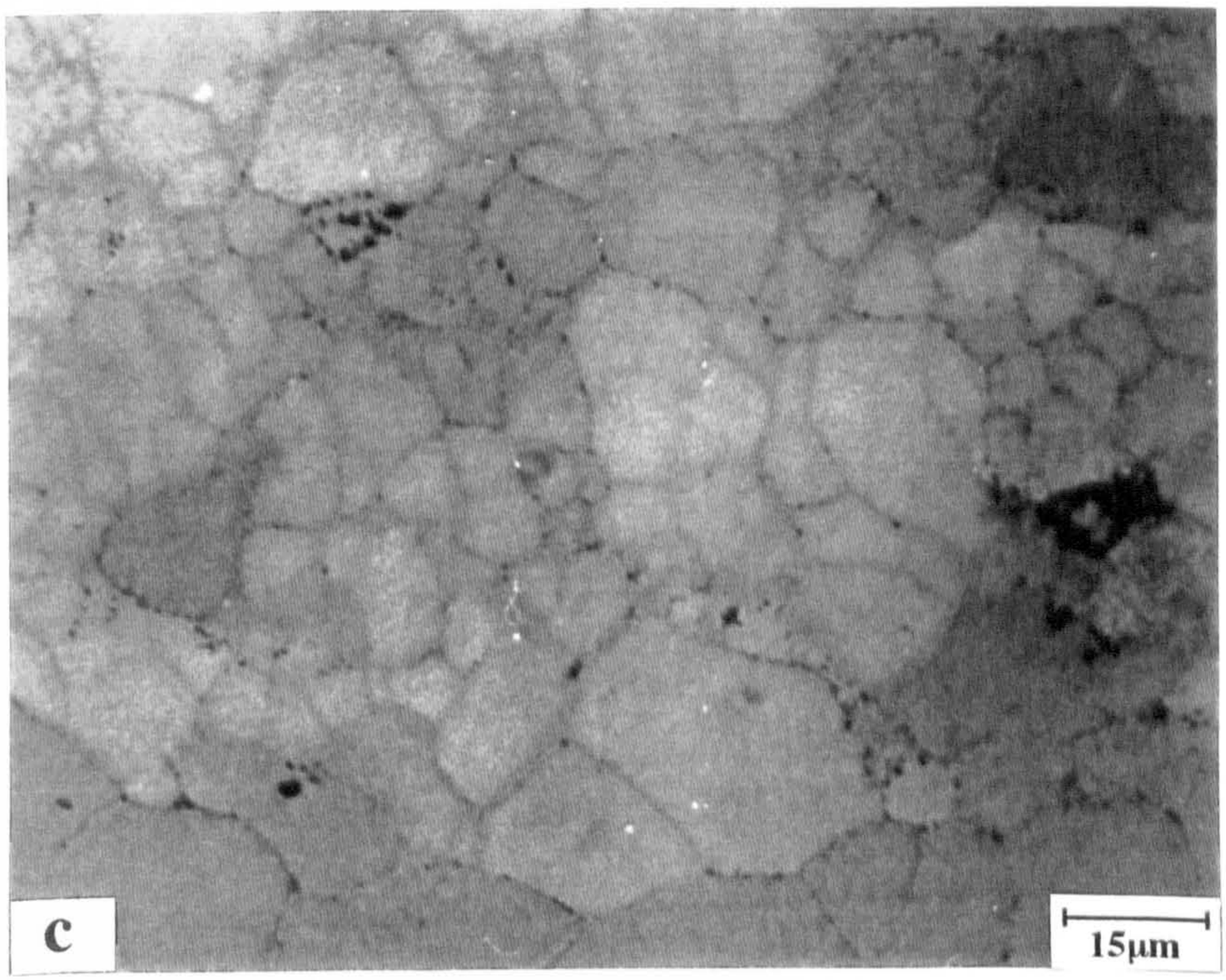


Fig 5.1.4

Die Cone Angle	Extrusion Temp (°C)	% of core recrystallisation	Grain size of core recrystallisation (μm)	Size of core subgrains (μm)
30°	400	12	10 -> 40	2 ->10
	430	16	10 -> 40	2 ->10
	460	21	10 -> 50	2 ->10
45°	400	4	10 -> 20	2 ->10
	430	8	10 -> 30	2 ->10
	460	10	10 -> 50	2 ->10
60°	400	8	10 -> 20	2 ->10
	430	15	10 -> 30	2 ->10
	460	16	10 -> 40	2 ->10
90°	400	10	10 -> 20	2 ->10
	430	15	10 -> 30	2 ->10
	460	20	10 -> 50	2 ->10

Fig 5.1.5 Variation in % recrystallisation, grain size, and subgrain size, with increasing extrusion temperature and die cone angle.

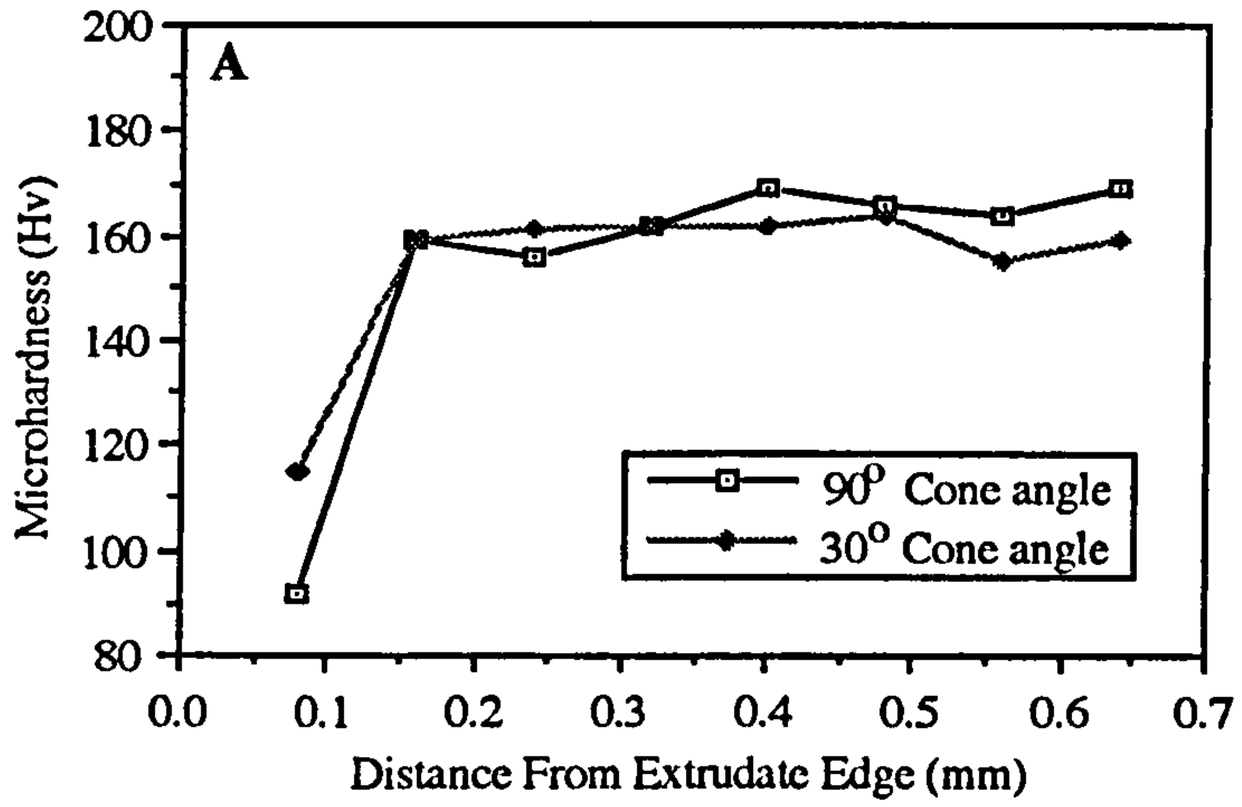


Fig 5.1.6 Variation in surface region microhardness values.
(a) 460°C extrusion temperature.
(b) 430°C extrusion temperature.

5.2 Transmission Electron Microscopy.

T.E.M analysis of the axi-symmetric extrudates was carried out in order to provide information upon the proportion and distribution of precipitates within the extrudates, together with a knowledge of the subgrain sizes. An in depth chemical analysis of the phases was considered unnecessary, since it was possible to identify the matrix and grain boundary precipitates to the required degree from the published literature[(1)-(6)(9)].

5.2.1 Variation in Microstructure with Processing

As with the optical analysis, transmission electron microscopy (T.E.M.) revealed the extrudate microstructures to be characterised by elongated original grains containing internal substructure, fig 5.2.1 (a).

Fig 5.2.1 (d) & (e) and fig 5.2.2 (a)->(c) illustrate typical microstructures obtained from underaged extrudates. In this condition, matrix precipitation was mainly limited to δ' and composite β' precipitation, with no evidence of significant S (Al_2 CuLi) or T_1 (Al_2CuLi) precipitation being observed. Grain boundary precipitation, fig 5.2.2 (c), together with constituent phases, fig 5.2.2 (b), were also observed. A complete analysis of the constituent phases was not carried out, since many researchers have previously established them to be based upon the Al-Fe-Cu system.

As ageing continued to the overaged condition the sizes of the homogeneously precipitated δ' phase and heterogeneously precipitated β' precipitates both increased. The incidence of T_1 and S phase precipitation also increased as ageing proceeded, fig 5.2.1 (b)&(c), and 5.2.2 (d),(e)&(f). The T_1 phase was apparent in the T.E.M micrographs, due to fringe contrast caused by the associated stacking faults. The S phase, however, has been reported to grow as rods and then to widen to form laths resulting in a corrugated sheet appearance[(2)(7)].

As ageing times increased the proportion of small grain boundary precipitates with associated δ' precipitate free zones, increased. These precipitates were observed to grow from an average of 0.05 μm in the under-aged condition to 0.1μm in the over-aged condition, with the presence of the P.F.Z.'s suggesting that they contained lithium. Researchers such as Mukapadyay[(1)] have also observed grain boundary precipitates, and by using x-ray E.D.S. analysis, he found these particles to be rich in copper (13-17 wt%), determining them to be based upon the Al-Li-Cu-Mg system. Other researchers[(1)(3)], however, have found that in AA 8090, I phase forms at the grain boundaries. The I phase has a composition based upon the Al-Cu-Li system (70% Al and 30% Cu), and is responsible for the P.F.Z formation. There are, therefore, conflicting results as to the specific composition of these grain boundary phases. The majority of evidence, however, does suggest these phases to be I phase, hence they will be referred to as such subsequently in this project.

majority of evidence, however, does suggest these phases to be I phase, hence they will be referred to as such subsequently in this project.

I phase precipitates of approximately 0.1μm in size are shown in fig 4.2.2(d). Fig 5.2.1 (a) also illustrates grain boundary precipitation, together with the outline of the elongated deformed grains and the internal subgrain structures.

Even though considerable variations in precipitation were observed as ageing occurred, no significant changes in precipitation were evident as the extrusion temperature and/or die cone angle increased.

Subgrain sizes ranging from 1->8μm were observed in all extrudates, with no significant changes in their sizes occurring as extrusion temperature or die cone angle increased.

Fig 5.2.1 **T.E.M. Micrographs.**

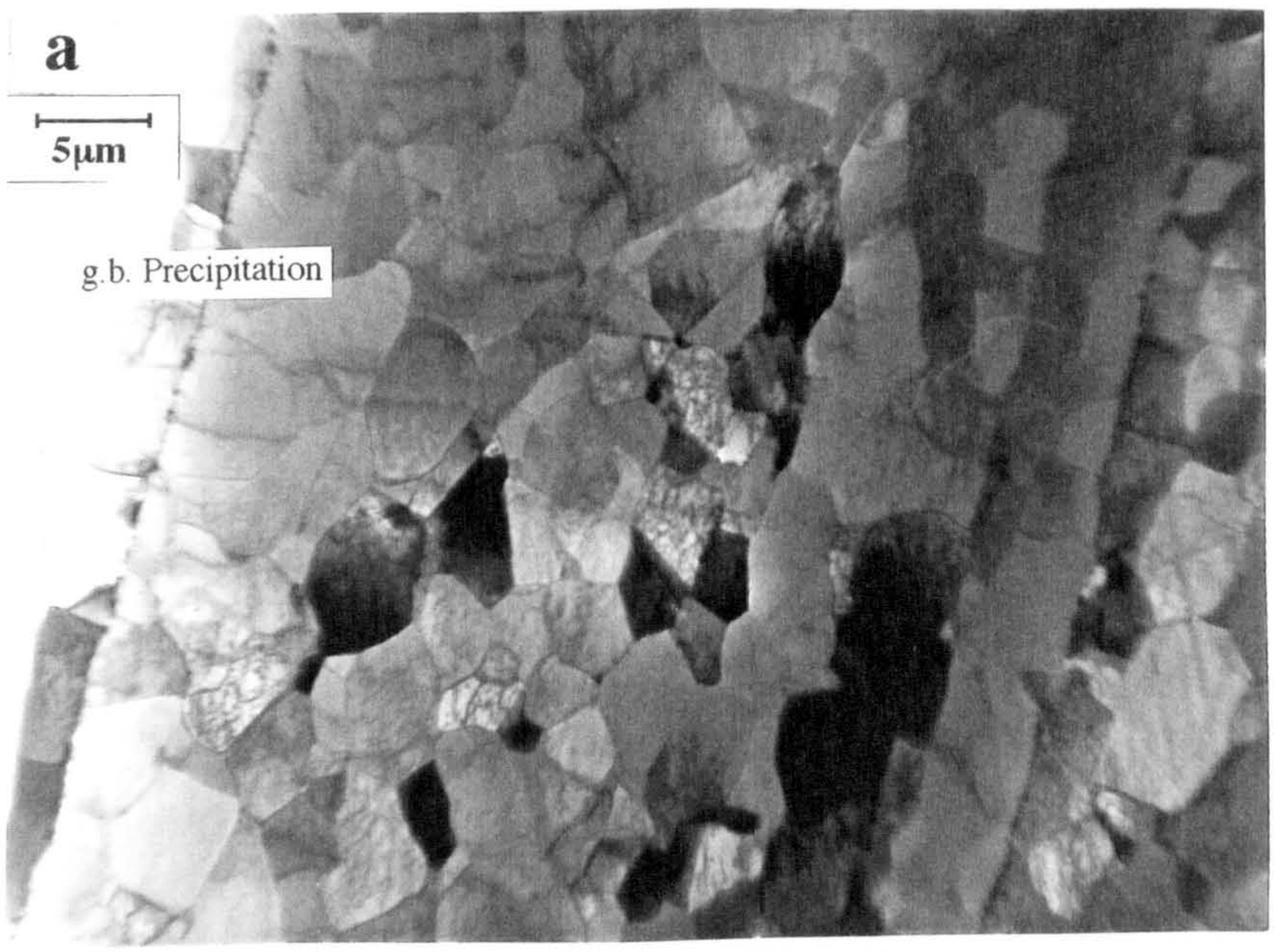
(a) 60° die cone angle.
460° C extrusion temperature.
Overaged condition.
Longitudinal section.
Core region of extrudate.
This micrograph illustrates the elongated nature of the original grains, together with internal substructure. Matrix precipitation, along with grain boundary I phase precipitation (Al-Cu-Li) are also evident.

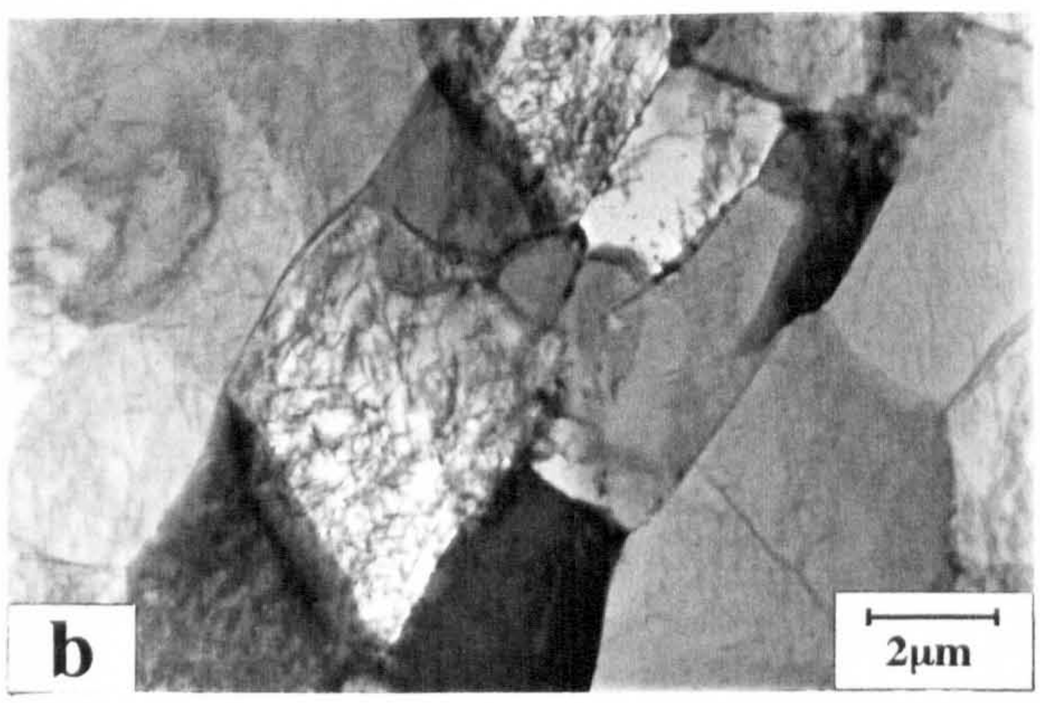
(b) Higher magnification of (a).

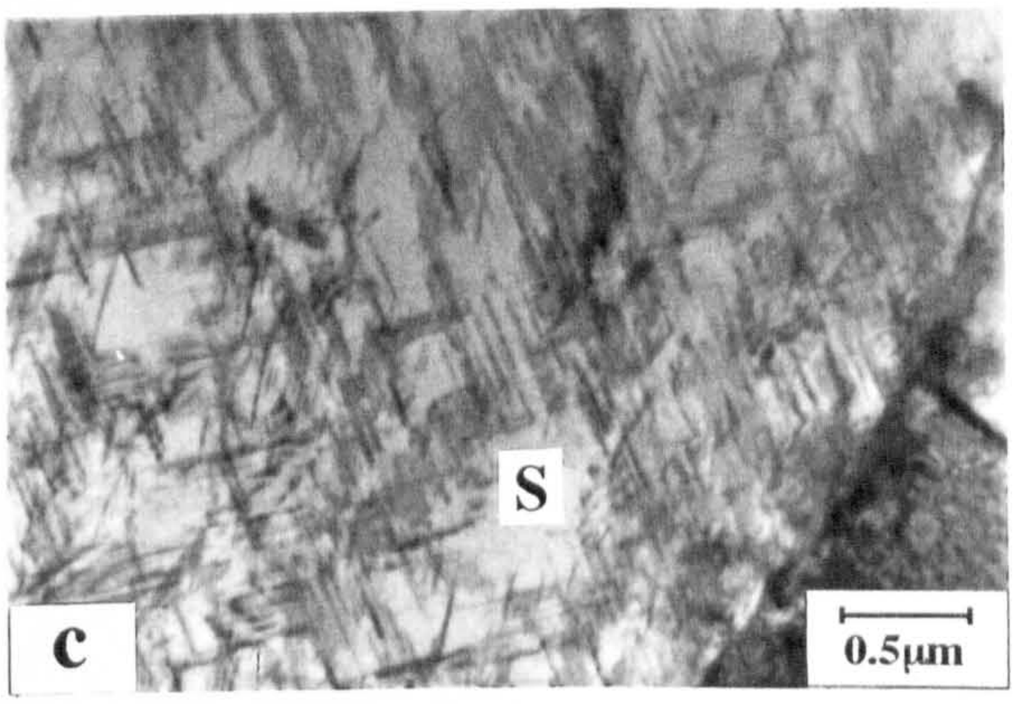
(c) Higher magnification of (b), highlighting the matrix S phase precipitation.

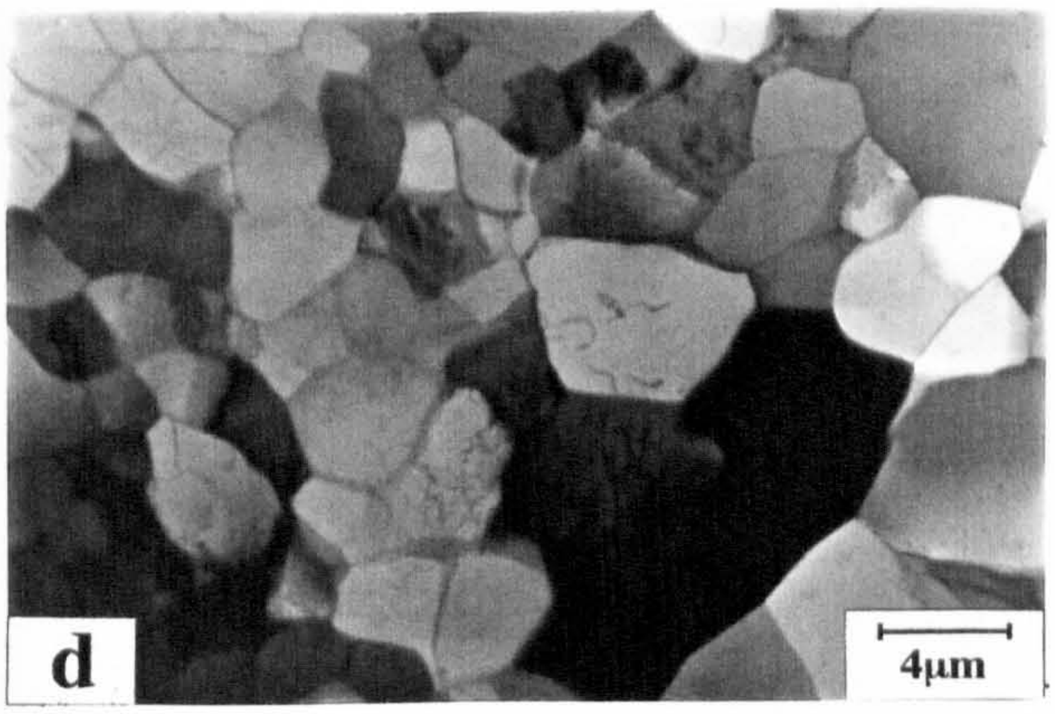
(d) 30° die cone angle.
400° C extrusion temperature.
Underaged condition.
Transverse section.
Core region of extrudate.

(e) Higher magnification of (d) illustrating the absence of matrix S an T_1 precipitation in the underaged condition.









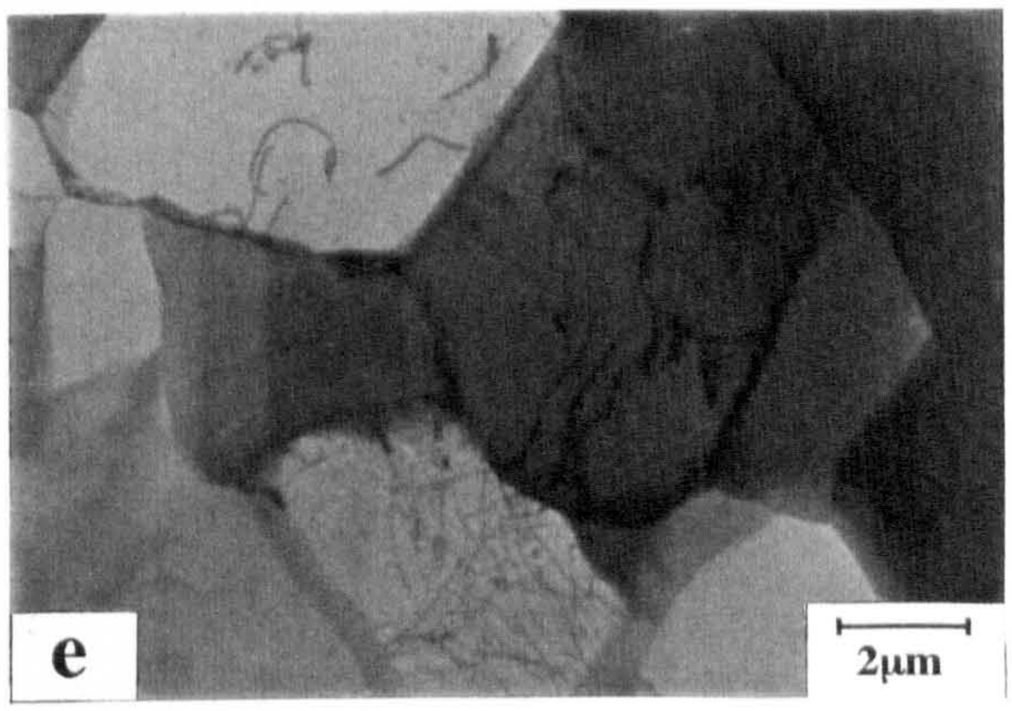


Fig 5.2.1

Fig 5.2.2 **T.E.M. Micrographs.**

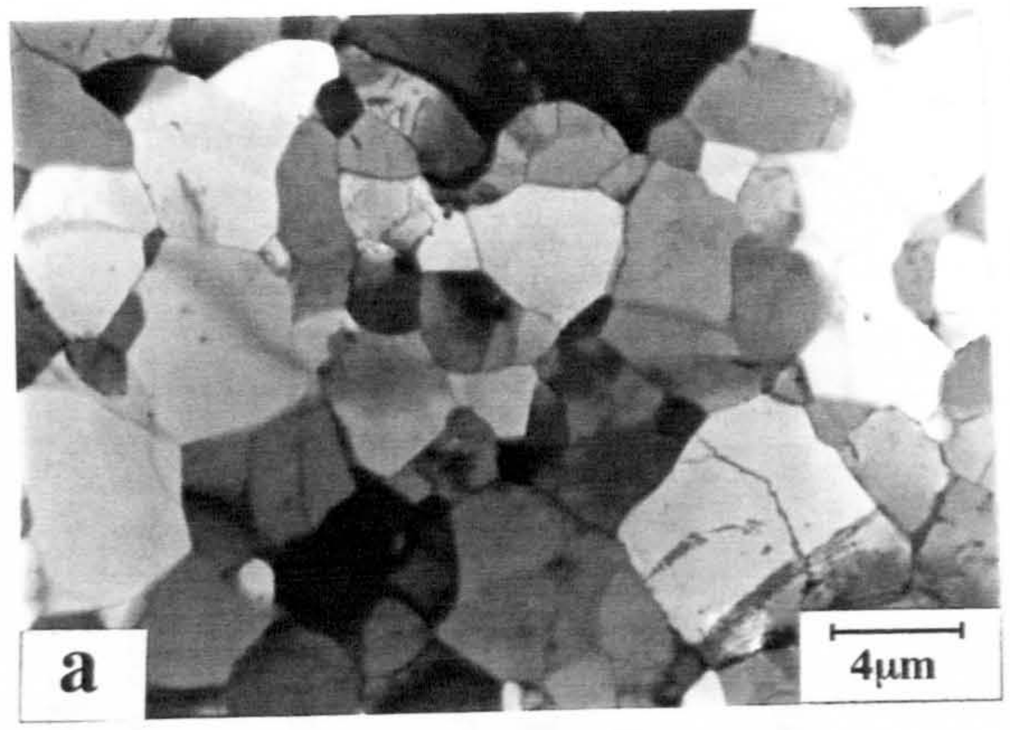
(a) 90° die cone angle.
400° C extrusion temperature.
Underaged condition.
Transverse section.
Core region of extrudate.

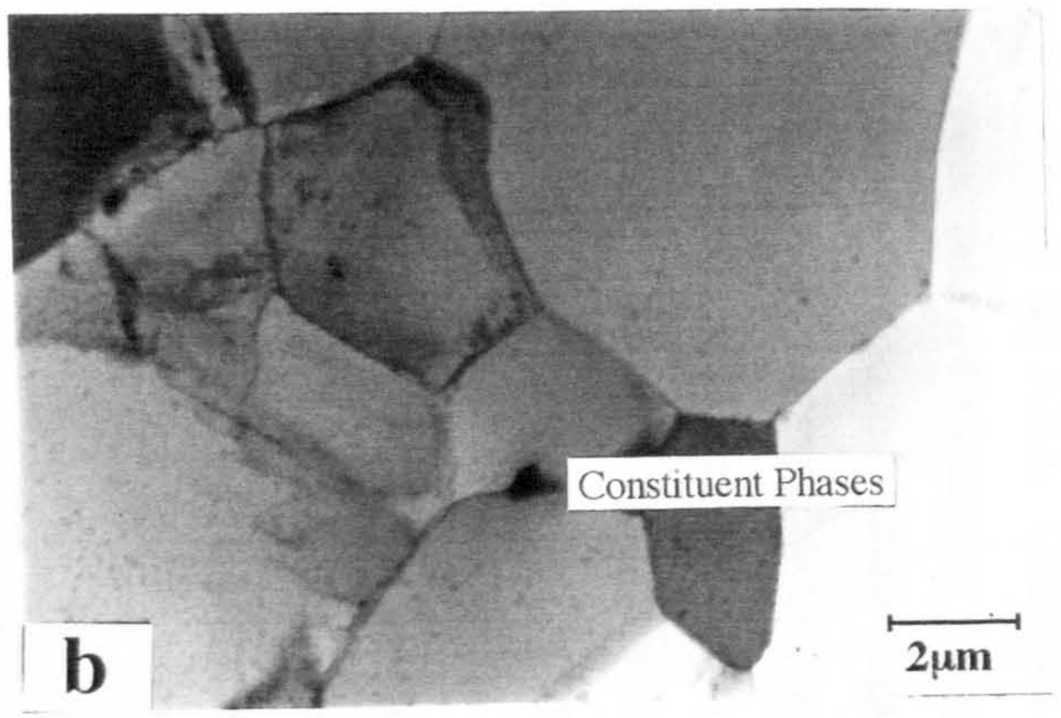
(b) Higher magnification of (a) illustrating the absence of significant matrix precipitation other than δ', which gave rise to the 'mottled' effect associated with the subgrains.

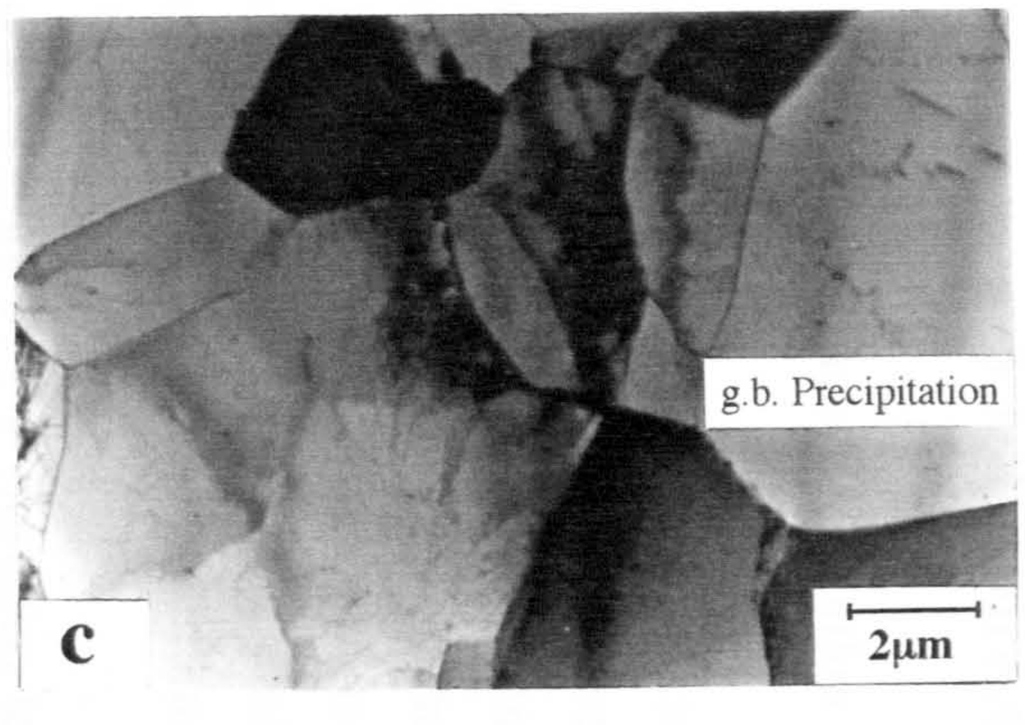
(c) 90° die cone angle.
460° C extrusion temperature.
Underaged condition.
Transverse section
Core region of extrudate.
These micrographs illustrate the absence of S and T_1 matrix precipitation within the underaged material.
δ' precipitation, along with dislocation loops, are clearly observed within the subgrains, however, and grain boundary precipitation of I phase, based upon the Al-Cu-Li system, is also clearly evident.

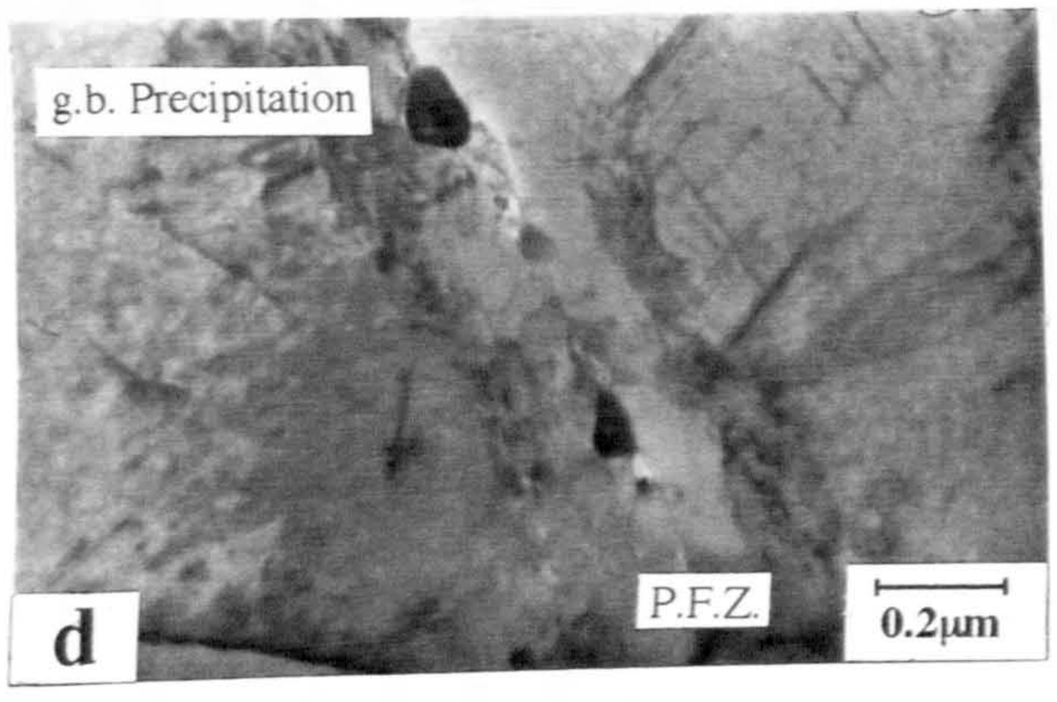
(d) 90° die cone angle.
400° C extrusion temperature.
Overaged condition.
Transverse section.
Core region of extrudate.
This micrograph illustrates the grain boundary precipitation of I phase (Al-Cu-Li), with associated precipitate free zones.

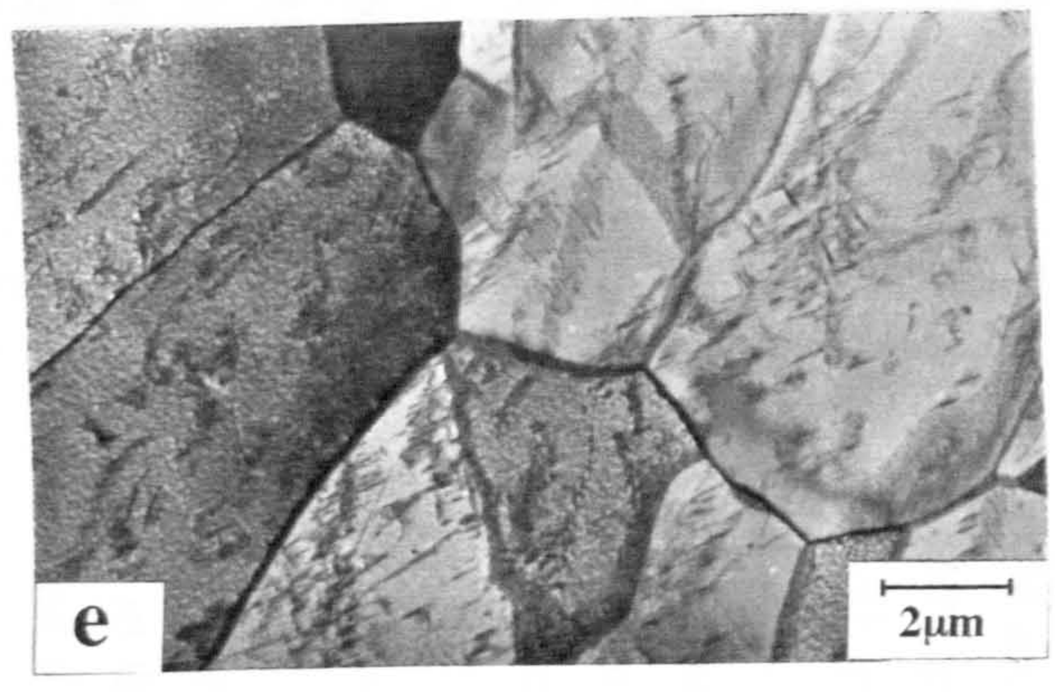
(e) & (f) 90° die cone angle.
460° C extrusion temperature.
Overaged condition.
Transverse section.
Core region of extrudate.
These micrographs illustrate the matrix precipitation of S phase, together with the δ' precipitation, which has given rise to the 'mottled' effect associated with the micrographs.


a
4μm


Constituent Phases
b
2μm


g.b. Precipitation
c
2μm


g.b. Precipitation
P.F.Z.
d
0.2μm


e
2μm

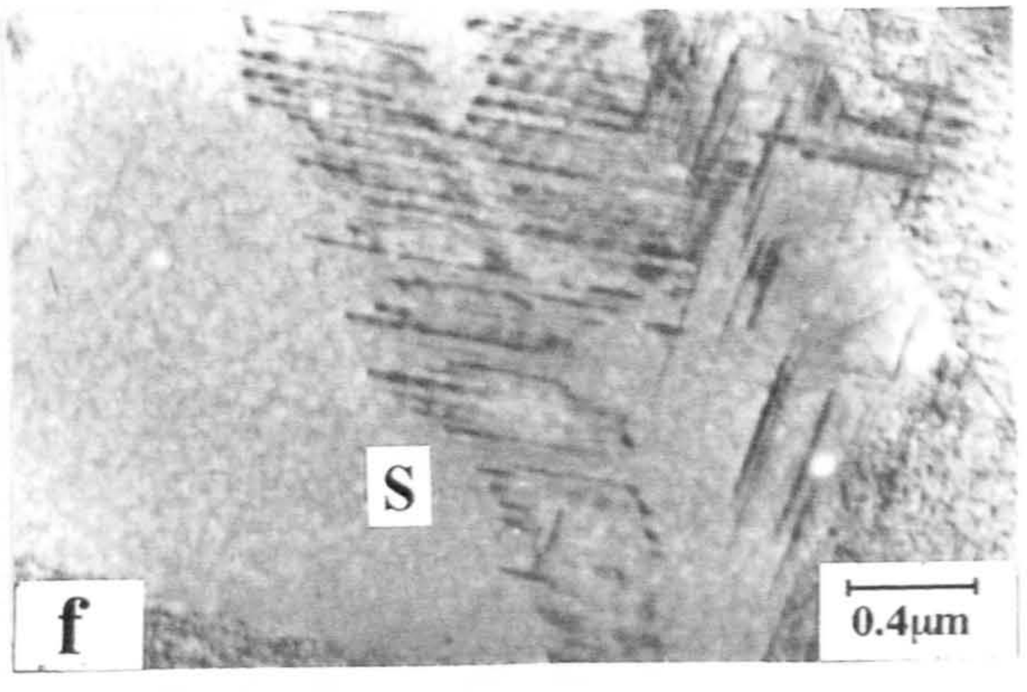

S
f
0.4μm

Fig 5.2.2

5.3 Texture Analysis

5.3.1 Texture Variation With Processing

In order to investigate the variation in texture with die cone angle and extrusion temperature, O.D.F. and pole figure analyses were carried out. O.D.F. analysis enabled percentage volume fractions of specific components to be calculated, whilst pole figure plots showed general trends in texture with variations in processing condition.

Figs 5.3.1->3 illustrate {111} pole figure plots obtained from extrusions carried out at different extrusion temperatures and using dies of different cone angle. As is clearly seen, all the axi-symmetric extrudates exhibited a <100> <111> double fibre texture system[1][2][3][4].

The variation in texture as the extrusion temperature increased was found to be insignificant, fig 5.3.1(b) & fig 5.3.3. Changes in die cone angle, however, did appear to cause slightly larger texture changes. Figs 5.3.1->2 illustrate pole figure plots obtained from extrudates produced using dies of different cone angle. Both plots illustrate double fibre texture systems, with the <111> fibre being most dominant. As the die cone angle increased, however, the intensity peaks along the <111> fibre altered position. A precise identification of the specific texture changes taking place as the die cone angle increased was impossible to obtain from the pole figure analysis, hence O.D.F was carried out.

The variations in texture with increases in die cone angle, obtained from the O.D.F. analysis, are tabulated in fig 5.3.4. Of all the texture components investigated the copper {112}<111> and S {124}<211> components were the most dominant for all cone angles, but as can be seen, no highly substantial or constant variations in these textures with cone angle were evident. The variations in the Brass, Goss and Cube texture components were also measured, but found to be very small.

5.3.2 Texture-Microstructure Correlations

Due to sample size requirements, all the textural analysis was carried out on longitudinally sectioned samples which incorporated the whole of the extrudate transverse section. Each sample, therefore, included the complete microstructural variation from the centre of the extrudate to the edge, hence the microstructural variation of the whole section had to be considered when seeking explanations for the texture variations.

Optical analysis revealed the basic extrudate microstructures to consist of elongated original grains with internal substructure. The volume fraction and grain size of

equiaxed recrystallised grains, was then observed to vary throughout this basic deformed structure, as the extrusion temperature and die cone angle increased.

Increases in extrusion temperature caused the proportion of recrystallisation to increase, but no correlations with texture were possible, since insignificant texture variations were identified.

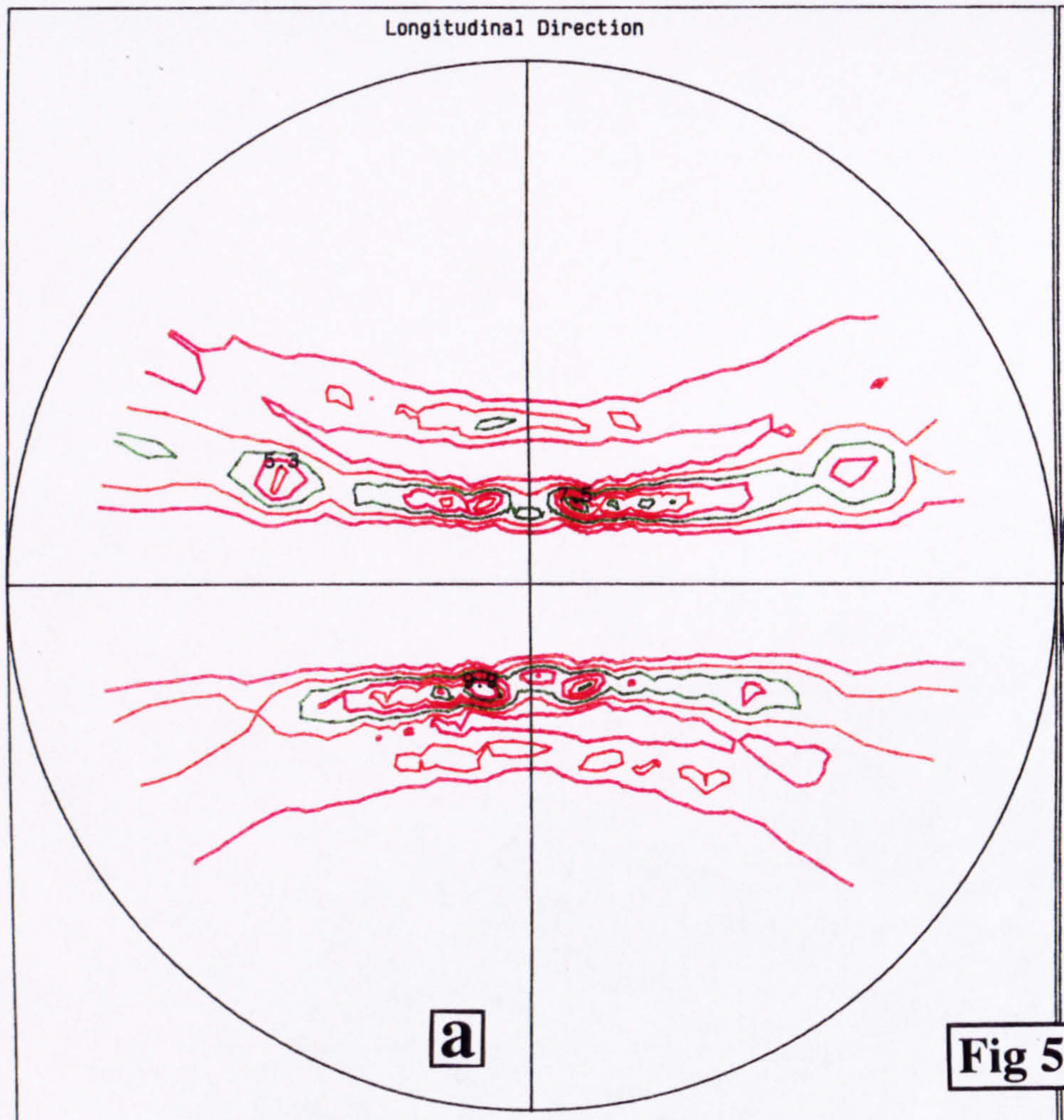
Increases in the cone angle also caused changes in the % recrystallisation. Die cone angle increases from 30° ->45° , decreased the percentage of core recrystallisation, whilst subsequent increases in die cone angle to 60° and then to 90° caused the proportion of recrystallisation to increase.

From comparison of these optical results with the observed changes in texture systems shown in fig 5.3.4, it appeared that decreases in recrystallisation corresponded to increases in S and copper texture components. From analysis of the 'slab' extrudates, however, a correlation between cube texture and increases in recrystallisation was identified. For the axi-symmetric extrusions the variation in cube texture did also increase as the recrystallisation increased, but the percentage texture changes were so small that no definite correlations could be stated.

Overall, therefore, it was observed that increases in die cone angle affected the extrudate texture systems to a greater extent than increases in extrusion temperature.

5.3.3 Conclusions

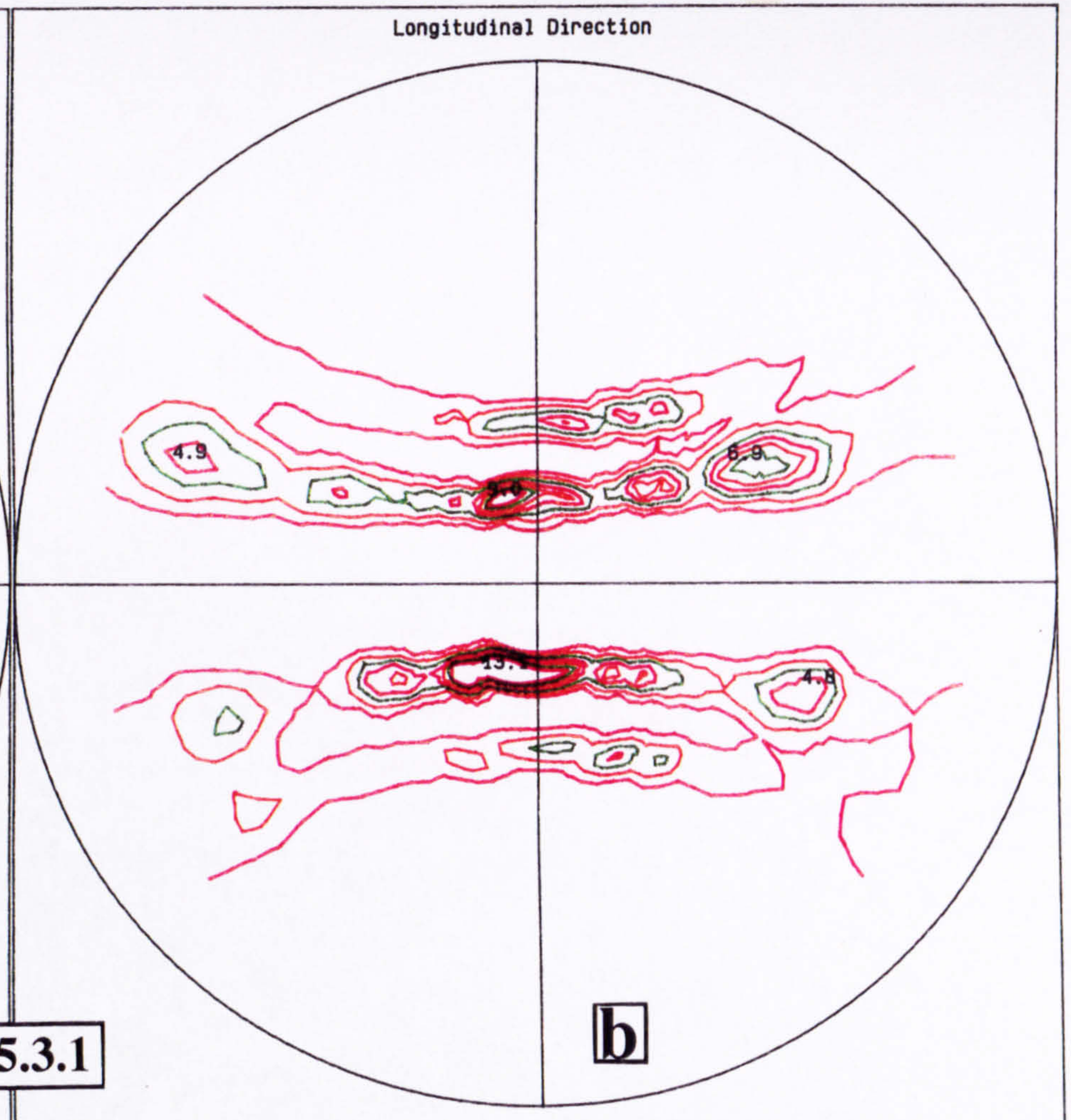
All the axi-symmetric extrudates, irrespective of processing conditions were characterised by a <100>,<111> double fibre texture. As the extrusion temperature increased, no significant or definite changes in the textures systems were observed, hence no correlations between texture and microstructure changes could be made. Changes in die cone angle did, however, appear to cause greater variations in texture. When subsequently correlated with microstructure, it appeared that decreases in recrystallisation corresponded to increases in S and Copper components. As with the 'slab' extrudates the cube texture components were observed to decrease as recrystallisation decreased, but these changes were so slight that no definite conclusion concerning this correlation could be drawn.



111 Pole figure

30° Die Cone Angle,
430 ℃ Extrusion Temperature.

SAMPLE: BEA000
IDENT.: #103 NCP/IMPERIAL COLLEGE EXTRUSION 30
Contour levels: 1.00 2.00 3.00 4.00 5.00 6.00 7.00

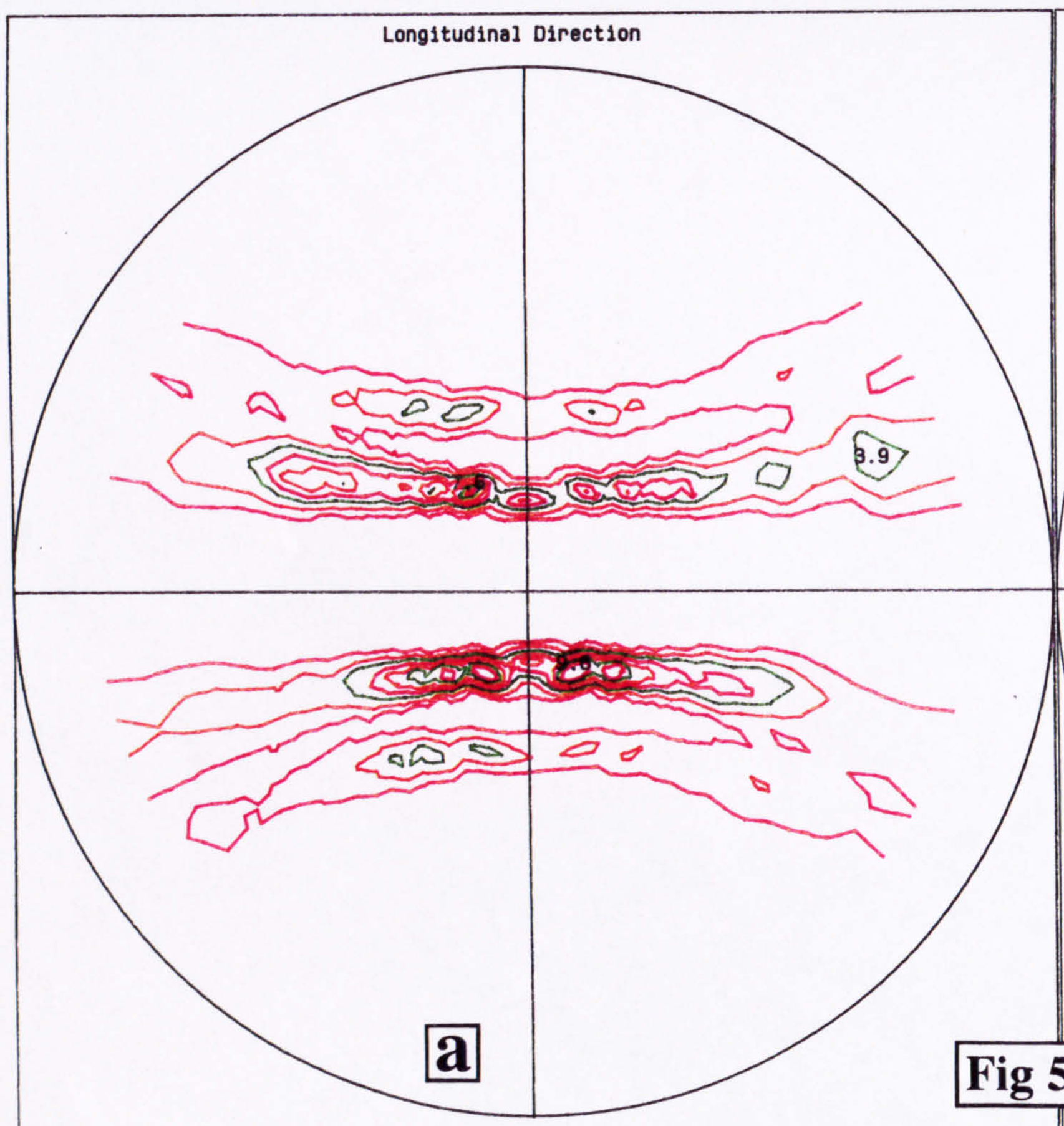


111 Pole figure

45° Die Cone Angle,
430 ℃ Extrusion Temperature.

SAMPLE: BEB000
IDENT.: #103 NCP/IMPERIAL COLLEGE EXTRUSION 45
Contour levels: 1.00 2.00 3.00 4.00 5.00 6.00 7.00

Fig 5.3.1



a

111 Pole figure

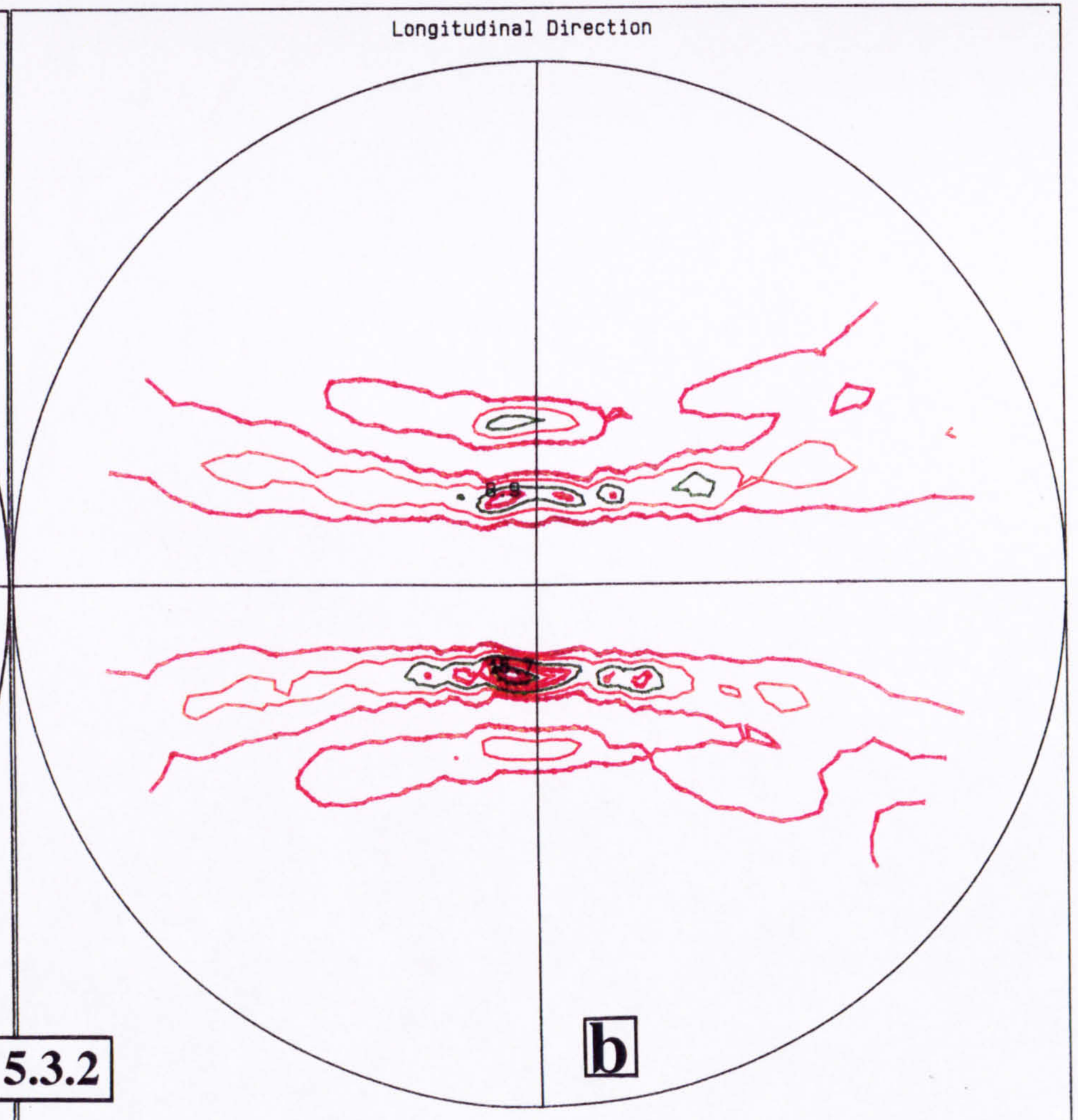
SAMPLE: BED000

IDENT.: #103 NCP/IMPERIAL COLLEGE EXTRUSION 60

Contour levels: 1.00 2.00 3.00 4.00 5.00 6.00 7.00

60° Die Cone Angle,
430 ℃ Extrusion Temperature.

Fig 5.3.2



b

111 Pole figure

SAMPLE: BEE000

IDENT.: #103 NCP/IMPERIAL COLLEGE EXTRUSION 90

Contour levels: 1.00 3.00 5.00 7.00 9.00 11.00 13.00

90° Die Cone Angle,
430 ℃ Extrusion Temperature.

163

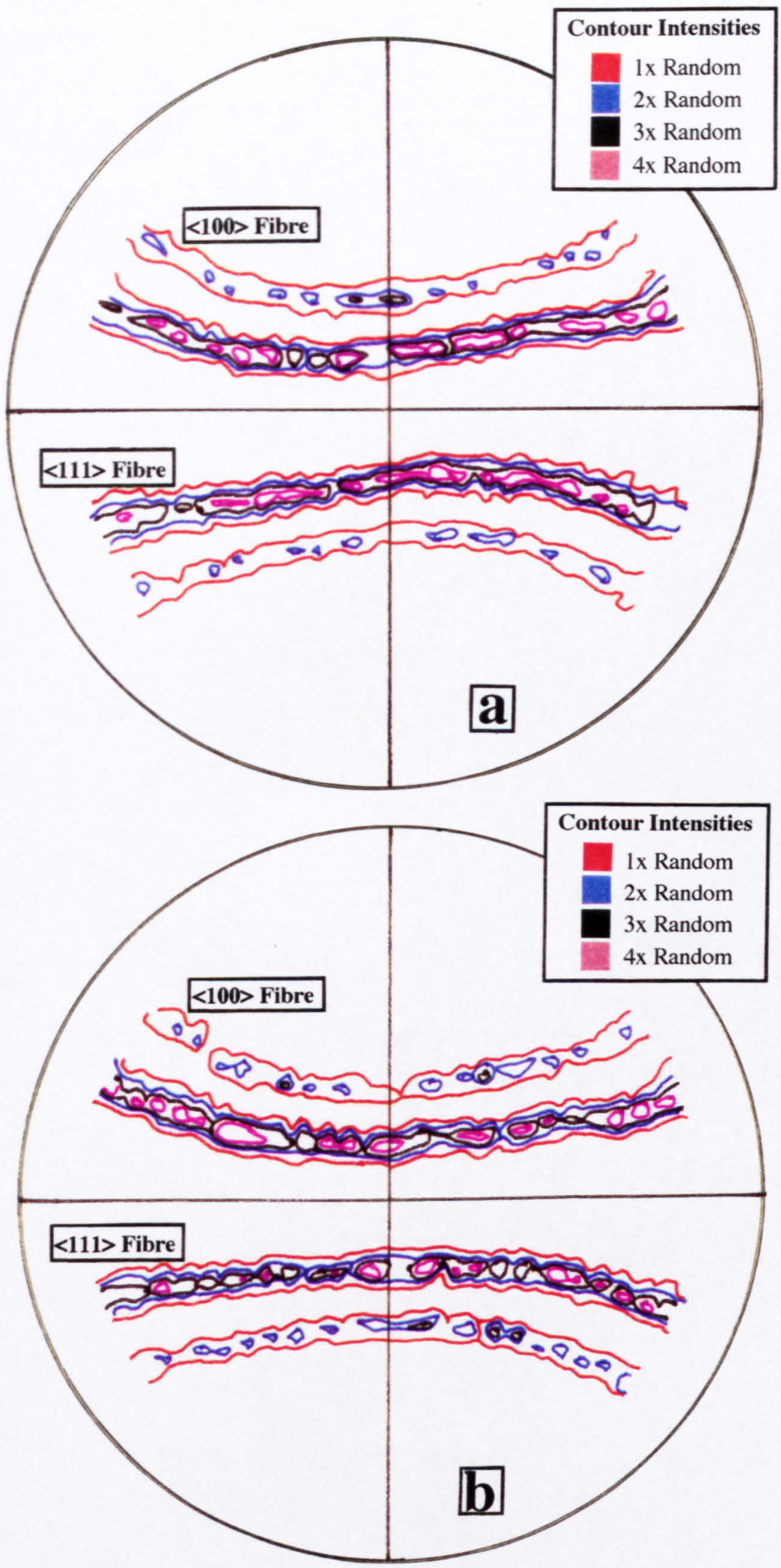


Fig 5.3.3.
{111} Pole figure Plots
(a) 45° Die Cone Angle, 400 °C Extrusion Temperature.
(b) 45° Die Cone Angle, 460 °C Extrusion Temperature.

Die Cone Angle	% Volume Fraction of Texture				
	CUBE	BRASS	COPPER	GOSS	S
30°	5.3	9.0	21.5	5.0	24.3
45°	4.3	9.3	23.7	5.5	27.5
60°	5.3	9.8	19.3	4.4	24.8
90°	5.6	10.3	19.4	4.2	24.1

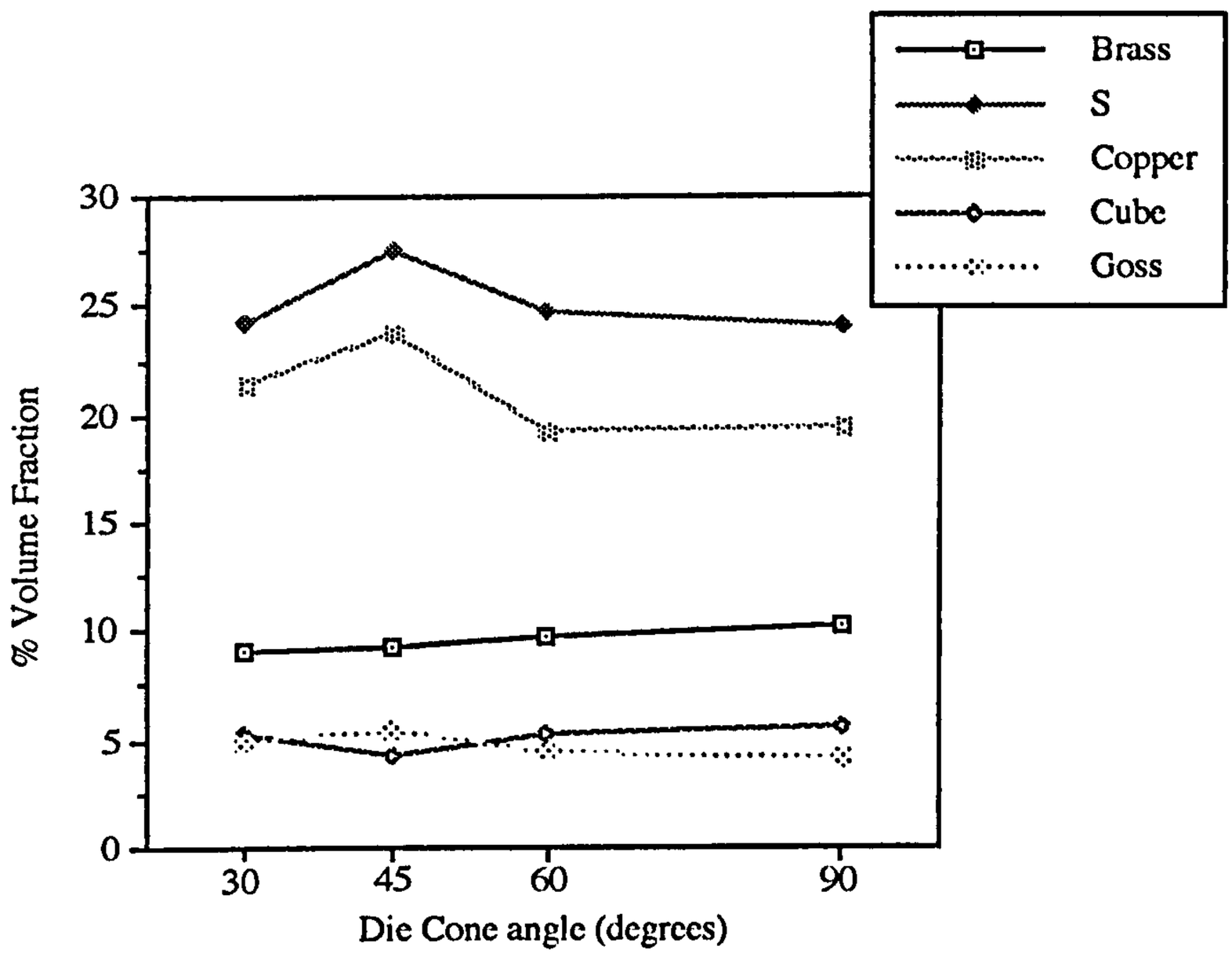


Fig 5.3.4 Variation in the % volume fraction of texture components with increasing die cone angle, for extrusions carried out at 430°C.

5.4 Deformation Flow Analysis

In order to establish the reasons for any property and microstructural variations occurring as a result of changes in die cone angle, analytical techniques that characterised the deformation process needed to be carried out. Several different techniques, of varying complexity, were utilised in this project in order to define the extrusion process:- (1) Split Gridded Billets.

(2) Visioplasticity.

(3) Finite Element Analysis.

The use of split gridded billets was the simplest analysis carried out, and provided information on the extrusion flow pattern. The visioplasticity analysis also produced distortion patterns, but these were then analysed in order to provide information on the deformation strain rates. The most complex technique employed was that of finite element analysis. This technique provided information upon extrusion load, strain rate, flow patterns and temperature distributions.

5.4.1 Split Gridded Billet Analysis

When considering extrusion it is often stated that some deformable substance, resistant to high temperature and pressure, must be introduced between the tooling surfaces and extrusion material in order to facilitate sliding. For aluminium alloys, however, the high surface finish of extrudates is associated with intimate contact between the extrusion metal and tooling, and is destroyed by the introduction of the deformable substance[1]. For this reason this project has considered unlubricated extrusion.

Figs 5.4.1 (a)->(d) illustrate the distortion patterns obtained from unlubricated extrusion of machined gridded billet, with each distortion pattern representing an instantaneous picture of the elemental distortions present. The machined grid lines were highlighted with black pen, and as can be seen the distortions present in the central regions of the deformation zone were easily distinguished. In the edge regions, however, separation of the various machined lines was impossible. As fig 5.4.1 (d) illustrates, the longitudinal machined lines A,B,C,D,E and F were easily identified, but flow line G could only be accurately mapped in the upper regions of the billet. Lower down in the more highly strained regions of the deformation zones the profile of line G was indicated as suggested by the striations on the split billet surface, but by no means could this be considered as definite.

Even with these short comings in the grid identification, it was evident that each elemental section, defined by the machined grid lines, deformed uniquely. Due to the unlubricated nature of the extrusions, the material immediately adjacent to the tooling remained in contact with the tooling throughout the extrusion stroke, or until disturbed

by the scraper pad. This essentially meant that a dead zone was formed for all cone angles, and due to the 'collection' of material from the walls, circular flow at the rear of the extrusion occurred.

Other consequences of this 'sticking' of the extruding material to the tooling surfaces were:- (i) significantly higher levels of shear deformation associated with the surface regions of the deformation zones and (ii) unlike the core regions of the extrudates, which were produced from consecutive sections within the deformation zone, the entire outer surfaces of all the extrudates were formed from material present at the dead metal zone surface, and situated initially at the immediate edge of the die orifice. Material from further back in the billet did not, therefore, form any part of the extreme outer surface regions of the extrudate[9]. The material flow associated with extrudate surface production was also investigated by Valberg[2]. In his investigation he also considered that the region supplying the whole of the extreme outer surface of the extrudate was concentrated around the dead metal zone.

In order to highlight all these features associated with the unlubricated extrusion, fig 5.4.2 represents a schematic diagram developed from observation of the distorted grid patterns, which clearly indicates the horizontally and vertically machined grid line distortions.

The general observation of figs 5.4.1(a)->(d) highlighted above allowed the basic distortion field characteristics to be identified, but comparison of figs 5.4.1 (a)->(d), allowed the degree to which the distortion fields varied with die cone angle to be investigated.

The gridded billets indicated that the actual volume of the dead metal zone formed upon the tooling surfaces decreased as the die cone angle was reduced. The size and shape of the 'effective' die cone angle, which consisted of dead metal plus tooling, however, increased as the die cone angle decreased. For the shear face die situation the 'effective' dead zone surface was curved in appearance. As the cone angle decreased, however, the line of the dead metal zone from the container to the die orifice became straighter, fig 5.4.3 (b) & (c).

The flow through the central regions of the deformation zone did not seem to be affected to any great extent by this variation in the 'effective' die cone angle, but some modification of the surface distortion was apparent. The 'straightening out' of the dead zone surface as cone angle decreased caused the onset of radial movement within the deformation zone to initiate further away from the die orifice. The resulting effects upon the level of redundant work and the rate of redundant deformation was less obvious.

Farag[3] investigated the variation in the strain (ideal and redundant) distribution across an extrudate section, as die cone angle varied, but determined only second order effects of die cone angle on the final redundant strains. Another quantitative way in

which the changes in redundant work manifest themselves, however, is in the variation of extrusion load. For a non lubricated extrusion the extrusion load depends upon the energy required for ideal and shear (redundant) deformation. The rates at which these two types of deformation occur, along with the temperature rise associated with the deformation, will also influence the energy requirements for extrusion.

Since the extrusion ratio for all the axi-symmetric extrudates was constant, the amount of ideal deformation occurring for all the extrusions was also constant. Any changes in extrusion load with cone angle were, therefore, either due to changes in the amount of redundant work, or changes in the rate of deformation and temperature rise during extrusion.

Fig 5.4.4 (c) indicates the observed variations in extrusion load. The extrusion load decreased with increasing cone angle, irrespective of the extrusion temperature. This would suggest, therefore, that the higher cone angle dies produced lower degrees of redundant work, compared with dies of lower cone angle.

5.4.2 Visioplasticity

Visioplasticity is a technique in which a distortion field is experimentally produced and then analysed to produce strain, strain rate and stress fields[4][5][6][7].

The strain, strain rate, and stress fields within the deformation zones, or the resultant strain distributions within the extrudate itself can be assessed. Both these analyses would indicate the effect of die cone angle upon flow, but the latter analysis would allow correlations between resultant strain and resultant microstructure to be made. Farag[3] carried out such a strain analysis, in which he extruded gridded billets, and summated the strains along streamlines. He developed strain distributions for various extrudates produced using different die cone angles, but did encounter problems in his analysis. He found the measurement of surface strains to be impossible, and the central strains that were measured showed little dependence upon die cone angle. Figs 5.4.1 (a)->(d) illustrate the distortion patterns obtained in this project from the extrusion of machined gridded billets. As can be seen, the only discernible strains were at the centre of the deformation zone, hence any analysis performed upon these patterns would, therefore, suffer from the same inadequacies as that of Farag's analysis. This prompted an investigation into the use of other methods, rather than machining, for producing the grid pattern. It was considered that a gold mesh laid into the machined grid lines may solve the problem of strain measurement within the surface regions. When annealed, the gold mesh would be capable of undergoing the strains associated with the surface regions without breaking, and when the extrudate and discard were photographed using X-rays, the greater absorption rate of the gold would cause the distortion field to be highlighted. Problems were encountered with this technique, however:-

(i) Distortions in the gold mesh occurred during assembly of the split billet.

(ii) Distortion of the gold mesh occurred during billet heat-up.

(iii) The integrity of the mesh was not maintained during billet upset.

The attainment of useful distortion fields, was, therefore, difficult, but several useable patterns were obtained. Fig 5.4.5 illustrates a typical X-ray contact print obtained from an extrusion carried out using a die with a 45° cone angle. The outline of the longitudinally orientated gold wire has been highlighted with black ink, and as can be seen occasional erratic deviations in the actual streamline were modified as suggested by the stable sections.

Appendix II outlines the analysis carried out upon several of these distortion patterns in order to produce strain rate fields, with the results obtained shown in fig 5.4.6.

There appeared to be no significant difference in the strain rate fields associated with the extrusion of the 8090 and 7075 alloys, when the 45° die cone angle was utilised, fig 5.4.6 (a) & (b). This suggested that the differences in the 7075 and 8090 working constants were not significant enough to affect the flow during extrusion. Changes in the strain rate fields brought about by variations in die cone angle are illustrated by comparison of fig 5.4.6 (a) & (c). In general it appeared that increasing the die cone angle increased the strain rate values. Due to differences in the sizes and shapes of the deformation zones, however, it was difficult to know which values should be compared.

5.4.4 Finite Element Analysis

Finite element analysis is a highly analytical technique which simultaneously solves equilibrium equations, yield criteria, material flow stress equations and constitutive equations, for elemental sections within the deformation zone.

Due to the complexity of the analysis computer assistance is required, and in this project a modified 'forge II' program was utilised. The basic outline of the analysis is shown in appendix III, and for any given material and tooling configuration inputs concerning:- (i) Friction conditions and (ii) Hot working equations, were required.

All the extrusions were carried out unlubricated, hence sticking friction was assumed. As for the hot working constants, 8090 aluminium was of main concern, but due to the limited availability of data, a mixture of both 8090 and other quaternary alloy hot working constants were utilised[8][9] . It was considered that the use of mixed hot working constants would not affect the flow results obtained from the finite element analysis. To illustrate this, finite element analysis was also carried out using accurate and complete 7075 hot working data. The results were then compared in order to establish the effects of substantial changes in hot working constants. The accuracy of the finite element analysis carried out upon the 7075 and 8090 material was also

checked by comparison with the visioplasticity results. The hot working constants employed are listed below:-

	7075	8090
LnA	27.54	24.01
n	7.8	2.28
α (m^2/Mn)	0.012	0.025
ΔH (J/mole)	155,336	153,000

Once carried out, the finite element analysis provided information upon extrusion loads, distortion fields, temperature fields and strain rate fields.

Flow Patterns

Flow line patterns obtained from the finite element analysis are illustrated in fig 5.4.7. By comparison with the visioplasticity results, and even the gridded split billet distortion patterns, it was evident that a fairly close prediction of the actual distortion fields was made by the finite element technique.

As with the previous results the finite element analysis predicted the actual distortion patterns to vary continuously throughout the extrusion process, hence a true 'steady state' period was not present during deformation.

This continual change in the distortion fields was due to the 'sticking' friction conditions prevailing during extrusion. All the tooling surfaces were, therefore, coated with a layer of 'stationary' material throughout the extrusion stroke or until passed by the ram. This lead to the heightening of elemental distortion levels, particularly in the surface regions, circular flow at the rear of the billet, and the continual variation in the deformation field.

Extrusion Loads

The extrusion load requirements predicted by the finite element analysis, together with experimentally obtained values, are tabulated in fig 5.4.4 (a) & (b) for the 8090 and 7075 alloys respectively.

Good correlations between the predicted and experimental extrusion loads were observed for the 7075 alloy extrusions, with all the predicted loads within 10% of the experimentally obtained values. The correlation between the experimental and predicted extrusion loads improved to 2% for the 8090 extrusions. These consistently good correlations, for both the 8090 and 7075 material, suggested that the finite element analysis was simulating the practical situation quite successfully, hence a high degree of confidence could be placed in the results obtained. This high level of correlation also suggested that the use of mixed 8090 hot working constants did not appear to affect the analysis to any significant degree.

As expected increases in extrusion temperature consistently decreased the extrusion load, due to the associated lowering of the material flow stress. Higher die cone angles were also associated with lower extrusion load requirements. Decreases of up to 31% were observed for the 7075 alloy and 21% for the 8090 alloy, which suggested a high dependence of extrusion load upon the specific distortion field patterns.

As already found, due to the friction conditions, a relatively thin layer of 'stationary' material existed adjacent to all the tooling surfaces. Around the junction of the liner and die these layers of material were observed to increase and form dead metal zones. Fig 5.4.3 (b)&(c) illustrate schematically the various distributions of 'stationary' material produced from the use of different tooling configurations. As the die cone angle increased the sizes of the dead zones were found to increase, but the distortion fields were found to be dependent upon the combined configuration of the dead zone and tooling, i.e. the 'effective' dead zone size and shape, which increased as the die cone angle decreased.

The dead zone formation upon the tooling surfaces occurred so as to minimise the total energy associated with both the ideal and redundant work of deformation. For the shear face die situation, no boundary conditions were imposed upon the dead zone size and shape by the die configuration. Consequently, the most energy efficient dead zone size and shape were developed, resulting in the most desirable deformation paths, and the lowest extrusion load requirements. As the die cone angle increased, however, the tooling modified the ideal dead zone formation, causing a decrease in the 'actual' dead zone size, but an overall increase in the 'effective' dead zone size. This caused an alteration to the lowest energy flow pattern, hence an increase in extrusion load.

With regard to the changes in the extrusion load requirements brought about by changes in alloy composition, the experimental results obtained from the 8090 and 7075 extrusions only differed by 1%->8%, whilst the predicted results obtained from the finite element analysis differed by just 2->7%. The closeness of these results, together with the fact that no alloy composition was consistently harder to extrude than the other, suggested that the changes in the working characteristics of the extruding alloy had little effect upon the load requirements.

Temperature Fields

Temperature field predictions made by the finite element analysis for various tooling configurations are illustrated in fig 5.4.8. It was consistently observed that the temperature increased along any given flow line, resulting in concentric temperature profiles of equi-temperature bands centred around the die orifice. As a result of the absence of a steady state period of deformation, however, the average extrusion temperatures throughout the deformation zone and billet were predicted to increase slightly as extrusion proceeded, fig 5.4.8. (a)&(b). The temperature distributions shown are, therefore, only representative of the temperature fields for certain stages of

extrusion. Even though the specific temperature values increased slightly during extrusion, however, the general concentric character of the temperature field distributions was maintained for the majority of the extrusion process.

With regard to the effect of die cone angle upon temperature distributions, decreases in die cone angle were predicted to cause the general temperature levels throughout the deformation zone to increase, but again the concentric character of the temperature fields within the deformation zones was maintained.

The general picture of the predicted temperature distributions within the deformation zone has been highlighted above. In the extruded product, however, the microstructures present depended upon the deformation history of the extruded material. Some idea of the material movement through these temperature fields, and assessment of the average temperature experienced by the extruded material was, therefore, necessary in order to offer explanations for the relationship between extrudate microstructures and processing conditions. Fig 5.4.3 (c) illustrates schematically the general areas within the billet that produced the transverse and longitudinal sections within the extrudate. By consideration of both the flow patterns and temperature fields, therefore, it was obvious that simply equating the transverse and longitudinal temperature profiles within the deformation zone to the transverse and longitudinal temperature histories experienced by the extruded material was inaccurate.

For transverse sections within the extrudate, it appeared that the centrally located elements experienced very similar temperature histories. In the surface regions of the transverse section, however, the material closer to the outer extrudate surface was subjected to higher average temperature during extrusion.

For longitudinal sections within the extrudates, it appeared that the material further back in the extrudate was subjected to higher average temperatures.

Changes in die cone angle did not affect the general trend of the transverse and longitudinal variations in temperature history within the extrudate, but the specific average temperatures throughout the extrudate, particularly in the surface regions, appeared to be higher when the lower die cone angles were used. This tended, therefore, to cause slight increases in the levels of transverse and longitudinal temperature variations within the extrudates.

The above conclusions were highly subjective and involved consideration of many factors of flow and temperature. In order to provide some quantitative analysis of the temperature histories present within the extruded product, therefore, the computer program was modified in order to provide a cumulative temperature compensated strain rate. These results are discussed later.

Strain Rate Fields

Strain rate field predictions made by the finite element analysis for various tooling configurations are illustrated in fig 5.4.9.(a)->(d).

Typically it was forecast that along any given flow line, the strain rate increased from the rear of the billet to the die orifice. The greatest strain rate values were predicted in the regions adjacent to the tooling and die orifice, whilst minimum values were expected in the central regions at the back of the billet and within the dead zones. In the deformation zones, therefore, strain rate distributions consisting of consecutive equi-strain rate bands decreasing in intensity from a maximum at the die orifice were present.

As with the temperature fields, the strain rate distributions were predicted to vary throughout the extrusion stroke. The strain rate fields illustrated are, therefore, only truly representative of an incremental stage of extrusion. It was evident, however, that even though specific strain rate values varied with extrusion stroke, the general concentric banded character of the strain rate distributions was maintained for the majority of the extrusion process. Fig 5.4.9.(a)->(d) illustrate how the basic strain rate distributions were maintained during extrusion with only the strain rate values around the die orifice varying to any significant degree as the extrusion took place.

Even though the strain rate distributions associated with each extrusion remained relatively constant throughout the majority of the extrusion, changes in the strain rate distributions did occur as die cone angle increased. The general banded appearance of the strain rate field was present for all die cone angles, but in the surface regions of the deformation zone decreasing the die cone angle was predicted to cause higher levels of strain rate to be experienced further away from the die orifice. This consequently altered the entire strain rate distributions.

In order to establish the accuracy of the strain rate field predictions, produced by the finite element analysis, comparisons between the predicted strain rate fields and those obtained experimentally from the visioplasticity technique were carried out. Since it had previously been established that a true steady state period was not present during extrusion, it was important to compare the strain rate fields produced at the same stage of extrusion. With this in mind it was observed that the visioplasticity technique and finite element analysis consistently produced similar strain rate field distributions. The only significant differences between the strain rate evaluations occurred in the immediate vicinity of the die orifice, where the visioplasticity analysis produced lower strain rate values than those predicted by the finite element analysis. This may have been caused by distortion measurement error during the visioplasticity analysis. Overall, therefore, the strain rate distributions and changes with tooling configuration predicted by the finite element analysis were considered accurate, with only a small level of doubt associated with the specific values obtained in the immediate vicinity of the die orifice.

Even though the above analysis has highlighted the general strain rate distribution within the deformation zone and the final strain rate at exit, the microstructure within

the extruded product depended upon the deformation history experienced by the material. Some idea of the material movement through these strain rate fields and assessment of the average strain rate experienced by the extruding material was, therefore, necessary in order to explain the correlation between microstructure and processing.

Fig 5.4.3 illustrates the position of material in the billet that formed the transverse sections within the extrudates, together with a typical flow line distribution. By comparison of all these diagrams with the strain rate fields, it was considered that, in general, the maximum strain rates and average strain rates experienced by the extruded material increased towards the surface regions of the extrudate. Die cone increases were also considered to increase the average strain rates associated with the surface regions of the extrudates.

These conclusions concerning the average strain rate histories experienced by the extruded material were highly subjective. In order to provide some quantitative analysis of the deformation histories present within the extruded product, therefore, the computer program was modified in order to provide a cumulative temperature compensated strain rate.

Temperature Compensated Strain Rate

As already mentioned the extrudate microstructure depended upon the temperature and strain rate histories experienced by the extruded material. Some idea of the deformation histories endured by the extruded material was developed by correlation of the temperature and strain rate fields, with the material flow during extrusion. The conclusions produced from this type of analysis were highly subjective, however, hence in order to provide some quantitative results, the computer program was modified to provide values for the temperature compensated strain rate throughout the deformation zone and within the extruded product. Before the computer program was altered, however, it was necessary to determine whether the cumulative Z values, average Z values or maximum Z values should be calculated in order to best correlate the microstructure with processing conditions. Average Z values would be influenced by the specific strain rate and temperature values together with the time period over which the deformation took place. The final microstructure, however, may be best represented by the Z values present during the final period of deformation, or the max Z values present during extrusion -provided that deformation at these values occurred for a sufficient time period that microstructural development could take place. Identification let alone determination of the Z values most appropriately representing the extrudate microstructure was, therefore, very difficult. For convenience a cumulative Z value was calculated in this project.

The cumulative Z values calculated by the finite element analysis are illustrated in fig 5.4.10.(a)->(d).

For all stages of extrusion, throughout every extrudate, the cumulative Z values were observed to increase from the centre of the extrudates to the surface. This was due to the greater severity in strain rate history experienced by the surface regions. Higher temperatures were also associated with the edge regions of the extrudate, but these were not sufficient to prevent the increase in cumulative Z values.

It was also observed that for any given longitudinal section within the extrudates, the cumulative Z values initially increased and then subsequently decreased from the front of the extrudate to the rear. This initial increase in the cumulative Z values was due to increases in the level of distortion associated with the material forming the extrudates. Once the flow was established as relatively constant, however, the influence of higher temperatures upon the incremental Z values, caused the cumulative Z to subsequently decrease.

Even though transverse and longitudinal variations in the cumulative Z values occurred for all die cone angles, the magnitude of the Z values and their specific variations throughout the extrudate, were dependent upon die cone angle. As the die cone angle decreased, the magnitude of the cumulative Z values throughout the extrudates decreased. Decreasing the die cone angle also decreased the transverse and longitudinal difference in the cumulative Z values.

Decreasing the die cone angle consequently lowered the specific cumulative Z values associated with each elemental section within the extrudates, and decreased the difference between the various cumulative Z values.

5.4.5 Discussion and Conclusions

In this project the effect of die cone angle upon the deformation process was characterised by a number of different techniques. It was shown that the extrusion of machined gridded split billets provided little information concerning the effect of die cone angle upon the extrusion process, other than illustrating the flow changes occurring within the central regions of the deformation zone. More information on the distortion fields associated with the deformation process was obtained from visioplasticity techniques incorporating the use of gold wire meshes. This technique also enabled strain rate fields within the deformation zones to be identified. The amount of information obtained from this technique was limited by practical difficulties, however, but the results obtained together with extrusion load data did allow the applicability of the finite element analysis to the practical situation to be established. The finite element analysis provided the most extensive information regarding the extrusion process, producing temperature, strain rate and Z distributions, together with extrusion load predictions.

In any extrusion process the strain, strain rate and temperature fields associated with each extrusion are influenced by:- (1) Tooling configurations.

(2) Friction conditions.

(3) Material deformation characteristics.

(4) Extrusion temperature and ratio.

Even though under the action of the imposed boundary and process conditions it was the material deformation characteristics that caused the observed strain, strain rate and temperature fields, it was found that the differences in the deformation characteristics between the 7075 and 8090 material did not affect load requirements, strain rate fields or temperature fields to any significant extent.

With regard to friction conditions 'sticking' friction was associated with each extrusion, which resulted in the presence of stationary material adjacent to all tooling surfaces and caused:-

(i) Continual modification of the flow pattern during extrusion, particularly in the surface regions of the deformation zone.

(ii) Maximum strains to occur in the outer regions of the deformation zone.

(iii) Circular flow at the rear of the extrudate, due to the scraping of the material from the tooling by the ram.

As a result, for any given set of process and tooling conditions, the analysis revealed the temperature profiles within the deformation zones of each extrusion to be characterised by concentric bands of decreasing temperature centred about the die orifice. The specific temperatures associated with each band increased as extrusion continued, but the general temperature distribution was maintained throughout the stroke. Strain rate values within the deformation zone were also predicted to decrease along the flow lines from a maximum at the die orifice. The resulting bands of equi-strain rate were not, however, as concentric about the die orifice as the temperature distributions.

As the extrusion temperature was increased the general temperature levels within the deformation zone naturally increased, but the concentric character of the temperature field were maintained. Also, as expected, changes in the tooling configurations significantly altered the material flow path. This in compliance with the fact that material flow occurred by the lowest energy input route given the prevailing boundary conditions caused the dead zone sizes and shapes to alter. As the die cone angle decreased, the energy requirements for extrusion increased, causing the extrusion load to increase and the general temperatures reached for a given stage of extrusion to rise. The modification in flow also caused the strain rate distribution and the specific strain rate values to alter.

All these changes in flow and subsequent changes in temperature and strain rate, caused the material in the extruded product to experience different processing histories.

From observation of the temperature and strain rate fields within the deformation zone and comparison with the material flow through these fields, it appeared that decreases in the die cone angle caused:-

(i) Increases in the general temperature levels throughout the deformation zone.

(ii) Increases in the average temperatures experienced by the material forming the extruded product.

(iii) Increases in the average temperature differences between the centre and surface of the extrudates.

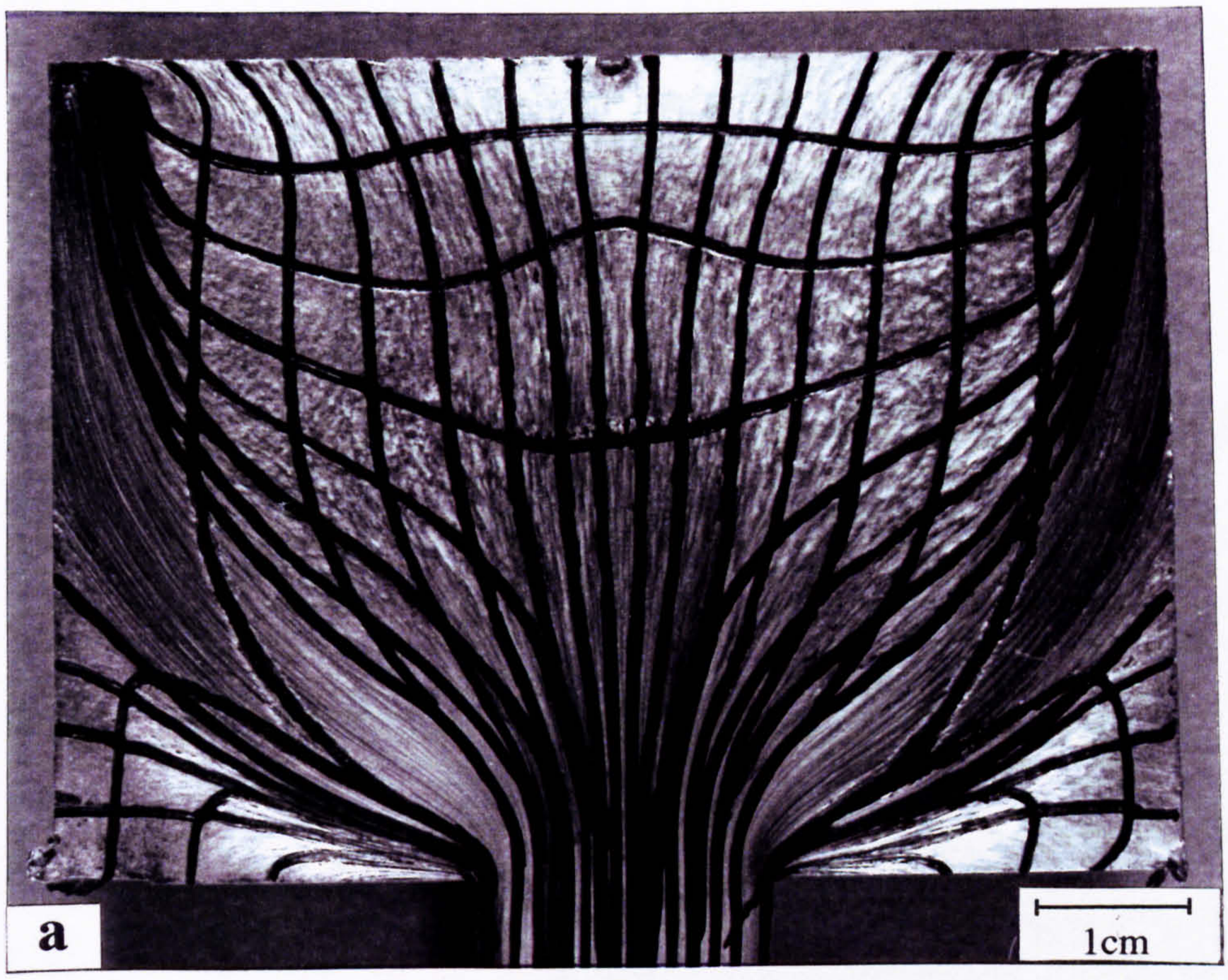
(iv) Higher levels of strain rate to be experienced at greater distances from the die orifice, particularly in the surface regions of the deformation zone.

(V) Increases in the average strain rate experienced by the material forming the extruded product

(vi) Increases in the average strain rate differences between the centre and surface regions of the extrudate.

(vii) Decreases in the specific cumulative Z values associated with each elemental section within the extrudates.

(viii) Decreases in the difference in the cumulative Z values between each elemental section within the extrudates.



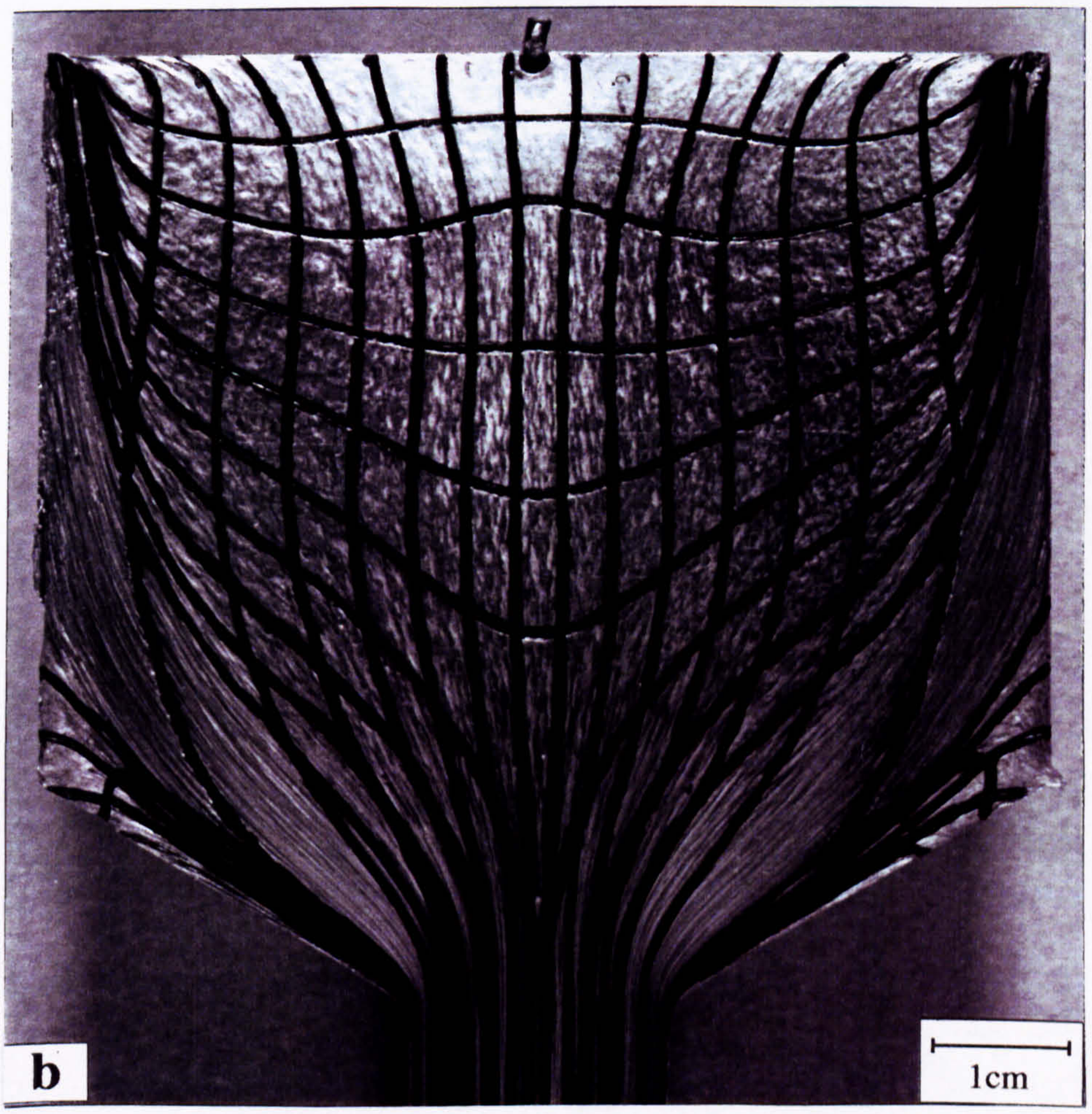


Fig 5.4.1 Distortion Patterns obtained from extrusion of machine gridded split billets at 430 °C.
(a) 90° Die Cone Angle.
(b) 60° Die Cone Angle

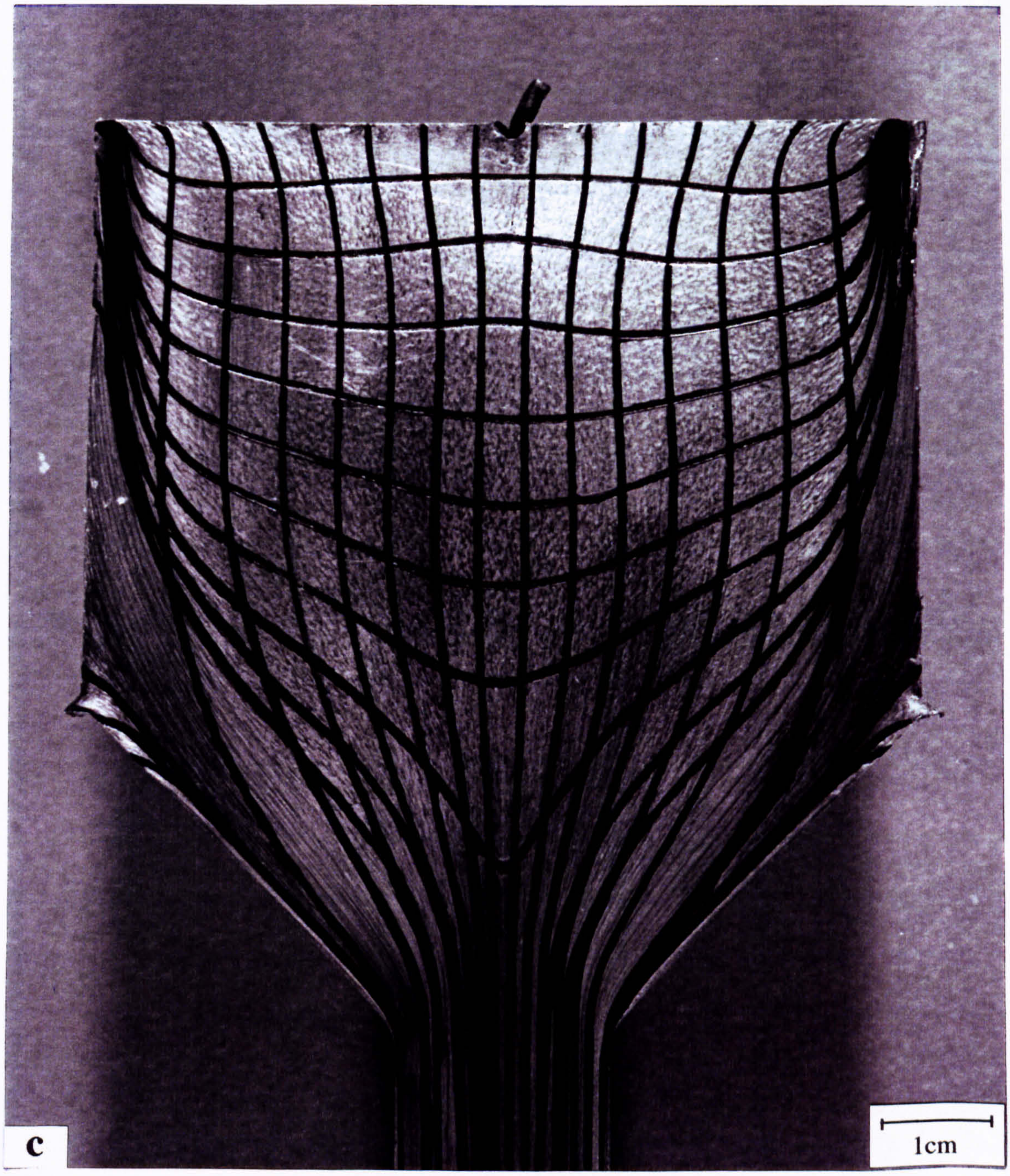


Fig 5.4.1 Distortion Patterns obtained from extrusion of machine gridded split billets at 430 °C. (c) 45° Die Cone Angle.

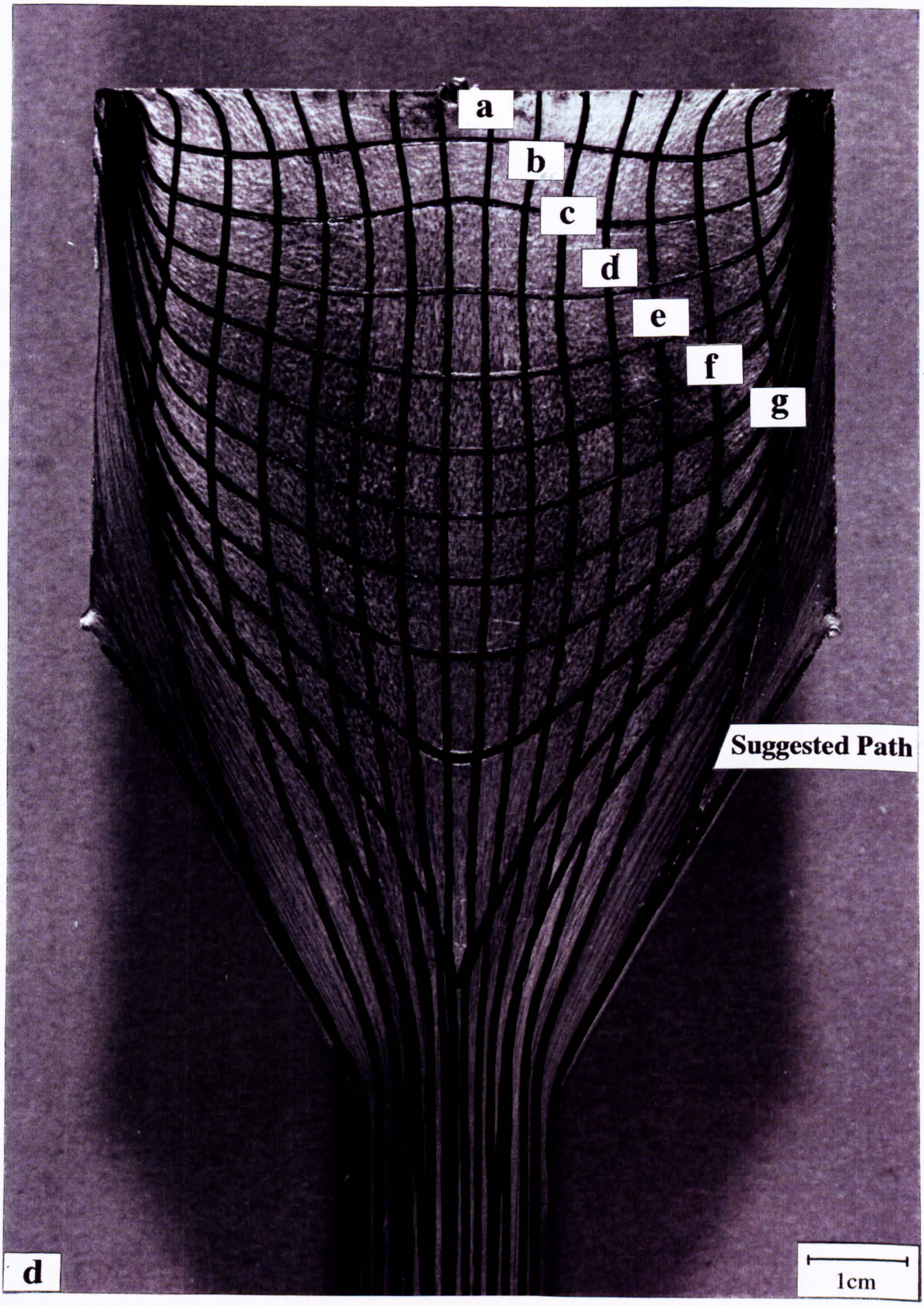
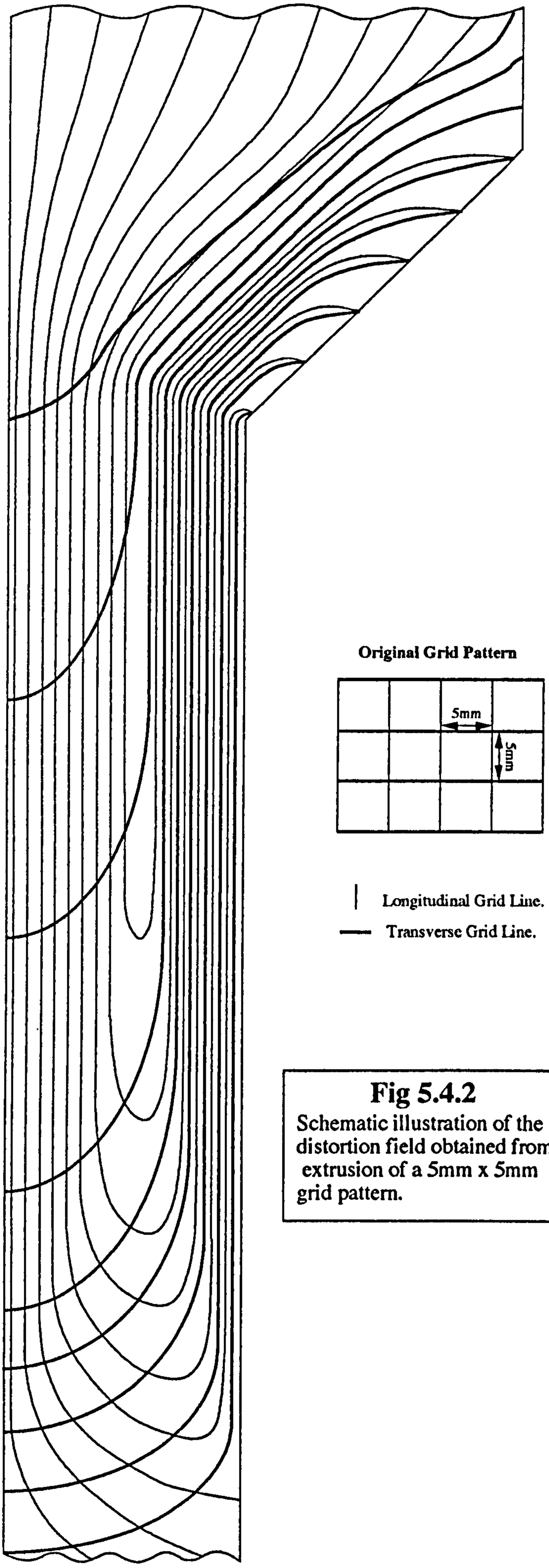


Fig 5.4.1 Distortion Patterns obtained from extrusion of machine gridded split billets at 430 °C. (d) 30° Die Cone Angle.

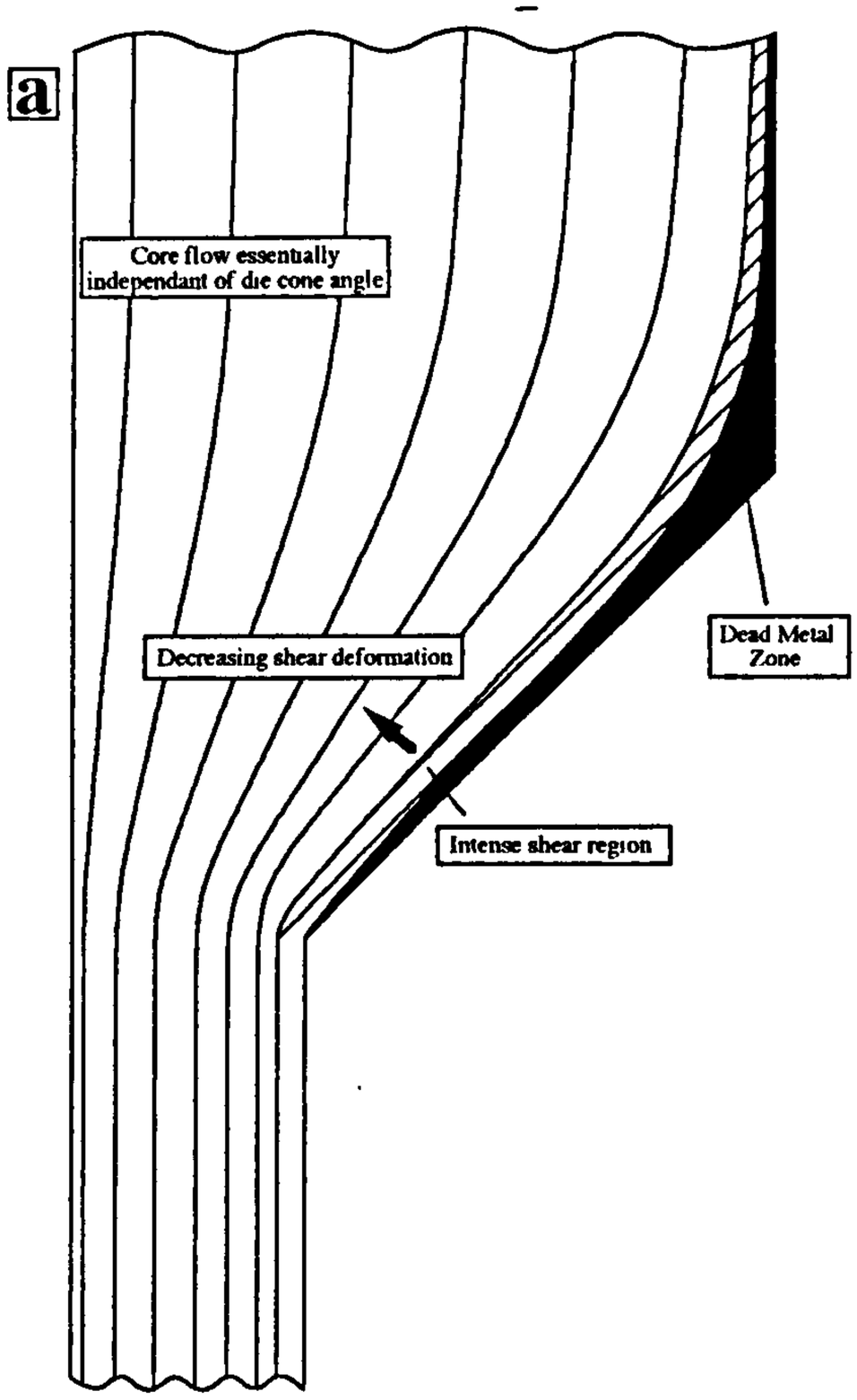


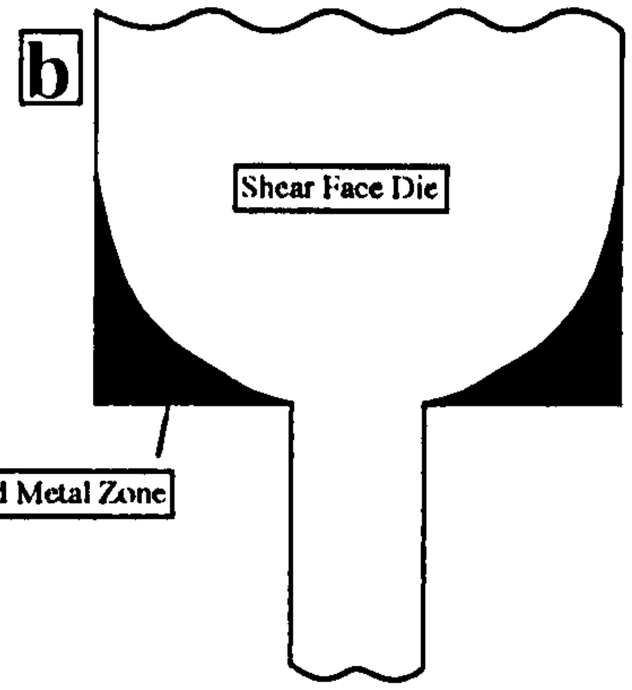
Original Grid Pattern

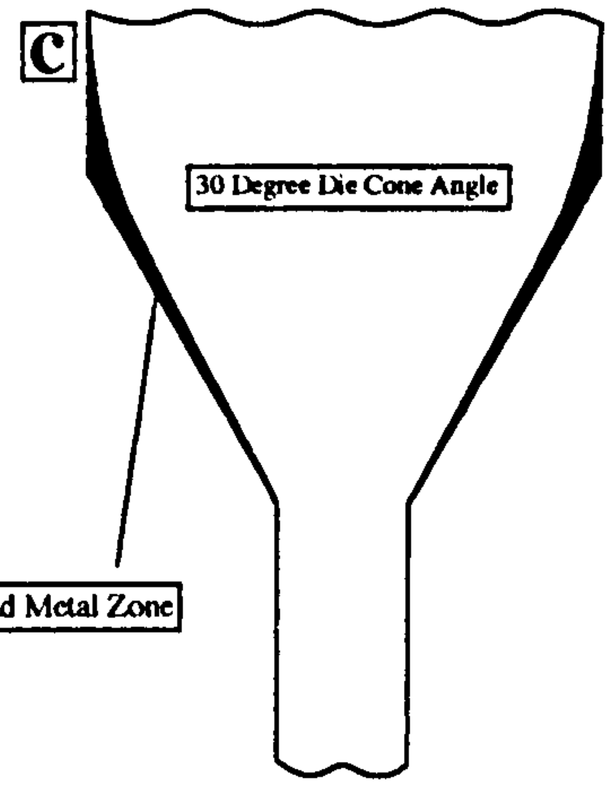
| Longitudinal Grid Line.

— Transverse Grid Line.

Fig 5.4.2
Schematic illustration of the distortion field obtained from extrusion of a 5mm x 5mm grid pattern.







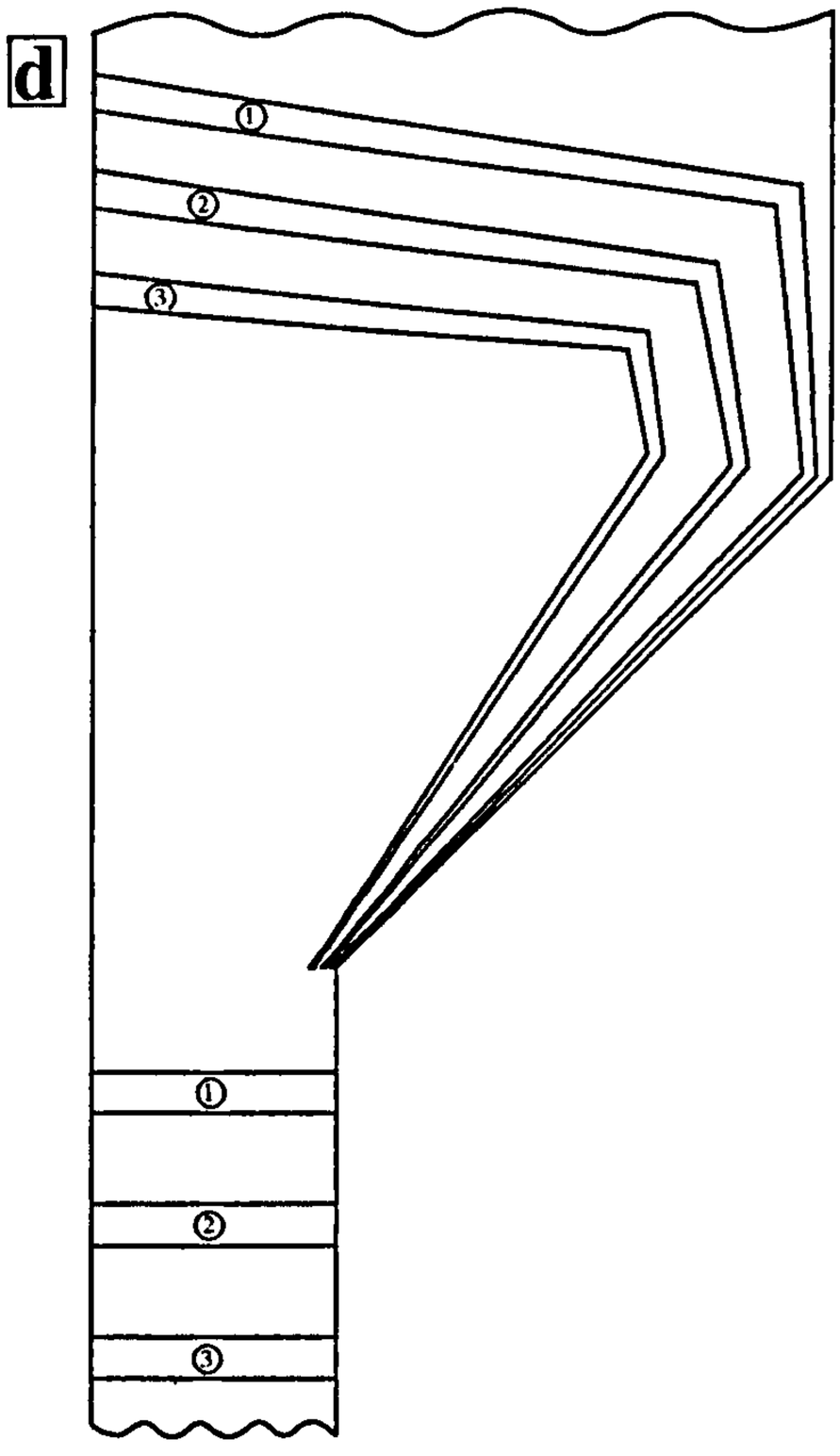


Fig 5.4.3

(a), (b) & (c) Schematic illustrations of the variation in dead metal zone formation as the die cone angle altered.
(d) Schematic relating the relative material positions in the deformation zone, with the transverse and longtiudinal sections within the extrudate.

a

	400°C Extrusion Temp	430°C Extrusion Temp			500°C Extrusion Temp
	Experimental	Experimental	Predicted	% difference	Experimental
30° Die Cone Angle	329	315	310	-2%	260
45° Die Cone Angle	296	285	290	+2%	222
60° Die Cone Angle	278	268	265	-1%	203
90° Die Cone Angle	260	248	240	+1%	185

b

	430°C Extrusion Temp		
	Experimental	Predicted	% difference
30° Die Cone Angle	331	317	-4%
45° Die Cone Angle	297	270	-9%
60° Die Cone Angle	266	253	-5%
90° Die Cone Angle	230	249	+8%

c

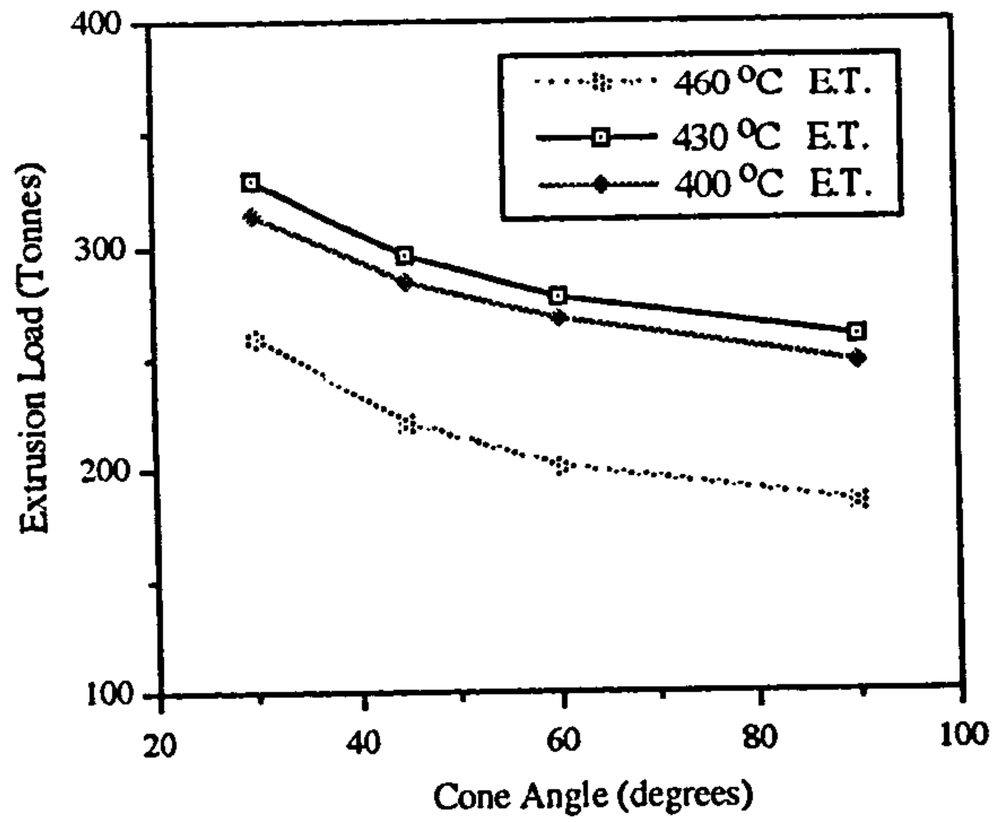
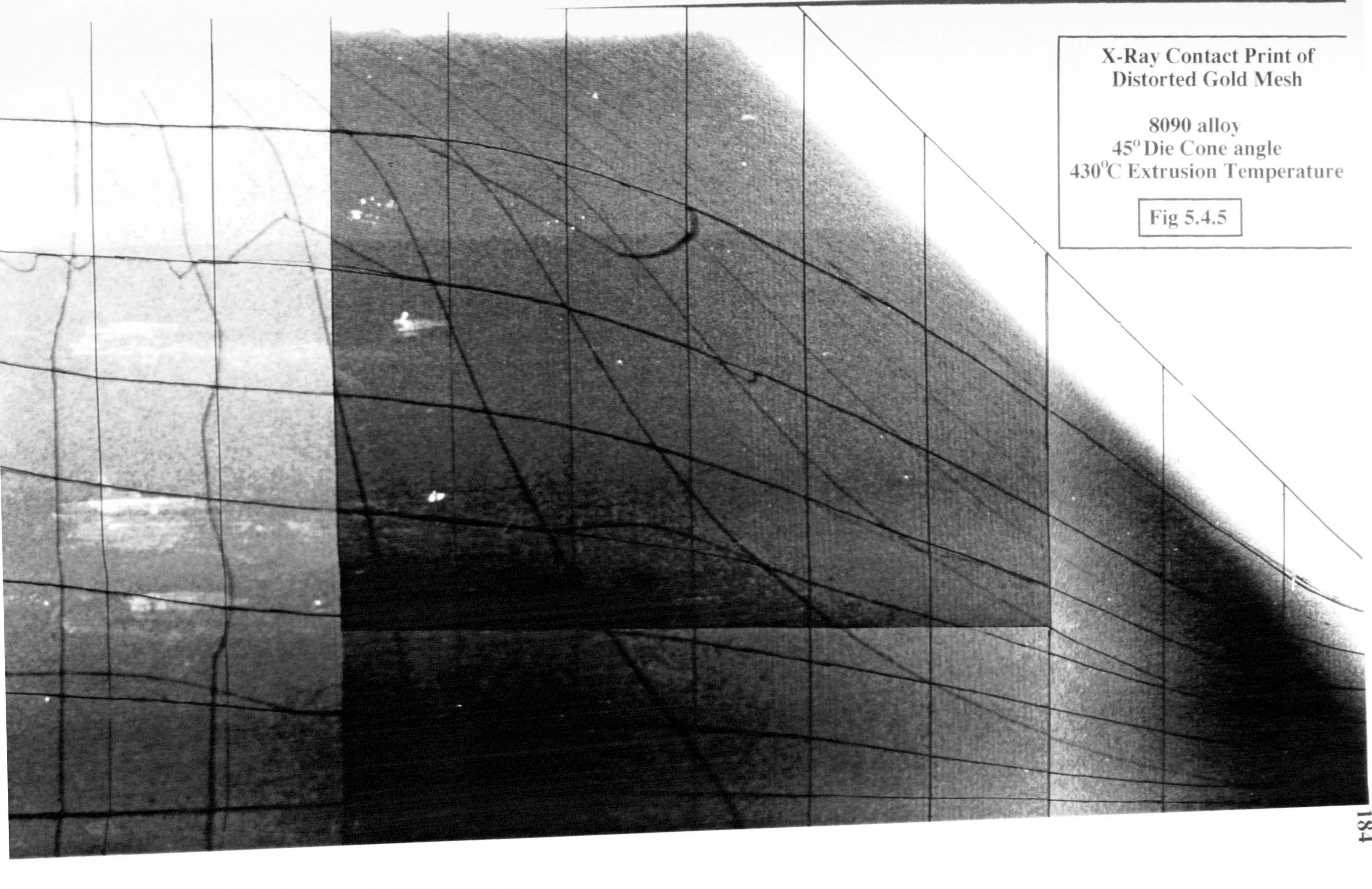


Fig 5.4.4

Variation in experimental and predicted extrusion loads (tonnes) with changes in processing conditions.
(a) Variation in the experimentally obtained and theoretically predicted extrusion loads as die cone angle and extrusion temperature were varied. 8090 alloy extrusions.
(b) Variation in the experimentally obtained and theoretically predicted extrusion loads as die cone angle increased. 7075 alloy extrusions.
(c) Graphical representation of the variations in extrusion load as die cone angle increased. 8090 extrudates.



X-Ray Contact Print of Distorted Gold Mesh

8090 alloy
45° Die Cone angle
430°C Extrusion Temperature

Fig 5.4.5

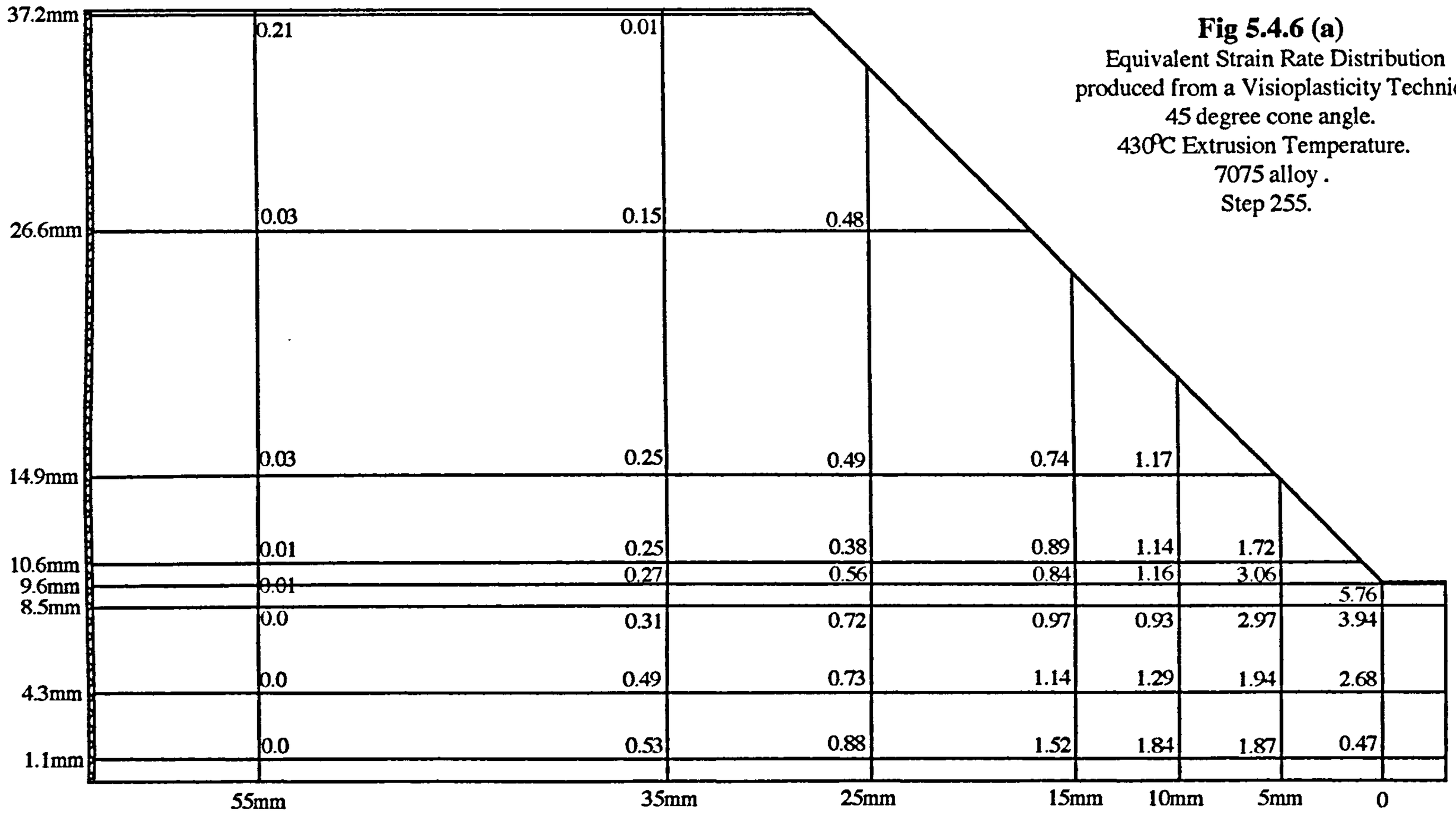


Fig 5.4.6 (a)
Equivalent Strain Rate Distribution
produced from a Visioplasticity Technique.
45 degree cone angle.
430°C Extrusion Temperature.
7075 alloy .
Step 255.

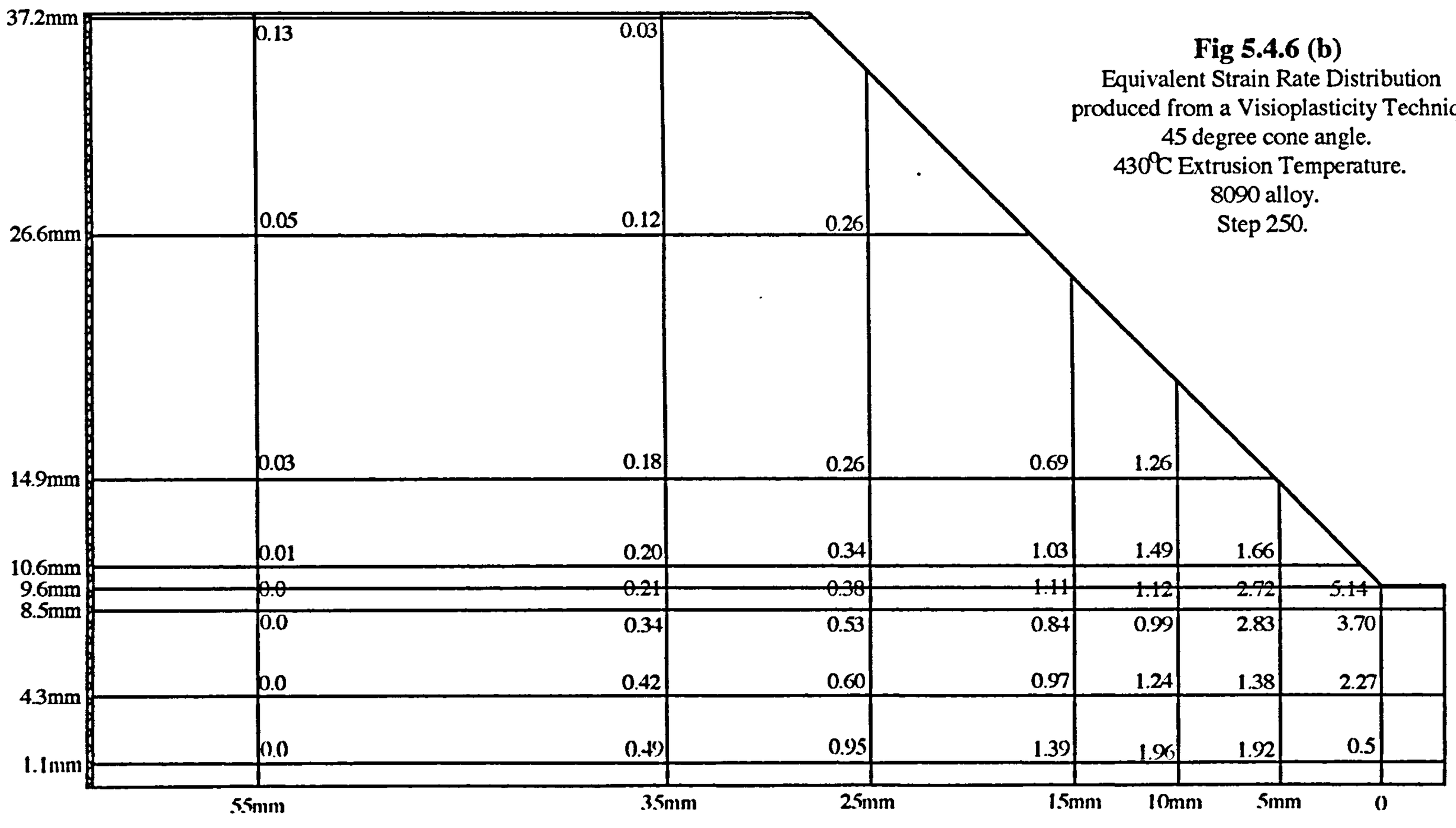


Fig 5.4.6 (b)
Equivalent Strain Rate Distribution
produced from a Visioplasticity Technique.
45 degree cone angle.
430°C Extrusion Temperature.
8090 alloy.
Step 250.

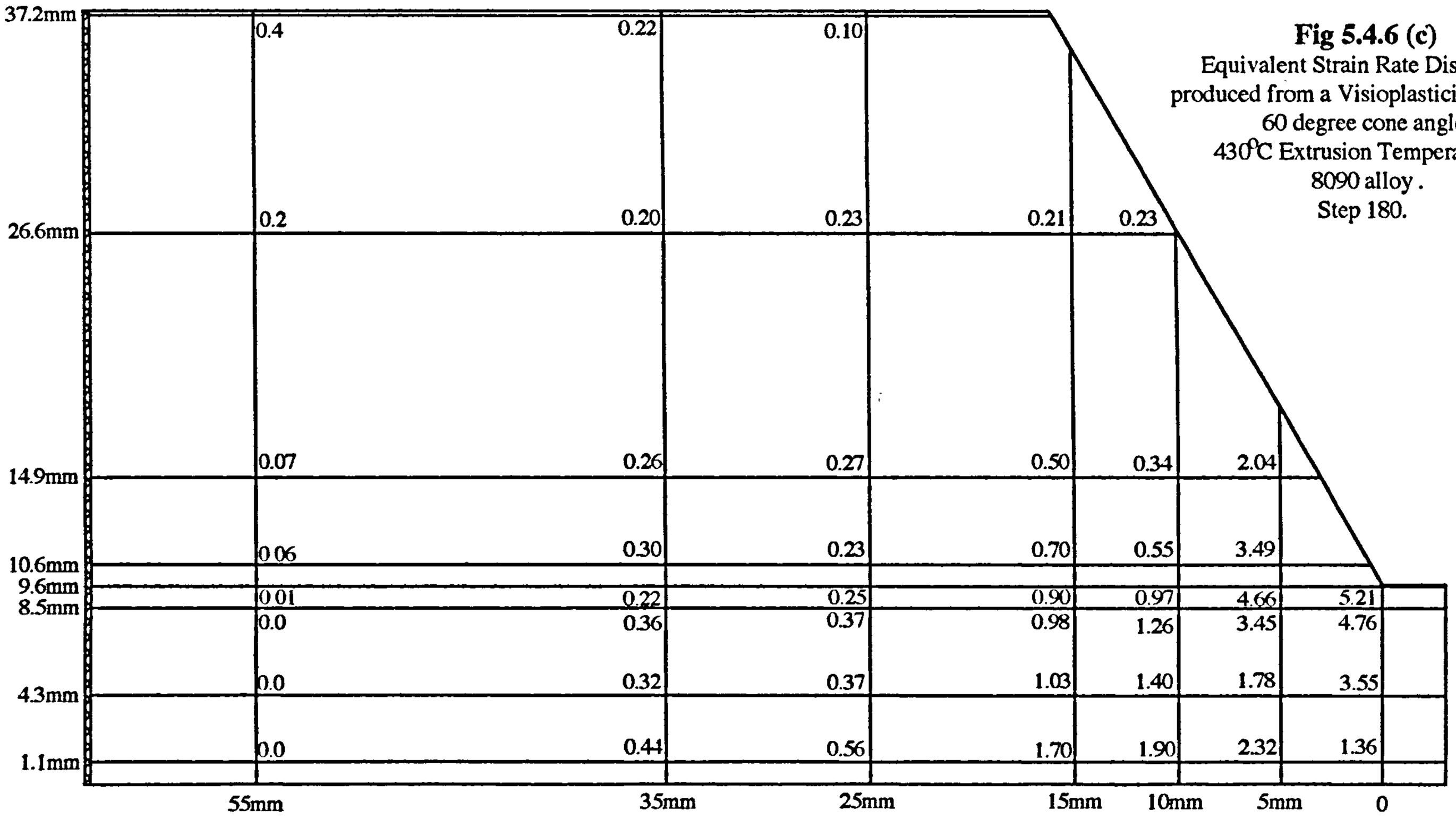
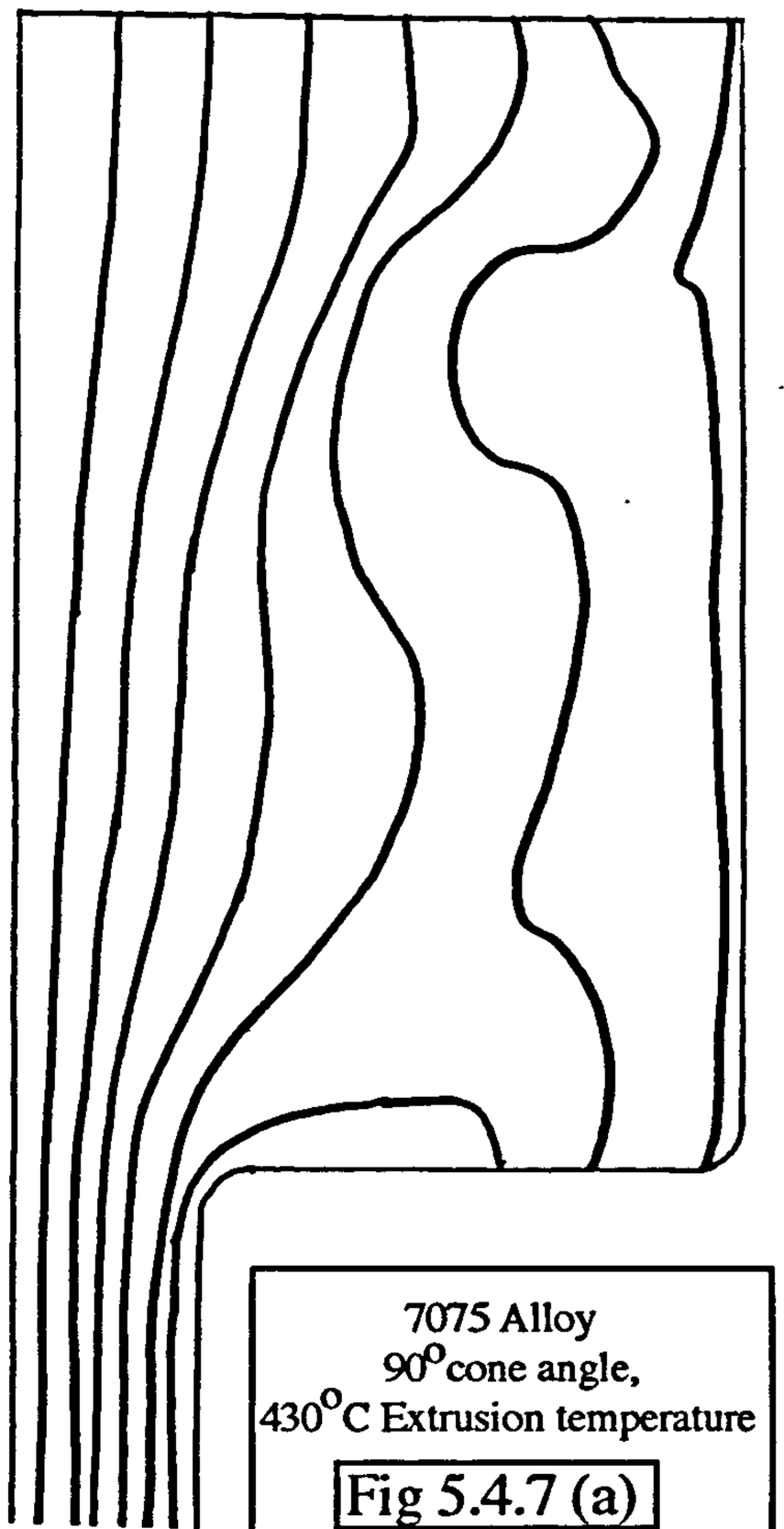
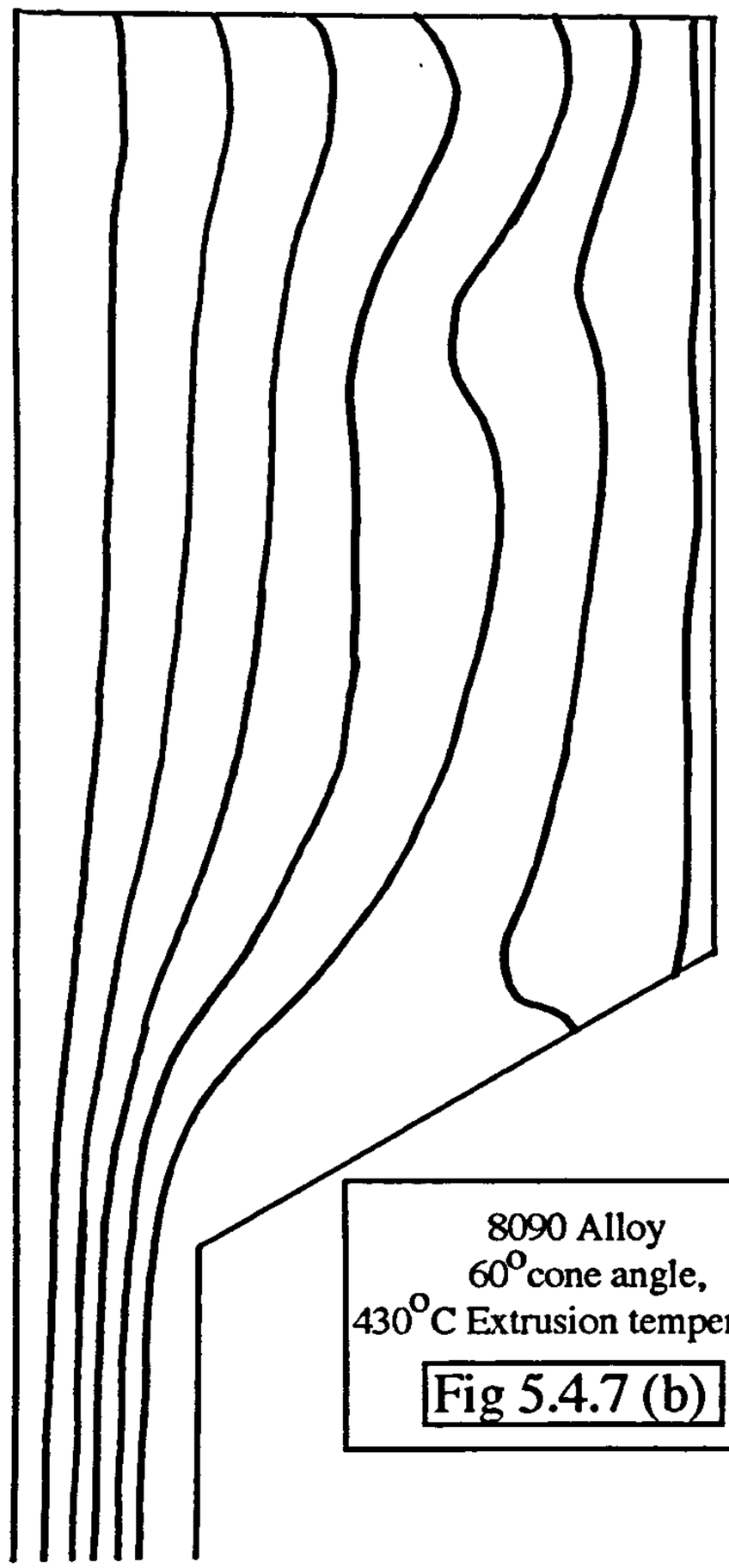


Fig 5.4.6 (c)
Equivalent Strain Rate Distribution
produced from a Visioplasticity Technique.
60 degree cone angle.
430°C Extrusion Temperature.
8090 alloy .
Step 180.



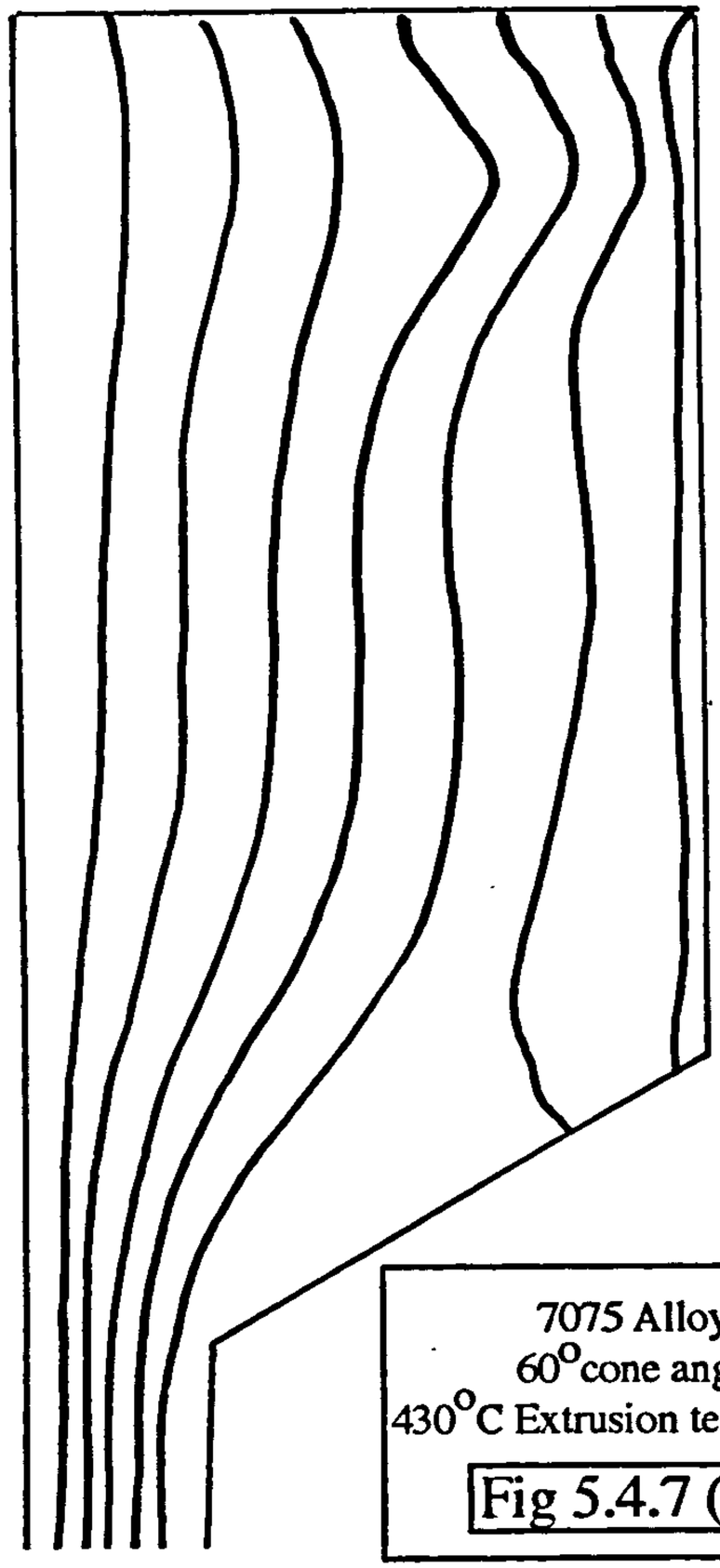
7075 Alloy
90°cone angle,
430°C Extrusion temperature

Fig 5.4.7 (a)



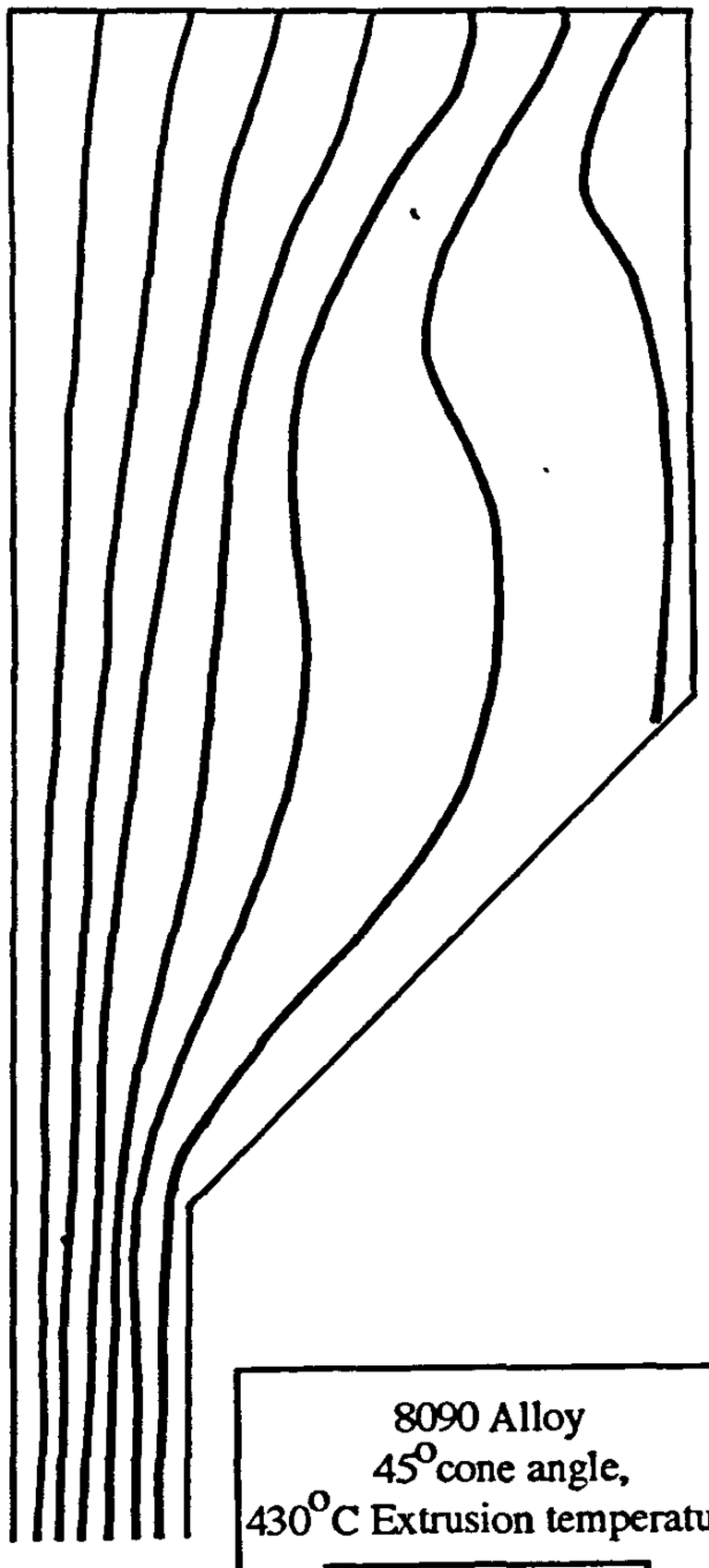
8090 Alloy
60°cone angle,
430°C Extrusion temperature

Fig 5.4.7 (b)



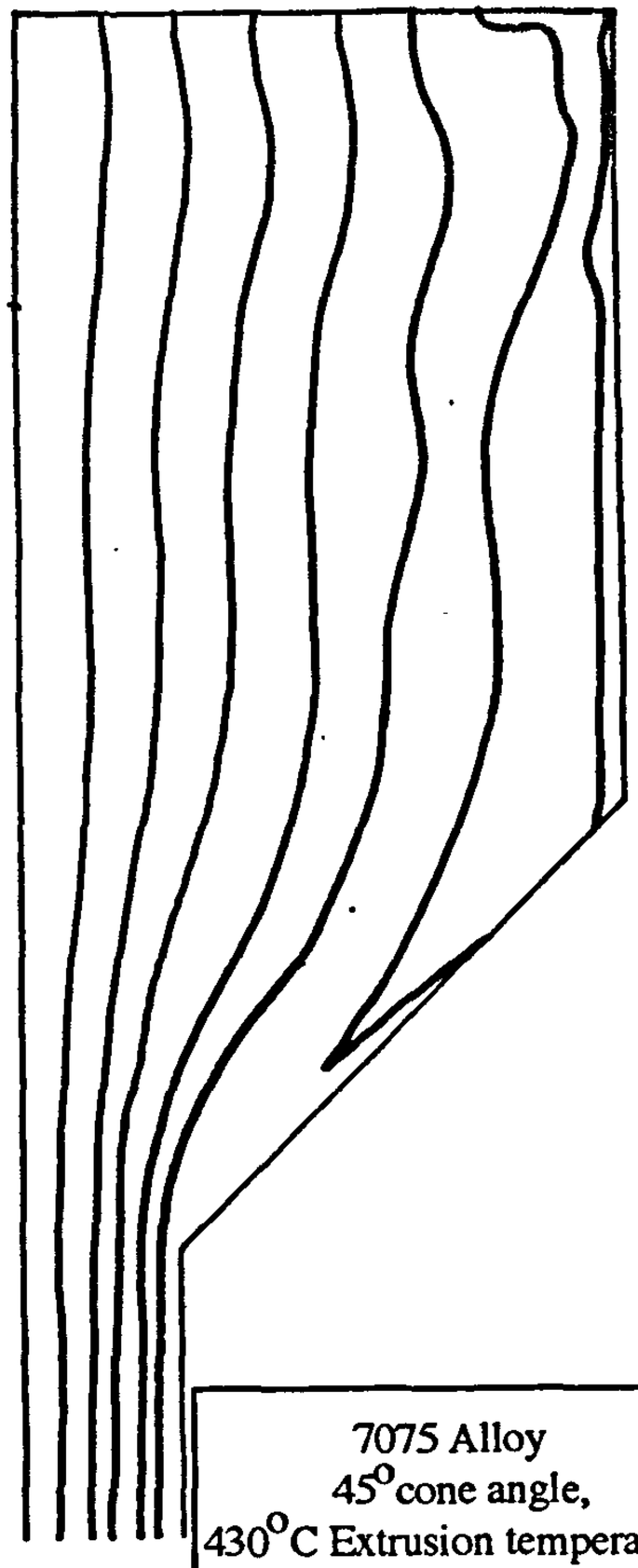
7075 Alloy
60°cone angle,
430°C Extrusion temperature

Fig 5.4.7 (c)



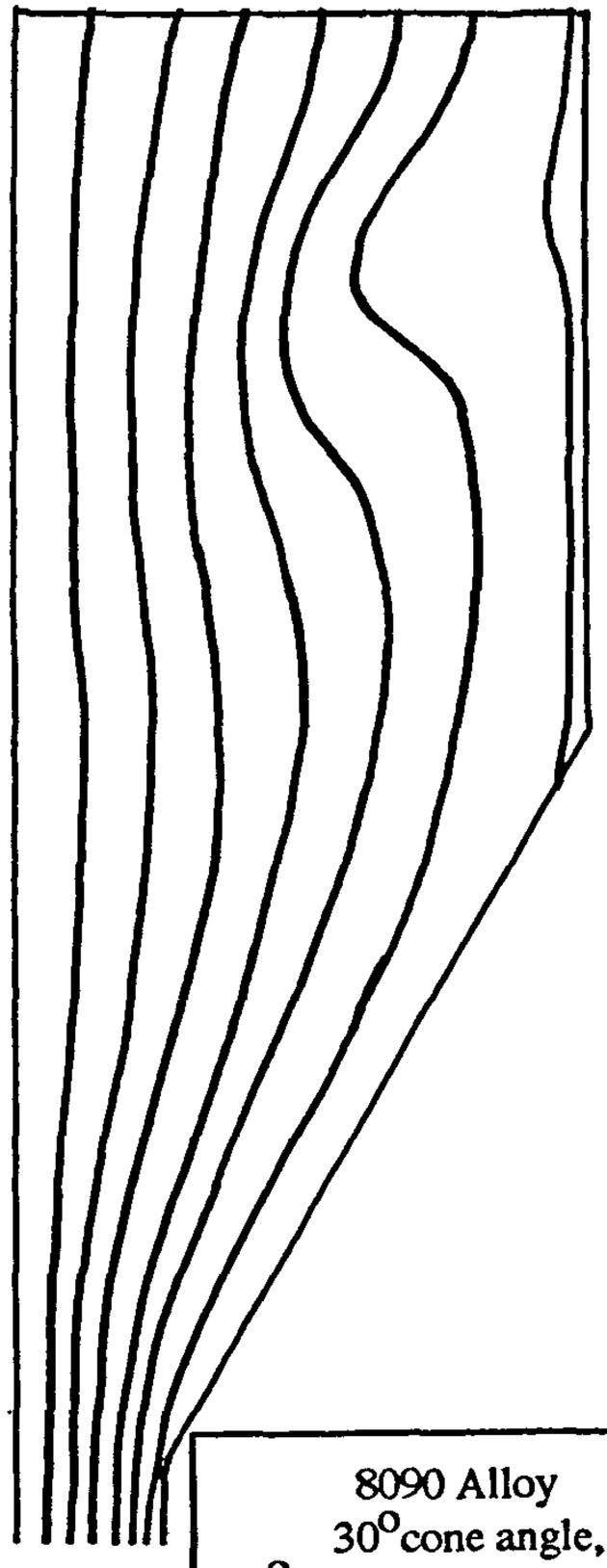
8090 Alloy
45°cone angle,
430°C Extrusion temperature

Fig 5.4.7 (d)



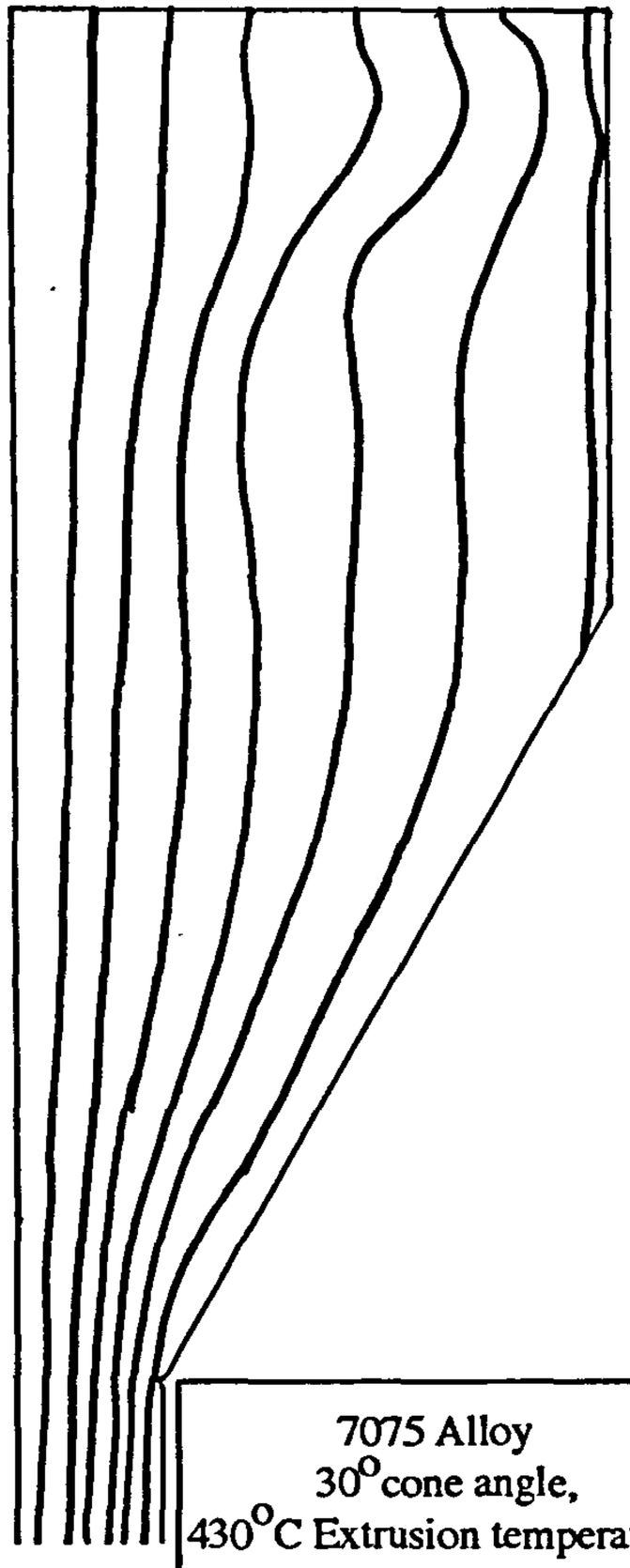
7075 Alloy
45°cone angle,
430°C Extrusion temperature

Fig 5.4.7 (e)



8090 Alloy
30°cone angle,
430°C Extrusion temperature

Fig 5.4.7 (f)



7075 Alloy
30°cone angle,
430°C Extrusion temperature

Fig 5.4.7 (g)

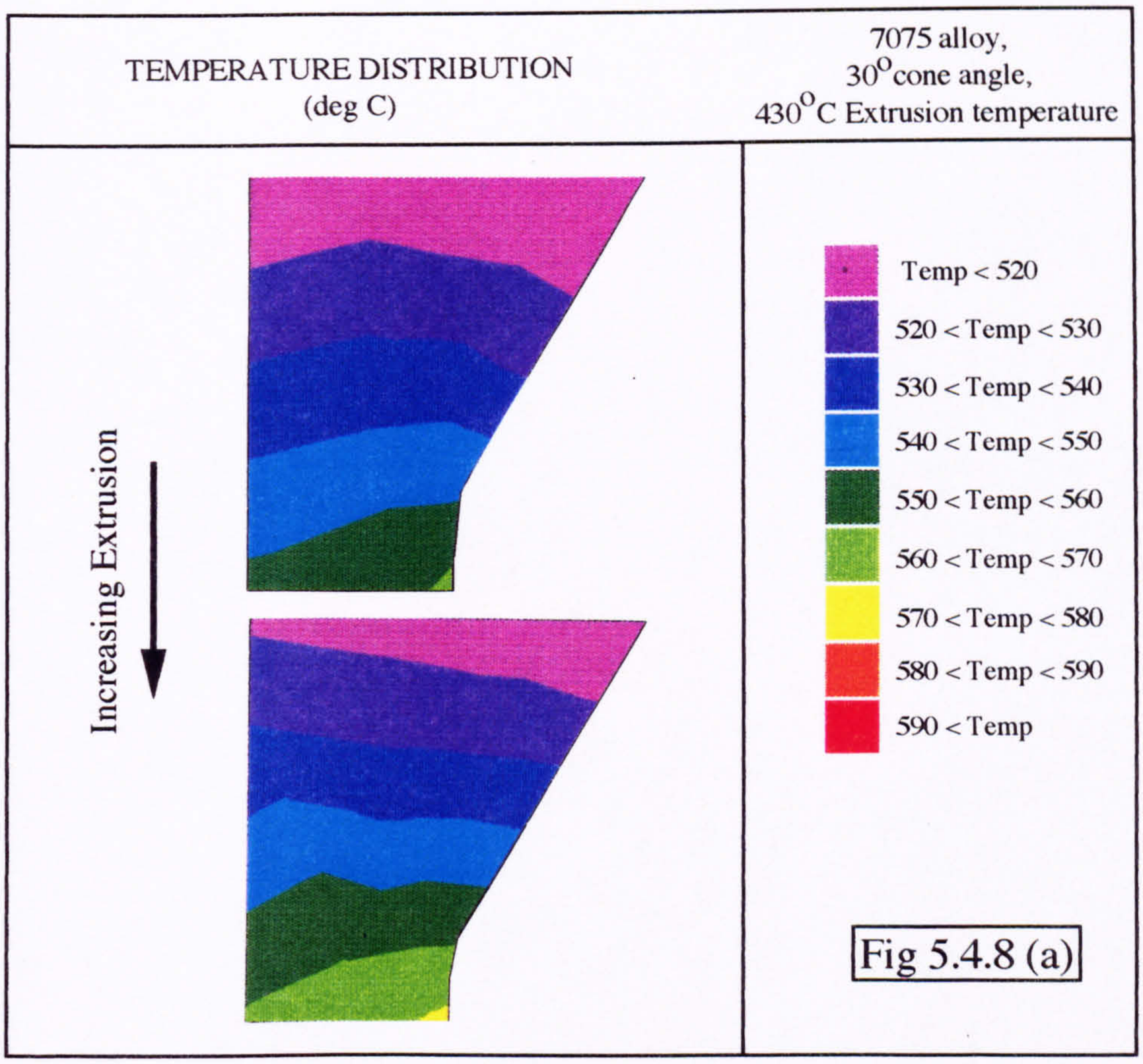


Fig 5.4.8 (a)

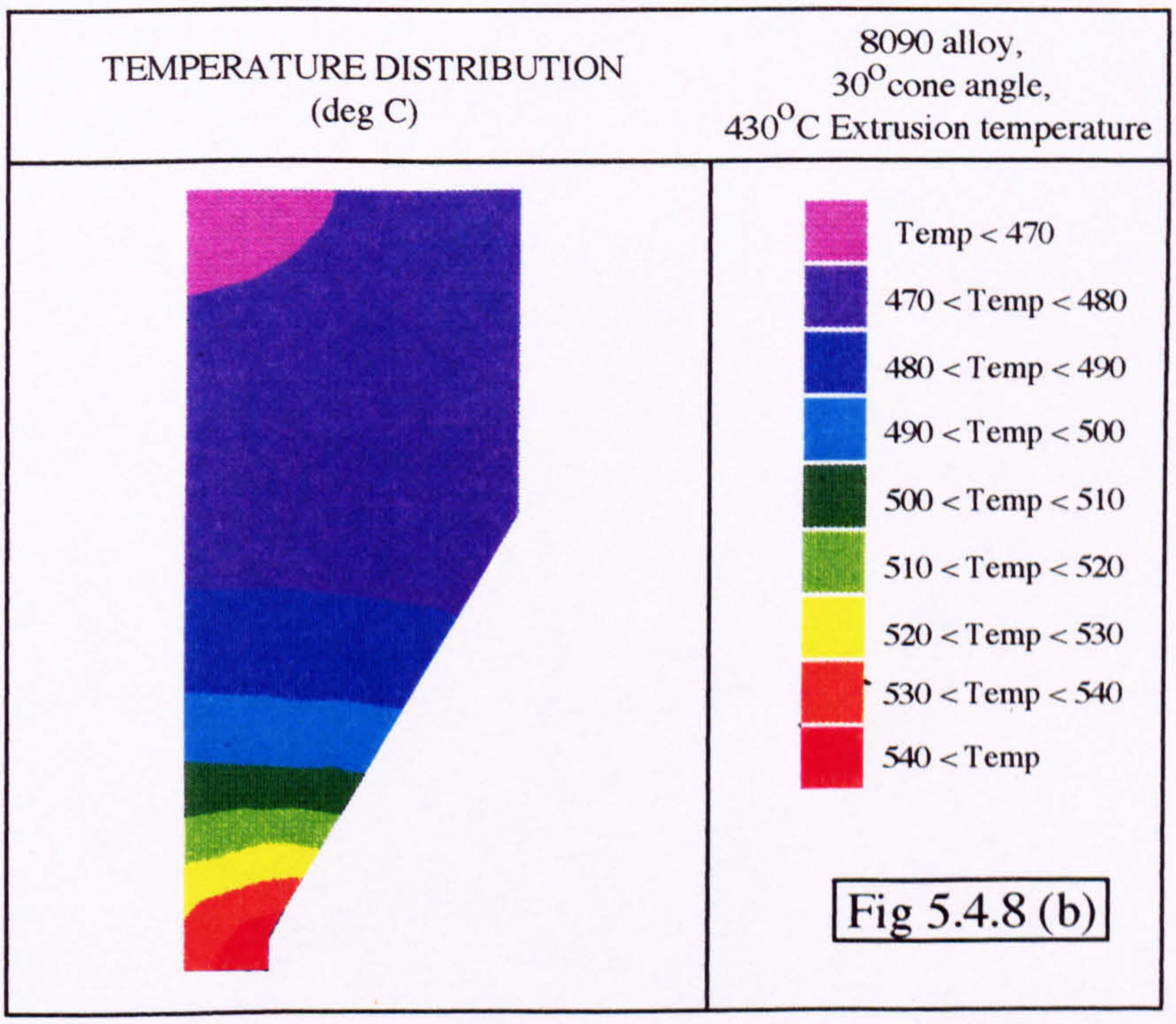


Fig 5.4.8 (b)

191

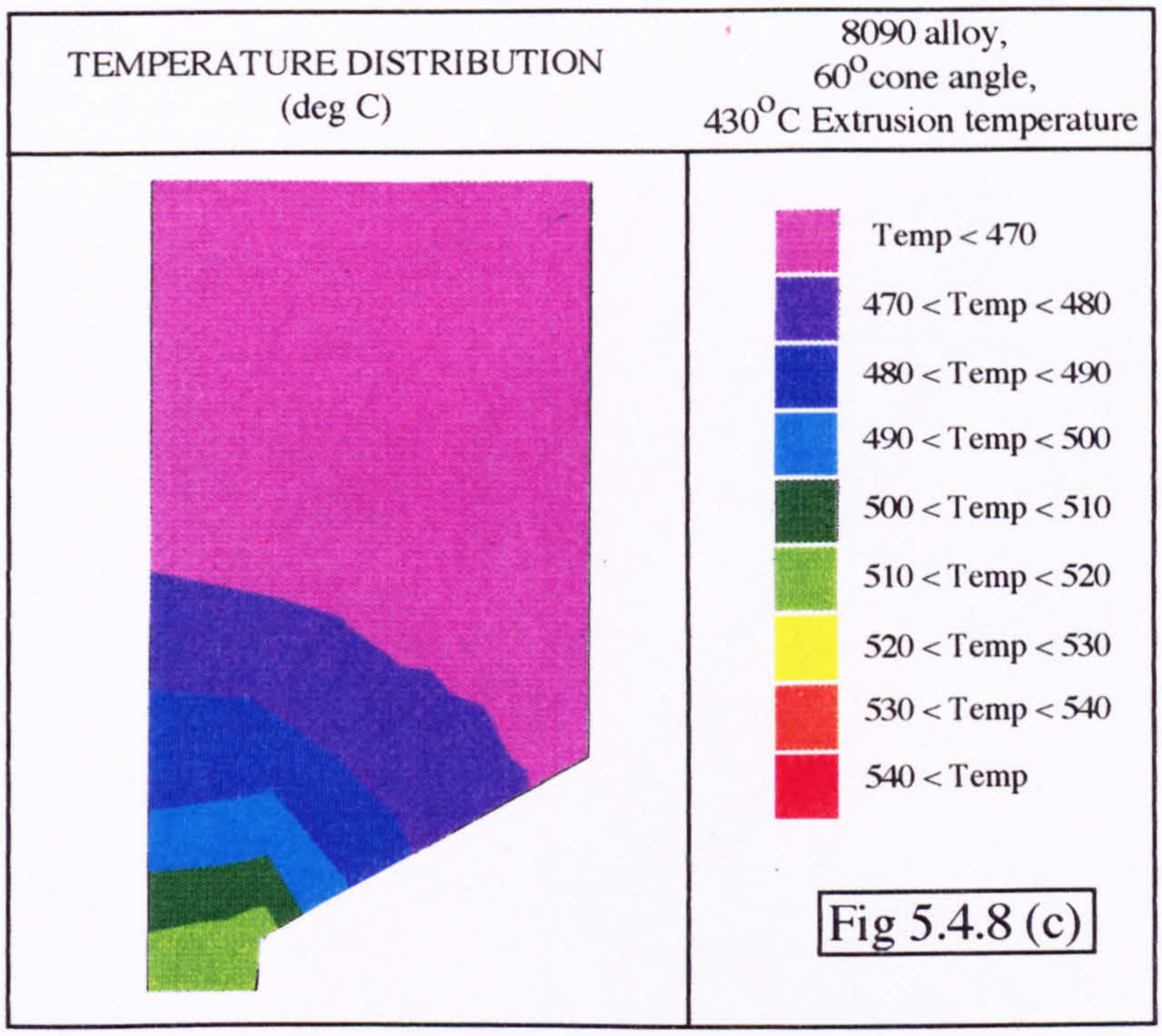


Fig 5.4.8 (c)

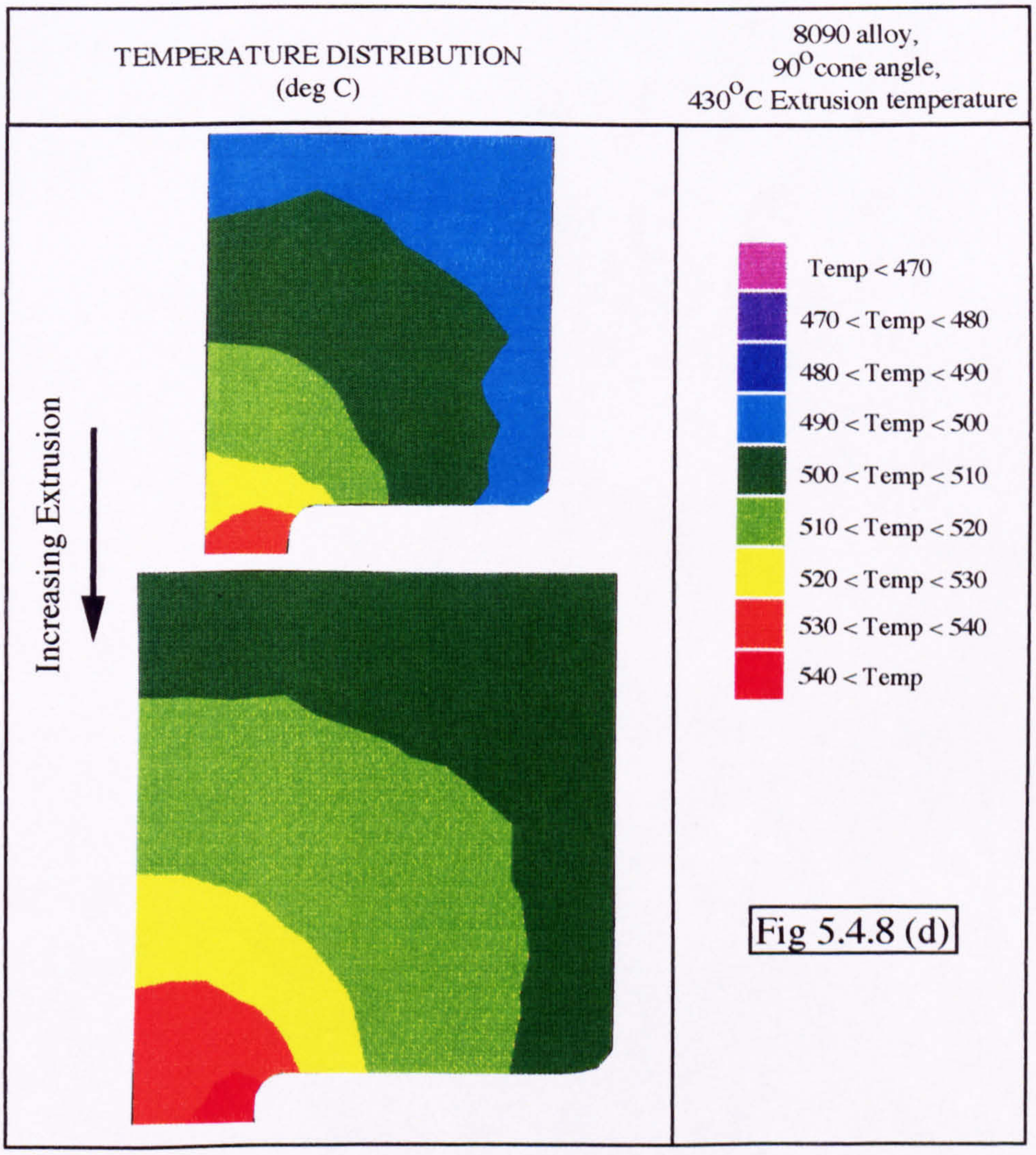
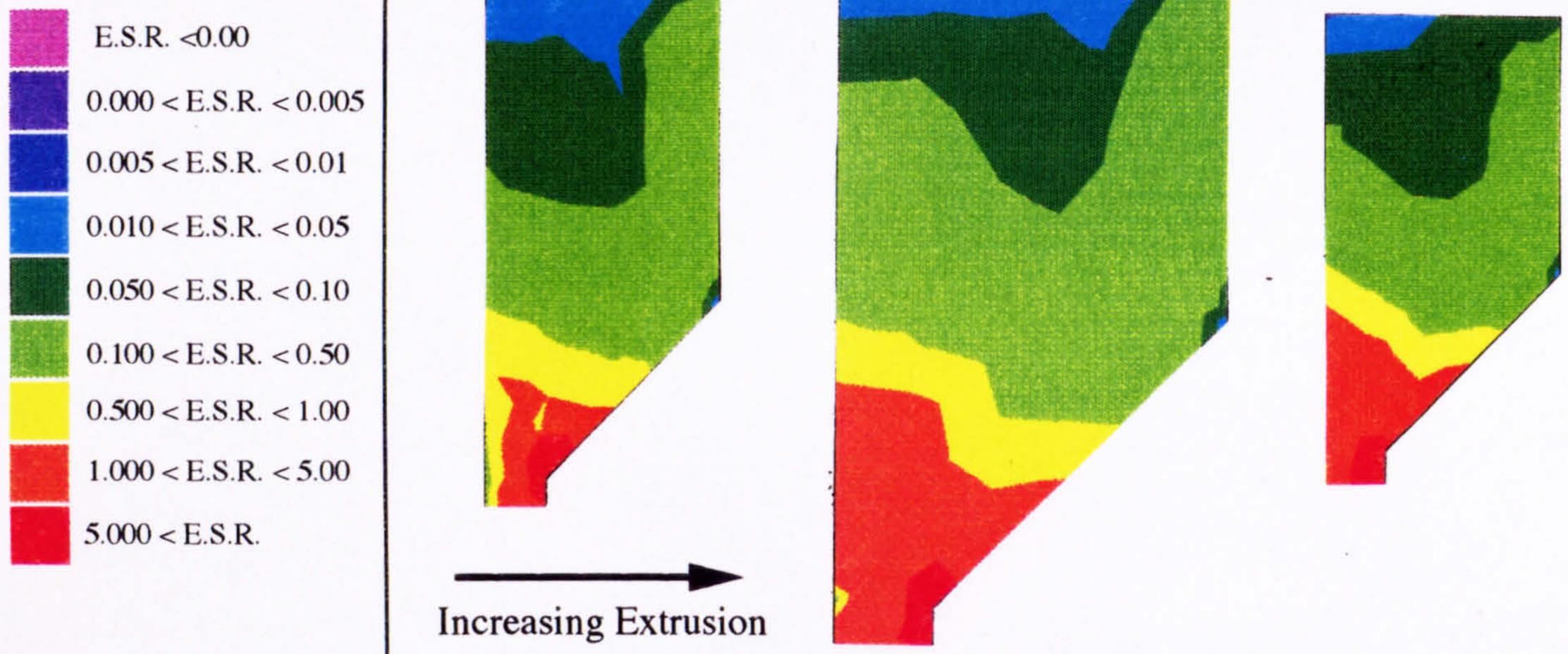


Fig 5.4.8 (d)

EQUIVALENT STRAIN RATE
(E.S.R.)
(SEC-1)

8090 alloy,
45°cone angle,
430°C Extrusion temperature

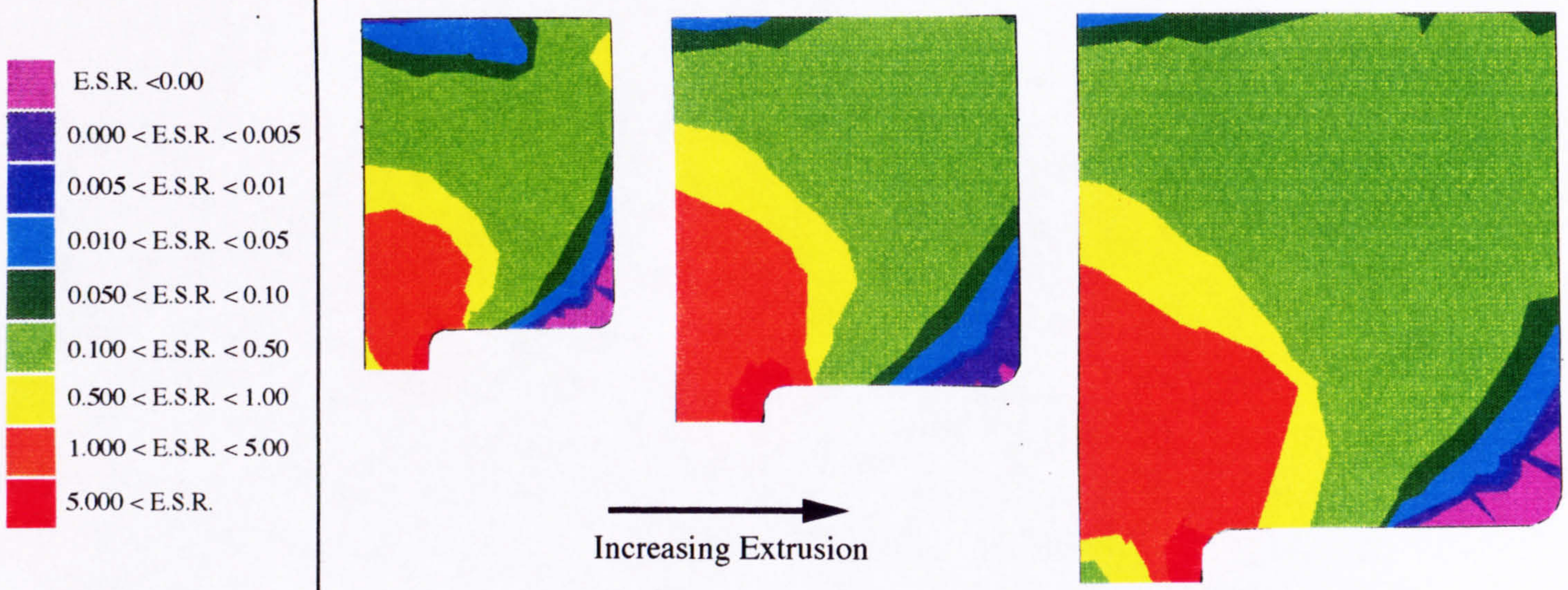
Fig 5.4.9 (a)



EQUIVALENT STRAIN RATE
(E.S.R.)
(SEC-1)

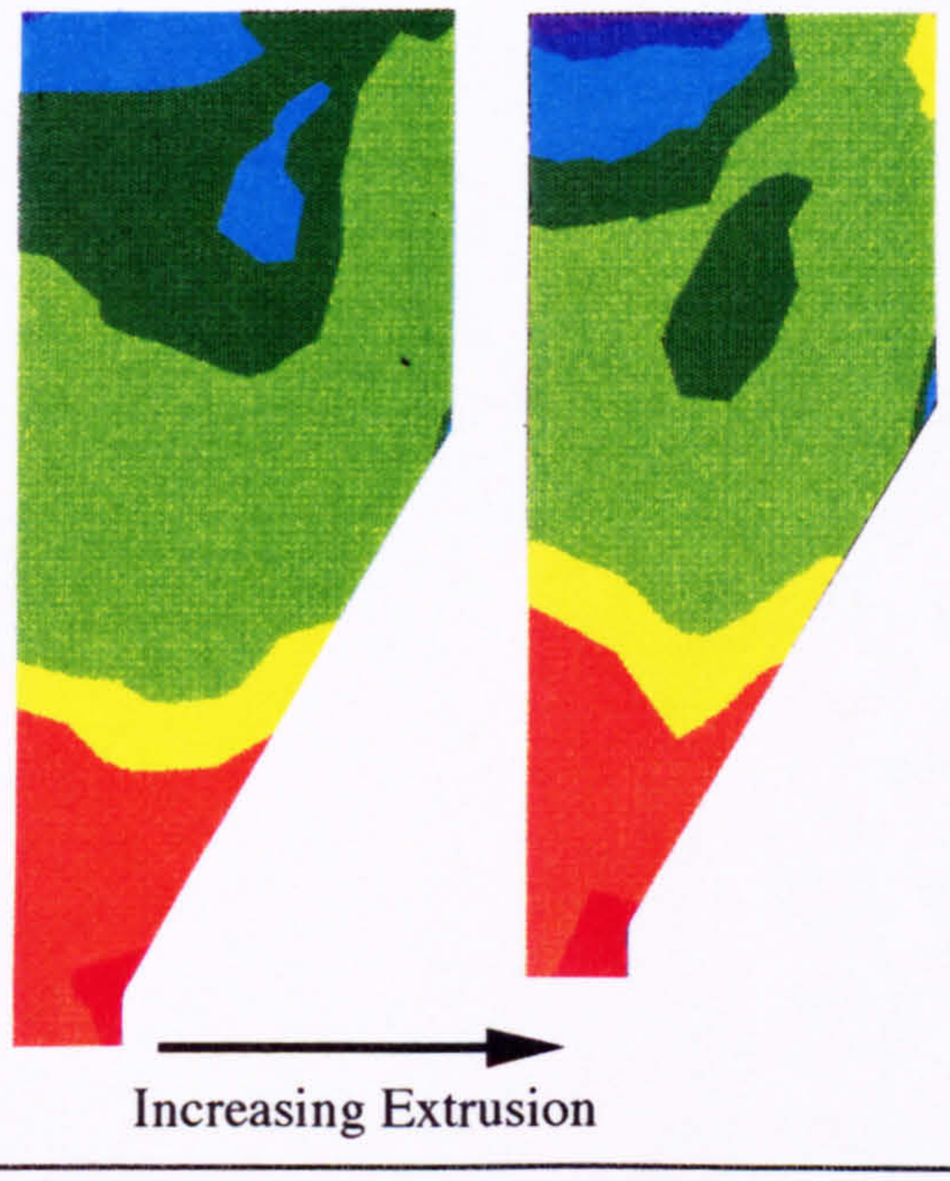
8090 alloy,
90°cone angle,
430°C Extrusion temperature

Fig 5.4.9 (b)



EQUIVALENT STRAIN RATE (E.S.R.)
(SEC-1)

8090 alloy,
30°cone angle,
430°C Extrusion temperature

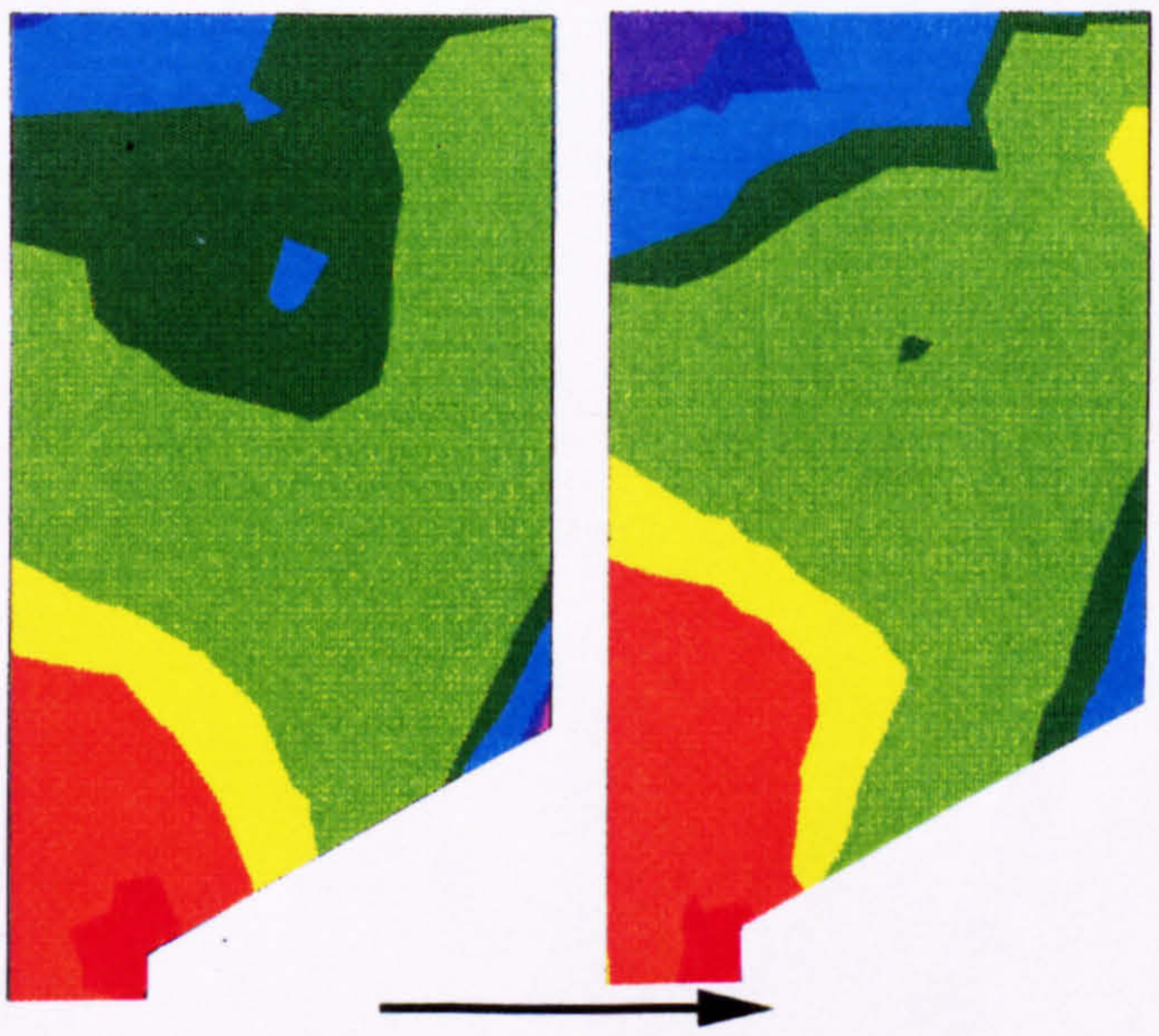


E.S.R. <0.00
0.000 < E.S.R. < 0.005
0.005 < E.S.R. < 0.01
0.010 < E.S.R. < 0.05
0.050 < E.S.R. < 0.10
0.100 < E.S.R. < 0.50
0.500 < E.S.R. < 1.00
1.000 < E.S.R. < 5.00
5.000 < E.S.R.

Fig 5.4.9 (c)

EQUIVALENT STRAIN RATE (E.S.R.)
(SEC-1)

7075 alloy,
60°cone angle,
430°C Extrusion temperature



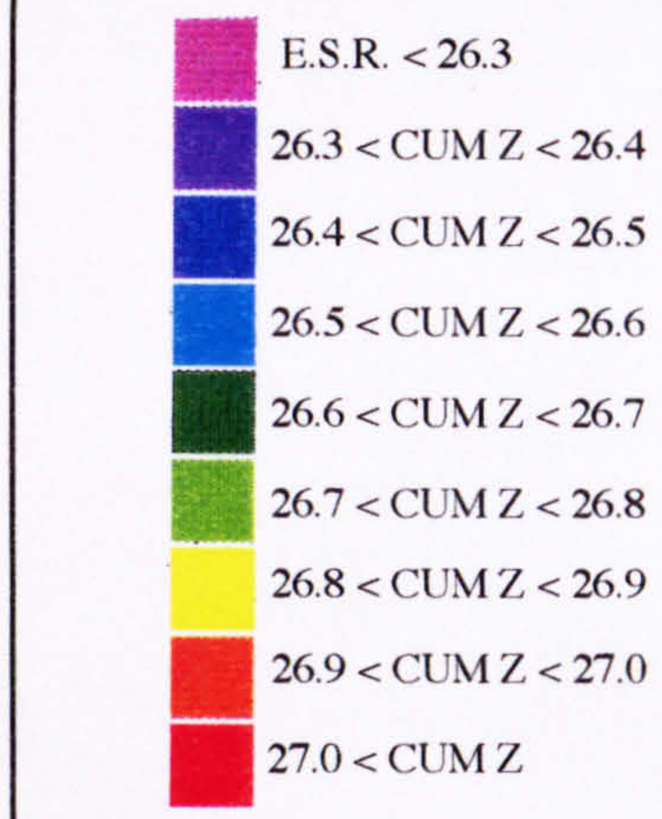
E.S.R. <0.00
0.000 < E.S.R. < 0.005
0.005 < E.S.R. < 0.01
0.010 < E.S.R. < 0.05
0.050 < E.S.R. < 0.10
0.100 < E.S.R. < 0.50
0.500 < E.S.R. < 1.00
1.000 < E.S.R. < 5.00
5.000 < E.S.R.

Fig 5.4.9 (d)

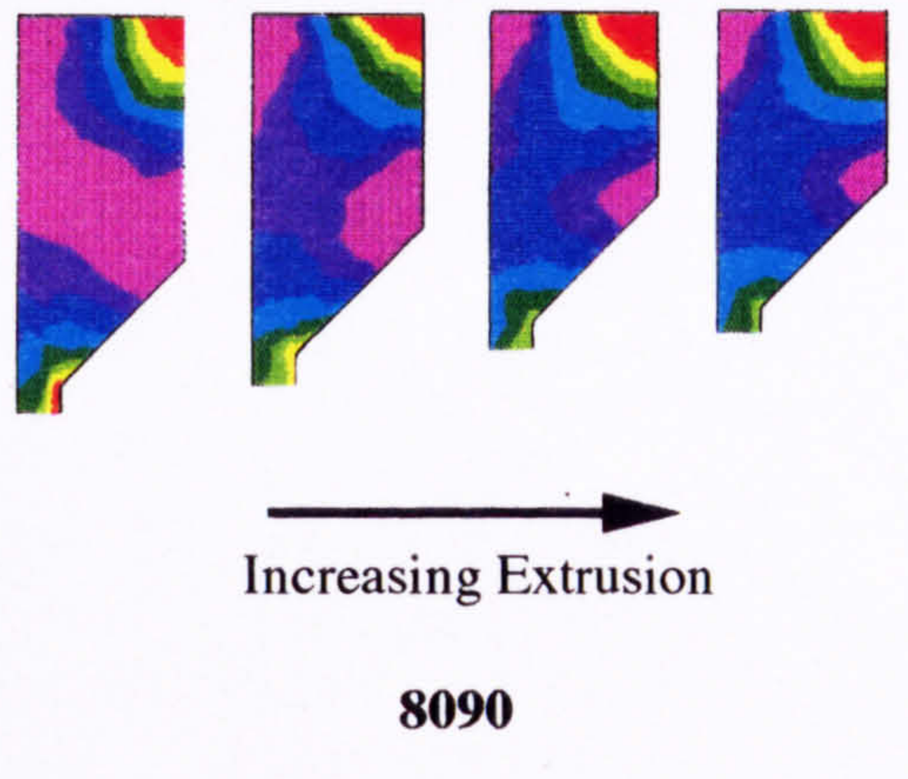
CUMULATIVE Z VALUE DISTRIBUTIONS

45°cone angle,
430°C Extrusion temperature

Fig 5.4.10 (a)



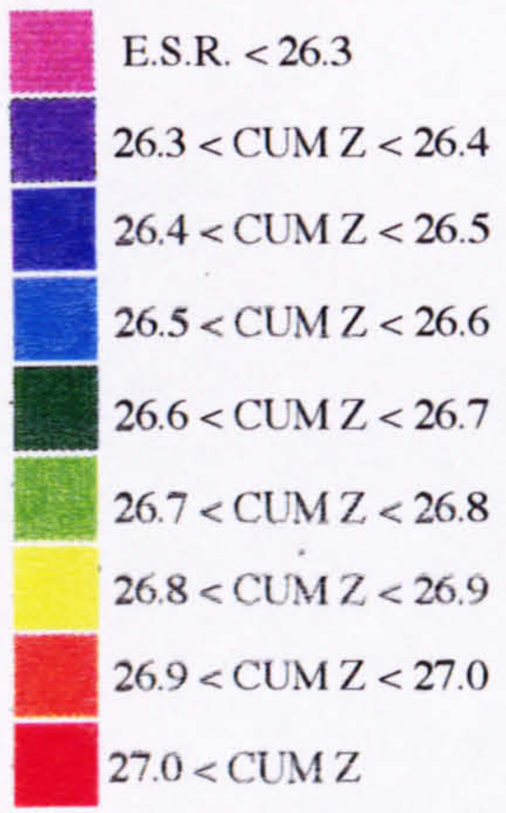




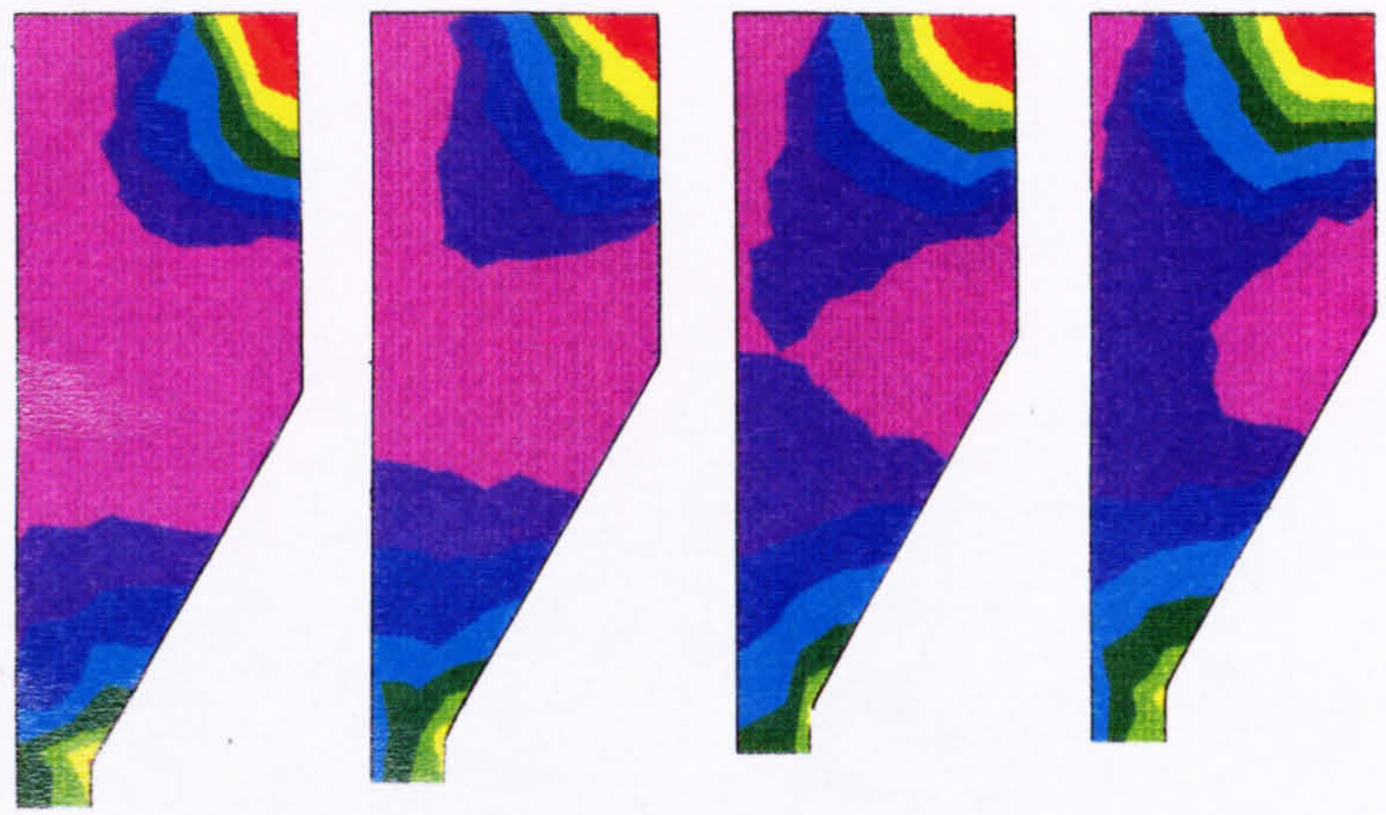
CUMULATIVE Z VALUE DISTRIBUTIONS

30°cone angle,
430°C Extrusion temperature

Fig 5.4.10 (b)





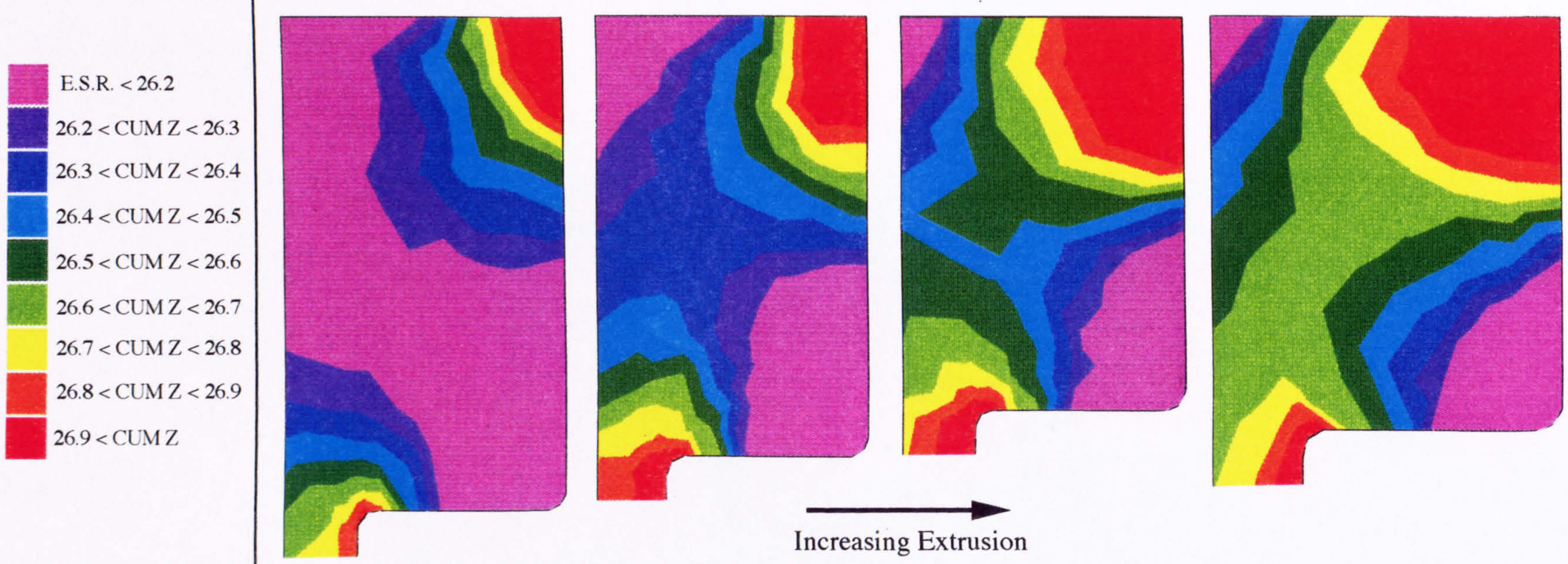


8090 ALLOY

CUMULATIVE Z VALUE DISTRIBUTIONS

90°cone angle,
430°C Extrusion temperature

Fig 5.4.10 (c)



5.5 Toughness Analysis

In this section, correlations between toughness, microstructure and processing conditions are made. The variation in toughness anisotropy with extrusion temperature and die cone angle, together with the variation in property values from the edge of the extrudate to the centre were also investigated.

Since anisotropy was investigated, two different types of toughness sample were required in order to measure the orthogonal toughness values. Short rod[1][2] specimens were used to measure the R-L toughness, and chevron notch bar specimens[3] to measure the L-R values. Even though two different fracture toughness specimens were used, section 4.4.1 did conclude that the different configurations and geometry of the samples did not affect the toughness measurements of the aged material, hence the R-L and L-R toughness values could be compared directly.

Since there were two different fracture orientations measured, a characterisation of the two different types of fracture was carried out initially, before the property variation with process conditions was discussed.

5.5.1 Fracture Characterisation

Fractographs obtained from S.E.M. analysis of failed R-L fracture samples are shown in figs 5.5.1->3. As can be seen the R-L failure was characterised by crack propagation along the line of the original grain boundaries, with relief features comparable in size to that of the subgrains and recrystallised grains. Not only were regions of subgrain/grain sized relief observed, however, but flatter regions ranging in size from 10->50μm and exhibiting a slightly 'rippled' or 'stepped' appearance were also evident.

T.E.M. analysis of the aged material revealed matrix precipitation of δ', T_1 and S, together with grain boundary I phase, and constituent phase stringers. Optical analysis also revealed the presence of small equiaxed recrystallised grains at the original grain boundaries. The following failure process was, therefore, identified in connection with these fractographs. Deformation was considered to begin upon primary slip systems, which, due to the presence of δ', resulted in intense shear regions[8][9] . Grain boundaries then impeded dislocation motion within these regions, creating dislocation pileups and strain concentration. At this point, operation of a secondary slip system became feasible. As the strain concentration at the grain boundaries increased, cracks nucleated at grain boundary precipitates, which then grew, causing an intergranular failure by a microvoid coalescence mechanism[4][5][6][7] . This process produced the relief features of comparable size with the subgrains and recrystallised grains. The flat faceted regions of little relief, however, were considered to occur as a consequence of transgranular failure causing breakdown of the intense coplanar regions within the

grains. Again a microvoid coalescence mechanism operated, causing voiding, but the operation of secondary slip systems also produced steps upon the fracture surface.

The transgranular failure was much more in evidence when the fractures produced from L-R samples were examined, figs 5.5.4->5. For this orientation of sample, it was necessary for the crack to propagate perpendicular to the original grains. Consequently, transgranular failure occurring by the breakdown of shear regions, was more common, hence the proportion of flat faceted areas with stepped topography increased. Intergranular failure was also evident within the L-R fractographs and again occurred by a microvoid coalescence crack propagation mechanism involving grain boundary precipitation.

As found with the 'slab' material, therefore, two different failure paths were identified during fracture- intergranular and transgranular. The specific path followed, hence the toughness, appeared to be dependent upon (i) The relative strengths of the grain boundary regions and the matrix coplanar shear regions and (ii) The testing orientation.

5.5.2 Effect of Die Cone Angle upon Toughness, Anisotropy and Centre to Surface Property Variations

The variations in the transverse toughness values with increases in die cone angle were found to be different from the longitudinal toughness value changes occurring as the die cone angle increased. It was necessary, therefore to investigate the correlations between processing and orthogonal property values separately.

Transverse (L-R) Toughness. The variations in the L-R toughness values with increases in die cone angle are tabulated in fig 5.5.7, and graphically shown in fig 5.5.8.(b)&(e).

As can be seen, the variation in toughness values with increases in die cone angle changes did not follow a constant trend. Instead, maximum L-R toughness values were observed for material produced using the die with a 45° cone angle, with the toughness values decreasing as the die cone angle was either decreased and increased from this value.

From S.E.M. analysis of the fracture surfaces, a correlation between the incidence of the flat faceted regions with 'stepped' or 'rippled' appearance and the toughness values, was evident. Figs 5.5.4. and 5.5.5.(c)&(d) illustrate L-R fractographs obtained from extrudates produced using dies with 45° cone angle. Transgranular failure is clearly evident, producing relatively flat regions of comparable size with the width of the original deformed grains, and exhibiting a 'rippled' or 'stepped' topography. Intergranular failure was also evident, however, with fracture relief corresponding to the recrystallised grain sizes clearly present. For extrudates produced from dies of any

other cone angle, the degree of these large transgranular failure regions was observed to decrease, and the degree of intergranular failure to increase, fig 5.5.5.(a)&(b). The decrease in transgranular failure was, therefore, associated with the observed decrease in L-R toughness values.

Optical analysis revealed the proportion of recrystallisation to decrease from 30° ->45° and then increase as the die cone angle was subsequently raised to 60° and 90° . Correlation of this microstructural change with the changes in fracture would, therefore, suggest that for the L-R failure, small recrystallised grains may act as points of stress concentration, thereby initiating intergranular failure before the breakdown of the transgranular region. The associated decrease in the applied stress necessary for failure would then lower the fracture toughness of the material.

T.E.M. analysis revealed no significant variations in precipitation or subgrain sizes as the cone angle varied. Other than the % recrystallisation, therefore, textural changes were the only other microstructural characteristic that varied with die cone angle changes. From section 5.3 it was found that the only significant texture variations with changes in die cone angle occurred in the S and copper texture components. These texture components exhibited an increase in intensity as the cone angle was increased from 30° to 45° and then a subsequent decrease as the die cone angle was increased to 60° and 90° . Increases in these texture components could, therefore, be associated with decreases in recrystallisation and increases in L-R toughness values. Since texture changes occurred concurrently with variations in the percentage of recrystallisation, however, the actual effects of die cone angle upon the deformed texture were difficult to separate from the effects of recrystallisation upon texture. Likewise, the definite effects of the changes in texture upon L-R toughness values could not be established, since concurrent changes in recrystallisation occurred.

Not only were the effects of die cone angle upon the core property values investigated, but attempts were also made to measure the L-R toughness values in the outer regions of the extrudates. Fig 5.5.4 (c) illustrates a typical fractograph obtained from L-R fracture samples produced from as close to the extrudate surfaces as possible. Failure in the transverse direction involved crack propagation across the elongated deformed grains, consequently transgranular, rather than intergranular failure was dominant, as indicated by the fractograph. No obvious differences in the appearance of the fracture surfaces obtained from the core and surface samples were, however, evident. The L-R toughness values obtained from the surface samples are tabulated in fig 5.7.3. As can be seen the near surface samples were found to be slightly tougher than the samples prepared from the core material. The property variations were, however, very small and did not alter significantly with die cone angle. Since microstructural differences were evident between the core and surface regions of the extrudates, this apparent absence of centre to surface property changes was attributed to the fact that the 'surface' sample

preparations could not be sufficiently removed from the core regions for crack propagation through the surface microstructures to occur. The core and surface toughness measurements were, therefore, virtually the same since microstructures associated with both the core and surface samples were virtually the same.

Microhardness testing was also used to identify any centre to surface variations in property values. The results are discussed in section 5.1, where they indicated a decrease in strength from the core of the extrudate to the surfaces.

Longitudinal (R-L) Toughness. The observed variations in the R-L toughness values occurring as a result of die cone angle increases are tabulated in fig 5.5.7, and shown graphically in 5.5.8.(a)&(d).

As with the L-R toughness, the variation in R-L toughness values with increases in die cone angle did not follow a constant trend. Minimum R-L toughness values were observed for extrudates produced using dies of 45° cone angle, with the toughness values increasing as the die cone angle was either decreased and increased from this value.

As already stated, optical analysis revealed decreases in the volume fraction of recrystallisation as the die cone angle rose from 30°->45°. Increases in the volume fraction of recrystallisation were then observed to increase as the die cone angle was increased to 60° and then to 90°. It was considered, therefore, that the increased volume fraction of recrystallisation enhanced the R-L toughness, by disrupting the crack propagation along the line of the original deformed grains. In addition to the variations in recrystallisation, microstructural analysis also revealed changes in the texture systems present. The texture analysis is discussed in section 5.3, but it did appear that the decreases in the S and copper texture components could be correlated with increases in R-L toughness values.

Overall, therefore, increases in the proportion of small (10->40 μm) recrystallised grains were considered to decrease L-R toughness values and increase the R-L toughness values. Increases in S and copper texture components could also be correlated with increases in L-R and decreases in R-L toughness values.

Since the L-R and R-L toughness values varied conversely with changes in die cone angle, the anisotropy of the extrudates also varied, fig 5.5.8.(c)&(f). For extrudates processed to either the underaged or overaged condition, maximum levels of anisotropy were associated with extrudates produced from dies of 45° cone angle. Lower levels of anisotropy were then associated with extrudates produced from dies with cone angles of 30° , 60° and 90° . For the underaged material, however, the minimum anisotropy values were obtained from material produced using the 30° die cone angle, whereas for the overaged material the shear face die produced minimum anisotropy values.

5.5.3 Effect of Extrusion Temperature upon Toughness and Anisotropy

The variations in toughness values occurring as the extrusion temperature increased are shown graphically in fig 5.5.10. The variations in toughness values were not considerable, but generally for every die cone angle used, increasing the extrusion temperature caused the R-L toughness values to increase and the L-R toughness values to decrease. S.E.M analysis of the R-L and L-R failures, however, revealed no discernible variations in the fracture appearance as the extrusion temperature was increased, figs 5.5.1, 5.5.2, 5.5.4 & 5.5.5.

Microstructurally, T.E.M. analysis revealed the precipitation changes within the extrudate to be negligible as the extrusion temperature increased. Optical analysis, however, revealed an increase in the amount of small (10->40μm) recrystallised grains. As previously stated the presence of the grain boundary recrystallisation was considered to enhance the disruption of the failure along the line of the deformed grains, thereby increasing the longitudinal toughness. With regard to transverse failure, however, the recrystallised grains were considered to act as points of discontinuity, hence caused a decrease in L-R toughness values. This consequently caused the anisotropy to decrease, but as fig 5.5.10. illustrates, generally only small changes in anisotropy with increases in extrusion temperature were observed for all die cone angles.

From these results, therefore, it was found that a low extrusion temperature would be preferable for improved L-R toughness values, whilst higher temperatures would generally improve R-L toughness values. The anisotropy would be decreased by using a high extrusion temperature.

5.4.4 Conclusions

(1) Fracture Characterisation

As with the slab material, the orthogonal failures within the aged axi-symmetric extrudates exhibited different fracture characteristics:-

R-L toughness specimens:- Due to the 'weakness' of the internal boundaries, R-L failure predominantly occurred by an intergranular microvoid coalescence failure mechanism. The boundary 'weakness' was caused by grain boundary precipitation, and accentuated by the strain concentration phenomena occurring within the material,- coplanar slip & P.F.Z formation. Transgranular failure was also evident, and again occurred by a microvoid coalescence, but was usually associated with transverse crack propagation.

L-R toughness samples:- Failure in the transverse direction involved crack propagation across the elongated deformed grains, and consequently transgranular

rather than intergranular failure occurred. The problem of crack growth along elongated grain boundaries at low applied stresses was, therefore, highly reduced. As a result the L-R toughness values were always higher than the R-L values. The mechanism of trans-granular crack propagation was microvoid coalescence, but relief on the transgranular fracture surface was relatively small. Steps were present on the fracture surface, however, due to the manifestation of secondary slip systems upon the fracture surface.

These results showed that the appearance of transgranular or intergranular failure in the aged material was highly dependent upon (i) The relative strengths of the grain boundary and shear regions, which in turn were found to be affected by grain boundary precipitation, and (ii) Fibering of the grains. The elongated nature of the grains encouraged R-L samples to exhibit intergranular failure and L-R samples to exhibit transgranular failure.

(2) Correlation Between Properties, Processing Conditions & Microstructure.

It was observed that the extrusion temperature affected toughness by its direct effect upon the recrystallisation present within the material. Die cone angle changes, however, were considered to affect the toughness values not only through the variations caused in recrystallisation, but also through the changes brought about in the deformed matrix.

Increasing the die cone angle from 30°->45° caused the % recrystallisation to increase. The % recrystallisation then decreased as the die cone angle increased to 60° and 90°.

The presence of the small equiaxed recrystallised grains at the original grain boundaries increased the energy requirements necessary for longitudinal crack propagation by enhancing the disruption of the crack propagation along the path of the original grain boundaries, whilst not increasing stress concentration levels significantly. With regard to transverse crack propagation, however, the recrystallised grains acted as grain boundary discontinuities. The increases in the proportion of the small (10->40μm) grain boundary recrystallisation consequently increased the R-L toughness values and decreased L-R toughness values.

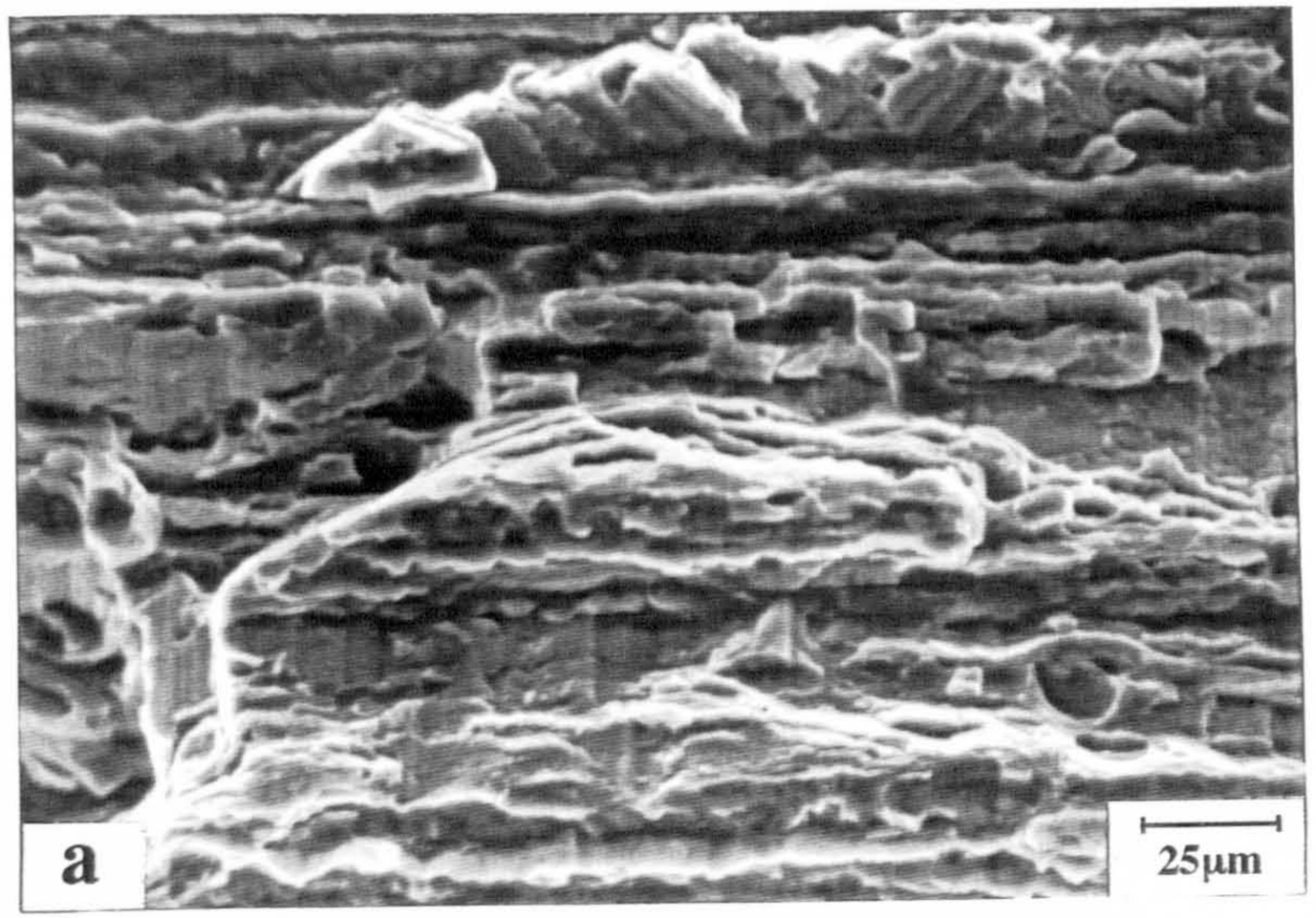
With regard to the variation in texture brought about by changes in die cone angle, it was observed that increases in the intensity of S and copper texture components corresponded to decreases in R-L toughness values and increases in L-R toughness values. It was impossible to definitely establish the effect of texture changes upon property values, however, since concurrent changes in recrystallisation also occurred. Likewise, it was difficult to establish whether the observed texture changes occurring with increases in die cone angle were as a result of changes in the deformed matrix orientation, or as a result of variations in recrystallisation.

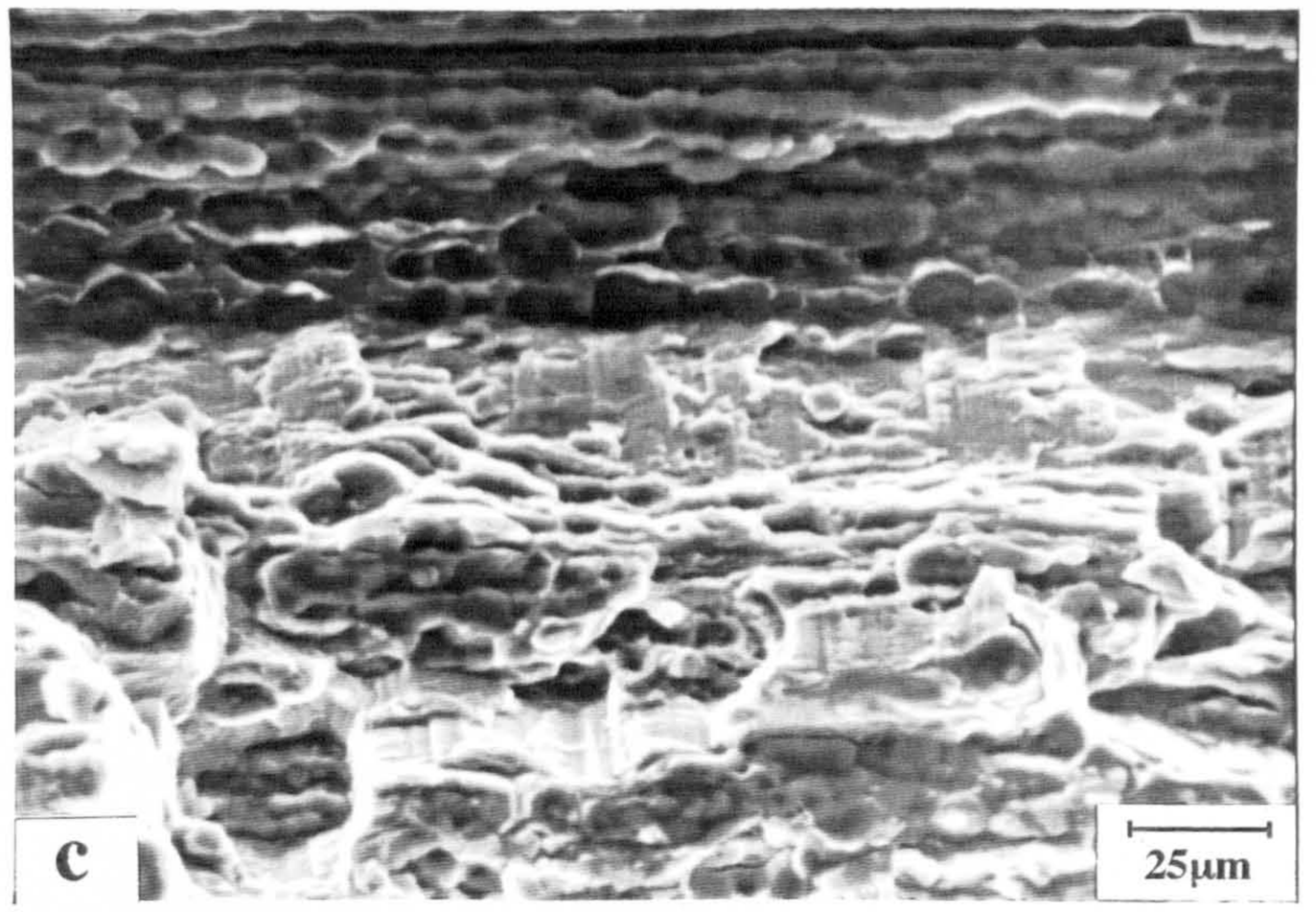
Differences in the R-L and L-R toughness variations with increases in die cone angle where, however, present between underaged and overaged material. These changes in the toughness variations were attributed to the effect of precipitation upon the deformation and fracture characteristics. Changes in recrystallisation and texture with increases in die cone angle consequently had differing effects upon the property values, due to the presence of differing precipitation. When considering the specific effects of recrystallisation and/or texture upon toughness values, therefore, the overall deformation and fracture characteristics of the material must be considered before individual microstructure property value correlations can be made. Recrystallisation was, therefore, considered to increase R-L toughness values and decrease L-R toughness values, with these effects being diluted by the presence of substantial grain boundary precipitation.

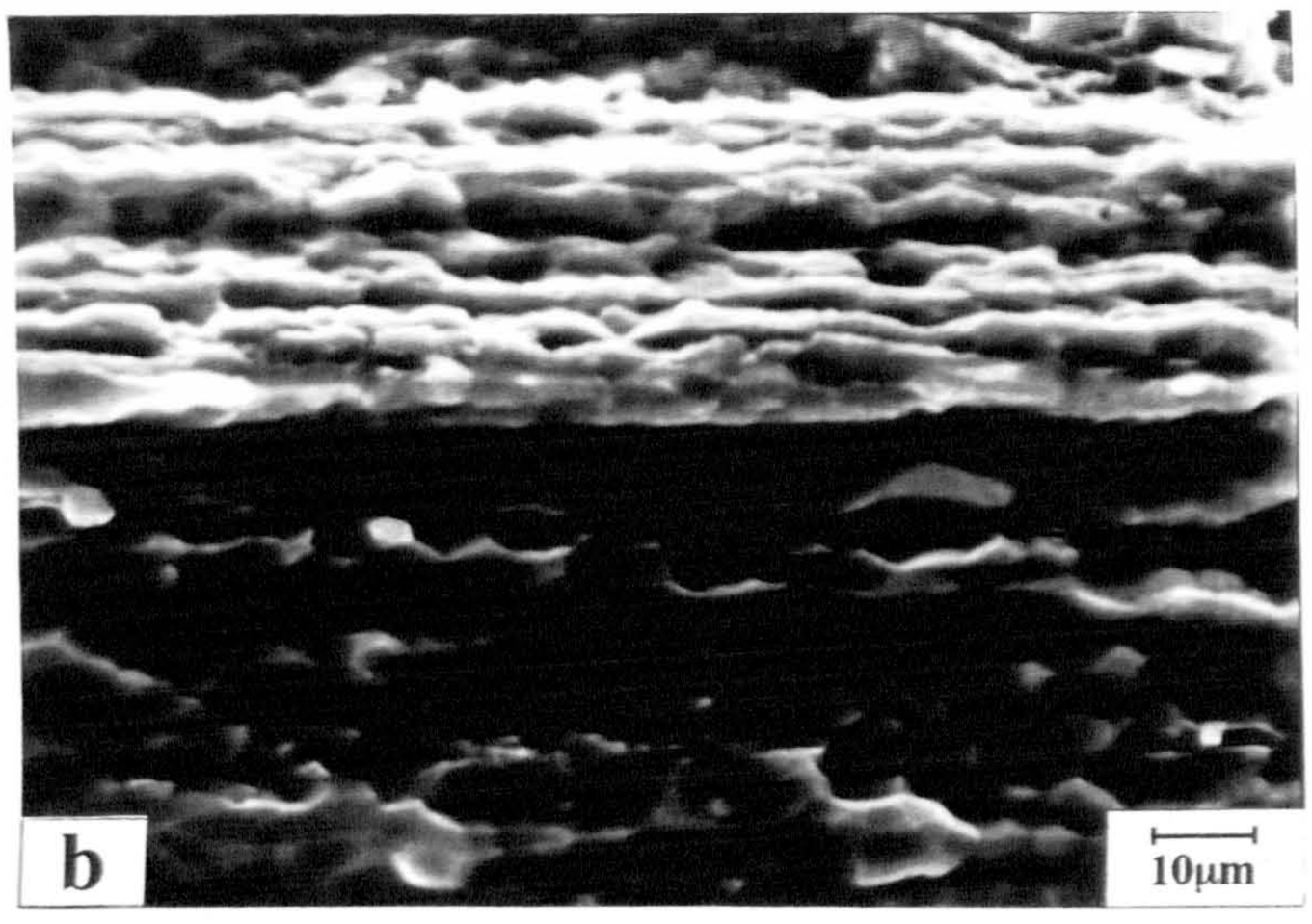
Due to this correlation between property values and recrystallisation, increases in the extrusion temperature consequently caused increased R-L toughness values and decreased L-R toughness values. The toughness anisotropy of the extrudates also decreased as the extrusion temperature rose. Depending upon the desired property values, therefore, the extrusion temperature could be altered in order to help control recrystallisation, and thereby property values. The 8090 limit diagrams must be consulted, however, because boundaries on the process conditions exist due to limitations on press capacity, tooling and surface quality[10][11].

The influence of die cone angle upon recrystallisation and texture also meant that die cone angle changes could also be used to modify property values.

Fig 5.5.1 (R-L) S.E.M. Fractographs.
Underaged condition.
Core regions of extrudates.
(a) 45° die cone angle.
400° C extrusion temperature.
(a) 90° die cone angle.
430° C extrusion temperature.
(c) & (d) 45° die cone angle.
430° C extrusion temperature.







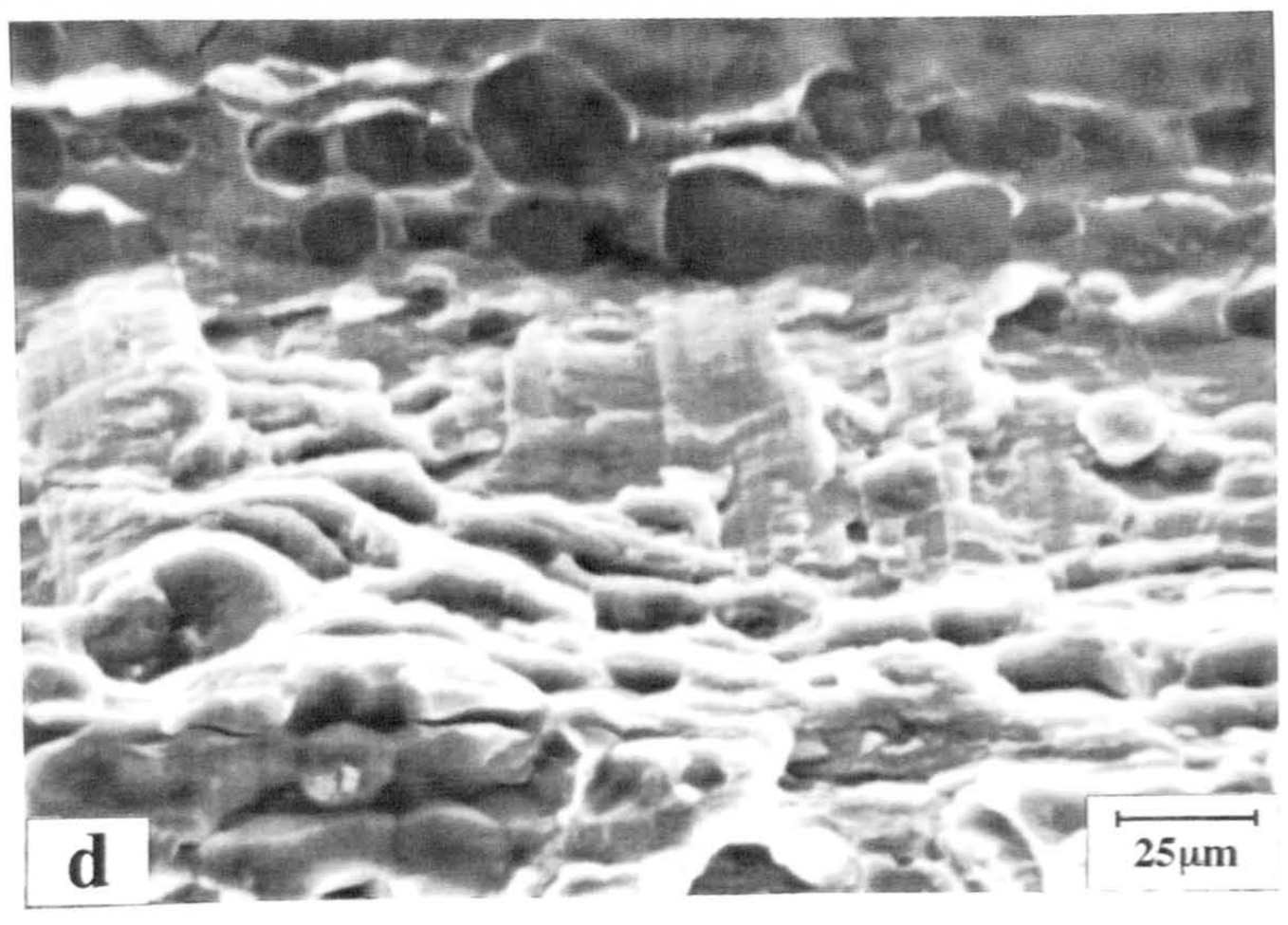


Fig 5.5.1

Fig 5.5.2 (R-L) S.E.M. Fractographs.
Underaged condition.
Core regions of extrudates.
460° C extrusion temperature.
(a) 30° die cone angle.
(b) 45° die cone angle.
(c) 60° die cone angle.
(d) 90° die cone angle.

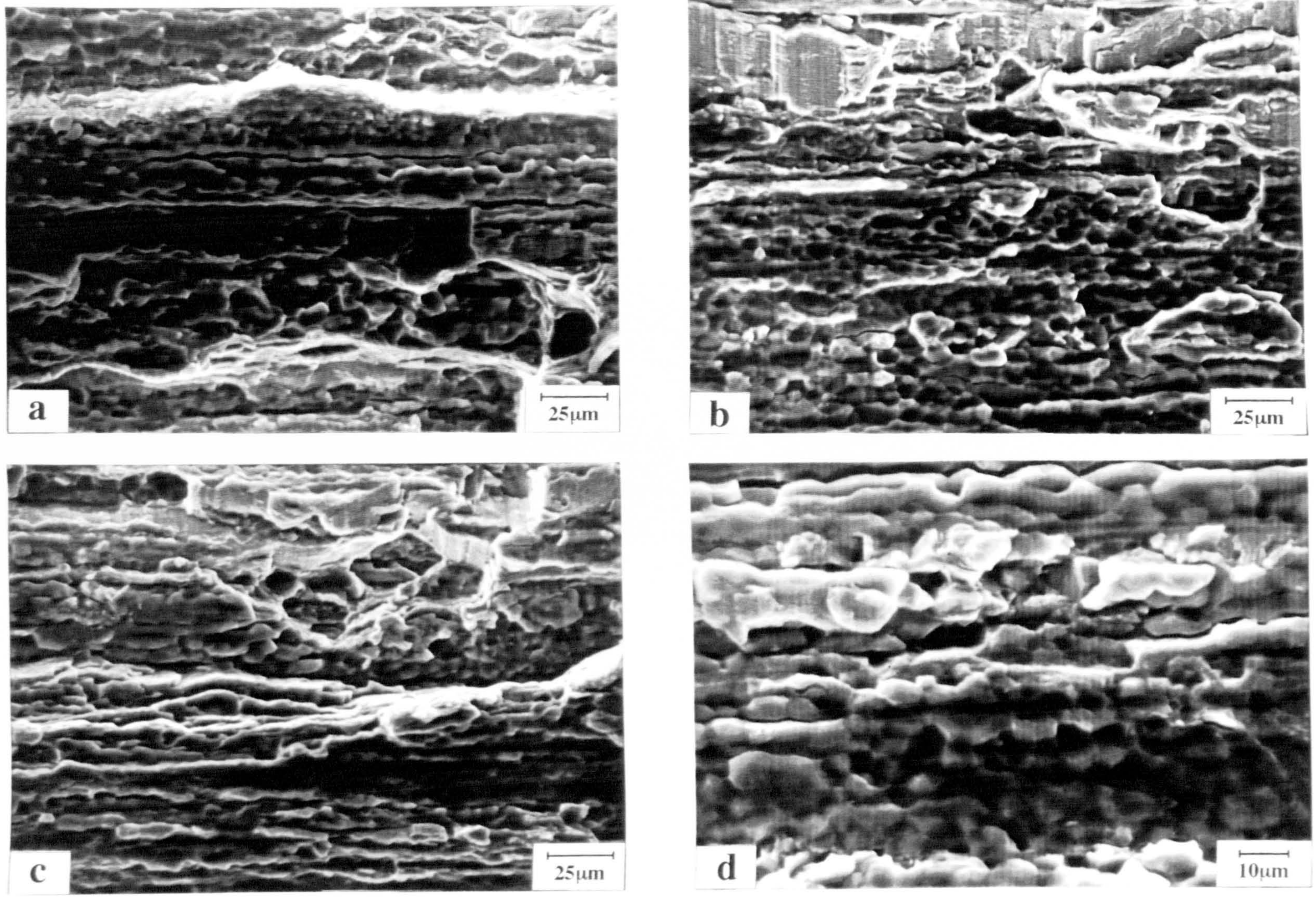
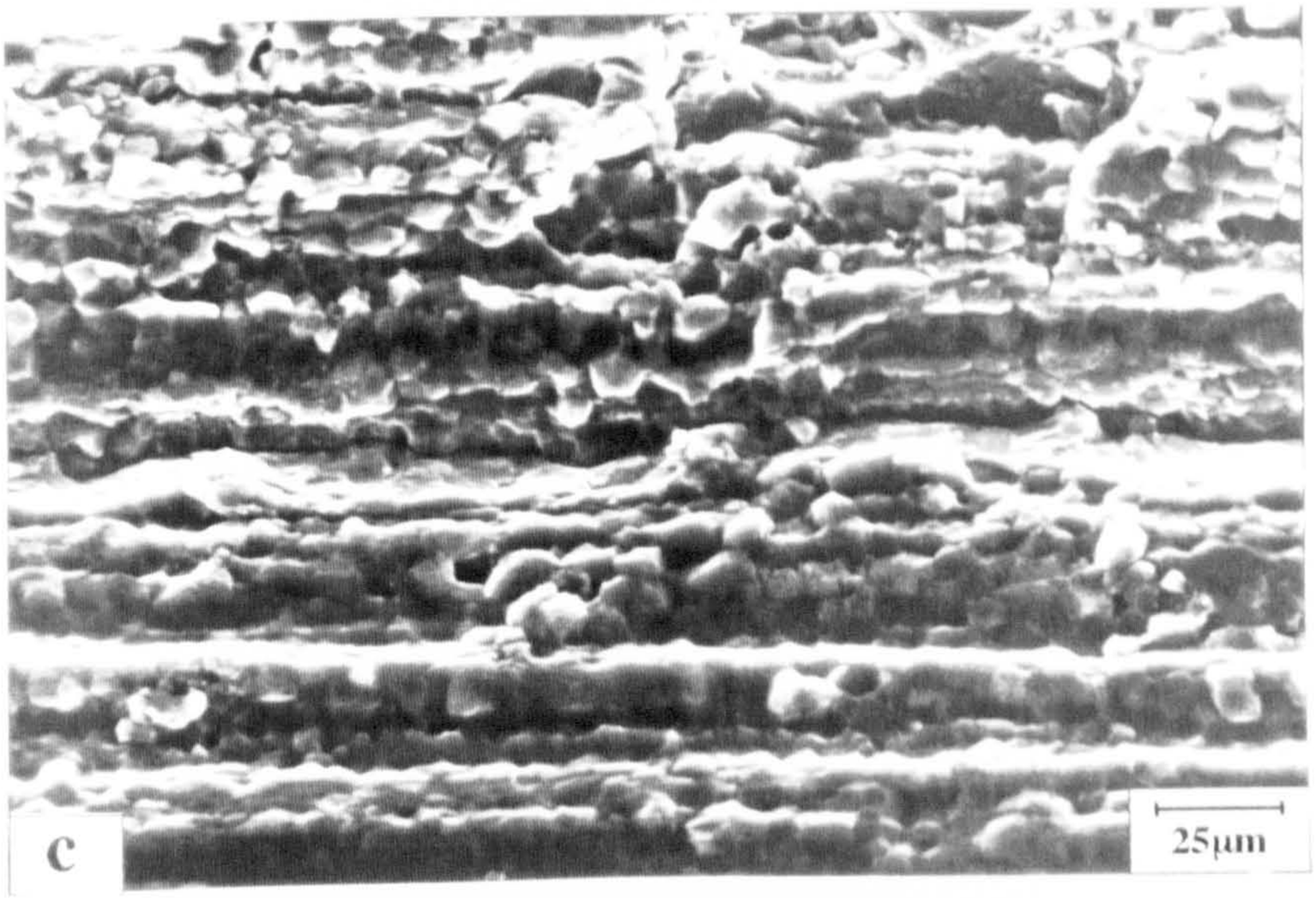
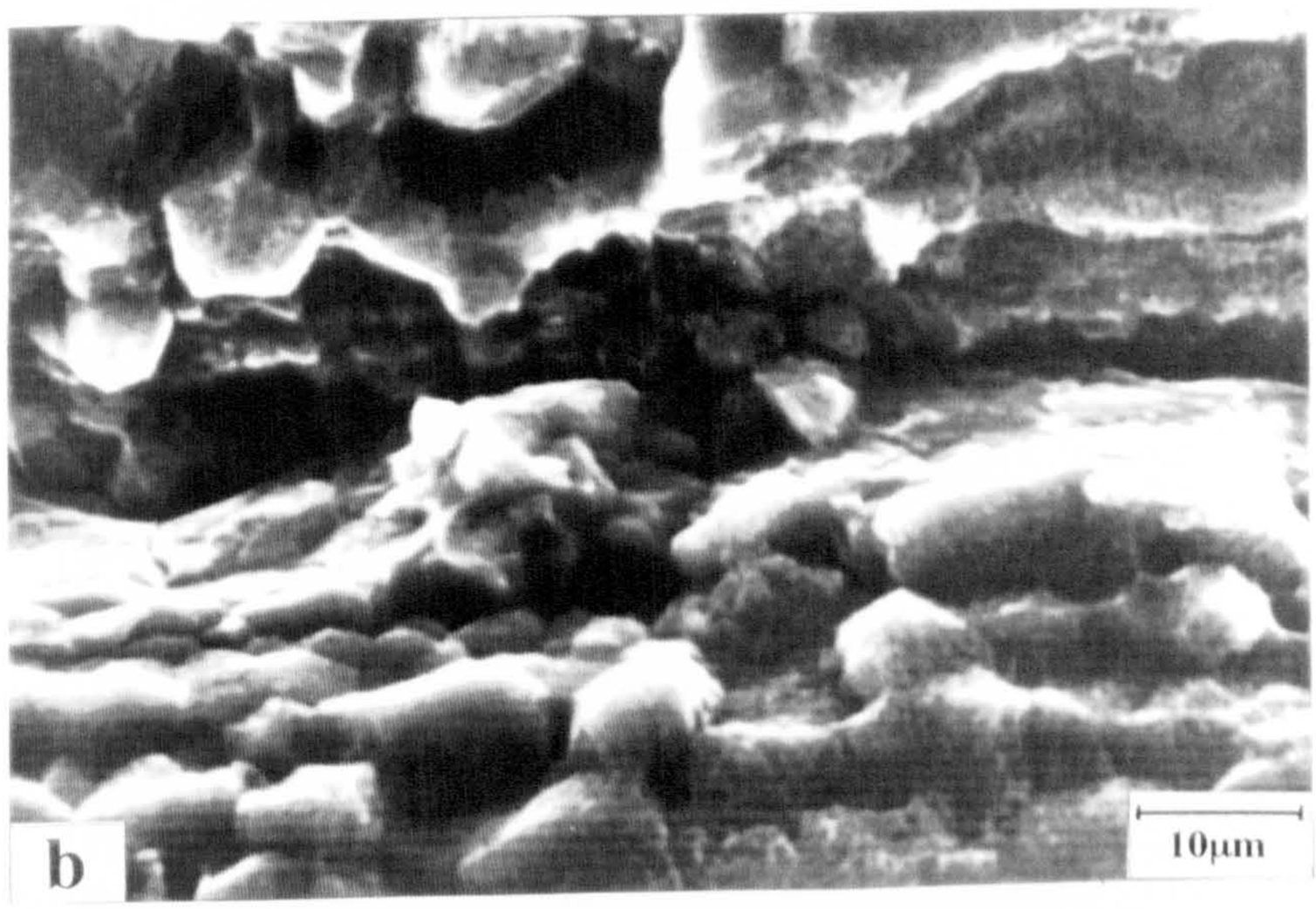


Fig 5.5.2

Fig 5.5.3 (R-L) S.E.M. Fractographs.
Overaged condition.
Core regions of extrudates.
430° C extrusion temperature.
(a) 60° Die cone angle.
(b) & (c) 30° die cone angle.





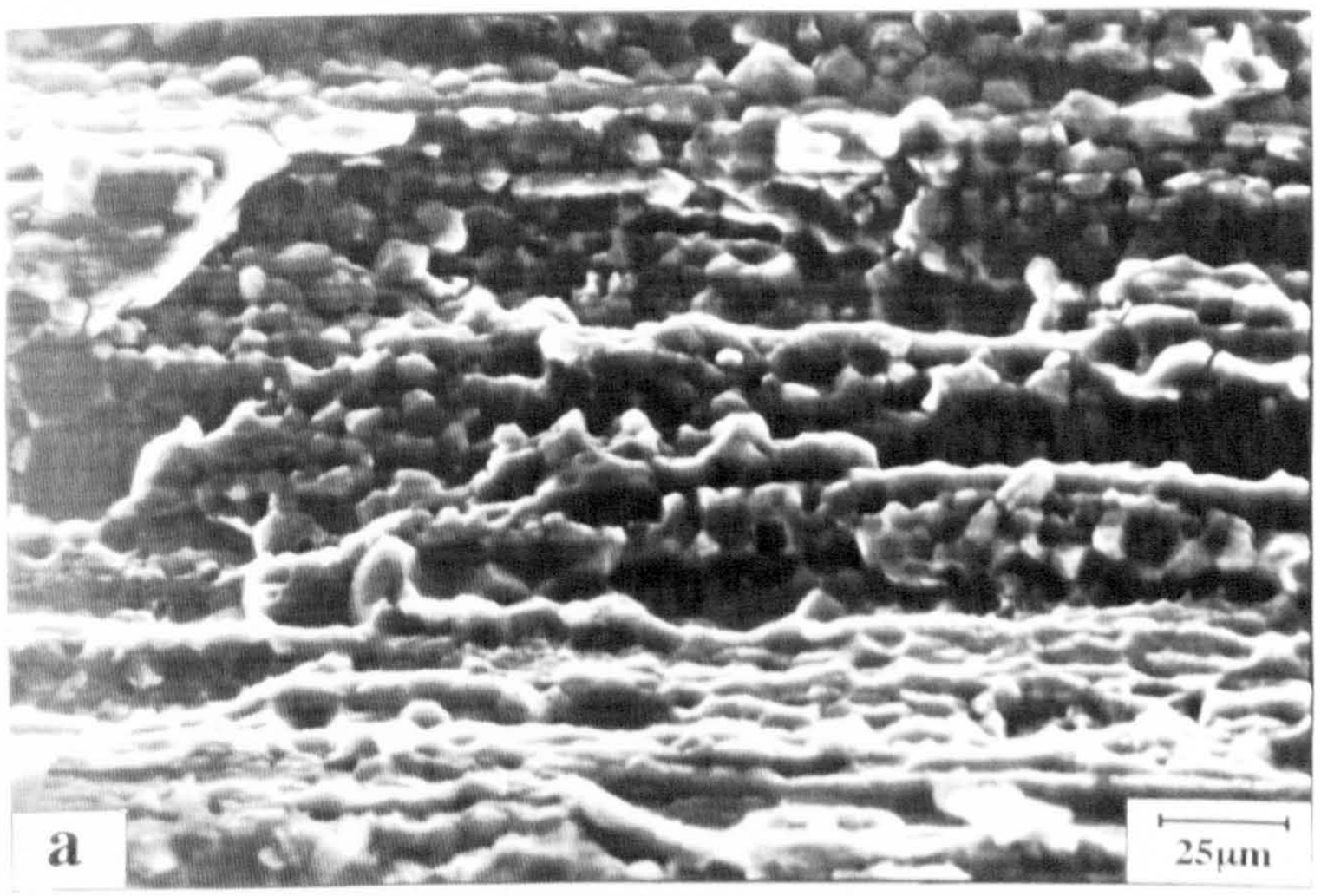
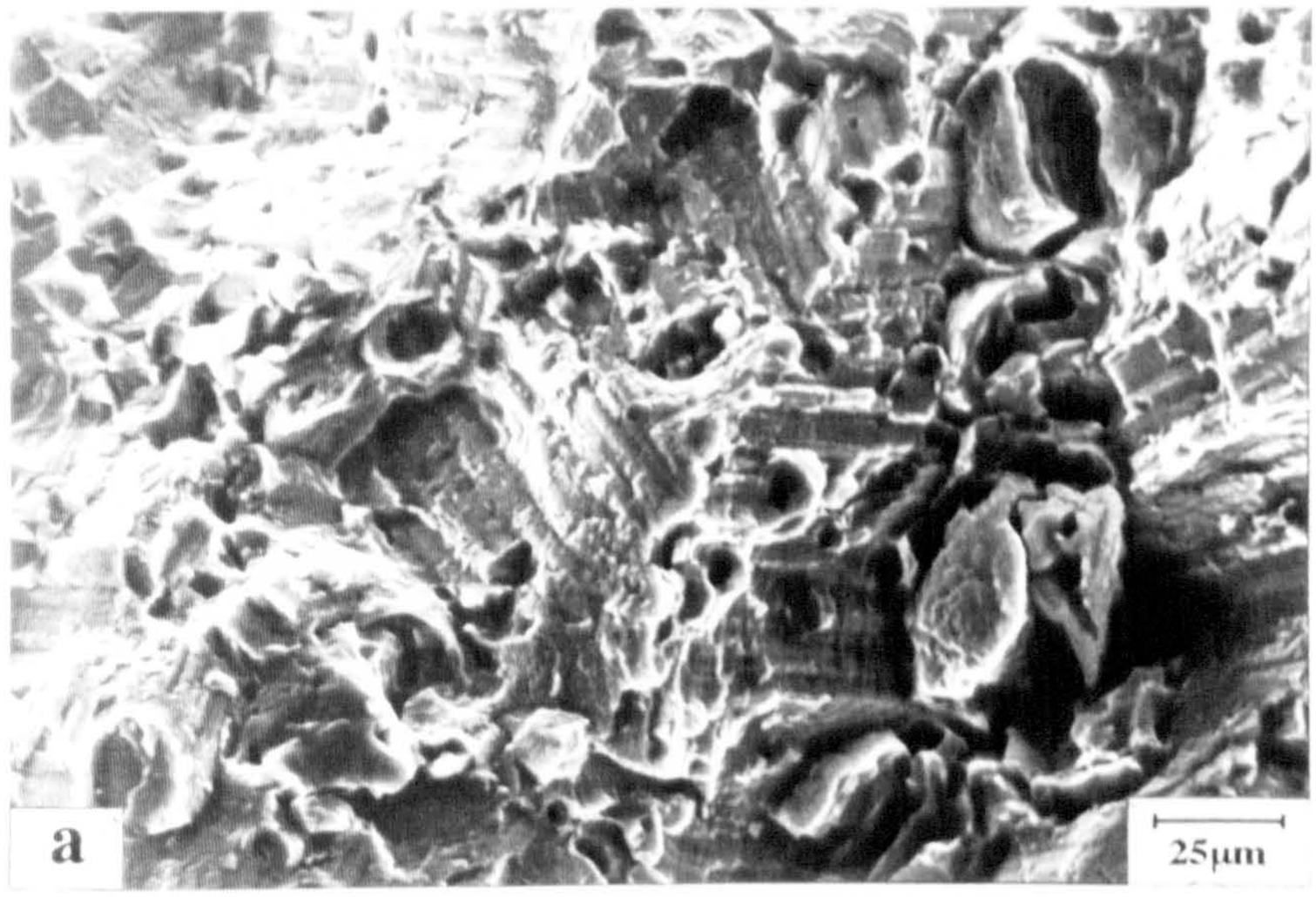
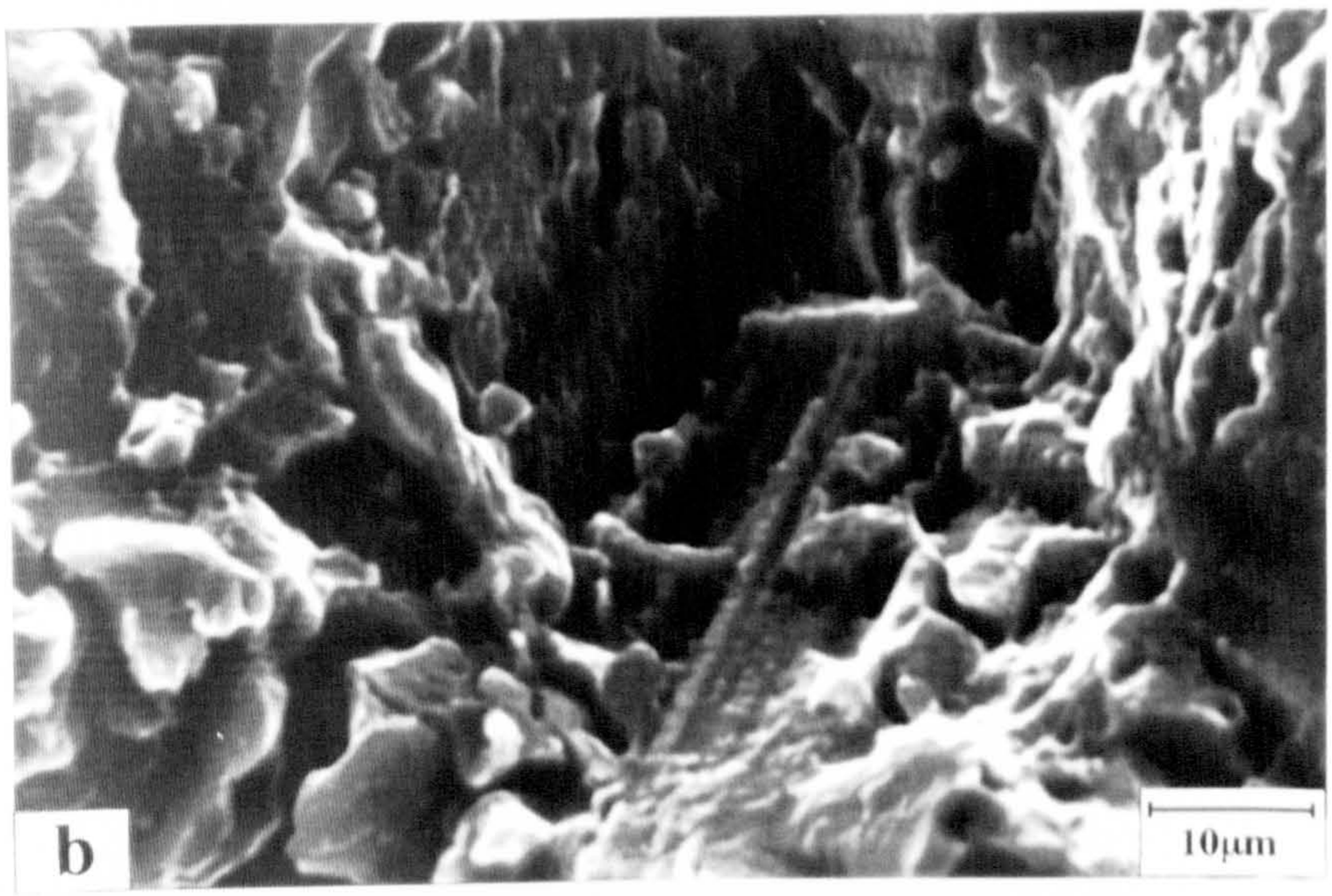


Fig 5.5.3

Fig 5.5.4 (L-R) S.E.M. Fractographs.
Underaged condition.
(a) 45° die cone angle.
430° C extrusion temperature.
Core of extrudates.
(a) 45° die cone angle.
460° C extrusion temperature.
Core of extrudates.
(c) 45° die cone angle.
430° C extrusion temperature.
Surface of extrudates.





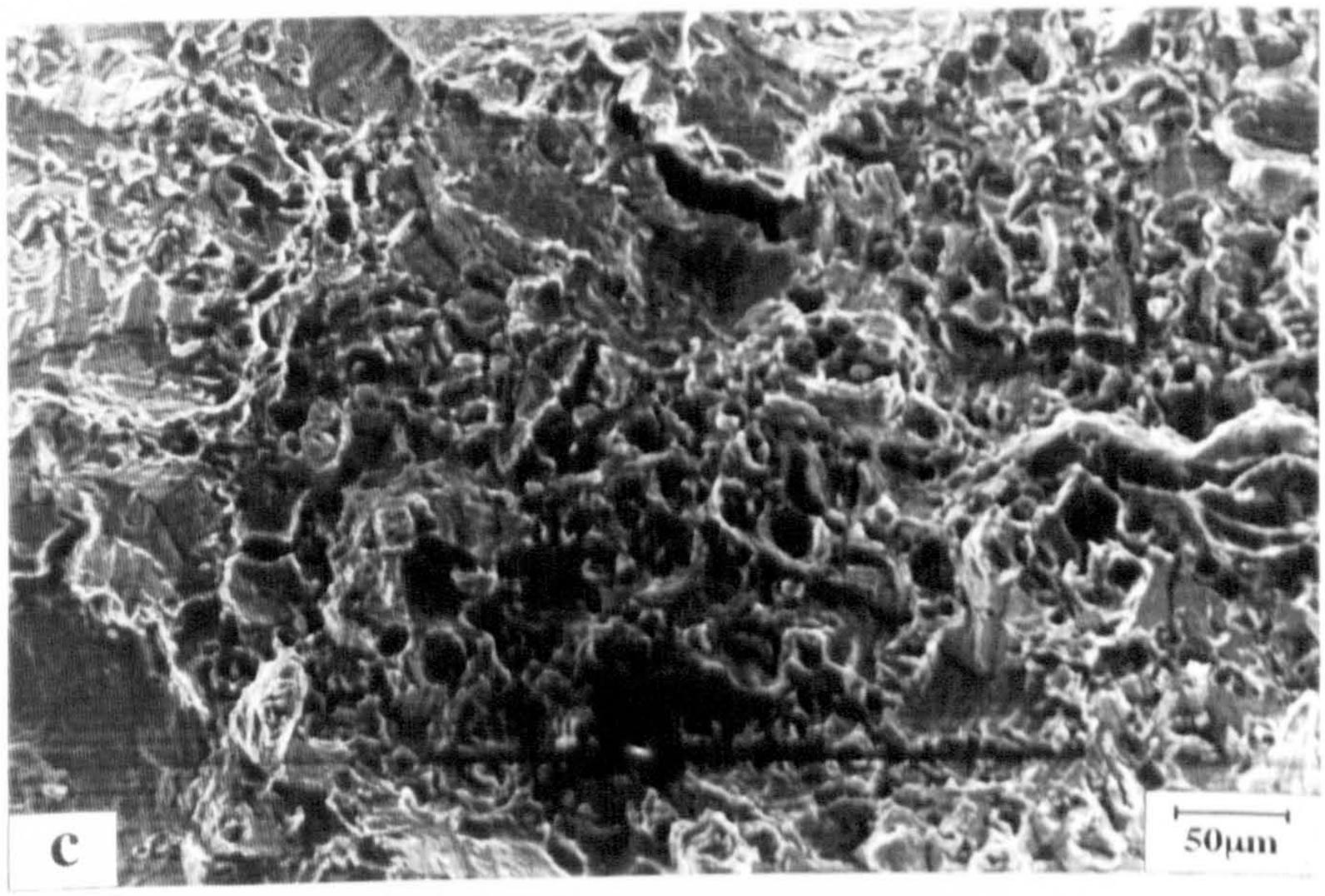
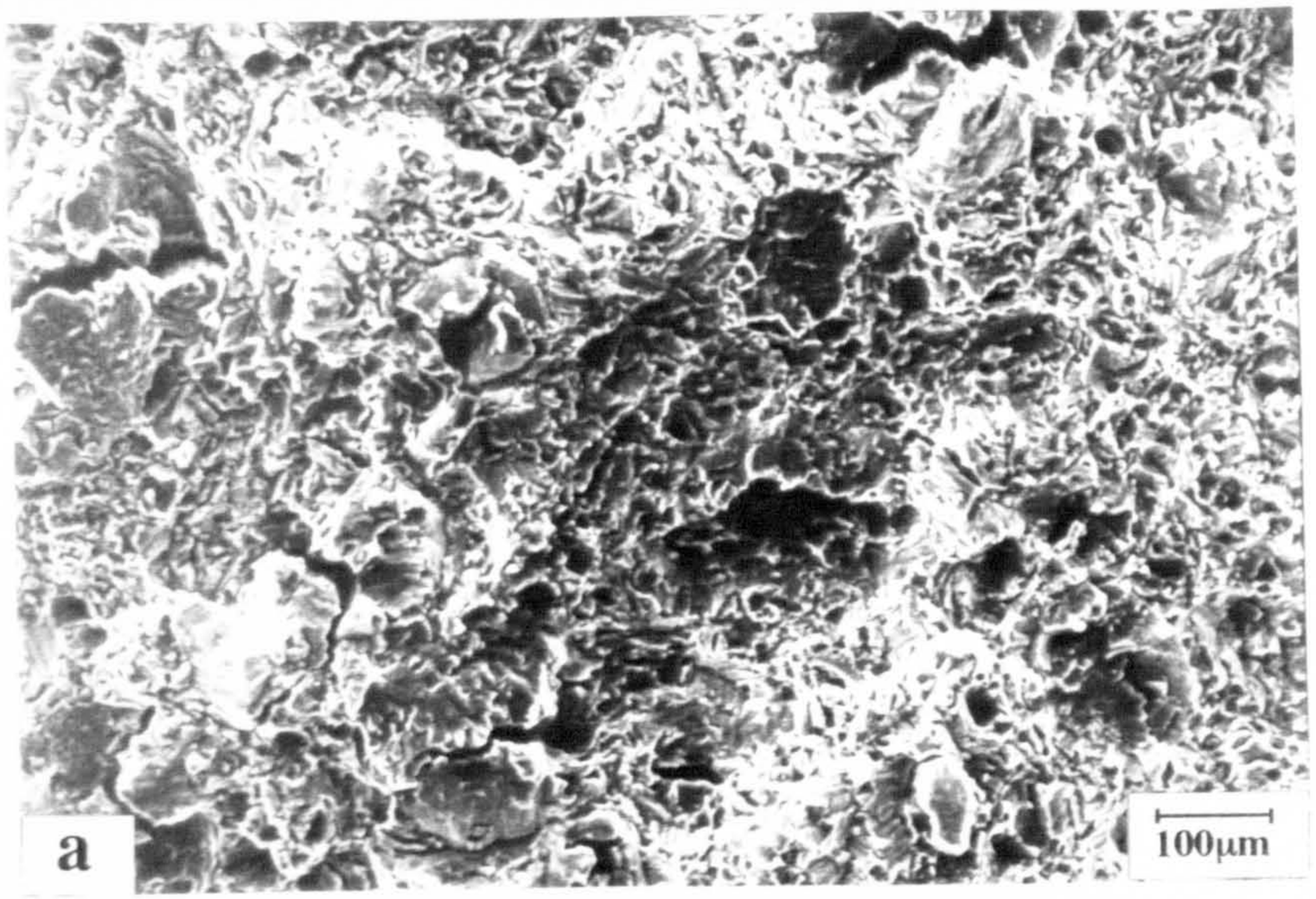
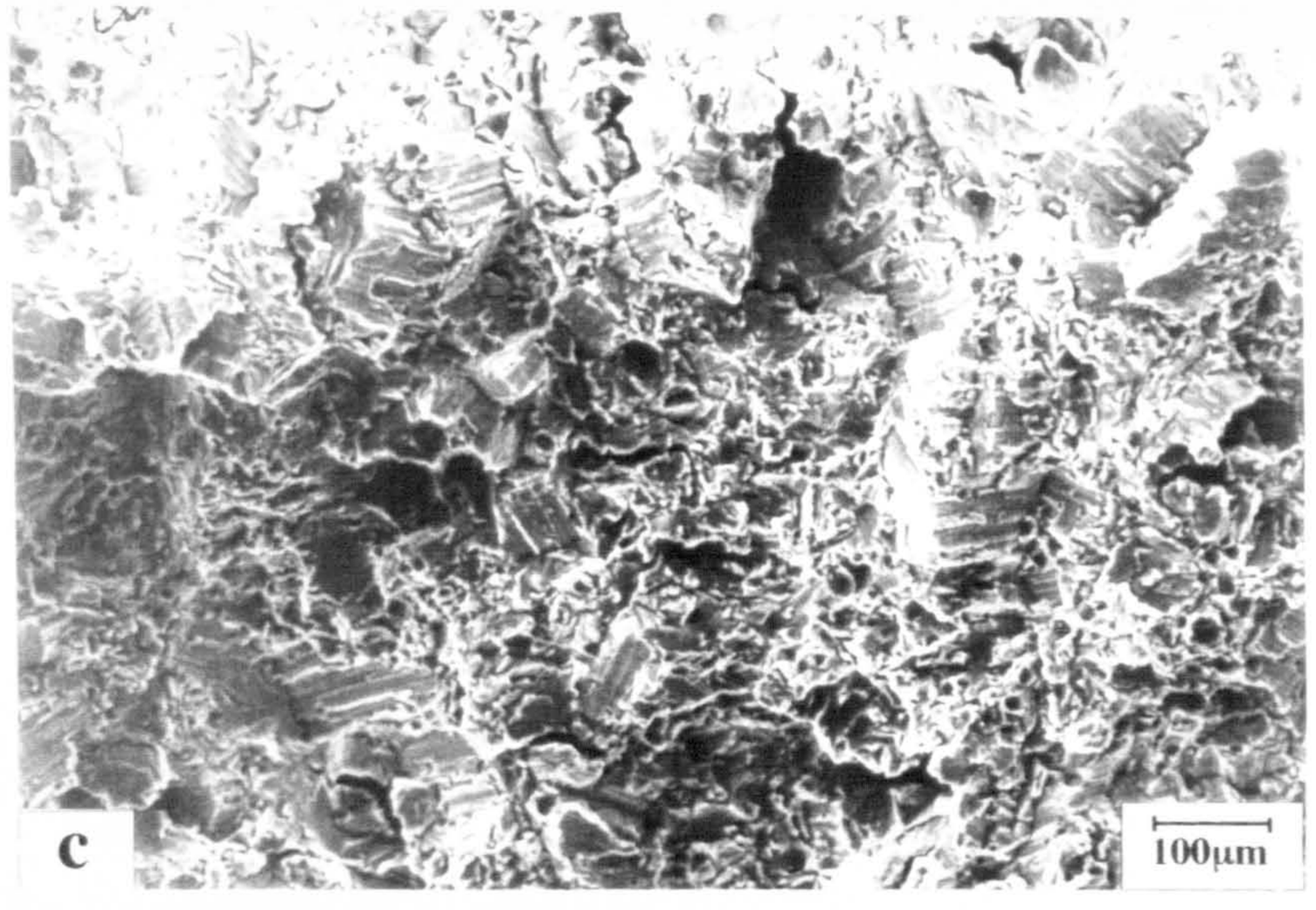
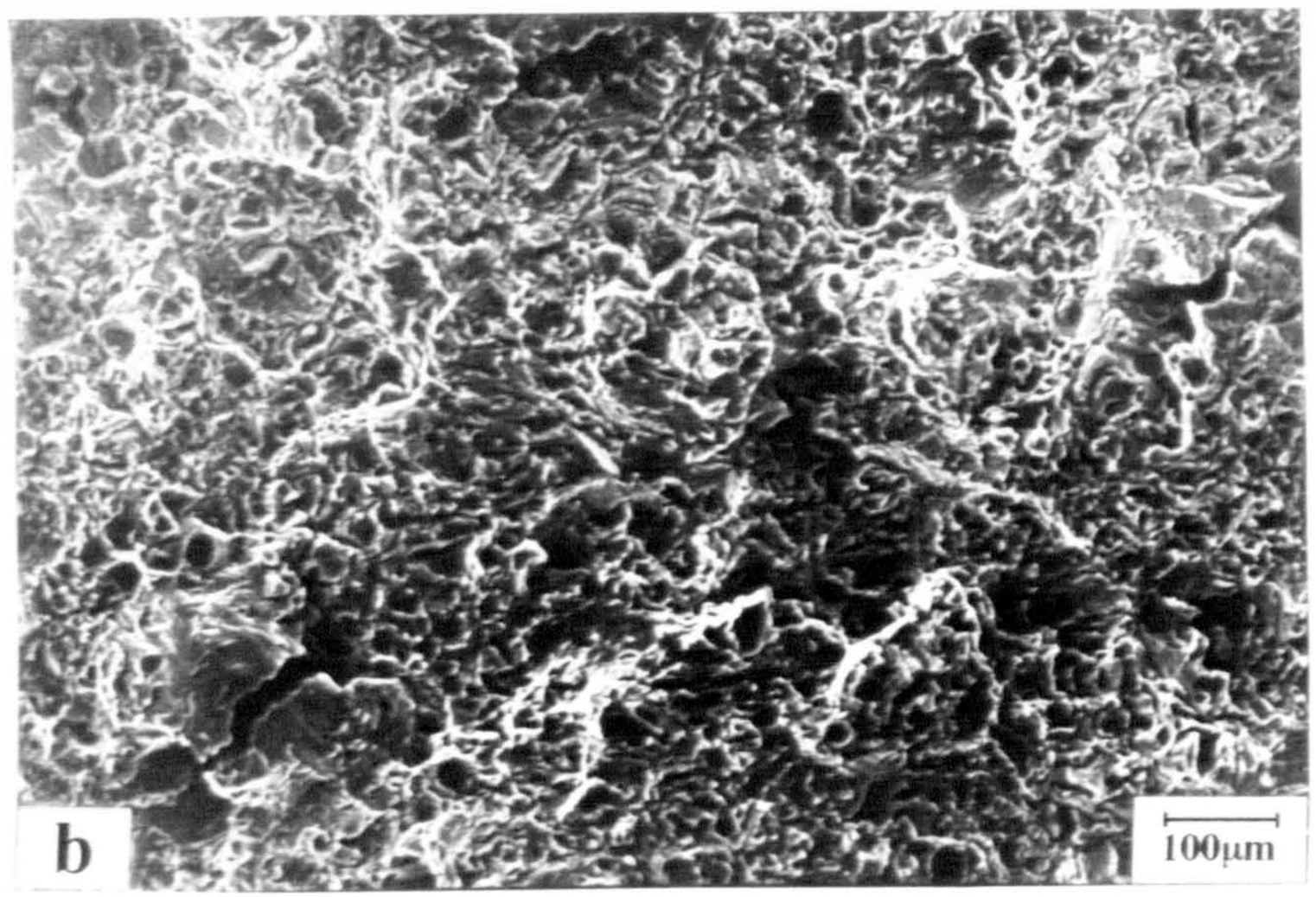


Fig 5.5.4

Fig 5.5.5 (L-R) S.E.M. Fractographs.
Underaged condition.
Core regions of extrudates.
400° C extrusion temperature.
(a) 30° die cone angle.
(b) 90° die cone angle.
(c) & (d) 45° die cone angle.







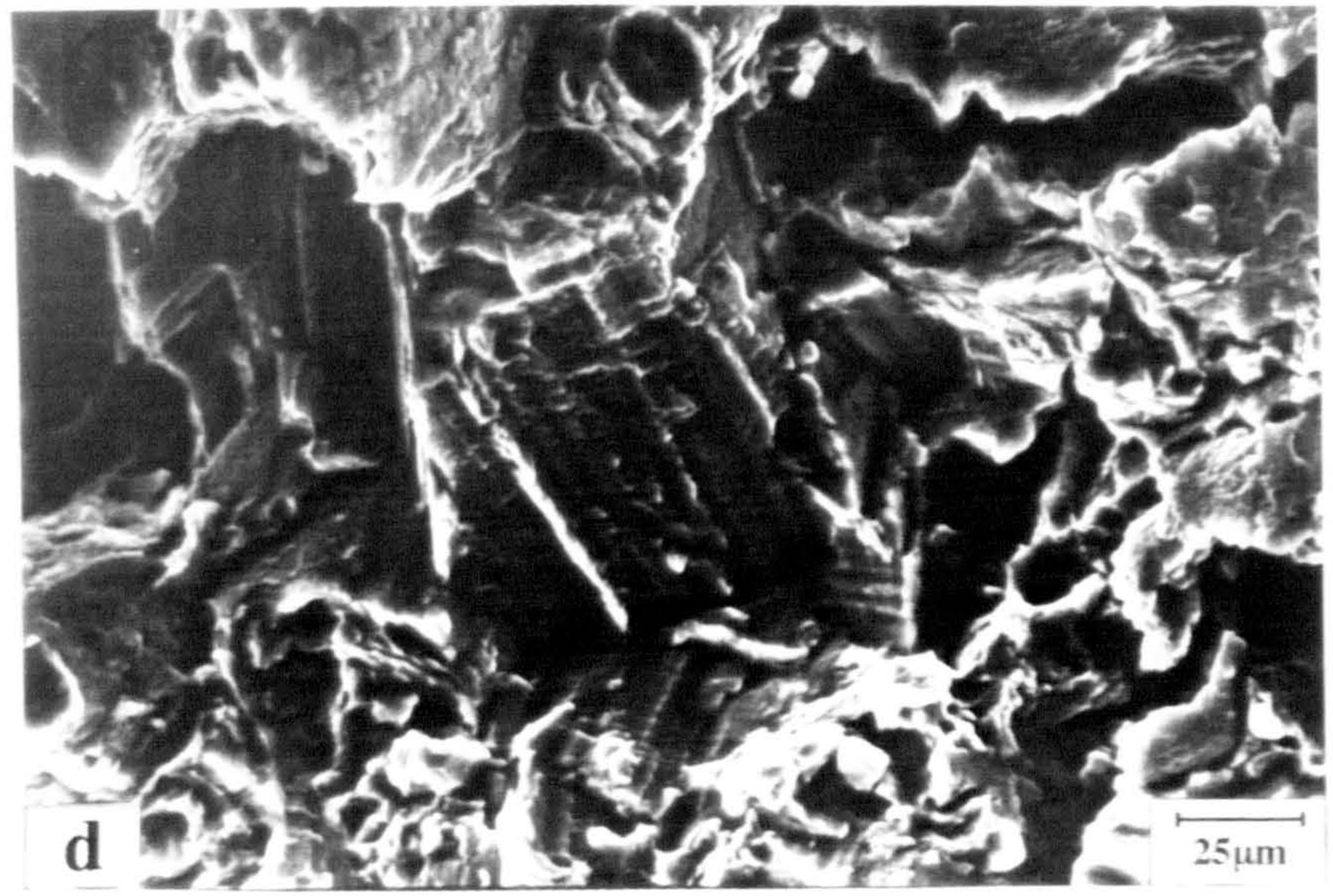
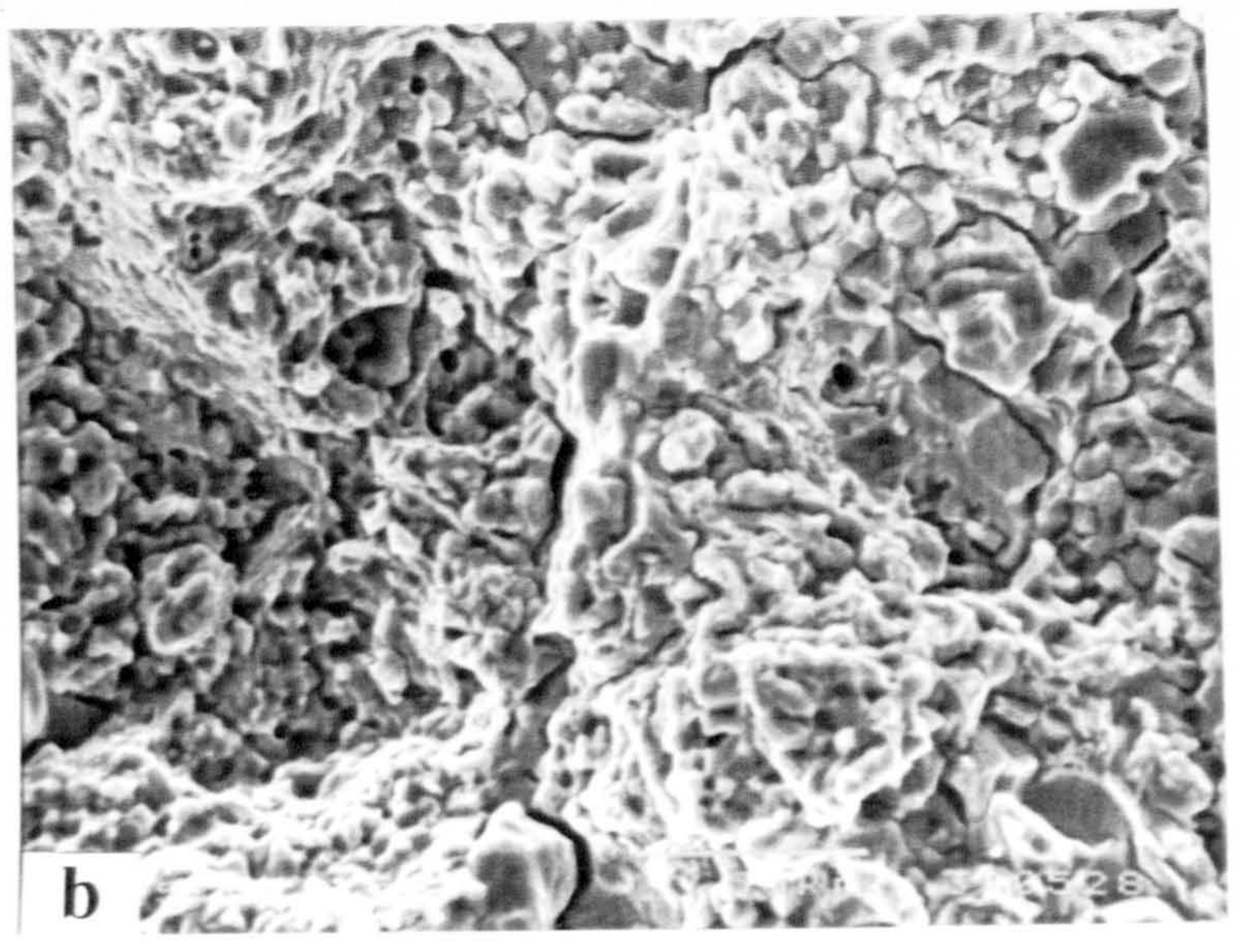


Fig 5.5.5

Fig 5.5.6 (L-R) S.E.M. Fractographs.
Overaged condition.
Core regions of extrudates.
460° C extrusion temperature.
(a) 30° die cone angle.
(b) 60° die cone angle.
(c) & (d) 45° die cone angle.



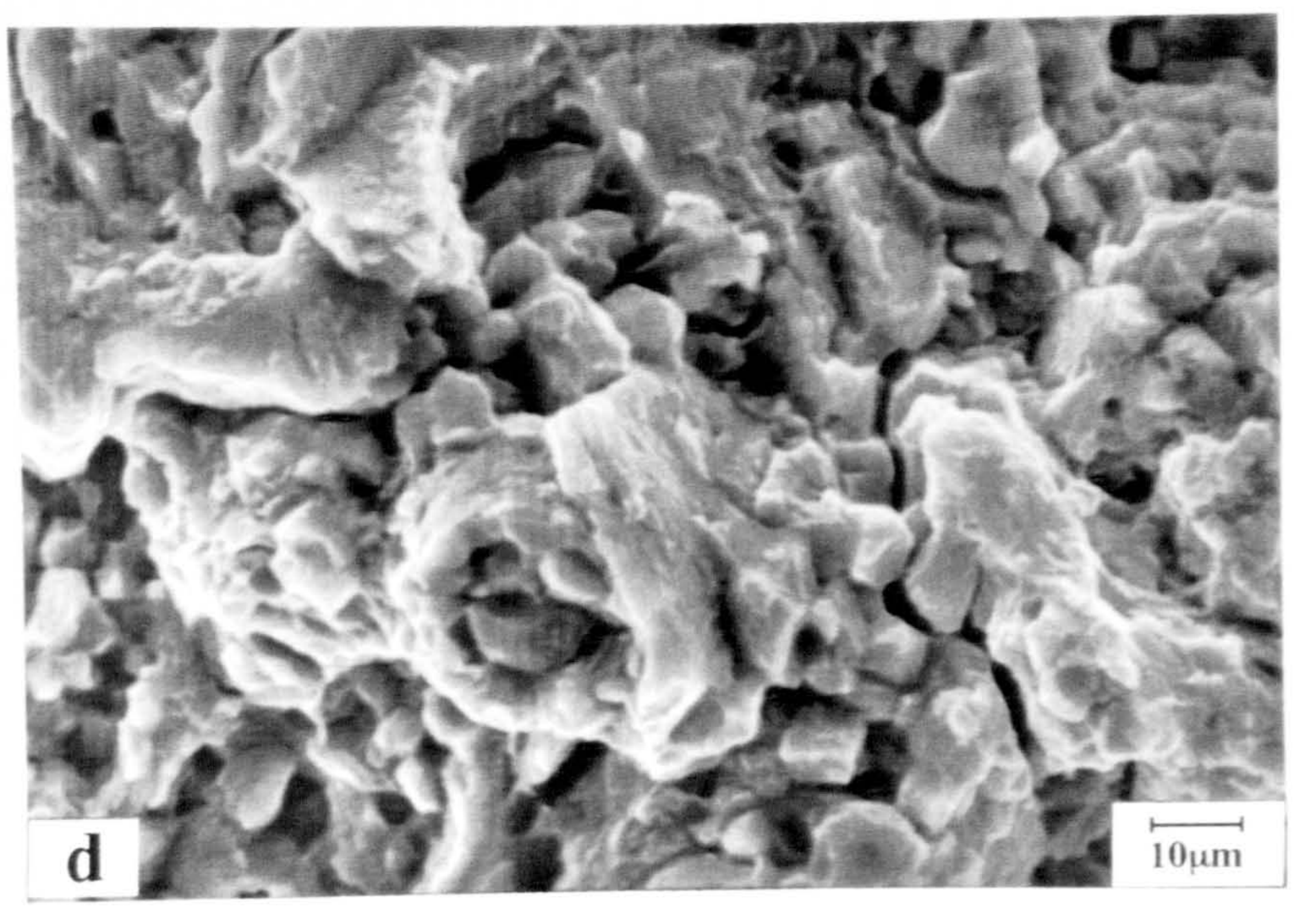


Fig 5.5.6

Ageing Cond.	Die Cone Angle	Extrusion Temp (°C)	(R-L) Toughness (MPam$^{1/2}$)	(L-R) Toughness (MPam$^{1/2}$)	(L-R)-(R-L) (MPam$^{1/2}$)
Under-aged	30°	400	22.1 (±0.3)	31.8 (±0.2)	9.7
		430	24.9 (±0.9)	31.3 (±0.2)	6.4
		460	25.8 (±0.5)	30.7 (±0.2)	4.9
	45°	400	18.1 (±0.4)	33.2 (±0.3)	15.1
		430	18.0 (±0.6)	32.0 (±0.3)	14
		460	18.5 (±0.3)	32.0 (±0.5)	13.5
	60°	400	19.3 (±0.4)	32.4 (±0.2)	13.1
		430	19.5 (±0.4)	31.6 (±0.4)	12.1
		460	19.8 (±0.3)	31.5 (±0.2)	11.7
	90°	400	21.6 (±0.2)	32.2 (±0.2)	10.6
		430	22.1 (±0.3)	31.5 (±0.3)	9.4
		460	22.9 (±0.3)	31.3 (±0.2)	8.4
Over-aged	30°	400	17.3 (±0.5)	30.2 (±0.5)	12.9
		430	18.5 (±0.8)	29.0 (±0.4)	10.5
		460	19.7 (±0.3)	28.4 (±0.4)	8.7
	45°	400	16.2 (±0.3)	30.4 (±0.2)	16.2
		430	17.6 (±0.5)	29.6 (±0.4)	12.0
		460	18.5 (±0.8)	28.3 (±0.5)	9.8
	60°	400	17.0 (±0.4)	29.7 (±0.2)	12.7
		430	17.8 (±0.5)	28.8 (±0.4)	11.0
		460	18.9 (±0.5)	27.5 (±0.5)	8.6
	90°	400	17.7 (±0.5)	29.0 (±0.5)	11.3
		430	19.5 (±0.3)	28.2 (±0.3)	8.7
		460	21.1 (±0.5)	27.0 (±0.5)	5.9

Fig 5.5.7 Variation in (R-L) and (L-R) fracture toughness values with changes in extrusion temperature and die cone angle.

Die Cone Angle	(L-R) Toughness		
	Surface	Centre	Surface
30°	32.1 (±0.5)	31.3 (±0.5)	32.2 (±0.7)
45°	32.3 (±0.2)	32.0 (±0.4)	32.4 (±0.5)
60°	32.4 (±0.6)	31.6 (±0.5)	32.4 (±0.8)
90°	32.0 (±0.8)	31.5 (±0.2)	32.1 (±0.5)

Fig 5.5.9 Variation in (L-R) toughness values from the centre of the extrudates to the surface. All extrudates were produced at 430°C, and aged to the underaged condition.

Fig 5.5.8 Variation in (R-L) and (L-R) toughness values with changes in die cone angle, for extrudates produced at different extrusion temperatures and aged to either the underaged or overaged conditions.

(a) Underaged material, 8090 alloy.
Variation in (R-L) toughness values with increases in die cone angle.

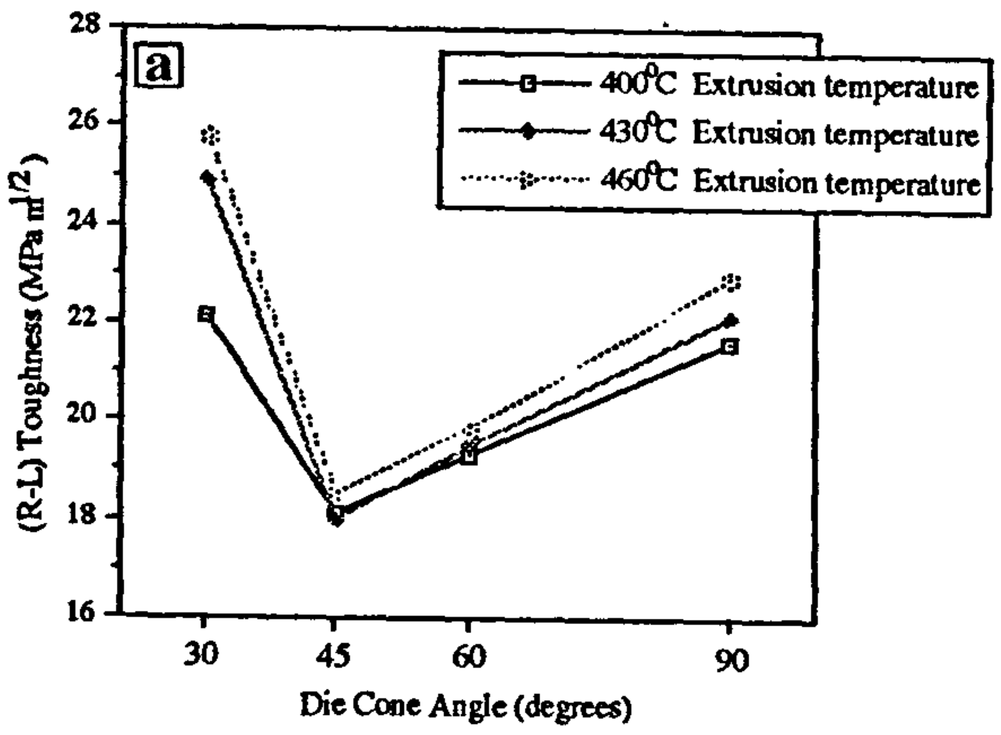
(b) Underaged material, 8090 alloy.
Variation in (L-R) toughness values with increases in die cone angle.

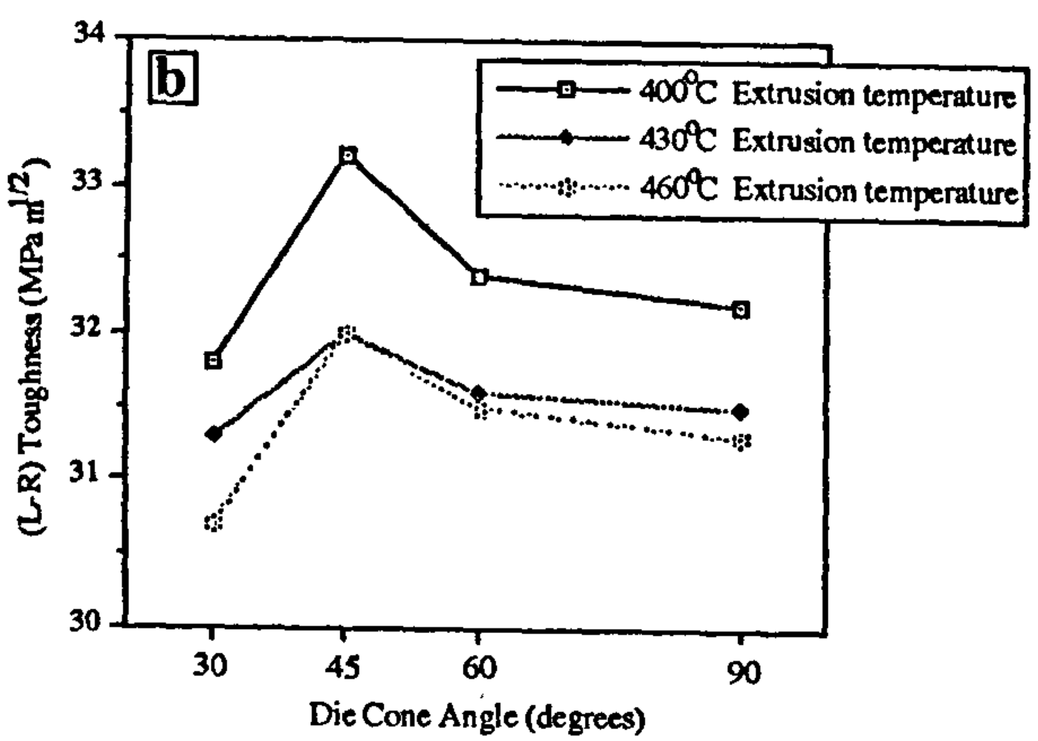
(c) Underaged material, 8090 alloy.
Variation in toughness anisotropy with increases in die cone angle.

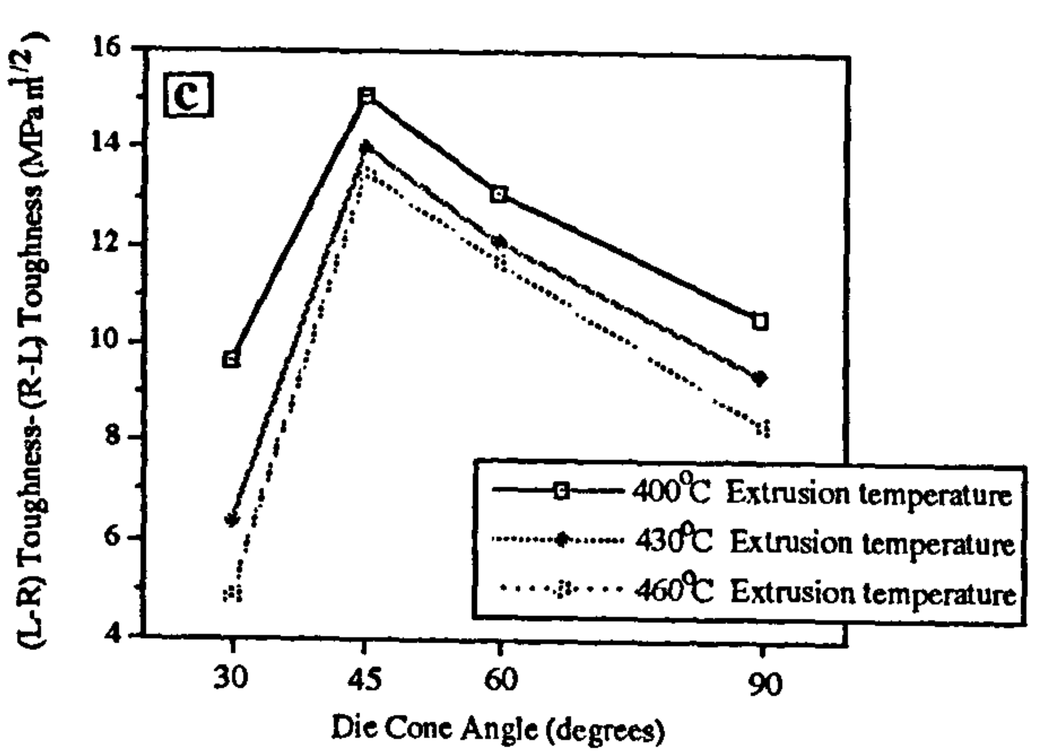
(d) Overaged material, 8090 alloy.
Variation in (R-L) toughness values with increases in die cone angle.

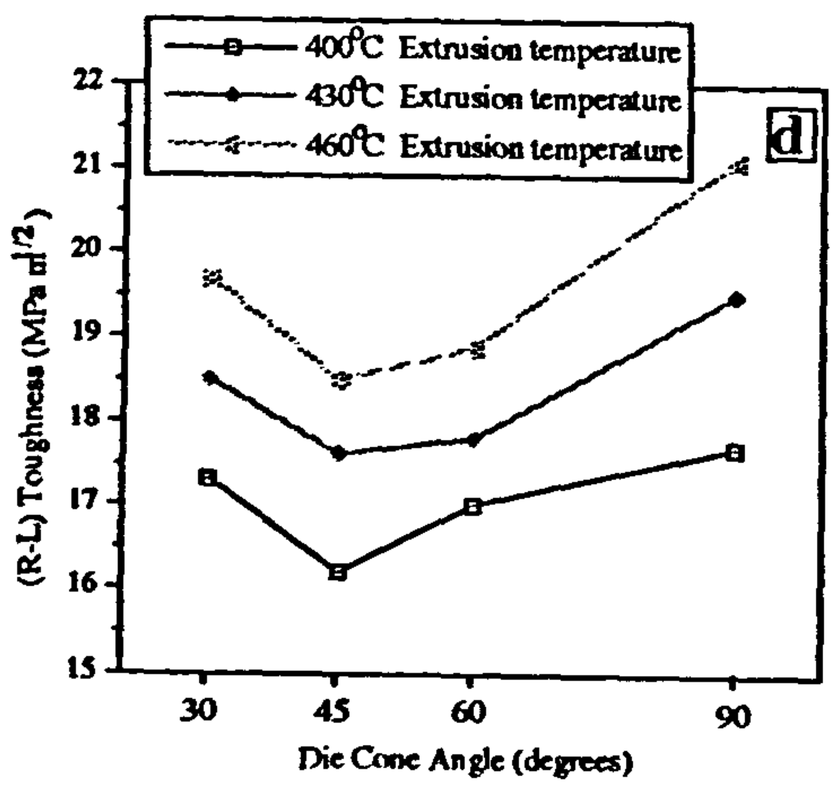
(e) Overaged material, 8090 alloy.
Variation in (L-R) toughness values with increases in die cone angle.

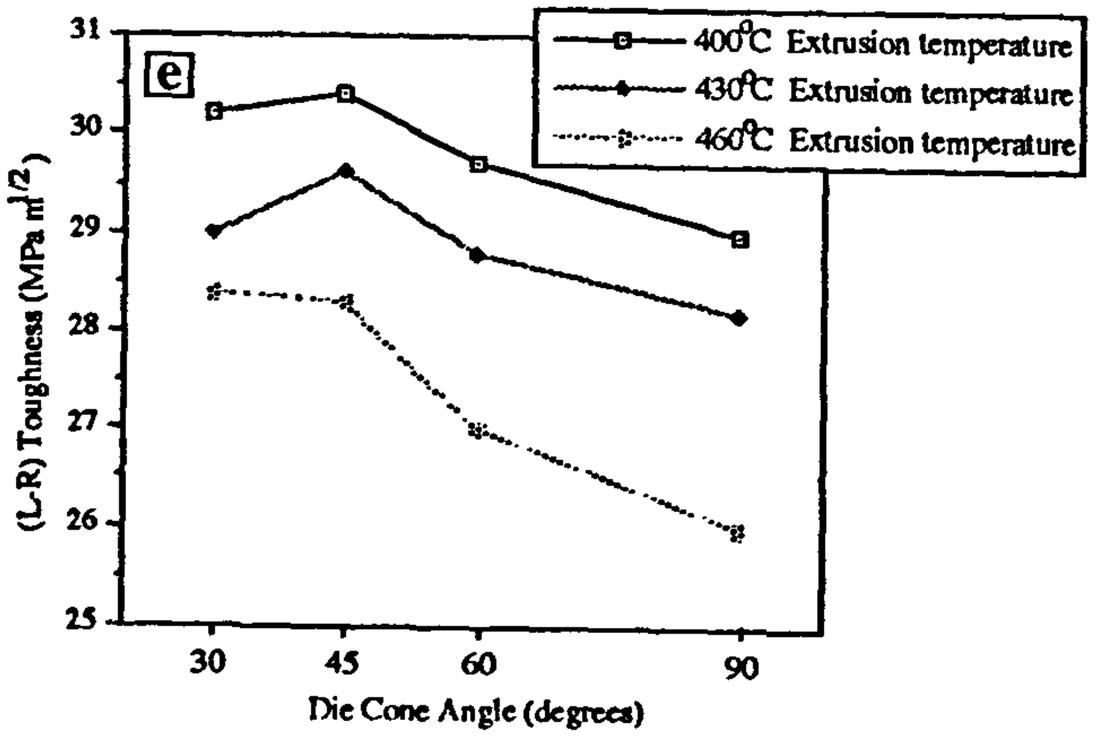
(f) Overaged material, 8090 alloy.
Variation in toughness anisotropy with increases in die cone angle.


a
400°C Extrusion temperature
430°C Extrusion temperature
460°C Extrusion temperature
(R-L) Toughness (MPa m^1/2)
Die Cone Angle (degrees)


b
400°C Extrusion temperature
430°C Extrusion temperature
460°C Extrusion temperature
(L-R) Toughness (MPa m^1/2)
Die Cone Angle (degrees)


c
400°C Extrusion temperature
430°C Extrusion temperature
460°C Extrusion temperature
(L-R) Toughness- (R-L) Toughness (MPa m^1/2)
Die Cone Angle (degrees)


d
400°C Extrusion temperature
430°C Extrusion temperature
460°C Extrusion temperature
(R-L) Toughness (MPa m^1/2)
Die Cone Angle (degrees)


e
400°C Extrusion temperature
430°C Extrusion temperature
460°C Extrusion temperature
(L-R) Toughness (MPa m^1/2)
Die Cone Angle (degrees)

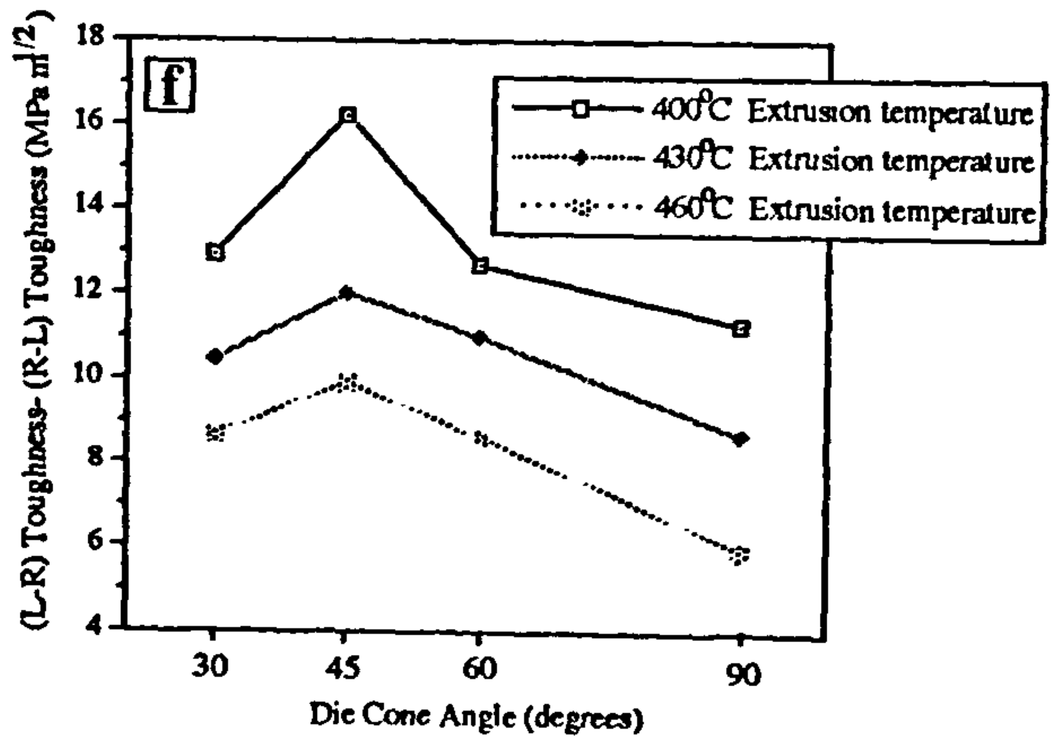

f
400°C Extrusion temperature
430°C Extrusion temperature
460°C Extrusion temperature
(L-R) Toughness- (R-L) Toughness (MPa m^1/2)
Die Cone Angle (degrees)

Fig 5.5.8

Fig 5.5.10 Variation in (R-L) and (L-R) toughness values with changes in extrusion temperature, for extrudates produced using dies of varying die cone angle and aged to either the underaged or overaged conditions.

(a) Underaged material, 8090 alloy.
Variation in (R-L) toughness values with increases in extrusion temperature.

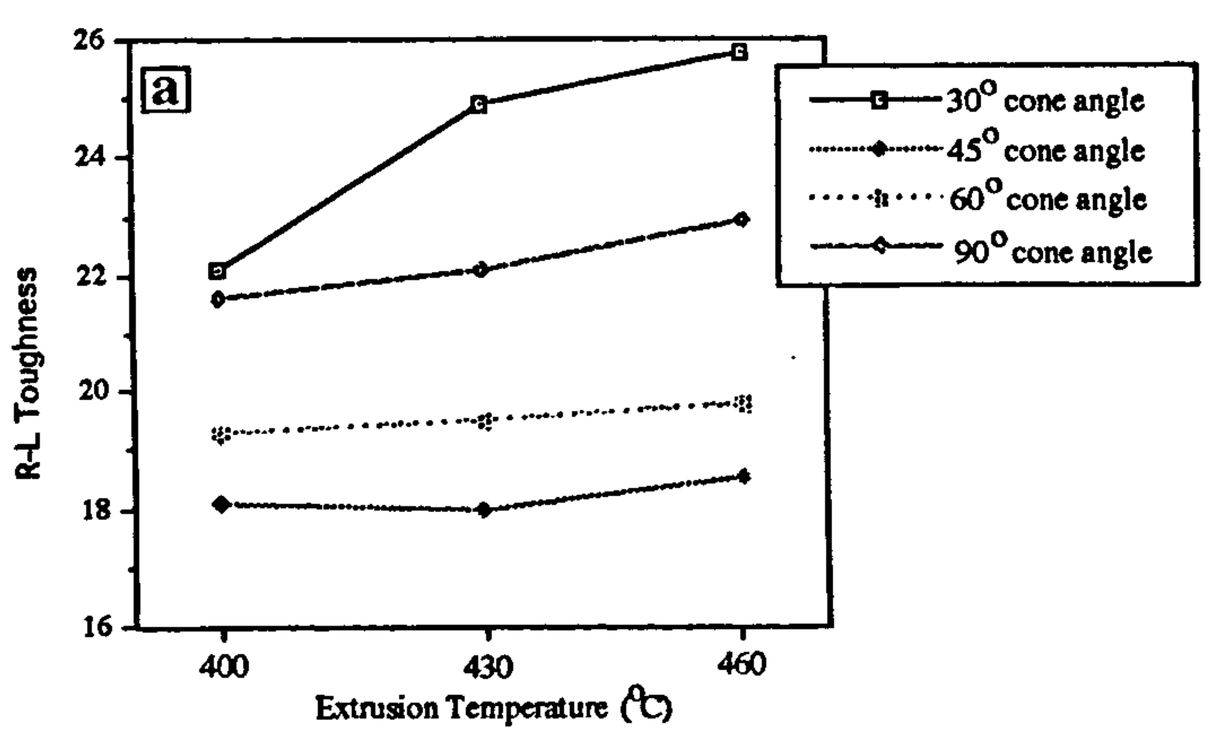
(b) Underaged material, 8090 alloy.
Variation in (L-R) toughness values with increases in extrusion temperature.

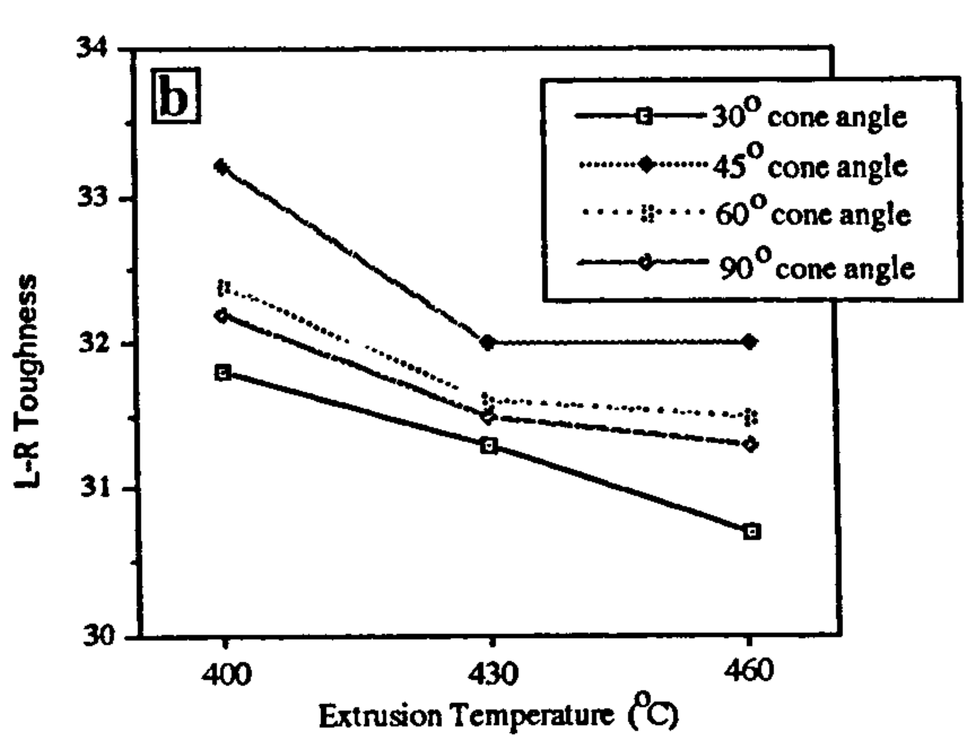
(c) Underaged material, 8090 alloy.
Variation in toughness anisotropy with increases in extrusion temperature.

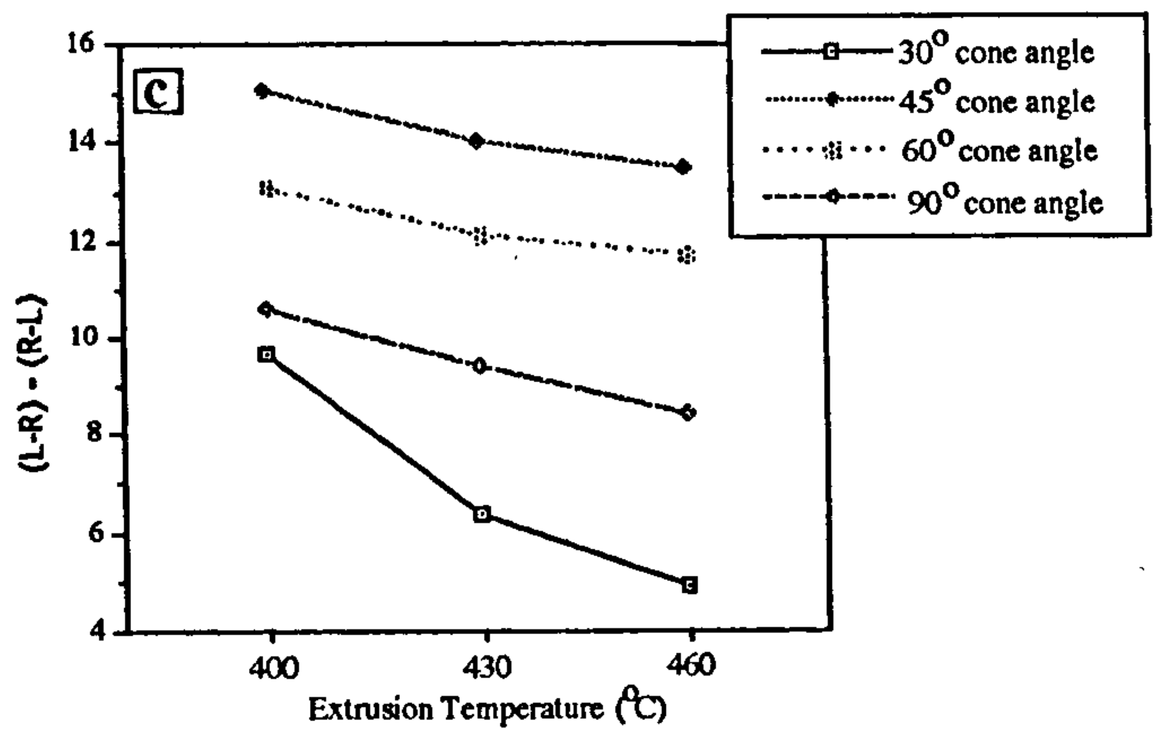
(d) Overaged material, 8090 alloy.
Variation in (R-L) toughness values with increases in extrusion temperature.

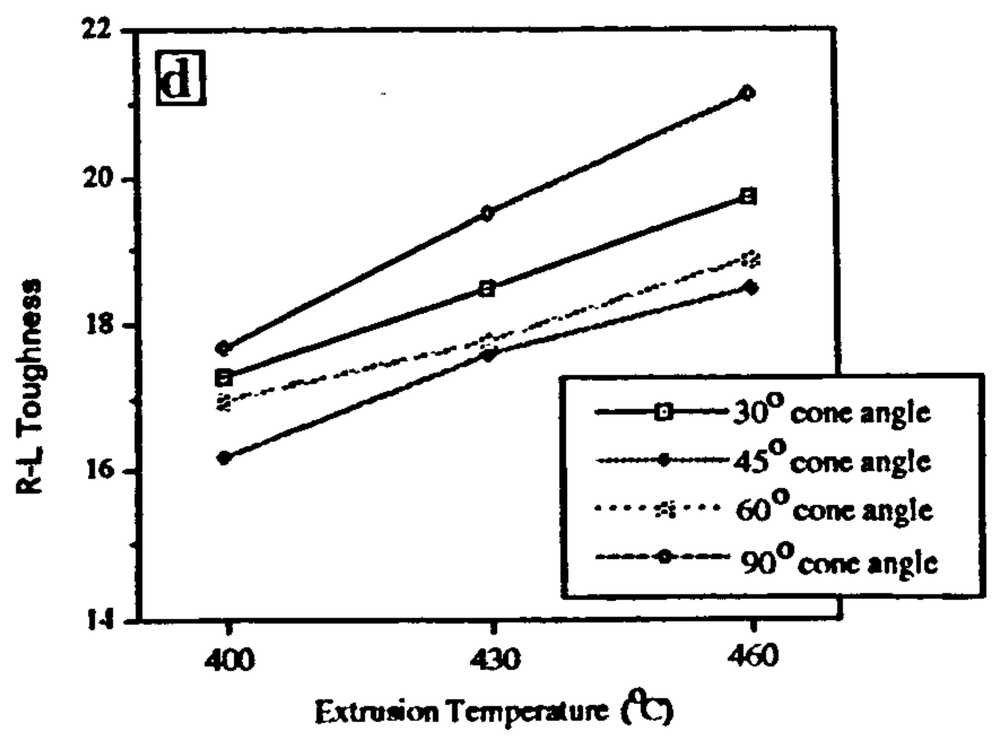
(e) Overaged material, 8090 alloy.
Variation in (L-R) toughness values with increases in extrusion temperature.

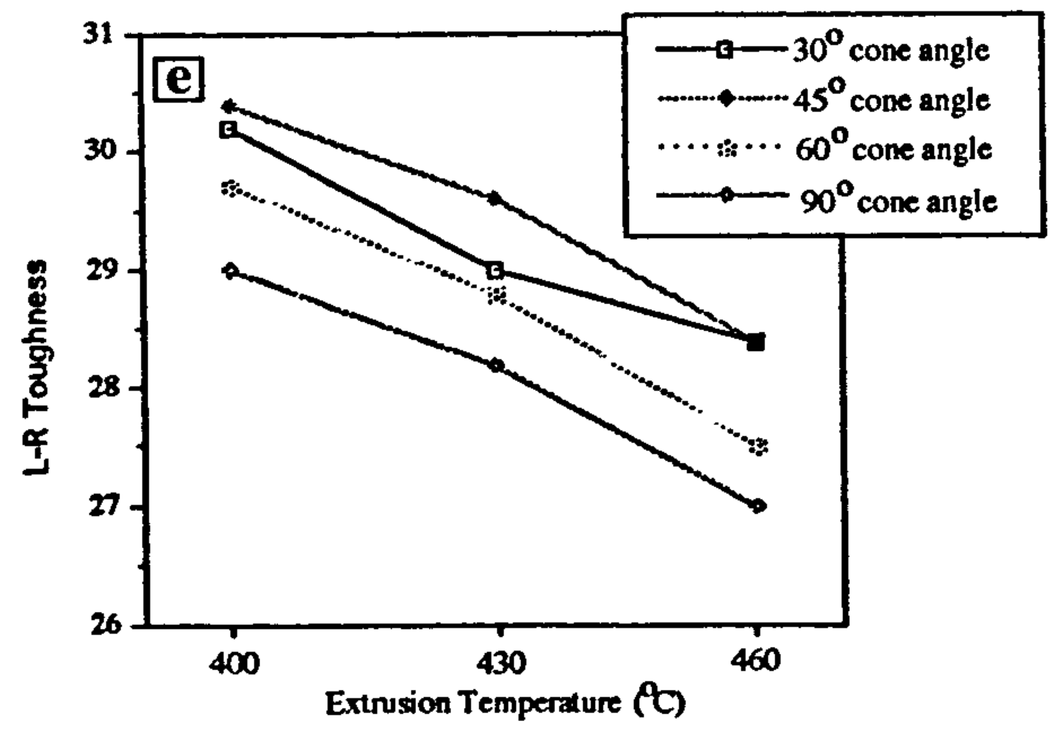
(f) Overaged material, 8090 alloy.
Variation in toughness anisotropy with increases in extrusion temperature.


a
R-L Toughness
Extrusion Temperature (°C)
30° cone angle
45° cone angle
60° cone angle
90° cone angle


b
L-R Toughness
Extrusion Temperature (°C)
30° cone angle
45° cone angle
60° cone angle
90° cone angle


c
(L-R) - (R-L)
Extrusion Temperature (°C)
30° cone angle
45° cone angle
60° cone angle
90° cone angle


d
R-L Toughness
Extrusion Temperature (°C)
30° cone angle
45° cone angle
60° cone angle
90° cone angle


e
L-R Toughness
Extrusion Temperature (°C)
30° cone angle
45° cone angle
60° cone angle
90° cone angle

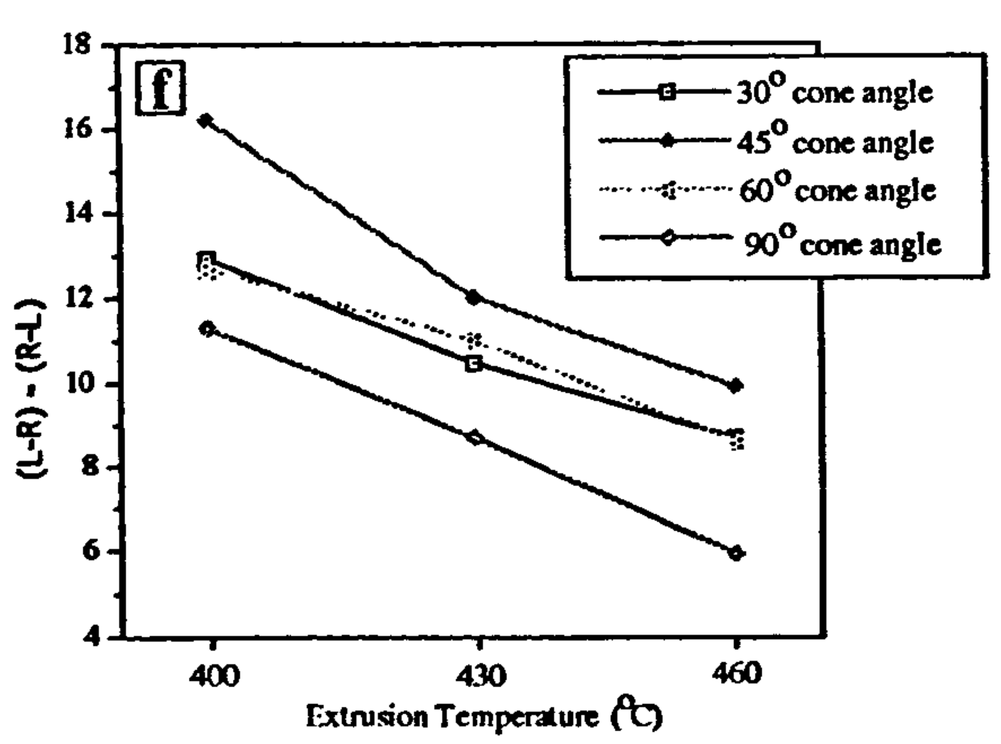

f
(L-R) - (R-L)
Extrusion Temperature (°C)
30° cone angle
45° cone angle
60° cone angle
90° cone angle

Fig 5.5.10

5.6 Tensile Properties

Table 5.6.1 tabulates the tensile property values obtained from aged extrudates produced at different extrusion temperatures and using dies of different cone angle. As with the 'slab' extrusions, yield stress, tensile strength and % elongation to failure were measured, but the variation in strength values were of main concern. The yield stress was calculated at 0.2% strain and the U.T.S. represented the stress at instability.

5.6.1 Variation in Tensile Properties with Die Cone Angle

Fig 5.6.1 tabulates the observed variations in the longitudinal yield stress and U.T.S values as the extrusion die cone angle was increased. From observation of the specific values it was difficult to develop any obvious correlation between the tensile property values and die cone angle. When the tensile results were represented graphically, however, certain consistencies in the variation in yield stress and U.T.S were evident, fig 5.6.2. The general % fluctuations in properties were low, however, hence caution was taken in concluding correlations between property values and processing conditions.

Fig 5.6.2 (a)&(b) illustrate the effect of die cone angle upon the yield stress and U.T.S. values of the underaged material. For all extrusion temperatures, decreases in the yield stress were associated with increases in die cone angle from 30° to 45° and from 60° to 90°. Increasing the die cone angle from 45° to 60°, however, caused an increase in yield stress. With regard to the U.T.S. values, strength levels were observed to increase with increases in die cone angle from 30° to 45° and from 60° to 90°. Decreases in U.T.S. values were, however, associated with increases in cone angle from 45° to 60°. From these results, therefore, it was indicated that the microstructural changes causing increases in yield stress, affected the work hardening capacity, hence U.T.S., in the opposite manner.

There are many microstructural factors that affect the yield stress and U.T.S of a material, such as grain size, texture, substructure and precipitation[1][2][3][4][8]. Optical analysis of the extrudates revealed the aged microstructures to be characterised by elongated original grains, grain boundary recrystallisation of small equiaxed grains, matrix precipitation of T_1, S & δ', and grain boundary I phase precipitation. As the die cone angle was varied, no significant change in the precipitation was observed, but microstructural analysis did reveal variations in recrystallisation and texture.

The proportion of grain boundary recrystallisation was observed to decrease as the die cone angle was increased from 30° ->45° and then subsequently to increase as the die cone angle was raised to 60° and 90°.

Textural analysis revealed negligible variations in cube, brass and Goss textures as cone angle varied, but more significant changes in copper and S texture components were evident. The S and copper texture components were observed to increase in intensity as the die cone angle was increased from 30° to 45° and then subsequently to decrease as the die cone angle was raised to 60° and 90°.

From comparison of these microstructural changes with the variation in property values and processing conditions, therefore, no correlations between property values and microstructure or processing conditions & microstructure for the underaged extrudates could be made. Even though correlations with microstructure were not possible, property-processing correlations could be simply stated. Maximum U.T.S. values were associated with extrusions produced using dies of 45° cone angle, whilst maximum yield stresses were present in extrudates produced using dies of 60° cone angle. The % fluctuations in property values with changes in die cone angle were relatively small, however, hence caution was placed in the definite nature of these property processing correlations.

In addition to the tensile properties of underaged material, tensile properties of overaged extrudates were also measured, and are illustrated graphically in fig 5.6.2 (c)&(d). The yield stress of the overaged material varied with die cone angle in the same manner as the underaged material, but slight differences in the variation of the U.T.S values were observed between the two aged conditions. The only microstructural difference observed between the underaged and overaged material that would affect U.T.S and not yield, was the grain boundary precipitation. This was, therefore, considered the cause for the change in the response of the U.T.S. values to variation in die cone angle. As with the underaged material, however, no correlations between properties and microstructure could be established. Even though correlations with microstructure were not possible, property-processing correlations could again be simply stated. Maximum U.T.S. values were associated with extrusions produced using dies of 90° cone angle, whilst maximum yield stresses were present in extrudates produced using dies of 60° cone angle.

5.6.2 Variation in Tensile Properties with Extrusion Temperature

The observed variation in the tensile property values with increases in extrusion temperature, for underaged and overaged extrudates are tabulated in fig 5.6.1 and graphically shown in fig 5.6.3. Irrespective of ageing condition or die cone angle, it was evident that increases in the extrusion temperature generally decreased the tensile property values. As found by other researchers[1][5][6][7].

Optical analysis of the aged extrudates revealed a small increase in the amount of recrystallisation as the extrusion temperature increased. The recrystallisation took the

form of small equiaxed grains, forming at original grain boundaries. The change in the overall grain size within the extrudates was, therefore, not substantial.

T.E.M and textural analysis revealed no significant variation in precipitation or texture as the extrusion temperature increased. Consequently even though only slight, the overall increases in grain size, together with decreases in the amount of substructure associated with the recrystallisation were considered responsible for the decrease in tensile properties.

5.6.3 Variation in Tensile Properties with Ageing Condition

The underageing and overageing times were chosen to correspond to the 80% strength level, hence the yield stress did not alter with ageing. Ageing from the underaged to overaged condition did, however, increase the U.T.S. and decrease the % elongation to failure, fig 5.6.1.

As ageing occurred, microstructural analysis revealed increases in δ', T_1 & S matrix precipitation, together with enhanced grain boundary I phase precipitation.

The grain boundary precipitation was not a factor in determining the material deformation characteristics, hence did not affect the yield stress[16] . The grain boundary precipitation did affect stress concentration within the extrudates, however, hence influenced the material failure mechanism and point of instability.

The matrix precipitation of δ', T_1 and S phases has been reported to affect both the yield stress and work hardening capacity of aluminium lithium alloys, due to their effect upon dislocation motion[9]->[15] . By far the greatest influence upon the deformation characteristics of Al-Li alloys, however, has been attributed to δ' precipitation. δ' precipitation has an ordered structure, hence encourages localised deformation. As ageing occurs the volume fraction of finely dispersed δ' precipitates increases up to the peak hardness. Continued ageing then causes the δ' precipitate sizes to increase, even though the volume fraction of δ' remains constant. The presence of δ' affects the deformation characteristics of the extrudates to such an extent that two different deformation models have been suggested for aged and non-aged materials[3] i.e. the Sachs and Taylor models. Both the Sachs and Taylor models predict the likelihood of slip occurring on a given slip system when the load is applied in a specified direction. The Sachs model is more applicable to aged material, due to the coplanar slip producing unhomogeneous slip.

In this project, the underageing and overageing times were both chosen to correspond to the 80% peak strength level, hence the yield stress did not alter with ageing. Even though ageing from the underaged to overaged condition was designed to produce constant yield stress levels, the work hardening capacity obviously decreased as ageing was carried out. This caused the U.T.S. and elongation values to decrease

5.6.4 Conclusions

For any given die cone angle, maximum longitudinal yield stress and U.T.S. values were associated with the lowest extrusion temperatures. This was attributed to the increased presence of the small (10->50μm) recrystallised grains present at the original grain boundaries.

With regard to the effect of die cone angle upon property values and microstructure, no correlations between the variations in die cone angle and the observed microstructural changes could be established. Simple property processing correlations could, however, be stated. The combined effects of the variations in recrystallisation and texture, brought about by changes in die cone angle, caused dies of 60° cone angle to produce extrudates with the highest yield stress values irrespective of ageing condition. The variation in the U.T.S values with changes in die cone angle were, however, dependent upon ageing condition. For the underaged material, extrudates produced using dies of 45° cone angle exhibited the maximum U.T.S. values, whereas for the overaged material the dies with 90° cone angle produced the highest U.T.S. values.

Ageing Cond.	Die Cone Angle	Extrusion Temp (°C)	Yield Stress (MPa)	Ultimate Tensile Stress (MPa)	% Elong.
Under-aged	30°	400	442 (±4)	483 (±5)	5.5
		430	443 (±7)	479 (±6)	5.9
		460	431 (±8)	469 (±5)	6.6
	45°	400	437 (±5)	492 (±5)	5.6
		430	433 (±4)	483 (±5)	5.4
		460	422 (±5)	477 (±5)	6.4
	60°	400	455 (±10)	489 (±12)	5.7
		430	440 (±5)	479 (±5)	5.8
		460	429 (±6)	472 (±5)	6.0
	90°	400	445 (±5)	493 (±5)	5.7
		430	436 (±6)	480 (±7)	5.6
		460	416 (±7)	475 (±10)	5.6
Over-aged	30°	400	450 (±5)	541 (±2)	4.3
		430	444 (±8)	533 (±6)	4.7
		460	436 (±8)	530 (±5)	5.1
	45°	400	443 (±8)	545 (±5)	4.9
		430	438 (±4)	539 (±2)	4.9
		460	426 (±10)	528 (±8)	5.0
	60°	400	454 (±8)	549 (±2)	4.8
		430	449 (±5)	538 (±5)	4.7
		460	441 (±6)	530 (±5)	5.1
	90°	400	442 (±2)	551 (±5)	4.3
		430	438 (±7)	545 (±8)	4.8
		460	429 (±8)	538 (±4)	5.1

Fig 5.6.1 Variation in longitudinal tensile property values with changes in die cone angle, extrusion temperature and ageing condition. Alloy A extrudates.

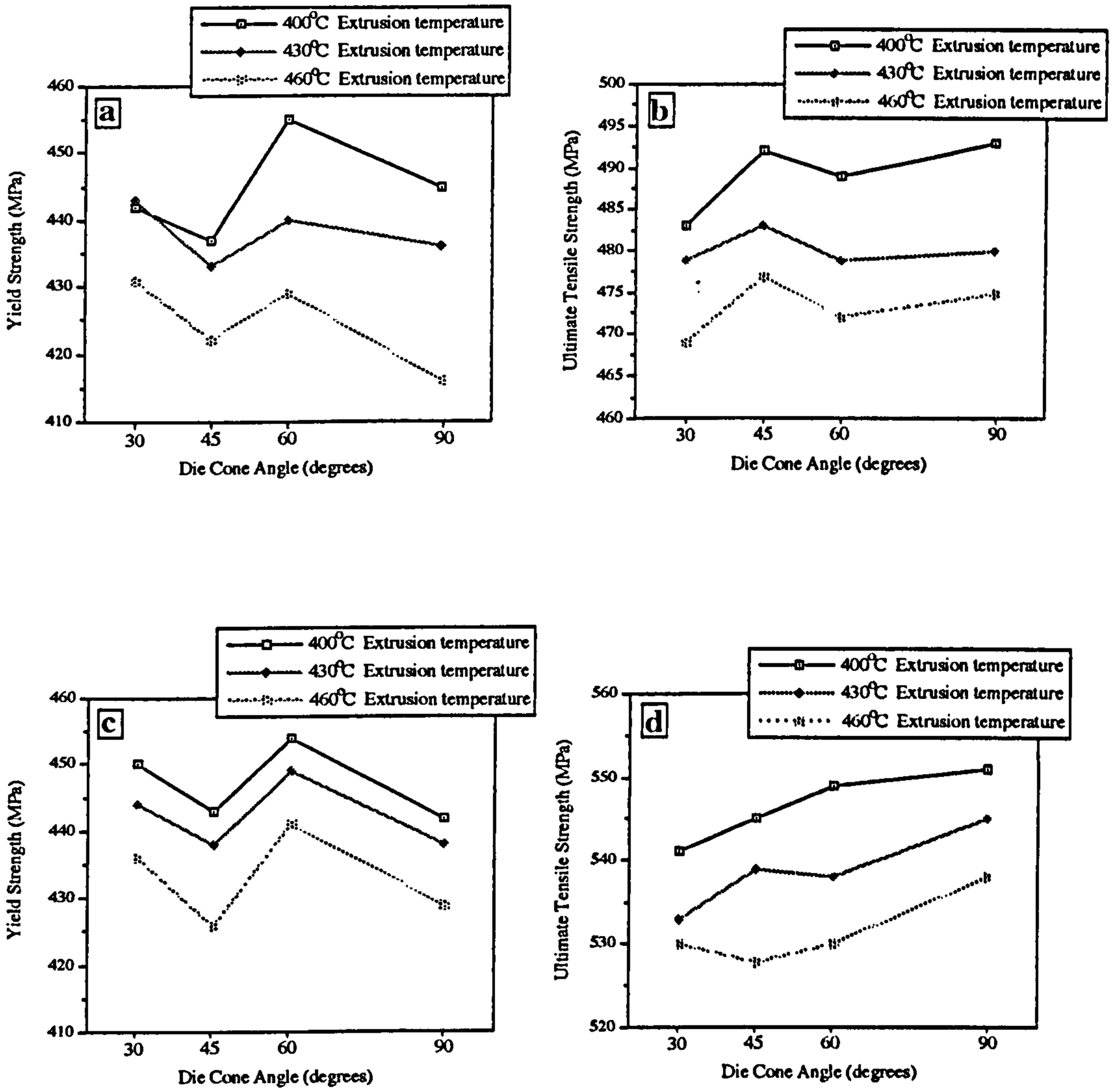
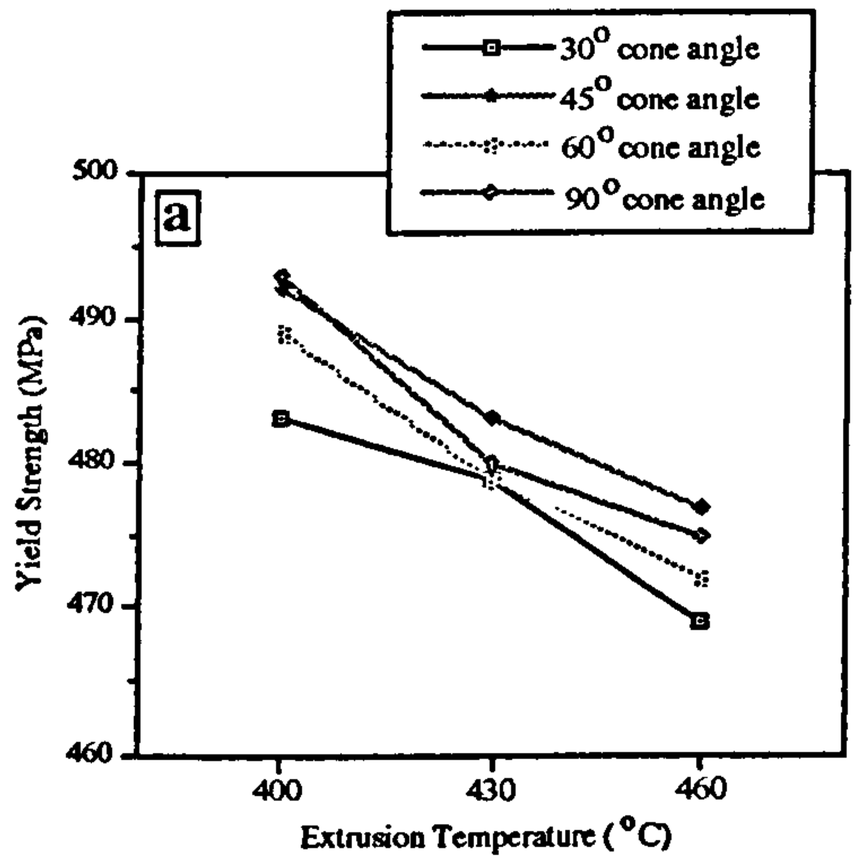
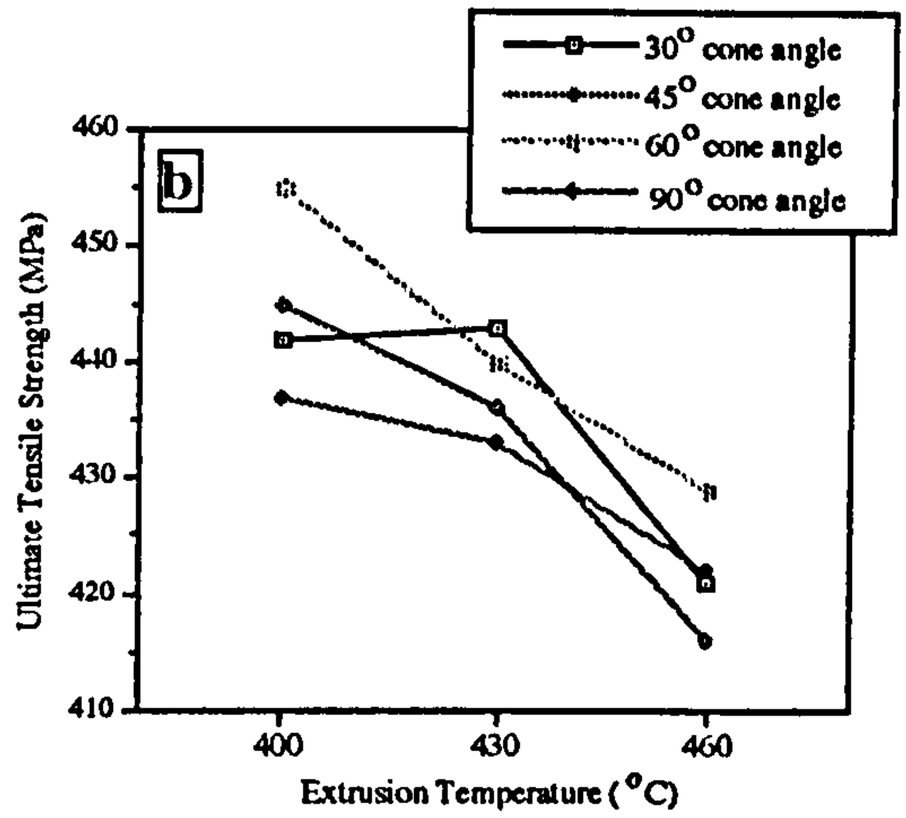
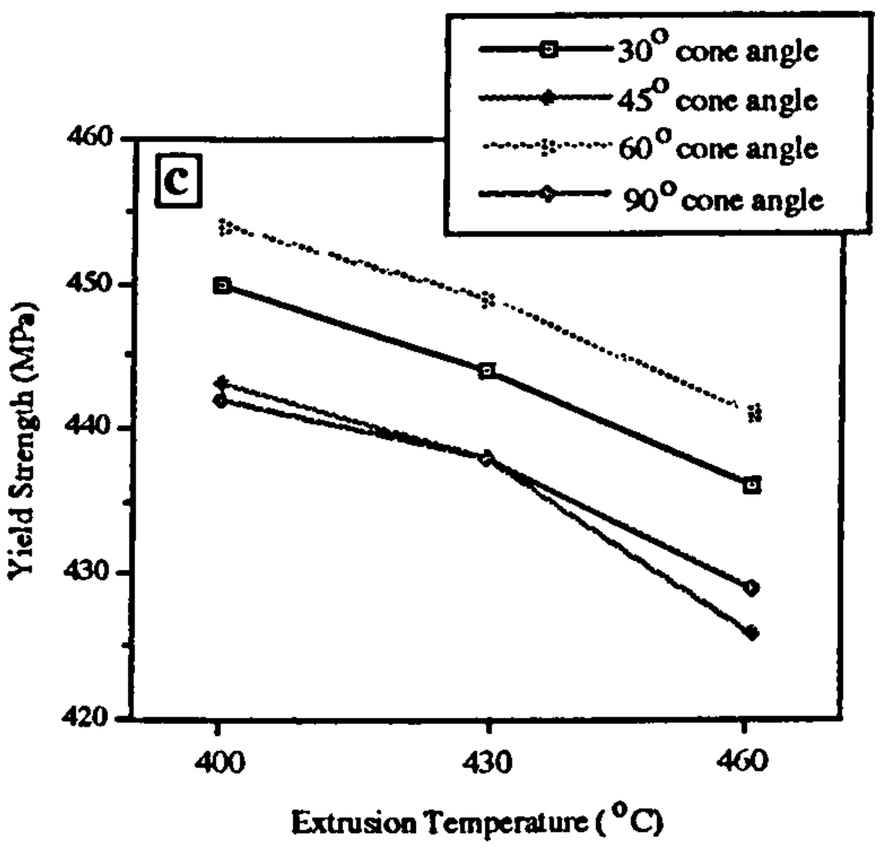


Fig 5.6.2.

Variation in Longitudinal tensile property values with increases in die cone angle.
(a) 8090 alloy, underaged condition.
Variation in yield stress values with increasing die cone angle.
(b) 8090 alloy, Underaged condition.
Variation in U.T.S. values with increasing die cone angle.
(c) 8090 alloy, overaged condition.
Variation in yield stress values with increasing die cone angle.
(b) 8090 alloy, overaged condition.
Variation in U.T.S. values with increasing die cone angle.







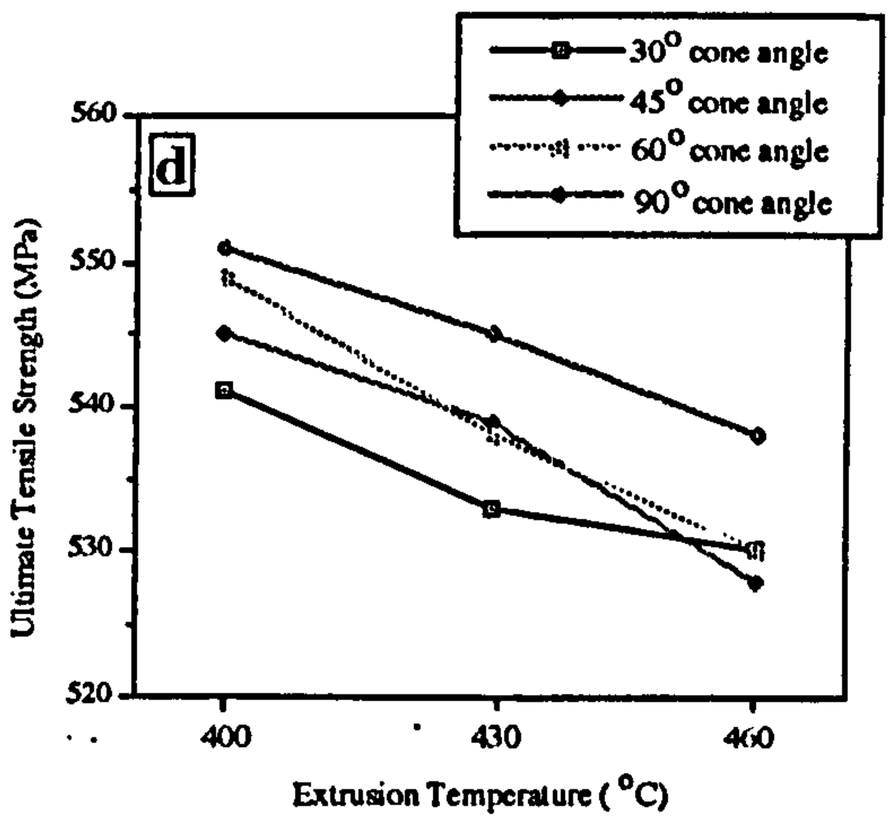


Fig 5.6.3

Variation in Longitudinal tensile property values with increases in extrusion temperature.
(a) 8090 alloy A, underaged condition.
Variation in yield stress values with increasing extrusion temperature.
(b) 8090 alloy A, underaged condition.
Variation in U.T.S. values with increasing extrusion temperature.
(c) 8090 alloy A, overaged condition.
Variation in yield stress values with increasing extrusion temperature.
(b) 8090 alloy A, overaged condition.
Variation in U.T.S. values with increasing extrusion temperature.

CHAPTER SIX

Conclusions and Further Work.

Many problems concerning extrudate toughness and anisotropy have been experienced in thin section extrusions. Correspondingly numerous processing variables have been altered in attempts to improve extrudate property values.

This project was initiated in order to commence work on a series of investigations that would determine the effects that modifying processing conditions had upon property values. The ultimate aim of the investigation sequence was to analyse the effects of using conically shaped dies for the production of thin bar extrudates. The two main areas of investigation carried out in this project towards this end were as follows:-

(i) Characterisation of the microstructure and properties of thin bar extrusion produced from shear face dies, in order to establish correlations between microstructure, property and processing conditions. This included analysis of a method that could successfully be used for the toughness measurement of thin extrudate sections.

(ii) Utilisation of the simplified situation of axi-symmetric extrusion to investigate the possibility of using conically shaped dies to modify the deformation field, hence property values of extruded material. This involved investigation in to visioplasticity techniques and finite element analysis, in order to define the deformation process.

The conclusions produced from the various analyses are indicated in each section and sub-section. The main conclusions produced from these areas are, however, indicated below:-

6.1 Conclusions

The 'slab' extrudates were characterised by elongated deformed grains possessing internal substructures, combined with grain boundary recrystallisation.

As processing conditions were varied, the volume fraction and size of the recrystallised grains, together with the texture systems present within the extrudates were the main microstructural features that altered.

Recrystallisation was found to be enhanced by increases in strain, strain rate and temperature, hence varied with changes in both extrusion temperature and extrusion/aspect ratio. With regard to the textural changes, cube texture components were related to recrystallisation, hence textural variations occurred whenever processing conditions altered the recrystallisation nucleation and growth rates. Rolling type deformation textures were also observed to increase as aspect ratio increased.

This dependence of the microstructure upon strain, strain rate and temperature not only caused variations in microstructures as processing conditions altered, but also caused considerable microstructural differences within each extrudate. For all the

extrudates the percentage volume fraction of recrystallisation increased from the centre of the extrudates to the surface regions, with increases in the size of the recrystallised grains also evident depending upon the specific combinations of extrusion temperatures and extrusion/aspect ratios. These transverse variations in microstructure were attributed to:-

(i) Increased strain, strain rate and temperature in the surface regions of the extrudates, which enhanced recrystallisation and grain growth.

(ii) Solute depletion in the surface regions, which may have enhanced recrystallisation and/or grain growth.

(iii) Textural differences between core and surface regions, which may have altered the recrystallisation nucleation and/or growth rates.

Longitudinal variations in microstructures were also evident within the extrudates. The % volume fraction of recrystallisation, along with the cube texture intensities were observed to increase from the 'front' of the extrudate to the 'rear'. This was attributed to the longitudinal increases in the average levels of temperature experienced by the extruded material, together with increased levels of straining, particularly in the extrudate surface regions.

The extrudate toughness values were dependant upon the energy requirements necessary for crack propagation through these microstructures, whilst the tensile properties were dependent upon the deformation and work hardening characteristics associated with the microstructures. Crack propagation was characterised as follows:-

T-L toughness specimens:- Due to the 'weakness' of the internal grain boundaries, T-L fracture occurred predominantly by an intergranular microvoid coalescence failure mechanism. The boundary 'weakness' was caused by grain boundary precipitation, and accentuated by the strain concentration phenomena occurring within the material - coplanar slip & P.F.Z formation. Transgranular failure was also evident, but was usually associated with transverse crack propagation. This failure occurred when the grain boundary strength and textural systems present within the material, were such that the shear stress developed within the coplanar slip regions reached transgranular failure initiation, before the shear stress necessary for boundary failure was achieved. The transgranular failure again occurred by a microvoid coalescence, with void initiation occurring at second phase matrix precipitates, β' particles, and at the junction of three or four slip bands.

L-T toughness samples:- Failure in the transverse direction involved crack propagation across the elongated deformed grains, and consequently transgranular rather than intergranular failure was necessary. The problem of crack growth along elongated grain boundaries at low applied stresses was, therefore, not present. As a result the L-T toughness values were always higher than the T-L values.

The mechanism of trans-granular crack propagation was microvoid coalescence, and the slightly corrugated appearance of the flat faceted transgranular regions was due to the manifestation of secondary slip systems upon the fracture surface.

The observed changes in recrystallisation and texture occurring as processing conditions altered, consequently affected both the toughness values and the tensile properties. The definite separation of the effects of recrystallisation and texture changes upon property values was difficult, however, since the microstructural variations occurred concurrently.

Increases in the volume fraction of small (10->20μm) recrystallised grains present at the original grain boundaries caused an increase in T-L toughness values, with the intensity of the increase reducing as ageing proceeded. The T-L toughness values, however, were decreased by the presence of the recrystallisation. As a consequence the anisotropy of the material also decreased. These increases in the longitudinal toughness values were attributed to the increased disruption of the crack propagation along the line of the original deformed grain boundaries. The transverse toughness values, however, decreased due to the enhanced stress localisation associated with the recrystallisation.

Not only were small recrystallised grains present, but certain combinations of extrusion temperature and extrusion/aspect ratio caused larger (20->100μm) recrystallised grains to be present. The increased presence of these larger recrystallised grains decreased both the longitudinal and transverse toughness properties, irrespective of ageing condition. The toughness anisotropy levels also decreased, due to the greater decreases in transverse properties than in longitudinal toughness properties. These decreases in toughness values were attributed to the increased levels of stress concentration associated with the larger grain sizes.

Increases in the recrystallisation also caused the longitudinal and transverse tensile properties to decrease. This was again attributed to the increased stress concentration associated with the larger grains, together with the decrease in substructure.

With regard to the texture changes, increases in the rolling deformation texture intensities caused the longitudinal toughness values to increase, and the transverse toughness values to decrease. The tensile strength values were also observed to decrease. The presence of double fibre textures compared with that of rolling type textures were also observed to decrease the longitudinal toughness properties and increase the transverse toughness values.

As already mentioned, however, it was difficult to assess the exact effects of texture upon properties, since the changes in recrystallisation occurred concurrently.

The correlations between microstructure and properties provided the explanations for the observed property changes as processing conditions altered. Direct correlations

between property values and processing conditions, however, were of the most practical importance.

Maximum longitudinal toughness properties were associated with moderate extrusion temperatures, which produced significant recrystallisation without extensive grain growth. The maximum transverse toughness properties, however, were associated with the lowest extrusion temperatures, where negligible recrystallisation occurred. Maximum tensile properties were also associated with low levels of recrystallisation, which corresponded to the lowest extrusion temperatures.

With regard to the effect of extrusion ratio and aspect ratio changes upon properties, it was observed that through changes in the deformation fields, increases in aspect ratio enhanced the formation of rolling type textures, and encouraged recrystallisation. Increases in extrusion ratio also caused increased recrystallisation, and consequently affected the texture systems present within the extrudates.

For the best combination of properties, therefore, moderate extrusion temperatures and extrusion/aspect ratios, which encouraged recrystallisation, but not grain growth, would be most suitable. From consideration of the texture, however, a high aspect ratio was considered preferable in order to increase the intensity of the rolling type deformation textures.

Even though it was evident that extrusion temperature and extrusion/aspect ratios may be used to modify property values, in practise the aspect ratio is usually fixed by product design requirements, hence may not be a variable processing parameter. For the axi-symmetric extrusions, however, tooling boundary conditions of die cone angle were additionally altered, in order to investigate whether or not the resulting flow changes could be used to modify properties, instead of the flow changes arising from extrusion/aspect ratio variation.

The microstructures of the axi-symmetric extrusions were characterised by elongated deformed grains with internal substructure, together with grain boundary recrystallisation. As with the 'slab' extrudates, recrystallisation was enhanced by strain, strain rate and temperature. Consequently microstructural changes were observed as the extrusion temperature and die cone angle varied. In addition, variations in microstructure were also observed within each extrudate. For all the extrudates, the % volume fraction of recrystallisation increased from the centre of the extrudates to the surface, with annuli of 100% recrystallisation consisting of significantly larger (20->100μm) grains at the extreme outer surface areas of the extrudates. The reasons suggested for these observed transverse variations in microstructure were the same as those proposed for the 'slab' material, and have been listed earlier.

The main difference between the axi-symmetric and 'slab' extrudate microstructures were associated with the texture systems present. The axi-symmetric extrudates were characterised by a <100> <111> double fibre texture systems, whereas in the 'slab'

extrudates rolling type textures were dominant. The high similarity in microstructure between the 'slab' and axi-symmetric extrudates, however, caused the fracture and deformation characteristics between the extrudates to be consistent. The presence of small equiaxed recrystallised grains consequently increased R-L toughness, decreased the L-R toughness, and decreased the longitudinal tensile strengths. Due to this converse movement in the orthogonal toughness values, increases in the presence of recrystallisation also caused the toughness anisotropy of the extrudates to decreased.

With respect to the texture systems present, increases in the intensity of S and copper texture components were correlated with decreases in R-L toughness and increases in L-R toughness values. This correlation may, however, have not only been due to the changes in the texture, but also the associated variations in recrystallisation.

Increases in extrusion temperature naturally increased the average temperature experienced by the extruded material. From observation of the temperature and strain rate fields within the deformation zones, and the subsequent comparison with the material flow through these fields, it was also found that decreases in die cone angle caused:-

(i) Increases in the general temperature levels throughout the deformation zone.
(ii) Increases in the average temperatures experienced by the material forming the extruded product.
(iii) Increases in the average temperature differences between the centre and surface regions of the extrudates.
(iv) Higher levels of strain rate to be experienced at greater distances from the die orifice, particularly in the surface regions of the deformation zone.
(v) Increases in the average strain rates experienced by the material forming the extruded product.
(vi) Increases in the average strain rate differences between the centre and surface regions of the extrudate.
(vii) Decreases in the specific cumulative Z values associated with each elemental section within the extrudates.
(viii) Decreases in the difference in the cumulative Z values between each elemental section within the extrudates.

The increases in extrusion temperature, consequently increased the percentage volume fraction of recrystallisation throughout the extrudates and increases in die cone angle caused variations in recrystallisation and texture dependent upon the specific die cone angle used. As with the 'slab' material, therefore extrusion temperature affected toughness by its direct effect upon the recrystallisation present within the material. Die cone angle changes, however, affected the toughness values not only through the

variations caused in recrystallisation, but also through changes brought about in the deformed matrix.

It was observed that for the underaged material, maximum R-L toughness values were observed in extrudates produced using die cone angles of 30° , for the overaged material, however, the 90° die cone angles produced the highest R-L toughness values. Maximum L-R toughness values occurred in extrudates produced using dies of 45° cone angle, irrespective of ageing condition. The highest yield stress values, were also found to correspond to a constant die cone angle -60° - irrespective of ageing condition. As with the R-L toughness values, however, the variation in U.T.S. values were dependent upon ageing condition. For the underaged material, extrudates produced using the die with the 45° cone angle exhibited the maximum U.T.S. values, whereas for the overaged material dies with 90° cone angle produced the highest U.T.S. values.

These changes in the processing property correlations as ageing conditions altered, were consequently due to differences in precipitation causing the changes in recrystallisation (volume fraction and size) and texture systems to have differing effects upon deformation and fracture characteristics. When considering the specific effects of processing conditions upon property values, therefore, the overall deformation and fracture characteristics of the material must be considered before individual processing-property correlations can be made. From the results obtained, however, it was evident that conical dies could be used to modify the property values of extrudates.

With regard to the effect of extrusion temperature upon properties, maximum R-L toughness values corresponded to the highest temperatures, whereas maximum L-R toughness values corresponded to the lowest temperatures. Maximum yield stress and U.T.S. values were also associated with the lowest extrusion temperatures and was attributed to the decreased presence of the small recrystallised grains. Extrusion temperatures could, therefore, also be used to modify property conditions.

6.2 Further Work

It has already been stated that this project was initiated in order to commence work on a series of investigations that would ultimately lead to the analysis of thin bar extrusion produced using conically shaped dies. The analysis carried out in this project identified correlations between properties, microstructure and processing for thin bar extrudates, and it also established possible property benefits obtainable from varying the die cone angle for axisymmetric extrusions.

The main areas of further work will, therefore, involve ideas for improving the analyses already carried out, along with analysis of 'slab' extrusions produced from conically shaped dies.

The property analyses already carried out on the extrudates were extensive, but more determination of surface property values may highlight the benefits from process condition variations to a greater extent. The microstructural analysis of the extrudates were also comprehensive, including T.E.M., optical, texture, and S.E.M.. No further optical or S.E.M. analysis of the extrudates would be beneficial, but in order to definitely establish the recrystallisation process, more T.E.M. work is required. A more in depth analysis of the extrudates under the transmission electron microscope may also reveal consistent precipitation changes with processing conditions that were not evident in this project.

Microtextural analysis would be beneficial, in order to identify the orientation of the individual grains and establish whether or not it is preferred nucleation or preferred growth occurring during the recrystallisation process. More localised textural analysis of the extrudates could also be used to help define transverse and longitudinal variations in texture. On a more macroscopic scale, O.D.F. analysis, rather than the pole figure plots, would also be much more useful for quantifying texture changes with processing.

Finally, in order to complete the required investigation, further work would involve the design and manufacture of conically shaped dies. The microstructural and property analysis of the extrudates, produced from these dies, would then enable the full benefits of using conically shaped dies for the improvement of thin bar extrudate properties to be established. To assist in the modelling of this extrusion, the use of finite element analysis could be used.

APPENDIX I

TOUGHNESS MEASUREMENT

Toughness Parameter

In order to quantify toughness, some sort of toughness parameter that indicates the ability of the material to resist crack propagation must be formulated. It must be noted, however, that the resistance to crack propagation will change with crack character, crack geometry and stress state, as well as with the mechanism of crack growth.

What is actually required for toughness quantification is a parameter which changes with the resistance of the material to crack propagation and can be related to the crack configuration. Critical values can then be used for design purposes.

Griffiths [1] initiated an analysis along these lines, by using an elastic energy approach to define the conditions for crack propagation. He suggested that crack growth would occur when the incremental decrease in the strain energy, $d(-U_a)$, associated with crack growth exceeded the incremental increase in surface energy occurring during crack advance, where U_a=the additional strain energy associated with the introduction of the crack.

This introduced the term, G, which is the strain energy release rate per unit area, and is essentially the elastic energy per unit crack surface area that is available for infinitesimal crack extension. G can be used as a fracture toughness measurement with a critical value, G_c, being obtained at failure.

Even though a value for G_c can be determined, it must be remembered that fracture toughness is a function of crack front speed[2][3], hence will depend upon the character of the crack. The crack character must, therefore, be quoted when determining G_c and indeed when quoting all fracture toughness parameters.

Another condition that must be considered when defining fracture toughness is the stress state ahead of the crack tip. This will influence the measured G_c, due to the differences in strains at a given applied stress as the material constraints are altered. If the conditions are of plain strain then the material strain is restricted to a minimum for a given applied stress and a limiting minimum value of G - termed G_{1C} - is obtained at failure.

Since G_{1C} is a minimum value for the material it can be used as a material property. If values of G at failure are to be compared between material, therefore, it is necessary to

(1) Establish the character of the crack

(2) Ensure plane strain conditions at the crack tip.

This approach by Griffiths was modified slightly by Irwin in order to introduce a degree of plasticity, but elastic theory was still applied.

Owing to practical difficulties of the energy approach, a stress intensity term was also developed by Irwin[1].

In this approach Irwin used linear elastic theory to define the crack tip stresses, in which K determined the magnitude of the elastic stress field. The term, K, was known as the stress intensity factor and was linearly related to stress and directly related to the square root of the crack size

$$K=C\sigma\sqrt{\pi a} \qquad \text{.....2.2.2}$$

$C=f\left(\frac{a}{w}\right)$ = This is a dimensionless parameter that depends upon the geometry of the specimen, w, and crack, a.

σ = applied stress

Irwin showed that the attainment of a critical stress intensity factor, K_c, is equivalent to the attainment of a critical stored elastic strain energy, G_c, hence G_c and K_c are related:-

$$G_{1C}=\frac{K_{1C}^2(1-v^2)}{E} \qquad \text{.....Plane strain} \qquad \text{.....2.2.3}$$

$$G_{1C}=\frac{K_{1C}^2}{E} \qquad \text{.....Plane stress}$$

In plane strain, material constriction causes a limit to the strain, hence the strain energy stored is less.

K will always give the same plastic zone size, hence the stresses and strains both inside and outside the plastic zone will be determined by K. As long as elastic theory holds true, therefore, the elastic stress intensity factor can be used to determine toughness, even in the presence of a degree of crack tip plasticity.

Testing Procedure

Once the toughness parameter has been defined the testing procedure necessary in order to obtain an accurate toughness measurement must be considered.

The British standard BS 5447 [8] incorporates all the above criteria regarding definition of the crack configuration, the stress state and the point of toughness measurement. This standard states the following for plane strain fracture toughness:- It is a property of a material indicative of the material's resistance to crack growth under conditions in which the stress at a short distance ahead of the crack front is predominantly triaxial (plane strain) and in which plastic deformation is limited. It is the critical value of K_1 at which significant extension of the crack occurs under the influence of a rising force under conditions of high constraint to plastic deformation.

Significant crack extension is defined in terms of force/displacement characteristics and for valid K_{1C} measurements to be made (ie elastic theory defines the crack tip stresses), both crack length and thickness should not be less than:

$$2.5\left(\frac{K_{1C}}{\sigma_y}\right)$$

Fatigue pre-cracking is also defined in this standard. This provides consistency in the starting crack and simulates an ideal plane crack with essentially zero crack tip radius, which complies with assumptions made in the stress intensity analysis.

The problems of fatigue pre-cracking and the need for large specimens, which are associated with this standard, may be overcome by the use of 'V' shaped notched specimens [3][4]. Crack growth from the point of a 'V' shaped slot within the specimen is initially stable, thus a real crack is obtained during the initial loading. This crack will then grow in a stable manner until eventually at a critical crack length, a_c, the crack will grow in an unstable manner. The value of a_c is dependent upon the specimen dimensions and not the material. The maximum load at the point $a=a_c$, however, is material dependent. A measure of toughness can, therefore, be carried out using the crack tip configuration and the maximum load at failure, i.e. the stress state at $a=a_c$ can be calculated and a toughness measurement produced. Examples of specimens which use the chevron notch are short rod toughness samples and chevron notch bar samples.

Chevron Notch Toughness Samples

Due to the lack of material availability, chevron notch specimens for toughness measurement were developed [3][4]. Chevron notch specimens are said to measure the energy required per unit area swept out by a quasistatically advancing mode 1 steady state crack tip in a material constrained to plane strain without the need for fatigue pre-cracking

Quasi-static cracking means that the increase in surface area occurs at such a rate, A, that the generation of kinetic energy is negligible compared with the work of cracking. Continuous quasi-static cracking is called stable cracking.

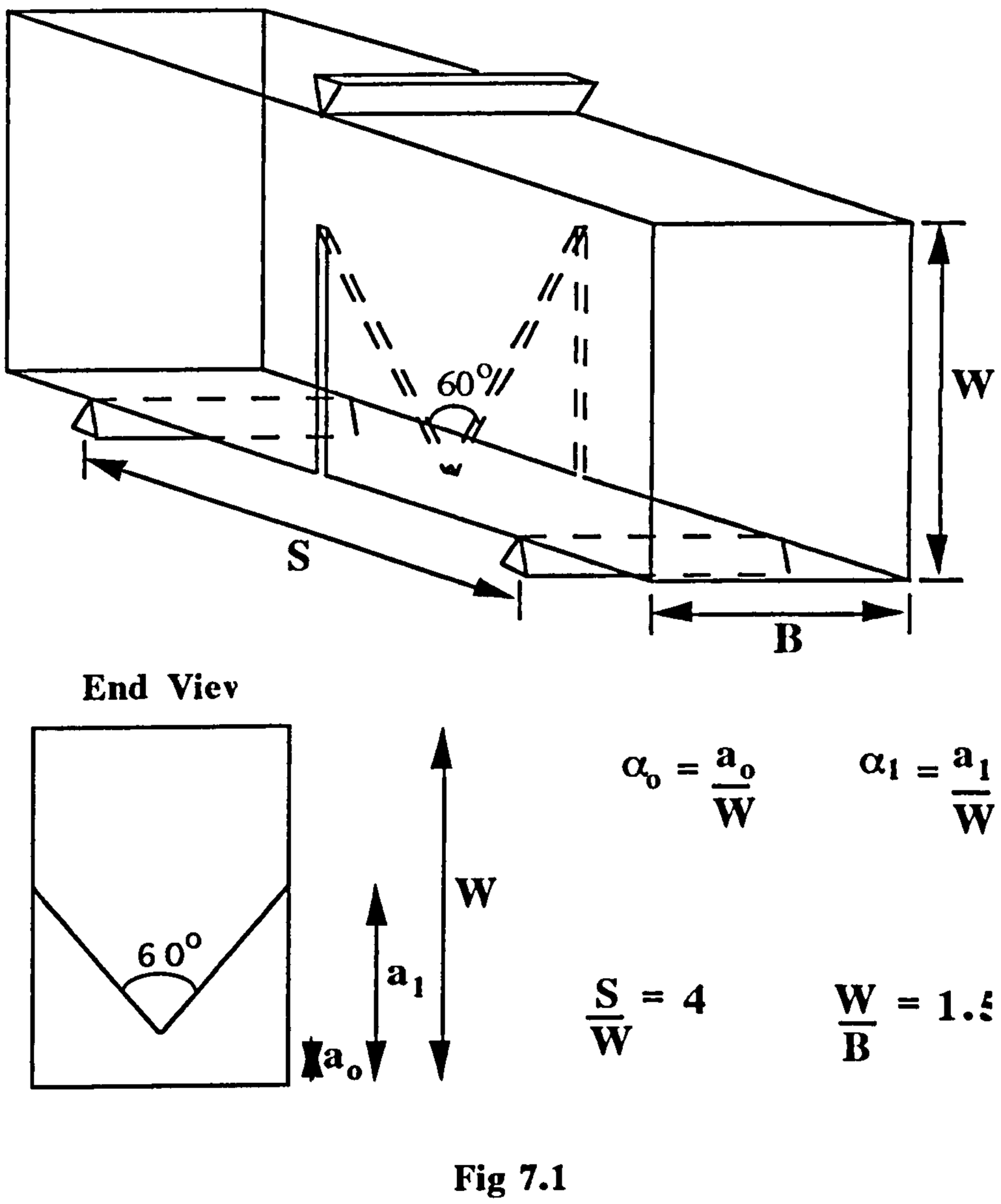


Fig 7.1

The above diagram shows the configuration of the chevron notch bar specimens, which are tested in three point bend.

The small size of the specimens, together with no fatigue pre-cracking may create the following problems:-

(1) For fatigue pre-cracking not to be required the crack must initiate and grow in the same way and show the same characteristics for every specimen tested. This has been accepted by some researchers [3][4], since restrictions are introduced, due to the nature of the 'V' shaped notch.

(2) When K_{1C} is measured from specimens too small to meet 'standard' minimum size requirements two basic assumptions may be violated:-

(i) The crack does not propagate under conditions of plane strain.

(ii) The specimen responds in an elastic-plastic manner rather than in an elastic manner.

For 'standard' specimens, which use straight through cracks, the central regions are in plane strain and the regions adjacent to the free surface are in plane stress. This results in shear lips being produced at the edge as the crack propagates. In order to ensure plane strain conditions over the majority of the crack front, therefore, the width of the

specimens must be above a given size. In the chevron notch samples however, because the plane stress state is restricted to the thickness of the slot machined into the specimen, the majority of the crack front is under plane strain condition and the shear lip formation is restricted to a relatively small area. Smaller specimens can be used, therefore, compared with the standard specimens.

The second problem of approximating elastic-plastic rather than elastic behaviour may be negligible when considering brittle materials, but when highly ductile materials such as aluminium are considered a certain amount of error may be present. This error may be reduced if plasticity is incorporated into the theory of the crack advancement.

Even if the previously mentioned assumptions of plane strain and elasticity are satisfied there is still one apparently major difference between the chevron notch and normal standard toughness tests and that is the use of the steady state crack advancement for the measurement of crack growth resistance. In normal standard tests the crack is considered not to attain the steady state configuration at toughness measurement, whereas in the chevron notch specimen it obviously does. Barker [3] suggested that both the standard tests e.g. ASTM test [7], and the chevron notch bar tests are based upon steady state crack growth and put forward several reasons for for this to be the case. He suggested that fatigue sharpened cracks require only very small crack advancements before attainment of the steady state configuration and since such tests as the ASTM E 399-74 test provide up to 2% crack growth before K_{IC} measurement, the steady state crack growth is most certainly attained.

He also suggested that because K_I approaches a limiting maximum value as the steady state crack develops, the maximum load value obtained during testing and used in K_{IC} calculation should correspond to steady state crack advancement. Steady state crack advancement is, therefore, a requirement of the test rather than an error. The maximum K_I value would only correspond to non-steady state crack growth if the transition region between crack initiation and steady state growth had a higher K_I value.

Toughness Calculation Using Chevron Notch Bars

In the testing procedure of the chevron notch bar samples the specimen is loaded and a crack initiates at the tip of the 'V'. The crack then grows in a stable manner under the action of an increasing load until, at a critical crack length, the load for further growth decreases. This critical crack length is constant for a given specimen geometry and loading configuration ie it is independent of the material.

It can be shown[5][6] that for chevron notch three point bend specimens the plane strain fracture toughness and the maximum load are related by:-

$$K_{1C} = \frac{P_{max}}{B\sqrt{w}} Y_c(\alpha_o, \alpha_1)$$

B = Specimen thickness

W = Specimen width

$Y_c(\alpha_o, \alpha_1)$ = Stress intensity factor geometrical coefficient

$$Y_c = \sqrt{\frac{1}{2}\left|\frac{dC_c(\alpha)}{d\alpha}\right|\left(\frac{\alpha_1 - \alpha_o}{\alpha_c - \alpha_o}\right)}\ \alpha=\alpha_c$$

$$\alpha_o = \frac{a_o}{W} \text{ and } \alpha_1 = \frac{a_1}{W}$$

The dimensionless critical crack length α_c is obtained from the solution to the following equation:-

$$\frac{1}{\alpha-\alpha_o}\frac{dC_c(\alpha)}{d\alpha} = \frac{d^2C_c(\alpha)}{d\alpha^2}$$

which is obtained from the equality necessary for crack advancement assuming linear elastic fracture mechanics

$$\frac{d(bG_{IC})}{da} = \frac{d}{da}\left(\frac{F_c^2}{2}\left(\frac{dc}{da}\right)\right)$$

if G_{1C} is assumed a material constant and if F is held constant as crack advances

$$G_{IC}\frac{d(b)}{da} > \frac{F_c^2}{2}\left(\frac{d^2c}{da^2}\right)$$

from the geometry of the crack

$$\frac{db}{da} = \frac{b}{a-a_o}$$

and it is known that at crack growth

$$G_{IC} = \frac{F_c^2}{2b}\left(\frac{dc}{da}\right)$$

substituting these into equation (1) the following is obtained:-

$$\frac{1}{a-a_o}\frac{dC}{da} = \frac{d^2C}{da^2}$$

It has been shown[4] that the above derivatives are to a good approximation independent of the specimen material properties and dependent only on the specimen geometry.

Once a_c and the form of the equation $C_c(\alpha)$ are known, $Y_c\ (\alpha_o, \alpha_1)$ can be calculated and K_{1C} found.

There are two approximate methods for the calculation of $C_c(\alpha)$:-

(1) Straight through crack assumption (S.T.C.A.)

(2) Bluhm's slice model.

Wu Shang Xian [5] used the chevron bar specimens for toughness determination of GCr15 bearing steel and by comparing results obtained from chevron notch bar samples (B=12mm, W=18mm and $\theta = 60^o$ with a slot width of 0.16mm), with results obtained from the ASTM E399-81 standard test,he found that the difference between the two models was minimised when $\alpha_o > 0.3$ and at these values of α_o the slice model was the most accurate. He, therefore, recommended the use of a chevron notch of $\alpha_o > 0.3$, and the slice model

He used the following expression for the determination of Y_c

$$Y_c(\alpha) = 5.639 + 27.44\alpha_o + 18.93\alpha_0^2 - 43.42\alpha_0^3 + 338.9\alpha_0^4$$

The above formula's suitability for Al-Li alloys will not be examined in this project, because material constraints will not permit the machining of 'standard' test specimens. Results obtained from the chevron notch bar specimens will be compared with toughness results obtained from short rod specimens, however, enabling the suitability of the chevron notch bar specimens and formula to be established.

We must remember that the equations shown above are derived under the assumptions of linear elastic behaviour. If gross plasticity occurs, such that L.E.F.M no longer applies, then the maximum load during testing will correspond to a plastic instability point rather than the point of unstable crack growth. If elastic-plastic behaviour is assumed then the following equations are derived from the compliance approach[3][4]:-

$$G_{IC} = \left(\frac{1+p}{1-p}\right)\frac{F^2}{2b}\left(\frac{dc}{da}\right)$$

$\left(\frac{1+p}{1-p}\right)$ = Plasticity factor, where $p = \frac{Dx_o}{Dx}$

Dx_o = crack opening remaining after unloading

Dx = Crack opening during loading

This produces the following:- $$K_{IC} = \left(\frac{1+p}{1-p}\right)^{1/2} K_Q$$

K_Q = The value obtained during testing if linear elastic behaviour is assumed, but in actual fact plasticity occurs. The equation shows that if plasticity does occur the measured K_{IC} will be an underestimate of the true K_{1C}.

APPENDIX II

Visioplasticity Deformation Analysis

Visioplasticity[1][3][4][5][6][7] is a technique in which a distortion field is experimentally produced and then analysed to produce strain, strain rate and stress distributions.

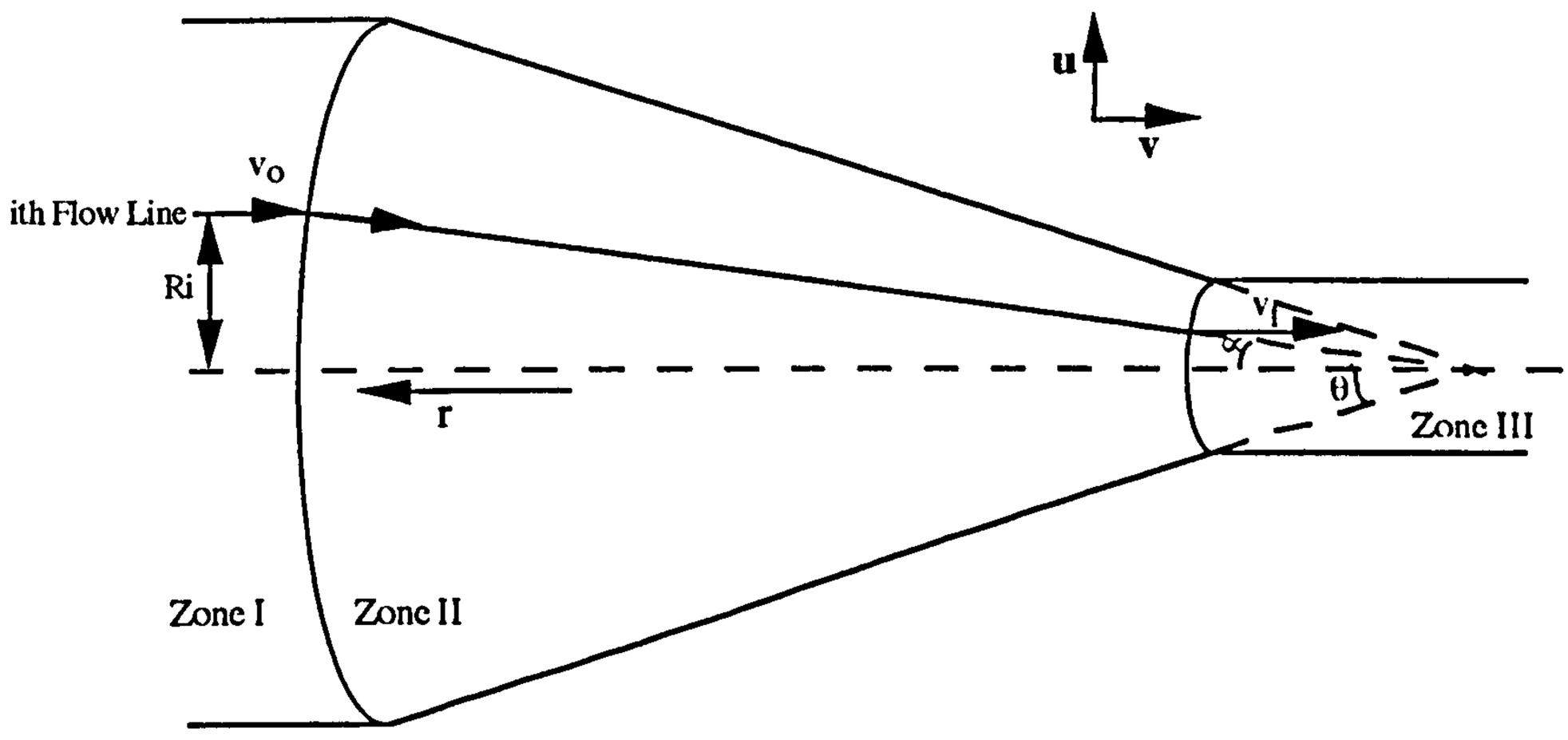
In this project, a visioplasticity analysis was carried out in order to obtain flow field and strain rate distributions. Simplification of the distortion field analysis was carried out by utilisation of a flow function, ψ_i, which was obtained from the initial conditions and defined as[5]:- .

$$\psi_i = \pi R_i^2 |v_o| \qquad \text{.....5.4.1}$$

ψ_i = The flow function along the ith flow line

v_o = Ram speed

R_i = Radius of the flow line before deformation begins



The radial and axial velocity components u and v, as shown above were, therefore, defined by:-

$$u = \frac{1}{2\pi r}\frac{d\psi}{dz} \qquad v = -\frac{1}{2\pi r}\frac{d\psi}{dr} \qquad \psi = \text{Flow function} \qquad \text{.....5.4.2}$$

the strain rates by:-

$$\dot{\varepsilon}_r = \frac{du}{dr} = -\frac{1}{2\pi r^2}\frac{d\psi}{dz} + \frac{1}{2\pi r}\frac{d^2\psi}{drdz}$$

$$\dot{\varepsilon}_z = \frac{dv}{dz} = -\frac{1}{2\pi r}\frac{d^2\psi}{drdz}$$

$$\dot{\varepsilon}_\theta = \frac{u}{r} = \frac{1}{2\pi r^2}\frac{d\psi}{dz}$$

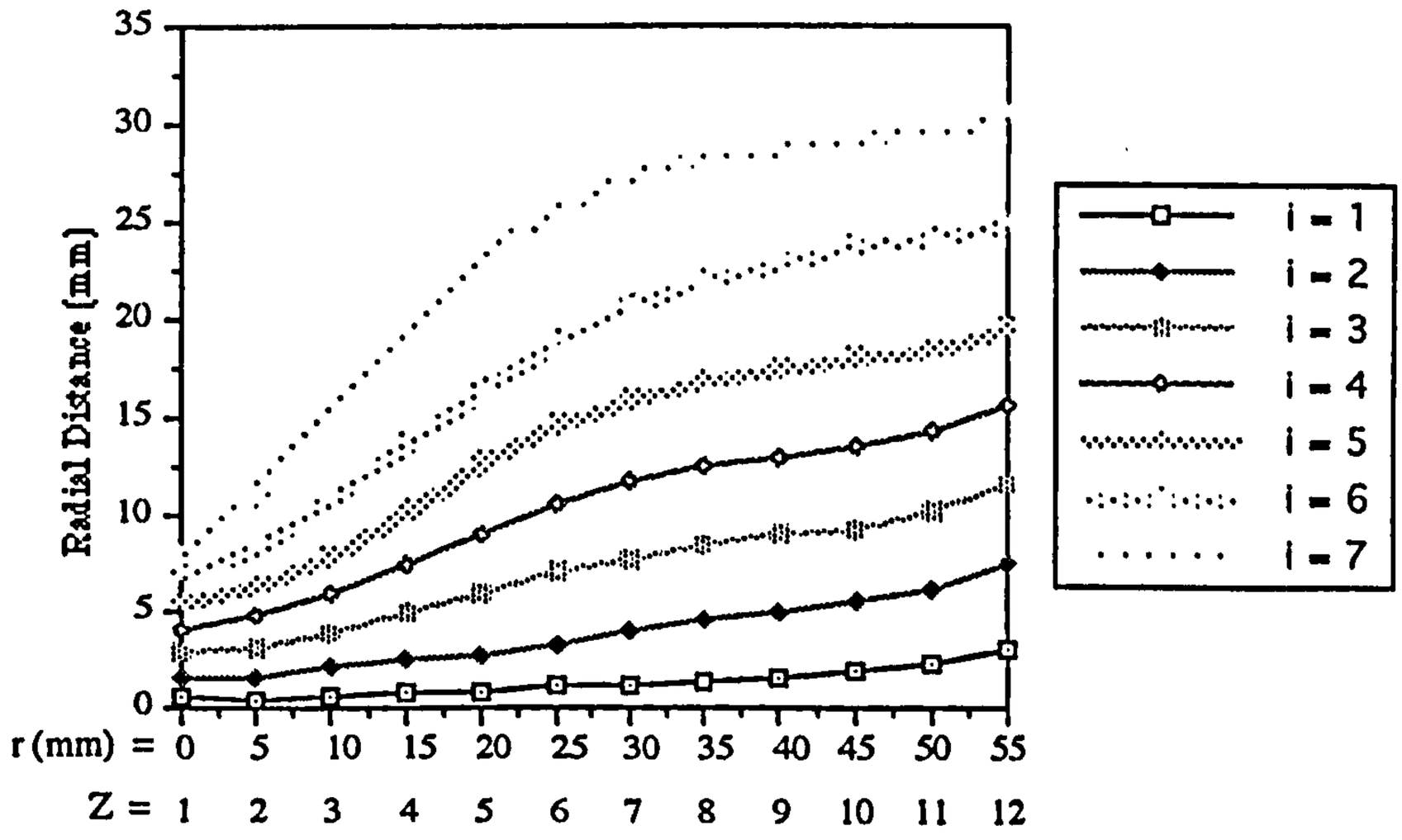
$$\dot{\gamma}_{rz} = \frac{du}{dz} + \frac{dv}{dr} = \frac{1}{2\pi r}\left[\frac{d^2\psi}{dz^2} - \frac{d^2\psi}{dr^2} + \frac{1}{r}\frac{d\psi}{dr}\right] \qquad \text{.....5.4.3}$$

and the effective strain rate by:-

$$= \sqrt{\frac{2}{3}(\dot{\varepsilon}_{rr}^2 + \dot{\varepsilon}_{\theta\theta}^2 + \dot{\varepsilon}_{zz}^2 + 2\dot{\gamma}_{zr}^2)} \qquad \text{.....5.4.4}$$

Experimental determination of the Distortion Field

The first step in the visioplasticity analysis was to experimentally determined a flow field. This was achieved through the use of split gridded billets, combined with gold wire mesh. The split gridded billets, plus gold mesh, were partially extruded and then X-rayed in order to obtain x-ray contact prints of the flow field. Measurements taken from the X-ray contact prints of the distorted gold wire meshes allowed the position of 7 flow lines at 12 different 'z' sections to be assessed. Curve fitting then allowed flow line profiles to be plotted:-



Previous researchers[4][5] have mentioned the 'noise' associated with the measurements made from the distortion field, suggesting various mathematical processes by which to smooth any functions obtained. The flow lines produced in this project were curve fitted by computer, hence noise produced from the actual measurement was reduced.

Once the streamlines were identified, the associated flow functions, ψ_i, for each 'i' flow line and 'z' section were then calculated using equation 5.4.1 above.

Plots of ψ vs r for each z section were then subsequently made. Differentiation of the function obtained, then allowed the $d\psi/dr$ values at any r value and for each z section to be established. The double differential of the $\psi=f(r)$ function with respect to r also enabled $d^2\psi/dr^2$ values to defined at any r value and for each z section.

In the same manner as highlighted above, $d\psi/dz$ and $d^2\psi/dz^2$ values could be obtained at selected positions within the distortion field. $d^2\psi/drdz$ values throughout the deformation zone, were produced by plotting $d\psi/dr$ values versus Z, and obtaining the gradient of the resulting curves associated with specific r and z values.

Once the values of $d\psi/dr$, $d\psi/dz$, $d^2\psi/dr^2$, $d^2\psi/dz^2$ and $d^2\psi/drdz$, were established at selected positions throughout the deformation zone, it was a simple matter of using equations 5.4.3 to obtain strain rate fields.

In brief, therefore, the visioplasticity evaluation of distortion and strain rate fields involved the following steps:-

(1) Experimental determination of streamline positions within the deformation zone, from assessment of distorted grid patterns.

(2) Evaluation of flow function throughout the deformation zone, using equation 5.4.1.

(3) Plotting of ψ vs r and ψ vs z, in order to obtain $\psi=f(r)$ and $\psi=f(z)$.

(4) Differentiation of $\psi=f(r)$ and $\psi=f(z)$ and determination of $d\psi/dr$, $d\psi/dz$, $d^2\psi/dr^2$, $d^2\psi/dz^2$.

(5) Plotting of $d\psi/dr$ values versus z to obtain $d\psi/dr= f(z)$

(6) Differentiation of $d\psi/dr=f(z)$ in order to determine $d^2\psi/drdz$ values throughout the deformation zone.

(7) Evaluation of strain rate fields using equation 5.4.3.

(8) Evaluation of effective strain rate by using equation 5.4.4.

APPENDIX III

Finite Element Analysis

Forge2 is a finite element based computer programme which allows the simulation of material behaviour during metal working operations such as forging, rolling and extrusion. It combines the simultaneous calculation of deformation, heat transfer and friction, leading to output information concerning tool loading, shape change, temperature/deformation distributions.

As mentioned in section 2.4.1, in order to produce a solution for the material deformation, many criteria need to be considered:-

(i) Equilibrium equations

(ii) yield criteria

(iii) Equations relating flow stress, strain rate and temperature.

(iv) Constitutive equations

(v) Boundary conditions

(vi) Heat transfer

In order to produce a solution therefore the Forge2 package requires information concerning (i) The material properties during deformation, (ii) the friction conditions between material and tooling and (iii) the thermal property considerations of both the material and tooling.

Material Properties During Deformation

A knowledge of the material flow stress during deformation is vital in order to model the deformation process. Many factors affect the flow stress of a material and several functions have been used to correlate the effects of temperature and strain rate upon flow stress values. The following hyperbolic sine relationship has been shown to provide the greatest applicability to hot working and was employed in this project:-

$$\dot{\bar{\varepsilon}} = A\,(\sinh\alpha\sigma)^n \exp(-Q/RT)$$

$\dot{\bar{\varepsilon}}$ = Mean equivalent strain rate

Q= Activation energy assumed independent of temperature and stress (J/mole)

T= Temperature (K)

R= Universal gas constant 8.314 J/Kmole

A(/s), a (m^2/MN) and n (no units) are empirically derived constants, independent of temperature and stress and in order to make use of the above equation, these three constants, along with the value of Q needed to be established.

Friction Conditions

Friction is defined as the resistance to relative sliding between two bodies in contact under normal load. Friction between the material and the tooling impedes free movement at the interface, thus can significantly affect the flow and the deformation of the material in many hot working operations.

The value of the coefficient of friction will depend upon the material being deformed, the surface quality of the tooling and the presence of any lubrication. In this project no lubrication was used during extrusion, hence sticking friction was assumed (coefficient of friction = 1).

Thermal Properties of the Material

As the material is deformed work is done to the material and most of this work is converted into heat, which will increase the temperature of the material.

In addition to the heat being generated by deformation, heat may be conducted to and from other adjacent elements. This will depend on the thermal conductivity of the material and the temperature gradient.

The total heat accumulated by the element will be the sum of the heat generated by deformation within the element and the heat conducted to or from the element. The increase in temperature will depend upon the specific heat capacity and density of the material.

The Forge2 package

The Forge2 package can be divided into three sections:-

- Pre-processing: setting up the programme for simulation.
- Simulation: performing the simulation.
- Post processing: analysing the results.

The pre-processing involves setting up three files:- The mesh file, the tooling file and the data file.

The mesh file contains information as to the initial dimensions of the material prior to deformation and defines the finite element mesh that is to be used.

The tooling file contains information as to the dimensions of the tooling, the movement of the tools during the deformation and defines any axis of symmetry.

The data file contains all the relevant data that the simulation programme needs to operate and is split into several sections or modules.

-The Fichier module gathers together all the names of the files to be used in the simulation.

-The Rheologie module gathers together the data defining the thermomechanical behaviour of the material, the initial temperature of the material, and the friction conditions between the material and the tooling.

-During simulation, if a large amount of deformation is experienced by the material, the original finite element mesh may become so distorted that calculations can no longer be performed on it. If this occurs the simulation programme will automatically re-mesh the material and transfer the relevant information form the old mesh to the new one. The Mayeur module gathers together the boundary conditions required for constructing a new mesh (if required) during the simulation.

Once the data, mesh and tooling files have been defined the simulation can be performed. Post-processing of the data files then allows working loads, temperature and strain rates to be drawn and deformation patterns visualised.

Appendix IV

Calculation of Z Values

As mentioned in section 2.4, Sellers and Tegart[1] adopted the general empirical equation relating steady state creep to stress and temperature, to hot working studies and produced the following equation:-

$$\dot{\bar{\varepsilon}} = A(\sinh \alpha \bar{\sigma}_f)^{n'} \exp\left(\frac{-\Delta H}{RT}\right)$$

$\bar{\sigma}_f$ = Mean equivalent flow stress

$\dot{\bar{\varepsilon}}$ = Mean equivalent strain rate

T = Absolute temperature

$-\Delta H$ = Activation energy

R = Universal gas constant

A, α and n' are experimentally determined temperature independent constants

($-\Delta H$) is the activation energy of the rate controlling deformation mechanism occurring, and $\Delta H = f(\sigma_{app}, T, S)$. At high temperatures ($-\Delta H$) has been found to be equivalent to the energy for self diffusion.

Re-arrangement of the above equation gives:-

$$\dot{\bar{\varepsilon}} \exp\left(\frac{\Delta H}{RT}\right) = A[\sinh(\alpha \bar{\sigma}_f)]^n$$

The L.H.S of the above expression incorporates both the strain rate and temperature of deformation, and is known as the temperature compensated strain rate or Zener-Hollomon parameter (Z), where $Z = \dot{\bar{\varepsilon}} \exp\left(\frac{\Delta H}{RT}\right)$

Hence the above equation can be written as :- $Z = A[\sinh(\alpha \bar{\sigma}_f)]^n$

The Zener Hollomon parameter incorporates the processing conditions of temperature and strain rate, hence as such, many researchers have found relationships between microstructure and Z values[2]. The calculation of the Zener Hollomon parameter may, therefore, be useful in order to develop relationships with the microstructure, hence properties, which may then be used to modify the processing variables to produce desired properties.

In order to achieve the calculation of the Z values, determination of the strain rate as well as the temperature is required.

Feltham[3] used the following equation for the calculation of mean equivalent strain rate:-

$$\dot{\bar{\varepsilon}} = \frac{\text{(Total strain, } \varepsilon.)}{\text{(Time taken to produce the strain, t)}}$$

where $\varepsilon = \text{Ln}R$

(R= Extrusion ratio)

&

$$t = \frac{\text{(Volume of die.)}}{\text{(Volume of metal extruded per unit time)}}$$

For axi-symmetric die of cone angle α, t is represented by:-

$$t = \frac{D}{6v\tan\alpha}$$

where v = ram speed, and D = Billet diameter

The equivalent strain rate can, therefore be represented by:-

$$\dot{\bar{\varepsilon}} = \frac{6v\text{Ln}R\tan\alpha}{D}$$

The extrusions used in this project were, however, mainly 'slab' extrusions. In order to compensate for the non-axisymmetric nature of the rectangular slab extrusion, the modified extrusion ratio, R' can be used. This R' value was suggested by T Sheppard and Wood[4] and has the form:-

$$R' = \frac{R\sqrt[2]{Pe}}{Pr}$$

Pe = Extrusion perimeter

Pr = Circumference of rod having same extrusion ratio.

REFERENCES

Introduction

(1) W.E. Quist and G. H. Narayanan and A.L. Wingert
Aluminium lithium alloys II (Eds. T.H. Sanders and E.A. Starke) Met. Soc. AIME p 313.
(2) C.J. Peel, B.E. Evans, C.A. Baker, D.A. Bennet,P.J. Gregson and H.M Flower
Aluminium lithium alloys II (Eds T.H. Sanders and E.A. Starke) Met. Soc. AIME p363.
(3) C.J. Peel, B Evans and D. McDarmaid
Aluminium lithium alloys III (Eds. C. Baker, P.J. Gregson, S.J. Harris and C.J. Peel) Inst. Metals, p27.
(4) W.S. Miller, A.J. Cornish, A.P. Titchener and P.A. Bennel
Aluminium lithium alloys II (Eds T.H. Sanders and E.A. Starke) Met. Soc. AIME p335
(5) K.K. Sankaran, V.M. Vasey-Glandon and E.J. Tuegel
Aluminium Lithium alloys V, M.C.E.P. (1989),.p1625
(6) Roy Woodward.
Metals and Materials Journal, February 1991 volume 7 No2, p96.
(7) A.F. Smith.
Aluminium Lithium VI (Eds. M. Peters and P.J. Winkler),DGM Informationgesellenschaft, p1305.
(8) M.A. Reynolds et al.
Aluminium Lithium VI (Eds. M. Peters and P.J. Winkler),DGM Informationgesellenschaft, p915.

2.1 Physical Metallurgy of Lithium Containing Aluminium Alloys

(1) L.P. Costas and R.P. Marshall.
Trans. Met. Soc. A.I.M.E. Vol 224, 1962, p970-974.
(2) E.D. Levine and E.J. Rapperport.
Trans. Met. Soc. A.I.M.E. vol 227, 1963, p1204-1208
(3) R. Nozato and G. Nakai.
Trans. J.I.M. vol 18, 1977, p679-689
(4) S. Fujikawa, Y. Izeki and K. Hirano.
Scripta. Met. vol 20, 1986, p1275-1280.
(5) D.B. Williams
Aluminium Lithium alloys V, M.C.E.P. (1989).
(6) D. B. Williams and J.W. Edington
Met. Sci., vol 9, 1975 p 529-532.
(7) S. Ceresara, G. Cocco, G. Fagherazzi and L. Schiffini.
Phil. Mag., vol 35, 1977, p373-378.
(8) C. Sigli and J.M. Sanchez.
Acta. Met. Vol 34, 1986 p1021-1028.
(9) A.G. Khachaturyan, T.F. Lindsey and J.W. Morris.
Met. Trans., vol 19A, 1988, p249-258.
(10) R Nozato and G. Nakai.
Trans. J.I.M., 18, 679, 1977.
(11) B.E. Noble and G.E. Thompson.
Met Sci. J., vol 5, 1971, p114-120.
(12) G. Cocco, L. Schiffini, S. Enzo and A. Benedetti.
Phys. Stat. Sol., vol 69A, 1982, p343-348.
(13) O. Jesrud and N. Ryum.
Mat. Sci. Eng., vol 64, 1984, p229-236.
(14) K. Mahaligam, B.B. Gu, G.L. Liedl and T. Sanders.

Acta. Met., vol 35, 1987, p483-498.
(15) A.K. Mukapadhyay, C.N.J. Titem H.M. Flower.
J.de Phys. collC3 vol 48, 1987, p439-446.
(16) J.M. Papazian, C Sigli and J.M. Sanchez.
Scripta. Met., vol 20, 1986, p201-206.
(17) S. Ceressara, A. Giarda, A. Sanchez.
Phil. mag., vol 35, 1977, p97-110.
(18) A. Livet, D. Block.
Scripta. Met., vol 10, 1985, p1147-1151.
(19) S. Spooner, D.B. Williams, C.M. Sung.
Aluminium lithium alloys III (Eds. C. Baker, P.J. Gregson, S.J. Harris and C.J. Peel) Inst. Metals,.p329
(20) Radmilovic, A.G. Fox, and G, Thomas.
Acta Metall, 37 (9) p2385, 1989.
(21) B.J. Shaui, H.T. Li, H.Y. Lee and Hayden Chen.
Met Trans., A21, p1133 (1990).
(22) M.S. Yu and Hayden Chen
Aluminium Lithium VI (Eds. M. Peters and P.J. Winkler),DGM Informationgesellenschaft. p77.
(23) S. Miyasato and G. Thomas.
Aluminium Lithium alloys V, M.C.E.P. (1989),.p633.
(24) A.G. Khachaturyan, T.F. Lindsey and J.W. Morris.
Met. Trans., vol 19A, 1988, p249-258.
(25) E.A. Starke et al.
J. of Metals., 33, p24, 1981.
(26) B.P. Gu et al
Mat. Sci. Eng., 76, p167, 1985.
(27) F.W. Gayle and J.B. Vandersande.
Scr. Metall. 18, p473, 1984.
(28) J.M. Silcock.
J. Inst.Met., 88,p357, 1959.
(29) S.F. Baumann and D.B. Williams.
Aluminium lithium alloys III (Eds. C. Baker, P.J. Gregson, S.J. Harris and C.J. Peel) Inst. Metals,.p17, 1983.
(30) B.Noble and G.E. Thompson.
Met. Sci. J., 6, p167, 1972.
(31) P.J. Gregson and H.M. Flower.
Acta Met., 33, p527, 1985.
(32) D.B. Williams.
Aluminium lithium alloys II (Eds. T.H. Sanders and E.A. Starke) Met. Soc. AIME p 89.
(33) M. Tomura et al.
J. Japan Inst. Metals, 34, p919, 1970.
(34) C.J. Peel et al.
Aluminium lithium alloys II (Eds. T.H. Sanders and E.A. Starke) Met. Soc. AIME, p363, 1984.
(35) G.W. Lorimer.
Met. Soc. A.I.M.E. 87, 1978.
(36) R.E. Crooks et al
Scripta Met., 17, p643, 1983.
(37) R.E. Crooks and E.A. Starke.

Metall. Trans. A., 15A, p1367, 1984.
(38) A. Mukapadyay.
Ph. D. Thesis University of London, 1988.
(39) N. Owen.
Ph.D. Thesis, university of London, 1987.
(40) A. Loiseau and G. Lapassat.
J. de Physique, coll C3, vol 47, 1986.
(41) M. Ahmed and T. Ericison.
Aluminium lithium alloys III (Eds. C. Baker, P.J. Gregson, S.J. Harris and C.J. Peel) Inst. Metals, p509.
(42) P.J. Gregson and H.M. Flower.
Acta Metall, Vol 33 p527, 1985.
(43) McAlister.
Alloy phase diagrams, 3, 177, 1982.
(44) H.K. Hardy and J.M. Silcock.
J. Inst. Met., 84, 423, 1955-56.
(45) J.M. Silcock.
J. Inst. Met., 88, 357, 1959-60.
(46) S.F. Baumann and D.B. Williams.
Scripta. metall. vol 18, 1984, p611.
(47) P.M. Kelly and R.B. Nicholson.
Prog. in mat. Sci. Vol 10 1963 p151.
(48) D. Raynor and J.M. Silcock
Metal. Sci. J. vol 4 1970 p121.
(49) J.M. Silcock.
J. of Inst. Metals 1959-60 vol 88 p357.
(50) R.H. Van Stone, T.B. Cox, J.R. Low and J.A. Psioda.
Int. metals rev. 1985 vol 30 no4 p151.
(51) E. J. Gyne, E.A. Starke.
J. of Met Sci. 21 1986 1553.
(52) T.H Sanders Jr. And E.S. Balmuth.
Met. Prog., 3, 32, 1978.

2.2 Mechanical Properties of Lithium Bearing Aluminium Alloys

(1) B.Noble, S.J.Harris and K.Dinsdale.
J.Mat.Sci. 16, 425, 1982.
(2) B.Noble, S.J.Harris and K.Dinsdale.
J.Mat.Sci. 17, 461, 1982.
(3) E,A, Starke, T.H. Sanders and I.G. Palmer.
J. Metals vol 8(33) p24 1981.
(4) F.W. Gayle, J.B. Vandersande and O.R. Singleton.
Aluminium alloys- their physical and mechanical properties vol II p767.
(5) A.K. Mukhopadhyay.
Ph.D. Thesis University of London, 1988.
(6) N.J. Owen.
Ph.D. Thesis University of London 1987.
(7) C.J. Peel, B Evans, C.A. Baker, D.A Bennett, H.M. Flower.
Aluminium lithium alloys II (Eds. T.H. Sanders and E.A. Starke) Met. Soc. AIME. p363 (1983).
(8) P.J. Gregson and H.M. Flower.
Acta. Met. vol33, p527, 1985.

(9) W.S. Miller, J White and D.J. Lloyd.
Aluminium Lithium alloy IV (Eds. G. Champier, B, Dubost, D Mainnay and L. Sabety), J. De Phys., 1987, p139.
(10) P. Sainfort and B. Dubost.
Aluminium Lithium alloy IV (Eds. G. Champier, B, Dubost, D Mainnay and L. Sabety), J. De Phys., 1987, p407.
(11) B.D. Williams
Aluminium lithium alloys II (Eds. T.H. Sanders and E.A. Starke) Met. Soc. AIME, p89
(12) T.H. Sanders, E.A. Ludwiezak and RR Sawtell.
Mat. Sci. Eng. 43 247 1980.
(13) J.C.Huang.
Ph.D. University of California 1986.
(14) J.M. Fragomeni, B.M. Hillberry and T.H. Sanders
Aluminium Lithium alloys V, M.C.E.P. (1989),.p837.
(15) O. Jensrud.
Aluminium lithium alloys III (Eds. C. Baker, P.J. Gregson, S.J. Harris and C.J. Peel) Inst. Metals, p441.
(16) P.Sainfort and P Guyot.
Aluminium lithium alloys III (Eds. C. Baker, P.J. Gregson, S.J. Harris and C.J. Peel) Inst. Metals, p420.
(17) J.G. Huang and A.J. Ardell.
Acta Metall. Vol 36 No11 1988 p2995.
(18) J.C. Huang and A. J. Ardell.
Mat. Sci. and Eng. A104 1988 p142.
(19) M. Furukawa, Y Miura and M Nemto.
Trans. Japan Inst. Metals, Vol 26 No4 1985 p230.
(20) J. Glaser.
M.Sc Thesis University of California May 1986.
(21) D. B. Williams, J. W. Edington.
Metal Sci. J. vol 9 1975 p529.
(22) L.M. Brown and R.K. Ham.
'Strengthening methods in Crystals' Edited by A kelly and R.B. Nicholson.
Halsted Press Div. 1971.
(23) S.F. Baumann and D.B. Williams.
Scripta. Metall. vol 18 1984 p611.
(24) P.M. Kelly and R.B. Nicholson.
Prog. in Mat. Sci. Vol 10 1963 p151.
(25) D. Raynor and J.M. Silcock.
Metal. Sci. J. vol 4 1970 p121.
(26) A.J. Foreman, M.J. Makin
Can. J. Phys.. vol 45 1967 p511.
(27) U.F. Kocks.
Phil Mag. Vol 14 1966 p1629.
(28) J.M. Silcock.
J. of Inst. Metals 1959-60 vol 88 p357.
(29) R.H. Van Stone, T.B. Cox, J.R. Low and J.A. Psioda.
Int. Metals Rev. 1985 vol 30 no4 p151.
(30) E. J. Gyne, E.A. Starke.
J. of Met Sci. 21, 1986, 1553.
(31) P.J. Gregson and H.M. Flower

Acta. Metall. 33, 527, 1985.
(32) B. Noble, S.J. Harris and K. Dinsdale.
Met. Sci. 16, 425, 1982.
(33) T.H. Sanders and E.A. Starke.
Acta. Metall. 30, 927, 1982.
(34) S.F. Baumann and D.B. Williams.
Aluminium lithium alloys II (Eds. T.H. Sanders and E.A. Starke) Met. Soc. AIME. p17.
(35) J.M. Silcock.
J. Inst. Met., 88, 357, 1959.
(36) B. Noble and G.E. Thompson.
Met sci. Tech. J., 6, 167, 1972.
(37) J.C. Huang and A.J. Ardell.
Aluminium Technology, London, 1987.
(38) J.M. Silcock.
J.Inst. Metals, 69, 203, 1960.
(39) K.V. Jata and E.A Starke.
Metall Trans A, 17A, 1011, 1986.
(40) T.H. Sanders and E.A. Starke Jr.
Aluminium Lithium alloys V, M.C.E.P. (1989), p 12.
(41) P.J. Gregson and H.M. Flower.
Acta Met., Vol 33, p527, 1985.
(42) R.E. Crooks et al.
Scripta Met., 17, 643, 1983.
(43) R.E. Crooks et al.
Met. Trans. A, 15A, 1367, 1984.
(44) A.K. Vasudevan and R.D. Doherty.
Acta. Metall, 35, 1193, 1987.
(45) A.K. Vesudevan and S. Suresh.
Mat Sci. Eng. 72, 1985, 37.
(46) S. Suresh and A.K. Vesudevan.
Acta, Metall. 35, 1987, 25.
(47) R.E. Lewis et al.
Aluminium Lithium alloy IV (Eds. G. Champier, B, Dubost, D Mainnay and L. Sabety), J. De Phys., 1987, C3-643.
(48) R.J. Sinho, T. Ahrens, G.J. Shiflet, E.A. Starke Jr.
Aluminium Lithium alloys V, M.C.E.P., 1989, 375.
(49) Ahrens and E.A. Starke Jr.
Aluminium Lithium alloys V, M.C.E.P., 1989, 385.
(50) G.N. Colvin and E.A. Starke Jr.
S.A.M.P.E. J., 19 1988, 10.
(51) K.T.V. Rao and R.O. Ritchie.
Mat Sci.Tech. 5 1989 p882.
(52) C.J. Peel, D. McDarmaid and D.Evans.
Aluminium alloys, Design development and application update, A.S.M. 1987 p315.
(53) H.J. Roven and E,.A Starke.
Recent Developements in Sci. and Eng of light alloys, Conf. proceedings, Oct 14-16 1991.
(54) G. Tempus, G Sharf and W. Calles.
Aluminium Lithium alloy IV (Eds. G. Champier, B, Dubost, D Mainnay and L. Sabety), J. De Phys., 1987, C3-187.

(55) H.L. Ewalds and R.J. Wanhill.
Fracture Mechanics Published by Arnold.
(56) B. Noble and G.E. Thompson.
Met. Sci. 1971, 5, 114.
(57) P.J. Gregson and H.M. Flower.
Acta Metall. 1985, 33, p527.
(58) D.B. Williams and J.W. Edington.
Met Sci. 1975, 9, 529.
(59) B.P. Gu, G.L. Liedt and J.H. Kulwicki and T.H. Sanders.
Mat. Sci.Eng. 1985, 70 217.
(60) F.W. Gayle and J.B. Vandersande.
Scripta Metal, 1984, 18, 473.
(61) G.P. Blakenship Jr. and E.A. Starke.
Aluminium Lithium VI (Eds. M. Peters and P.J. Winkler),DGM Informationgesellenschaft. p187.
(62) F.W. Gayle and J.B. Vandersande.
Scripta Metal, 1984, 18, 473.
(63) P.F. Ashton, D.S. Thompson, F.W. Gayle.
Aluminium alloys-physical and mechanical properties.E.M.A.S. (1986), 403.
(64) E.A. Starke et al.
J. Metals, 8, (33), 24, 1981.
(65) P.J. Gregson and H.M. Flower.
Acta Metall, 33, 527, 1985.
(66) W.A. Cassada, G.J. Shiflet and E.A. Starke.
'Aluminium alloys II (ed E.A. Starke and T.H. Sanders) volume II, p695, 1986, Warley Engineering Advisory Servive.

2.3 Textural Systems of Wrought Aluminium Lithium alloys

(1) D.J. Willis.
Metals Forum, 1 No2, June 1978.
(2) H.J. Bunge.
Int. Mats. Review, 32 No6, 265, 1987.
(3) G.J. Davies, D.J. Goodwill and J.S. Kallend.
J. Appl. Cryst. 4, 67, 1971.
(4) A.W. Bowen.
Mat. Sci. and Tech., vol. 6 Nov 1990.
(5) I. Dillamore and W. Roberts.
'Preferred orientation in wrought and annealed metals', Metall. Rev., 1965, 10, p271.
(6) J.R Hirsch.
Mat. Sci. and Tech., vol 6 November 1990.
(7) D. Juul Jensen, N. Hansen and F.J Humphreys.
Acta. Metall. Vol. 33 No12 1985.
(8) G. Tempus, G. Scharf and W. Calles.
Aluminium Lithium alloy IV (Eds. G. Champier, B. Dubost, D Mainnay and L. Sabety),.J. De Physique, C3-187 Sept. 1987.
(9) N. Hansen, T. Leffers and J.K. Kjens
Acta Metall 29, 1523, 1981.
(10) R.J. Roe.
J. Appl. Phys., 37, 1966, p2069.
(11) D.V. Wilson.
Metals Tech., 1975, p8.

(12) H. Hu.
Texture, 1974, 1, p233.
(13) T. Leffers et al.
Proc. ICOTOM 8, 265, 1987, Warrendale, PA, The Metallurgical Society of AIME.
(14) J Hirsch and K Lucke.
Acta Metall., 1988, 36, 2863.
(15) H Mecking.
Proc. ICOTOM 6, 53, 1981, Tokyo, Iron and Steel Institute of Japan.
(16) U. F. Kocks, and H Chandra.
Acta Metall., 1982, 30, 665.
(17) P. Van Houtte.
Proc. 7th Int. Conf. on strength of Metals and Alloys, ICSMA 7, Pergamon Press.

2.4 Hot working Process

(1) B. Avitzur.
'Metal forming processes and analysis' Mcgraw and Hill 1968.
(2) J. Halling and L.A. Mitchell.
Int. J. Mech. Sci. 7, 277, 1965.
(3) A.H. Shabaik.
J. Eng. for Ind., p1225 Nov. 1972.
(4) A.H. Shabaik and E.G. Thomsen.
J. Eng. for Ind., p343 May 1968.
(5) N. Cristescu.
Int. J. Mech. Sci., 18, 45, 1976.
(6) A. Shabaik and S. Kobayashi.
J. Eng. for Ind., p339 May 1967.
(7) Thomsen, Yang and Kobayashi.
Mechanics of Plastic Deformation in Metal Processing. McMillan press N.Y. 1965.
(8) J.J. Jonas, C.M Sellars and W.J. McTegart.
Metallurgical Reviews vol 14, 1969.
(9) M.G. Tutcher.
PhD Thesis university of London (1979).
(10) F.J.Humphreys.
Acta. Metall. 25, 1323, 1977.
(11) L.A.Pacheco Rodriguez.
PhD Thesis, University of London March 1980.
(12) J.H. Weber
Aluminium Lithium VI (Eds. M. Peters and P.J. Winkler),DGM
Informationgesellenschaft, p935.
(13) C.M. Sellars and W.J. McG Tegart.
International Metallurgical Reviews. 1971 vol 17 review 158.
(14) T Altan and F.W. Boulger.
Journal of Engineering for industry Nov 1973 p1009.
(15) S.J. Paterson.
PhD Thesis. University of London 1981.
(16) C.M. Sellars and W.J. McG Tegart.
Metallurgical science review 1966 63 p731.
(17) F Gayle, J VandeSande and O Singleton.
Aluminium alloys physical and mechanical properties volume II
conference proceedings 15-20 June 1986 E.M.A.S.
(18) H Ormerod and W.J. McG Tegart.

J. Inst. Met., 89, p94 1960->61.
(19) H McQueen.
Met. Trans. 18A, p807 1977.
(20) T. Sheppard and D Raybould.
J.I.M. 1973 101 p73.
(21) J. Cotner and W.J. McG Tegart.
J.I.M. 1969, 97.
(22) T Sheppard and M.G. Tutcher.
Met. Sci. 14 p579 1980.
(23) T.Sheppard, N.C. Parson and M.A. Zaidi.
Met. Sci. 17 p481 1983.
(24) A Mukapadyay.
PhD Thesis. University of London. 1988.

4.1 Optical Analysis

(1) N.C. Parsons and T Sheppard.
Aluminium lithium alloys III (Eds. C. Baker, P.J. Gregson, S.J. Harris and C.J. Peel) Inst. Metals, p226.
(2) J.J. Jonas, C.M. Sellars and W.J. McG Tegart.
Metall.. Rev. 1969 14, 1.
(3) A Mukapadyay.
PhD Thesis. University of London, 1988.
(4) P.L. Makin and W.M. Stobbs.
Aluminium lithium alloys III (Eds. C. Baker, P.J. Gregson, S.J. Harris and C.J. Peel) Inst. Metals, p392.
(5) H.E. Friedrich and R. Mussack.
Aluminium Lithium alloys V, M.C.E.P. (1989), p1615.
(6) I.G. Palmer, W.S. Miller, D.J. Lloyd and M.J. Ball.
Aluminium lithium alloys III (Eds. C. Baker, P.J. Gregson, S.J. Harris and C.J. Peel) Inst. Metals, p565.
(7) T.H. Sanders Jr and E.A. Starke Jr.
Aluminium Lithium alloys V, M.C.E.P. (1989), p1.
(8) T. Sheppard and E.P. Wood.
Metals Technology, 1980, p58.

4.2 T.E.M.

(1) A Mukapadyay
PhD Thesis. University of London, 1988.
(2) Owen.
PhD Thesis. University of London, 1987.
(3) M.A. Reynolds, E. Creed, S. A. Court and P.J. Gregson.
Aluminium Lithium alloys V, M.C.E.P. (1989), p915.
(4) Xia Xiaoxin and john W Martin.
Aluminium Lithium alloys V, M.C.E.P. (1989),.p315.
(5) G.W. Lorimer.
Met. Soc. AIME 87 (1978).
(6) M.D. Ball and H Lagrace.
Al-Li III Inst. Metals p584 (1985)
(7) S.C. Jha, T.H. Sanders and M.A. Dayananda.
Acta. Metall, 35, No2, 473, 473, 1987.
(8) P.J. Gregson and H.M. Flower
Acta Met. vol 33 p527 (1985).

(9) G. Tempus, G. Scharf and W. Calles.
Aluminium Lithium alloy IV (Eds. G. Champier, B, Dubost, D Mainnay and L. Sabety),.J. De Physique, C3-187 Sept. 1987.

4.3 Texture Analysis

(1) M.J. Bull.
Aluminium lithium alloys III (Eds. C. Baker, P.J. Gregson, S.J. Harris and C.J. Peel) Inst. Metals,.p402 (1986).
(2) M.J. Bull.
Aluminium lithium alloys III (Eds. C. Baker, P.J. Gregson, S.J. Harris and C.J. Peel) Inst. Metals,.p402 (1986).
(3) G. Tempus, G. Scharf and W. Calles.
Aluminium Lithium alloy IV (Eds. G. Champier, B, Dubost, D Mainnay and L. Sabety),.J. De Physique, C3-187 Sept. 1987.
(4) A.W. Bowen.
Mat. Sci. and Tech., vol. 6 Nov 1990.
(5) P.J. Partridge.
International Materials Review,1990, vol 35, no1 p37.
(6) D. Juul Jensen, N. Hansen and F.J Humphreys.
Acta. Metall. Vol. 33 No12 1985.
(7) G. Tempus, G. Scharf and W. Calles.
J. De Physique p187 Sept. 1987.
(8) J.R Hirsch.
Mat. Sci. and Tech., vol 6 November 1990.
(9) D.K Denzer, P.A. Hollinshead.
Aluminium Lithium VI (Eds. M. Peters and P.J. Winkler),DGM Informationgesellenschaft. p903.
(10) A.W. Bowen.
Aluminium Lithium VI (Eds. M. Peters and P.J. Winkler),DGM Informationgesellenschaft. p327.

4.4 Toughness Analysis

(1) S.P. Lynch.
Mat.Sci. and Eng. 1991 p25.
(2) A.K. Vasudevan and R.D. Doherty.
Acta. Metall, vol 35 no6 p1193 (1987).
(3) E. Hornborgen and H. Kreye.
J. Mat. Sci., vol 17 p979 (1982).
(4) C. Verdu, J.M. Gentzbittel and R. Fougeres.
Aluminium Lithium alloys V, M.C.E.P. (1989), p899.
(5) K.T. Venhalsewatra Rao, R.O. Ritchie.
Mats. Sci. and Tech. Sept 1989 Vol 5 p882.
(6) W.S. Miller, J. White and D.J. Lloyd.
Journal De physique Colleque C3, Supplement 9, Tom 48 sept 1987 p139.
(7) Owen.
Ph.D. Thesis, University of London, 1987.
(8) T.H. Sanders Jr, E.A. Ludwuzak and R.R. Sawlett.
Mat. Sci. Eng., 43 (1980) p247.
(9) S. Suresh, A.K. Vasudevan, M. Tosten and P.R. Howell.
Acta Metall, 35, (1987), p25.
(10) K.M. Galenby, M.A. Reynolds, J. White and I.G. Palmer.
Aluminium Lithium alloys V, M.C.E.P. (1989), p909
(11) W.S. Miller, J. White and M.A. Reynolds.

J.De. Phys. C3, sup 9, tom 4 (1987), p151.
(12)J. White, and W.S. Miller.
J.De. Phys. C3, sup 9, tom 4 (1987).
(13) Stanley, J Cieslak.
Alcoa Application Engineering division, May 26th 1985.
(14) L.M. Barker.
Int. J. of fracture, vol 15, no6, 1979.
(15) Wu Shang-Xian.
Int. J. of fracture, vol 19, 1982.
(16) G. Tempus, G. Scharf and W. Calles.
Aluminium Lithium alloy IV (Eds. G. Champier, B. Dubost, D Mainnay and L. Sabety),.J. De Physique, C3-187 Sept. 1987.
(17) M.H. Shillingberg and R.F. Ashton.
Aluminium Lithium alloy IV (Eds. G. Champier, B, Dubost, D Mainnay and L. Sabety), J. De Phys., 1987, p179.
(18) N. C. Parsons and T.Sheppard.
Aluminium lithium alloys III (Eds. C. Baker, P.J. Gregson, S.J. Harris and C.J. Peel) Inst. Metals,.p222.

4.5 Tensile Analysis

(1) M.A. Reynolds and Creed.
Aluminium Lithium alloy IV (Eds. G. Champier, B, Dubost, D Mainnay and L. Sabety), J. De Phys., 1987, C3-195.
(2) W.S. Miller et al.
Aluminium Lithium alloys V, M.C.E.P. (1989), p1799
(3) G. Tempus, G. Scharf and W. Calles.
Aluminium Lithium alloy IV (Eds. G. Champier, B, Dubost, D Mainnay and L.Sabety),.J. De Physique, C3-187 Sept. 1987.
(4) H.M. Flower et al.
Aluminium Lithium alloys V, M.C.E.P. (1989), p743.
(5) N.C. Parsons, T. Sheppard.
Aluminium Lithium alloys II (Eds. T.H. Sanders and E.A. Starke) Met. Soc. AIME p53.
(6) N.C. Parsons, T. Sheppard.
Aluminium lithium alloys III (Eds. C. Baker, P.J. Gregson, S.J. Harris and C.J. Peel) Inst. Metals,.p222.
(7) D.K. Denzer et al.
Aluminium Lithium VI (Eds. M. Peters and P.J. Winkler),DGM Informationgesellenschaft. p903.
(8) M.A. Reynolds and E. Creed.
Aluminium Lithium VI (Eds. M. Peters and P.J. Winkler),DGM Informationgesellenschaft. p915.
(9) S.F. Baumann and D.B. Williams.
Aluminium lithium alloys II (Eds. T.H. Sanders and E.A. Starke) Met. Soc. AIME. p17.
(10) J.M. Silcock.
J. Inst. Met., 88, 357, 1959.
(11) J.M. Silcock.
J.Inst. Metals, 69, 203, 1960.
(12) R.E. Crooks et al.
Scripta Met., 17, 643, 1983.
(13) R.E. Crooks et al.
Met. Trans. A, 15A, 1367, 1984.
(14) T.H. Sanders and E.A. Starke.

Acta. Metall. 30, 927, 1982.
(15) D.J. Nichols and J.W. Martin.
J. Mater. Sci. 26, 1991, p552.
(16) A.K. Vasudevan and R.D. Doherty.
Acta. Metall., vol 35, No6, p1193 (1987).
(17) M.H. Shillingberg and R.F. Ashton.
Aluminium Lithium alloy IV (Eds. G. Champier, B, Dubost, D Mainnay and L. Sabety),
J. De Phys., 1987,.p179.

5.1 Optical Analysis

(1) H.E.Friedrich and R. Mussack.
Aluminium Lithium alloys V, M.C.E.P. (1989), p1615 V
(2) H.M. Flower, P.J. Gregson.
Mat Sci. and Tech vol 3 p81 1987.

5.2 T.E.M.

(1) A Mukapadyay.
PhD Thesis. University of London.1988.
(2) Owen Thesis.
Ph.D. Thesis, University of London, 1987.
(3) M.D. Ball and H. Lagrace.
Al-Li III Inst.Metals p584 (1985).
(4) M.A. Reynolds et al.
Aluminium Lithium alloys V, M.C.E.P. (1989), p915.
(5) Xia Xiaoxin and john W Martin.
Aluminium Lithium alloys V, M.C.E.P. (1989), p315.
(6) P.J. Gregson and H.M. Flower.
Acta Met. vol 33 p527 (1985).
(7) G.W. Lorimer.
Met. Soc. AIME 87 (1978).
(8) W.S. Miller, J. White and D.J. Lloyd.
Aluminium Lithium alloy IV (Eds. G. Champier, B, Dubost, D Mainnay and L. Sabety),
J. De Phys., 1987,p139.

5.3 Texture Analysis

(1) D.K Denzer, P.A Hollinshead.
Aluminium Lithium VI (Eds. M. Peters and P.J. Winkler),DGM
Informationgesellenschaft. p903.
(2) M.J. Bull.
Aluminium lithium alloys III (Eds. C. Baker, P.J. Gregson, S.J. Harris and C.J. Peel) Inst. Metals,.p402 (1986).
(3) G. Tempus, G. Scharf and W. Calles.
Aluminium Lithium alloy IV (Eds. G. Champier, B, Dubost, D Mainnay and L. Sabety),.J. De Physique, C3-187 Sept. 1987.
(4) A.W. Bowen.
Mat. Sci. and Tech., vol. 6 Nov 1990.

5.4 Deformation Flow Analysis

(1) Richard Chadwick.
Metals and Materials, May 1970, p201.
(2) H. Valberg and Thorbjoern Loeken.
Proceedings: 5th International Aluminium Extrusion Technology Seminar.(E.T. 1992) p529.
(3) M.M. Farag, C.M. Sellars.
Metals Technology May 1975, p220.

(4) A.H. Shabaik.
J. of Eng. for Ind., p1225, Nov1972.
(5) A. Shabaik and S. Kobayashi.
J. of Eng. for Ind. p339 May 1967.
(6) A. Shabaik andE.G. Thomsen.
J. of Eng. for Ind. p343 May 1968.
(7) Erich G Thomsen.
Mechanics of plastic deformation in metal processing, McMillan press, 1965.
(8) M.N. Niikura, K Lakahashi.
Aluminium lithium alloys III (Eds. C. Baker, P.J. Gregson, S.J. Harris and C.J. Peel) Inst. Metals, p213.
(9) Martin Lefsta.
Proceedings: 5th International Aluminium Extrusion Technology Seminar.(E.T. 1992) p503.
(10) N.C. Parson and T. Sheppard.
Aluminium lithium alloys III (Eds. C. Baker, P.J. Gregson, S.J. Harris and C.J. Peel) Inst. Metals, p222.

5.5 Toughness

(1) Stanley, J Cieslak.
Alcoa Application Engineering division, May 26th 1985.
(2) L.M. Barker.
Int. J. of fracture, vol 15, no6, 1979.
(3) Wu Shang-Xian.
Int. J. of fracture, vol 19, 1982.
(4) A.K. Vasudevan and R.D. Doherty.
Acta. Metall, vol 35 no6 p1193 (1987).
(5) E. Hornborgen and H. Kreye.
J. Mat. Sci., vol 17 p979 (1982).
(6) C. Verdu, J.M. Gentzbittel and R. Fougeres.
Aluminium Lithium alloys V, M.C.E.P. (1989),.p899.
(7) Owen.
Ph.D. Thesis, University of London, 1987.
(8) T.H. Sanders Jr, E.A. Ludwuzak and R.R. Sawlett.
Mat. Sci. Eng., 43 (1980) p247.
(9) S. Suresh, A.K. Vasudevan, M. Tosten and P.R. Howell.
Acta metall, 35, (1987), p25.
(10) M.H. Shillingberg and R.F. Ashton.
Aluminium Lithium alloy IV (Eds. G. Champier, B, Dubost, D Mainnay and L. Sabety), J. De Phys., 1987, p179.
(11) N. C. Parsons and T.Sheppard.
Aluminium lithium alloys III (Eds. C. Baker, P.J. Gregson, S.J. Harris and C.J. Peel) Inst. Metals, p222.

5.6 Tensile

(1) M.A. Reynolds et al.
Aluminium Lithium alloy IV (Eds. G. Champier, B, Dubost, D Mainnay and L. Sabety), J. De Phys., 1987, C3-195.
(2) W.S. Miller et al.
Aluminium Lithium alloys V, M.C.E.P. (1989), p1799.
(3) G. Tempus, G. Scharf and W. Calles.
Aluminium Lithium alloy IV (Eds. G. Champier, B, Dubost, D Mainnay and L. Sabety),.J. De Physique, C3-187 Sept. 1987.

(4) H.M. Flower et al.
Aluminium Lithium alloys V, M.C.E.P. (1989), p743.
(5) N.C. Parsons, T. Sheppard.
Aluminium lithium alloys II (Eds. T.H. Sanders and E.A. Starke) Met. Soc. AIME p53.
(6) N.C. Parsons, T. Sheppard.
Aluminium lithium alloys III (Eds. C. Baker, P.J. Gregson, S.J. Harris and C.J. Peel) Inst. Metals, p222.
(7) D.K. Denzer et al.
Aluminium Lithium VI (Eds. M. Peters and P.J. Winkler),DGM Informationgesellenschaft. p903.
(8) M.A. Reynolds and E. Creed.
Aluminium Lithium VI (Eds. M. Peters and P.J. Winkler),DGM Informationgesellenschaft. P915.
(9) S.F. Baumann and D.B. Williams.
Aluminium lithium alloys II (Eds. T.H. Sanders and E.A. Starke) Met. Soc. AIME. p17.
(10) J.M. Silcock.
J. Inst. Met., 88, 357, 1959.
(11) J.M. Silcock.
J.Inst. Metals, 69, 203, 1960.
(12) R.E. Crooks et al.
Scripta Met., 17, 643, 1983.
(13) R.E. Crooks et al.
Met. Trans. A, 15A, 1367, 1984.
(14) T.H. Sanders and E.A. Starke.
Acta. Metall. 30, 927, 1982.
(15) D.J. Nichols and J.W. Martin.
J. Mater. Sci. 26, 1991, p552.
(16) A.K. Vasudevan and R.D. Doherty.
Acta. Metall., vol 35, No6, p1193 (1987).

Appendix 1

(1) H.L. Ewalds, R.J.H.Wanhill.
'Fracture Mechanics' Published by Arnold.
(2) C Gurney and Y.W. Mai.
Eng. Fract. Mech., 1972, vol4, p853.
(3) L.M. Barker.
Int. J. of Fract., vol 15, No6, Dec 1979.
(4) L.M. Barker.
Eng. Fract. Mech., 1977, vol9, p361.
(5) Wu Shang Xian.
Eng. Fract. Mech., vol 19, No2, p221.
(6) Wu Shang Xian.
Int. J. of Fract., Vol 19, 1982.
(7) A.S.T.M. E399-74.
'Standard Method of Test for Plane Strain Fracture Toughness of Metallic Material'.
(8) B.S. 5447, 1977.
'Method of Test for:- Plane Strain Fracture Toughness of Metallic Materials'.

Appendix II

(1) Richard Chadwick.
Metals and Materials, May 1970, p201.
(2) H. Valberg and Thorbjoern Loeken.

Proceedings: 5th International Aluminium Extrusion Technology Seminar.(E.T. 1992) p529.
(3) M.M. Farag, C.M. Sellars.
Metals Technology May 1975, p220.
(4) A.H. Shabaik.
J. of Eng. for Ind., p1225, Nov1972.
(5) A. Shabaik and S. Kobayashi.
J. of Eng. for Ind. p339 May 1967.
(6) A. Shabaik and E.G. Thomsen.
J. of Eng. for Ind. p343 May 1968.
(7) Erich G Thomsen.
Mechanics of Plastic Deformation in Metal Processing, McMillan press, 1965.

Appendix IV

(1) C.M. Sellars and W.J. McG Tegart.
Metallurgical Science Review 1966 63 p731.
(2) T.H. Sanders Jr., A.F. Grandt.
Aluminium Lithium alloys V, M.C.E.P. (1989), p273.
(3) P. Feltham.
Metal Treatment and Drop Forging, 23, p440, 1976.
(4) T. Sheppard and E.P. Wood.
Metals Technology, 1980, p58.

BIBL. LONDIN. UNIV.